UTS UNIVERSITY OF TECHNOLOGY SYDNEY

Harnessing the Interaction between Gold Nanoparticles and *Escherichia coli* to Develop a Label-Free Sensor

Camilla Gazzana

Thesis submitted in fulfilment of the requirements for the degree of

Doctor of Philosophy

under the supervision of Michael B. Cortie,

University of Technology Sydney
Faculty of Science

December 2025

CERTIFICATE OF ORIGINAL AUTHORSHIP

I, Camilla Gazzana declare that this thesis is submitted in fulfilment of the requirements for the award of Doctor of Philosophy, in the School of Mathematical and Physical Sciences in the Faculty of Science at the University of Technology Sydney.

This thesis is wholly my own work unless otherwise referenced or acknowledged. In addition, I certify that all information sources and literature used are indicated in the thesis.

This document has not been submitted for qualifications at any other academic institution.

This research was supported by an Australian Government Research Training Program (RTP) Scholarship doi.org/10.82133/C42F-K220.

Production Note:
Signature removed prior to publication.

Camilla Gazzana

December 2025

COVID-19 IMPACT STATEMENT

The experimental work performed as part of this thesis was impacted significantly as a result of the COVID-19 pandemic, particularly throughout 2020 and 2021.

Extended periods of lock-downs and/or heavily restricted access to campus facilities, including research laboratories, significantly delayed research progress. Delivery times for consumable orders of equipment and reagents became drastically lengthened, and a decrease in working technical staff resulted in less available support for laboratory equipment and stock maintenance.

It was not feasible to fully transition the research presented within this thesis to an online-only based format, due to the experimental nature of the research. Consequently, the overall scope of the study is less than originally intended.

Contents

List of Figures ix

List of Tables xxvii

Equations xxviii

Abbreviations xxix

Acknowledgements xxxiii

Abstract xxxiv

Chapter 1: 1

Introduction 1

1.1 Motivation and Overview 2

1.2 Research Outputs and Publications To Date 4

Chapter 2: 6

Review of Literature 6

2.1 Introduction 7

2.2 Brief Overview of Common Synthetic Routes of Gold Nanoparticles 8

2.2.1 Mechanism of Citrate Gold Nanoparticle Formation 9

2.3 Optical Properties of Gold Nanoparticles 10

2.4 Factors Affecting the Localized Surface Plasmon Resonance (LSPR) 11

2.5 Surface Functionalization of Gold Nanoparticles, Colloidal Stability and Aggregation 12

2.6 Gold Nanoparticle Stability with Age 13

2.7 *Escherichia coli* as a Model Gram-Negative Bacteria 15

2.8 *Escherichia coli* Behaviour in Luria-Bertani Broth 18

2.8.1 Gold Nanoparticle Behaviour in Luria-Bertani Broth 19

2.9 Phases of Bacterial Growth Under Batch Culture Conditions 21

2.10 Gold Nanoparticle Interactions with Cells 23

2.10.1 Interaction of Gold Nanoparticles with *Escherichia coli* – A Surface-based Interaction? 24

2.11 Current Methods for Detection of Bacteria 26

2.11.1 Biosensors for the Detection of Bacteria 29

2.11.2 Desirable Characteristics of Biosensors 34

2.12 Research Gaps and Questions 34

2.12.1 Thesis Aims and Objectives 35

Chapter 3: 37

Gold Nanoparticle Synthesis & Characterization 37

3.1 General 38

3.2 Introduction 38

3.2.1 *In Situ* Synthesis of Tetrachloroauric Acid from Solid Gold 38

3.2.2 Synthesis and Functionalization of a Range of Gold Nanoparticles 40

3.3 Experimental Design and Methods 41

3.3.1 Chemicals and Materials 41

3.3.2 Synthesis of Tetrachloroauric Acid 41

3.3.3 Synthesis of Citrate Gold Nanoparticles from $HAuCl_4$ 42

3.3.4 Washing of As-Synthesized Citrate Gold Nanoparticles 43

3.3.5 Synthesis of CTAB Stabilized Gold Nanoparticles via the Seeded Growth Method (Silver-Free Method) 43

i) Gold Seeds 43

ii) Synthesis of Seeded ‘Pink’ CTAB Stabilized Gold Nanoparticles 44

3.3.6 Synthesis of Gold Nanoparticles via the Seeded Growth Method (Containing Silver Nitrate) 44

i) Gold Seeds 44

ii) Synthesis of Seeded Gold Nanoparticles 44

3.3.7 Conjugation of Bovine Serum Albumin to Gold Nanoparticles . 45

3.3.8 Conjugation of Thiolated-Poly(Ethylene Glycol) Carboxylic Acid to Gold Nanoparticles 45

3.4 Characterization of Gold Nanoparticles 46

3.4.1 Sample Characterization Using Ultraviolet-Visible (UV-Vis) Spectroscopy 46

3.4.2 Sample Characterization Using Dynamic Light Scattering (DLS) 46

3.4.3 Sample Preparation for Scanning Electron Microscopy 46

3.4.4 Sample Preparation for Transmission Electron Microscopy (TEM) 46

3.5 Results and Discussion 47

3.5.1 UV-Vis Characterization of As-synthesized Citrate AuNPs 47

3.5.2 UV-Vis Characterization of Washed Citrate AuNPs 48

3.5.3 UV-Vis Characterization of 'Pink' CTAB Stabilized AuNPs 49

3.5.4 UV-Vis Characterization of Seeded AuNPs Containing Silver Nitrate 50

3.5.5 UV-Vis Characterization of Bovine Serum Albumin Conjugated Citrate AuNPs 51

3.5.6 UV-Vis Characterization of Thiolated-Poly(Ethylene Glycol) Carboxylic Acid Conjugation to Citrate AuNPs 53

3.5.7 UV-Vis Characterization of Anti-Lipopolysaccharide Antibody Conjugated PEG-AuNPs 54

3.6 Dynamic Light Scattering (DLS) Characterization of AuNPs 55

3.7 Scanning Electron Microscopy (SEM) Characterization of AuNPs . 57

3.7.1 SEM of As-synthesized AuNPs 57

3.7.2 Size Distribution of As-synthesized AuNPs from SEM 58

3.8 Transmission Electron Microscopy (TEM) Characterization of AuNPs 59
3.8.1 TEM of As-synthesized Citrate AuNPs 59
3.8.2 TEM of Washed Citrate AuNPs 60
3.8.3 TEM of 'Pink' CTAB AuNPs 61
3.8.4 Size Distribution of 'Pink' CTAB AuNPs 62
3.8.5 TEM of AuNPs Synthesized via the Seeded Growth Method 'Purple' CTAB AuNPs (Containing Silver Nitrate) 63
3.8.6 Size Distribution of AuNPs (Seeded Growth Method) – 'Purple' CTAB AuNPs 64
3.8.7 TEM of BSA, Thiol-PEG-COOH and Antibody Conjugated AuNPs 66
3.9 Summary, Conclusions and Discussion 66
Chapter 4: 69
Gold Nanoparticle & Live *Escherichia coli* Experiments 69
4.1 General 70
4.2 Introduction 70
4.3 Experimental Design and Methods 71
4.3.1 Chemicals and Materials 71
4.3.2 Preparation for Bacterial Culturing 71
4.3.3 Culturing of *Escherichia coli* 72
4.3.4 Preparation of Live *E. coli* for Assays 72
4.3.5 Live *E. coli* and Gold Nanoparticle Assays 72
4.3.6 Concentration of Gold Nanoparticles Used in Assays 72
4.4 Results 74
4.4.1 Optical Spectra of Gold Nanoparticle and *E. coli* Interactions .. 74

4.4.2 Live *E. coli* and As-synthesized Citrate AuNPs Time Point Assays 85

4.4.3 Live *E. coli* and Washed Citrate AuNPs Time Point Assays 90

4.4.4 Live *E. coli* and As-synthesized Citrate AuNP Assays at Elevated Temperature (37°C) 96

4.4.5 Live *E. coli* and Washed Citrate AuNP Assays at Elevated Temperature (37°C) 101

4.5 Summary, Conclusions and Discussion 106

Chapter 5: 109

Gold Nanoparticle & Heat-Killed *Escherichia coli* Experiments 109

5.1 General 110

5.2 Introduction 110

5.3 Experimental Design and Methods 112

5.3.1 Chemicals and Materials 112

5.3.2 Preparation for Bacterial Culturing 112

5.3.3 Preparation of Heat-Killed *E. coli* for Assays 113

5.3.4 Heat-Killed *E. coli* and Gold Nanoparticle Assays 113

5.3.5 Concentration of Gold Nanoparticles Used in Assays 114

5.4 Results and Discussion 115

5.4.1 Optical Spectra of AuNP and Heat-Killed *E. coli* Interactions 115

5.4.2 Washed Citrate AuNP and Heat-Killed *E. coli* Assays at Elevated Temperature (37°C) 127

5.5 Summary, Conclusions and Discussion 132

Chapter 6: 136

Investigation of Gold Nanoparticle & *Escherichia coli* Interactions via Transmission Electron Microscopy 136

6.1 General 137

6.2 Introduction 137

6.2.1 Extracellular Proteins Associated with *Escherichia coli* Growth 138

6.2.2 Uranyl Acetate as a Fixative and Contrast Agent for Biological Specimens using Transmission Electron Microscopy 140

6.3 Experimental Design and Methods 142

6.3.1 Chemicals and Materials 142

6.3.2 Preparation of Extra Heat-Killed *E. coli* for Assays and Electron Microscopy 142

6.3.3 Preparation of Biological and Mixed Samples for Transmission Electron Microscopy 143

6.4 Results and Discussion 144

6.4.1 Concentration of Gold Nanoparticles Used in Assays 144

6.4.2 Transmission Electron Micrographs of Control Samples 144

6.4.3 Transmission Electron Micrographs of Gold Nanoparticles and Live *Escherichia coli* 150

6.4.4 Transmission Electron Micrographs of Gold Nanoparticle and Heat-Killed *E. coli* Interactions 159

6.4.5 Transmission Electron Micrographs of Gold Nanoparticle and Extra Heat-Killed *E. coli* Interactions 168

6.5 Summary, Conclusions & Discussion 175

6.5.1 Summary 175

6.5.2 Conclusions and Discussion 176

Chapter 7: 180

Conditioned Media & Gold Nanoparticle Experiments 180

7.1 General 181

7.2 Introduction 182

7.3 Experimental Design and Methods 183

7.3.1 Concentration of Gold Nanoparticles Used in Assays 183
7.3.2 Gold Nanoparticle Stability in Luria-Bertani Broth 184
7.3.3 Preparation of Extra Heat-Killed *E. coli* for Assays 185
7.3.4 Preparation of Conditioned Media 186
7.3.5 Conditioned Media and Gold Nanoparticle Assays 187
7.4 Results and Discussion 188
7.4.1 Experiments to Investigate the Role of Bacterial Metabolites in AuNP Aggregation 188
7.4.2 Unintuitive Gold Nanoparticle Characteristics in Conditioned Media Assays: The Role of Ageing 218
7.5 Summary, Conclusions and Discussion 225
Chapter 8: 228
Development of a Sensing Platform for *Escherichia coli* 228
8.1 Introduction 229
8.2 Experimental Design and Methods 230
8.2.1 Materials and Methods 230
8.2.2 Numerical Methods 231
8.2.3 Optical Parameters 231
8.3 Results and Discussion 234
8.3.1 Regression of Optical Variables 234
8.4 Summary, Conclusions and Discussion 237
Chapter 9: 239
Conclusions, Discussion & 239
Future Directions 239
9.1 Conclusions 240
9.2 Future Directions 243
References 245

List of Figures

Figure 1: Schematic diagram of a Gram-negative cell wall. It is significantly more complex in structure than the Gram-positive cell wall, consisting of an inner and outer membrane, periplasmic space containing 1-2 layers of peptidoglycan (generally 2 - 8 nm) and lipopolysaccharide (LPS) anchored via Lipid A to the outer membrane.[69] Inner membrane ~ 5 nm, periplasm ~ 17 nm. The outer membrane is not a phospholipid bilayer, and the inner leaflet is a phospholipid, while the outer layer is comprised of glycolipids and LPS.[70] 16

Figure 2: Schematic diagram of lipopolysaccharide (LPS); the outermost (complex) molecule anchored to the outer membrane of Gram-negative cell walls via Lipid A. LPS is divided into three main sections: Lipid A, which has little variation and is identical in bacteria of the same species; the core oligosaccharide which consists of the inner and outer cores as well as the O-polysaccharide region which is sometimes referred to as the O-antigen. The O-antigen is responsible for eliciting host-immune responses and can be rapidly modified to escape immune responses.[69, 71] 17

Figure 3: Schematic diagram of a Gram-positive cell wall. Although significantly more simple in composition than the Gram-negative cell wall, it is both thicker (15 - 80 nm) and more homogeneous in nature. The Gram-positive cell wall consists of a single plasma membrane and the cell wall which is comprised of peptidoglycan layers, teichoic acids and lipoteichoic acids.[69] Teichoic acids consist of long anionic polymers.[70] 18

Figure 4: Schematic representation of biosensors used for the detection of bacteria/bacterial metabolites or by-products.[111, 116-118] 30

Figure 5: Apparatus setup used for the synthesis of tetrachloroauric acid from gold metal. Redrawn from King et al.[164] 42

Figure 6: Schematic representation of gold nanoparticle synthesis using the citrate reduction method pioneered by Turkevich[20] in 1951. 43

Figure 7: UV-vis spectra of as-synthesized citrate AuNPs (via the Turkevich[20] method). The single plasmon peak centred around 527 nm is characteristic of spherical AuNPs of approximately 20 nm diameter. 47

Figure 8: UV-vis spectrum of as-synthesized citrate AuNPs which have aggregated; the characteristic plasmon peak has decreased in attenuance and red-shifted to 533 nm, while an additional plasmon peak has appeared at 733 nm. 48

Figure 9: UV-Vis spectra of washed citrate AuNPs, prepared from as-synthesized citrate AuNPs, subjected to two rounds of centrifugation and resuspension in MQ (λ_{max} = 526 nm). 49

Figure 10: UV-vis spectrum of 'Pink' CTAB stabilized AuNPs, synthesized via the seeded method and displaying a relatively narrow plasmon peak (λ_{max} = 533 nm). 50

Figure 11: UV-Vis spectrum of AuNPs synthesized via the seeded growth method containing silver nitrate and stabilized by CTAB. The resulting AuNPs appeared purple to the naked eye (λ_{max} = 549 nm). 51

Figure 12: UV-Vis spectrum of BSA conjugated citrate AuNPs. 52

Figure 13: UV-Vis spectrum of thiolated-poly(ethylene glycol) carboxylic acid conjugated as-synthesized AuNPs. 53

Figure 14: UV-Vis spectrum of PEG-AuNPs subsequent to conjugation with anti-LPS antibodies through the terminal carboxylic end of the PEG linker. 54

Figure 15: Scanning electron micrographs ((a) and (b)) of as-synthesized citrate AuNPs, representative of colloidal samples used experimentally. Scale bars = 100 nm. 57

Figure 16: Size distribution histogram of as-synthesized AuNPs, as obtained from the measurements from 100 particles imaged using SEM. Mean particle size (diameter) was determined to be 23.9 nm ± 4.9 nm. .. 58

Figure 17: Representative transmission electron micrographs of as-synthesized AuNPs ((a) and (b)). 59

Figure 18: Representative transmission electron micrograph of washed citrate AuNPs. 60

Figure 19: Representative transmission electron micrograph ((a) and (b)) of 'pink' CTAB stabilised AuNPs. 61

Figure 20: Size distribution histogram of 'pink' CTAB stabilized AuNPs, as determined from the measurement of > 150 particles (n = 173). Mean particle size (diameter) was found to be 29.2 nm $\pm$ 3.7 nm. 62

Figure 21: Representative transmission electron micrographs ((a) and (b)) of AuNPs synthesized via the seeded growth method and stabilized with CTAB. 63

Figure 22: Size distribution histogram of AuNPs synthesized via the seeded growth method, containing silver nitrate, as determined from the measurement of > 150 particles (n = 168). Mean particle size (diameter) was determined to be 34.4 nm $\pm$ 5.5 nm. The resulting AuNPs appeared purple to the naked eye. 64

Figure 23: Comparison of the relative size (diameter, nm) distributions for the as-synthesized AuNPs (red bars), pink CTAB AuNPs (pink bars) and purple CTAB AuNPs (purple bars). 65

Figure 24: Schematic of the general set-up of an *E. coli* and AuNP assay in a 96-well plate. Each serial dilution is prepared in triplicate (n = 3) and all resulting spectra are the average of triplicate scans. 74

Figure 25: Attenuance of live *E. coli* in LB, measured at 600 nm over time, plotted against starting bacterial concentration (CFU/mL). Data points are the average of triplicate scans. 75

Figure 26: UV-vis spectra of as-synthesized citrate AuNPs assayed with serial dilutions of live *E. coli* in MQ and measured immediately post assay; (a) shows a close-up region of the relative positions of the LSPR peaks, and inset (b) shows the spectra over the entire range of monitored wavelengths (nm). 76

Figure 27: UV-vis spectra of as-synthesized citrate AuNPs assayed with serial dilutions of live *E. coli* in MQ and measured after overnight incubation at room temperature; (a) shows a close-up region of the relative positions of the LSPR peaks, and inset (b) shows the spectra over the entire range of monitored wavelengths (nm)..... 77

Figure 28: UV-vis spectra of as-synthesized citrate AuNPs assayed with serial dilutions of live *E. coli* in LB and measured immediately post assay; (a) shows a close-up region of the relative positions of the red-shifted plasmon peaks, and inset (b) shows the spectra over the entire range of monitored wavelengths (nm)..... 78

Figure 29: UV-vis spectra of as-synthesized citrate AuNPs assayed with serial dilutions of live *E. coli* in LB and measured after overnight incubation at ambient temperature; (a) shows a close-up region of the relative positions of the red-shifted plasmon peaks, and inset (b) shows the spectra over the entire range of monitored wavelengths (nm). 79

Figure 30: UV-vis spectra of washed citrate AuNPs assayed with serial dilutions of live *E. coli* in MQ and measured immediately post assay; (a) shows a close-up region of the relative positions of the LSPR peaks, and inset (b) shows the spectra over the entire range of monitored wavelengths (nm). 81

Figure 31: UV-vis spectra of washed citrate AuNPs assayed with serial dilutions of live *E. coli* in MQ and measured after overnight incubation at ambient temperature; (a) shows a close-up region of the relative positions of the LSPR peaks, and inset (b) shows the spectra over the entire range of monitored wavelengths (nm)..... 82

Figure 32: UV-vis spectra of washed citrate AuNPs assayed with serial dilutions of live *E. coli* in LB and measured immediately post assay. (a) shows a close-up region of the relative positions of the red-shifted plasmon peaks, and inset (b) shows the spectra over the entire range of monitored wavelengths (nm)..... 83

Figure 33: UV-vis spectra of washed citrate AuNPs assayed with serial dilutions of live *E. coli* in LB and measured after overnight incubation at ambient temperature. (a) shows the rescaled spectra with saturated signals A and B omitted, and inset (b) shows the all spectra, including the saturated optical signals from the highest starting concentrations of bacteria. 84

Figure 34: UV-vis spectra of as-synthesized citrate AuNPs assayed with serial dilutions of live *E. coli* in LB, t = 0 h. (a) shows a close-up region of the relative positions of the red-shifted plasmon peaks, and inset (b) shows all spectra over the entire range of monitored wavelengths (nm). 86

Figure 35: UV-vis spectra of as-synthesized citrate AuNPs assayed with serial dilutions of live *E. coli* in LB, t = 8 h. (a) shows a close-up region of the relative positions of the red-shifted plasmon peaks, and inset (b) shows all spectra over the entire range of monitored wavelengths (nm). 87

Figure 36: UV-vis spectra of as-synthesized citrate AuNPs assayed with serial dilutions of live *E. coli* in LB, t = 10 h. (a) shows a close-up region of the relative positions of the red-shifted plasmon peaks, and inset (b) shows all spectra over the entire range of monitored wavelengths (nm). 88

Figure 37: UV-vis spectra of as-synthesized citrate AuNPs assayed with live *E. coli* in LB, t = 12 h. (a) shows a close-up region of the relative positions of the red-shifted plasmon peaks, and inset (b) shows all spectra over the entire range of monitored wavelengths (nm). 89

Figure 38: UV-vis spectra of washed citrate AuNPs assayed with live *E. coli* in LB. Concentrations of *E. coli* range from 5 x 10^7 – 5 cells/mL, t = 0. (a) shows a close-up region of the relative positions of the red-shifted plasmon peaks, and inset (b) shows all spectra over the entire range of monitored wavelengths (nm). 91

Figure 39: UV-vis spectra of washed citrate AuNPs assayed with live *E. coli* in LB, t = 4 h. (a) shows a close-up region of the relative positions of the red-shifted plasmon peaks, and inset (b) shows all spectra over the entire range of monitored wavelengths (nm). 92

Figure 40: UV-vis spectra of washed citrate AuNPs assayed with live *E. coli* in LB, t = 8 h. (a) shows a close-up region of the relative positions of the red-shifted plasmon peaks, and inset (b) shows all spectra over the entire range of monitored wavelengths (nm)..... 93

Figure 41: UV-vis spectra of washed citrate AuNPs assayed with live *E. coli* in LB, t = 10 h. (a) shows a close-up region of the relative positions of the red-shifted plasmon peaks, and inset (b) shows all spectra over the entire range of monitored wavelengths (nm)..... 94

Figure 42: UV-vis spectra of washed citrate AuNPs assayed with live *E. coli* in LB, t = 12 h. (a) shows a close-up region of the relative positions of the red-shifted plasmon peaks, and inset (b) shows all spectra over the entire range of monitored wavelengths (nm)..... 95

Figure 43: UV-vis spectra of as-synthesized citrate AuNPs assayed with live *E. coli* in LB at 37°C. Concentrations of *E. coli* range from 5 x 10^7 – 5 cells/mL, t = 0. (a) shows a close-up region of the relative positions of the red-shifted plasmon peaks, and inset (b) shows all spectra over the entire range of monitored wavelengths (nm)..... 97

Figure 44: UV-vis spectra of as-synthesized citrate AuNPs assayed with live *E. coli* in LB at 37°C, t = 8 h, 45 m. (a) shows a close-up region of the relative positions of the red-shifted plasmon peaks, and inset (b) shows all spectra over the entire range of monitored wavelengths (nm)..... 98

Figure 45: UV-vis spectra as-synthesized citrate AuNPs assayed with live *E. coli* in LB at 37°C, t = 10 h, 30 m. (a) shows a close-up region of the relative positions of the red-shifted plasmon peaks, and inset (b) shows all spectra over the entire range of monitored wavelengths (nm). 99

Figure 46: UV-vis spectra of as-synthesized citrate AuNPs assayed with live *E. coli* in LB at 37°C, t = 12 h, 15 m. (a) shows a close-up region of the relative positions of the red-shifted plasmon peaks, and inset (b) shows all spectra over the entire range of monitored wavelengths (nm)..... 100

Figure 47: UV-vis spectra of washed citrate AuNPs assayed with live *E. coli* in LB at 37°C. Concentrations of *E. coli* range from 5 x 10^7 – 5

cells/mL, t = 0. (a) shows a close-up region of the relative positions of the red-shifted plasmon peaks, and inset (b) shows all spectra over the entire range of monitored wavelengths (nm). 102

Figure 48: UV-vis spectra of washed citrate AuNPs assayed with live *E. coli* in LB at 37°C, t = 3 h, 30 m. (a) shows a close-up region of the relative positions of the red-shifted plasmon peaks, and inset (b) shows all spectra over the entire range of monitored wavelengths (nm). 103

Figure 49: UV-vis spectra of washed citrate AuNPs assayed with live *E. coli* in LB at 37°C, t = 10 h, 30 m. (a) shows a close-up region of the relative positions of the red-shifted plasmon peaks, and inset (b) shows all spectra over the entire range of monitored wavelengths (nm). 104

Figure 50: UV-vis spectra of washed citrate AuNPs assayed with live *E. coli* in LB at 37°C, t = 12 h, 15 m. (a) shows a close-up region of the relative positions of the red-shifted plasmon peaks, and inset (b) shows all spectra over the entire range of monitored wavelengths (nm). 105

Figure 51: (left) Schematic representation of live E. coli working solution prepared in a centrifuge tube and (right) the preparation of the heat-killed E. coli working solution, prepared by placing the live working solution in a heating block for 30 min. 113

Figure 52: Schematic of the general set-up of an *E. coli* and AuNP assay in a 96-well plate. Each serial dilution is prepared in triplicate (n = 3) and all resulting spectra are the average of triplicate scans. 114

Figure 53: Attenuance of heat-killed E. coli in LB, measured at 600 nm over time, plotted against starting bacterial concentration (CFU/mL). Data points are the average of triplicate scans. 116

Figure 54: UV-vis spectra of as-synthesized citrate AuNPs assayed with 10-fold serial dilutions of heat-killed *E. coli* in MQ and measured immediately post assay. (a) shows a close-up region of the relative positions of the LSPR peaks, and inset (b) shows the spectra over the entire range of monitored wavelengths (nm). 117

Figure 55: UV-vis spectra of as-synthesized citrate AuNPs assayed with 10-fold serial dilutions of heat-killed *E. coli* in MQ and measured after overnight incubation at ambient temperature. (a) shows a close-up region of the relative positions of the LSPR peaks, and inset (b) shows the spectra over the entire range of monitored wavelengths (nm). 119

Figure 56: UV-vis spectra of as-synthesized citrate AuNPs assayed with serial dilutions of heat-killed *E. coli* in LB and measured immediately post assay. (a) shows a close-up region of the relative positions of the red-shifted plasmon peaks and inset (b) shows the spectra over the entire range of monitored wavelengths (nm). 120

Figure 57: UV-vis spectra of as-synthesized citrate AuNPs assayed with serial dilutions of heat-killed *E. coli* in LB and measured after overnight incubation at ambient temperature. (a) shows a close-up region of the relative positions of the red-shifted plasmon peaks and inset (b) shows the spectra over the entire range of monitored wavelengths (nm). 121

Figure 58: UV-vis spectra of washed citrate AuNPs assayed with serial dilutions of heat-killed *E. coli* in MQ and measured immediately post assay. (a) shows a close-up region of the relative positions of the red-shifted plasmon peaks and inset (b) shows the spectra over the entire range of monitored wavelengths (nm). 123

Figure 59: UV-vis spectra of washed citrate AuNPs assayed with serial dilutions of heat-killed *E. coli* in MQ and measured after overnight incubation at ambient temperature. (a) shows a close-up region of the relative positions of the red-shifted plasmon peaks and inset (b) shows the spectra over the entire range of monitored wavelengths (nm). 124

Figure 60: UV-vis spectra of washed citrate AuNPs assayed with 10-fold serial dilutions of heat-killed *E. coli* in LB and measured immediately post assay. (a) shows the spectra over the entire range of monitored wavelengths (nm), and inset (b) shows a close-up region of the relative positions of the red-shifted plasmon peaks. 125

Figure 61: UV-vis spectra of washed citrate AuNPs assayed with 10-fold serial dilutions of heat-killed *E. coli* in LB and measured after overnight incubation at ambient temperature. (a) shows the spectra over the entire range of monitored wavelengths (nm), and inset (b) shows a close-up region of the relative positions of the red-shifted plasmon peaks. 126

Figure 62: UV-vis spectra of washed citrate AuNPs assayed with 10-fold serial dilutions of heat-killed E. coli in LB at 37°C, measured immediately post assay. (a) shows a close-up region of the relative positions of the red-shifted plasmon peaks, and inset (b) shows the spectra over the entire range of monitored wavelengths (nm)..... 128

Figure 63: UV-vis spectra of washed citrate AuNPs assayed with 10-fold serial dilutions of heat-killed *E. coli* in LB at 37°C, t = 3 h 30 min. (a) shows a close-up region of the relative positions of the red-shifted plasmon peaks, and inset (b) shows the spectra over the entire range of monitored wavelengths (nm)..... 129

Figure 64: UV-vis spectra of washed citrate AuNPs assayed with serial dilutions of heat killed *E. coli* in LB at 37°C, t = 10 h 30 min. (a) shows a close-up region of the relative positions of the red-shifted plasmon peaks, and inset (b) shows the spectra over the entire range of monitored wavelengths (nm)..... 130

Figure 65: UV-Vis spectra of washed citrate AuNPs assayed with 10-fold serial dilutions of heat-killed *E. coli* in LB at 37°C, t = 12 h 15 m. (a) shows a close-up region of the relative positions of the red-shifted plasmon peaks, and inset (b) shows the spectra over the entire range of monitored wavelengths (nm)..... 131

Figure 66: Representative transmission electron micrographs of protein aggregates a) amyloid fibrils and b) amorphous aggregates. Reproduced with permissions from Chandel et al.[199]..... 139

Figure 67: Representative transmission electron micrograph of as-synthesized AuNPs stained with 2% (w/v) UA. 145

Figure 68: Representative transmission electron micrographs (a) and b)) of live *E. coli* controls stained with UA. White arrows in b) indicate amyloid-like fibril protein aggregates. 146

Figure 69: Representative transmission electron micrograph a) of a heat-killed *E. coli* cell stained with UA. Insets b) and c) show magnified regions of the labelled boxes in a). 147

Figure 70: Representative transmission electron micrographs (a) and b)) of heat-killed *E. coli* controls stained with UA. 148

Figure 71: Representative transmission electron micrographs (a) and b)) of extra heat-killed *E. coli* controls stained with UA. White arrows indicate areas of cytoplasmic condensation. 149

Figure 72: Representative transmission electron micrograph a) of live *E. coli* incubated with as-synthesized AuNPs, aliquoted immediately post-assay and stained UA. Insets b), c) and d) show the magnified regions in a) indicated by labelled boxes. 151

Figure 73: Representative transmission electron micrograph b) of live *E. coli* incubated with as-synthesized AuNPs, aliquoted immediately post-assay and stained UA. Insets a), c) and d) show the magnified regions in b) indicated by labelled boxes. 152

Figure 74: Representative transmission electron micrograph a) of live *E. coli* incubated with as-synthesized AuNPs, aliquoted 2 h post-assay and stained with UA. Insets b) and c) show magnified regions in a) as indicated by the labelled boxes. 153

Figure 75: Representative transmission electron micrographs of aliquots taken from a sample of live *E. coli* incubated with as-synthesized AuNPs, 2 h post-assay and stained with UA. a) shows an *E. coli* cell, b) shows a semi-fused cluster of AuNPs aggregated within amyloid-like fibril aggregates and c) shows an amyloid-like fibril (left) and a disordered, amorphous aggregate (right). 154

Figure 76: Representative transmission electron micrograph a) of live *E. coli* incubated with washed AuNPs, aliquoted immediately post-assay and stained with UA. Insets b) and c) show magnified regions of a) as indicated by the labelled boxes. 155

Figure 77: Representative transmission electron micrograph a) of live *E. coli* incubated with washed AuNPs, aliquoted immediately post-assay and stained with UA. Insets b), c) and d) show magnified regions of a) as indicated by the labelled boxes. 156

Figure 78: Representative transmission electron micrograph a) of live *E. coli* incubated with washed AuNPs, aliquoted 2 h post-assay and stained with UA. Insets b) and c) show the magnified regions indicated by the labelled white boxes in a). White arrows indicate areas of inner membrane shrinkage. 158

Figure 79: Representative transmission electron micrographs (a) and d)) of live *E. coli* incubated with washed AuNPs, aliquoted 2 h post-assay and stained with UA. Insets b) and c) show the magnified regions indicated by the labelled white boxes in d) and a) respectively. Black arrows in a) indicate amorphous aggregates, white ovals denote clusters of unfused AuNP aggregates and white arrows indicate areas of inner membrane shrinkage. 158

Figure 80: Representative transmission electron micrographs (a) and b)) of heat-killed *E. coli* incubated with as-synthesized AuNPs, aliquoted immediately post-assay and stained with UA. White arrows indicate areas of inner membrane shrinkage and black areas denote cytoplasmic shrinkage. 160

Figure 81: Representative transmission electron micrographs of aliquots taken from a sample of heat-killed *E. coli* incubated with as-synthesized AuNPs, aliquoted immediately post-assay and stained with UA. a) shows an amyloid-like fibril aggregate, and b) a disordered amorphous aggregate. 161

Figure 82: Representative transmission electron micrographs (a) and b)) of heat-killed *E. coli* incubated with as-synthesized AuNPs, aliquoted 2 h post-assay and stained with UA. White arrows denote disruption to the cell envelope and dispersion of cellular material. 162

Figure 83: Representative transmission electron micrographs (a) and b)) of heat-killed *E. coli* incubated with as-synthesized AuNPs, aliquoted 2 h post-assay and stained with UA. 163

Figure 84: Representative transmission electron micrographs (a) and b)) of heat-killed *E. coli* incubated with washed AuNPs, aliquoted immediately post-assay and stained with UA. 164

Figure 85: Representative transmission electron micrographs of aliquots taken from a sample of heat-killed *E. coli* incubated with washed AuNPs, aliquoted immediately post-assay and stained with UA. a) shows AuNPs aggregating on a quasi-spherical surface, likely to be an empty cell envelope/dispersed LPS, and b) shows an *E. coli* cell exhibiting significant morphological defects. 165

Figure 86: Representative transmission electron micrographs (a) and b)) of heat-killed *E. coli* incubated with washed AuNPs, aliquoted 2 h post-assay and stained with UA. 166

Figure 87: Representative transmission electron micrographs of aliquots taken from a sample of heat-killed *E. coli* incubated with washed AuNPs, aliquoted 2 h post-assay and stained with UA. a) shows a cell with severe morphological defects and cytoplasmic condensation, b) shows a bacterium with the cell envelope severely disrupted and AuNPs associated with its surface, and c) shows an amyloid-like fibril associated with, and in the vicinity of aggregated AuNP clusters. 167

Figure 88: Representative transmission electron micrographs (a) – c)) of extra heat-killed *E. coli* incubated with as-synthesized AuNPs, aliquoted immediately post-assay and stained with UA. 169

Figure 89: Representative transmission electron micrographs (a) – c)) of extra heat-killed *E. coli* incubated with as-synthesized AuNPs, aliquoted immediately post-assay and stained with UA. 170

Figure 90: Representative transmission electron micrographs (a) – c)) of extra heat-killed *E. coli* incubated with as-synthesized AuNPs, aliquoted 2 h post-assay and stained with UA. 171

Figure 91: Representative transmission electron micrographs (a) – c)) of extra heat-killed *E. coli* incubated with as-synthesized AuNPs, aliquoted 2 h post-assay and stained with UA. 171

Figure 92: Representative transmission electron micrographs (a) – c)) of extra heat-killed *E. coli* incubated with washed AuNPs, aliquoted immediately post-assay and stained with UA. 172

Figure 93: Representative transmission electron micrographs (a) and b)) of a sample of extra heat-killed *E. coli* incubated with washed AuNPs, aliquoted immediately post-assay and stained with UA. b) shows a cluster of quasi-aggregated (unfused) AuNPs surrounded by proteinaceous material (denoted by white arrow in b)). 173

Figure 94: Representative transmission electron micrographs (a) and b)) of extra heat-killed *E. coli* incubated with washed AuNPs, aliquoted 2 h post-assay and stained with UA. 174

Figure 95: Representative transmission electron micrographs (a) and b)) of extra heat-killed *E. coli* incubated with washed AuNPs, aliquoted 2 h post-assay and stained with UA. White arrows indicate areas of disrupted cell division. 175

Figure 96: Schematic representation of the preparation of various conditioned media used within the present chapter. 187

Figure 97: UV-vis spectra of as-synthesized AuNPs with 10-fold serial dilutions of conditioned media from live *E. coli* at ambient temperature, t = 0. a) shows a magnified region of the LSPR peaks and inset b) shows all spectra over the entire range of monitored wavelengths (nm). 191

Figure 98: UV-vis spectra of as-synthesized AuNPs with 10-fold serial dilutions of conditioned media from live *E. coli* at ambient temperature, t = 4 h. a) shows a magnified region of the LSPR peaks and inset b) shows all spectra over the entire range of monitored wavelengths (nm). 192

Figure 99: UV-vis spectra of as-synthesized AuNPs with 10-fold serial dilutions of conditioned media from live E. coli at ambient temperature, t = 10 h. a) shows a magnified region of the LSPR peaks and inset b) shows all spectra over the entire range of monitored wavelengths (nm)..... 193

Figure 100: UV-vis spectra of as-synthesized AuNPs with 10-fold serial dilutions of conditioned media from live *E. coli* at ambient temperature, t = 12 h. a) shows a magnified region of the LSPR peaks and inset b) shows all spectra over the entire range of monitored wavelengths (nm)..... 194

Figure 101: UV-vis spectra of as-synthesized AuNPs with 10-fold serial dilutions of conditioned media from heat-killed *E. coli* at ambient temperature, t = 0. a) shows a magnified region of the LSPR peaks and inset b) shows all spectra over the entire range of monitored wavelengths (nm). 196

Figure 102: UV-vis spectra of as-synthesized AuNPs with 10-fold serial dilutions of conditioned media from heat-killed *E. coli* at ambient temperature, t = 12 h. a) shows a magnified region of the LSPR peaks and inset b) shows all spectra over the entire range of monitored wavelengths (nm). 197

Figure 103: UV-vis spectra of as-synthesized AuNPs with 10-fold serial dilutions of conditioned media from heat-killed *E. coli* at ambient temperature, t = 14 h. a) shows a magnified region of the LSPR peaks and inset b) shows all spectra over the entire range of monitored wavelengths (nm). 198

Figure 104: UV-vis spectra of as-synthesized AuNPs with 10-fold serial dilutions of conditioned media from extra heat-killed *E. coli* at ambient temperature, t = 0. a) shows a magnified region of the LSPR peaks, inset b)

shows all spectra over the entire range of monitored wavelengths (nm), and inset c) shows the magnified region of interest indicated in b). 200

Figure 105: UV-vis spectra of as-synthesized AuNPs with 10-fold serial dilutions of conditioned media from extra heat-killed *E. coli* at ambient temperature, t = 6 h. a) shows a magnified region of the LSPR peaks, inset b) shows all spectra over the entire range of monitored wavelengths (nm), and inset c) shows the magnified region of interest indicated in b). 201

Figure 106: UV-vis spectra of as-synthesized AuNPs with 10-fold serial dilutions of conditioned media from extra heat-killed *E. coli* at ambient temperature, t = 10 h. a) shows all spectra over the entire range of monitored wavelengths (nm), and inset b) shows a magnified region of the LSPR peaks. 202

Figure 107: UV-vis spectra of as-synthesized AuNPs with 10-fold serial dilutions of conditioned media from extra heat-killed *E. coli* at ambient temperature, t = 14 h. a) shows all spectra over the entire range of monitored wavelengths (nm), and inset b) shows a magnified region of the LSPR peaks. 203

Figure 108: UV-vis spectra of washed AuNPs with 10-fold serial dilutions of conditioned media from live *E. coli* at ambient temperature, t = 0. a) shows a magnified region of the LSPR peaks and inset b) shows all spectra over the entire range of monitored wavelengths (nm). 206

Figure 109: UV-vis spectra of washed AuNPs with 10-fold serial dilutions of conditioned media from live *E. coli* at ambient temperature, t = 4 h. a) shows a magnified region of the LSPR peaks and inset b) shows all spectra over the entire range of monitored wavelengths (nm). 207

Figure 110: UV-vis spectra of washed AuNPs with 10-fold serial dilutions of conditioned media from live *E. coli* at ambient temperature, t = 8 h. a) shows a magnified region of the LSPR peaks and inset b) shows all spectra over the entire range of monitored wavelengths (nm). 208

Figure 111: UV-vis spectra of washed AuNPs with 10-fold serial dilutions of conditioned media from heat-killed *E. coli* at ambient

temperature, t = 0. a) shows a magnified region of the LSPR peaks and inset b) shows all spectra over the entire range of monitored wavelengths (nm). 210

Figure 112: UV-vis spectra of washed AuNPs with 10-fold serial dilutions of conditioned media from heat-killed *E. coli* at ambient temperature, t = 4 h. a) shows a magnified region of the LSPR peaks and inset b) shows all spectra over the entire range of monitored wavelengths (nm). 211

Figure 113: UV-vis spectra of washed AuNPs with 10-fold serial dilutions of conditioned media from heat-killed *E. coli* at ambient temperature, t = 8 h. a) shows a magnified region of the LSPR peaks and inset b) shows all spectra over the entire range of monitored wavelengths (nm). 212

Figure 114: UV-vis spectra of washed AuNPs with 10-fold serial dilutions of conditioned media from extra heat-killed *E. coli* at ambient temperature, t = 0. a) shows a magnified region of the LSPR peaks and inset b) shows all spectra over the entire range of monitored wavelengths (nm). 214

Figure 115: UV-vis spectra of washed AuNPs with 10-fold serial dilutions of conditioned media from extra heat-killed *E. coli* at ambient temperature, t = 4 h. a) shows a magnified region of the LSPR peaks and inset b) shows all spectra over the entire range of monitored wavelengths (nm). 215

Figure 116: UV-vis spectra of washed AuNPs with 10-fold serial dilutions of conditioned media from extra heat-killed *E. coli* at ambient temperature, t = 8 h. a) shows a magnified region of the LSPR peaks and inset b) shows all spectra over the entire range of monitored wavelengths (nm). 216

Figure 117: UV-vis spectra of fresh, as-synthesized AuNPs with LB, illustrating the evolution of the spectra over time, measured every 2 h. a)

shows all spectra over the entire range of monitored wavelengths (nm), and inset b) shows a magnified region of the LSPR peaks. 221

Figure 118: UV-vis spectra of aged, as-synthesized AuNPs with LB, illustrating the evolution of the spectra over time, measured every 2 h. a) shows all spectra over the entire range of monitored wavelengths (nm), and inset b) shows a magnified region of the LSPR peaks. 222

Figure 119: UV-vis spectra of fresh washed AuNPs with LB, illustrating the evolution of the spectra over time, measured every 2 h. a) shows all spectra over the entire range of monitored wavelengths (nm), and inset b) shows a magnified region of the LSPR peaks. 223

Figure 120: UV-vis spectra of aged washed AuNPs with LB, illustrating the evolution of the spectra over time, measured every 2 h. a) shows all spectra over the entire range of monitored wavelengths (nm), and inset b) shows a magnified region of the LSPR peaks. 224

Figure 121: Screen-shot from the program PLASMOFIT, showing how a measured spectrum (green) can be decomposed into an exponentially decaying background (blue), two LSPR peaks (‘peak 1’ and ‘peak 2’) and a small contribution from interband transitions. The model has twelve variable parameters but in practice only eight of them are used, with the other four being held constant at values dependent on the system investigated. .. 232

Figure 122: Evolution of the optical parameters of the washed AuNPs incubated at ambient temperature with 10-fold serial dilutions of live *E. coli* at different times. a) 0 h, b) 4 h, c) 8 h and d) 12 h incubation times. The error bars were obtained for each bacterial concentration using the minimum and maximum limits of the triplicate scans. 235

Figure 123: Graphs showing the position of the second plasmon peak (nm) resulting from the incubation of live *E. coli* with washed AuNPs at ambient temperature, allowing the inference of the starting concentration of *E. coli* in CFU/mL. a) after 6 h incubation, and b) after 8 h incubation. Inner pink zones denote the 95% confidence interval for the mean of several

measurements. Light pink zones denote the 95% confidence interval for an individual measurement. 237

List of Tables

Table 1: Table of constituents of LB, organised by amino acid & amino acid derivatives, vitamins and sugars.[74, 76, 77] 20

Table 2: Table summarizing bacterial limits of detection associated with sensing techniques for bacteria. 33

Table 3: Zeta-potentials of AuNPs at various pH values, reported in mV ± the standard deviation for each set of measurements. 55

Table 4: Concentration of As-Synthesized and Washed AuNPs used in assays, reported with respect to concentration of gold in g/L and g/100 µL, as well as particles/m^3 and particles/100 µL. 73

Table 5: Concentration of As-Synthesized and Washed AuNPs used in assays, reported with respect to concentration of particles/m^3 and particles/100 µL. 115

Table 6: Concentration of As-Synthesized and Washed AuNPs used in assays..... 144

Table 7: Concentration of As-Synthesized and Washed AuNPs used in assays, reported with respect to concentration of particles/m^3 and particles/100 µL. 184

Table 8: Table of optical parameters that contribute to the UV-vis spectra of AuNP and *E. coli* assays, showing their potentially variable parameters. The cells highlighted in green are those that were fixed at a value taken from an average of all scans..... 233

Table 9: Comparison of r^2 values for as-synthesized AuNPs assayed with live *E. coli* at ambient temperature 236

Table 10: Comparison of r^2 values for washed AuNPs assayed with live *E. coli* at ambient temperature 236

Equations

$$\mathrm{C}(r) = \mathrm{C}^{\circ} \exp\left(\frac{2\gamma V\mathrm{m}}{rRT}\right) \tag{1}$$

$$\frac{dX}{dt} = -k_d X \tag{2}$$

$$\Delta T = -\frac{n_p\, \Delta H}{\mathrm{C}_p} \tag{3}$$

$$A = B_k + G_1 + G_2 + I_B \tag{4}$$

$$B_k = E_{820\,nm} + (E_{400\,nm} - E_{820\,nm}) \cdot e^{-E_d(\lambda - 400)} \tag{5}$$

$$G_n = H_n \cdot e^{-\frac{(eV - P_n)^2}{2W_n{}^2}} \tag{6}$$

$$y = ae^{(-e^{b-cx})} \tag{7}$$

Abbreviations

µL	microlitre
Ag/AgCl	silver/silver chloride
$AgNO_3$	silver nitrate
Al	aluminium
anti-LPS	anti-lipopolysaccharide (antibody)
Au	gold
Au^0	gold (non-ionic)
Au^{3+}	gold (cationic, 3+)
AuNPs	gold nanoparticles
B	boron
bio-TEM	biological transmission electron microscopy
BSA	bovine serum albumin
BSC	biology safety cabinet
Ca	calcium
CFU/mL	colony forming units per millilitre
C-H	carbon-hydrogen
CH_3	methane
Cl_2	chlorine
Co	cobalt
C-O	carbon-oxygen
conc.	concentrated
$-COO^-$	carboxylate anion
COOH	carboxylate functional group
Cr	chromium
cspB	cold shock protein from *Bacillus subtilis*
cspF	cold shock-like protein from *Escherichia coli*
cspI	cold shock protein (from CspA family of *Escherichia coli*)
CTAB	cetyltrimethylammonium bromide
Cu	copper
DFT	density functional theory

DLS	dynamic light scattering
DNA	deoxyribonucleic acid
E. coli	*Escherichia coli*
EDC	N-(3-dimethylaminopropyl)-N'-ethylcarbodiimide
ELISA	enzyme-linked immunosorbent assay
EM	electromagnetic
eV	electron volt
g	gram(s)
GCB1-3	gold colloid batch (1 -3)
h	hour(s)
$HAuCl_4$	tetrachloroauric acid
HCl	hydrochloric acid
HNO_3	nitric acid
ICP-MS	inductively coupled plasma mass spectrometry
IMS	immuno-magnetic separation
IR	infrared radiation
K	potassium
$KMnO_4$	potassium permanganate
kV	kilovolt
L	litre
LAMP	loop-mediated isothermal amplification
LB	Luria-Bertani
log_{10}	logarithm base 10
LPS	lipopolysaccharide
LSPR	localized surface plasmon resonance
LTSP	long-term stationary phase
M	molar concentration
ME	magnetoelastic
mg	milligram(s)
Mg	magnesium
mL	millilitre(s)
mM	millimolar
Mn	manganese
MNP	metal nanoparticle

Mo	molybdenum
MQ	milliQ water/ultra-pure water
mV	millivolt(s)
Na	sodium
Na/K	sodium/potassium
Na^+	sodium cation
$Na_2S_2O_3$	Sodium thiosulfate
$NaBH_4$	sodium borohydride
NaCl	sodium chloride
NaOH	sodium hydroxide
NASBA	nucleic acid sequence-based amplification
NGS	next generation sequencing
N-H	nitrogen-hydrogen
NH2	amino functional group
NHS	n-hydroxysuccinimide
Ni	nickel
NIR	near-infrared
nm	nanometre
NPs	nanoparticles
OD_{600}	optical density at 600 nm
OH	alcohol functional group
O-H	oxygen-hydrogen
P	phosphorous
Pb	lead
PBS	phosphate buffered saline
PCR	polymerase chain reaction
PEG	poly(ethylene glycol)
PEG-AuNPs	poly(ethylene glycol) conjugated gold nanoparticles
pH	potential of hydrogen
pK_a	acid dissociation constant (log scale)
pK_b	base dissociation constant (log scale)
QCM	quartz crystal microbalance
RMS	root mean square

rpm	revolutions per minute
SAXS	small-angle X-ray scattering
Se	selenium
SEM	scanning electron microscopy
SERS	surface enhanced Raman spectroscopy
SH	mercapto functional group
Si	silicon
SO_2^-	sulfite anion
SPR	surface plasmon resonance
Sr	strontium
t	time
TEM	transmission electron microscopy
thiol-PEG-COOH	thiolated-poly(ethylene glycol) conjugated gold nanoparticles
tris-HCl	tris (hydroxymethyl) aminomethane hydrochloride
UA	uranyl acetate
UV	ultraviolet
UV-vis	ultraviolet-visible
V	volume
VBNC	viable but non-culturable
w/v	weight per volume
WGS	whole genome sequencing
x g	multiples of Earth's standard gravitational acceleration
XANES	X-ray absorption near-edge spectroscopy
Zn	zinc
ΔH	enthalpy change
ΔT	total temperature change
ζ -potential	zeta potential
λ_{max}	wavelength of highest absorption or attenuance
℃	degrees Celsius

Acknowledgements

Thank you to my supervisors, Emeritus Professor Michael Cortie, Professor Andrew McDonagh and Professor Stella Valenzuela, for their supervision, leadership and advice throughout my candidature. It has been a lengthy and often tumultuous process, but none of you threw in the towel on me, and I'm grateful for that.

A special thank you to Andrew for introducing me to Mike and Stella – if you hadn't done so, this thesis wouldn't exist and maybe I'd be an expert in a totally different field. Thank you to Stella for always being available and helpful. Mike, you've been a wonderful mentor. I appreciate all your help, support and guidance over the years. Yes, even in spite of your rants about Microsoft and your semi-retirement throwing a spanner in the works.

Thanks to the University of Technology Sydney and to the Australian Government RTP for project support. Thank you in particular to the technical staff in the chemistry, biology and physics departments, and the countless lab members I've shared lab space with over the years. In particular, thank you to Dr Matthew Phillips for his help with the conditioned media assays. I wasn't going to mention anyone by name, but you didn't leave me much choice here.

An even bigger thank you to the people who have supported me over the years, you know who you are. A lot of you have seen me through my worst, and will hopefully see me through my best – on the other side of this. I appreciate you all.

Finally, I would sincerely like to thank my thesis reviewers. Thank you for your thoughtful and incredibly detailed feedback, which led to a lot of personal and academic growth, and what I hope is reflected as a significant improvement in my resulting thesis.

Abstract

Gold nanoparticles (AuNPs) are widely used across multiple disciplines due to their highly desirable and readily tuneable properties. In particular, their ease of synthesis, characterization, biocompatibility and optical properties make them attractive candidates for biological sensing applications. In this thesis, I show how the properties of AuNPs can be exploited to develop a sensor for *Escherichia coli* (*E. coli*). This bacterium is a well-characterized Gram-negative micro-organism, frequently associated with significant disease, infections, and the contamination of food and water. Disease and infection remain a leading threat to public health and wealth; foodborne illnesses have been estimated to cost Australia $2.44 billion annually, with *E. coli* alone contributing to an estimated $100 million/year. Consequently, the early, rapid and accurate detection of micro-organisms is imperative in the management of outbreaks, prevention of serious infections and timely identification and removal of contaminated products. *E. coli* was employed as a model Gram-negative bacterium to establish the proof-of-concept basis of the proposed sensor.

Herein, the synthesis of various AuNPs, from the precursor tetrachloroauric acid prepared *in situ* is presented. The resulting colloids were characterized using a range of techniques including ultraviolet-visible (UV-vis) spectroscopy, dynamic light scattering (DLS) and electron microscopy. In particular, the citrate AuNPs (24 nm), synthesized via the Turkevich method, were found to be most useful within the present study, and were used for subsequent assays with various preparations of *E. coli* (live, heat-killed and extra heat-killed). It was found that removal of excess surface-associated citrate from the AuNPs (i.e. washed AuNPs) increased their propensity to aggregate within the bacterial samples, and therefore attain better sensitivity within the proposed system. Importantly, assays were conducted in a non-specific, nutrient rich growth medium, Luria-Bertani (LB) broth to allow for the growth of low numbers of bacteria to within detectable levels

over a few hours in the presence of the AuNPs. The high ionic strength of the LB resulted in an initial aggregation of the AuNPs, whereby a second red-shifted LSPR peak appeared. However, it was found that the second (newly formed) LSPR peak was more sensitive to further aggregation within the AuNP/bacterial mixtures compared to the initial LSPR peak of the colloid.

Further changes to the optical properties of the AuNPs from the proliferation of the bacteria could be used to infer the starting concentration of the bacteria (CFU/mL); the wavelength of the second, red-shifted LSPR peak (nm), its associated inflection point, the attenuance at 400 nm, and spectral correlation (with respect to a reference spectrum) were found to be the most useful spectral parameters. Use of these select optical parameters resulting from the assays between live *E. coli* and washed AuNPs enabled a limit of detection of ~ 15 CFU/mL at the 95% confidence interval for an individual measurement, after 8 h incubation at ambient temperature. This could be improved to ~ 2 - 3 CFU/mL if several individual measurements were taken and averaged.

The proposed sensor developed herein has advantages over traditional, ‘gold standard’ methods of detection such as plate counting, polymerase chain reaction (PCR) and other molecular- or immunological-based methods, as comparatively, it does not require skilled personnel to operate, does not involve the use of expensive equipment (a basic UV-vis spectrometer is sufficient), is relatively cheap to make (requires very little gold to produce the initial AuNPs) and does not require costly bio-recognition elements that also decrease the longevity of the sensor (limited shelf-life and strict storage conditions). Some of these aforementioned detection methods may also be very time-intensive, with plate counting requiring a minimum of 24 h (often more) incubation post sample processing. Literature shows a highly variable range of limits of detection, from ~ 10 – 10^5 CFU/mL (technique and bacterial species dependent) to 2500 CFU/mL (plate counting).

A suggested mechanism by which the interaction between the AuNPs and bacteria occurs is presented; incubation of the *E. coli* with AuNPs in LB resulted in aggregation of the colloid that increased with time. This aggregation however, did not occur exclusively on the surfaces on the bacteria and was found to also occur in and around the proteinaceous materials arising from the bacterial cells. Interactions with the AuNPs were observed to result in disrupted and damaged morphologies of the bacterial cells, giving rise to further leakage of cellular materials from the cells. This in turn contributed to the *further* aggregation of the AuNPs within the system. It was consequently determined that the *in situ* proliferation of the live *E. coli* in the presence of the AuNPs was an integral aspect of the concentration-dependent optical signals resulting from their interaction.

Chapter 1:

Introduction

1.1 Motivation and Overview

Disease and infections as a result of food- or waterborne pathogen contamination remain a significant threat to public safety, human health and economic property globally.[1-3] *Escherichia coli* (*E. coli*) is an extensively studied and well-characterised Gram-negative bacterium, often chosen as a model for Gram-negative bacteria in general due to the vast number of studies on its behaviour under various conditions.[4] In addition, *E. coli* is a zoonotic pathogen of significant concern, and the ease with which it can be transmitted from person-to-person or contaminate food and water sources has resulted in numerous outbreaks.[5-8]

Despite *E. coli* naturally existing in the intestinal tracts of humans and several animals as a harmless organism, there are multiple strains of this bacteria which can cause a range of diseases of varying levels of severity. These include, but are not limited to: intestinal disease, neonatal meningitis, urinary tract infections, gastroenteritis or fatal haemolytic uremic syndrome.[1] Transmission of this micro-organism tends to originate from the faecal contamination of food or water sources through irrigation, human handling and failure to effectively decontaminate harvesting or slaughterhouse/post-processing equipment.[5, 6]

Although not all strains of *E. coli* are capable of causing infection and disease, it is one of the most common sources of food and water contamination; consequently *E. coli* is recommended as the most specific bacterial indicator for wastewater monitoring in Australia.[9] It is thus of great importance to be able to rapidly and accurately detect *E. coli*.[1]

Besides the severity of the illnesses which may result from infections caused by *E. coli*, there are also significant economic costs associated with treating those afflicted, the removal and/or recall of contaminated products, and the decontamination of all potentially implicated processing facilities. Unfortunately, as I will show in Chapter 2, existing testing/detection methods for *E. coli* are often expensive and generally require skilled personnel. Within this thesis, I will show how this problem can potentially be solved by using gold nanoparticles (AuNPs) to form a label-free sensor for live *E. coli*.

The effectiveness of the proposed sensor was vastly enhanced by a simple novelty that I will describe in detail within the thesis; in brief, by placing the bacteria in a growth medium that simultaneously contained the AuNPs, a greater sensitivity and concentration-dependent relationship between the starting bacterial CFU/mL and AuNP-signal was achieved.

In Chapter 2, I review the literature pertaining to AuNPs, their synthesis, stability and interactions with cells. I also touch on *E. coli* as a model Gram-negative bacterium, bacterial growth in batch culture and current methods in use for the detection of bacteria. In Chapter 3, I show how the AuNPs used were synthesized and characterized using techniques including ultraviolet-visible (UV-vis) spectroscopy, dynamic light scattering (DLS), scanning electron microscopy (SEM) and transmission electron microscopy (TEM). In particular, I demonstrate that it is possible to obtain colloidally stable 'washed' citrate AuNPs that have a reduced amount of surface-associated citrate. The comparatively lower colloidal stability (and higher sensitivity) of the washed AuNPs compared to the unmodified, "as-synthesized" AuNPs has important implications for the proposed sensor and is discussed throughout the thesis.

In Chapter 4, I present the results of assays of AuNPs with live *E. coli* at both ambient and elevated temperatures (37°C). The effect of bacterial concentration on the observed optical properties of the AuNP/bacterial mixtures was pronounced. Did this seemingly concentration-related effect require the presence of live bacteria (and their proliferation), or would the sensing also be possible with the equivalent concentrations of heat-killed preparations of bacteria? In Chapter 5, I present the results of assays between AuNPs and heat-killed *E. coli*, repeating the experiments performed with live bacteria in the previous Chapter in an attempt to answer this question.

Subsequently the interactions between the AuNPs and various preparations of *E. coli* are explored via TEM in Chapter 6, to allow for a visual assessment of what had only been explored spectroscopically up to this point. Further to this, Chapter 7 investigates the role and impact of the *E. coli* growth, metabolism and cellular by-products on the AuNPs, using conditioned media. The assays between the AuNPs and conditioned media yielded some surprising, yet important results on the age-related stability of citrate AuNPs. Thereafter, Chapter 8 presents the numerical modelling of select optical

parameters that were used in the development of the proposed sensor platform. And finally, in Chapter 9, I present a brief overall conclusion and discuss the findings from thesis.

1.2 Research Outputs and Publications To Date

The investigation of AuNP-based assays for the detection of pathogens in food was the subject of review at the very beginning of this project. This was conducted together with colleages in Thailand and resulted in the very well-cited paper (80 citations on Scopus at time of writing)

1. D. Pissuwan, C. Gazzana, S. Mongkolsuk, and M.B. Cortie, Single and multiple detections of foodborne pathogens by gold nanoparticle assays, *Wiley Interdisciplinary Reviews: Nanomedicine and Nanobiotechnology*, vol.12(1), 2020, article e1584. https://doi.org/10.1002/wnan.1584

During my candidature, I delivered two conference presentations describing my on-going experimental work, results and implications:

2. C. Gazzana, S. Valenzuela, A. McDonagh, M. Cortie, Exploiting the interaction between live Escherichia coli and citrate Au nanoparticles to form a label-free diagnostic test for bacterial contamination, *Gold 2022*, Quebec City July 2022, and

3. C. Gazzana, S. Valenzuela, A. McDonagh, M. Cortie, Exploiting the interaction between live *E. coli* and citrate Au nanoparticles to form a label-free diagnostic test for bacterial contamination, *13th International Nanomedicine Conference*, 19-21 June 2023, Sydney, Australia.

A comprehensive journal paper demonstrating how the experimental results contained within this thesis can be harnessed to generate a concentration-sensitive, label-free sensor using citrate AuNPs to detect live bacteria, using *E. coli* as a model Gram-negative bacterium. Status of paper is “some revisions requested” at time of thesis submission.

4. C.R. Gazzana, M.J. A. Phillips, S.M. Valenzuela, A.M. McDonagh and M.B. Cortie, Label-free detection of live bacteria using growth medium enhanced with Au nanoparticles, in 'revision' phase, *Biochemical and Biophysical Research Communications*

The above listed publications and presentations describe the *need* for a sensor, *how* it can be constructed, and what limits of detection can be achieved, but they do not directly address how and why the sensor works. To resolve the how and why of the sensing mechanism, further exploration of why the washed AuNPs provide a better basis for a sensor compared to the as-synthesized AuNPs. Additionally, further insights into the contributing and competing stabilizing/destabilizing factors within the complex sample matrices (i.e. growth medium containing AuNPs) affecting the AuNPs will be the focus of the final paper resulting from my thesis work:

5. C. Gazzana, S. Valenzuela, A.M. McDonagh and M.B. Cortie, On the mechanisms of bacterially-induced aggregation of gold nanoparticles, to be submitted.

Chapter 2:

Review of Literature

2.1 Introduction

As mentioned in the introductory chapter, the primary aim of this thesis is to investigate whether unmodified, label-free gold nanoparticles (AuNPs) can be utilized as a useful sensor for live bacteria, using *Escherichia coli* (*E. coli*) as a model Gram-negative bacterium. Within the present chapter, I briefly review the current understanding of the properties of AuNPs, what is known regarding their interactions with bacteria in general, and *E. coli* specifically. Finally, I briefly review current state-of-the-art bacterial detection and quantification methods to provide context for the work that is presented within this thesis.

Gold nanoparticles (AuNPs) are ultra-small particles of gold, with at least one dimension within the range of 1 - 100 nm. They may be synthesized in a range of shapes, including spheres, rods and triangles. At the nanoscale, the behavior of electrons at or near surfaces or interfaces become important; this results in new and specific electronic, therapeutic, catalytic and photonic characteristics that can be exploited.[10] These properties differ from both the bulk and individual components of the nanomaterials, and are size dependent and hence tunable.[11] AuNPs are widely used as model systems for the exploration of catalysis, phase transfer, self-assembly, electron-transfer theories and crystal growth.[12] The use of AuNPs is also prolific within the biomedical field, with applications ranging from diagnostics, biosensors, therapeutics, specific cell/tumor targeting and theranostics, to drug delivery.[10]

The widespread use of AuNPs across multiple disciplines is a result of their highly desirable and tunable properties. These include: large surface-to-volume ratio, inertness, high electron density, ease of synthesis and functionalization, biocompatibility, low cytotoxicity, attractive optical properties and photothermal capabilities.[10, 11, 13-17] Comparing AuNPs to organic and inorganic chromophores, AuNPs > 2 nm in diameter have a significantly larger extinction cross-section, with the ability to reach very high (close to 100%) light-to-heat conversion efficiencies in addition to the ability to amplify electromagnetic fields within nm distances from the particle's surface.[18] Many methods exist for the synthesis of AuNPs, and can be grouped into physical, chemical, biological or hybrid-type syntheses.

2.2 Brief Overview of Common Synthetic Routes of Gold Nanoparticles

Physical methods generally involve laser ablation of bulk materials into their nano-counterparts, with focal spot, irradiation time and repetition rate of the irradiation capable of tuning the size distribution and surface plasmon resonance (SPR) of the resulting AuNPs.[13]

Chemical synthesis methods are generally considered 'bottom-up' approaches, in particular, those which involve the reduction of dissolved gold (precursor) ions under select conditions to allow the subsequent growth of aggregates or clusters of gold atoms to form the resulting AuNPs.[19] One of the most well-known wet chemical methods for the synthesis of spherical AuNPs is the Turkevich method,[20] involving the reduction of Au^{3+} to Au^{0} through the addition of reducing agents such as sodium citrate, ascorbic acid or amino acids. Here, the resulting size of the AuNPs can be controlled through variation of the amount of reducing agent, and, in some instances, may also be stabilized/capped with the reducing moiety.[19, 21] Chemical methods may also include seed-mediated growths whereby small nanoparticles are used as seed 'templates' onto which fresh metallic ions are reduced, allowing the growth of the NPs on top of the surface of the seed particles. A benefit to chemical synthesis is the ease with which these methods can generally be performed, as well as their relatively low cost. Despite this, the use of toxic chemicals, risk of dangerous byproducts and residual contamination from chemicals used as precursors/reducing agents are all potential disadvantages to consider.[19]

To counteract these drawbacks and limit the potential negative consequences to the environment, particularly those related to large-scale production, green or biosynthetic methods have been developed and are becoming increasingly popular.[21] The focus of these synthetic routes follows that of green chemistry; to reduce or exclude the use of hazardous chemicals, in turn leading to AuNPs which are more suitable for biomedical applications. Green, or biosynthetic methods for the synthesis of AuNPs often utilize either plant sources or microorganisms in a two-step process which does not require a significant increase in pressure or temperature.[22] In general, the biological extract (fungal, plant or bacterial-based) is used to reduce the $HAuCl_4$ solution, after which

various biocompounds within the extracts are responsible for the growth and stabilization of the resulting AuNPs. When microorganisms are used to synthesize AuNPs, this may be carried out either extracellularly or intracellularly, depending on the microorganism involved, with enzymes and proteins being the main biomolecules involved in the formation.[22, 23]

Hybrid-type synthesis methods may involve a combination of one or more of the above synthetic techniques; for example, Sylvestre et al.[24] have reported the successful synthesis of monodisperse and very stable 2 – 2.5 nm AuNPs formed through laser ablation in the presence of biomolecule α-cyclodextrin. In this instance, the cyclodextrin served to reduce the size of the resulting AuNPs, act as a surface stabilizing agent and enabling tight control of the monodispersity. In contrast, when no biomolecules were added, significantly larger particles were formed with a much higher dispersity and tendency to aggregate.[24]

2.2.1 Mechanism of Citrate Gold Nanoparticle Formation

A proposed mechanism of citrate-AuNP formation has been derived from in situ ultraviolet-visible (UV-vis) spectroscopy, X-ray absorption near-edge spectroscopy (XANES) and small-angle X-ray scattering (SAXS), suggesting a multi-step process.[25]

The first phase of AuNP formation has two parts: initially, within about 60 seconds of the synthesis, rapid nucleation occurs whereby approximately 20% of the gold precursor is converted into polydisperse nuclei. This is followed by the merging and aggregation of the nuclei, resulting in a decrease in both the number of particles and polydispersity. This was found to occur within ~ 20 min of synthesis, and particles had (on average) doubled in size.

The second stage of growth occurs between 25 – 50 min. Herein, particles continue to grow, increasing in average size while further decreasing in polydispersity. The number of particles within the system, however, remain fairly constant. The particle growth during this stage can be described by the “growth by diffusion” model – in this

instance, the rate of reduction of the Au(III) precursor ions is the rate limiting factor, controlling the rate of growth of the Au onto the particles via diffusional growth.

Phase three involves the rapid consumption of remaining Au(III) precursor ions within solution, resulting in a further increase in particle size and decrease in polydispersity, occurring between 50 – 70 min of synthesis. The final phase of AuNP formation involves the rapid growth of the particles to their final size, proceeding until the complete consumption of precursor materials within the system.[25]

A more recent study,[26] also considering extensive dynamic light scattering (DLS) data of the investigated systems suggests a slightly different mechanism of formation. The authors propose the following: Initially, nanoclusters of < 5 nm are formed. These nanoclusters in turn form a network of gold nanowires of varying sizes, continuing to grow until they begin to fragment. Subsequently, individual AuNPs are reported to form from the fragments of the Au nanowires.

Critical factors governing this process were found to be, in particular, the ratio of the sodium citrate to $HAuCl_4$ and temperature of the system during reduction. Careful control of these factors enables the fragmentation of the (intermediate) nanowires into stable colloidal particles. It is worth noting that it is possible to ‘arrest’ the reaction and obtain the intermediate nanowires if the ratio of reactants it sufficiently small, or the temperature is too low for the reaction to proceed.[26]

2.3 Optical Properties of Gold Nanoparticles

The highly desirable optical properties of AuNPs are related to their surface plasmons; plasmons are the collective oscillations of free electrons which occur at well-defined frequencies in metals and can also be described as negatively charged clouds of electrons which become coherently displaced from their equilibrium position around lattices of positively charged ions. In the case of AuNPs, where the nanoscale results in a particle size comparable to metal skin depth, it is possible for incident light to penetrate the metal to polarize the conduction electrons to result in non-propagating excitations termed localized surface plasmon resonances (LSPRs). When an AuNP is

much smaller than the wavelength of the light, these oscillations are distributed over the entirety of the particle with the positively charged lattice acting as a 'regenerative force' to pull the polarized electrons back into the lattice - similar to a mass-spring harmonic oscillator.[18]

2.4 Factors Affecting the Localized Surface Plasmon Resonance (LSPR)

Many factors can influence the LSPR of AuNPs and a change in its frequency will result in a colour change of the colloidal gold; these factors include effective electron mass, dielectric medium (including capping agent(s)), density of electrons, particle size, aggregation state, geometry, orientation and shape.[27, 28] Both the position and width of the LSPR peak (measured as absorption) are dependent on the size and inter-particle distance of the AuNPs, while the intensity of the LSPR is related to the concentration of the colloid.[29] When AuNPs are functionalized, the characteristic LSPR peak becomes shifted and dampened due to the attachment of molecules to the surface; this change may be monitored by the total shift in LSPR position in addition to broadening or appearance of additional LSPR peaks. This change is also a result of the change in the refractive index of the medium immediately surrounding the particles and forms the basis of localized surface plasmon resonance (LSPR) sensors.[30]

As the LSPR is very sensitive to many factors, especially the shape of the nanoparticle, it is possible to 'tune' the LSPR to desired wavelengths for specific applications. In general, increasing the size of AuNPs will result in a red shift (longer wavelength) of the attenuance (total sum of scattered, absorbed and reflected light), while increasing the anisotropy of the particles results in the presence of additional LSPR bands from the excitation of additional plasmon modes.[28, 31] This red shift, which is observed with an increase in particle size, is a result of the differences in frequency of the surface plasmon oscillations of the free surface electrons.[29] For example, spheres have a single LSPR band whereas spheroids and rods exhibit a second red-shifted band, where one is a result of the excitation along the long axis and the other a result of the excitation along the short axis. When considering more complex shapes such as

triangular nanoprisms, four LSPR peaks can often be observed, resulting from the out-of-plane, in-plane quadrupoles, in-plane dipole and weak out-of-plane dipole.[31]

2.5 Surface Functionalization of Gold Nanoparticles, Colloidal Stability and Aggregation

Extensive research has been devoted to the functionalization of AuNPs with targeting moieties. The goal is usually to increase the specificity, selectivity, longevity and, in some instances, ability to cross biological membranes that they would otherwise be excluded from.[32, 33] In some instances, the surface 'capping agents' may serve a dual purpose; not only do they coat the surface of the particles, increasing their colloidal stability, they may also enable selective targeting to specific cells or sites of interest. Conversely, the opposite may be true, where 'stealth'-like properties can be imparted to reduce AuNP recognition by the immune system.[32, 34-36]

There are many approaches that can be used to functionalize the surface of AuNPs – these can involve ionic or electrostatic interactions between the surface of the gold particles and a charged moiety, hydrophobic interactions or via the formation of dative bonds between the conducting electrons of the gold and atoms such as sulfur.[14, 36, 37] Depending on the intended use of the AuNPs, they have been functionalized with polymers, small molecule ligands, dendrimers, surfactants and biomolecules. These may include (but are not limited to) serum albumins (SA), biotin, streptavidin, DNA (single or double stranded), RNA, antibodies, polyvinylpyrrolidone (PVP), and poly(ethylene glycol) (PEG).[36-40]

It is imperative to maintain stability of AuNPs in order to preserve their desirable properties for end use; AuNP stability can be classified into either gravitational or colloidal stability. Gravitational stability refers to the ability of AuNPs to withstand the migration of individual particles via sedimentation mechanisms, whereas colloidal stability is related to the aggregation (irreversible) or agglomeration (reversible)[41] of the particles.[42] (Note that aggregation or agglomeration may often be followed by sedimentation anyway). The stability of AuNPs in high ionic strength media is of great concern and interest in a biomedical context as in vivo and in vitro applications alike

involve the use of high ionic strength media and complex biological matrices.[38] For example, bacterial testing often requires AuNPs to be subjected to bacterial growth media which may contain a multitude of multivalent ions and/or high NaCl content which can lead to immediate and irreversible aggregation of AuNPs. Similarly, in vivo administration involves AuNPs interacting with complex biological matrices, with the need to overcome several 'challenges' before reaching their desired target;[43] these will vary depending on route of administration which include oral, transdermal, nasal, intravenous or via the blood-brain barrier.[44]

In some instances, the controlled or partial aggregation of AuNPs can be beneficial as a method to colourimetrically and/or spectroscopically detect target analytes.[45-49] The strategy of monitoring the aggregation of AuNPs can be implemented to colourimetrically detect target analytes, and is the basis of a multitude of AuNP-based assays, including many of the once ubiquitous COVID RAT lateral flow assays. This exploits the strong absorption and light scattering properties of AuNPs that are both size and inter-particle dependent, as well as their extinction coefficients which are more than 1000 times greater than highly absorbing organic dyes. This may result in colourimetric changes which are capable of high sensitivity,[48] high specificity (often where targeting moieties are employed),[45, 47, 50, 51] and colour changes which may be tracked with the naked eye.[45, 46, 50, 51]

While it is possible to track the colour changes associated with AuNP aggregation visually in some instances, more subtle changes in NP shape, size, dielectric medium or aggregation state may require the use of ultraviolet-visible (UV-Vis) spectroscopy to monitor the wavelength and shape of the resulting LSPR. Consequently, UV-Vis is a rapid, simple and relatively inexpensive probe for the monitoring and (partial) characterization of AuNPs.

2.6 Gold Nanoparticle Stability with Age

The age of AuNPs plays a role in their stability,[52-54] with processes such as Ostwald ripening (or coarsening),[55-58] fusion of particles,[53] disruption or degradation of their

surface capping moieties,[52, 59] as well as storage conditions (such as pH, temperature, additives etc.)[60] contributing to long-term colloidal stability.

There are three common types of ripening processes that can be observed in metal nanoparticle (MNP) populations, particularly those containing ultrasmall (≤ 5 nm diameter) or disperse size populations. These include Ostwald, Smoluchowski, and digestive ripening; all of which lead to size instability.[55]

Ostwald ripening can be described most simply as the growth of larger NPs at the expense of their smaller counterparts within the population, and is a major process that occurs both during synthesis and beyond.[55] Colloidal MNPs become more unstable the smaller the particle size, as a result of the relative increasing higher surface area and curvature. This relationship can be explained by the Gibbs-Thomson equation, where the phase instability is expressed in terms of the solubility concentration C(*r*), of a particle with a radius *r.*

$$\mathrm{C}(r) = \mathrm{C}^{\circ} \exp\left(\frac{2\gamma V\mathrm{m}}{rRT}\right) \qquad (1)$$

Diameters of ~ 5 nm were found to be the 'critical size' below which instability, melting temperature, cohesive energy and surface tension are no longer able to be sufficiently described by the Gibbs-Thomson equation, instead becoming more sensitive to local effects.[56]

The structure and coordination of the citrate layers on the surface of AuNPs contribute to their stability and time-dependent surface rearrangements.[54, 61] Understanding the structure and coordination of the citrate layers affords a more holistic understanding of the potential surface interactions between citrate-AuNPs, and how this may change with time (and storage conditions). The work of Grys et al.[54] has shown through surface-enhanced Raman spectroscopy (SERS) and density functional theory (DFT) calculations, that the citrate coordination to AuNPs is predominantly bidentate, and can be controlled through modification of the protonation state. The citrate coordination was found to become increasingly more complex in the presence of

interfering ions (e.g. chloride, excess citrate, etc.), and with the presence and movement of gold adatoms along the Au facets.

The three pK_a values of citrate (3.13, 4.67, and 6.39)[62] correspond to the central and terminal carboxylate groups respectively – therefore the pH of the colloid strongly influences the degree of protonation and dominant mode of citrate coordination. For example, colloids at pH < 6.8 have shown bidentate bridging via the central carboxylate, while colloids at pH > 6.8 exhibit coordination through the terminal carboxylate moieties, independent of the central -COOH. Monodentate binding has also been observed in chloride-rich environments, where surface-chlorides may interrupt the citrate-Au coordination, leading to decreased stability.

Time-dependent rearrangements ("ageing") occurring on the surface of citrate-AuNPs have been observed, and are associated with the emergence and migration of gold adatoms. The citrate-adatom coordination ultimately affords additional stability to the AuNPs, from the decreased ability of competing moieties to displace the citrate coordinated with the gold adatoms. It is possible however, to 'refresh' aged citrate-AuNPs through the etching of their surfaces to remove the weakly bound gold adatoms, using a strong oxidiser such as tetrachloroauric acid ($HAuCl_4$). When aged citrate-AuNPs are boiled in the *absence* of a strong oxidising agent, an increased in adatoms coordinated to citrate is instead observed.[54]

2.7 *Escherichia coli* as a Model Gram-Negative Bacteria

Escherichia coli (*E. coli*) was chosen as a model Gram-negative bacterium as it has been extensively studied, its behaviour under various conditions is well understood, including, but not limited to, its interactions with nanoparticles.[4, 63-66] In particular, *E. coli* is a clinically relevant pathogenic microorganism of concern, as one of the most common sources of food and water contamination.[67] Consequently, it is recommended as the most reliable specific bacterial indicator for wastewater monitoring in Australia.[9]

Annually, it is estimated that foodborne illnesses cost Australia alone $2.44 billion; of this, *E. coli* is estimated to be responsible for $100 million/year.[68] This enormous sum

is an amalgamation of the social and economic costs associated with decontamination, recall and treatment efforts, as well as the development of new treatment and prevention strategies. Thus, the rapid and accurate detection of *E. coli* is imperative to save time, money and the health of people.[2]

As mentioned, *E. coli* is a Gram-negative bacterium; therefore, its outermost surface is decorated by lipopolysaccharide (LPS) (see **Figure 1** below and **Figure 2** for a more detailed breakdown of LPS). This differs greatly from Gram-positive bacteria and their cell walls, which are comparatively simpler in structure and composition (see **Figure 3**) than their Gram-negative counterparts, which notably lack the outer membrane and LPS.

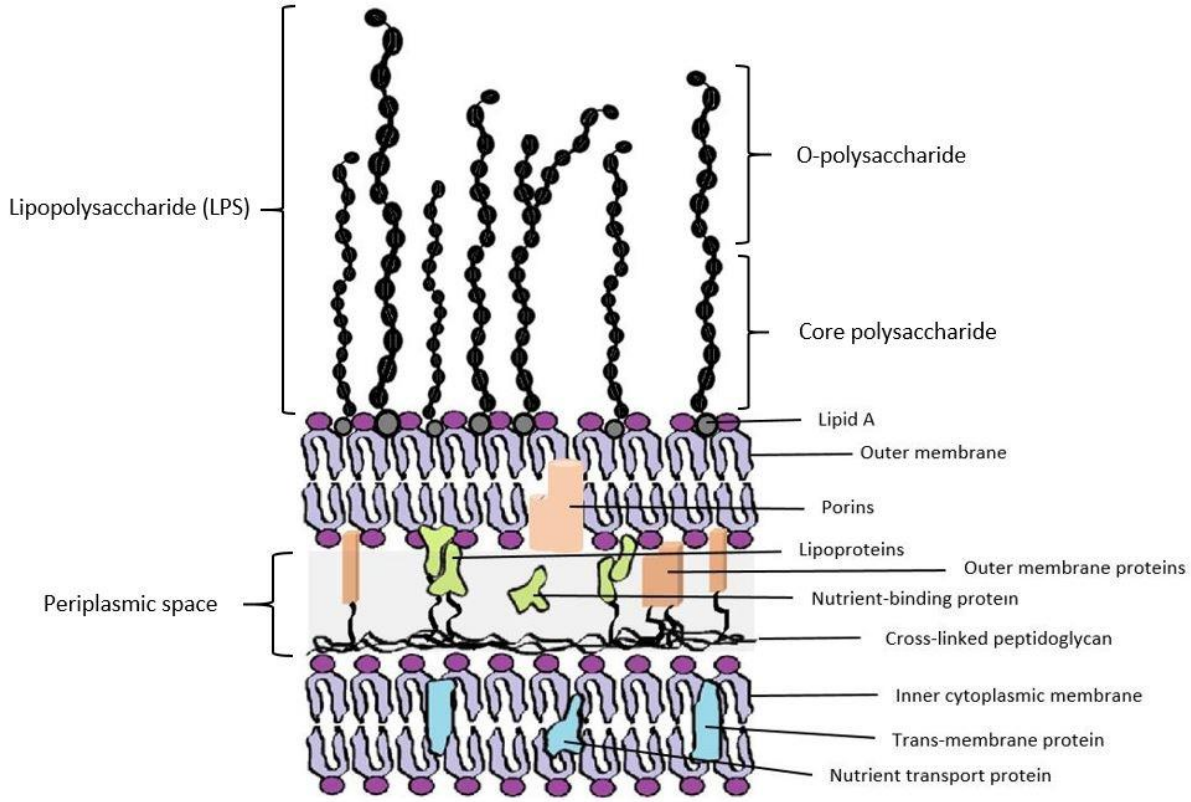

Figure 1: Schematic diagram of a Gram-negative cell wall. It is significantly more complex in structure than the Gram-positive cell wall, consisting of an inner and outer membrane, periplasmic space containing 1-2 layers of peptidoglycan (generally 2 - 8 nm) and lipopolysaccharide (LPS) anchored via Lipid A to the outer membrane.[69] Inner membrane ~ 5 nm, periplasm ~ 17 nm. The outer membrane is not a phospholipid

bilayer, and the inner leaflet is a phospholipid, while the outer layer is comprised of glycolipids and LPS.[70]

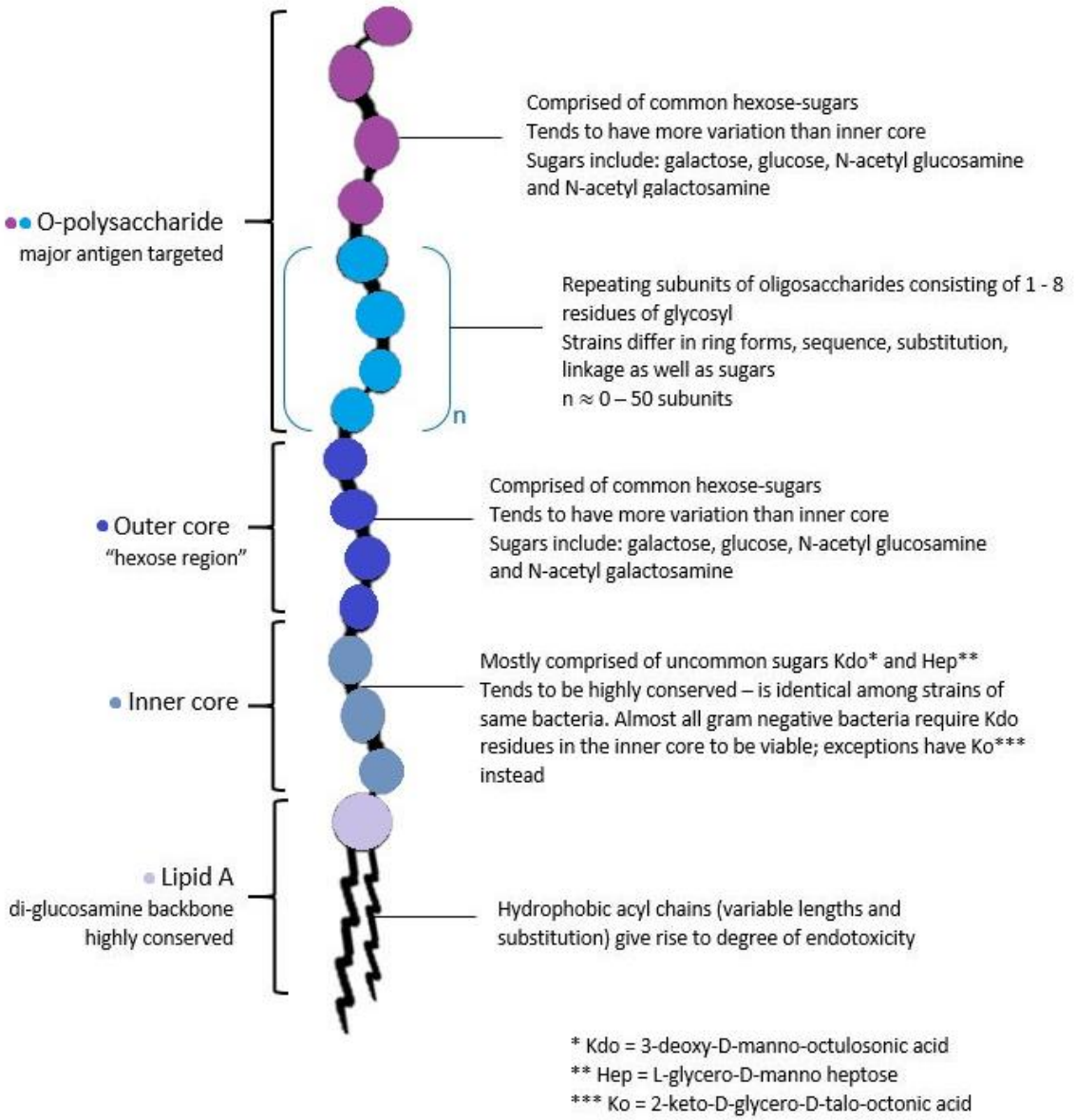

Figure 2: Schematic diagram of lipopolysaccharide (LPS); the outermost (complex) molecule anchored to the outer membrane of Gram-negative cell walls via Lipid A. LPS is divided into three main sections: Lipid A, which has little variation and is identical in bacteria of the same species; the core oligosaccharide which consists of the inner and outer cores as well as the O-polysaccharide region which is sometimes referred to as the O-antigen. The O-antigen is responsible for eliciting host-immune responses and can be rapidly modified to escape immune responses.[69, 71]

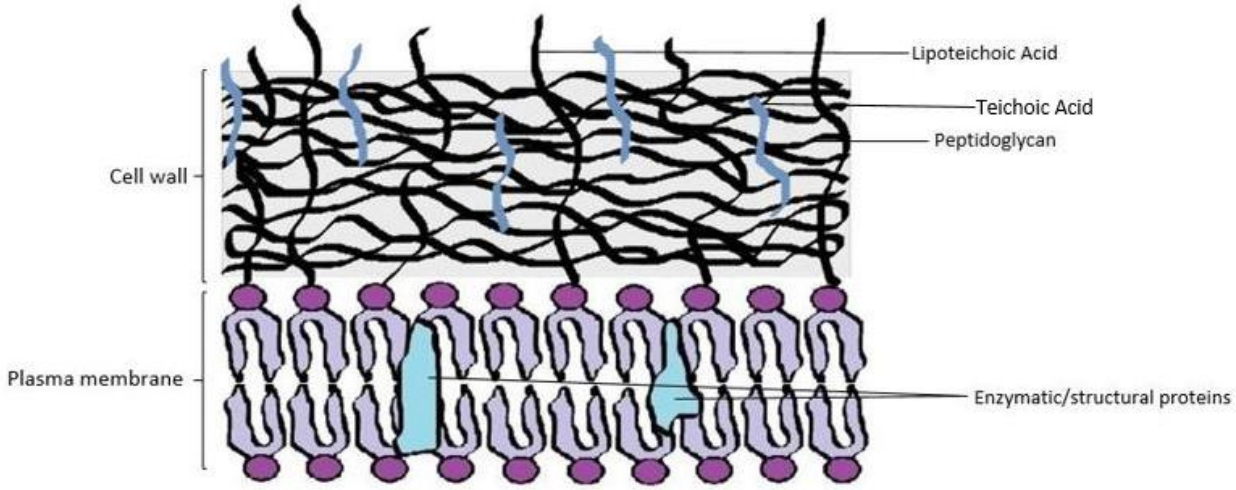

Figure 3: Schematic diagram of a Gram-positive cell wall. Although significantly more simple in composition than the Gram-negative cell wall, it is both thicker (15 - 80 nm) and more homogeneous in nature. The Gram-positive cell wall consists of a single plasma membrane and the cell wall which is comprised of peptidoglycan layers, teichoic acids and lipoteichoic acids.[69] Teichoic acids consist of long anionic polymers.[70]

2.8 *Escherichia coli* Behaviour in Luria-Bertani Broth

An understanding of the surface characteristics of the target analyte may help to understand and predict the way in which various AuNPs will (potentially) interact with the bacteria in select matrices to produce a detectable response.

The work of Sherbet et al.[72] has shown that the surface of unmodified *E. coli* has amino, carboxyl and sulfhydryl groups, all of which are charged species that will readily interact with AuNPs. However, at high ionic strengths, the surfaces of *E. coli* behave less like a smooth surface and more like an uneven surface with “hills and valleys”, although the charged groups within these valleys become ‘shielded’ and unable to exert their charge.[72]

Luria-Bertani (LB) broth is a common and effective growth medium for *E. coli* that contains tryptone (a pancreatic digest of casein), resulting in a medium rich in amino

acids and proteins. It has been shown that amino acids will competitively adsorb to AuNPs through several functional groups; -CH_3, -COOH, -NH_2, -OH, -SH and aromatic rings through π-metal interactions.[73]

2.8.1 Gold Nanoparticle Behaviour in Luria-Bertani Broth

The composition of Luria-Bertani (LB) broth is as follows: 10 g of tryptone, 5 g of yeast extract, 10 g of NaCl, per 1 L of water, autoclaved.[74] The two major organic components of this nutrient broth, tryptone (a pancreatic digest of bovine casein), and yeast extract (an autodigest of *Saccharomyces cerevisiae*),[75] are often not well-defined by manufacturers or suppliers. This can be problematic when investigating systems as sensitive as those containing un-conjugated AuNPs, where it is essential to understand the composition of system as fully as possible.

The individual components of LB can be further broken down into amino acids, carbohydrates and sugars, vitamins and trace elements.[74, 76, 77] (See **Table 1** for a comprehensive list, including structures). The trace elements in LB are likely to originate from yeast extract,[77] and include the following: Al, B, Ca, Co, Cr, Cu, K, Mg, Mn, Mo, Na, Ni, P, Pb, Se, Si, Sr, V and Zn. The ionic species sulfite (SO_2^-) has also been identified from the analysis of tryptone.[76]

The high ionic strength of LB, in addition to the presence of multiple trace elements and compounds (amino acids, vitamins and sugars), containing functional groups that will readily interact with AuNPs, contribute to the colloidal instability within the complex media. This generally results in the formation of NP-NP aggregates, which are reflected in the optical spectra as the appearance of an additional red-shifted ‘aggregation’ peak, ~ 700 - 750 nm. This aggregation occurs to a greater degree and faster in the instance of washed AuNPs (i.e. those with a lower surface coverage of citrate), and to a lesser degree, or not at all when functionalised by moieties such as PEG chains which may ‘shield’ the AuNPs from destabilisation. (See results in Chapters 4, 5 and 6).

Table 1: Table of constituents of LB, organised by amino acid & amino acid derivatives, vitamins and sugars.[74, 76, 77]

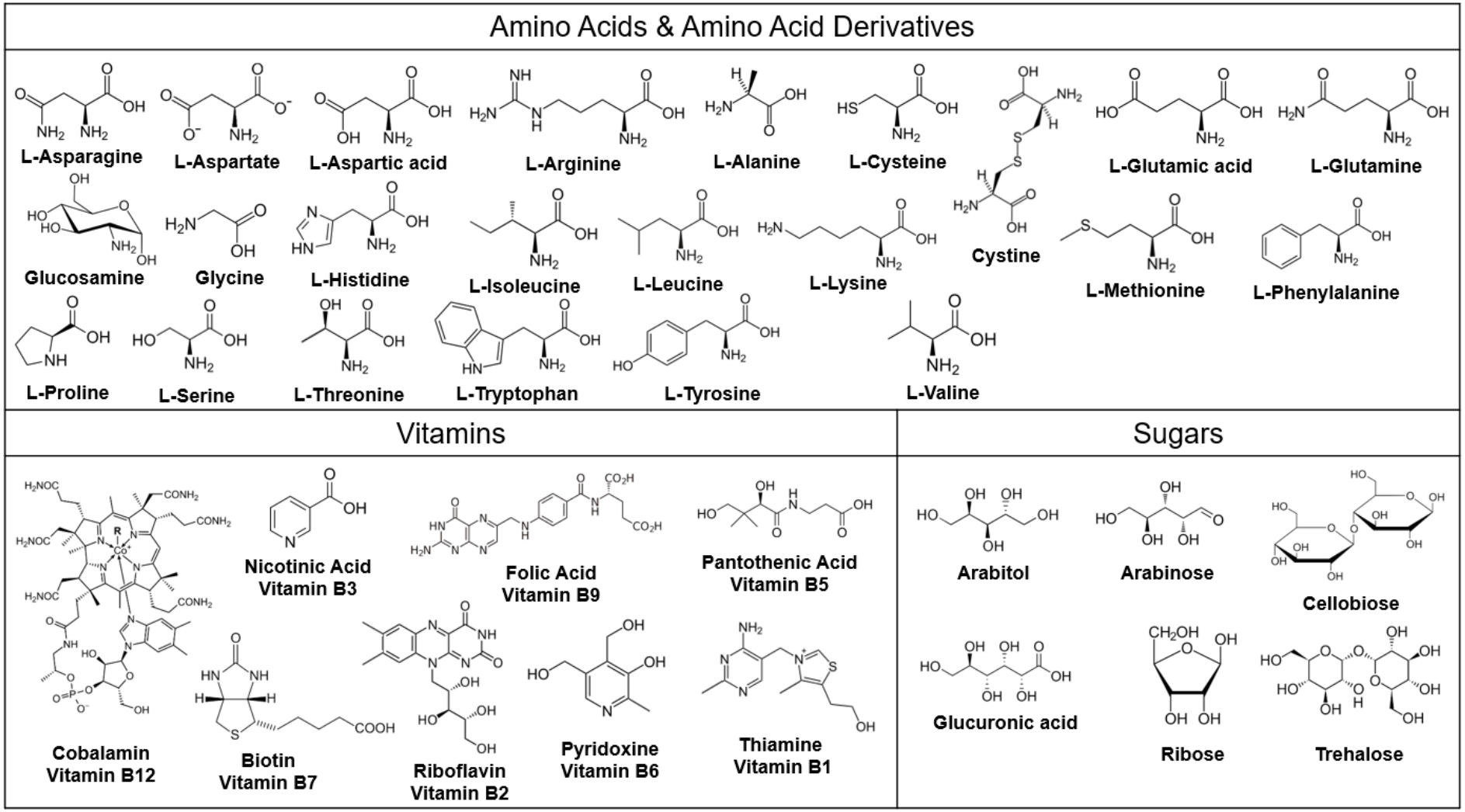

2.9 Phases of Bacterial Growth Under Batch Culture Conditions

Bacterial growth, when pertaining to that of pure and isolated bacteria in batch liquid culture, can be broken down into five phases; the lag, exponential, stationary, death and long-term stationary phase.[78] Each of these distinct phases of growth are associated with typical physiological changes within a bacterial population, with their own unique, reproducible growth rates and features.[79] The lag phase is the first phase observed, where the rate of growth is almost zero and occurs when fresh media is inoculated. This phase is defined as the transition to the exponential phase after the initial bacterial population has doubled and is thought to be a result of the initially low concentrations of exoenzymes and nutrients which may leak from growing cells.[78, 79] The length of time in which a batch culture remains in the lag phase is a result of both the species of bacteria as well as the length of time the cells have remained in a state of starvation.[78]

The exponential phase is the most rapid phase of growth possible under the optimal growth conditions of batch culture, with the rate of cells increasing proportionally to the number of cells present at any particular time. The time taken for a cell division to occur is referred to the doubling time or the generation time, while the number of cells at any given time can be expressed mathematically as being equal to 2^n after n number of divisions. This can be determined from the linear section of a semi-log plot of a bacteria's growth vs. time.[79] The exponential growth phase may also be thought of as a period of steady-state growth, whereby there is great reproducibility of the physiological state of the bacteria, given the same medium and strain of bacteria.

During steady-state growth, all intrinsic cell parameters remain constant when measured as cell population averages. These include the mean density, volume and macromolecular composition of the cells. Conversely, the extrinsic parameters associated with the cell population (i.e. number of cells/mL, optical density or turbidity of the culture, amount of DNA and RNA/mL etc.) increase exponentially with the same doubling time. The growth medium, including temperature, composition and pH all remain constant within the limits of detection for cells during steady-state growth.

When pertaining to the growth of *E. coli* in LB, this tends to transition to the next growth phase at an optical density at 600 nm (OD_{600}) of 0.6 - 1.0.[74, 80]

The third phase of bacteria growth is the stationary phase, characterized by a state of no net growth. During this phase there is still bacterial growth, however the rate of growth is balanced by an equal rate of cell death. The stationary phase within batch culture may be reached for a multitude of reasons, most commonly due to the exhaustion of a primary energy or essential nutrient source, although a multitude of stress factors may also induce this. One such scenario involves the buildup of cellular waste products to levels that inhibit bacterial growth and induce toxicity, although this is generally only the case in batch cultures with very high cell densities. When viewed in the context of a bacterial growth curve, the stationary phase can be observed as a plateau, representing the equilibrium between cell division and death. The growth which occurs at this point is largely due to endogenous metabolism, whereby dead or dying cells are lysed and become a source of nutrients.[78, 79]

Bacterial cells within the stationary phase exhibit drastically reduced metabolic activity and increased resistance to external stressors, functionally behaving more akin to ‘spores’. In general, stationary phase cells tend to be smaller and rounder compared to their exponential phase counterparts as a result of lack of nutrients and increased stress. Significant decreases in energy-consuming processes such as protein synthesis are also observed during this phase.[79, 81]

The death phase is often thought of as the final phase of growth and is represented by a net loss of viable cells within the population. Within the death phase, however, there is still a small portion of the cell population which may continue to metabolize and divide. The rate of the death phase is often exponential, yet (usually) slower than the initial exponential growth phase and can be described by the equation:

$$\frac{dX}{dt} = -k_d X \tag{2}$$

where k_d is the specific death rate.[79]

The long-term stationary phase (LTSP) is the final distinct phase of growth in batch culture and is most similar to conditions experienced in a natural environment in that it is a heterogeneous environment where cells experience a multitude of stresses and changing conditions. This requires cells to adapt to cycles of “feast and famine” through which nutrients are continuously recycled. These nutrients originate from the detritus of approximately 99% of the cell population that have lysed and released their cellular contents in the death phase, as no new nutrients are added to the batch culture. Survival of cells in LTSP, therefore requires an increased ability to metabolize single amino acids and nucleic acids as carbon sources. Interestingly, three genes belonging to the cold shock protein family (cspB, cspF, and cspI) have been found to be upregulated in LTSP in the absence of cold stress, indicating not only that LTSP has a distinct transcriptional program, but also that there may be novel functions for proteins up- or downregulated at different growth phases.[82, 83]

2.10 Gold Nanoparticle Interactions with Cells

The extent to which AuNPs interact with cells – both eukaryotic and prokaryotic – is influenced by several factors, many of which are not yet well understood or characterized. In the context of eukaryotic cells (which include mammalian but not bacterial cells), it has been determined that there are two main mechanisms by which NPs can be internalized by cells; pinocytosis and phagocytosis. (Both of these processes are subsets of the more general process known as endocytosis). These mechanisms are dependent on the size of the NPs as well as cell type. For example, pinocytosis is a less specialized process and can be subcategorized into macro- and micropinocytosis which are mediated by different receptors for larger (> 0.2 μm) and smaller (10 – 200 nm) diameter particles, respectively. In contrast, phagocytosis only occurs for particles > 0.5 μm and in specific cell types such as monocytes and macrophages.[84] It has also been found that AuNPs of 50 nm diameter are readily internalized via receptor-mediated endocytosis more efficiently than smaller (14 nm) and larger (74 nm) AuNPs of the same shape and surface capping (citrate).[85]

In the context of prokaryotes, the mechanisms by which particles may enter or be taken up by cells include: facilitated diffusion, group translocation and active transport.

Facilitated diffusion involves the passive diffusion of solutes through specific gene-encoded membrane channels. Although this is a simple transport mechanism, it is not very energy efficient. Group translocation is similar to facilitated diffusion in that solutes enter the cell through membrane-bound carriers, however, once the solutes have entered the cell, they are converted into charged moieties to prevent their diffusion back out of the same channels.

Active transport, in contrast, involves specific steric recognition and coupling between transporter (membrane-bound) proteins and solutes, with unmodified solutes becoming released into the cytoplasm of cells. For example, Gram-negative bacteria have outer membrane receptors (porins) which facilitate energetic coupling of certain complexes for transport across the cell membrane. These transporters in Gram-negative bacteria generally use either non-membrane soluble, solute binding proteins or they are 'piggy-back' off ionic potential channels (e.g. proton of Na^+ ion pump) to facilitate transport.[86]

2.10.1 Interaction of Gold Nanoparticles with *Escherichia coli* – A Surface-based Interaction?

There are some generally accepted mechanisms by which AuNPs are reported to interact with bacteria, yet there remains a disparity in the literature, with some studies reporting cytotoxic, antibacterial effects,[21, 66, 87] and others reporting the opposite (see the work by Zhang et al.[88] for an in-depth review).

Some of these discrepancies can be attributed to the key variables such as NP size, shape/geometry, surface capping, charge (ζ-potential), age of particles, pH (including buffers), and characteristics of target analytes. Although the core of the NP (Au in this instance) remains the same, any changes to the aforementioned variables may affect the downstream fate of the AuNPs.

When NPs are introduced into a complex biological environment – e.g. in cell culture or *in vivo*, it has been demonstrated that protein coronas form through the adsorption of serum and other (extracellular) proteins.[89-97] This protein corona evolves over time,

with the initially formed ‘soft’ corona reflecting the relative abundance of proteins/adsorbates within the system that have an affinity to the NPs. With time, this evolves into a ‘hard’ corona, comprised of high-affinity, tightly-bound proteins and moieties that displace the more weakly associated proteins that had formed the soft corona.[43, 91] The evolving protein coronas play an important role in the biological fate of the NPs, influencing key factors including targeting efficiency and recognition, cell uptake, kinetics and signal transduction. In some instances, the formation of the protein corona can be beneficial to antigen-antibody interactions, supporting sandwich-type immunoassays. In other instances, however, the protein corona masks the ability of small-molecule functionalized NPs to specifically bind to target cells or receptors.[89, 91, 93]

Protein-NP complexes form on both cationic and anionic AuNPs; however, both were found to result in negatively charged complexes. The key difference arose from the resulting structures of the adsorbed proteins; taking bovine serum albumin (BSA) as a model protein due to its abundance in biological matrices and high affinity to NPs, those adsorbed to anionic NPs maintained their secondary structure. In contrast, BSA molecules adsorbed to cationic AuNPs exhibited denaturation and were consequently associated with scavenger cell receptors as opposed to albumin receptors, as was found to be the case with BSA-NP complexes formed from anionic NPs.[43] The initial shape of the NP has also been found to influence the composition of the protein corona. The work of Nandakumar et al.[92] suggests protein binding to the surface of AuNPs corresponds with the structure of the NP. For example, spiked AuNPs displayed cylindrical symmetry (of the spiked regions) closely resembling that of the fibrillar proteins adsorbed, with concave areas in the areas between the spikes enabling the unique adsorption of small globular proteins. Comparatively, the smoother surfaces of the spherical AuNPs allowed for the adsorption of larger proteins.[92] Similar work has shown that changing the shape/geometry of AuNPs from spherical to rod affects both protein adsorption to the surface and consequently the NP-cell associations.[91]

2.11 Current Methods for Detection of Bacteria

There are a growing number of methods for detecting and quantifying bacteria in varying matrices, each with their associated advantages and limitations. Due to the importance of rapid and reliable monitoring for the presence of pathogenic microorganisms in water (for consumption and recreation), food processing and production, as well as in clinical settings, this area of research continues to grow and develop rapidly.[98-101]

In general, the methods for the detection of bacteria can be classified into conventional culture-based methods, and rapid, sensor-based techniques. The former includes methods such as bacterial culture, which remains the “gold standard” in microbial detection and quantification, despite its comparatively unimpressive detectable range of pathogens in culture media (~2.5 x 10^3 CFU/mL) and laborious nature (time, instrumentation and skilled human resources).[99]

Bacterial culture is usually followed by biochemical and/or immunological confirmatory tests, further extending the total time from sampling through testing to acquisition of results. Another significant downfall to conventional culture-based methods, is their inability to reliably and accurately detect three significant (potential) metabolic states of pathogenic bacteria – sub-lethally injured, viable but non-culturable (VBNC) or dormant.[102, 103] These altered metabolic states may be induced by external stress factors, many of which are encountered during food processing or other decontamination efforts, leading to an inability of these bacteria to be cultured using conventional media. These bacterial states still pose a threat however, as, upon removal of the stress factors or upon certain stimuli, it is possible for this population to regain activity and culturability.[100]

Bacteriophages have a high specificity and affinity for their respective host cells; as they are only able to replicate inside live cells, phage-based methods can be used to demonstrate cell viability.[100] Bacteriophage-based biosensors have become a promising platform for the detection of bacterial pathogens using plaque assays, or through the sensing of the bacterial analytes (cellular contents) when coupled with

transducers. Examples of such phage-based biosensors include those that are electrochemical, magnetoelastic (ME), incorporate surface plasmon resonance (SPR) optical sensing, and quartz crystal microbalances (QCM).[104]

Within the category of immunological methods are techniques such as enzyme-linked immunosorbent assays (ELISA) and immuno-magnetic separation (IMS). These techniques are based on specific binding interactions between antigens and antibodies, generally affording higher sensitivity and specificity. However, sample enrichment is often a requirement prior to sample analysis, being regarded as a major limitation of these methods. Additionally, the high cost of antibodies and antigens is often considered another drawback.[98, 99]

Molecular-based methods such as polymerase chain reaction (PCR), and isothermal amplification - including loop-mediated isothermal amplification (LAMP) and nucleic acid sequence-based amplification (NASBA), are comparatively more sensitive and specific in comparison to the aforementioned techniques as they target and amplify specific regions of a pathogen's genetic material. PCR is the most commonly used of these techniques, although standard PCR does not indicate the viability of detected cells, with complementary end-point techniques or the incorporation of viability dyes becoming necessary to assess the overall viability of the tested population.[98-101]
LAMP can be considered advantageous over PCR, using only three pairs of primers (in conjunction with DNA polymerase) for specific binding to target nucleic acids. The high specificity of this technique enables the amplification of target DNA, even when non-target DNA is present within a sample. Instead, the risk of non-specific binding arising from primer-primer hybridisations increases with the use of multiple primers, resulting in 'template-free amplification', or false positives. Additionally, numerous temperature cycles, long reaction times and specialised (costly) equipment are not required for LAMP.[98, 99, 105]

NASBA is a more sensitive, rapid and selective molecular-based method of detection for *viable* pathogenic microorganisms, utilising RNA amplification. This technique is capable of amplifying target RNA up to a billion-fold, within 2 h at a constant temperature in the range of 41 – 55°C. Not only does NASBA amplify target nucleic acids to a higher degree, and in a shorter time-frame when compared to conventional

PCR, but, in addition, specialised equipment is not necessary for this technique. However, this comes at the cost of pre-enrichment, taking away from the rapid nature of the detection technique, making this less suitable where rapid detection and quick turn-around of results are required.[99, 106]

There are also many spectroscopic techniques that are able to be used for the detection and quantification of bacterial species. The overarching principle of spectroscopic techniques is based on the interaction of targets or analytes with electromagnetic (EM) radiation that is then monitored as absorption, emission, or diffraction spectra. Raman, and surface enhanced Raman spectroscopy (SERS) are examples of spectroscopic techniques that analyse the inelastic scattering of laser light with samples to monitor the frequency changes. These spectral shifts give information on the rotational, vibrational and low-frequency transitions in molecules, allowing for analysis of molecular-structure.[107] SERS affords much higher sensitivity than traditional Raman spectroscopy through the use of 'nanotags' such as noble metal NPs, whereby the detectable EM fields are amplified by 6 – 10 orders of magnitude, as a result of the excitation of localised surface plasmons (LSP) from noble metal NPs. Although this is a very sensitive and powerful technique, the detected signal is material and substrate-dependent, often requiring sample preparation to separate and/or concentrate target microorganisms from complex food matrices.[98, 107] The limitations of lengthy sample preparation, poor reproducibility and contamination of samples can be circumvented by the integration of microfluidic/lab-on-a-chip systems to SERS substrates to combine pre-treatment, detection and identification of target organisms. However, an external Raman spectrometer is still required, becoming a limiting factor.[107, 108]

Near-infrared (NIR) spectroscopy allows for the continuous monitoring of the fundamental vibrational responses between functional chemical bonds (such as N-H, O-H, C-H, C-O and other organic molecules) within the spectral region of 780 – 2500 nm. Although this is a rapid technique, enabling the continuous and non-destructive monitoring of food-samples in real-time, the samples analysed are generally light and temperature sensitive, requiring alternate light sources to prevent degradation. Additionally, signals within the infrared (IR) region tend to be dominated by water, a major (and essential) component of bacterial organisms and food products.[98]

Sequencing methods can provide comprehensive information on detected pathogens, including species-level information, recognition of genes conferring antimicrobial resistance in addition to information allowing the tracking of bacterial outbreaks. Sequencing methods include techniques such as whole genome sequencing (WGS), of which Sanger sequencing and Maxam-Gilbert sequencing were among the first popularized iterations.[98, 109] Next generation sequencing (NGS) is a successor within the suite of sequencing techniques, capable of reducing reaction volumes to the microscale while sequencing millions of fragments simultaneously. Despite the advantages NGS has in relation to cost, speed and sample processing, the (base pair) read length and precision of Sanger sequencing continues to outperform NGS, with the exception of genomic re-sequencing.[109, 110]

The aforementioned techniques for the detection and quantification of bacterial pathogens are by no means exhaustive, with new, hyphenated, and improved methods being developed with urgency in an attempt to mitigate the huge economic and social burden associated with the downstream effects of bacterial contamination and infection.[2, 68] A particular focus within current and emerging literature is the development of analytical biosensors, notably for the rapid, cost-effective, and often portable monitoring of pathogenic bacteria.[99] Recent increased public awareness and scrutiny of health and disease-causing agents (e.g. the COVID-19 pandemic)[111] has led to further demand for detection techniques to become increasingly rapid, specific, reliable, cost-effective (cheap) and portable, thus enabling their adoption and use by laypeople, especially in the context of low-resource settings.[99, 101, 112]

2.11.1 Biosensors for the Detection of Bacteria

The increasing need for rapid, sensitive, accurate and portable detection platforms has seen a rise in popularity of biosensors, in both clinical and research sectors.[111] Biosensors as a concept were first introduced in 1962, taking the form of an oxidase enzyme amperometric oxygen electrode for the detection of glucose. Subsequent improvement in the field of nanotechnology saw an increasingly multidisciplinary approach to biosensor development, involving aspects of engineering, chemistry, biology and other disciplines.[113-115] A biosensor can be defined as a self-integrated

system that is capable of providing specific information (qualitative or quantitative), utilizing biological recognition elements in conjunction with a transducer to convert bio-interactive processes into measurable signals that are further processed into useable data displays.[114] Figure 4 (below) illustrates the general features of a biosensor, with specific reference to detection of bacteria and/or bacterial metabolites.

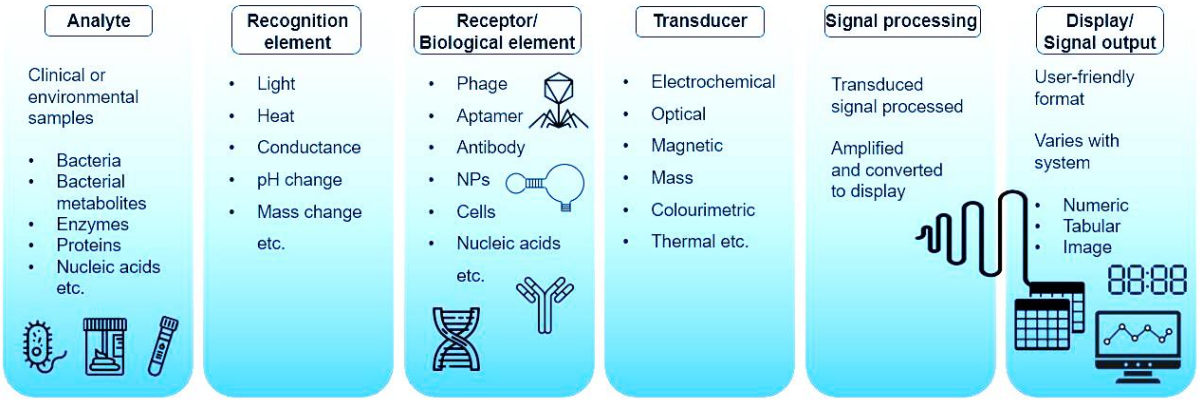

Figure 4: Schematic representation of biosensors used for the detection of bacteria/bacterial metabolites or by-products.[111, 116-118]

Given that the principal components of a biosensor consist of the analyte, bio-recognition element and the transducer, it is possible to characterize biosensors based on either the transducer or the bio-recognition element. For example, with reference to the bio-recognition elements, biosensors may be immuno- (antigens, antibodies, aptamers etc.), enzymatic, nucleic acid based (DNA, RNA etc.), whole-cell or microbial-biosensors. Within this sub-section, I will be referring to biosensors based on their transducers; i.e. piezoelectric (quartz crystal microbalance, acoustic wave etc.), thermometric (heat, calorimetric), electrochemical (potentiometric, amperometric, impedimetric etc.) or optical (absorption, refraction, reflection, transmission, fluorescence, LSPR etc.).[117, 119-121]

Piezoelectric biosensors exploit the wave acoustic principle whereby certain materials produce electrical charges when mechanically stressed. These types of biosensors generally employ a quartz crystal coated with gold electrodes in conjunction with a bio-recognition element, such that when the quartz crystal interacts with analytes of interest, the mass of the crystal will change and measurable oscillations occur. The

frequency of these oscillations depends on the mass of the crystal and its coating; absorption of analytes to the crystal surface results in a change in mass, altering the frequency of the oscillations. These can be measured electrically and used to quantify the mass change within the system.[114]

Thermometric, or thermal biosensors are based on the measurement of one of the fundamental characteristics of biological reactions – the measurement of the total heat energy absorbed or released within a reaction (ΔT). In general, thermal biosensors utilize reactors containing immobilized enzymes, where the analyte solution is passed through the site-active column via flow injection. Thermal transducers (e.g. thermopiles or thermistors) are positioned along the enzyme-column to allow the measurement of thermal signals as the enzymes convert substrates to products. Thermometric-based detection is particularly beneficial for the monitoring of multiple reactions simultaneously as the total temperature change measured within the system (ΔT) is proportional to the enthalpy (ΔH) and the total number of product molecules (n_p) generated, and inversely proportional to the heat capacity (C_p). i.e.

$$\Delta T = -\frac{n_p \, \Delta H}{C_p} \qquad (3)$$

[122]

Electrochemical biosensors are a very commonly used type of biosensor, based on the measurement of electrochemical signals that are generated during bio-interaction processes, leading to the consumption or generation of electrochemical species such as electrons. The benefits of electrochemical sensors lie in their ability to be used in turbid media, their ability to be miniaturized with little difficulty, and their high level of sensitivity which is comparable to classic instrumentation.[123] Electrochemical sensing generally requires three electrodes: a reference, working and counter electrode. The reference electrode may be comprised of Ag/AgCl for example, the working electrode combines the chosen bio-recognition element with the physiochemical transducer, and the third counter electrode is then kept separate from the reaction site at the working electrode in order to maintain a stable potential.[114] Electrochemical sensors can be further sub-classified into potentiometric, conductometric and amperometric biosensors, depending on the electrochemical property measured.[123]

Optical biosensors present a non-invasive, reliable and near real-time analytical tool for the monitoring of biological analytes. These sensors are based on the measurement of optical phenomena resulting from biological events via methods stemming from fluorescence, UV-vis absorption, transmission, chemiluminescence, bioluminescence, surface plasmon resonance (SPR)/localised surface plasmon resonance (LSPR), refractive index (RI), laser light scattering and others.[114, 119] Some of the advantages of optical biosensors, particularly those that have been integrated (e.g. with microfluidics or other techniques), include their capacity for continuous monitoring, high specificity and sensitivity in addition to their cost-effectiveness.[124-126] In particular, optical biosensors provide the potential for minimally invasive *in vivo* measurements (i.e. continuous monitoring of glucose, heart rate and other health metrics), parallel sample processing and kinetic analysis of the biological event(s) being investigated.[119, 126]

Below, **Table 2** summarises some of the limits of detection associated with the sensing techniques mentioned within Section 2.11. I also guide the readers to the recent work of Zhao et al.[127] that provides a more comprehensive review of detection limits for various techniques that can be applied to the detection of bacteria in food samples.

Table 2: Table summarizing bacterial limits of detection associated with sensing techniques for bacteria.

Sensing technique		Limit of Detection	Ref.
Bacterial culture		1 – 2.5 x 10^3 CFU/mL	99, 128, 129
Biochemical		10^4 CFU/mL; 14 - 1600 cells/100 mL	128-130
Immunological	ELISA	6 log CFU/mL	131
	IMS – hyphenated detection	1 – 10^5 CFU/mL	132
	LFIA	1-1000 CFU/mL	127
Phage-based	Electrochemical	10^2 CFU/mL	133
	Magnetoelastic (ME)	5 x 10^2 – 1.5 x 10^3 CFU/mL	134
	SPR/optical	10^2 – 10^3 CFU/mL	134
	QCM	1 – 10^3 CFU/mL	134, 135
Molecular	PCR	0.1-10 CFU/mL	127
	LAMP	5 copies/reaction	136, 137
	NASBA	1 copy/reaction	136
Spectroscopic	Raman/SERS	0.25 - 10^5 CFU/mL	138
	NIR	10^1 – 10^9 CFU/mL	139
Sequencing	WGS	60x detection of single nucleotide polymorphisms (SNPs)	140
	NGS	6 – 1.3 x 10^5 cells/mL	141
Biosensors	Piezoelectric (QCM)	10^2 CFU/mL	142
	Thermometric	10^3 CFU/mL	143
	Electrochemical	1-100 CFU/mL	127
Optical	Fluorescence	< 10 µg L^{-1}	111
	UV-vis	10^5 CFU/mL	111, 144
	Chemiluminescence	52 CFU/mL	145
	Bioluminescence	10^3 CFU/mL	146
	SPR/LSPR	10 CFU/mL	147
	RI	29 CFU/mL	148
	Laser light scattering	1 CFU/25 g	149

2.11.2 Desirable Characteristics of Biosensors

There are certain characteristics that are required for a biosensor to be effective and reliably implemented. The following specifications can be used as a general guide to assess different aspects of a biosensor's performance, and assist in the optimization of biosensors for commercialization.[122]

- **Sensitivity:** relationship between the change in concentration of the analyte and the generated signal intensity from the transducer.[150]
- **Selectivity:** ability of the sensor to accurately distinguish between specific analyte(s) of interest in a sample containing non-target analytes or contaminants.[118]
- **Linearity:** attribute demonstrating the accuracy of the measured response, based on a set of measurements of different concentrations (of the target analyte), to a straight line.[118]
- **Stability:** with reference to labeled methods – the time over which the bio-recognition element (e.g. protein/enzyme/aptamer) retains its activity. With reference to label-free methods – the time over which the biosensor is able to be used without detrimental effects to sensing and outputs.[151, 152]
- **Reproducibility:** ability to fabricate multiple biosensors that are functionally identical and will produce identical responses to target analytes.[153]
- **Limit-of-detection:** minimum concentration of target analyte(s) that can be distinguished with reasonable reliability from a sample without the target analyte(s).[154]

2.12 Research Gaps and Questions

The preceding discussion of the current state of literature has highlighted some important issues. Firstly, there is very little doubt that a cheap and easily used sensor for bacterial contamination would be readily welcomed in a point-of-care or field-testing context for either food or water samples. This would meet widespread social needs in both developed and developing countries by increasing accessibility to, decreasing

costs of and improving the speed of testing for potentially life-threatening bacterial contamination.

The literature shows that although there is a litany of techniques established to detect and/or quantify bacteria, they are often limited by their requirements for highly trained personnel, the need for expensive analytical instrumentation and/or preconditioned analytes. It is a limitation of the existing techniques that prevents their deployment in a field testing context and use by laypeople for these reasons. This creates an opportunity to develop such a sensor.

The review of literature has also shown that existing techniques for bacterial detections have a wide range of limits-of-detection, for example with PCR capable of detection down to 0.1 CFU/mL. However, more traditional methods such as plate-culturing has a limit-of-detection around 2500 CFU/mL, which although may seem high, is deemed sufficiently sensitive for the monitoring of a number of bacterial microorganisms in many products for use and/or consumption by the agricultural and food industry. i.e. the majority of food and water that is safe for use and/or consumption is not sterile, it has below a certain number of (species-specific) microorganisms.

2.12.1 Thesis Aims and Objectives

While it has been shown by others that labelled AuNPs are able to selectively attach to target molecules or analytes of interest (e.g. bacteria), the use of unlabelled AuNPs as a sensing platform has not been as thoroughly explored. The use of unlabelled AuNPs offer the benefits of lower costs and in the case of bio-functionalised AuNPs in particular, higher stability and longevity, since bio-moieties are notoriously susceptible to degradation in storage, usually require special storage conditions and have relatively short shelf lives. The caveat to this is that the use of unlabelled AuNPs are unlikely to be selective to specific bacterial species, and will likely interact with a wide range of microorganisms.

Further testing with a range of different strains of *E. coli* as well as additional Gram-negative bacteria and Gram-positive bacteria, at a range of different AuNP

concentrations is required to gain an understanding of whether the underlying interactions between the AuNPs and bacteria is able to be fine-tuned enough to be implemented as a sensor that is able to distinguish between bacterial species. However, as will be explored within this thesis, as a proof-of-concept and basis for Gram-negative bacterial detection and quantification, is that the presence and starting CFU/mL of a sample of live *E. coli* can be accurately determined using unlabelled citrate AuNPs.

Many sensors that utilise AuNPs require the pre-conditioning or growth of the bacterial sample prior to the addition of the AuNPs for sensing to occur, while those that simultaneously allow for the growth of the bacteria in a medium simultaneously containing the AuNPs have been significantly less investigated. Consequently, several questions need to be addressed:

- Does the presence of the AuNPs within the growth medium have an effect on the growth of the bacteria?
- Given that the effect on the AuNPs is likely to be from both the growth medium, LB (via the formation and evolution of the protein corona) as well as the bacteria present within the test samples, can a usable signal be extracted from just the microorganisms present?
- If the answer to the former question is yes, what is the limit-of-detection of such a system?

Having now provided the context for my work, I will proceed in the following chapters to describe how I created a sensitive and accurate, label-free biosensor platform for the detection of live bacteria, using *E. coli* as a model Gram-negative bacterium.

Chapter 3:

Gold Nanoparticle Synthesis & Characterization

3.1 General

The following section provides detailed information on the techniques applied in this project for the synthesis and characterization of the gold nanoparticles. In all cases, glassware used in the synthesis and/or manipulation of gold nanoparticles was first cleaned by soaking in *aqua regia* solution (3 parts conc. HCl to 1 part conc. HNO_3) overnight before rinsing liberally with MilliQ water (MQ). The purpose of this was to remove residual or trace ionic impurities from glassware, which could lead to the destabilisation and aggregation of colloidal suspensions.

In general, most published syntheses of gold nanoparticles start with solid $HAuCl_4$. This substance is deliquescent which introduces some uncertainty to quantities used experimentally. It is also exceedingly expensive, being sold at about 5 to 6 times the cost of the gold that it contains.[155] This posed a significant problem with regards to the scalability and costs associated with synthesis of considerable quantities of AuNPs; therefore, a viable alternative to the use of commercially available $HAuCl_4$ (s) was sought.

Another issue examined within the current chapter was the question of which type of AuNP to use for sensing. I will show that, despite the simplicity of the Turkevich synthesis of citrate stabilised AuNPs, these AuNPs produced the most appropriate AuNP for the purposes of the present project.

3.2 Introduction

3.2.1 *In Situ* Synthesis of Tetrachloroauric Acid from Solid Gold

Tetrachloroauric acid ($HAuCl_4$) is a well-known precursor used in the chemical synthesis of AuNPs,[10, 11, 13, 18, 27, 52, 54, 156-161] and is commonly purchased as a solid (hydrate) from chemical manufacturers and suppliers. It is less commonly produced *in situ* prior to further use. There are few production pathways traditionally employed on a large(r) scale, including the dissolution of solid gold in aqua regia (3:1 conc. HCl: HNO_3) and the hydrogen peroxide/HCl dissolution of gold solid.

The traditional aqua regia synthesis of tetrachloroauric acid[162] is a multi-step process involving the initial dissolution of solid gold by reaction with aqua regia at 60 - 80°C. This is followed by denitration of the chloroauric acid, whereby excess nitric acid is removed by repeated addition and evaporation of concentrated HCl to prevent the crystallisation of nitrates. Finally, the solution is cooled to temperatures between 0 and 5°C to give crystals of $HAuCl_4.xH_2O$. While this method is tried and true, it involves multiple highly hazardous steps, with the production of toxic nitrogen oxide (NO_x) gases as the nitric acid decomposes, requiring a high level of specialized ventilation. Additionally, large volumes of concentrated HCl must be used to remove the excess nitric acid, preventing the accumulation and crystallization of nitrates which pose additional hazards, including their strong oxidising ability and potential for explosive reactions. Any residual nitrates that remain as impurities in the final product require additional rigorous purification steps, potentially reducing the overall yield.[162, 163] Alternatively, newer methods have replaced nitric acid, instead utilising the reaction between hydrogen peroxide and concentrated HCl to eliminate nitrogen-based by-products and impurities, producing water as a (reaction) product and achieving an overall yield of 98%.[162, 163]

Through the application and refining of early chemistries used in the industrial processing of gold (and other noble metals), the reaction of gold metal with chlorine gas was shown by King et al.[164] to be a straightforward and comparatively safe method to produce $HAuCl_4$ *in situ*, able to be used for the preparation of AuNPs without further preparation. This was found to be comparatively cheaper than purchasing of solid $HAuCl_4$ from chemical suppliers, the precise concentration of the Au in solution is easily determined from the starting mass of gold used, and the reaction is highly scalable. Importantly, this method is inherently less hazardous and has a higher product purity than the traditional and most commonly employed aqua regia dissolution of gold.[164]

3.2.2 Synthesis and Functionalization of a Range of Gold Nanoparticles

The surface capping, charge (ζ-potential) and functionalisation of the AuNPs are all relatively simple variables to change, control and measurement, while reportedly having significant downstream effects on their interactions in biological contexts and for sensing purposes.[89-97] Consequently, both negatively charged (citrate-capped) and positively charged (cetyltrimethylammonium bromide (CTAB)-capped) AuNPs were synthesized and characterized in this Chapter.

CTAB AuNPs synthesized from Au seeds were originally intended to be gold nanorods (AuNRs); after several unsuccessful synthesis attempts, it was determined that ease of synthesis, reproducibility and scalability should be prioritised. This was not feasible with the AuNRs and so work was continued using the citrate AuNPs.

Conjugation of biomolecules to AuNPs has been demonstrated[34, 37, 40, 42, 165, 166] to impart additional stability and/or improve functionality with respect to targeting of analytes. Within the present Chapter, bovine serum albumin (BSA), thiolated-poly(ethylene glycol) and anti-lipopolysaccharide (anti-LPS) were initially explored as methods to improve the stability of the Au colloids and to improve the targeting specificity of the AuNPs to the target analyte (*E. coli*).

Again, when considering the scalability, cost and shelf-life of the AuNPs employed within the sensor, the use of biomolecules can significantly increase the associated cost of production (thus reducing scalability). Some biomolecules must also be stored at low-temperatures to retain their functionality (e.g. antibodies), while the citrate AuNPs can remain at ambient temperatures for extended periods of time (> 1 year) without deleterious effects. Therefore, although a range of AuNPs were initially synthesized and functionalized, in the interest of pursuing the design of a low-cost, low-tech sensor technology, unfunctionalized or *label-free* citrate AuNPs were used in further experimental work.

3.3 Experimental Design and Methods

3.3.1 Chemicals and Materials

The following chemicals and materials were used as purchased, without further purification, as per the methods in subsequent sections: hydrochloric acid (36 %) and nitric acid (70 %) (RCI Labscan), potassium permanganate (Avantor® Chemicals), Ultrapure Milli-Q (MQ) water (Sartorius, 18.2 MΩ cm), gold pellets (99.99 % purity) (AGS Metals, Australia), cetyltrimethylammonium bromide (CTAB) (Alfa Aesar), anti-LPS antibody (Origene Technologies, USA), thiolated-poly(ethylene glycol) carboxylic acid (PurePEG, USA), phosphate buffered saline, phosphate buffer, tris-hydrochloride, hydrochloric acid (32 %) and potassium hydroxide pellets (Chem supply), sodium thiosulfate pentahydrate, tri-sodium citrate dehydrate, L-ascorbic acid and silver nitrate (Ajax Chemicals), sodium borohydride, bovine serum albumin (BSA), N-(3-dimethylaminopropyl)-N'-ethylcarbodiimide (EDC) and N-hydroxysuccinimide (NHS) (Sigma Aldrich).

3.3.2 Synthesis of Tetrachloroauric Acid

The method detailed by King et al.[164] was used. Briefly, concentrated HCl (36 %) was slowly added to a side-arm flask containing excess $KMnO_4$ (s) to generate Cl_2 (g) which was passed through a closed system into a flask containing MQ (10 mL) and four gold pellets (1.451 g) (**Figure 5**). Unreacted Cl_2 (g) was passed into a chemical scrub-trap containing a saturated solution of $Na_2S_2O_3$ (aq). The reaction mixture was stirred at 60°C until the pellets had dissolved completely (approximately 4 days), and the resulting solution diluted to 25 mL, giving a final stock solution of 253.5 mM $HAuCl_4$. The final concentration of $HAuCl_4$ was determined by inductively coupled plasma-mass spectrometry (ICP-MS) and found to be quantitatively related to the initial mass of solid Au used. This is due to the elimination of the need to weigh out deliquescent solid $HAuCl_4$ and the very small losses of associated gold solution during synthesis. Overall, this procedure allows for the precise and convenient preparation of stock solution.

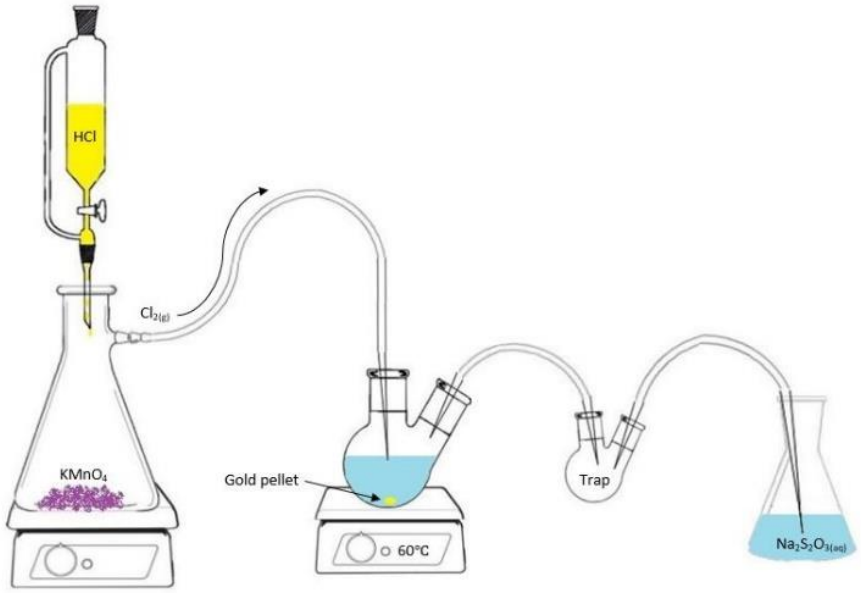

Figure 5: Apparatus setup used for the synthesis of tetrachloroauric acid from gold metal. Redrawn from King et al.[164]

3.3.3 Synthesis of Citrate Gold Nanoparticles from $HAuCl_4$

24 nm citrate AuNPs were synthesized via the Turkevich[20] method (**Figure 6**). The stock solution of $HAuCl_4$ (100 mL) was diluted to 1 mM with MQ and heated to 90°C. To the hot and vigorously stirring solution, tri-sodium citrate dehydrate (114 mg) in MQ (10 mL) was added rapidly. The resulting solution turned clear, then blue, before proceeding to a deep burgundy colour, indicating the successful formation of AuNPs. The solution was held between 90 – 100°C (*without boiling*) for a further 15 min before cooling to ambient temperature. Four separate colloidal solutions were prepared using this method and termed 'gold colloid batch 1, 2 etc.' (GCB1 etc.), or 'as-synthesized AuNPs' for ease of reference.

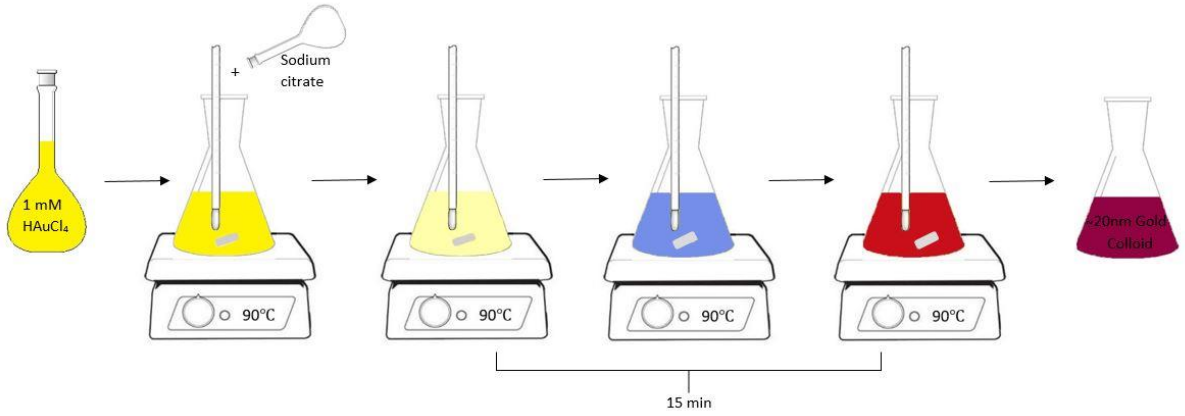

Figure 6: Schematic representation of gold nanoparticle synthesis using the citrate reduction method pioneered by Turkevich[20] in 1951.

3.3.4 Washing of As-Synthesized Citrate Gold Nanoparticles

As-synthesized citrate AuNPs were subjected to two cycles of centrifugation/ resuspension in MQ to remove excess citrate from the surface of the AuNPs.[167] Briefly, NPs were centrifuged at 8000 rpm for 15 min at ambient temperature, the supernatant removed, and pellet re-suspended in the desired volume of MQ. Four independent batches of AuNPs were prepared by this route.

3.3.5 Synthesis of CTAB Stabilized Gold Nanoparticles via the Seeded Growth Method (Silver-Free Method)

i) Gold Seeds

A slightly modified version of the method employed by Sánchez-Iglesias et al.[168] was used. Gold seeds were synthesized via the rapid reduction of $HAuCl_4$ (10 mL, 0.25 mM) in aqueous cetyltrimethylammonium bromide (CTAB, 50 mM) in the presence of citric acid (5 mM) to which freshly prepared $NaBH_4$ (0.25 mL, 25 mM) was added. The seed solution was prepared and stirred vigorously at ambient temperature, with the change in colour from light yellow to brown, indicating the formation of gold seeds. The resulting solution was stirred for an additional 2 min, sealed and placed in an oil bath at 80°C for 90 min under gentle stirring, resulting in a gradual colour change from

brown to red. After 90 min, the seeds were removed from the oil bath and stored at ambient temperature for subsequent use.

ii) Synthesis of Seeded 'Pink' CTAB Stabilized Gold Nanoparticles

A growth solution of CTAB (100 mL, 8 mM), and $HAuCl_4$ (625 µL, 50 mM) was stirred vigorously at ambient temperature for 15 min before L-ascorbic acid (625 µL, 100 mM) was added and the mixture vigorously shaken until colourless. Subsequently, an aliquot of thermally-aged gold seeds (580 µL) was added and shaken vigorously. The resulting solution was left undisturbed overnight at ambient temperature. The resulting AuNPs were a light pink colour to the naked eye.

3.3.6 Synthesis of Gold Nanoparticles via the Seeded Growth Method (Containing Silver Nitrate)

i) Gold Seeds

A slightly modified version of the method employed by T. K. Sau et al.[169] was used. To a 7.5 mL solution of 0.1 M CTAB, 250 µL of 0.01 M $HAuCl_4$ was added and mixed by gentle inversion. To the mixture, 600 µL of 0.01 M ice-cold $NaBH_4$ was rapidly injected and mixed via rapid inversion for 2 min before resting at ambient temperature for a minimum of 2 h. The seed solution could be used for up to 1 week.

ii) Synthesis of Seeded Gold Nanoparticles

To a 4.75 mL solution of 0.1 M CTAB, 200 µL of 0.01 M $HAuCl_4$ and 30 µL of 0.01 M $AgNO_3$ were added in order with gentle mixing between additions. Subsequently, 32 µL of freshly prepared L-ascorbic acid was added and mixed via gentle inversion before the addition of 10 µL of the seed solution as prepared above, followed by gentle mixing for ~ 10 sec. The resulting AuNP solution was left undisturbed for ≥ 3 h.

3.3.7 Conjugation of Bovine Serum Albumin to Gold Nanoparticles

Conjugation of bovine serum albumin (BSA) to AuNPs was performed through direct mixing of an aqueous solution of BSA with colloidal as-synthesized AuNPs. To 100 µL of AuNPs, 24 µL of BSA (1 mg/mL) was added and the resulting solution briefly vortexed. The minimum concentration of BSA required to stabilise AuNPs had previously been established by D. Pissuwan[170] and was used for all conjugation experiments. Complete surface coverage with BSA was confirmed by the addition of phosphate buffered saline (PBS, 0.01 M, monovalent ions only) which did not induce aggregation.

3.3.8 Conjugation of Thiolated-Poly(Ethylene Glycol) Carboxylic Acid to Gold Nanoparticles

A modified version of the method employed by H. Hinterwirth et al.[171] and E. Haller et al.[172] was used. In brief, 1 µL of HS-PEG_{12}-CH_2CH_2COOH solution was added to 800 µL of as-synthesized AuNPs and stirred at ambient temperature overnight. Subsequently, the mixture was washed twice with MQ, centrifuged (13 400 rpm, 15 min, ambient temperature) and resuspended in MQ.

3.3.8.1 Conjugation of Anti-LPS Antibodies to PEG-AuNPs

To the linker-AuNP pellet, 100 µL of EDC (N-(3-dimethylaminopropyl)-N'-ethylcarbodiimide, 12 mM) and 100 µL of NHS (N-hydroxysuccinimide, 12 mM) were added and stirred for 2 h. Thereafter, AuNPs were centrifuged (13 400 rpm, 15 min, ambient temperature), the supernatant discarded and pellet resuspended in 1 mL phosphate buffer (50 mM, pH 7.5) to which 1 µL of anti-LPS antibody solution (1 mg/mL) was added. Conjugation was left undisturbed to proceed for 24 h before washing with tris-HCl (50 mM, pH 7.5) 3 times to reduce non-specific –COOH interactions.

3.4 Characterization of Gold Nanoparticles

3.4.1 Sample Characterization Using Ultraviolet-Visible (UV-Vis) Spectroscopy

Ultraviolet-Visible (UV-Vis) spectroscopy for gold nanoparticle colloidal solutions was carried out using an Agilent Cary 60 Dual Beam UV-vis spectrophotometer with a deuterium UV lamp. In general, colloids were monitored from 300 – 800 nm in disposable plastic cuvettes unless otherwise specified. Scans were performed in triplicate (n = 3) and reported values are the average of the resulting triplicate spectra.

3.4.2 Sample Characterization Using Dynamic Light Scattering (DLS)

Samples were analysed using a Malvern Panalytical Zetasizer with a measurement angle of 173°. Samples were placed in disposable folded capillary cells (DTS1070, ATA Scientific) for all DLS measurements. Where the pH of the sample was adjusted, this was performed by the drop-wise addition of either 0.1 M HCl or 0.1 M KOH until the desired pH was attained. Scans were performed in at least triplicate (n = 3) for each sample, with additional scans performed for samples displaying greater levels of fluctuation in their readings (n = 6), with reported results being the average of all scans.

3.4.3 Sample Preparation for Scanning Electron Microscopy

Samples were imaged using a Zeiss Supra 55VP SEM on pre-cleaned silicon wafer substrates (1 x 1 cm). Samples were drop-cast (~ 5 µL) and spread gently with a clean toothpick left to dry under an upturned petri-dish to avoid dust or other particulate contamination. No conductive metal coating prior to imaging was required for AuNP-only samples.

3.4.4 Sample Preparation for Transmission Electron Microscopy (TEM)

Samples were imaged using a FEI Tecnai T20 (200 kV TWIN) TEM equipped with a Gatan 894 x 2k x 2k camera with samples drop-cast onto holey formvar/carbon support films (ProSciTech). Briefly, samples were drop-cast onto fresh TEM grids by

placing 3 x 10 µL drops on top of each other and left to dry under an upturned petri-dish to avoid contamination while drying. No staining or further preparation was required for AuNP-only samples.

3.5 Results and Discussion

3.5.1 UV-Vis Characterization of As-synthesized Citrate AuNPs

The following UV-Visible spectra of the as-synthesized citrate AuNPs were almost identical, with a single LSPR peak at 527 nm (**Figure 7**). The sample GCB4 (spectrum not shown) had a very slightly red-shifted LSPR (528 nm), but maintained the same peak shape and peak width as GCB1 - 3, indicating colloidal stability and similar particle size; the slight red-shifting can be attributed to a very slight increase in particle size, which in turn results in a difference in frequency of the surface plasmon oscillations of the free surface electrons.[29] If there was aggregation occurring within the samples, a second (further) red-shifted peak would appear ~ 730 nm (**Figure 8**).

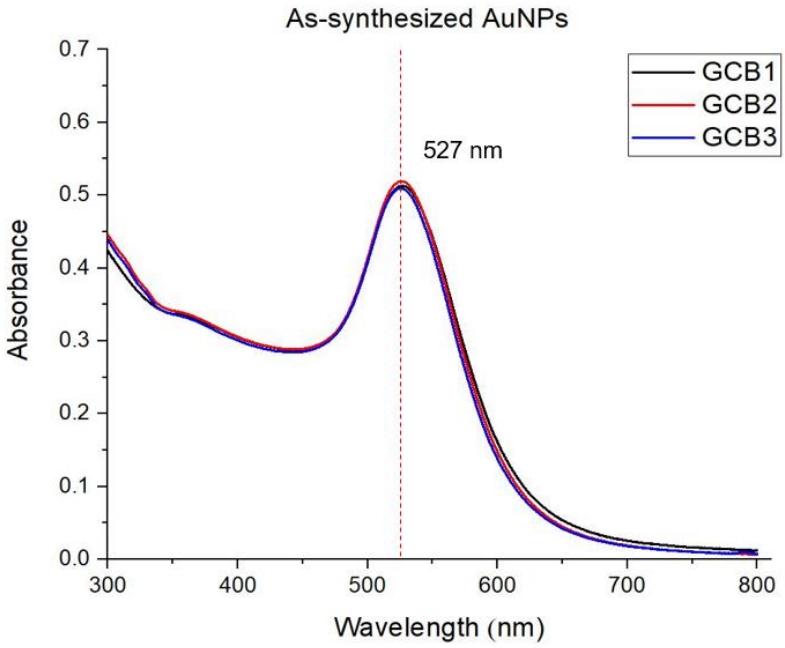

Figure 7: UV-vis spectra of as-synthesized citrate AuNPs (via the Turkevich[20] method). The single plasmon peak centred around 527 nm is characteristic of spherical AuNPs of approximately 20 nm diameter.

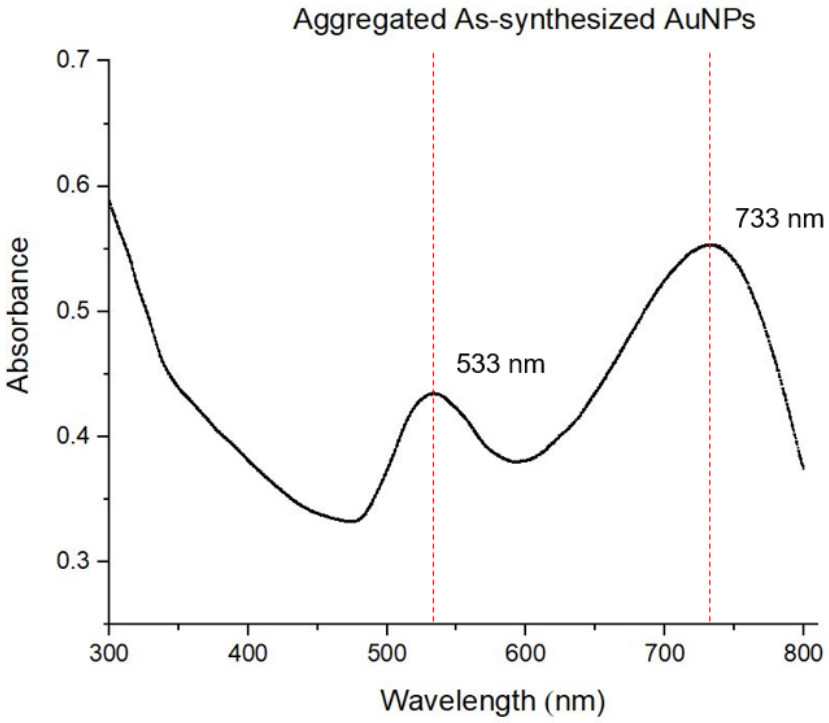

Figure 8: UV-vis spectrum of as-synthesized citrate AuNPs which have aggregated; the characteristic plasmon peak has decreased in attenuance and red-shifted to 533 nm, while an additional plasmon peak has appeared at 733 nm.

Aggregated AuNPs were obtained upon addition of as-synthesized AuNPs to a cuvette for UV-vis measurement. Upon contact with the walls of the cuvette, the colloid immediately underwent rapid (partial) aggregation, visibly changing from wine-red to blue and remaining in the quasi-aggregated blue state that has two distinct plasmon peaks (**Figure 8** above), indicating there was some type of contaminant present within the seemingly clean cuvette. This highlights the ease and speed with which citrate AuNPs are able to aggregate.

3.5.2 UV-Vis Characterization of Washed Citrate AuNPs

Subjecting the as-synthesized citrate AuNPs to washing in order to remove excess citrate coating from their surfaces maintained the similarities between colloidal batches. An increase in the attenuance can be attributed to the overall concentration

of the measured colloid, with the LSPR peak remaining the same (λ_{max} = 526 nm) for all samples, indicating a high level of similarity between samples (**Figure 9**).

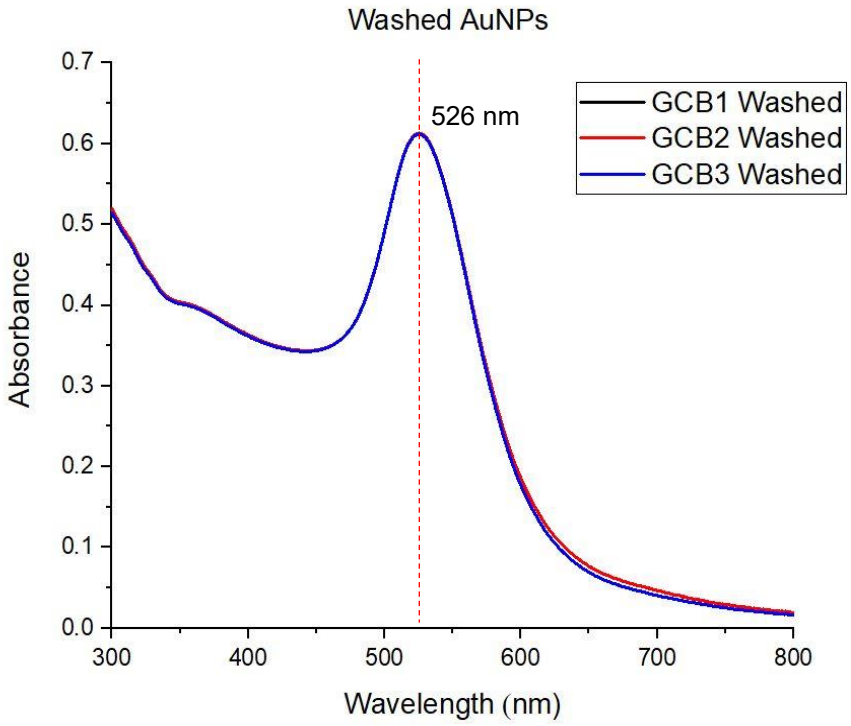

Figure 9: UV-Vis spectra of washed citrate AuNPs, prepared from as-synthesized citrate AuNPs, subjected to two rounds of centrifugation and resuspension in MQ (λ_{max} = 526 nm).

3.5.3 UV-Vis Characterization of 'Pink' CTAB Stabilized AuNPs

The UV-visible spectrum of CTAB stabilized AuNPs is shown below in **Figure 10**. The resulting particles appeared pink to the naked eye and were henceforth called 'pink' CTAB AuNPs. The relatively narrow LSPR peak centred at 533 nm suggests that a nearly monodisperse sample had formed.

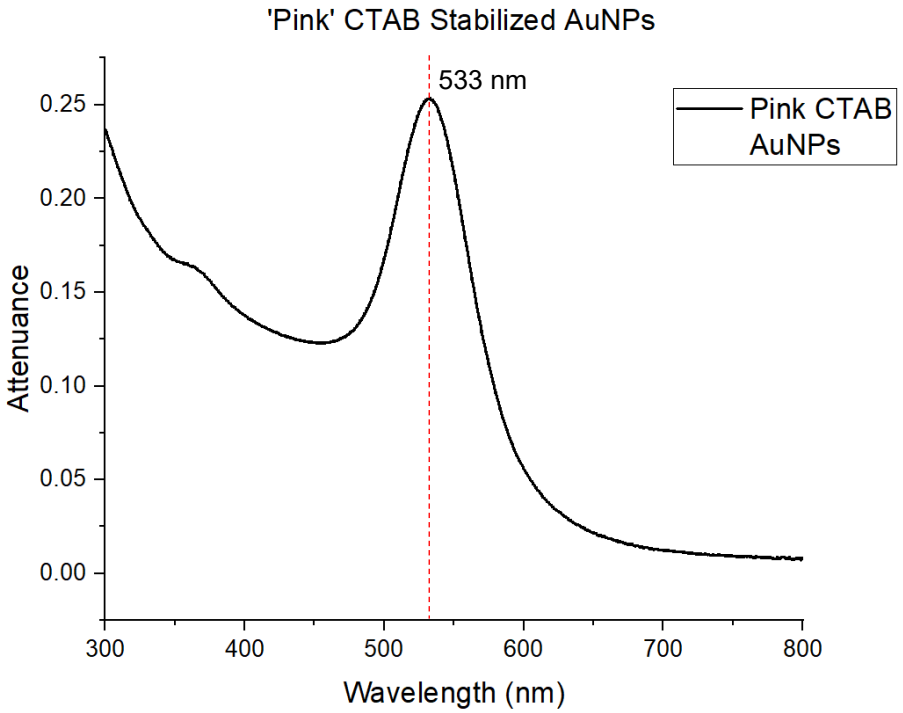

Figure 10: UV-vis spectrum of 'Pink' CTAB stabilized AuNPs, synthesized via the seeded method and displaying a relatively narrow plasmon peak (λ_{max} = 533 nm).

3.5.4 UV-Vis Characterization of Seeded AuNPs Containing Silver Nitrate

The UV-visible spectrum of AuNPs synthesized via the seeding method and containing $AgNO_3$ is shown below (**Figure 11**). Similar to the 'pink' CTAB AuNPs, the stabilising agent was CTAB (as opposed to citrate), and the resulting AuNPs appeared purple to the naked eye. The single LSPR peak, centred on 549 nm, is slightly more red-shifted than those observed previously; the peak width is similarly slightly wider. These both indicate the resulting AuNPs were slightly larger in size and either *more* polydisperse, or had a smaller inter-particle distance.

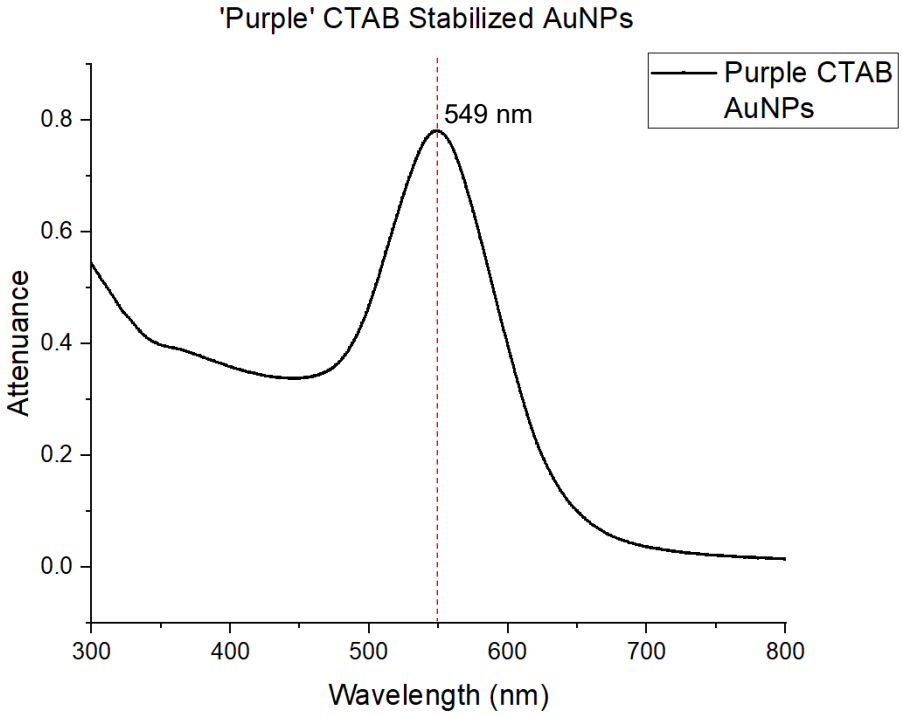

Figure 11: UV-Vis spectrum of AuNPs synthesized via the seeded growth method containing silver nitrate and stabilized by CTAB. The resulting AuNPs appeared purple to the naked eye (λ_{max} = 549 nm).

3.5.5 UV-Vis Characterization of Bovine Serum Albumin Conjugated Citrate AuNPs

The conjugation of citrate stabilized AuNPs with BSA was successful, with the AuNPs remaining colloidal post functionalization. This is evidenced by the red-shift of the LSPR by ~ 4 nm, caused by an increase in the refractive index of the medium which immediately surrounds the AuNPs, while the peak shape remains largely unchanged (see **Figure 12** below).

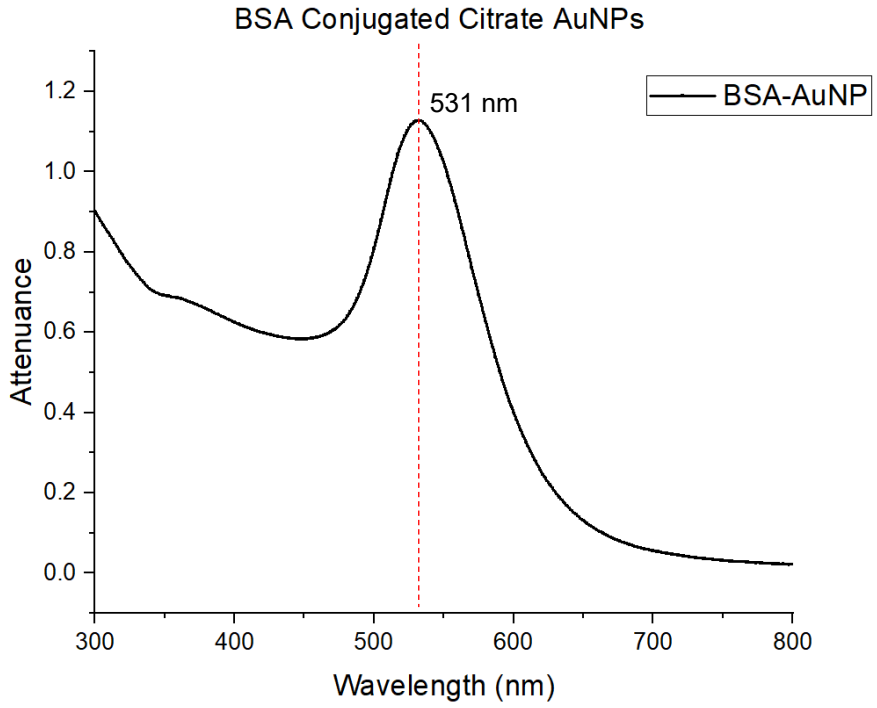

Figure 12: UV-Vis spectrum of BSA conjugated citrate AuNPs.

The overall shape of the plasmon peak has remained consistent from as-synthesized AuNPs to BSA coated, which is indicative of colloidal stability. There was a slight red-shift of λ_{max} from 527 nm to 531 nm, suggesting a slight increase in size of the particles and refractive index surrounding the particles, supporting the successful conjugation of BSA to the surface of the AuNPs. This was accompanied by a slight deepening in colour, visible to the naked eye.

3.5.6 UV-Vis Characterization of Thiolated-Poly(Ethylene Glycol) Carboxylic Acid Conjugation to Citrate AuNPs

Functionalization of as-synthesized citrate AuNPs with thiolated-PEG-carboxylic acid was successful, with the resulting conjugates remaining colloidally stable. As seen previously, the conjugation resulted in a slight red-shift of the LSPR due to the increase in the refractive index of the medium immediately surrounding the AuNPs (see **Figure 13**).

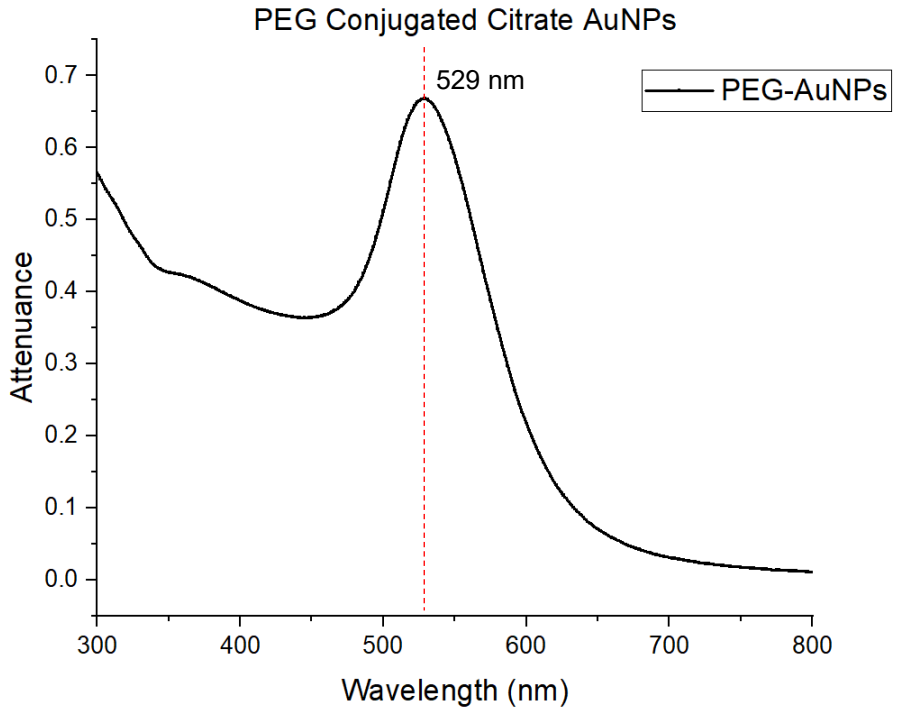

Figure 13: UV-Vis spectrum of thiolated-poly(ethylene glycol) carboxylic acid conjugated as-synthesized AuNPs.

When compared to the spectrum of the as-synthesized citrate AuNPs, they appear almost identical, indicating the colloidal stability of the conjugated NPs. The slight red-shift of the plasmon peak from λ_{max} = 527 nm (as-synthesized citrate) to λ_{max} = 529 nm further supports the successful conjugation of the thiol-PEG-carboxylic acid to the AuNPs.

3.5.7 UV-Vis Characterization of Anti-Lipopolysaccharide Antibody Conjugated PEG-AuNPs

The semi-oriented ligation of anti-LPS antibodies to the carboxylic acid ends of the thiolated-PEG linkers was successful, with the resulting AuNPs remaining colloidal. The LSPR peak red-shifted by 11 nm due to a significant increase in the refractive index of the medium immediately surrounding the AuNPs due to the presence of the antibodies. The successful conjugation was also supported by the slight peak dampening and broadening which can be seen below (**Figure 14**), as compared to the as-synthesized citrate particles.

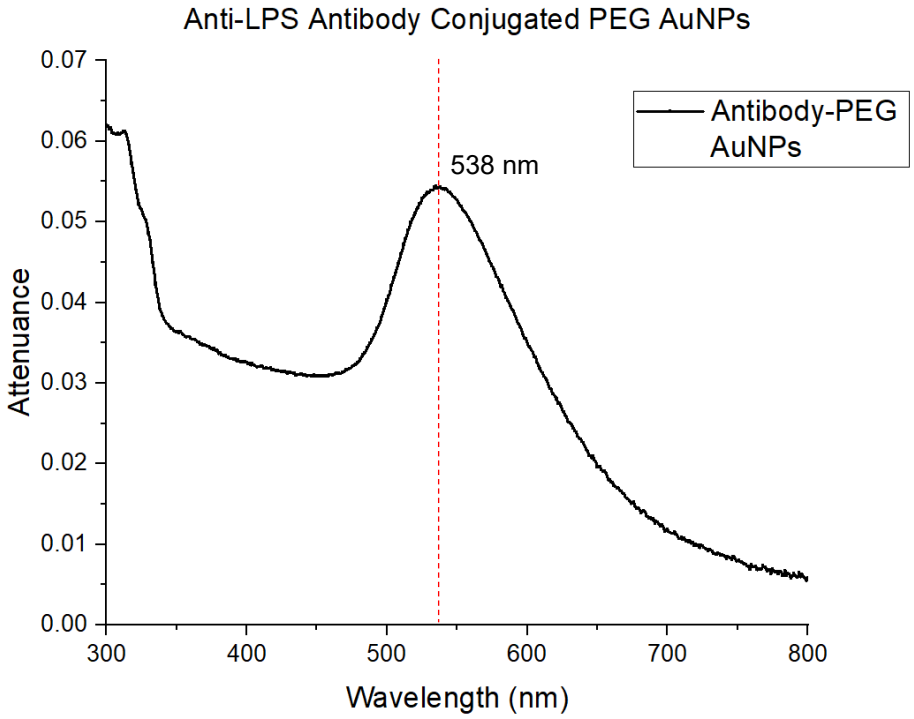

Figure 14: UV-Vis spectrum of PEG-AuNPs subsequent to conjugation with anti-LPS antibodies through the terminal carboxylic end of the PEG linker.

The broadening and red shifting of the plasmon peak from λ_{max} = 527 nm to λ_{max} = 538 nm is indicative of the successful ligation of the anti-LPS antibodies to the PEG-AuNPs in addition to an overall increase in particle size.

3.6 Dynamic Light Scattering (DLS) Characterization of AuNPs

Dynamic light scattering was used to measure the ζ -potentials, or hydrated surface charge of the synthesized and functionalized AuNPs. The zeta-potential is the electrical potential at the interface between a solid particle in solution and the surrounding solution, resulting from the presence of charged species.[173]

All ζ-potential measurements were performed in at least triplicate (n = 3) (see Section 4.2 of the current Chapter for additional details), with the recorded results an average and reported in mV ± the standard deviation for each measurement in **Table 3** below. Each sample was measured at their as-synthesized pH, as well as at pH 5, 7 and 9. Where the pH of samples needed adjustment prior to testing, drop-wise addition of either 0.1 M HCl or 0.1 M KOH was added until the desired pH was attained. Where the ζ value for the "Unmodified pH" is listed as the same as that for the pH 5 value, the pH of the initial colloid was ~ 5, therefore no adjustment prior to ζ-potential measurement for pH 5 was required (indicated by * in **Table 3** below).

Table 3: Zeta-potentials of AuNPs at various pH values, reported in mV ± the standard deviation for each set of measurements.

Nanoparticle Sample	**ζ -potential (mV)**			
	Unmodified pH	**pH 5**	**pH 7**	**pH 9**
As-synthesized	* -43.73 ± 0.87	-43.73 ± 0.87	-41.60 ± 0.12	-53.15 ± 0.40
Washed	* -34.63 ± 0.21	-34.63 ± 0.21	-38.00 ± 1.95	-35.83 ± 0.79
BSA-AuNPs	-6.81 ± 0.46	-0.33 ± 0.08	-19.90 ± 1.45	-0.25 ± 0.33
'Pink' CTAB	* 58.00 ± 8.71	58.00 ± 8.71	38.20 ± 1.27	27.13 ± 0.25
'Purple' CTAB	51.43 ± 2.01	51.20 ± 1.08	37.03 ± 0.93	36.98 ± 1.84
PEG-AuNPs	-27.27 ± 0.55	-31.90 ± 2.76	-51.27 ± 6.05	-0.27 ± 0.14

Light scattering techniques such as DLS are commonly used in the determination of size, colloidal state, polydispersity and zeta potential. Instances where there is high conductivity, the sample concentration is too high or low, or other factors such as large particle size(s) may contribute to sedimentation and overall colloidal instability, the reliability of DLS measurements may decrease, and therefore associated standard deviations tend to increase. Malvern Panalytical report[174] that one can expect a typical standard deviation value to be within approximately 10% of the mean obtained. This value can be expected to become larger, particularly when the zeta potential gets closer to zero (overall decrease in colloidal stability). Therefore, a standard deviation of ~ 2 mV or ~ 10% of the mean (whichever is larger) is typical.[174] Where the standard deviation is reportedly higher, (i.e. in the case of pink CTAB AuNPs at pH 5), it is possible that the high concentration of CTAB crystals in solution increased the overall conductivity of the solution and therefore increased the standard deviation associated with the measurements.

3.7 Scanning Electron Microscopy (SEM) Characterization of AuNPs

3.7.1 SEM of As-synthesized AuNPs

The scanning electron micrographs (**Figure 15** below) are representative of the as-synthesized citrate colloid. From the images, the particles appear to be mostly spherical and approximately 24 nm in diameter.

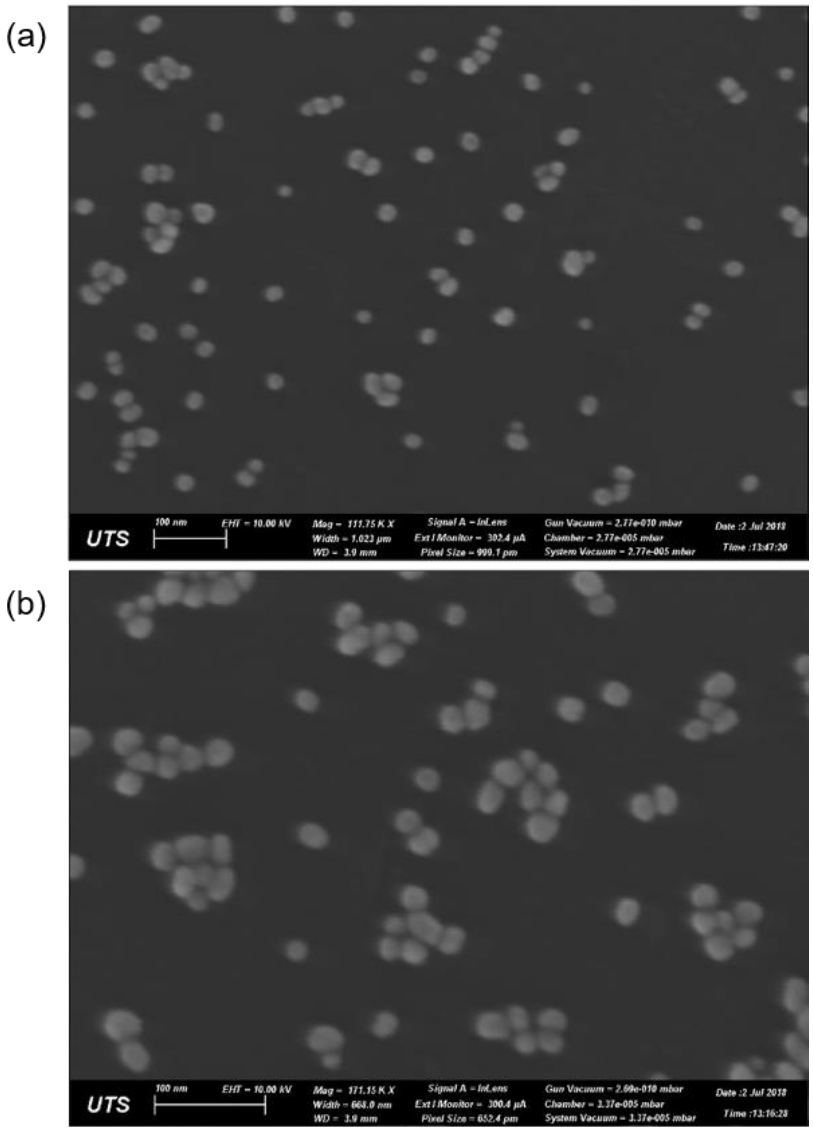

Figure 15: Scanning electron micrographs ((a) and (b)) of as-synthesized citrate AuNPs, representative of colloidal samples used experimentally. Scale bars = 100 nm.

3.7.2 Size Distribution of As-synthesized AuNPs from SEM

The size distribution of the measured as-synthesized citrate AuNPs shows the mean particle size to be ~ 24 nm, with a slight skewedness towards the presence of smaller particle sizes, still within an acceptable range for the Turkevich [20] method (**Figure 16**).

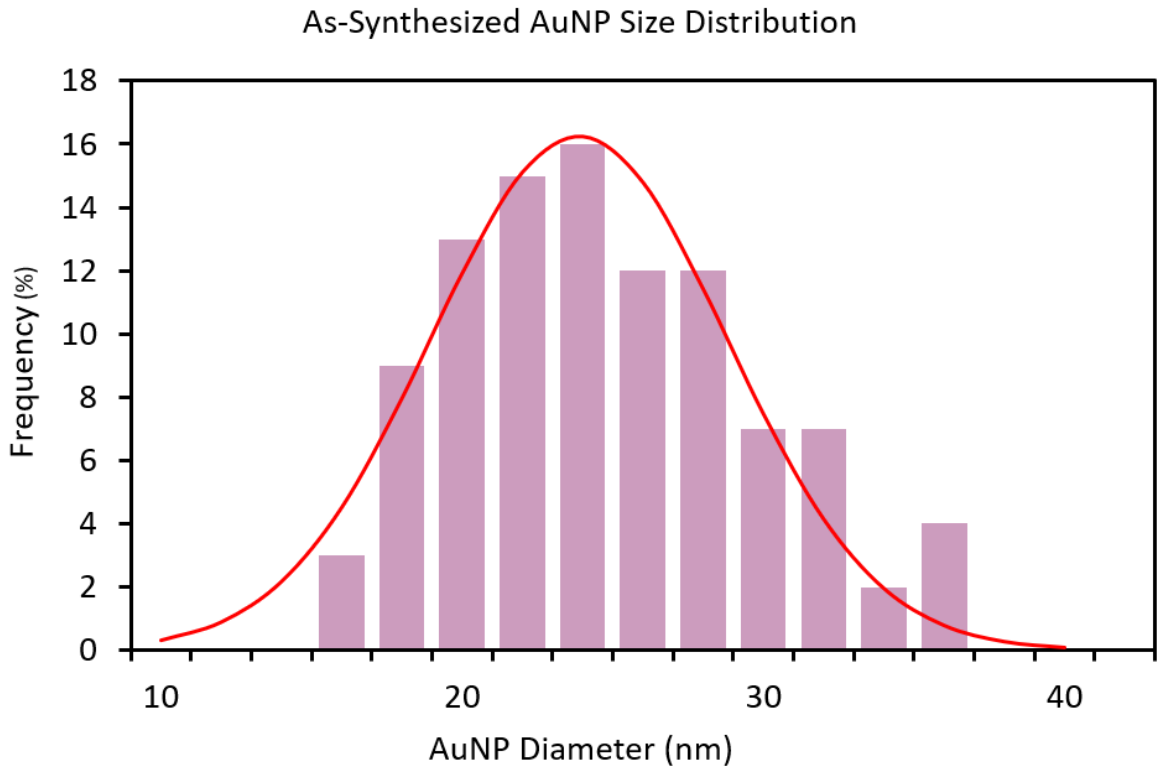

Figure 16: Size distribution histogram of as-synthesized AuNPs, as obtained from the measurements from 100 particles imaged using SEM. Mean particle size (diameter) was determined to be 23.9 nm ± 4.9 nm.

The normal distribution curve (red line) constructed from the measured mean and standard deviation indicates the as-synthesized AuNPs were reasonably normally distributed with respect to their distribution of measured diameters (nm), with a slight skew towards the larger sizes (> 30 nm).

3.8 Transmission Electron Microscopy (TEM) Characterization of AuNPs

3.8.1 TEM of As-synthesized Citrate AuNPs

Transmission electron micrographs of as-synthesized citrate AuNPs were acquired in order to better visualize the size and morphology of the individual particles. As can be seen below (**Figure 17**), the citrate AuNPs are quasi-spherical in shape and display polycrystallinity (as seen in the darker sections of the particles).

(a) (b)

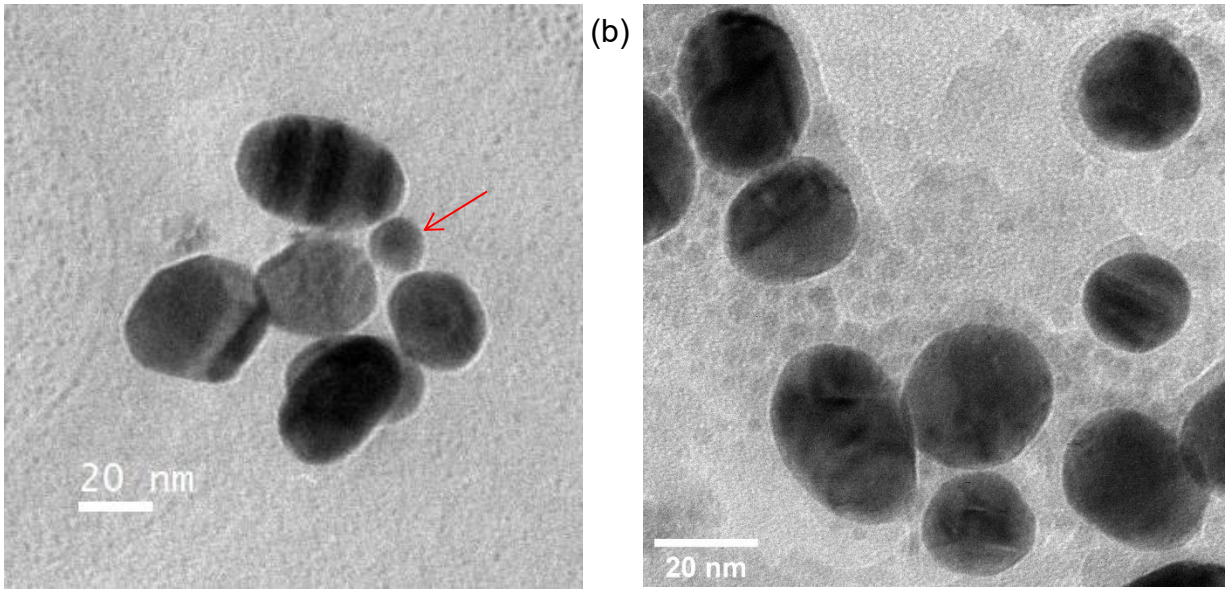

Figure 17: Representative transmission electron micrographs of as-synthesized AuNPs ((a) and (b)).

The presence of the significantly smaller NP (indicated by red arrow in (a)) is not uncommon when using this synthetic route, and has been postulated to be a result of incomplete Ostwald ripening which has been observed at certain molar ratios of citrate: gold chloride during synthesis.[157]

3.8.2 TEM of Washed Citrate AuNPs

Transmission electron microscopy of washed citrate AuNPs was used to visualize the morphology of the particles post removal of the excess citrate capping/stabilising layer. As can be seen below (**Figure 18**), some of the particles have begun to fuse, which may be a result of the reduced amount of surface citrate and therefore lower charge repulsion between the particles. However, this may also be a result of the way the particles have dried on the surface of the TEM grid which can result in aggregation as the solvent (ultra-pure water) evaporates.

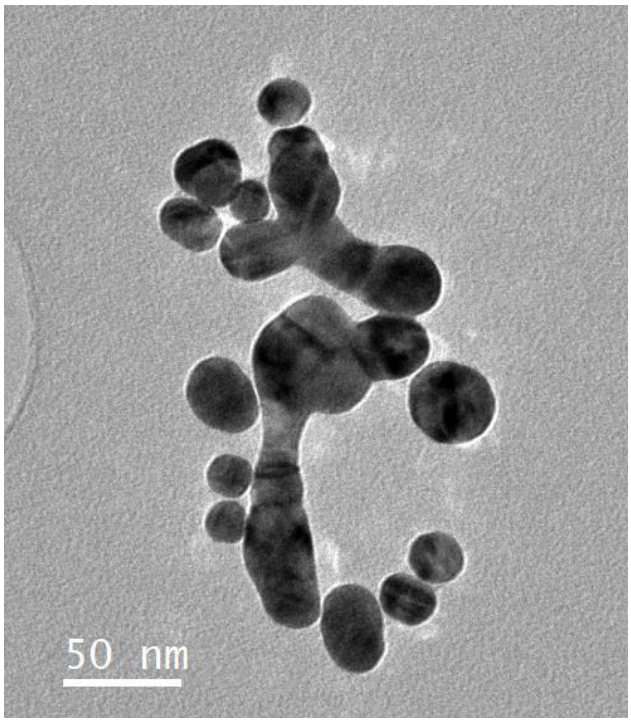

Figure 18: Representative transmission electron micrograph of washed citrate AuNPs.

Although the overall solution remained colloidal, the above image captures an example of small aggregates which may form during the washing process in which the excess citrate capping/stabilising layer is removed, increasing the tendency of the AuNPs to aggregate.

3.8.3 TEM of 'Pink' CTAB AuNPs

Transmission electron micrography of CTAB stabilized 'pink' AuNPs was used to confirm the size and morphology of the synthesized colloid. The resulting particles were found to be predominantly faceted on at least one edge, with the presence of truncated prisms and square shaped AuNPs as opposed to the spherical morphologies observed with citrate AuNPs (compare **Figure 19** below with **Figure 17**).

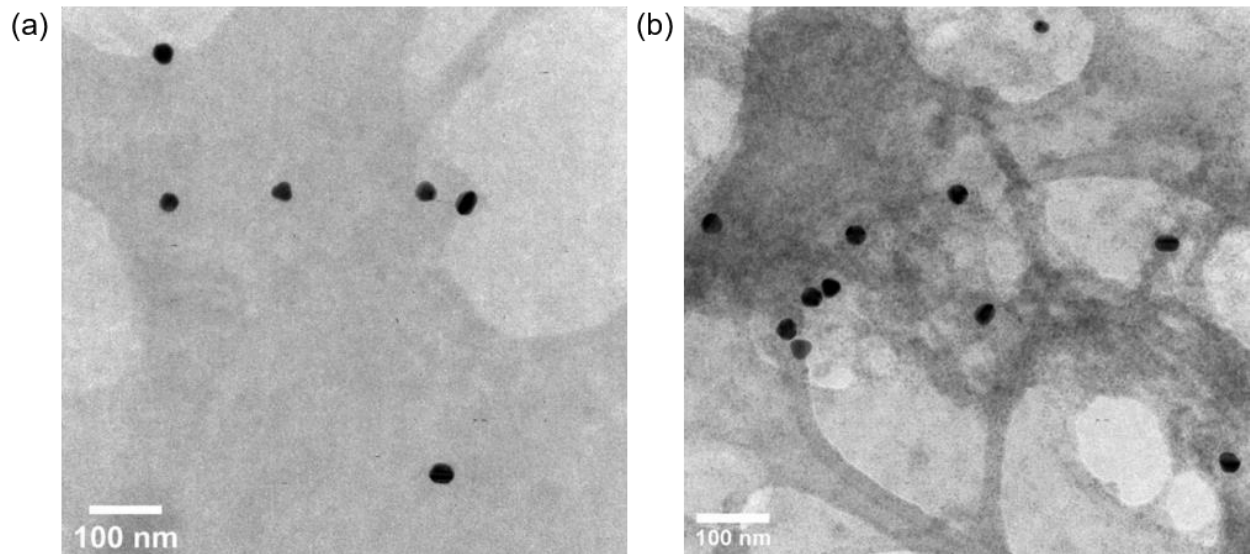

Figure 19: Representative transmission electron micrograph ((a) and (b)) of 'pink' CTAB stabilised AuNPs.

The particles remain very well dispersed, even upon drying. The edges of the majority of particles (> 150) imaged are somewhat faceted, with the presence of some truncated prism- and square shaped AuNPs observed.

3.8.4 Size Distribution of 'Pink' CTAB AuNPs

The size distribution of the 'pink' CTAB AuNPs was determined from the measurement of 173 particles and was found to have a narrower size distribution than the citrate AuNPs synthesized via the Turkevich[20] method. The average particle size was found to be ~ 29 nm with a standard deviation of 3.7 nm (see **Figure 20** below).

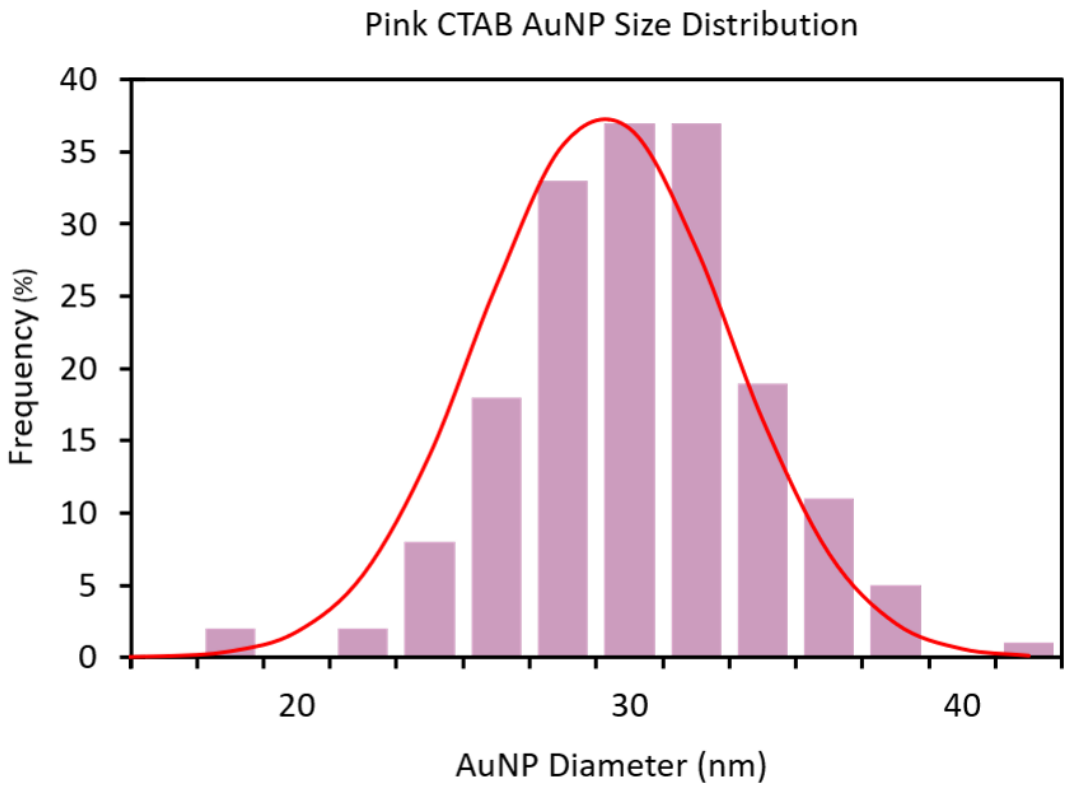

Figure 20: Size distribution histogram of 'pink' CTAB stabilized AuNPs, as determined from the measurement of > 150 particles (n = 173). Mean particle size (diameter) was found to be 29.2 nm $\pm$ 3.7 nm. A 'normal' distrubution is shown in red, but it can be seen that the actual distribution is slightly skewed to larger sizes.

The normal distribution curve (red line) in **Figure 20** above shows the size distribution of the pink CTAB AuNPs is almost symmetrically distributed, with a slight skew towards sizes ≥ 30 nm in diameter.

3.8.5 TEM of AuNPs Synthesized via the Seeded Growth Method 'Purple' CTAB AuNPs (Containing Silver Nitrate)

Transmission electron micrography was used to confirm the size and morphology of the seeded CTAB AuNPs containing silver nitrate. This sample, while colloidal, was significantly more polydisperse than those previously synthesized and characterized. The majority of particles imaged were anisotropic, featuring multiple shapes and faceted edges (**Figure 21**).

(a) (b)

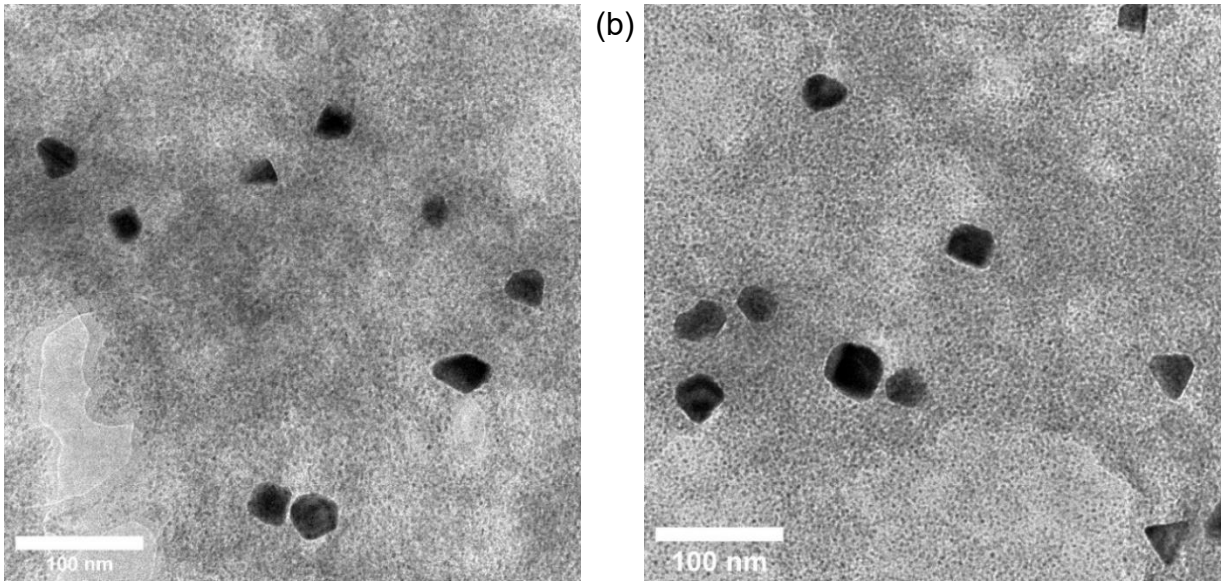

Figure 21: Representative transmission electron micrographs ((a) and (b)) of AuNPs synthesized via the seeded growth method and stabilized with CTAB.

The AuNPs remain well-dispersed, however they are fairly polydisperse and anisotropic, featuring multiple shapes with the majority of particles observed presenting faceted edges – more so compared to the 'pink' CTAB AuNPs.

3.8.6 Size Distribution of AuNPs (Seeded Growth Method) – 'Purple' CTAB AuNPs

The size distribution of the seeded CTAB AuNPs containing silver nitrate was determined from a measurement of 168 particles. The colloid was determined to have a mean particle diameter of ~ 34 nm with a standard deviation of 5.5 nm (see **Figure 22** below).

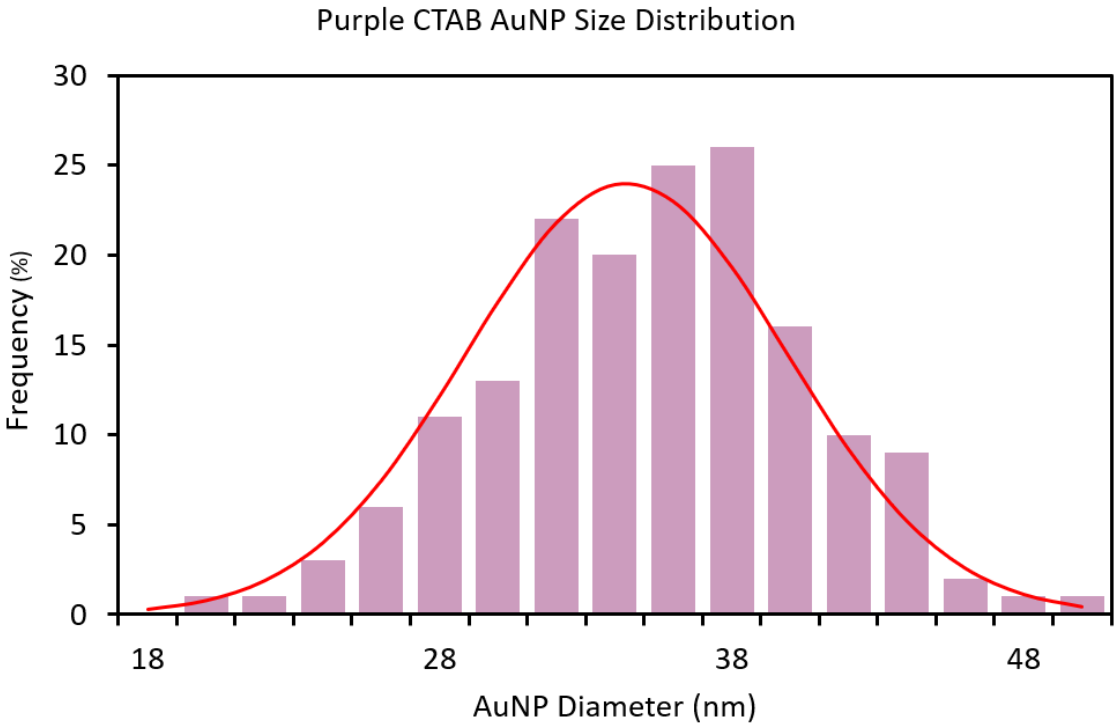

Figure 22: Size distribution histogram of AuNPs synthesized via the seeded growth method, containing silver nitrate, as determined from the measurement of > 150 particles (n = 168). Mean particle size (diameter) was determined to be 34.4 nm $\pm$ 5.5 nm. The resulting AuNPs appeared purple to the naked eye.

The purple CTAB AuNPs have a wider range of particle sizes, although the mean size was only ~ 5 nm larger compared to the pink CTAB AuNPs. The distribution of the purple CTAB AuNPs is similarly fairly symmetrical, following the red normal distribution curve to a good approximation, with a slight skew towards particles of 38 nm in diameter.

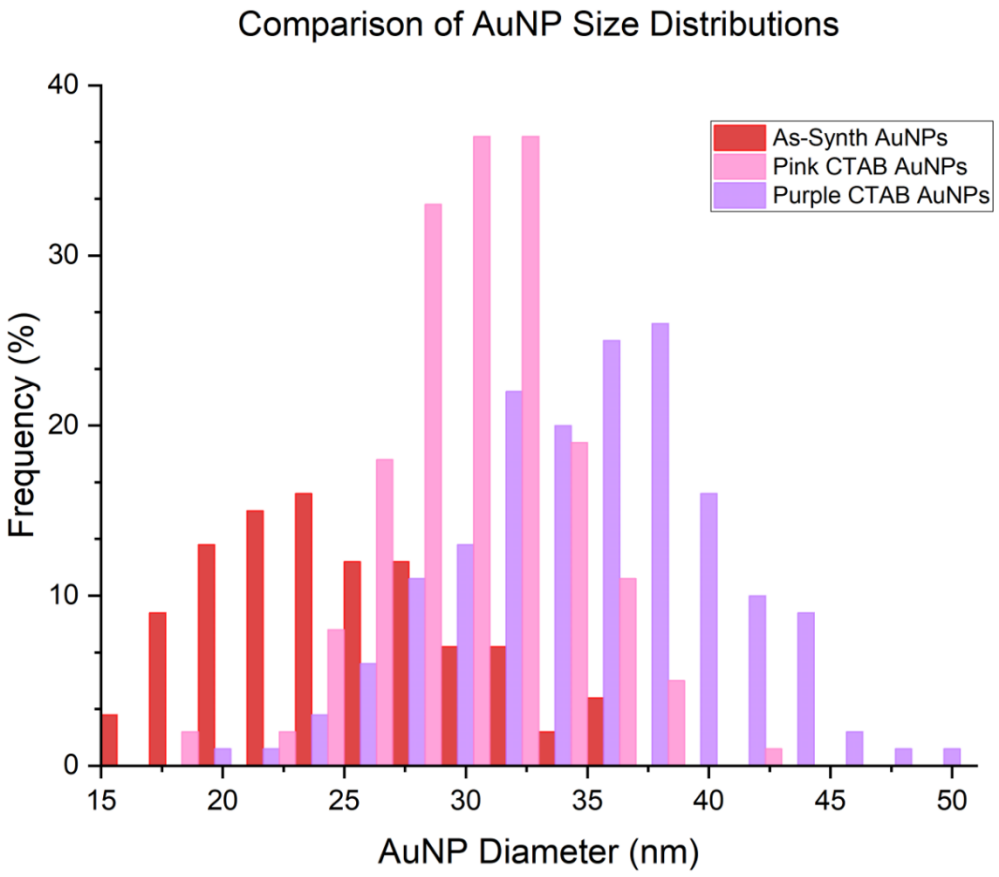

Figure 23: Comparison of the relative size (diameter, nm) distributions for the as-synthesized AuNPs (red bars), pink CTAB AuNPs (pink bars) and purple CTAB AuNPs (purple bars).

Direct, side-by-side comparison of the different AuNP preparations by size distributions readily highlights the effect the synthetic route has on the spread of the resulting AuNP sizes. Particularly when comparing the pink and purple CTAB AuNP distributions. The purple CTAB AuNPs have a much larger particle size distribution (higher polydispersity) while the pink CTAB AuNPs are much more tightly clustered around their mean diameter. The key difference between their synthesis was the use of silver nitrate ($AgNO_3$) in the case of the purple CTAB AuNPs; $AgNO_3$ has been demonstrated to affect and partially direct the growth of Au nanostructures, dictating the size at which the Au seed undergoes symmetry breaking.[175] However, higher (relative to $HAuCl_4$) concentrations of $AgNO_3$ have been shown to result in larger sized particles with higher aspect ratios.[176] Any contamination present within the system, or lack of control thermodynamically or kinetically (i.e. addition of reagents not timed

correctly), and the resulting size distribution and shapes of the colloid may be drastically affected.[175-177]

3.8.7 TEM of BSA, Thiol-PEG-COOH and Antibody Conjugated AuNPs

Due to the highly carbonaceous nature and the 'lightness' of the elements comprising BSA, thiol-PEG-COOH and antibodies, it is not possible to effectively visualize these structures using TEM unless a low voltage (such as 80 – 120 kV) and/or a negative stain is first applied.[178] Negative staining involves the application of a heavy-metal containing salt to the specimen to be imaged, allowing an electron image to be generated by the differential scattering of electrons caused by the significant difference in density and thickness of the specimen and the stain.[179] As such, it was determined to be more appropriate to monitor the conjugation of BSA, thiol-PEG-COOH and anti-LPS antibodies through UV-vis spectrometry and DLS (zeta potential and size measurements).

3.9 Summary, Conclusions and Discussion

Within the present chapter I have used a relatively uncommon procedure to synthesize precise concentrations of $HAuCl_4$ stock solution that was then used to produce gold nanoparticles by a variety of means. These included the Turkevich[20] method, employing sodium citrate as both the reducing agent and surfactant to provide stability for the resulting NPs, as well as seeded growth methods (with and without the addition of $AgNO_3$) where ascorbic acid acted as the reductant and CTAB induced the growth of the resulting NPs, spatially controlling the oxidation of gold ions and crystal growth, finally acting as the stabilising surfactant.[180]

AuNPs synthesized via the Turkevich method were 24 nm in diameter, quasi-spherical in shape, had a single LSPR at 527 nm and a net negative ζ-potential ~ 40 mV (slightly less negative for washed AuNPs), appearing a deep red colour to the naked eye. In contrast, the AuNPs produced using ascorbic acid and CTAB in the absence of $AgNO_3$ were 29 nm in diameter, quasi-spherical, with the majority of particles having at least one faceted edge. These particles appeared pink to the naked eye and had a positive

ζ-potential of 58 mV, owing to the cationic stabilising surfactant, CTAB. When AuNPs were synthesized via the seeded growth method using ascorbic acid and CTAB *in* the presence of $AgNO_3$, the resulting particles were 34 nm in diameter with more polydispersity observed within the imaged samples. There was a single LSPR observed at 549 nm, resulting in a colloidal solution that appeared purple to the naked eye and the sample had a positive ζ-potential of 51.2 mV.

BSA-AuNPs were found to have a single LSPR at 531 nm, a slightly deeper red colour when compared to as-synthesized citrate AuNPs and a less negative ζ-potential of -12 mV. Thiol-PEG-COOH-AuNPs had a single LSPR at 529 nm and similarly presented with a slightly deeper colour when compared to as-synthesized AuNPs. In contrast to the BSA-AuNPs, the thiol-PEG-COOH-AuNPs were closer in ζ-potential to citrate AuNPs, likely owing to the carboxylic (charged) end of the PEG moiety. Lastly, the antibody-thiol-PEG-COOH-AuNPs had a single, broad and slightly dampened LSPR at 538 nm and displayed a deeper red colour which was comparable to the as-synthesized citrate AuNPs.

Investigation of the zeta-potential in relation to colloidal stability and pH was pursued as it has been previously demonstrated that modification of the colloidal pH plays an often-overlooked role in AuNP stability and functionalization. In the case of citrate AuNPs, the pH of the colloid determines how protonated or deprotonated the stabilizing citrate moieties are; citric acid has three acidic functional (-COOH) groups that are able to coordinate with the gold, however, the conformation of the adsorbed citrate (and therefore, the 'strength' of the coordination with the gold surface) varies with pH. It has been hypothesized that the citrate is best able to stabilize colloidal AuNPs when in the fully deprotonated form. In contrast, when the citrate is partially or fully protonated, there are less charged $-COO^-$ groups available to coordinate with, and stabilize the AuNPs, making them more susceptible to competition from species other than citrate, potentially leading to destabilization and/or aggregation.[61] The relationship between pH and colloidal stability is closely related to the pK_a (or pK_b) value(s) of the AuNP capping moieties, and can be predicted/monitored with the Henderson-Hasselbach equation.[62]

Modification of the pH of colloidal AuNP solutions not only influences the ratio of protonated: deprotonated stabilizing moieties, it has also been shown to influence the binding and packing of more complex species and biomolecules to the surface of AuNPs. This can include the folding of proteins or peptides as well as the formation of monolayers and chemical switching of film morphologies on the surface of Au, ultimately influencing the binding and packing of these complexes to the Au surfaces.[181]

Some of the types of AuNPs that were synthesized and further functionalised were subsequently found to be less suitable as the basis for a sensing platform. These included citrate AuNPs that had been conjugated with BSA, thiol-PEG-COOH and the CTAB-stabilised AuNPs. In general, the citrate AuNPs that were additionally functionalised, displayed greater stability in higher ionic strength conditions; for example, a greater amount of NaCl solution was required to cause aggregation of the colloids. I will later briefly show, however, that the colloidal stability of these types of particles was disadvantageous from the perspective of detecting bacteria.

Although the use of antibodies has been reported to afford greater selectivity and sensitivity in relation to the specific targeting and binding to target organisms/analytes of interest,[32, 98-101, 170, 172] the associated high costs, limited shelf-life, and specific (low temperature) storage requirements, ultimately make their incorporation into the design of the present sensor a limitation. The work described in this chapter confirmed the distinct advantages of using Turkevich-route AuNPs where feasible. Ultimately, the use of antibody-conjugated AuNPs was not pursued beyond this chapter of work, with the goal of developing a label-free, aggregation-based AuNP sensor, with lower costs, ease of synthesis and design, longer shelf-life and potentially broader applications.

Having synthesized and characterised a range of AuNPs, I will now proceed to describe how they interact with batch cultures of *Escherichia coli* (*E. coli*) in the following chapters.

Chapter 4:

Gold Nanoparticle & Live *Escherichia coli* Experiments

4.1 General

The following Chapter provides detailed information on the techniques applied in this project for the growth and assaying of live bacteria with gold nanoparticles. For detailed information regarding the synthesis and characterization of gold nanoparticles used, see Chapter 3.

4.2 Introduction

Currently, there are discrepancies within the literature pertaining to how AuNPs interact with bacteria, owing to the vast number of key differences/variables within the tested systems. Briefly, it has not yet been unambiguously established whether, and how AuNPs bind to the surfaces of Gram-negative bacteria; i.e. do they always bind to the surfaces of the bacteria, or if it is only under certain circumstances, what are the controlling factors behind this interaction. For further details, see Chapter 2, Section 10 (and 10.1 with particular reference to the interaction of AuNPs with *E. coli*). The experimental work within this Chapter seeks to document the (optical) interactions between spherical citrate stabilised, 24 nm AuNPs and *Escherichia coli* in a non-selective, nutrient-dense culture medium, Luria-Bertani (LB) broth. This knowledge will be essential for developing an AuNP-based sensor technology for (Gram-negative) bacteria.

In order to establish a sensor platform, the baseline interactions of the AuNPs within the system must first be established rigorously – i.e. calibrated against a range of known concentrations of live *E. coli*. Herein, the prepared bacterial stock solutions were serially diluted to attain a concentration range of between approximately 5×10^7 and 5×10^0 CFU/mL. The resulting optical interactions of these samples with as-synthesized and washed AuNPs were monitored via UV-vis spectroscopy over time with the following objectives:

- to monitor the evolution of the optical parameters within the system over time
- to determine if incorporation of AuNPs into the system provides a means to amplify the signal(s) useful for sensing

- to gain an understanding of how the *in situ* growth of *E. coli* affects the measurable signal of the AuNPs
- to find the optimum time required for the sensor

4.3 Experimental Design and Methods

4.3.1 Chemicals and Materials

The following chemicals and materials were used as purchased, without further purification, as per the methods in subsequent sections: tryptone, yeast extract, NaCl, and agar (Sigma Aldrich), ethanol (70%) (Chem Supply). *Escherichia coli* BL21 (DE3) (New England Biolabs, Inc.). For all other chemicals and materials, refer Chapter 3, Section 3.1.

4.3.2 Preparation for Bacterial Culturing

All solid Luria-Bertani (LB) agar plates were prepared by pouring a small amount of hot, liquid LB-agar (10 g tryptone, 5 g yeast extract, 10 g NaCl, 15 g agar to 1 L of water, autoclaved) into sterile petri dishes in a Class II laminar flow cabinet (Biology Safety Cabinet; BSC). The LB-agar was allowed to cool and set before lids were placed on the dishes and they were stored inverted at 4°C until required.

The BSC was sterilised before and after each use by cleaning the surfaces with 70% ethanol, followed by 15 – 20 minutes of UV light exposure. The laminar flow in the BSC ensures no aerosols generated within the cabinet are released into the immediate environment as well as maintaining sterility of materials within the cabinet by filtering incoming air-flow.

For liquid cultures, Luria-Bertani (LB) broth (10 g tryptone, 5 g yeast extract, 10 g NaCl to 1 L of water, autoclaved) was used under sterile conditions.

4.3.3 Culturing of *Escherichia coli*

Escherichia coli BL21 (DE3) Competent cells (New England Biolabs, Inc.) were grown from a frozen glycerol stock by gently touching a sterile inoculation loop onto the surface of the glycerol stock before introducing the inoculation loop into 2 – 3 mL of sterile LB broth and stirring vigorously. The resulting broth was incubated overnight in a lateral shaking incubator at 37°C and 200 rpm.

4.3.4 Preparation of Live *E. coli* for Assays

Working solutions of *E. coli* broth were first prepared by incubating a single colony of *E. coli* in sterile LB overnight and adjusting the optical density at 600 nm (OD_{600}) to 0.1 which is approximately 5 x 10^7 cells/mL (live *E. coli* working solution).[74, 182]

4.3.5 Live *E. coli* and Gold Nanoparticle Assays

To a 96-well plate, 100 µL of *E. coli* working solution was added to the top well and serially diluted down the column from A – H from ~ 5 x 10^7 – 5 cells/mL, using either MQ or sterile LB. Where lanes are diluted with MQ, the initial aliquot of bacterial working solution is in LB, therefore the amount of LB is also serially diluted in each well. To each well, 100 µL of AuNPs were added. Control wells consisted of either 100 µL of sterile LB or MQ in place of *E. coli* working solutions, to which 100 µL of AuNPs were then added. The resulting absorbance spectra were subsequently measured and recorded using a Tecan i-control infinite 200Pro from either 450 – 800 nm or 400 – 1000 nm in 1 nm increments.

4.3.6 Concentration of Gold Nanoparticles Used in Assays

Control spectra of experimentally used preparations/aliquots of as-synthesized and washed AuNPs were used to determine the concentrations for both colloids. For the calculations, it was assumed all particles were 24 nm in diameter (mean size), the Q_{ext} in water was calculated using the λ_{spr} from control spectral and used in conjunction with the starting concentration of Au (g/L) to calculate the number of particles/m^3.

The resulting concentrations (in particles/m^3) for both the as-synthesized and washed AuNPs were cross-checked with the results obtained using the method outlined in the work of Haiss et al.[183] and were in perfect agreement.

Table 4: Concentration of As-Synthesized and Washed AuNPs used in assays, reported with respect to concentration of gold in g/L and g/100 µL, as well as particles/m^3 and particles/100 µL.

	As-Synthesized AuNPs	**Washed AuNPs**
Conc. Au (g/L)	0.0616	0.0346
Conc. Au (g/100 µL)	6.16×10^{-6}	3.46×10^{-6}
Conc. (particles/m^3)	4.24×10^{17}	2.49×10^{17}
Conc. (particles/100 µL)	4.24×10^{10}	2.49×10^{10}

Washing AuNPs through centrifugation and resuspension of the AuNP pellet results in a loss of a small proportion of AuNPs that remain in the discarded supernatant. These are often (relatively) smaller AuNPs that remain suspended, as using sufficient centrifugal speeds or forces to completely pellet the AuNPs can destabilise the colloid and lead to aggregation and an inability to fully resuspend the pelleted particles.

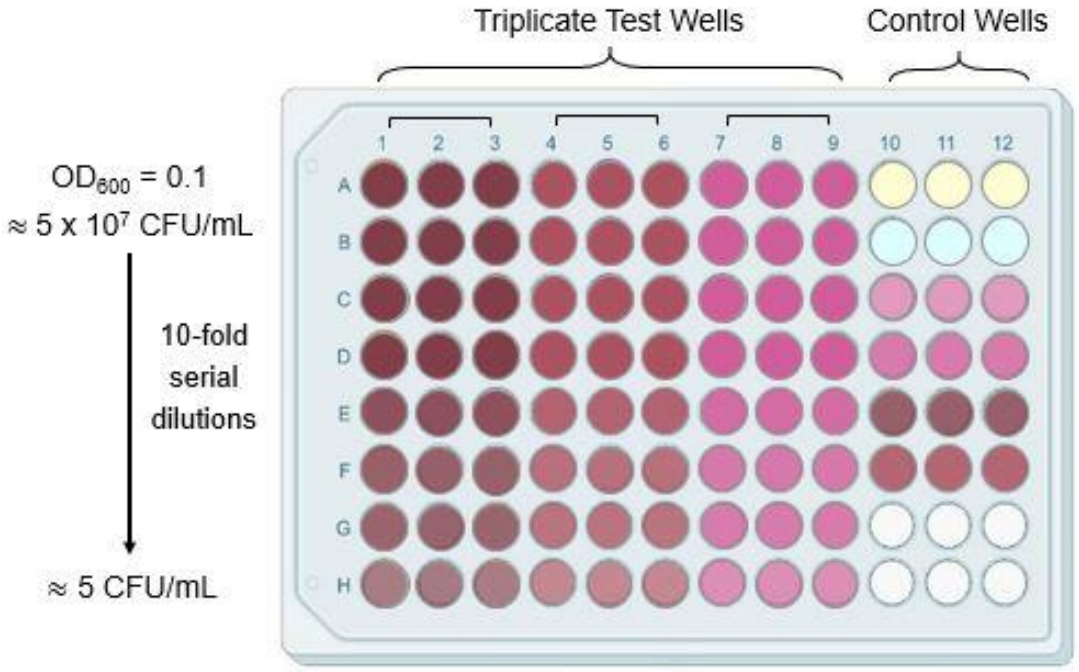

Figure 24: Schematic of the general set-up of an *E. coli* and AuNP assay in a 96-well plate. Each serial dilution is prepared in triplicate (n = 3) and all resulting spectra are the average of triplicate scans.

4.4 Results

4.4.1 Optical Spectra of Gold Nanoparticle and *E. coli* Interactions

The following section contains data from the assays of AuNPs with live *E. coli.* The live *E. coli* working solutions were prepared according to the procedure outlined in Section 4.3 of the current Chapter. Results were recorded immediately post assay and again after an overnight incubation at ambient temperature. Assays were performed with as-synthesized and washed AuNP preparations in both MQ and LB.

Prior to presenting the resulting UV-vis spectra arising from the interactions between the live *E. coli* and the AuNPs they were assayed with, I will first show the optical contributions from the live *E. coli* in LB only.

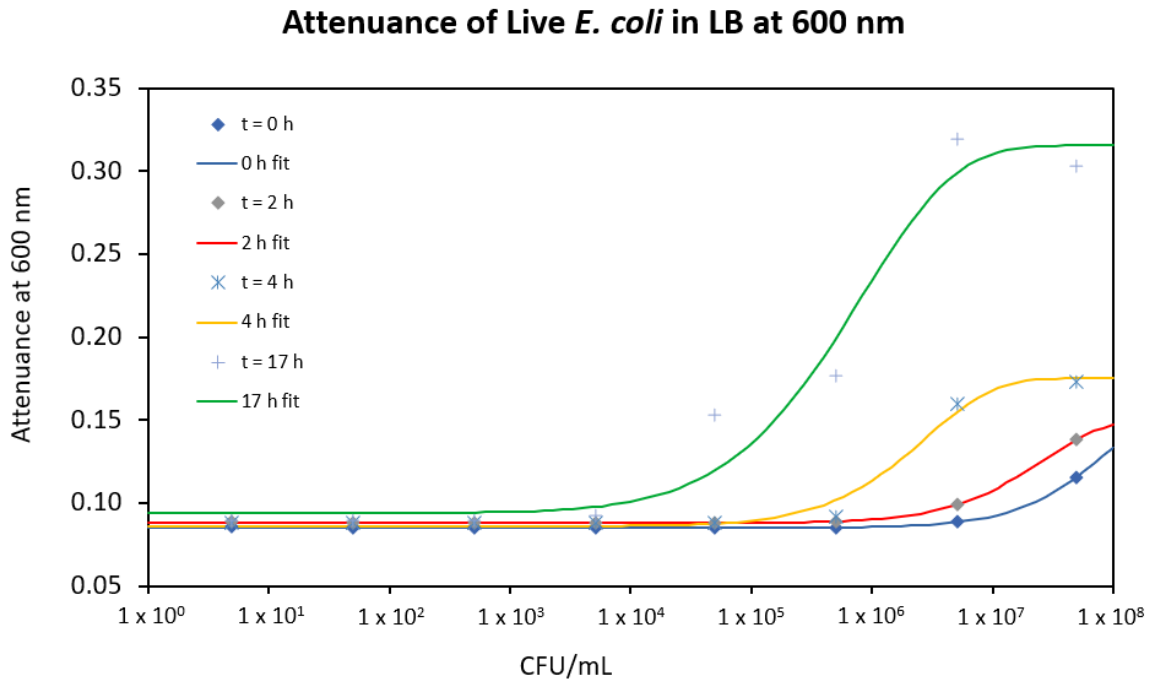

Figure 25: Attenuance of live *E. coli* in LB, measured at 600 nm over time, plotted against starting bacterial concentration (CFU/mL). Data points are the average of triplicate scans.

As demonstrated in **Figure 25** above, in general, the greater the starting concentration of the bacteria (CFU/mL), the faster the turbidity of the sample aliquot increased. This can be attributed to the growth of the live bacteria within the sample, increasing the turbidity of the medium. It is important to note however, that starting concentrations below ~ 1 x 10^4 CFU/mL contained too few bacteria to produce a measurable effect on the attenuance within 17 h of incubation at ambient temperature. Given the abundance of nutrients available to the bacteria and the observed growth trends, there is little doubt that the turbidity of these samples would have eventually increased given sufficient incubation times (> 17 h).

4.4.1.1 As-Synthesized Citrate AuNP and *E. coli* Assays

Assays containing as-synthesized citrate AuNPs and *E. coli* were performed and the absorbance spectra were collected immediately post assay (t = 0). Subsequently, the closed 96-well plates were left to incubate overnight (ambient temperature) prior to

measuring their absorbance spectra again to observe any changes in aggregation over time. Similarly, each of the resulting spectra are the average of triplicate scans.

Each serial dilution of *E. coli* was prepared separately, using a single-channel micro-pipette, in triplicate, prior to the addition of AuNPs. Subsequently, each of the presented optical spectra are the average of triplicate scans.

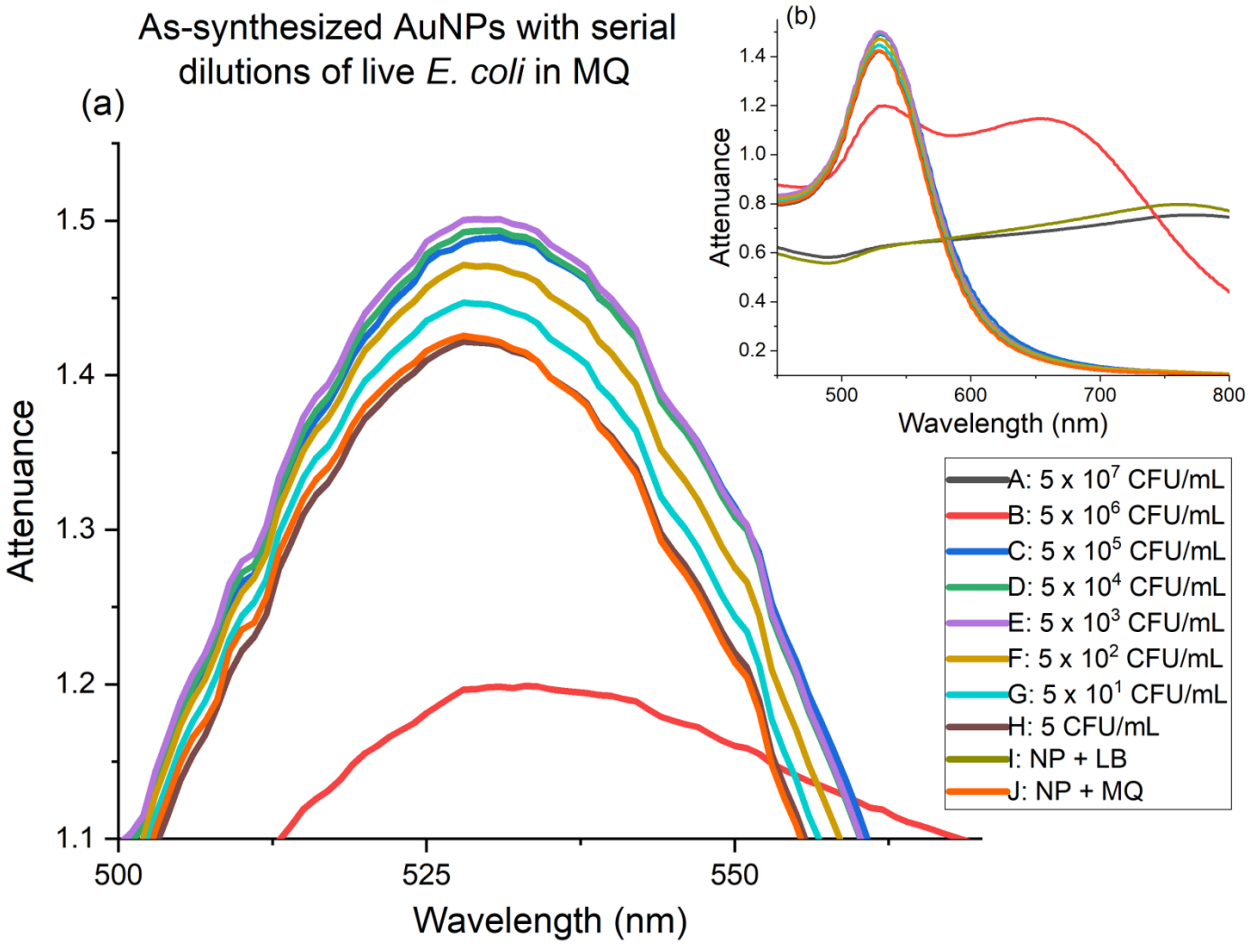

Figure 26: UV-vis spectra of as-synthesized citrate AuNPs assayed with serial dilutions of live *E. coli* in MQ and measured immediately post assay; (a) shows a close-up region of the relative positions of the LSPR peaks, and inset (b) shows the spectra over the entire range of monitored wavelengths (nm).

There are significant levels of aggregation within the NP + LB control (I, army green line) very similar to the sample containing the highest concentration (5 x 10^7 CFU/mL) of live *E. coli* (A, black line). The sample containing 5 x 10^6 CFU/mL (B, red line) presents an interesting second, red-shifted aggregation peak, while the original LSPR

peak has dampened and broadened when compared to the lower concentrations of live bacteria tested. Of particular note is that the 5 CFU/mL sample (H, dark brown line) appeared almost identical to that of the NP + MQ control (J, orange line). This suggests that the as-synthesized AuNPs at the tested concentration cannot readily be used to differentiate between 5 CFU/mL and MQ (negative control).

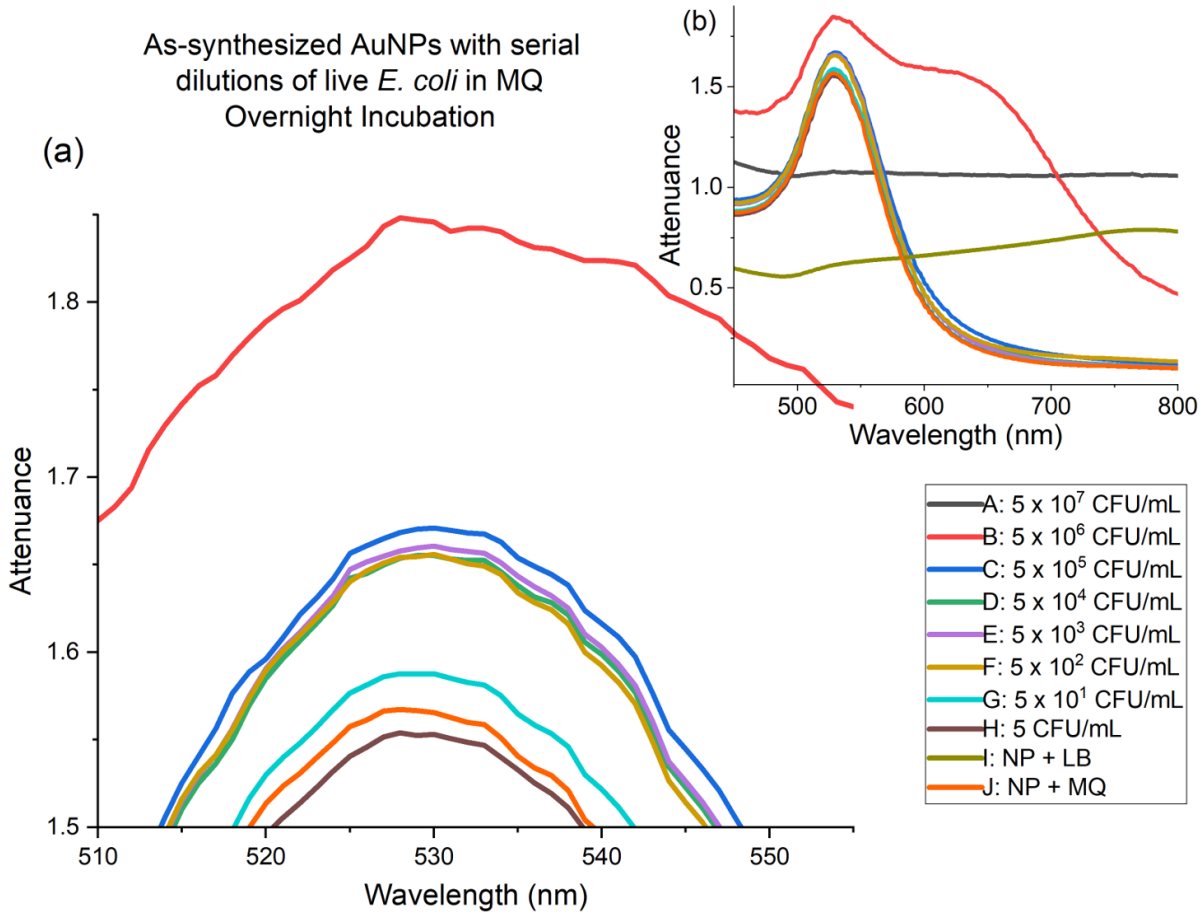

Figure 27: UV-vis spectra of as-synthesized citrate AuNPs assayed with serial dilutions of live *E. coli* in MQ and measured after overnight incubation at room temperature; (a) shows a close-up region of the relative positions of the LSPR peaks, and inset (b) shows the spectra over the entire range of monitored wavelengths (nm).

After overnight incubation of the as-synthesized AuNPs and live *E. coli* in MQ, there was an evolution of the UV-vis spectra whereby the overall attenuance of the samples increased, and the LSPR peaks broadened (**Figure 27** above). This indicates that the live *E. coli* were able to proliferate within the system (i.e. in the presence of as-synthesized AuNPs + MQ, ambient temperature) within the timeframe monitored. In

the case of concentrations ≤ 5 x 10^5 CFU/mL (C, dark blue line), the proliferation of *E. coli* was insufficient to cause enough aggregation of the colloid to induce a second red-shifted plasmon peak.

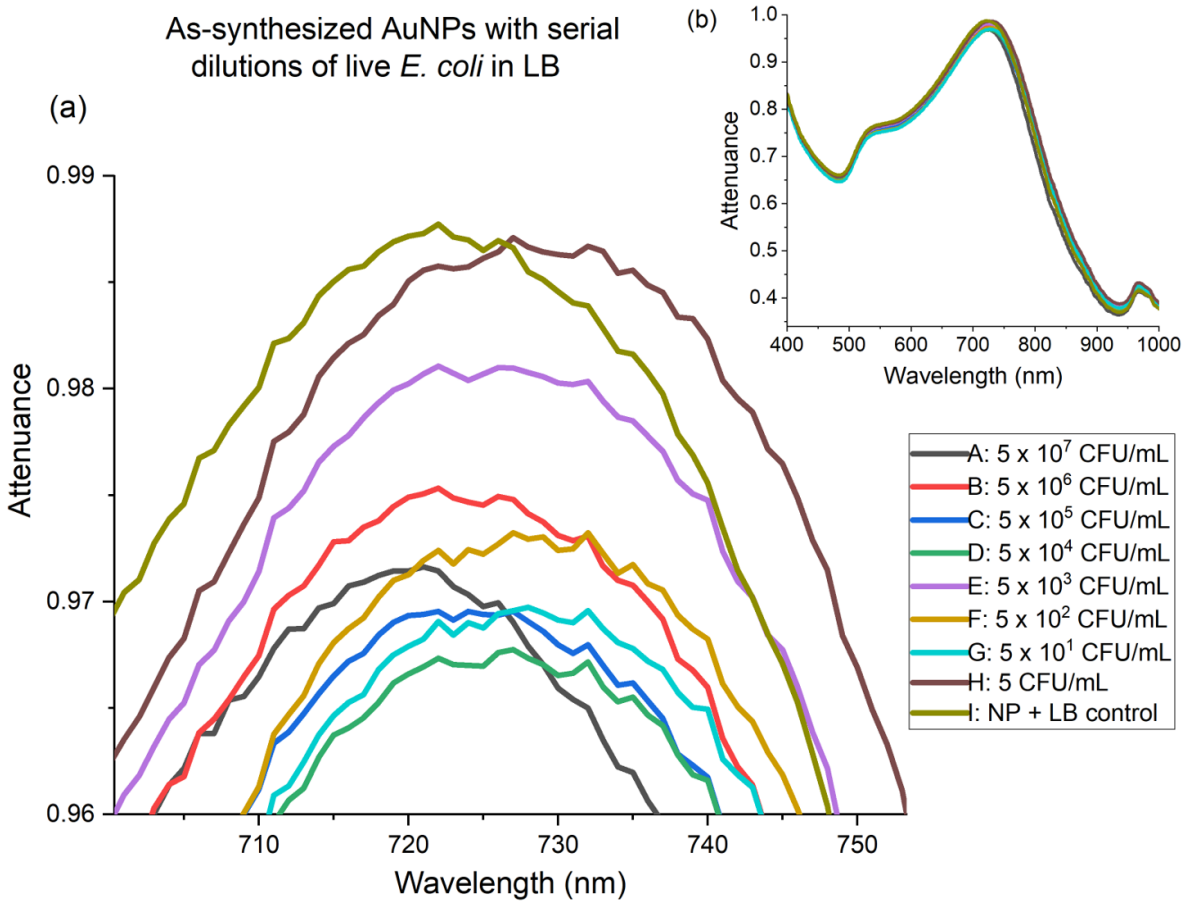

Figure 28: UV-vis spectra of as-synthesized citrate AuNPs assayed with serial dilutions of live *E. coli* in LB and measured immediately post assay; (a) shows a close-up region of the relative positions of the red-shifted plasmon peaks, and inset (b) shows the spectra over the entire range of monitored wavelengths (nm).

As-synthesized AuNPs assayed with serial dilutions of live *E. coli* in LB resulted in UV-vis spectra with two distinct plasmon peaks (**Figure 28**); the initial LSPR (from the colloidal gold) that became dampened, broadened and slightly red-shifted to ~ 535 nm, as well as the appearance of an additional further red-shifted 'aggregation' peak ~ 725 nm. The initial assay did not show significant differences between the different concentrations of bacteria assayed with the AuNPs, suggesting an incubation period may be necessary for differentiation.

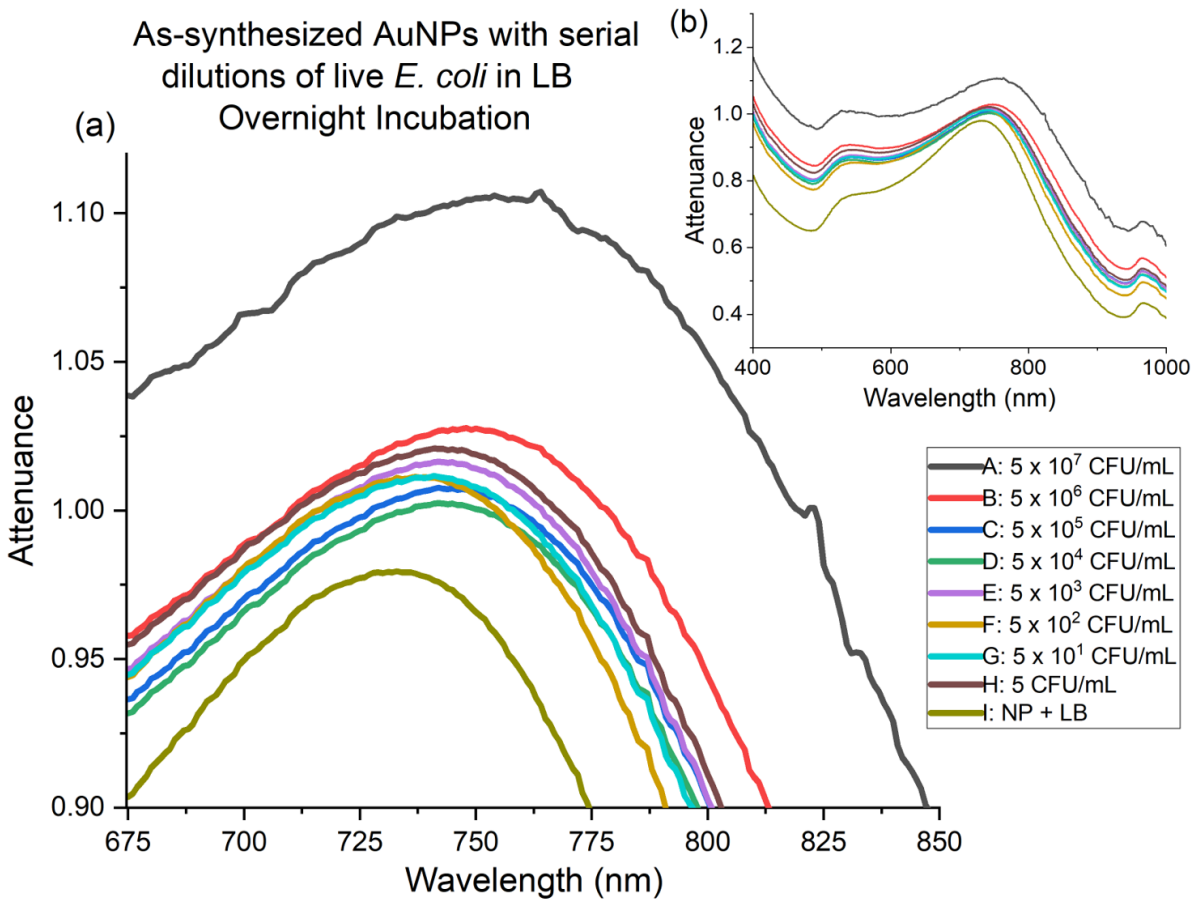

Figure 29: UV-vis spectra of as-synthesized citrate AuNPs assayed with serial dilutions of live *E. coli* in LB and measured after overnight incubation at ambient temperature; (a) shows a close-up region of the relative positions of the red-shifted plasmon peaks, and inset (b) shows the spectra over the entire range of monitored wavelengths (nm).

After overnight incubation of as-synthesized AuNPs with live *E. coli* in LB, a (relatively higher, compared to MQ) increase in attenuance, peak broadening and red-shifting was observed for all concentrations of *E. coli* tested (compare **Figure 29** with **Figure 27**). This indicates that the *E. coli* was able to proliferate within the system (as-synthesized AuNPs + LB, ambient temperature) and affect a measurable change to the colloidal AuNPs. There are only very slight differences in the attenuance and second peak position of all tested concentrations of bacteria ≤ 5 x 10^5 CFU/mL. This suggests that the as-synthesized AuNPs are not sensitive enough to the system to be able to distinguish between the lower bacterial concentrations, and/or the overnight incubation may not be the optimum length of time.

When comparing the UV-vis spectra resulting from the assays of the as-synthesized AuNPs with live *E. coli* in MQ, and those in LB, the control spectra (NP + LB) allude to difference in (age-related) stability of the AuNPs. All conditions and variables (except those deliberately varied) were kept consistent, with the MQ assays being performed when the AuNPs were comparatively 'fresh'. This is reflected in the rapid aggregation of the colloid and loss of the LSPR peak ~ 527 nm. This level of aggregation was not observed in the NP + LB controls in assays using comparatively aged AuNPs (i.e. assays in LB), as evidenced by the residual, albeit dampened and red-shifted LSPR at ~ 530 nm, in addition to the appearance of the strongly red-shifted aggregation peak ~ 750 nm.

4.4.1.2 Washed Citrate AuNP and *E. coli* Assays

The assays that were conducted with as-synthesized citrate AuNPs were repeated with washed citrate AuNPs, i.e. citrate AuNPs that were subjected to two cycles of washing and resuspension in MQ (see Chapter 3, Section 3.3) in order to remove excess surface associated citrate that may affect electrostatic interactions between the AuNPs and bacteria. By removing excess surface-associated citrate, the AuNPs become more susceptible to aggregation that may lead to increased instability in certain systems, however this may be favourable in some circumstances where the desired aggregation of AuNPs (as a detection mechanism) is beneficial.

The role of citrate can be thought of as threefold: it acts as a reducing agent, enabling the formation of the AuNPs via reduction aqueous Au^{3+} to Au^{0}, a pH regulator throughout this process, and stabilising agent through imparting electrostatic repulsions between particles. However, an excess of citrate can compete for the surface of the AuNPs, impeding subsequent chemistries applied to the colloid or even lowering their sensing capabilities.[26, 167, 184] Reducing the amount of surface-associated citrate has been demonstrated to improve the reliability and reproducibility of subsequent functionalization of citrate AuNPs,[167] therefore washing of the as-synthesized AuNPs was conducted prior to (some) assays to assess whether reducing the surface-associated citrate was beneficial in this context.

It is of note that the concentration of the washed AuNPs is significantly less than that of the as-synthesized AuNPs used experimentally (in both g of Au/L and particles/m^3). This is for a few reasons: there are additional steps involved in the preparation of the washed AuNPs, making it imperative to conserve the amount of colloid used; the washing of the AuNPs results in a net loss of Au from the colloid, and the washed AuNPs were more sensitive to aggregation, therefore the rationale was a less concentrated colloid would still result in the desired aggregation.

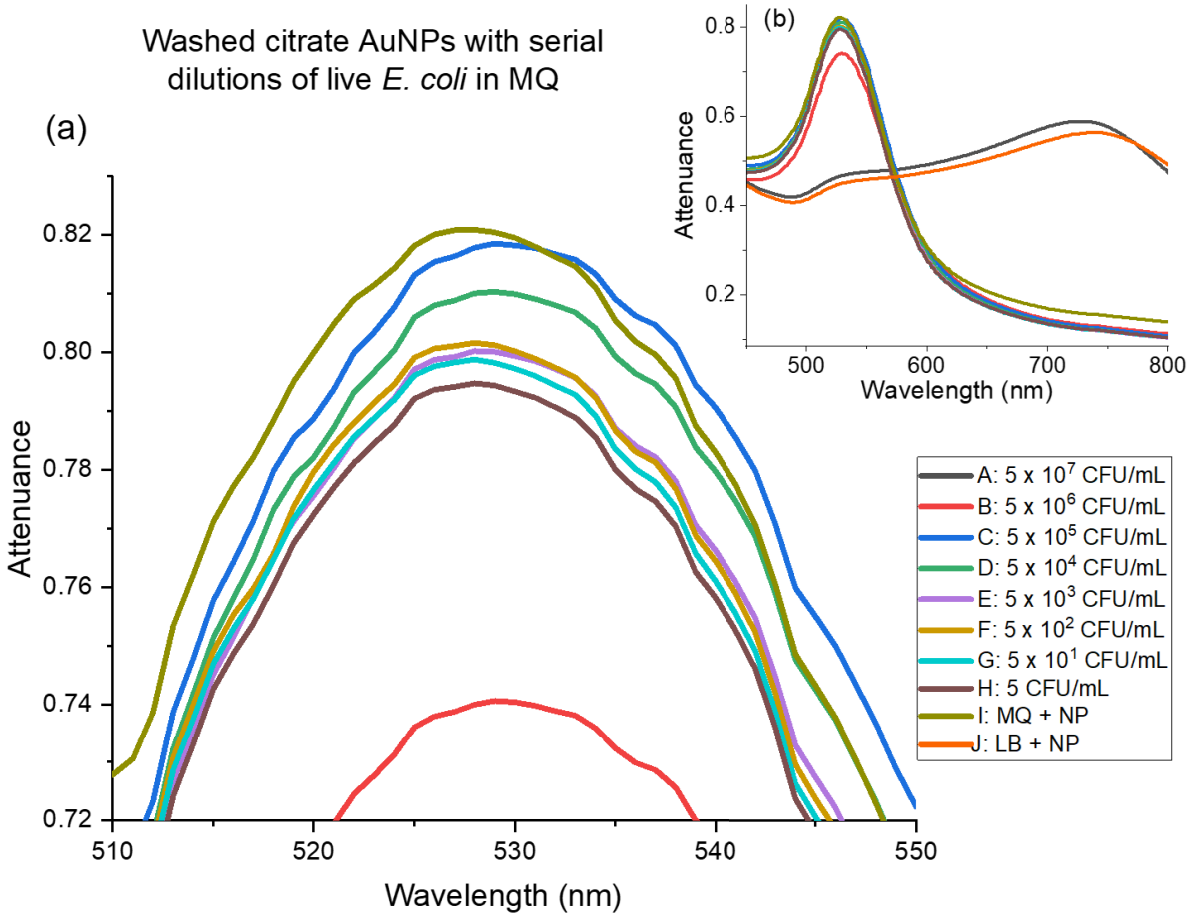

Figure 30: UV-vis spectra of washed citrate AuNPs assayed with serial dilutions of live *E. coli* in MQ and measured immediately post assay; (a) shows a close-up region of the relative positions of the LSPR peaks, and inset (b) shows the spectra over the entire range of monitored wavelengths (nm).

The highest concentration of bacteria tested, 5 x 10^7 CFU/mL (A, black line) caused significant aggregation of the washed AuNPs, resulting in a similar optical response to

the NP + LB control, while 5 x 10^6 CFU/mL (B, red line) resulted in LSPR peak dampening. All other concentrations tested were not significantly different to the AuNP + MQ control (I, army green line), **Figure 30**.

Without proliferation of the *E. coli* in the presence of the AuNPs, the initial (immediate) assay in MQ cannot be used to readily distinguish between the tested concentrations of bacteria.

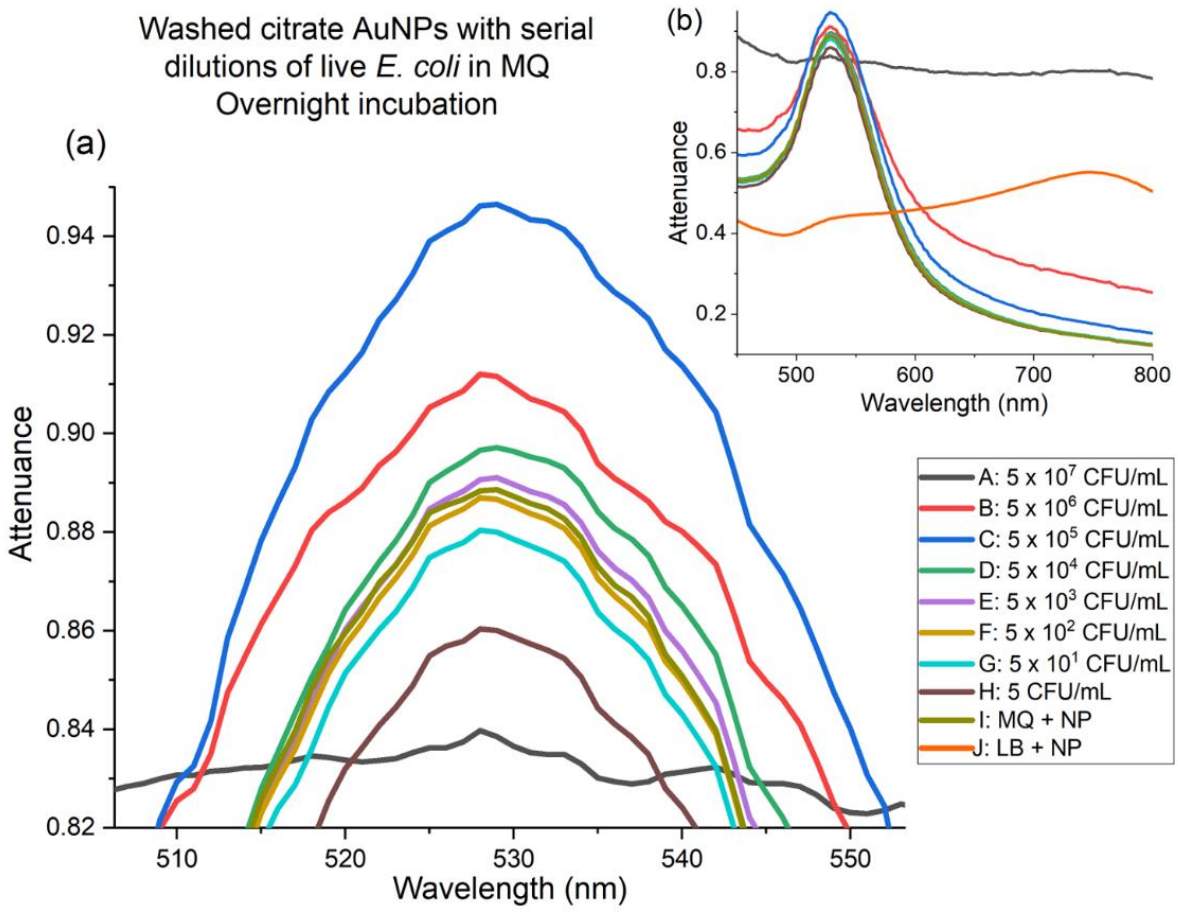

Figure 31: UV-vis spectra of washed citrate AuNPs assayed with serial dilutions of live *E. coli* in MQ and measured after overnight incubation at ambient temperature; (a) shows a close-up region of the relative positions of the LSPR peaks, and inset (b) shows the spectra over the entire range of monitored wavelengths (nm).

When compared to the initial assay, there had been a moderate amount of bacterial growth in the samples that initially contained ≥ 5 x 10^4 CFU/mL (compare **Figure 31** and**Figure 30**). There was more of a separation between the resultant LSPR peaks,

coupled with some peak broadening, evidencing the growth of bacteria within the samples. This is particularly true for the sample initially containing 5 x 10^6 CFU/mL (B, red line); the peak broadening and tailing > 600 nm suggests the colloid was beginning to aggregate/undergo size-broadening within the AuNP population. The optical signal for the sample initially containing 5 x 10^7 CFU/mL (A, black line) had become completely saturated, resulting in a total loss of the LSPR peak (i.e. flocculation).

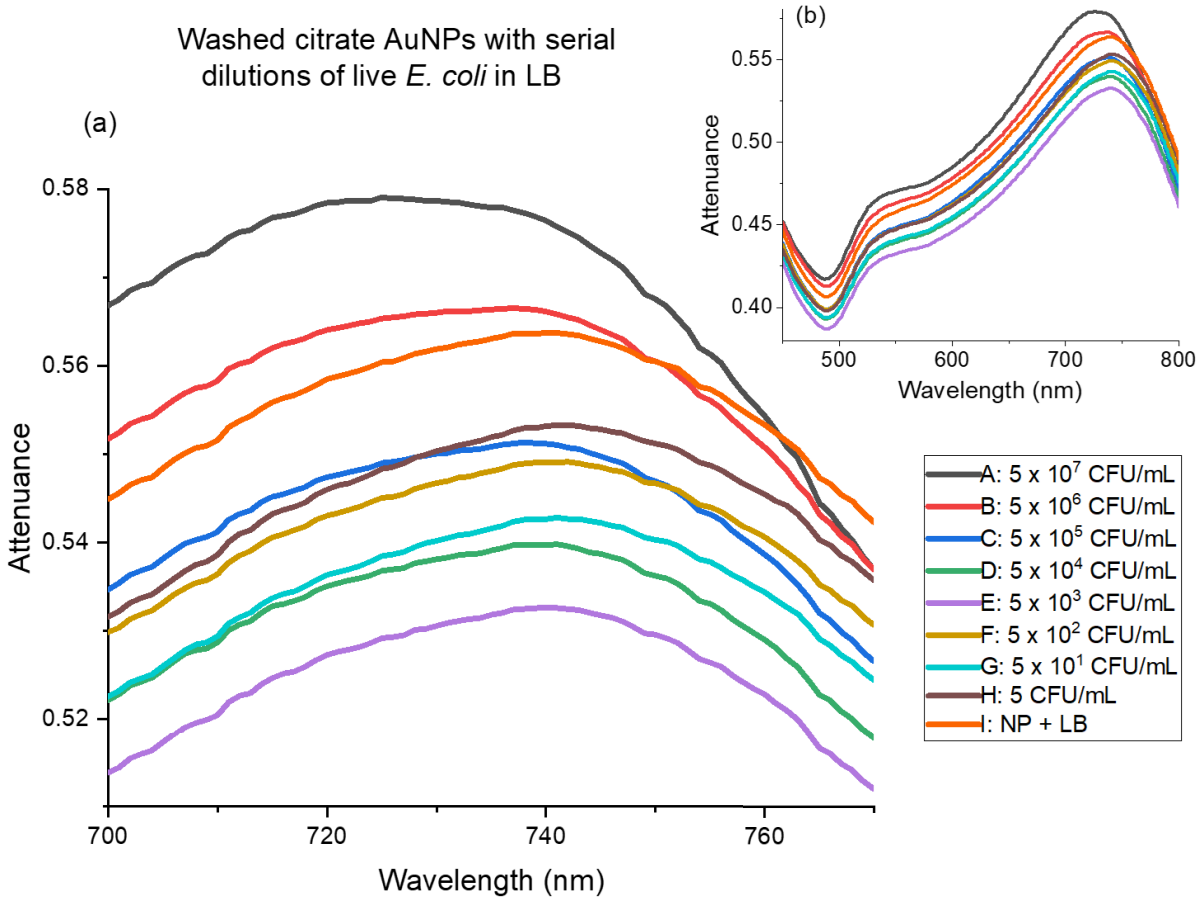

Figure 32: UV-vis spectra of washed citrate AuNPs assayed with serial dilutions of live *E. coli* in LB and measured immediately post assay. (a) shows a close-up region of the relative positions of the red-shifted plasmon peaks, and inset (b) shows the spectra over the entire range of monitored wavelengths (nm).

When compared to the as-synthesized citrate AuNP assay with live *E. coli* in LB, the washed AuNPs resulted in greater observable differences between the red-shifted LSPR peaks of the samples (compare **Figure 32** with **Figure 28**). In particular, it was

easier to distinguish between the highest and lowest concentrations of bacteria assayed with the respective colloids. This suggests the washed AuNPs were more sensitive to the starting CFU/mL of the live *E. coli* in LB at the tested concentrations.

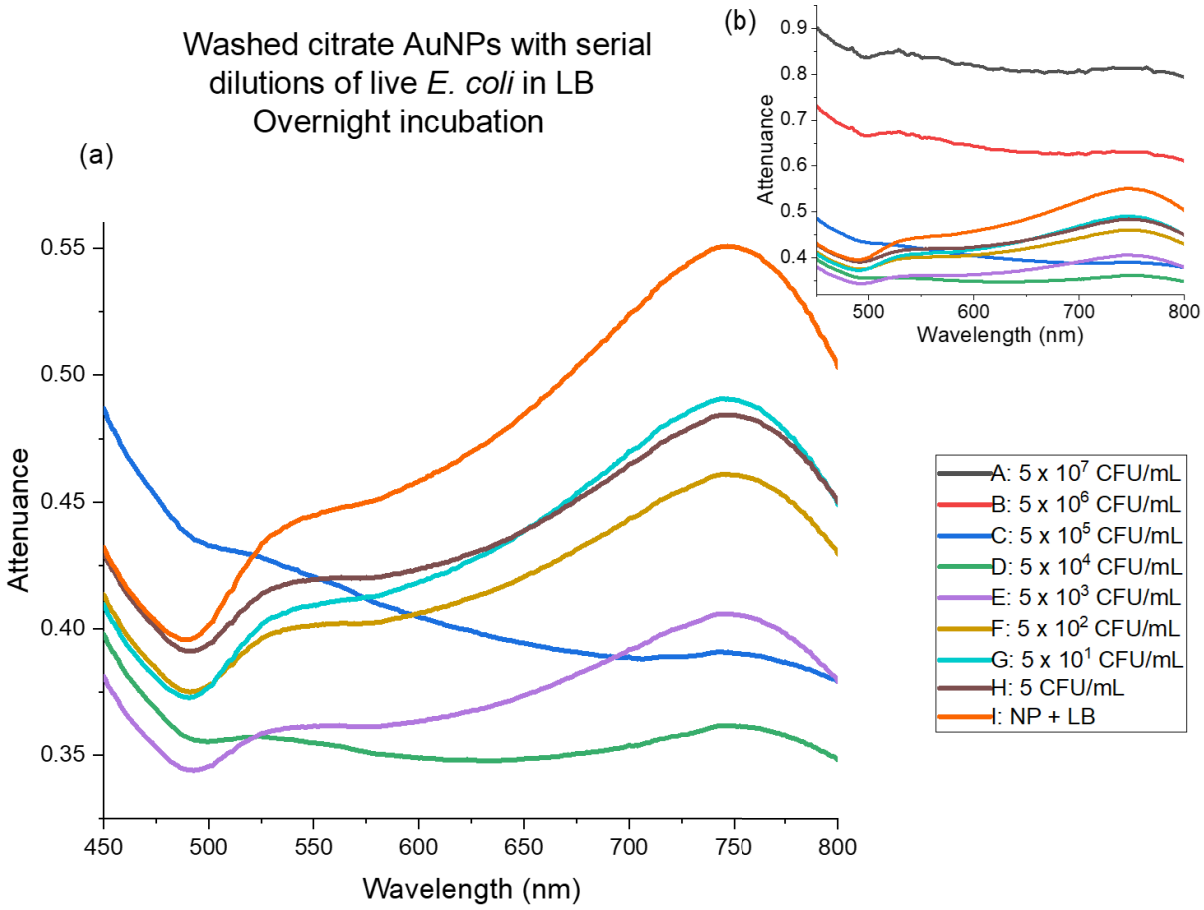

Figure 33: UV-vis spectra of washed citrate AuNPs assayed with serial dilutions of live *E. coli* in LB and measured after overnight incubation at ambient temperature. (a) shows the rescaled spectra with saturated signals A and B omitted, and inset (b) shows the all spectra, including the saturated optical signals from the highest starting concentrations of bacteria.

Overnight incubation in LB and the presence of washed AuNPs (**Figure 33**) resulted in the saturation (complete loss of LSPR peaks) of the optical signals for the two highest starting concentrations of bacteria tested (samples A and B, black and red lines respectively). All other lower concentrations tested resulted in a red-shifted, broadened and dampened LSPR peak. The growth of the *E. coli* evident within the

samples initially containing both 5 x 10^4 and 5 x 10^5 CFU/mL (D and C, green and dark blue lines respectively) appeared to be nearing their saturation, as evidenced by the almost complete loss (significant dampening) of the second, red-shifted aggregation peak present within the spectra.

4.4.2 Live *E. coli* and As-synthesized Citrate AuNPs Time Point Assays

The following UV-visible spectra show the changes in the optical readings (measured as attenuance) when as-synthesized citrate AuNPs were assayed with live *E. coli* in LB from concentrations of ~ 5 x 10^7 – 5 cells/mL. Each sequential scan was approximately 2 h apart, allowing for the tracking of the aggregation of AuNPs with respect to time. It can be seen that as time increases, so did the aggregation of the AuNPs; this effect was more pronounced in the samples containing higher concentrations of *E. coli* and is evidenced by the red-shifting and broadening of the LSPR peaks. The increase in attenuance over time in all samples (except the AuNP and LB control) was likely due to the proliferation of the *E. coli* in the presence of the AuNPs.

The omitted (sequential) spectra can be found in Appendix A, and have been excluded from this section for ease of reading.

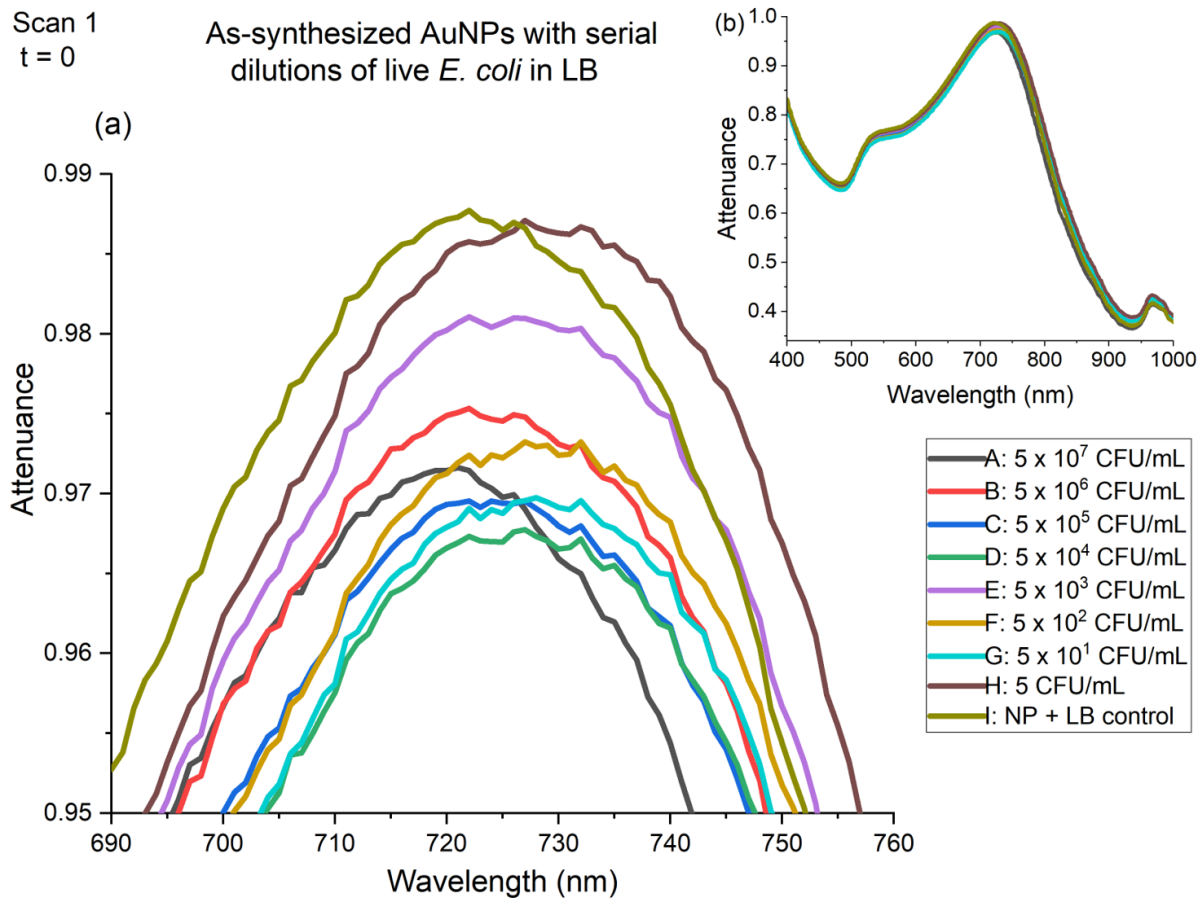

Figure 34: UV-vis spectra of as-synthesized citrate AuNPs assayed with serial dilutions of live *E. coli* in LB, t = 0 h. (a) shows a close-up region of the relative positions of the red-shifted plasmon peaks, and inset (b) shows all spectra over the entire range of monitored wavelengths (nm).

The initial assay between as-synthesized AuNPs and serial dilutions of live *E. coli* in LB resulted in spectra displaying two distinct plasmon peaks; the initial LSPR from the AuNPs that had become significantly dampened and red-shifted from 527 nm to ~ 530 nm, and an additional, further red-shifted 'aggregation' peak ~ 730 nm that is greater in attenuance than the initial LSPR associated with the colloidal gold. This implies the majority of the AuNPs within the system have aggregated, and is consistent with how the samples appeared visually (the red colloid rapidly turned grey-blue upon being added to the assay samples, indicating aggregation).

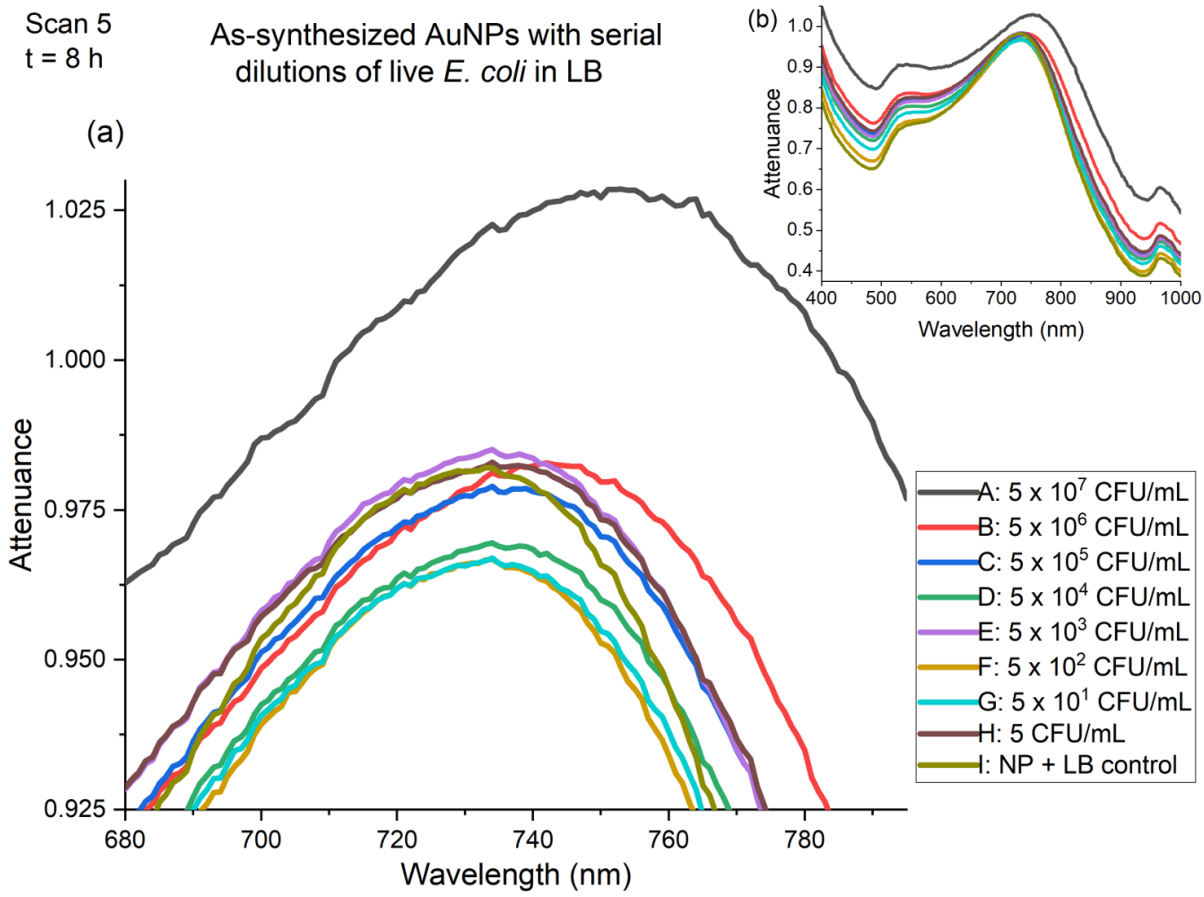

Figure 35: UV-vis spectra of as-synthesized citrate AuNPs assayed with serial dilutions of live *E. coli* in LB, t = 8 h. (a) shows a close-up region of the relative positions of the red-shifted plasmon peaks, and inset (b) shows all spectra over the entire range of monitored wavelengths (nm).

After 8 h of incubation at ambient temperature in the presence of as-synthesized AuNPs (**Figure 35**), there was notable change within the samples. This is evidenced by the additional aggregation displayed by the AuNPs (peak broadening, red-shifting). The evolution of the aggregation peak and increase in attenuance can be attributed to the proliferation of *E. coli* in the presence of the AuNPs.

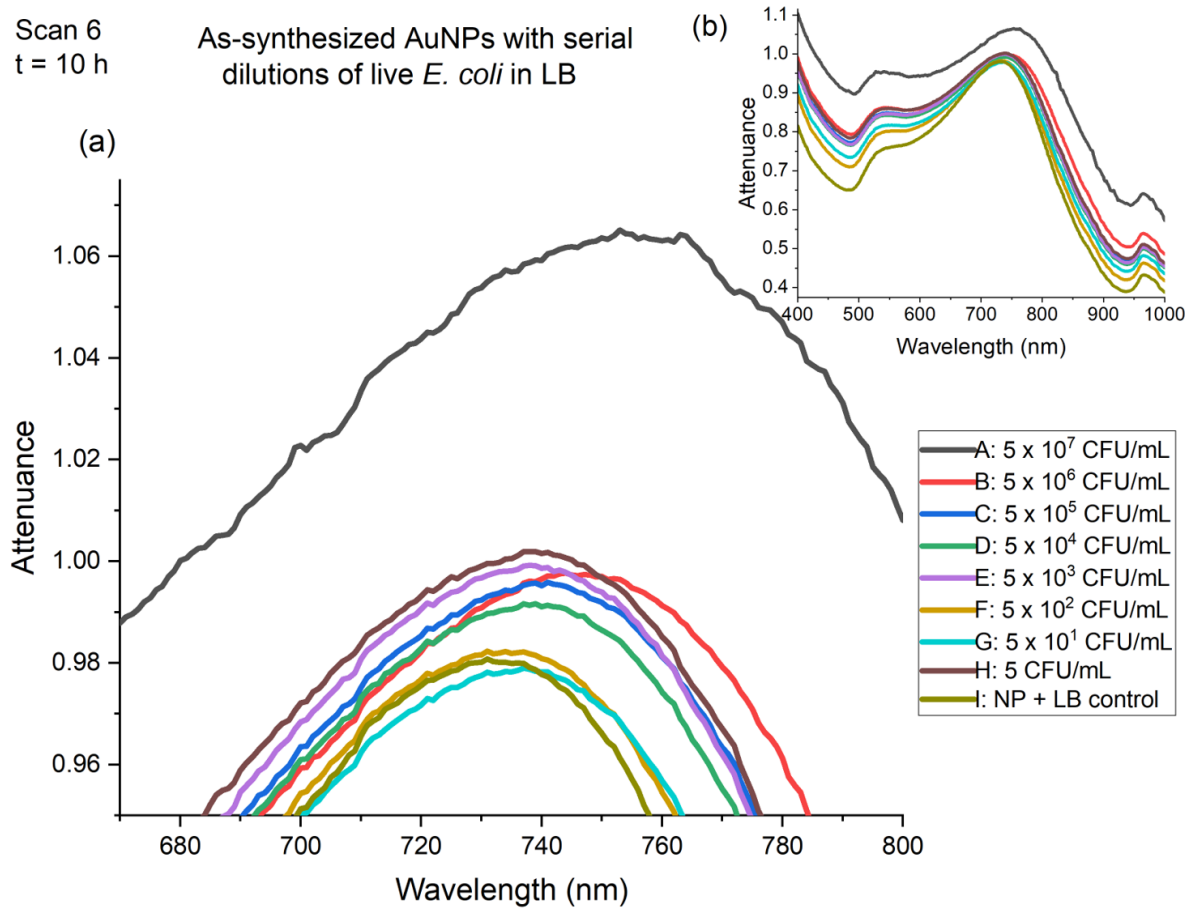

Figure 36: UV-vis spectra of as-synthesized citrate AuNPs assayed with serial dilutions of live *E. coli* in LB, t = 10 h. (a) shows a close-up region of the relative positions of the red-shifted plasmon peaks, and inset (b) shows all spectra over the entire range of monitored wavelengths (nm).

Additional growth of the *E. coli* within the samples has resulted in further aggregation and increase in attenuance of the AuNPs. Only the sample (intially) containing the highest concentration of bacteria (5 x 10^7 CFU/mL – A, black line) has produced a significantly distinguishable spectrum from the lower tested concentrations of bacteria. All (initial) concentrations of bacteria ≤ 5 x 10^6 CFU/mL have decreased slightly in attenuance since scan 5 (**Figure 35**).

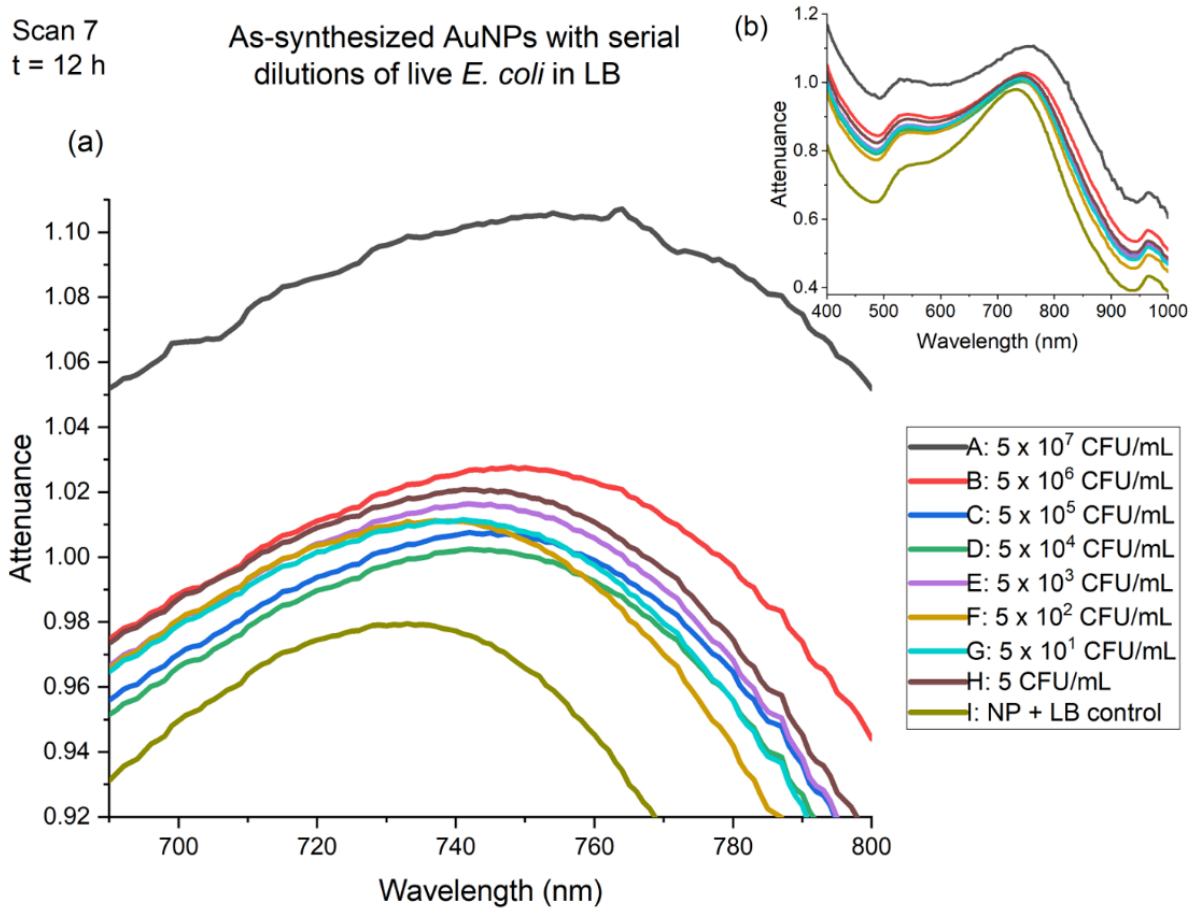

Figure 37: UV-vis spectra of as-synthesized citrate AuNPs assayed with live *E. coli* in LB, t = 12 h. (a) shows a close-up region of the relative positions of the red-shifted plasmon peaks, and inset (b) shows all spectra over the entire range of monitored wavelengths (nm).

All samples show further aggregation and peak broadening when compared to the previous scan at 10 h (**Figure 36**), with all samples remaining distinguishable from the control (I, army green line), suggesting further growth of the bacteria within the test samples.

4.4.3 Live *E. coli* and Washed Citrate AuNPs Time Point Assays

The following UV-visible spectra show the changes in the optical readings (measured as attenuance) when washed citrate AuNPs are assayed with live *E. coli* in LB from concentrations of ~ 5 x 10^7 – 5 cells/mL. Each sequential scan was approximately 2 h apart, allowing for the tracking of the aggregation of AuNPs with respect to time.

These differ from the previous assays in that the AuNPs have a reduced amount of surface associated citrate, and therefore a less negative surface charge (zeta potential), which has the potential to impact their interaction with analytes or targets of interest (in this instance, *E. coli*). Conversely, this also results in reduced stability of the AuNPs as the surface citrate serves as a stabilizing agent with respect to the AuNPs.

When comparing the optical responses of the washed citrate AuNPs to the as-synthesized citrate AuNPs, the initial downwards slope of the spectra (between 400 – 500 nm) appear steeper, with the initial peak around 520 nm less pronounced than those observed in their as-synthesized citrate counterparts. In addition, the peaks are broader and appear to have a more pronounced ‘tail hook’ in the region from 900 – 1000 nm. Although the *E. coli* are able to grow in the presence of both the as-synthesized and washed AuNPs, the stability of the washed AuNPs resulted in broader and flatter red-shifted peaks as the bacteria multiplied and affected an increase in the attenuance.

The relative attenuance of the following spectra resulting from *E. coli* and washed AuNPs are *lower* than those observed for the as-synthesized AuNP assays, as a consequence of the (relatively) lower concentration of washed AuNPs used.

Omitted (sequential) spectra can be found in Appendix A, and have been excluded from this section for ease of reading.

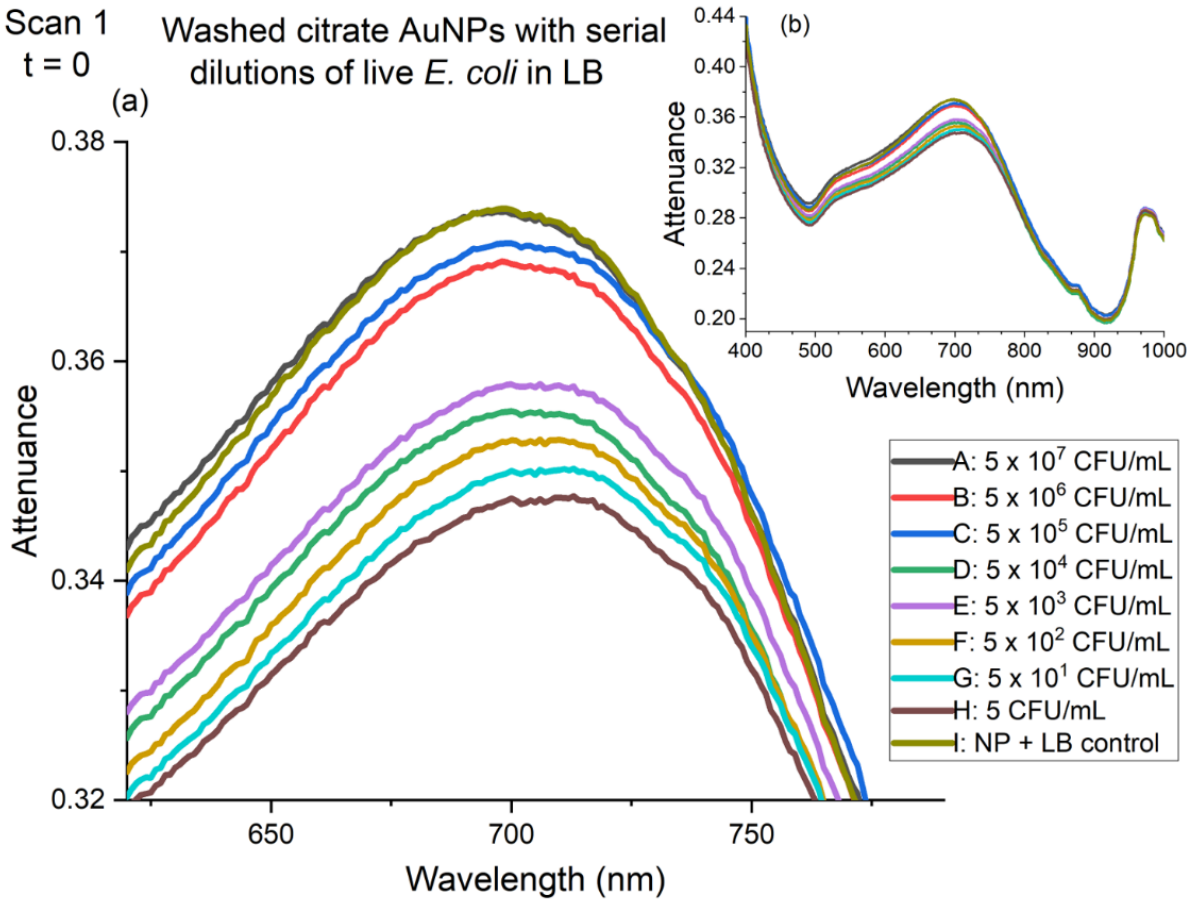

Figure 38: UV-vis spectra of washed citrate AuNPs assayed with live *E. coli* in LB. Concentrations of *E. coli* range from 5 x 10^7 – 5 cells/mL, t = 0. (a) shows a close-up region of the relative positions of the red-shifted plasmon peaks, and inset (b) shows all spectra over the entire range of monitored wavelengths (nm).

The initial assay between washed citrate AuNPs and the serial dilutions of live *E. coli* in LB resulted in red-shifted and broadened LSPR peaks around 700 nm. Concentrations of bacteria between 5 x 10^7 – 5 x 10^5 CFU/mL (A-C, black, red and dark blue lines) produced close to overlapping spectra with the NP + LB control (I, army green line), while the lower bacterial dilutions 5 x 10^4 – 5 CFU/mL (D - H, dark green, purple, tan, light blue and dark brown lines) resulted in spectra that were more readily distinguishable from the higher concentrations.

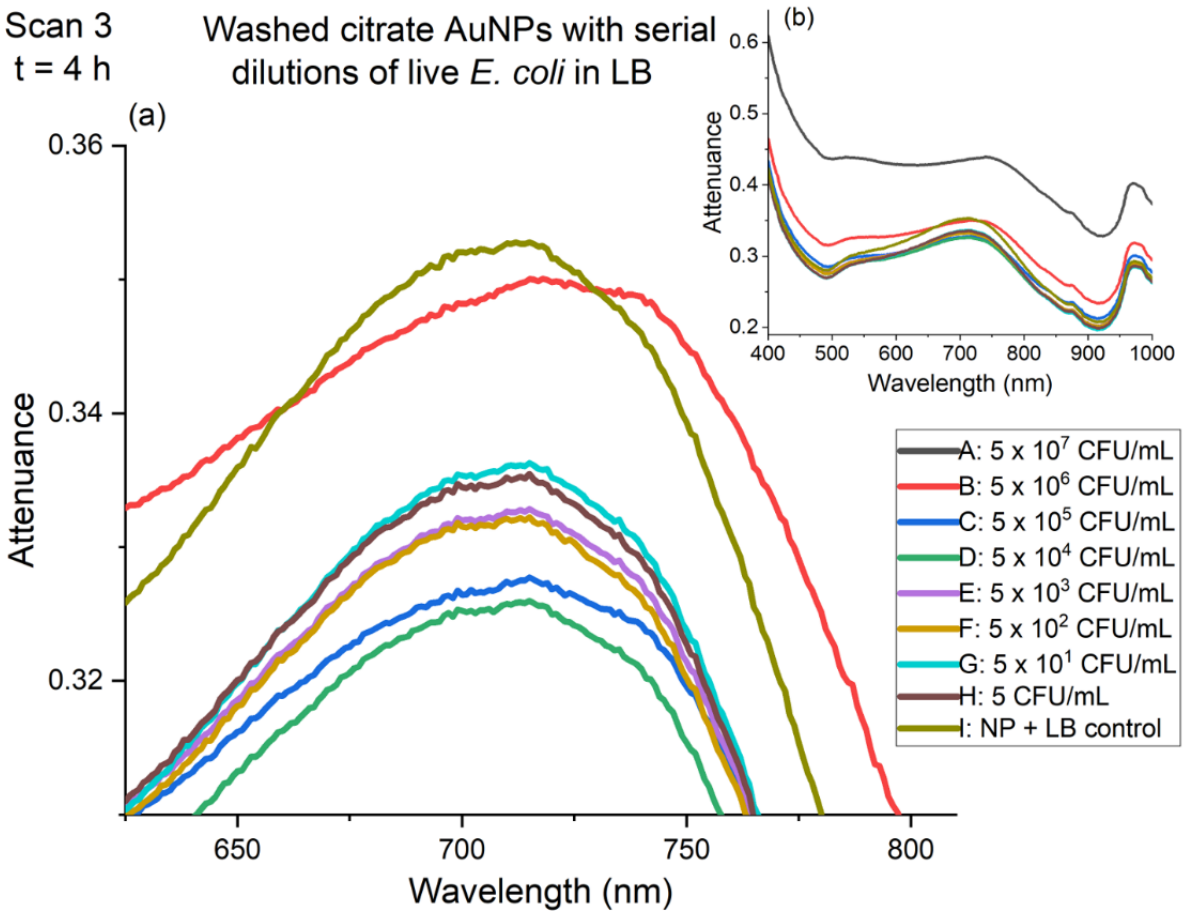

Figure 39: UV-vis spectra of washed citrate AuNPs assayed with live *E. coli* in LB, t = 4 h. (a) shows a close-up region of the relative positions of the red-shifted plasmon peaks, and inset (b) shows all spectra over the entire range of monitored wavelengths (nm).

All test samples have shown evidence of decreased AuNP stability and increased aggregation, as evidenced in peak broadening and a decrease in attenuance. The exceptions are 5 x 10^6 and 5 x 10^7 CFU/mL which have increased in attenuance, likely due to the comparatively higher amount of bacterial growth within the test wells, increasing the overall turbidity of the sample wells and therefore the attenuance.

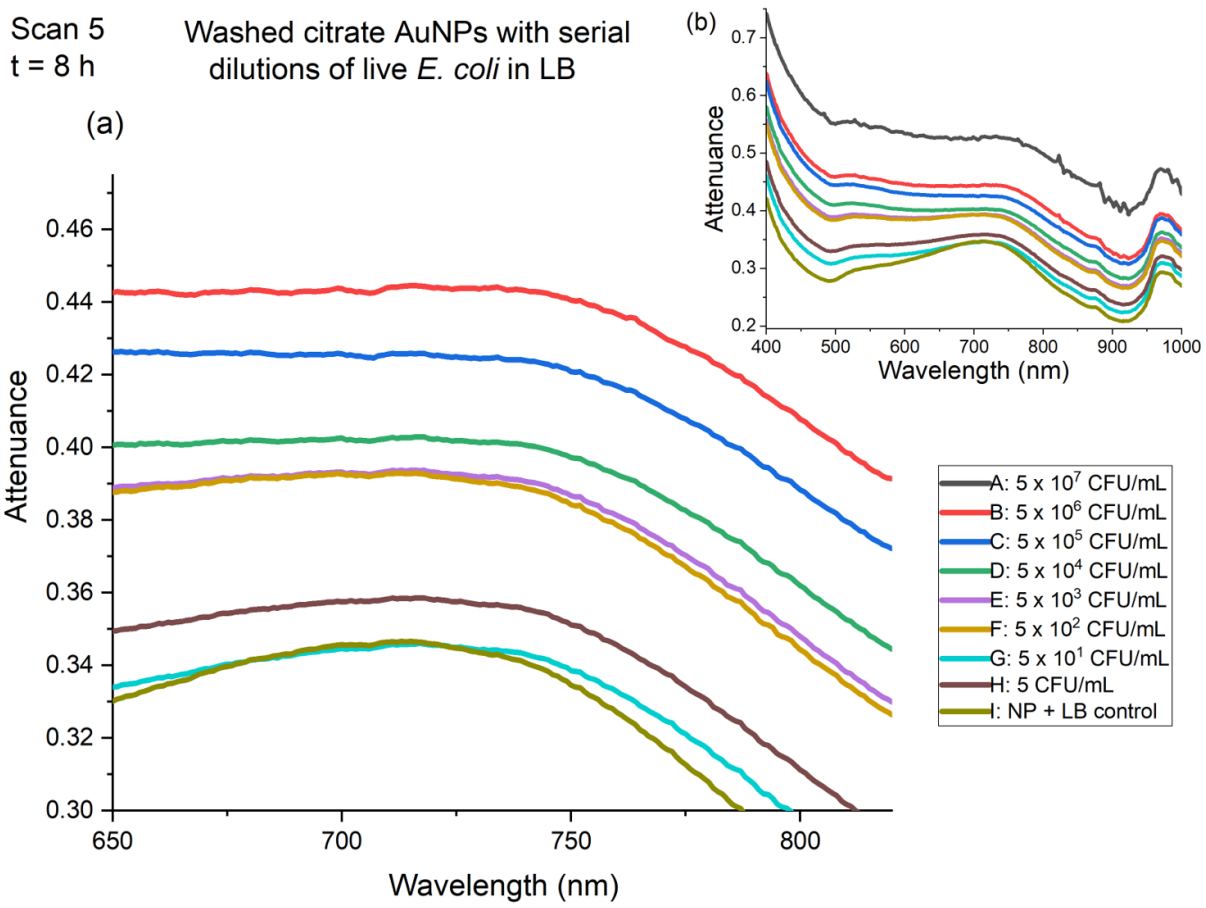

Figure 40: UV-vis spectra of washed citrate AuNPs assayed with live *E. coli* in LB, t = 8 h. (a) shows a close-up region of the relative positions of the red-shifted plasmon peaks, and inset (b) shows all spectra over the entire range of monitored wavelengths (nm).

All tested bacterial dilutions have resulted in significant aggregation of the washed colloids, evidenced by the further peak dampening and flattening. The initial shouldered LSPR ~ 530 nm has almost entirely disappeared, suggesting the ratio of colloidal:aggregated AuNPs is skewed heavily towards the aggregated particles. The red-shifted 'aggregation' LSPR has become increasingly flattened and dampened for all bacterial dilutions, while increasing in attenuance as a reflection of the continued bacterial growth.

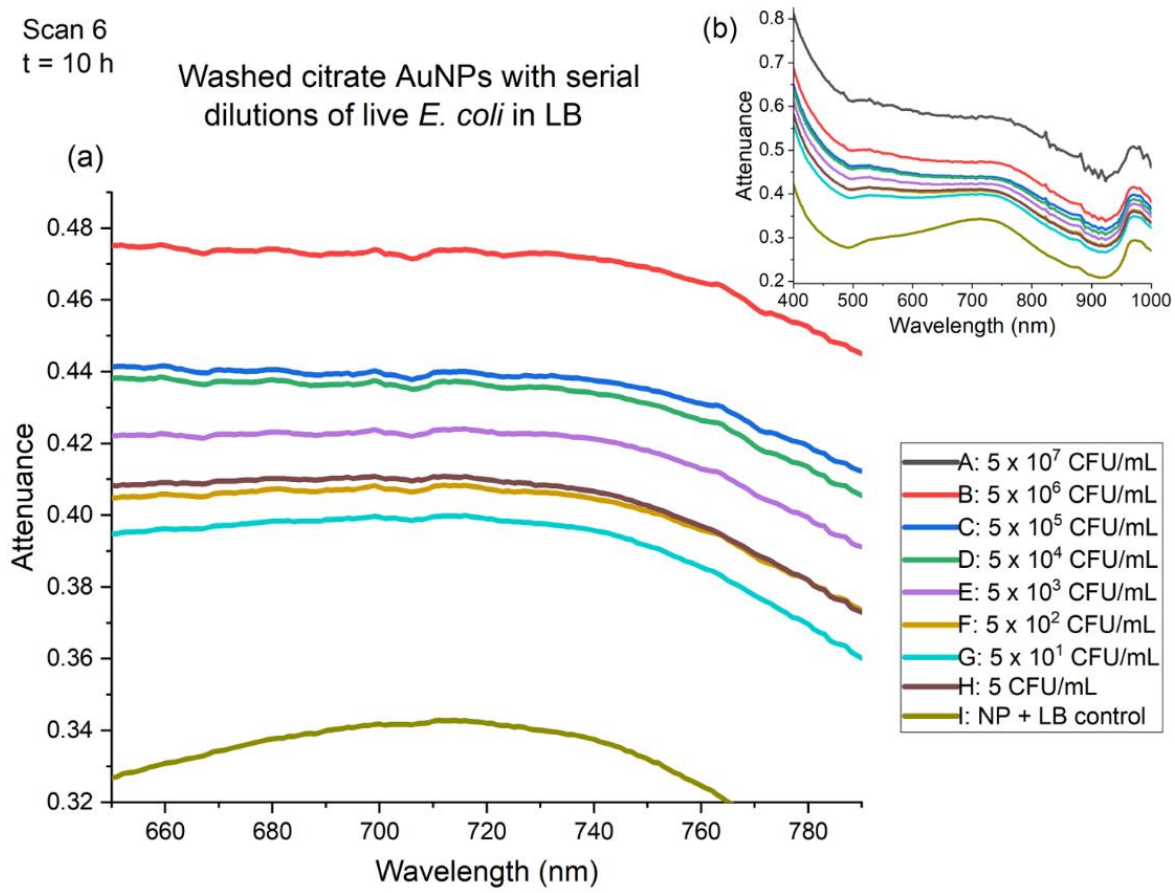

Figure 41: UV-vis spectra of washed citrate AuNPs assayed with live *E. coli* in LB, t = 10 h. (a) shows a close-up region of the relative positions of the red-shifted plasmon peaks, and inset (b) shows all spectra over the entire range of monitored wavelengths (nm).

All test samples have increased in attenuance, likely due to the growth of *E. coli* within the test wells. This is coupled with an increase in NP aggregation as evidenced by further peak broadening and flattening while the control sample remains largely unchanged from t = 8 h (**Figure 40**). The increased noise in the 5 x 10^7 CFU/mL (A, black line) spectrum is likely a consequence of the (proportionally greater) increased turbidity from bacterial growth, compared to the lower initial bacterial dilutions.

All bacterial dilutions can be distinguished from the NP + LB control after 10 h incubation in LB in the presence of washed AuNPs, although not all concentrations can be readily distinguished from each other.

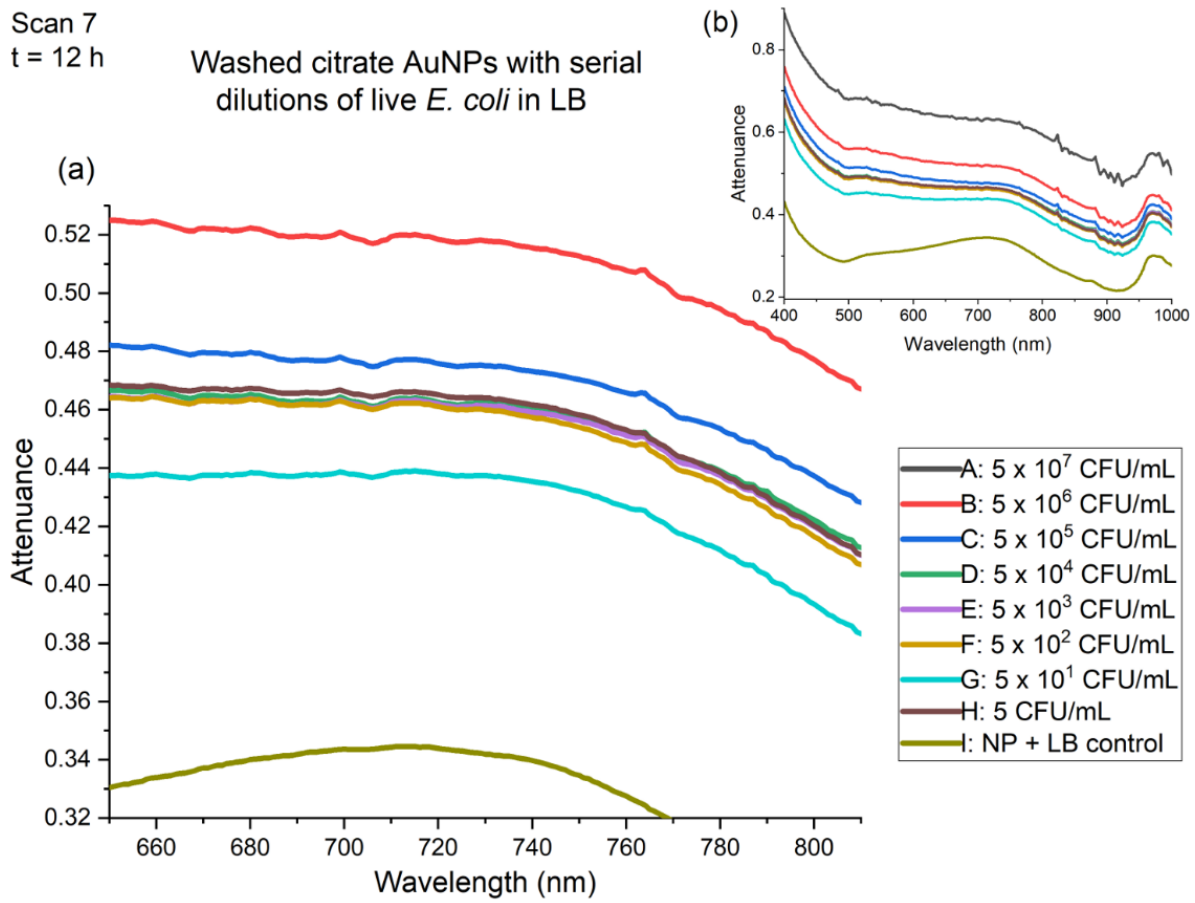

Figure 42: UV-vis spectra of washed citrate AuNPs assayed with live *E. coli* in LB, t = 12 h. (a) shows a close-up region of the relative positions of the red-shifted plasmon peaks, and inset (b) shows all spectra over the entire range of monitored wavelengths (nm).

All test samples have increased in attenuance and have aggregated further; slight peak broadening can be observed in all test samples, owing to the instability of the washed AuNPs coupled with bacterial growth. Although some of the initial bacterial dilutions are distinguishable from the NP + LB control (I, army green line), the spectra resulting from the initial 5 x 10^4 – 5 x 10^2 and 5 CFU/mL dilutions (D - F & H, dark green, purple, tan and dark brown lines) resulted in overlapping spectra.

4.4.4 Live *E. coli* and As-synthesized Citrate AuNP Assays at Elevated Temperature (37°C)

The following UV-visible spectra show the changes in the optical readings (measured as attenuance) when as-synthesized citrate AuNPs are assayed with live *E. coli* in LB at 37°C, from concentrations of ~ 5 x 10^7 – 5 cells/mL. As the 96-well plate was required to reach the desired assay temperature before optimal growth conditions for the bacteria could be met, it is most appropriate to consider the temperature of the first scan as somewhere between room temperature and 37°C, with scan 2 allowing sufficient time for samples to reach the desired temperature. Each sequential scan was approximately 1 hour, 45 min apart, allowing for the tracking of the aggregation of AuNPs with respect to time while providing optimal growth conditions for the bacteria (nutrient broth and 37°C).

Omitted sequential spectra can be found in Appendix A, and have been excluded from this section for ease of reading.

It is most useful to compare the presented spectra below to those resulting from the assays of live *E. coli* with as-synthesized citrate AuNPs conducted at ambient temperature. As such, direct comparisons will be made between the two sets of experiments, with the spectra resulting from comparable time-points used to illustrate the key findings.

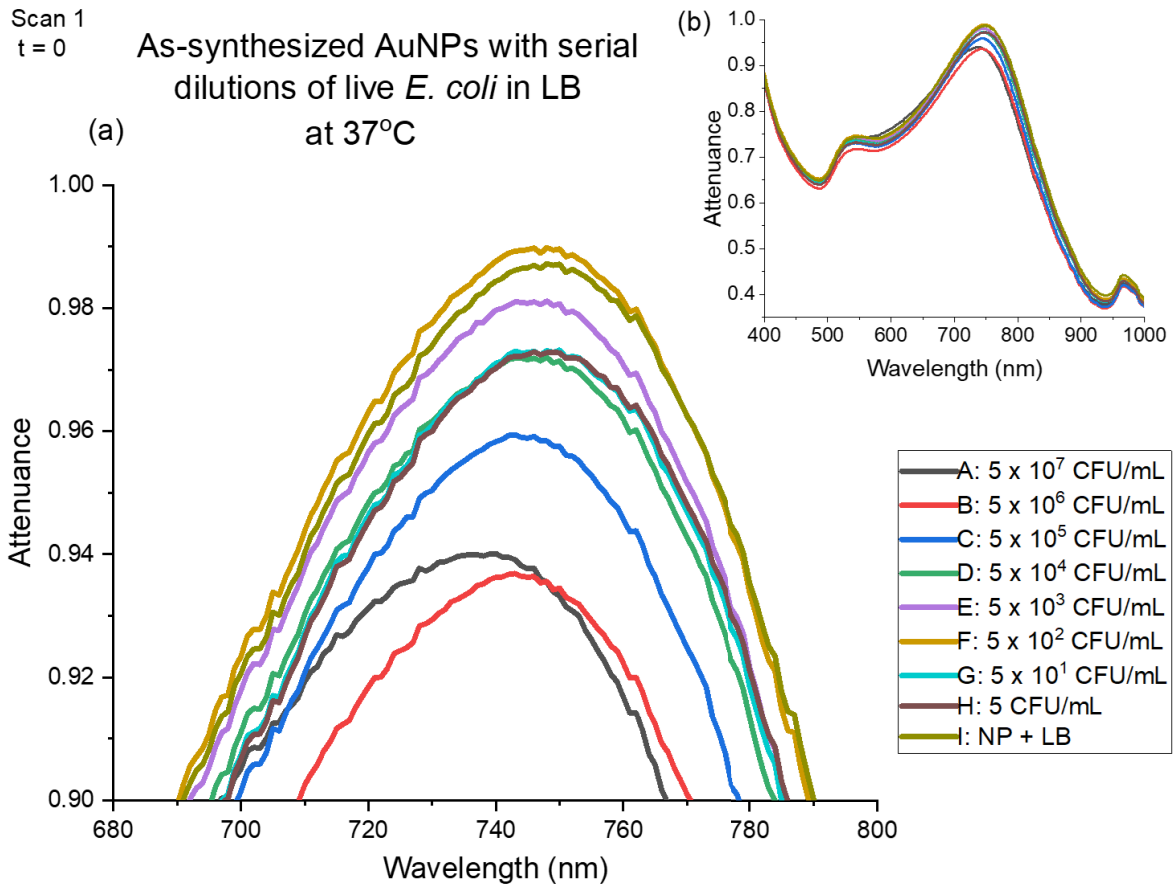

Figure 43: UV-vis spectra of as-synthesized citrate AuNPs assayed with live *E. coli* in LB at 37°C. Concentrations of *E. coli* range from 5 x 10^7 – 5 cells/mL, t = 0. (a) shows a close-up region of the relative positions of the red-shifted plasmon peaks, and inset (b) shows all spectra over the entire range of monitored wavelengths (nm).

When compared to the same assay performed at ambient temperature (**Figure 34**), there are no major differences between the resulting spectra at this stage. The average width(s) of the resultant red-shifted LSPR peaks ~ 740 nm are comparatively wider by at approximately 10 nm. In both sets of experiments (ambient temperature and 37°C), the resultant spectra are fairly clustered and overlapping at t = 0.

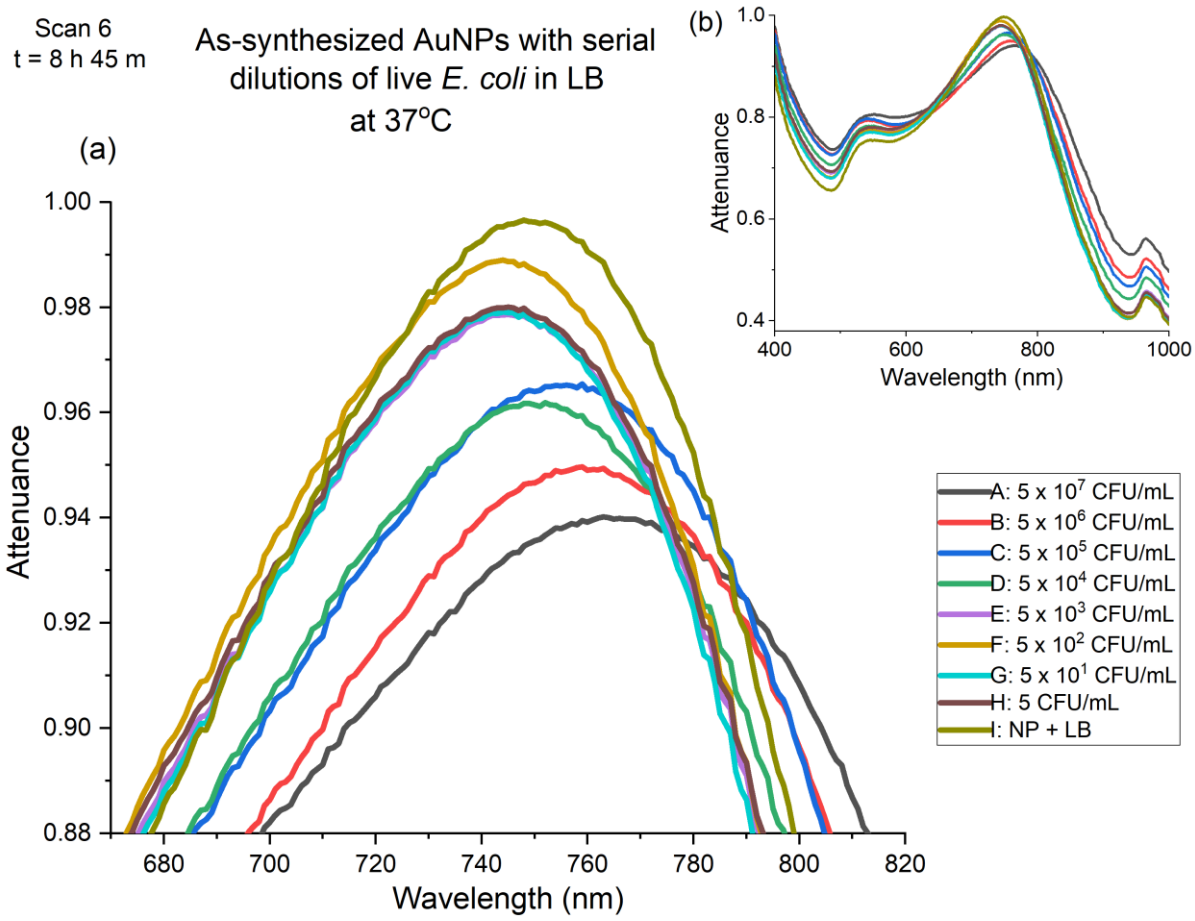

Figure 44: UV-vis spectra of as-synthesized citrate AuNPs assayed with live *E. coli* in LB at 37°C, t = 8 h, 45 m. (a) shows a close-up region of the relative positions of the red-shifted plasmon peaks, and inset (b) shows all spectra over the entire range of monitored wavelengths (nm).

Comparing the above **Figure 44** with **Figure 35** (comparable experimental equivalent at ambient temperature), the red-shifted LSPR peaks resulting from the 37°C incubation with as-synthesized AuNPs are less tightly clustered, with the sample initially containing the highest concentration of bacteria (5 x 10^7 CFU/mL – A, black line) exhibiting the lowest relative attenuance. At ambient temperature, this same tested concentration produced a spectrum with the highest relative attenuance.

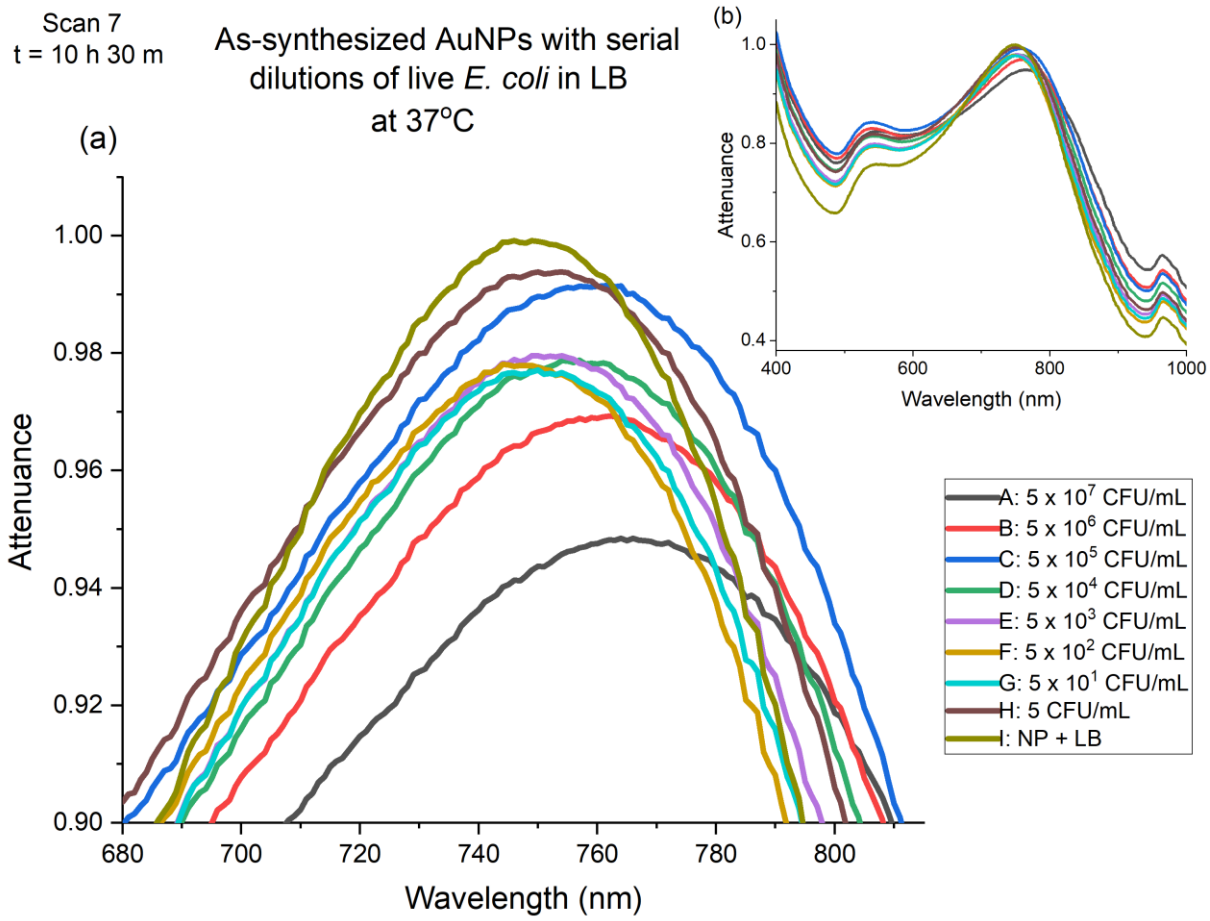

Figure 45: UV-vis spectra as-synthesized citrate AuNPs assayed with live *E. coli* in LB at 37°C, t = 10 h, 30 m. (a) shows a close-up region of the relative positions of the red-shifted plasmon peaks, and inset (b) shows all spectra over the entire range of monitored wavelengths (nm).

Compared to **Figure 36** (10 h incubation at ambient temperature), **Figure 45** above exhibits spectra that are comparatively broader and have a lower relative attenuance. The exception to this is A (5 x 10^7 CFU/mL, black line), which has the lowest attenuance of all samples. The increased peak broadening and decreased attenuance indicate a higher level of aggregation experienced by the as-synthesized colloids when assayed with live *E. coli* at 37°C compared to ambient temperature. This may be in part due to the faster proliferation of the bacteria within the samples.

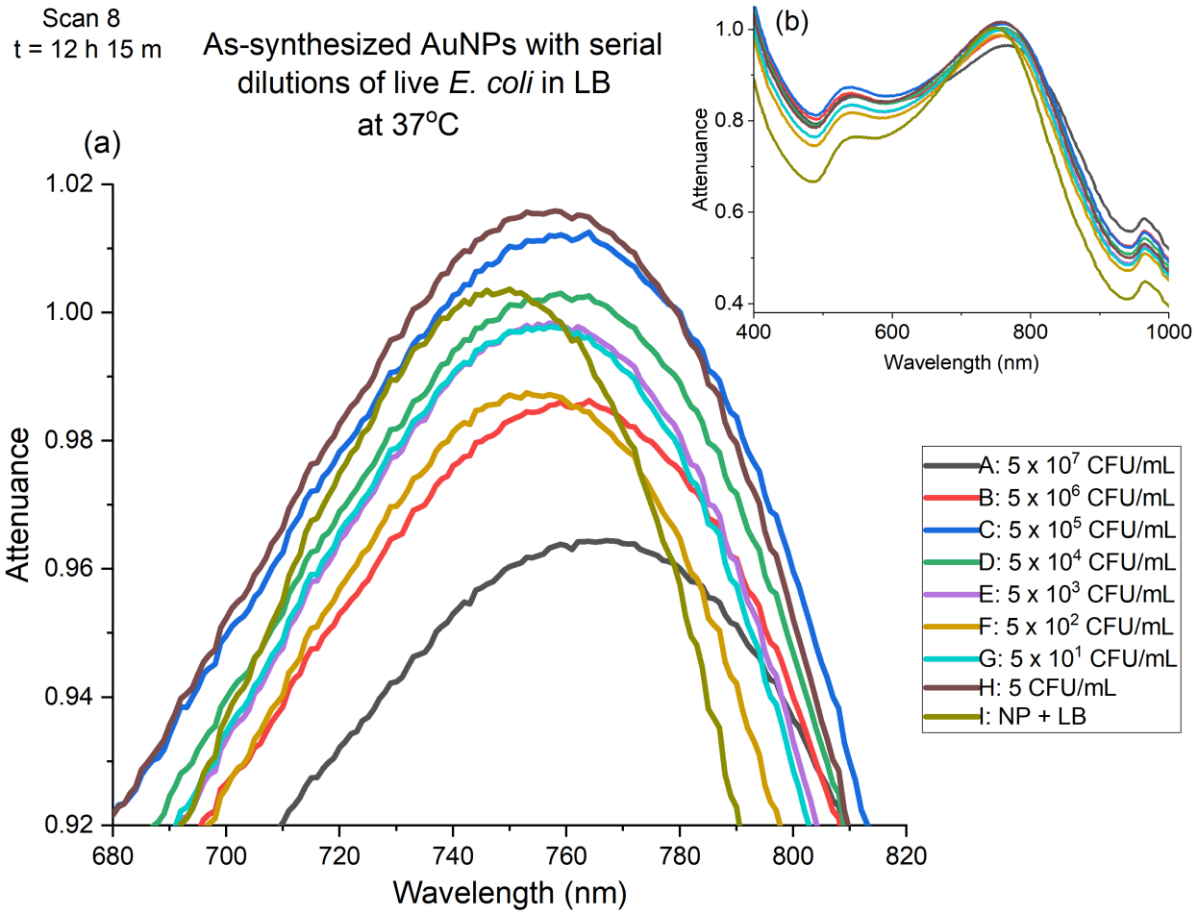

Figure 46: UV-vis spectra of as-synthesized citrate AuNPs assayed with live *E. coli* in LB at 37°C, t = 12 h, 15 m. (a) shows a close-up region of the relative positions of the red-shifted plasmon peaks, and inset (b) shows all spectra over the entire range of monitored wavelengths (nm).

Comparing the 12 h incubations at ambient temperature (**Figure 37**) and 37°C (**Figure 46** above), the elevated temperature assay resulted in comparatively narrower and further red-shifted LSPR 'aggregation' peaks. In both instances, all tested bacterial dilutions produced spectra that were distinguishable from the NP + LB controls.

4.4.5 Live *E. coli* and Washed Citrate AuNP Assays at Elevated Temperature (37°C)

The following UV-visible spectra show the changes in the optical readings (measured as attenuance) when washed citrate AuNPs are assayed with live *E. coli* in LB at 37°C from concentrations of ~ 5 x 10^7 – 5 cells/mL. As the 96-well plate was required to reach the desired temperature (37°C) before optimal growth conditions for the bacteria could be met, it is most appropriate to consider the temperature of the first scan as somewhere between ambient temperature and 37°C, with scan 2 allowing sufficient time for samples to reach the desired temperature. Each sequential scan was approximately 1 hour, 45 min apart, allowing for the tracking of the aggregation of AuNPs with respect to time while providing optimal growth conditions for the bacteria (nutrient broth and 37°C).

Omitted sequential spectra can be found in Appendix A, and have been excluded from this section for ease of reading.

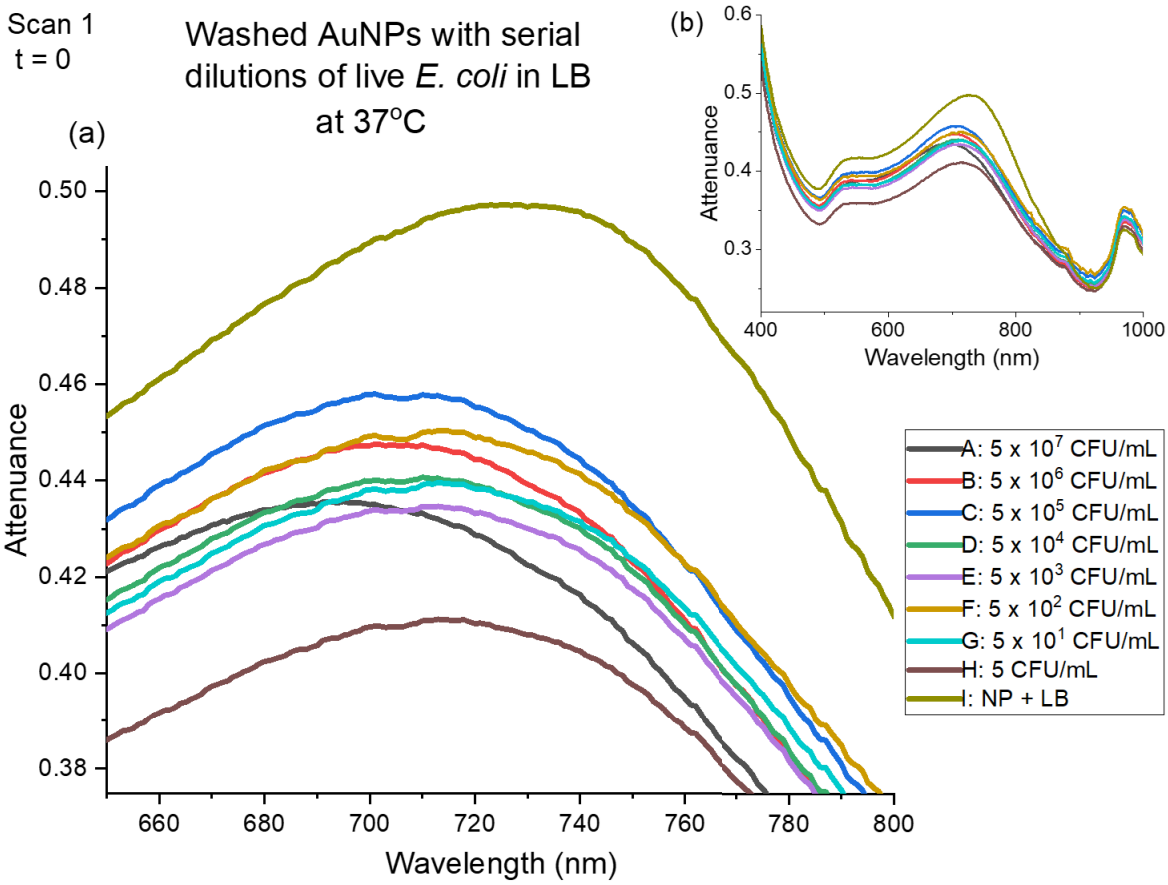

Figure 47: UV-vis spectra of washed citrate AuNPs assayed with live *E. coli* in LB at 37°C. Concentrations of *E. coli* range from 5 x 10^7 – 5 cells/mL, t = 0. (a) shows a close-up region of the relative positions of the red-shifted plasmon peaks, and inset (b) shows all spectra over the entire range of monitored wavelengths (nm).

In comparison to the initial assay between washed AuNPs and live *E. coli* at ambient temperature (**Figure 38**), the same assay conducted at 37°C (**Figure 47** above) resulted in all tested concentrations of bacteria exhibiting a distinguishably lower attenuance compared to the NP + LB control. At ambient temperature, the three highest concentrations of bacteria resulted in spectra that were difficult to distinguish from the control.

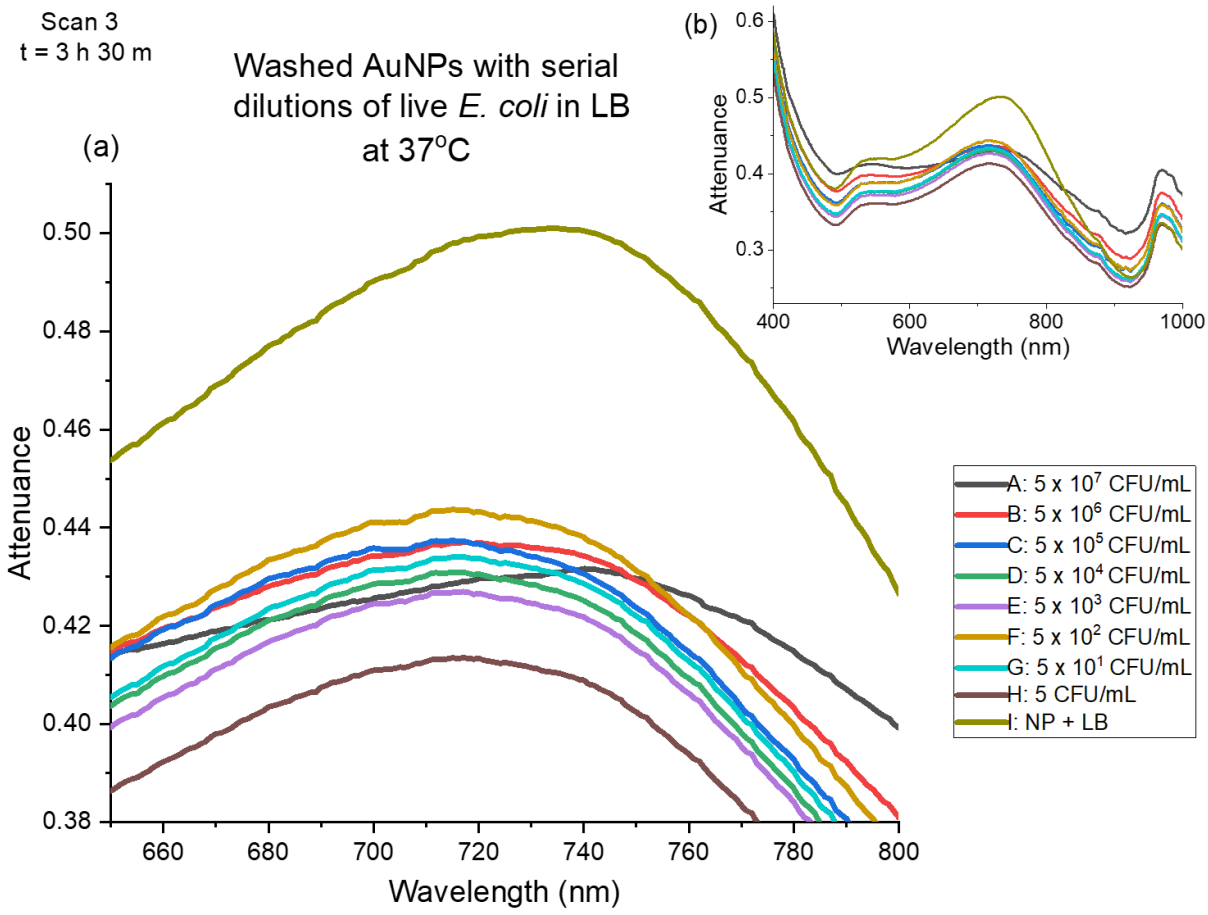

Figure 48: UV-vis spectra of washed citrate AuNPs assayed with live *E. coli* in LB at 37°C, t = 3 h, 30 m. (a) shows a close-up region of the relative positions of the red-shifted plasmon peaks, and inset (b) shows all spectra over the entire range of monitored wavelengths (nm).

Comparing the 4 h assay between washed AuNPs and live *E. coli* at ambient temperature (**Figure 39**) with the 3.5 h assay at 37°C (**Figure 48**), the spectra resulting from the elevated temperature equivalent have broader and slightly more red-shifted 'aggregation' LSPR peaks (~ 710 nm compared to ~ 720 nm). Additionally, the attenuance of all tested bacterial dilutions were lower in the 37°C assay, indicating a higher level of aggregation at the higher temperature.

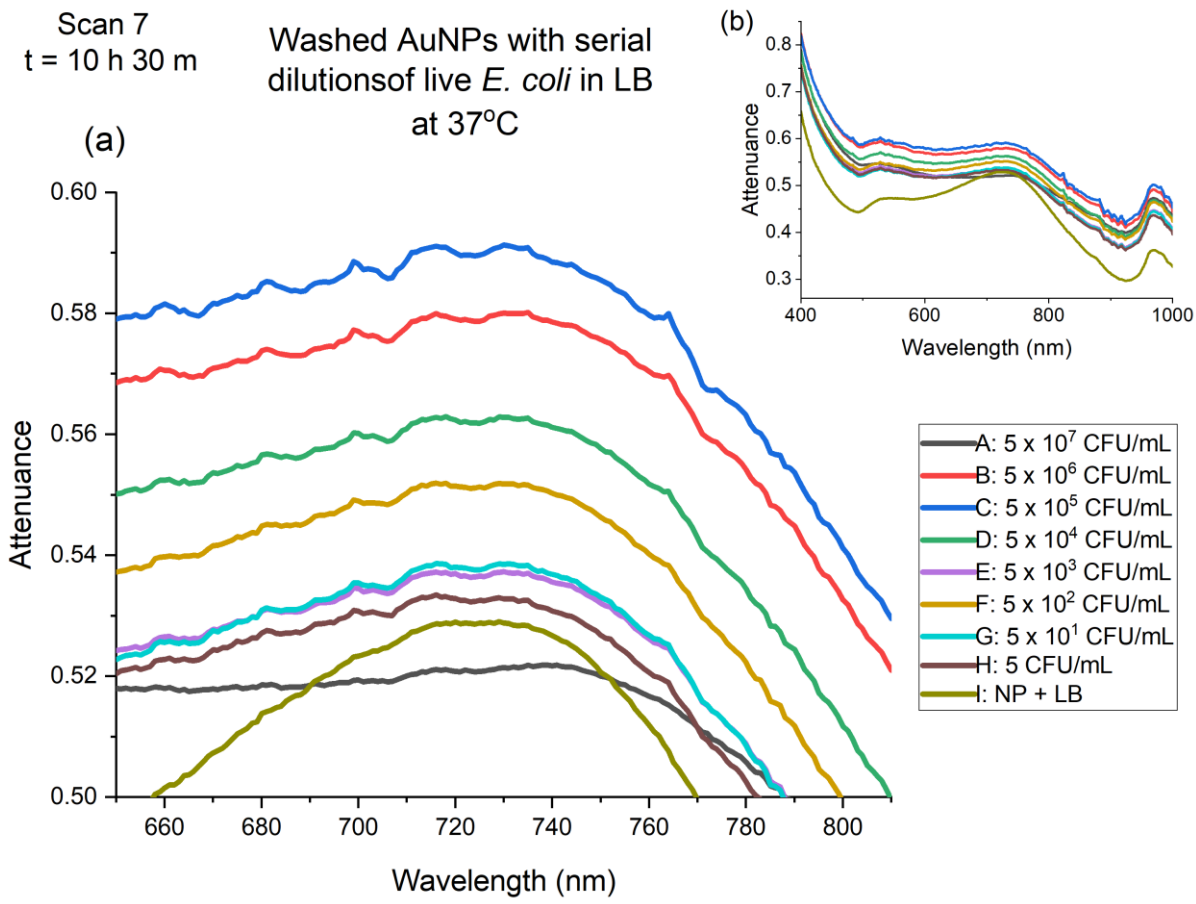

Figure 49: UV-vis spectra of washed citrate AuNPs assayed with live *E. coli* in LB at 37°C, t = 10 h, 30 m. (a) shows a close-up region of the relative positions of the red-shifted plasmon peaks, and inset (b) shows all spectra over the entire range of monitored wavelengths (nm).

Comparing the 37°C washed AuNP with live *E. coli* in LB assay (**Figure 49**) with the ambient temperature equivalent assay (**Figure 41**), the elevated temperature assay has, at this time, resulted in spectra that are comparatively *less* aggregated. This is supported by the more defined red-shifted 'aggregation' LSPR that is present ~ 730 nm. These same LSPR peaks have less definition in the ambient temperature assay (**Figure 41**) and also have a lower (relative) attenuance. Additionally, the 37°C assay (**Figure 49** above), resulted in a better separation between the average red-shifted LSPR peaks for the majority of the tested bacterial dilutions.

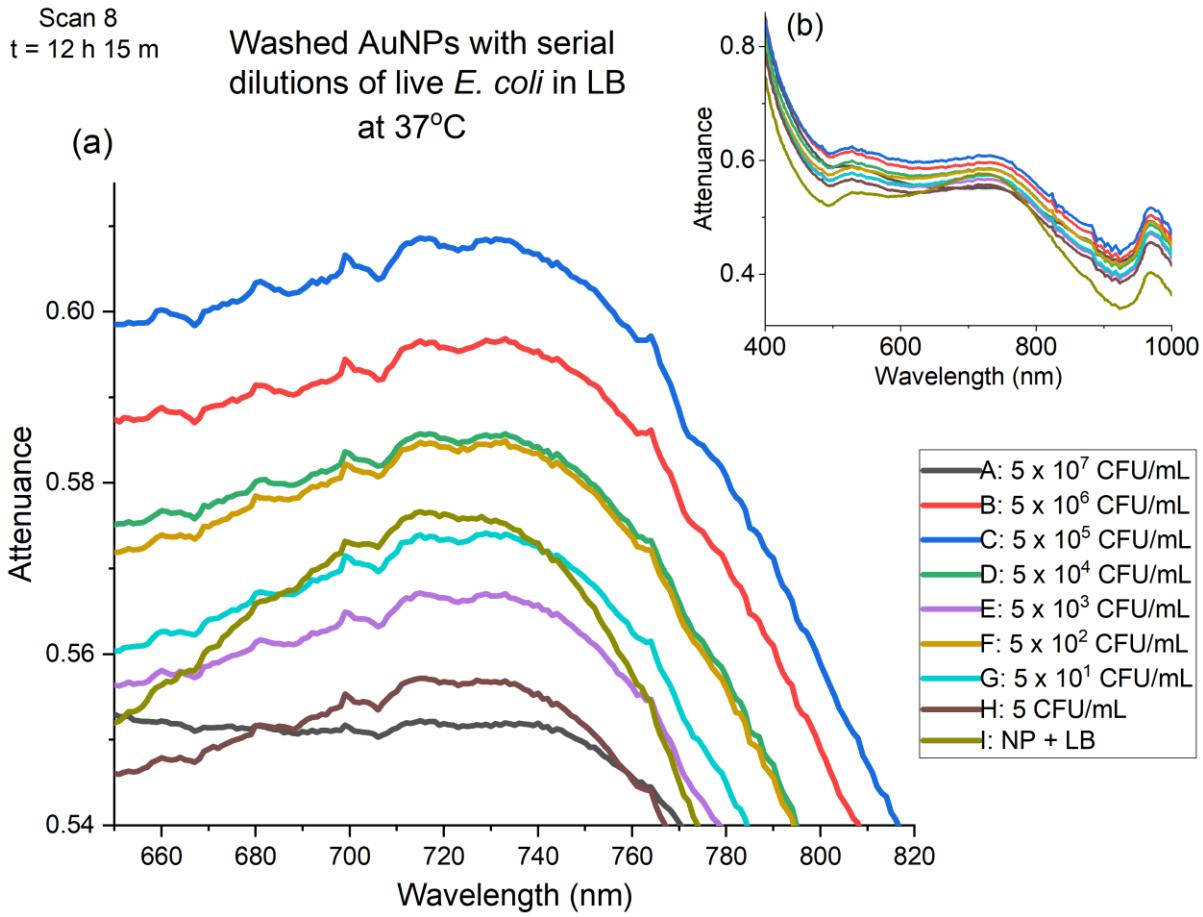

Figure 50: UV-vis spectra of washed citrate AuNPs assayed with live *E. coli* in LB at 37°C, t = 12 h, 15 m. (a) shows a close-up region of the relative positions of the red-shifted plasmon peaks, and inset (b) shows all spectra over the entire range of monitored wavelengths (nm).

After ~ 12 h of incubation at 37°C, all tested dilutions of bacteria are still able to be differentiated from the NP + LB (I, army green line) control. There is an increased level of noise observed in all samples, presumably due to the increased turbidity resulting from bacterial growth, and perhaps also in part due to condensation forming on the lid of the well-plate due to the increased temperature of the experiment.

Comparing the above **Figure 50** with its equivalent assay at ambient temperature (**Figure 42**), there appears to be less aggregation within the 37°C assay. This is evidenced by the comparatively higher attenuance and narrower/more defined LSPR peaks.

4.5 Summary, Conclusions and Discussion

Within the present chapter I have used UV-vis spectroscopy to investigate the optical interactions between as-synthesized citrate AuNPs, washed citrate AuNPs and live *Escherichia coli* in both ultra-pure water (MQ) and a bacterial growth medium (LB). Due to the unique optical and physicochemical properties of AuNPs, in particular their high sensitivity to changes in the environment, the optical monitoring of their aggregation state was used as a metric for their interaction with the tested bacterial dilutions.

When assays were performed in MQ, the initial bacterial aliquot/highest concentration of bacteria tested was in LB, with each sequential 10-fold serial dilution performed with MQ; therefore, the aggregation of these samples are in part due to the (relatively) high ionic strength of the bacterial growth medium in addition to the presence of bacteria.

Bacterial concentrations between approximately 5×10^7 - 5 CFU/mL were investigated to determine if the tested AuNPs presented a viable sensing tool for the presence of (moderately) low concentrations of *E. coli*. Time and (increased, relative to ambient temperature) temperature were also investigated to ascertain if these variables had an effect on the interactions between the tested AuNPs and live *E. coli.*

When both as-synthesized and washed AuNPs were assayed with live *E. coli* in MQ (**Figure 26** and **Figure 31**), only concentrations ≥ 5×10^6 CFU/mL (B, red curves) were sufficient to produce aggregation of the colloids that could be used for sensing purposes. The remaining (lower) tested concentrations of bacteria remained mostly indistinguishable from each other and controls, with minor differences in the spectra becoming noticeable only after an overnight incubation (in the case of washed citrate AuNPs). Considering the relative ionic strength of the test samples and bacterial dilutions, this supports the hypothesis that additional aggregation of the AuNPs *or* displacement of the capping citrate moieties is imperative to the interactions of the AuNPs with the bacterial cells, enabling the 'sensing' of the bacteria. This consequently ruled out the use of MQ water, or other low ionic strength media, as the diluent for further assay development.

In the case of as-synthesized citrate AuNPs assayed with live *E. coli* in LB, there were initially no discernable differences in the spectra produced amongst the different concentrations of bacteria (with reference to the initial measurement assay, **Figure 28**). However, when allowed to incubate overnight at ambient temperature, the as-synthesized citrate AuNPs could be used to differentiate between the control sample and all samples containing bacteria; despite this, the as-synthesized AuNPs were not sensitive enough to the initial CFU/mL, and may thus only sufficiently act as a binary sensor to determine if *E. coli* was present or not in the initial test sample.

When considering the results of the as-synthesized AuNPs with live *E. coli* in LB at ambient temperature, as time progressed, so too did the level of aggregation. There are likely a few contributing factors to this – with an increase in time, the protein corona of the AuNPs evolves – i.e. the adsorbed amino acid, protein and peptide moieties from the LB (and bacterial growth) become more strongly bound to the surfaces of the Au, displacing the weakly-bound citrate. This will proceed more rapidly in the case of washed AuNPs, since there is both less surface-citrate for 'competitors' to displace and the citrate is less densely packed around the surface of the Au.

In summary, the aggregation of the colloid will increase with time, due to both the ions in the LB and to the increasing presence of organic moieties generated by the bacteria.

Elevating the temperature of the assays was investigated to determine if providing optimal growth conditions for the bacteria (nutrient-dense broth, 37°C) would increase the efficiency and/or ability of the tested AuNPs to act as a sensor for live *E. coli*. This however, did not significantly improve the sensing ability or efficiency of sensing in the case of either as-synthesized or washed AuNPs. This point will be further expanded upon in subsequent Chapters.

Differences between the ambient temperature and elevated (37°C) assays can likely be attributed not only to the faster, more consistent growth of the live *E. coli* within the system, but also to the increased thermal energy within the system. Elevating the temperature would result in increased reaction rates, likely including those involving the displacement of the citrate from the surface of the AuNPs.

The work within this Chapter highlights the fact that the sensitivity of this sensor platform depends critically on the proliferation of the live bacteria during an incubation period. The sensitivity of the scheme depends critically on whether the AuNPs are washed or densely citrate-capped. The *in situ* proliferation of the bacteria, in a high ionic strength medium that has resulted in a quasi-aggregated colloid (i.e. the presence of a red-shifted 'aggregation' LSPR peak) amplifies the effect of the bacterial growth on the optical properties of the gold colloid in an exploitable way. This importance of this mechanism will be further discussed and explored in the following Chapter, in which the interactions between heat-killed *E. coli* and AuNPs are examined.

Chapter 5:

Gold Nanoparticle & Heat-Killed *Escherichia coli* Experiments

5.1 General

It was shown in the previous chapter that the development of the optical properties of the mixtures containing LB, AuNPs and live bacteria depended strongly on the incubation time. The problem is, however, that the origin of this phenomenon could arguably depend upon the time-dependent evolution of the protein corona around the nanoparticles (from the components of the LB) and/or on a time-dependent aggregation processes requiring only the proliferation of the live bacteria during incubation. As discussed in Chapter 2, the available literature rarely directly addresses these factors. The purpose of the present chapter is to compare that situation to one in which the viability of the starting bacterial inoculation has been reduced significantly by a heat treatment process. In this way the role of bacterial proliferation is able to be more readily isolated from the time-dependent chemical and/or structural changes at the surface of the nanoparticles. Accordingly, this chapter is focussed on a discussion of the techniques applied in this project for the growth and assaying of heat-killed bacteria with gold nanoparticles. For detailed information regarding the synthesis and characterization of gold nanoparticles used, see Chapter 3. For detailed information regarding the preparation for general bacterial culturing and the results of live *E. coli* assays with gold nanoparticles, see Chapter 4.

5.2 Introduction

In order to determine if the degree to which the *in situ* proliferation of *E. coli*, as opposed to the mere presence of bacterial cells, is an essential component of the sensing mechanism of the proposed sensor, a series of experiments were conducted using heat-killed bacterial suspensions. Heat-treatments previously demonstrated[4] to significantly reduce the viability but not completely kill the bacterial suspensions were applied, simulating pasteurization (or other similar heat-based) decontamination strategies that are used in real-world scenarios.[185-188] This was to establish if the proposed system was able to:

- Reliably detect and/or quantify the starting CFU/mL of heat-killed *E. coli*

- Distinguish between live and heat-killed preparations of *E. coli* and
- Facilitate the recovery of any sub-populations of sub-lethally injured or viable but non-culturable (VBNC) bacteria

It is well established that *E. coli* is a pathogen of concern with the potential to contaminate both water and food products, leading to deleterious health effects.[189-191] However, it is less commonly known that the use of rainwater tanks to supply domestic home water systems also presents a risk from the contamination of faecal, pathogenic and opportunistic bacteria, including *E. coli*. The resulting hygienic quality of said rainwater then becomes dependent on its pasteurization to reduce the microbial load.[187]

One of the common approaches to the control of microorganisms within products for consumption or use (i.e. food or water) is heat, to thermally inactivate bacterial cells.[187, 188, 192-194] While there are additional physical (high pressure processing, irradiation, pulsed electric fields), chemical (chlorination, sodium hypochlorite, peroxyacetic acid, organic acids) and biological methods (probiotics, enzymes, bacteriophages, bacteriocins) which can be implemented to control microbial populations, each has their own associated limitations and applicability which must be considered.[191]

Due to the common application of heat processes such as blanching, pasteurization and sterilization as decontamination strategies, heat treatment was chosen as mechanism to considerably reduce the viability of the *E. coli* in testing.[4, 195] This is significant, particularly in products for consumption, due to the presence of small populations of cells which may survive decontamination efforts, leading to sub-populations of sub-lethally injured cells or those which enter a viable but non-culturable (VBNC) state.[196-198] Sub-lethally injured bacteria are of great concern to human health due to their ability to undergo repair or resuscitate under favourable conditions, such as in the presence of nutrients or in the human gastrointestinal system.

The heat treatment employed experimentally was chosen to mimic real-world scenarios in which levels of bacterial contamination are lowered to within

acceptable levels or below detectable limits at the time of testing, with the potential for a small number of viable bacteria remaining. As determined by differential scanning calorimetry, heat treating *E. coli* at 70°C resulted in 7-$\log_{10}$-unit reductions in cell viability, corresponding to denaturation of ribosomal units.[4]

5.3 Experimental Design and Methods

5.3.1 Chemicals and Materials

All chemicals and materials used within the current Chapter are the same as those listed previously. I refer the readers to Sections 3.1 of Chapters 3 and 4 for the complete details. Relevant methodologies to the current Chapter and experiments will be repeated herein for ease of reference.

5.3.2 Preparation for Bacterial Culturing

All solid Luria-Bertani (LB) agar plates were prepared by pouring a small amount of hot, liquid LB-agar (10 g tryptone, 5 g yeast extract, 10 g NaCl, 15 g agar to 1 L of water, autoclaved) into sterile petri dishes in a Class II laminar flow cabinet (Biology Safety Cabinet; BSC). The LB-agar was allowed to cool and set before lids were placed on the dishes and they were stored inverted at 4°C until required.

The BSC was sterilised before and after each use by cleaning the surfaces with 70% ethanol, followed by 15 – 20 minutes of UV light exposure. The laminar flow in the BSC ensures no aerosols generated within the cabinet are released into the immediate environment as well as maintaining sterility of materials within the cabinet by filtering incoming air-flow.

For liquid cultures, Luria-Bertani (LB) broth (10 g tryptone, 5 g yeast extract, 10 g NaCl in 1 L of water, autoclaved) was used under sterile conditions.

5.3.3 Preparation of Heat-Killed *E. coli* for Assays

Working solutions of *E. coli* broth were prepared by incubating a single colony of *E. coli* in sterile LB overnight and adjusting the optical density at 600 nm (OD_{600}) to 0.1 which is approximately 5 x 10^7 cells/mL (live *E. coli* working solution).[74, 182] For heat-killed *E. coli*, the OD_{600} was first adjusted to 0.1 before the broth was subjected to heating at 75°C, 30 min to significantly reduce the viability (heat-killed *E. coli* working solution).[4]



Figure 51: (left) Schematic representation of live E. coli working solution prepared in a centrifuge tube and (right) the preparation of the heat-killed E. coli working solution, prepared by placing the live working solution in a heating block for 30 min.

5.3.4 Heat-Killed *E. coli* and Gold Nanoparticle Assays

To a 96-well plate, 100 µL of heat-killed *E. coli* working solution was added to the top well and serially diluted (10-fold) down the column from A – H from ~ 5 x 10^7 – 5 cells/mL, using either MQ or sterile LB. Where lanes are diluted with MQ, the initial aliquot of bacterial working solution was in LB, therefore the amount of LB was also serially diluted in each well. To each well, 100 µL of AuNPs were added. Control wells consisted of either 100 µL of sterile LB or MQ in place of *E. coli* working solutions, to which 100 µL of AuNPs were then added. The resulting absorbance spectra were subsequently measured and recorded using a Tecan i-

control infinite 200Pro from either 450 – 800 nm or 400 – 1000 nm in 1 nm increments.

Each serial dilution of *E. coli* was prepared separately, using a single-channel micro-pipette, in triplicate, prior to the addition of AuNPs. Subsequently, each of the presented optical spectra are the average of triplicate scans.

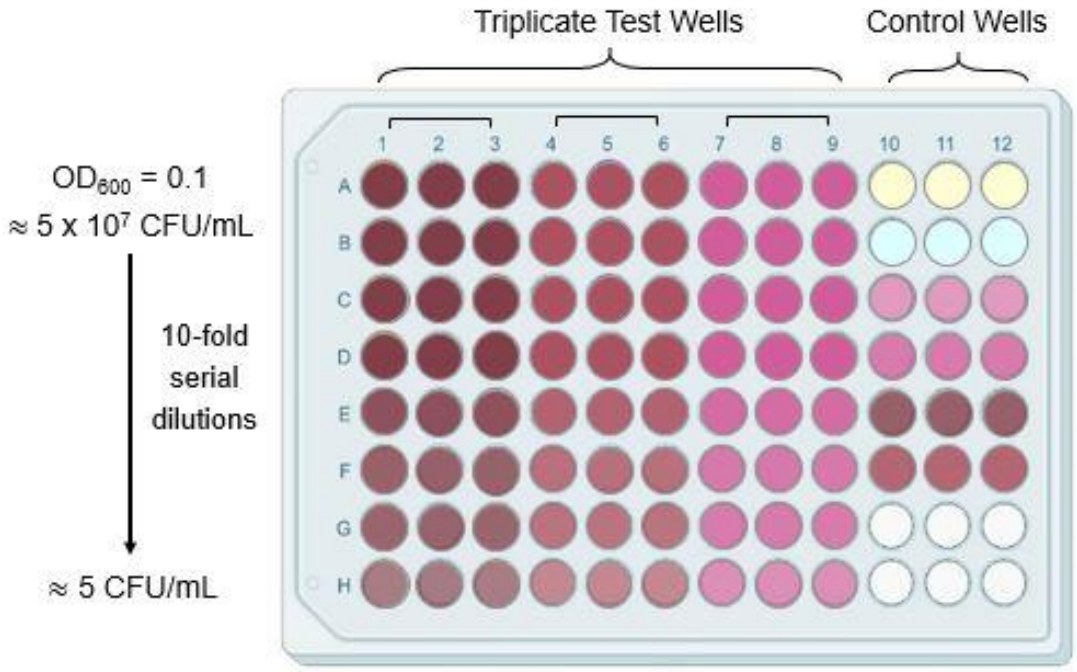

Figure 52: Schematic of the general set-up of an *E. coli* and AuNP assay in a 96-well plate. Each serial dilution is prepared in triplicate (n = 3) and all resulting spectra are the average of triplicate scans.

5.3.5 Concentration of Gold Nanoparticles Used in Assays

As detailed in Chapter 4, Section 3.6, it was assumed all particles were 24 nm in diameter (mean size), the Q_{ext} in water was calculated using the λ_{spr} from control spectral and used in conjunction with the starting concentration of Au (g/L) to calculate the number of particles/m^3. The concentrations of as-synthesized and washed AuNPs are reported in **Table 5** below for ease of reference.

Table 5: Concentration of As-Synthesized and Washed AuNPs used in assays, reported with respect to concentration of particles/m^3 and particles/100 µL.

	As-Synthesized AuNPs	**Washed AuNPs**
Conc. (particles/m^3)	4.24×10^{17}	2.49×10^{17}
Conc. (particles/100 µL)	4.24×10^{10}	2.49×10^{10}

5.4 Results and Discussion

5.4.1 Optical Spectra of AuNP and Heat-Killed *E. coli* Interactions

The following section contains the results from the assays of AuNPs with heat-killed *E. coli.* The heat-killed *E. coli* working solutions were prepared according to the procedure outlined in Section 5.3. Results were recorded immediately post assay and again after an overnight incubation at ambient temperature. Assays were performed with as-synthesized and washed AuNP preparations in both MQ and LB.

Each serial dilution of *E. coli* was prepared separately, using a single-channel micro-pipette, in triplicate, prior to the addition of AuNPs. Subsequently, each of the presented optical spectra are the average of triplicate scans.

Prior to presenting the resulting UV-vis spectra arising from the interactions between the heat-killed *E. coli* and the AuNPs they were assayed with, I will first show the optical contributions from the heat-killed *E. coli* in LB only, **Figure 53**.

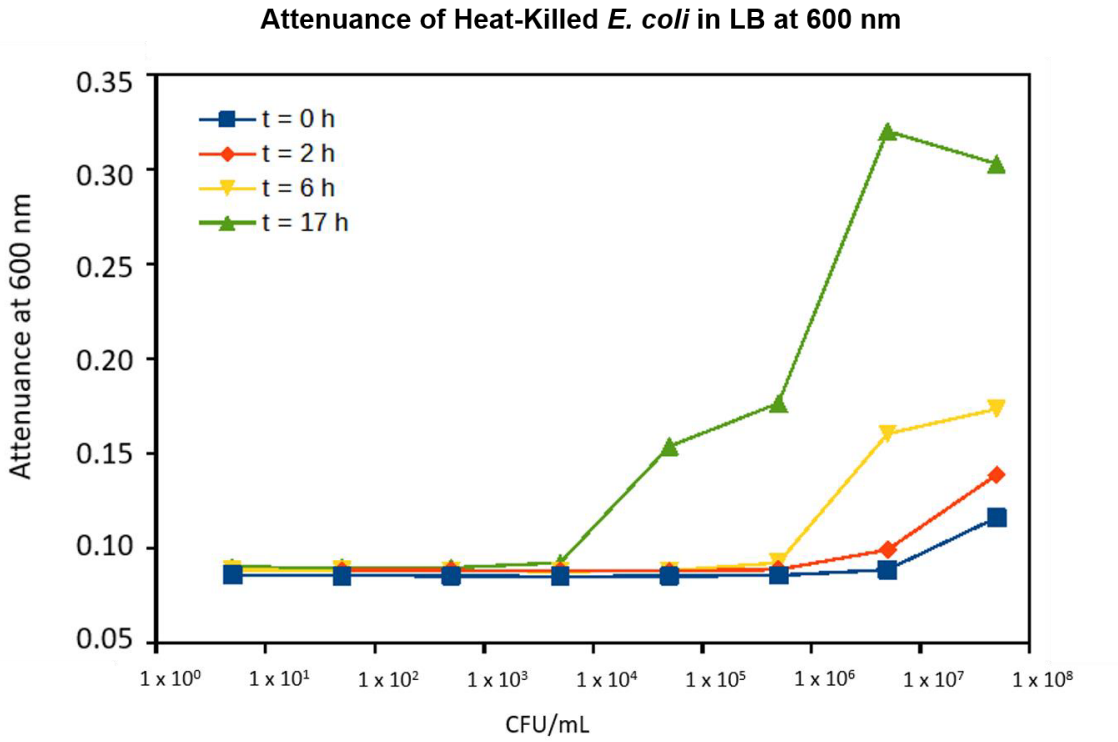

Figure 53: Attenuance of heat-killed E. coli in LB, measured at 600 nm over time, plotted against starting bacterial concentration (CFU/mL). Data points are the average of triplicate scans.

The data in **Figure 53** above shows that the heat-killed preparations of *E. coli* retained a small number of viable cells post heat treatment. Populations of viable cells started from very low numbers (compare to the much higher attenuance of live *E. coli* in LB in Chapter 4) and had a longer lag phase before resuming growth. In general, the higher the starting concentration (CFU/mL equivalent) of heat-killed *E. coli*, the faster the recovery and growth of the bacteria became detectable via the increase in attenuance. This supports the hypothesis that the resumption of growth in the samples comes from a small sub-population of sub-lethally injured cells that after a period of time (lag phase), have undergone sufficient repair within the conditions of the system to resume growth.

Although there was no noticeable increase in attenuance by 17 h incubation for starting concentrations of heat-killed *E. coli* preparations < 5 x 10^3 CFU/mL, it is reasonable to expect that those samples would also eventually have an increase

in attenuance, so long as the initial aliquots contained a few bacterial cells capable of repair and eventual (resumption of) growth.

5.4.1.1 As-synthesized Citrate AuNPs and Heat-Killed E. coli Assays

Assays containing as-synthesized citrate AuNPs and heat-killed *E. coli* were performed according to the procedures outlined in Section 5.3, to the purpose of comparing their optical responses to those obtained between the live *E. coli* and as-synthesized AuNPs, presented in the previous Chapter. The optical spectra were collected immediately post assay, and again after an overnight incubation at ambient temperature.

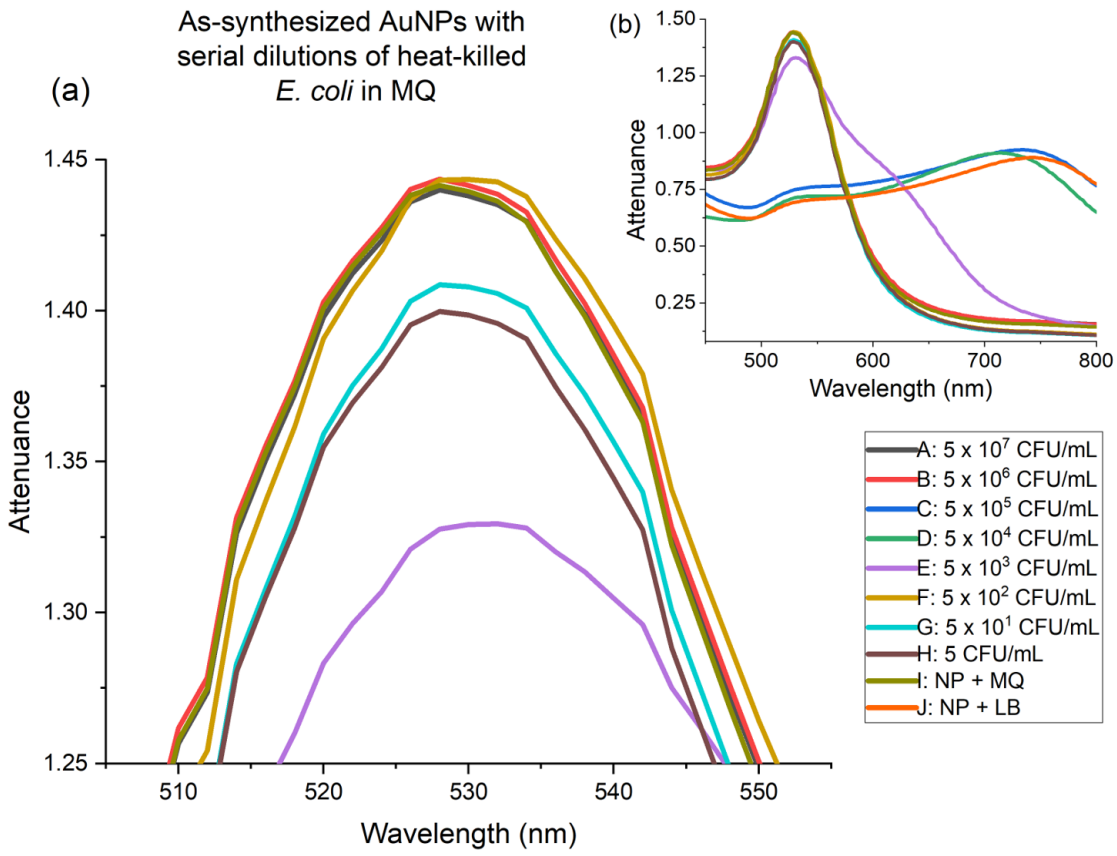

Figure 54: UV-vis spectra of as-synthesized citrate AuNPs assayed with 10-fold serial dilutions of heat-killed *E. coli* in MQ and measured immediately post assay. (a) shows a close-up region of the relative positions of the LSPR peaks, and inset (b) shows the spectra over the entire range of monitored wavelengths (nm).

Comparing the UV-vis spectra of the heat-killed *E. coli* with as-synthesized AuNPs in MQ (**Figure 54**) to those resulting from the assay of live *E. coli* with as-synthesized AuNPs (**Figure 26**), there was a greater level of aggregation caused by the heat-killed *E. coli*. This is evidenced by the decreased attenuance of all samples, as well as the emergence of the second red-shifted LSPR peak in samples containing heat-killed bacterial concentrations between 5 x 10^5 – 10^4 CFU/mL (C and D, dark blue and green lines). In contrast, these second red-shifted LSPR peaks resulted only from live bacterial concentrations ≥ an order of magnitude greater.

Similar to what was seen in the live assay counterpart (**Figure 26**), a small shoulder is forming in sample E (5 x 10^3 CFU/mL, purple line), suggesting the colloid is aggregating and beginning to form the second red-shifted aggregation LSPR peak. Interestingly, the two highest dilutions of heat-killed bacteria did not result in significant aggregation of the as-synthesized AuNPs in MQ, perhaps due to the bacterial suspensions containing an 'optimal concentration' of cells and/or proteinaceous material to stabilise the colloid.

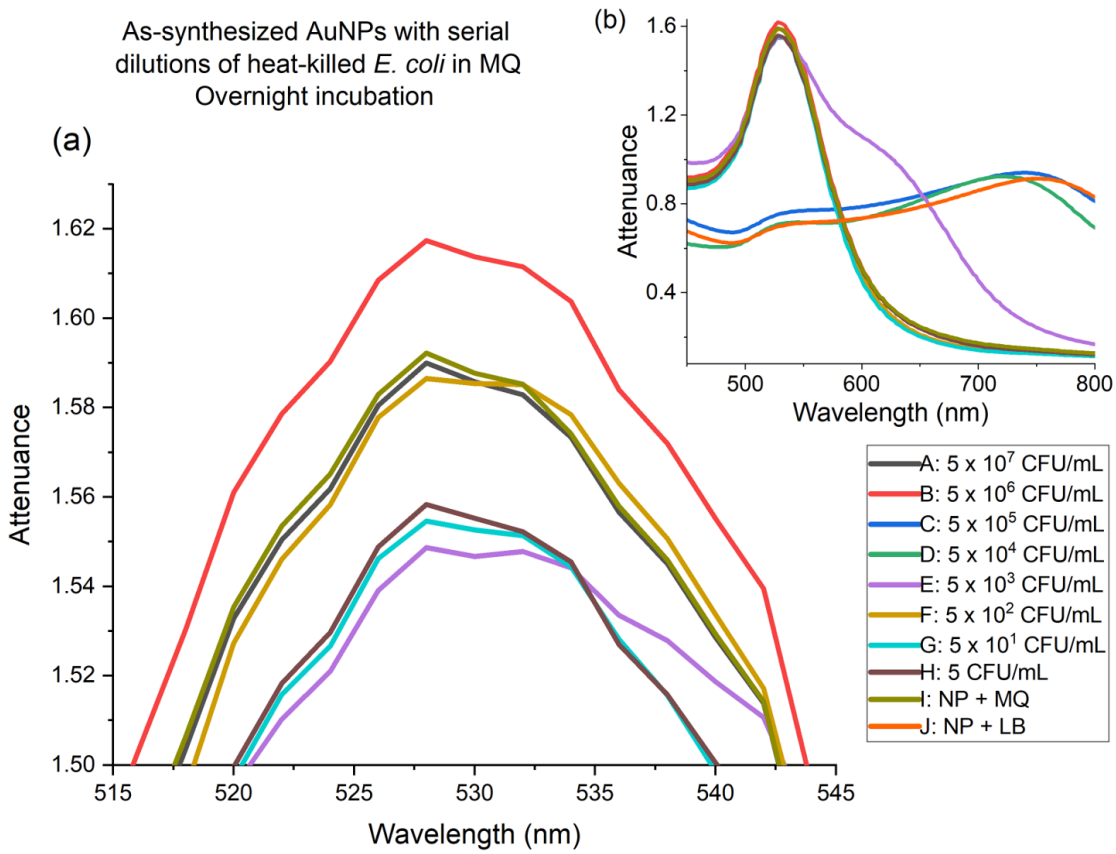

Figure 55: UV-vis spectra of as-synthesized citrate AuNPs assayed with 10-fold serial dilutions of heat-killed *E. coli* in MQ and measured after overnight incubation at ambient temperature. (a) shows a close-up region of the relative positions of the LSPR peaks, and inset (b) shows the spectra over the entire range of monitored wavelengths (nm).

After overnight incubation of heat-killed *E. coli* in the presence of as-synthesized AuNPs at ambient temperature, the attenuance of all samples increased. This suggests there was bacterial growth at all tested bacterial dilutions, therefore, as mentioned earlier the heat-treatment did not fully kill all of the bacterial cells, and the system (i.e. heat-killed *E. coli* in MQ and the presence of as-synthesized AuNPs) is able to support the recovery and growth of sub-lethally injured *E. coli* at ambient temperature.

Further aggregation was observed within the system after an overnight incubation at ambient temperature. However, when comparing the spectra of samples exhibiting a single LSPR peak to those with two peaks, the more red-shifted of

the two LSPR peaks were more sensitive to the starting concentration of the bacterial solutions. This suggests that the initial LSPR of the colloid is not as sensitive to the initial bacterial concentrations and/or red-shifting with (slight) aggregation of the colloid in comparison to the red-shifted aggregation LSPR peak.

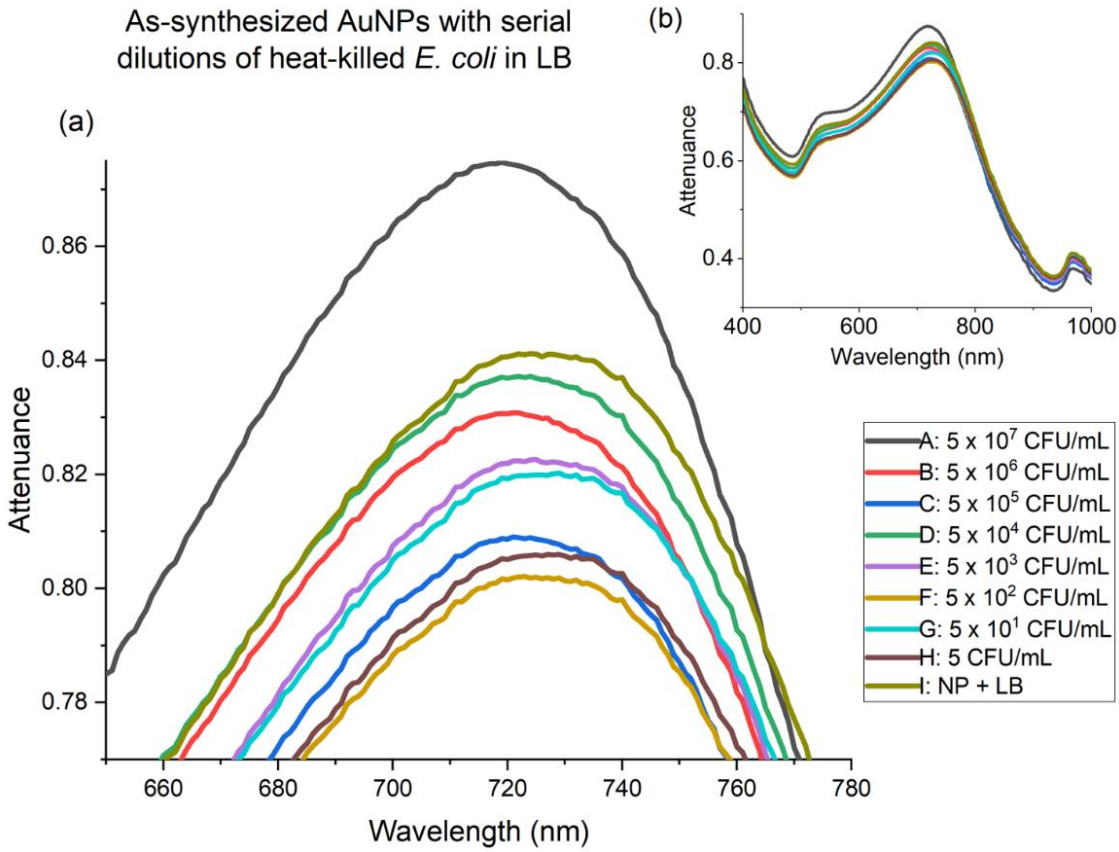

Figure 56: UV-vis spectra of as-synthesized citrate AuNPs assayed with serial dilutions of heat-killed *E. coli* in LB and measured immediately post assay. (a) shows a close-up region of the relative positions of the red-shifted plasmon peaks and inset (b) shows the spectra over the entire range of monitored wavelengths (nm).

Compared to the live bacterial assay with as-synthesized AuNPs (see **Figure 28** in Chapter 4), there appears to be a more consistent pattern to the red-shifting of the resulting spectra. This is in addition to a decrease in attenuance of all samples, indicating that the heat-killed bacteria resulted in additional aggregation of the AuNPs when compared to the live bacteria.

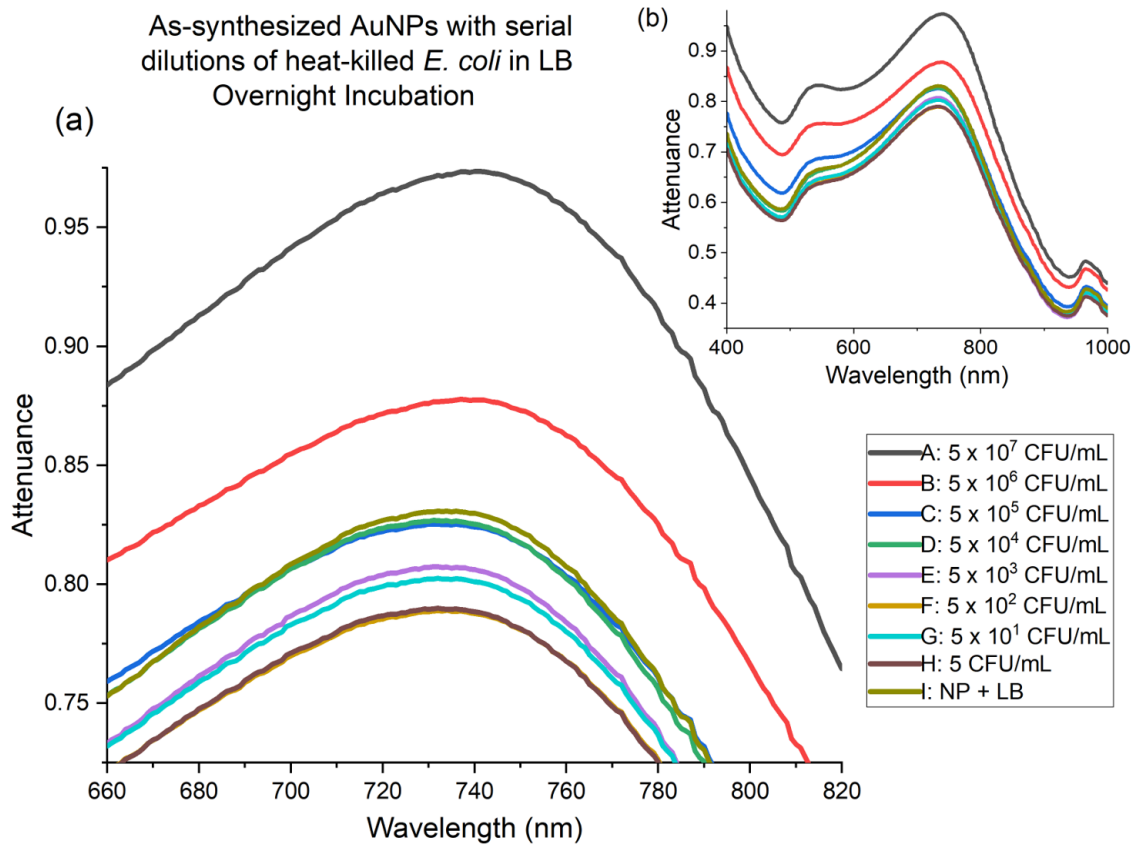

Figure 57: UV-vis spectra of as-synthesized citrate AuNPs assayed with serial dilutions of heat-killed *E. coli* in LB and measured after overnight incubation at ambient temperature. (a) shows a close-up region of the relative positions of the red-shifted plasmon peaks and inset (b) shows the spectra over the entire range of monitored wavelengths (nm).

Overnight incubation of the heat-killed *E. coli* in LB and the presence of as-synthesized AuNPs resulted in further aggregation of the AuNPs without complete collapse of the colloid (i.e. saturation of the sensing capacity of the AuNPs did not occur).

The increased aggregation of all AuNP samples is evidenced by additional red-shifting and dampening of LSPR peaks (compare **Figure 57** above with the initial assay, **Figure 56**). Further to this, bacterial growth resulted in an overall increase in attenuance of all tested samples. When compared to the overnight assay in MQ (**Figure 55**), here, the growth of the bacteria appears to be greater, likely

owing to the nutrient-rich LB, which is able to facilitate the repair of sub-lethally injured cells and general growth of bacteria.

5.4.1.2 Washed Citrate AuNPs and Heat-Killed E. coli Assays

The assays conducted with as-synthesized citrate AuNPs and heat-killed *E. coli* were repeated with washed citrate AuNPs, i.e. as-synthesized AuNPs that were subjected to two cycles of washing (see Section 3.4 of Chapter 3) to remove excess surface-associated citrate that may affect the electrostatic interactions between the particles and bacteria.

Although the removal of excess citrate reduces the overall stability of the AuNPs, particularly within complex systems and those of high ionic strength, this decreased stability can also be beneficial where the controlled or targeted aggregation within a system acts to detect targets of interest.

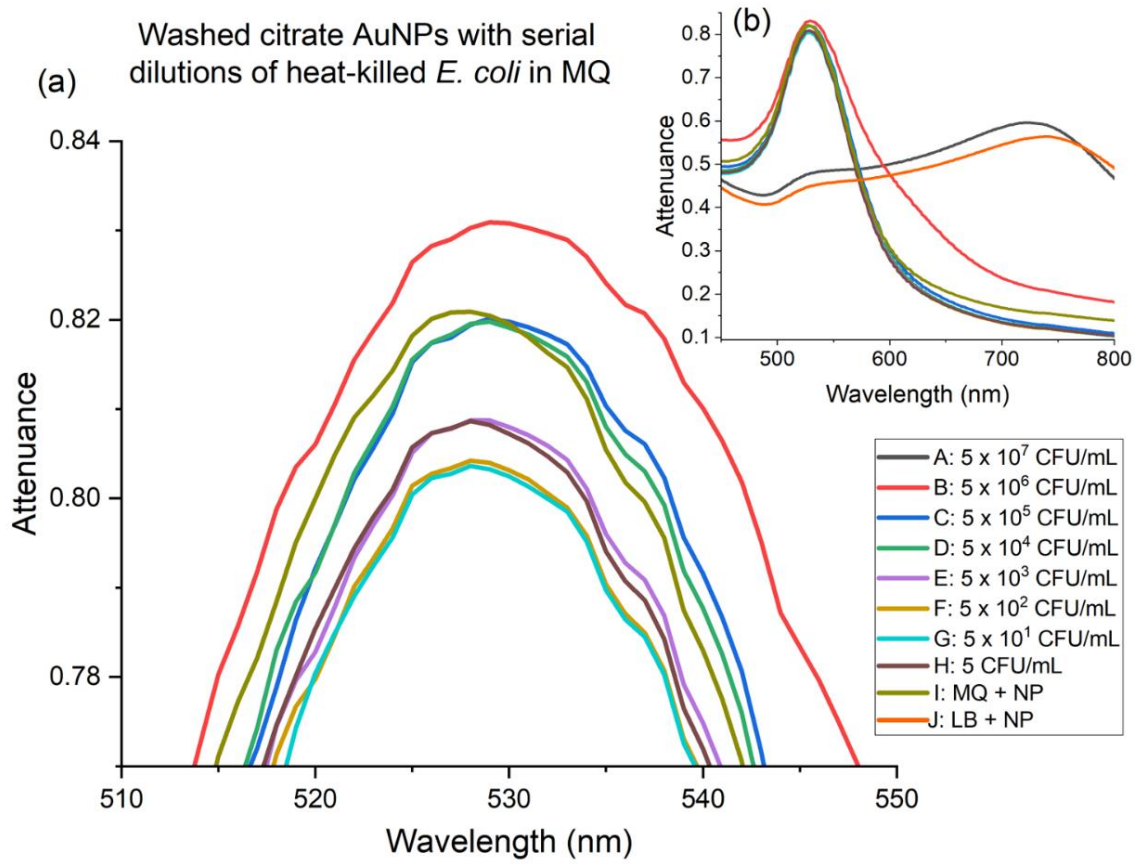

Figure 58: UV-vis spectra of washed citrate AuNPs assayed with serial dilutions of heat-killed *E. coli* in MQ and measured immediately post assay. (a) shows a close-up region of the relative positions of the red-shifted plasmon peaks and inset (b) shows the spectra over the entire range of monitored wavelengths (nm).

There are no appreciable differences between the resultant spectra for the initial assays between live *E. coli* with washed AuNPs in MQ (**Figure 30**) and heat-killed *E. coli* with washed AuNPs in MQ (**Figure 58** above).

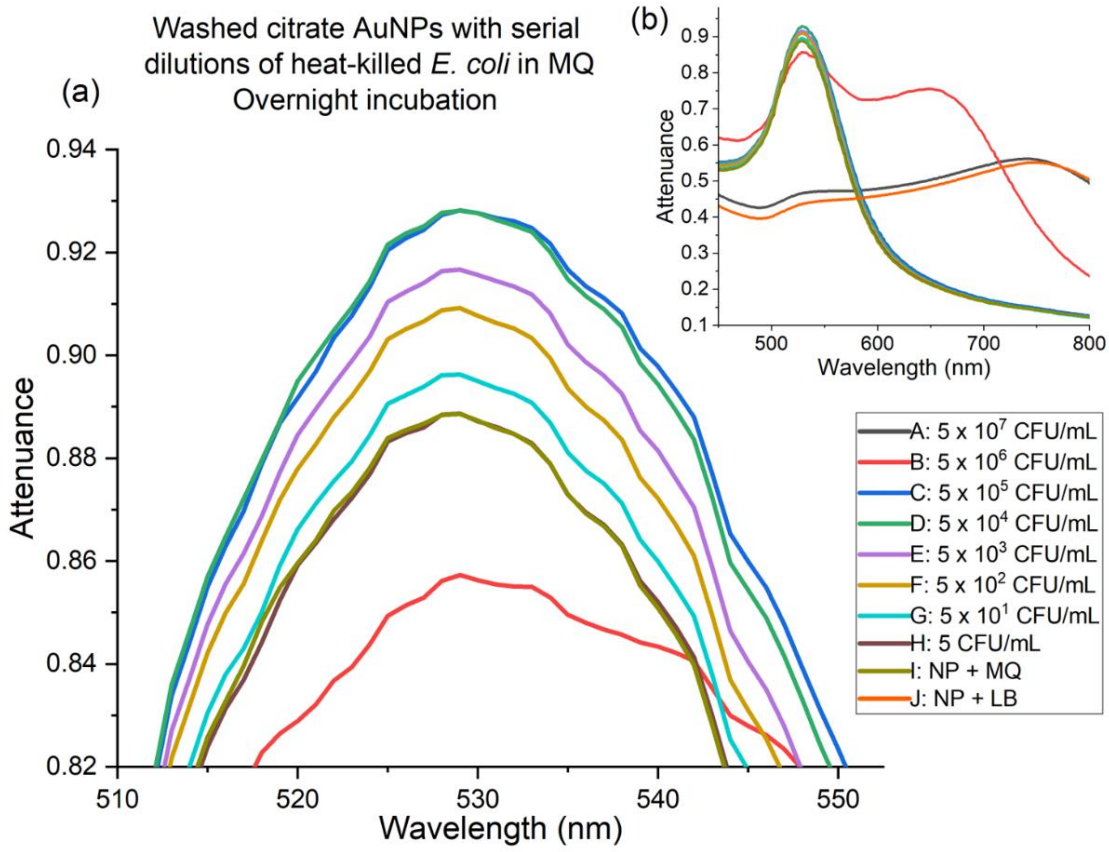

Figure 59: UV-vis spectra of washed citrate AuNPs assayed with serial dilutions of heat-killed *E. coli* in MQ and measured after overnight incubation at ambient temperature. (a) shows a close-up region of the relative positions of the red-shifted plasmon peaks and inset (b) shows the spectra over the entire range of monitored wavelengths (nm).

After overnight incubation at ambient temperature in the presence of washed citrate AuNPs, there was noticeable growth of the heat-killed bacterial dilutions (attenuance of all samples increased), resulting in further aggregation of the colloids within the samples initially containing 5 x 10^7 and 5 x 10^6 CFU/mL (A and B, black and red lines). Of particular note is the evolution of the 'shoulder' in the red curve (B) – this appears to be an in-between semi-aggregated state between the single LSPR of the colloidal state of the AuNPs and the two LSPR peaks where the initial LSPR becomes significantly dampened and broadened (i.e. A, black curve) as the AuNPs becoming increasingly aggregated.

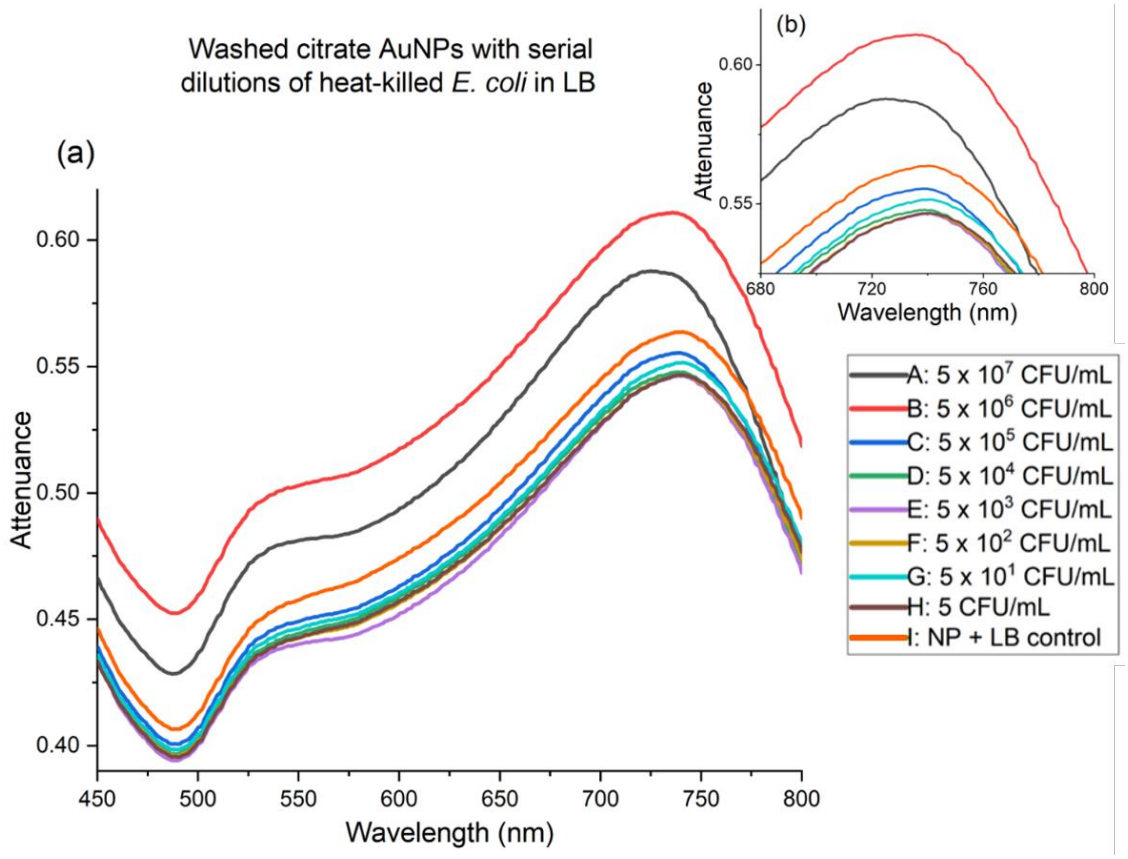

Figure 60: UV-vis spectra of washed citrate AuNPs assayed with 10-fold serial dilutions of heat-killed *E. coli* in LB and measured immediately post assay. (a) shows the spectra over the entire range of monitored wavelengths (nm), and inset (b) shows a close-up region of the relative positions of the red-shifted plasmon peaks.

When initial assays between washed AuNPs and heat-killed *E. coli* were performed in a high ionic strength medium (LB, **Figure 60** above), as opposed to a low ionic medium, (MQ, **Figure 58**) the initial LSPR peak of the colloids (526 nm) became significantly dampened, with an additional and more prominent red-shifted LSPR peak appearing ~ 750 nm. The relative attenuance of all tested bacterial dilutions were lower when compared to those from the MQ assay (**Figure 58**), indicating a higher level of aggregation within the LB assay. The two highest concentrations of heat-killed bacteria tested (A and B, black and red lines) exhibited higher attenuances relative to all lower dilutions (≤ 5 x 10^5 CFU/mL) and were thus most distinguishable from both the control and the lower concentrations of bacteria.

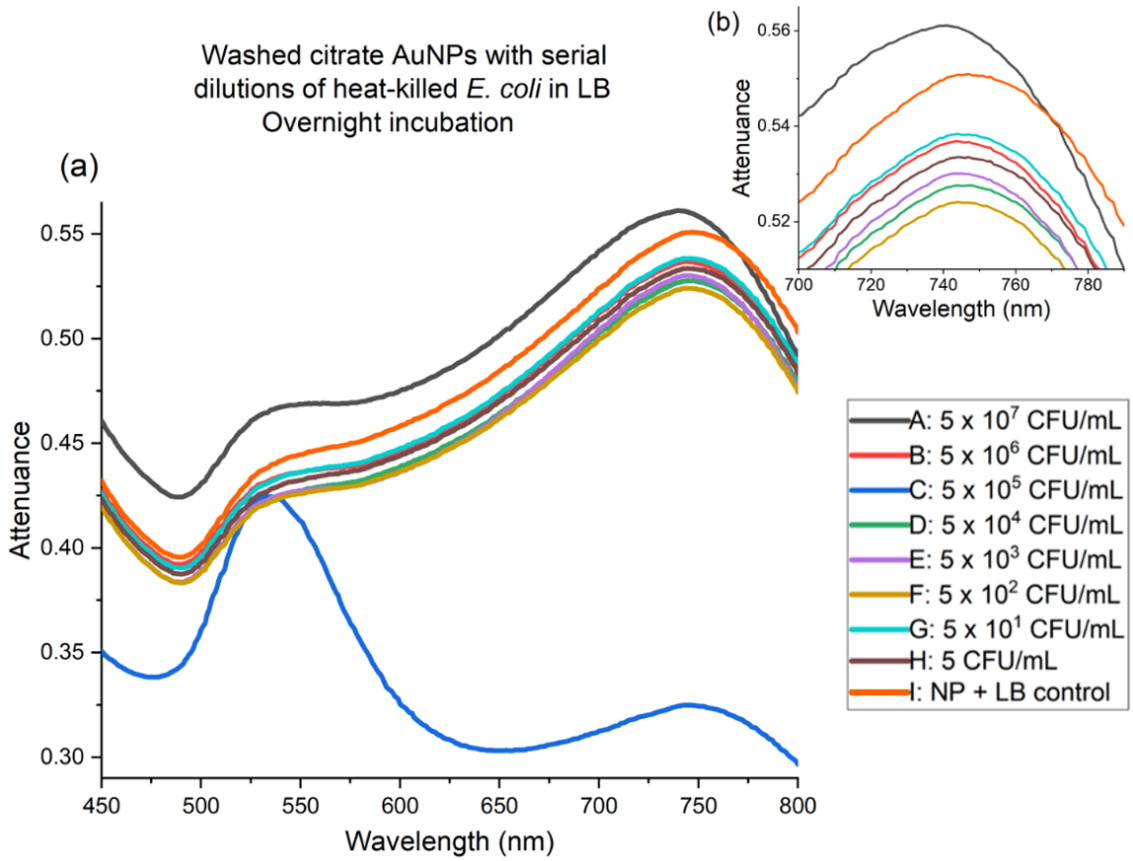

Figure 61: UV-vis spectra of washed citrate AuNPs assayed with 10-fold serial dilutions of heat-killed *E. coli* in LB and measured after overnight incubation at ambient temperature. (a) shows the spectra over the entire range of monitored wavelengths (nm), and inset (b) shows a close-up region of the relative positions of the red-shifted plasmon peaks.

Overnight incubation of the heat-killed *E. coli* in the presence of washed AuNPs at ambient temperature resulted in additional growth of the bacteria, and consequently further aggregation of the AuNPs.

There has been a slight decrease in attenuance of the sample containing the (initial) highest concentration of bacteria (A, black curve), although the optical response of that sample remains appreciably higher than all other tested dilutions. The remaining concentrations of bacteria tested have not differed dramatically from the initial measurements obtained, with the exception of 5 x 10^5 CFU/mL (C, dark blue curve) which appears to be in a quasi-aggregated state,

whereby the red-shifted aggregation LSPR has dramatically decreased in attenuance and the initial LSPR has become relatively more prominent. This suggests this sample contains a higher relative proportion of semi-unaggregated particles and the proportion of larger, more aggregated clusters of AuNPs (likely associated with bacteria and their leaked contents) have flocculated, thus no longer contributing to the LSPR at 750 nm. From this, and the highly variable nature of *E. coli* growth in LB, we can reasonably determine that the interactions between the washed citrate AuNPs and heat-killed *E. coli* in LB are a dynamic and highly variable process.

5.4.2 Washed Citrate AuNP and Heat-Killed *E. coli* Assays at Elevated Temperature (37°C)

The following UV-visible spectra show the changes in the optical readings (measured as attenuance) when washed citrate AuNPs are assayed with heat-killed *E. coli* in LB at 37°C, from concentrations of ~ 5 x 10^7 – 5 cells/mL.

As the 96-well plate was required to reach the desired assay temperature before optimal growth conditions for the bacteria could be met, it is most appropriate to consider the temperature of the first scan as somewhere between ambient temperature and 37°C, with subsequent scans allowing sufficient time for samples to reach the desired temperature. Each sequential scan was approximately 1 hour 45 min apart, allowing for the tracking of the aggregation of AuNPs with respect to time, while providing optimal conditions for the growth and repair of bacteria (nutrient broth and 37°C).

Omitted sequential spectra can be found in Appendix A, and have been excluded from this section for ease of reading.

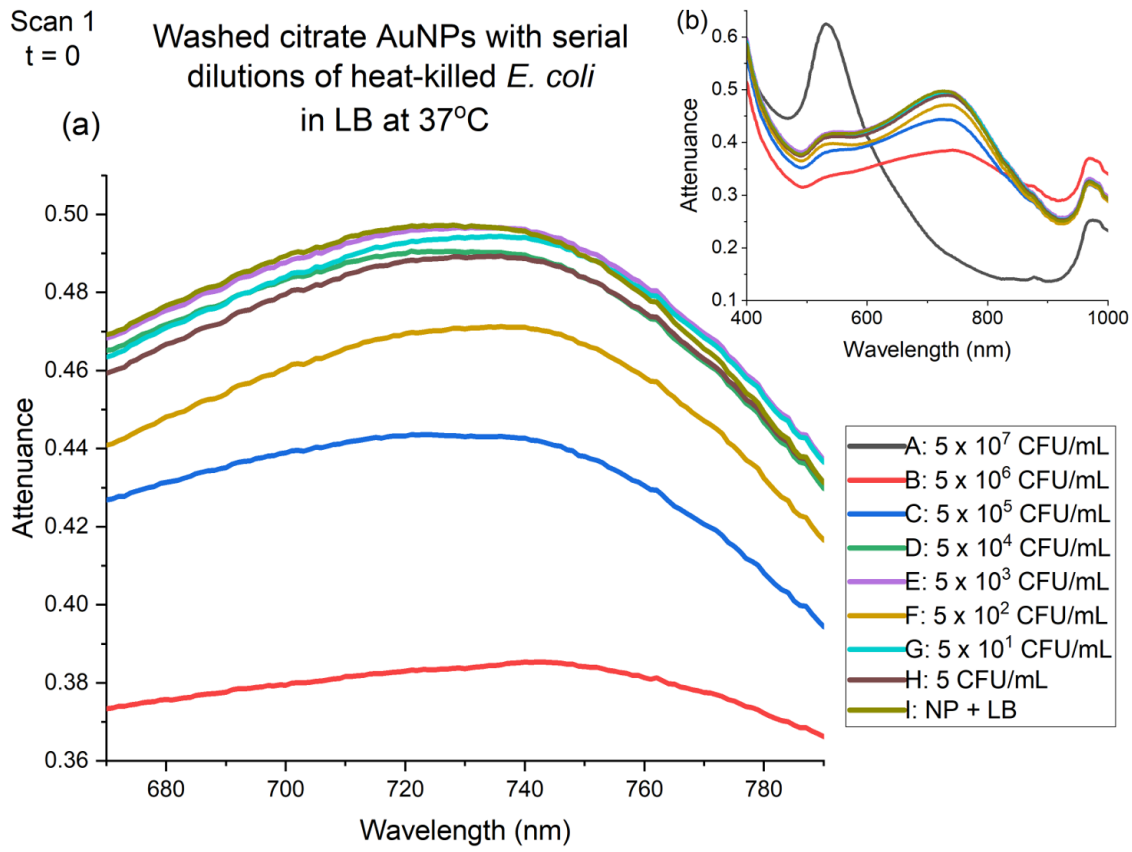

Figure 62: UV-vis spectra of washed citrate AuNPs assayed with 10-fold serial dilutions of heat-killed E. coli in LB at 37°C, measured immediately post assay. (a) shows a close-up region of the relative positions of the red-shifted plasmon peaks, and inset (b) shows the spectra over the entire range of monitored wavelengths (nm).

Comparison of the heat-killed *E. coli* assay with washed AuNPs at 37°C (**Figure 62** above) to the live equivalent (**Figure 47**), revealed that the higher concentrations of heat-killed bacteria (≥ 5 x 10^5 CFU/mL) resulted in spectra that were readily distinguishable from the control (I, army green line), while the remaining concentrations could not. In contrast, the live *E. coli* assayed with washed AuNPs (**Figure 47**), at all tested CFU/mL resulted in spectra that could be differentiated from the control.

In **Figure 62** above, the highest bacterial dilution, 5 x 10^7 CFU/mL (A, black line) remained colloidal, i.e. the initial LSPR peak was not significantly dampened and the characteristic red-shifted LSPR ~ 740 nm was not observed. This suggests

that within the samples initially contaiing 5 x 10^7 CFU/mL of heat-killed *E. coli*, there was an optimal concentration of proteinaceous material within the sample matrix to stabilise the AuNPs.

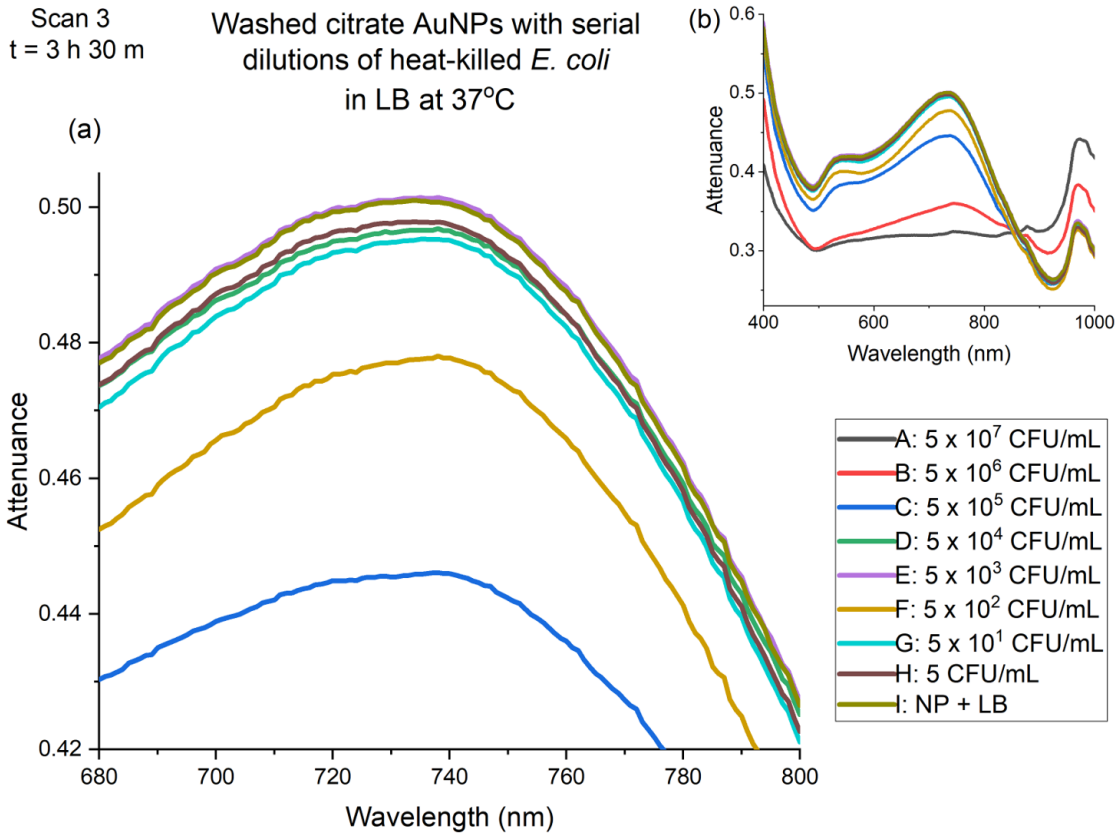

Figure 63: UV-vis spectra of washed citrate AuNPs assayed with 10-fold serial dilutions of heat-killed *E. coli* in LB at 37°C, t = 3 h 30 min. (a) shows a close-up region of the relative positions of the red-shifted plasmon peaks, and inset (b) shows the spectra over the entire range of monitored wavelengths (nm).

Between scan 1 and scan 3 of the heat-killed *E. coli* with washed AuNPs at 37°C (compare **Figure 63** above with **Figure 62**), there has been an appreciable evolution of the second, red-shifted aggregation LSPR peak for all bacterial concentrations ≤ 5 x 10^6 CFU/mL; the increase in these red-shifted LSPR peaks indicate a higher proportion of the AuNPs within the system have increased in size, while less of the initial colloid remains (relatively) unaggregated. The exception to this was the sample initially containing the highest concentration of

heat-killed bacteria (A, black line), that had almost entirely aggregated to the point where no LSPR peaks were detectable.

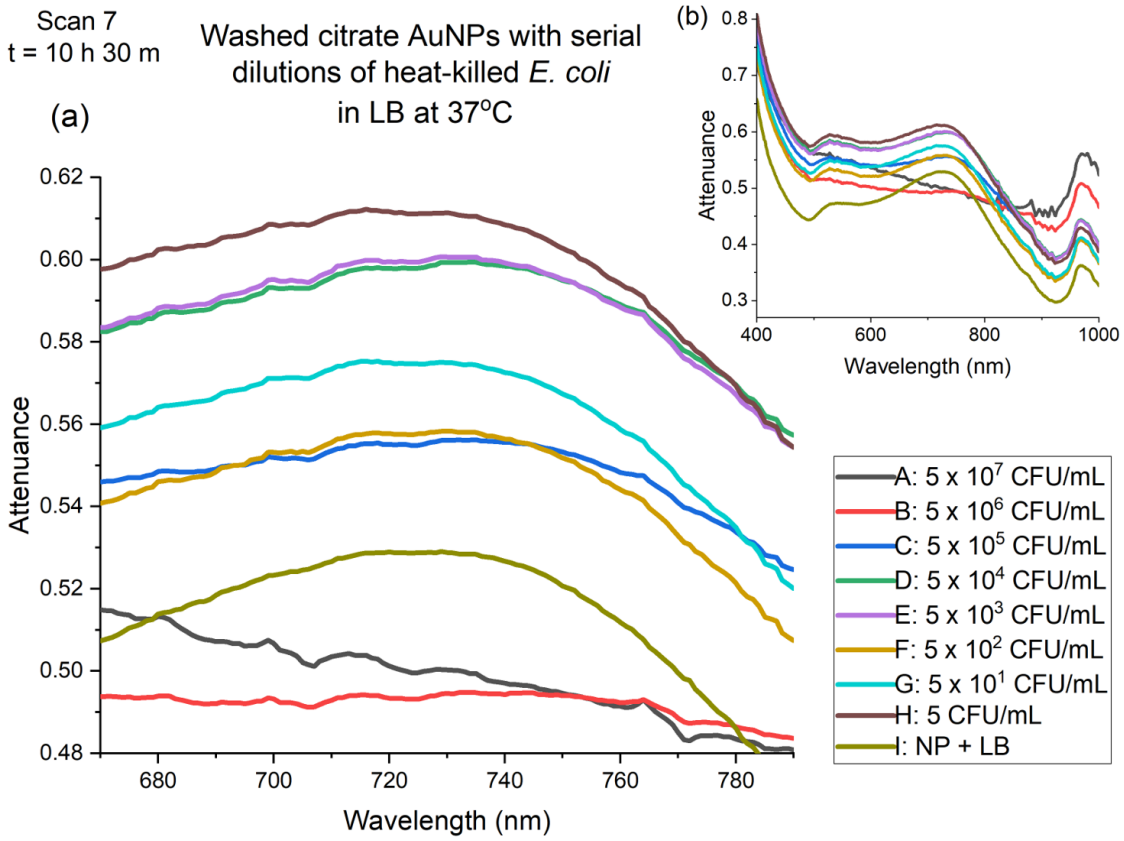

Figure 64: UV-vis spectra of washed citrate AuNPs assayed with serial dilutions of heat killed *E. coli* in LB at 37°C, t = 10 h 30 min. (a) shows a close-up region of the relative positions of the red-shifted plasmon peaks, and inset (b) shows the spectra over the entire range of monitored wavelengths (nm).

Comparison of **Figure 49** and **Figure 64** above revealed that after ~ 10.5 h at 37°C, assays with washed AuNPs resulted in spectra appreciably different from the controls for both live and heat-killed *E. coli*. In the case of heat-killed *E. coli* however, the samples that initially contained the highest bacterial concentrations (A and B, black and red lines) had completely flocculated, as indicated by the absence of any/all LSPR peaks. The concurrent increase in attenuance within those same samples indicates that the bacteria has continued to grow, resulting in the continued aggregation and eventual collapse of the AuNPs.

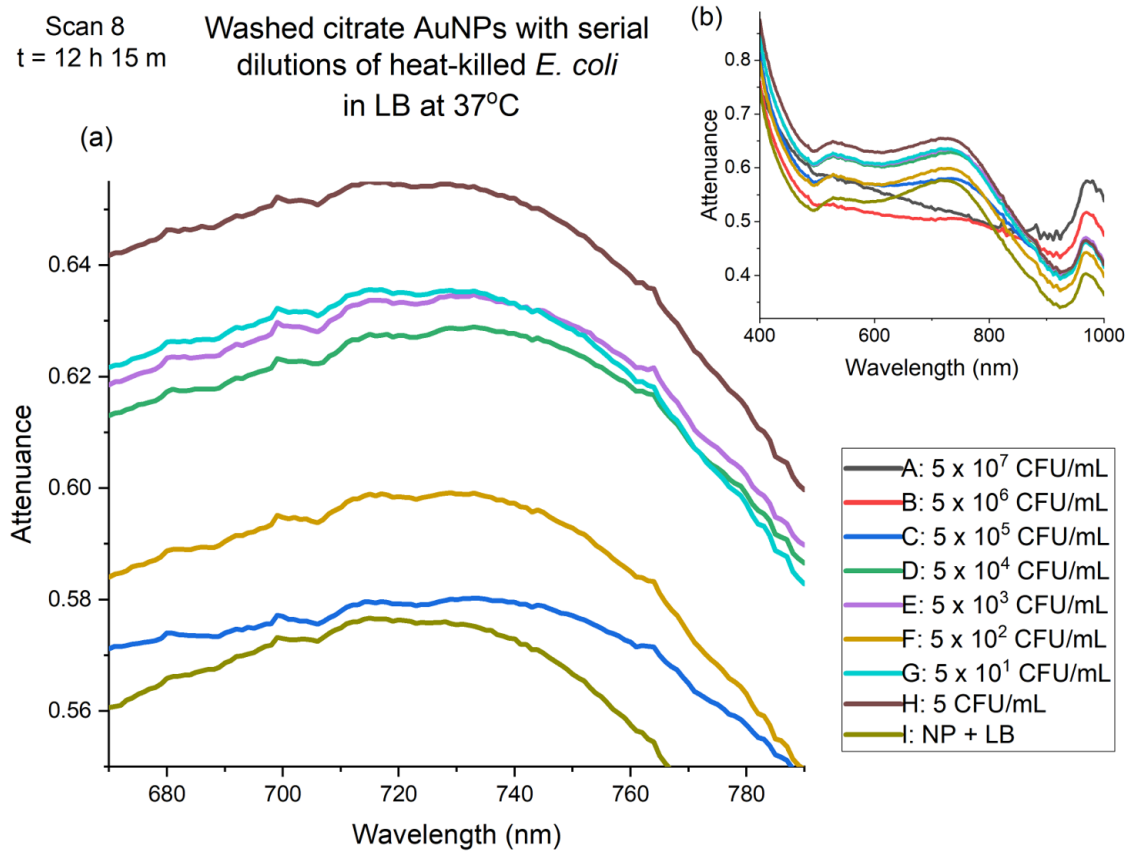

Figure 65: UV-Vis spectra of washed citrate AuNPs assayed with 10-fold serial dilutions of heat-killed *E. coli* in LB at 37°C, t = 12 h 15 m. (a) shows a close-up region of the relative positions of the red-shifted plasmon peaks, and inset (b) shows the spectra over the entire range of monitored wavelengths (nm).

Comparing the resulting spectra from the live *E. coli* assay with washed AuNPs at 37°C (**Figure 50**) to the heat-killed *E. coli* equivalent (**Figure 65** above) revealed that the live bacteria caused a higher degree of aggregation to the washed colloid, as was evidenced by the comparatively flatter and broader LSPR peaks observed in **Figure 50**. This likely resulted from the increased bacterial proliferation as the bacteria was untreated. The heat-killed assay, after ~ 12 h of incubation at 37°C (**Figure 65**) resulted in spectra for all tested concentrations of heat-killed bacteria that were distinguishable from the control. The increased attenuance compared to the previous scan suggests the bacteria had continued to grow, contributing to the aggregation of the colloid within the system.

5.5 Summary, Conclusions and Discussion

Within the present chapter I have investigated the optical interactions between as-synthesized citrate AuNPs, washed citrate AuNPs and heat-killed *Escherichia coli* in both ultra-pure water (MQ) and a bacterial growth medium (LB) through UV-vis spectroscopy. Due to the optical and physical properties of AuNPs, monitoring of their aggregation state was used as a metric for their interaction with the tested bacterial solutions. The experiments reported in this chapter utilized the experimental conditions discussed in Chapter 4 but examined *E. coli* that had been subjected to heat treatment prior to assaying.

As with Chapter 4, the assays that were performed in MQ had the initial bacterial aliquot (highest CFU/mL) in LB, with each sequential serial dilution performed with MQ; therefore, aggregation of these samples are in part due to the high ionic strength of the LB in which the *E. coli* was suspended. All bacterial concentrations ranged from approximately 5×10^7 – 5 CFU/mL (10-fold serial dilutions), and were investigated to determine if the tested AuNPs presented a viable sensing tool for the presence of low concentrations of heat-treated *E. coli*. This is of particular significance in food and water safety, where heat treatments are commonly employed to reduce the microbial load to within safe, consumable limits.[187] It was found that the tested conditions supported the recovery and growth of heat treated, sub-lethally injured *E. coli*; i.e. sub-lethally injured (and possibly VBNC) *E. coli* were able to recover and resume growth in the presence of both as-synthesized and washed AuNPs.

When as-synthesized citrate AuNPs were assayed with heat-killed *E. coli* in MQ (**Figure 54**), the lowest concentration of bacteria sufficient to produce a notable aggregation of the colloid when monitored spectroscopically, was 5×10^3 CFU/mL (E, purple curve). In contrast to the trend of increasing bacterial concentration resulting in increased aggregation of the colloids, the two highest concentrations of bacteria tested (5×10^7 – 10^6 CFU/mL, black and red curves **Figure 54**), did not exhibit aggregation of the colloid, even after an overnight incubation at ambient temperature. This is a surprising result, which suggests there is a certain

concentration range within which the colloid is able to be stabilized by the proteinaceous milieu within the sample matrix, either originating in part from the LB, and from the bacterial cells. Deviation from this concentration results in the aggregation of the colloid, as was seen by the aggregation of the colloid in LB only (control) and at heat-killed bacterial concentrations within the range of 5 x 10^5 – 10^3 CFU/mL.

In contrast, as-synthesized citrate AuNPs assayed with heat-killed *E. coli* in LB (**Figure 56**) resulted in significant aggregation of colloids at all CFU/mL tested. This can in part be attributed to the high(er) ionic strength of the samples (compare LB to MQ), however, direct comparison between the MQ and LB assays must take into consideration the controls of the NP + LB only. As will be discussed in later chapters, the age of the colloid affects the stability and therefore the degree of aggregation. The assays conducted in MQ were performed with relatively fresh colloids, thus they were less stable and more prone to aggregation in high ionic strength matrices. In contrast, the assays conducted with LB used the same colloids that had aged, becoming more stable and therefore more resistant to aggregation. The same trend was observed with washed citrate AuNPs with respect to the age of the colloids and will be discussed further in Chapter 7.

The relatively lower colloidal stability of the washed AuNPs compared to the as-synthesized AuNPs resulted in the appearance of a second, red-shifted aggregation LSPR peak, notably in assays conducted in LB (**Figure 60** and**Figure 61**), but also in samples with high bacterial concentrations (e.g. **Figure 58** and**Figure 59**, samples A, B and LB controls). This second, red-shifted LSPR peak was found to be more sensitive to the starting CFU/mL of the heat-killed bacteria, particularly as the initial LSPR dramatically decreased in attenuance and size relative to the second LSPR. This is consistent and reflective of the continued increase in aggregation of the colloid over time, gradually progressing to a complete collapse of the AuNPs in some instances.

Flocculation was observed to a lesser degree when AuNPs were assayed with heat-killed *E. coli* compared to live *E. coli*, suggesting that the *in situ* growth of

the bacteria is the most important contribution to the aggregation and eventual collapse of the colloid. This answers the question posed at the beginning of this Chapter.

However, when the growth of the bacteria is slower (i.e. in the case of the heat-killed *E. coli*), the resulting spectra of the colloids were more distinguishable from each other, as well as the controls. There appears to be a few competing/simultaneous phenomena within the AuNP/bacteria mixtures – the red-shifted, second LSPR forms as a result of the aggregation state of the colloid, the attenuance of the samples gradually increases up to a certain threshold as a result of the growth of the bacteria. Beyond this threshold, the attenuance begins to decrease gradually (peak dampening), red-shift and broaden, reflective of the further aggregation of the colloid. This 'threshold' relates to the concentration of the colloid and ionic strength of the medium they are in, as well as any moieties present within the sample matrix that may either stabilize or de-stabilize the colloid.

Initially, a greater level of aggregation was observed in the assays of heat-killed *E. coli* with as-synthesized and washed AuNPs. This can be attributed to the appreciably higher concentration of proteinaceous material within the heat-killed sample matrix as a result of the heat treatment of the bacteria. This suggests that chemical changes to the environment do play a role in the aggregation, albeit one that is secondary to the proliferation of bacteria. However, as time progressed and there was sufficient time for the growth of bacteria, it was found that the live bacteria resulted in more peak dampening and broadening compared to the heat-killed cells. Thus, over time, the growth of the bacteria results in an increase of proteinaceous milieu, contributing to the aggregation and eventual collapse of the colloid within the system.

Increasing the temperature to 37°C did not seem to notably improve the speed or sensitivity of the sensing for either the as-synthesized or washed AuNPs overall (taking into account the initial measurements were unlikely to have been equilibrated to 37°C). However, in the case of the heat-killed bacteria, the assay required approximately 7 h incubation (see Appendix A) before all concentrations

of the heat-killed bacteria were able to be distinguished from the control. Thereafter the washed AuNPs were more able to distinguish between samples containing live bacteria and the controls (AuNPs + LB) compared to heat-killed bacteria. This may in part be due to the difference between the protein coronas that form in the matrices of the live *E. coli* compared to the heat-killed *E. coli* and its subsequent effect on the downstream interactions and aggregation of the colloids.

Chapter 6:

Investigation of Gold Nanoparticle & *Escherichia coli* Interactions via Transmission Electron Microscopy

6.1 General

In this chapter, the interactions of the synthesized gold nanoparticles (AuNPs) with live or heat-killed preparations of bacteria are examined in detail. The detailed information on the techniques applied in this project for the preparation and imaging via the transmission electron microscopy (TEM) of *Escherichia coli* samples, with and without gold nanoparticles, is included in this chapter. For information and transmission electron microscopy characterization of gold nanoparticles only, see Chapter 3.

6.2 Introduction

A deeper understanding of the ways in which the interactions between the AuNPs and the *E. coli* occur within the proposed system is required than what can be afforded by UV-visible spectroscopy; it was originally postulated that the evolution of the red-shifted plasmon peak ~ 750 nm would be the result of AuNPs aggregating on the surfaces of, and associated almost exclusively with the bacterial cells contained within the test samples (not including those that had initially aggregated due to the high ionic strength of the LB). Extensive TEM imaging of the various *E. coli* preparations and the *E. coli*/AuNP sample mixtures previously investigated and characterized through UV-vis spectroscopy was performed to visualise:

- The interactions between the as-synthesized and washed AuNPs with live, heat-killed and extra heat-killed preparations of *E. coli*
- The effect of the heat-treatment(s) on the *E. coli* (with respect to appearance of the bacteria and how the AuNPs subsequently interact with them)
- Where the AuNPs are aggregating within the systems, and to determine if there is a difference between the preparations of *E. coli* or the type of AuNP (as-synthesized vs. washed)

6.2.1 Extracellular Proteins Associated with *Escherichia coli* Growth

As discussed in the preceding Chapters, the proposed sensor involves the *in situ* growth of the *E. coli* in the presence of the AuNPs. Consequently, changes to the growth medium are likely to have an effect on the detectable optical signals from the AuNPs. As *E. coli* proliferate, the composition of the LB is changing as nutrients are depleted, but more importantly, a number of proteinaceous moieties are released into the sample matrix.[199, 200] These proteins readily interact with the AuNPs, displacing the loosely-bound citrate moieties and ultimately contribute to the aggregation of the colloid.

To best understand the observations and features present within the following transmission electron micrographs containing *E. coli*, I first guide the readers to **Figure 66** below, reproduced with permissions from Chandel et al.[199] The below **Figure 66**shows two distinct forms of protein aggregates, amyloid fibrils (a)), and amorphous aggregates (b)) as visualized via TEM. Although both amyloid fibrils and amorphous aggregates are the result of protein misfolding and aggregation, their morphologies are considered *ordered* and *disordered*, respectively.[199]

In addition to protein aggregate formation, one must consider the leakiness of *E. coli* cells, even in the absence of external stimuli. This leakiness however, is appreciably affected by factors that influence the cellular envelope, for example the insertion or deletion of genes affecting membrane formation/stability and permeability, as well as factors such as osmotic shock and heat.[200-204]

This cell leakiness is distinctly different from cell lysis, usually resulting in the release of periplasmic contents into the surrounding medium, whilst lysis results in the release of contents from the entire cell, including DNA, proteases and other cellular proteins. It is possible to have populations of cells that are “leaky but still viable” in which cell lysis is kept to a minimum.[204]

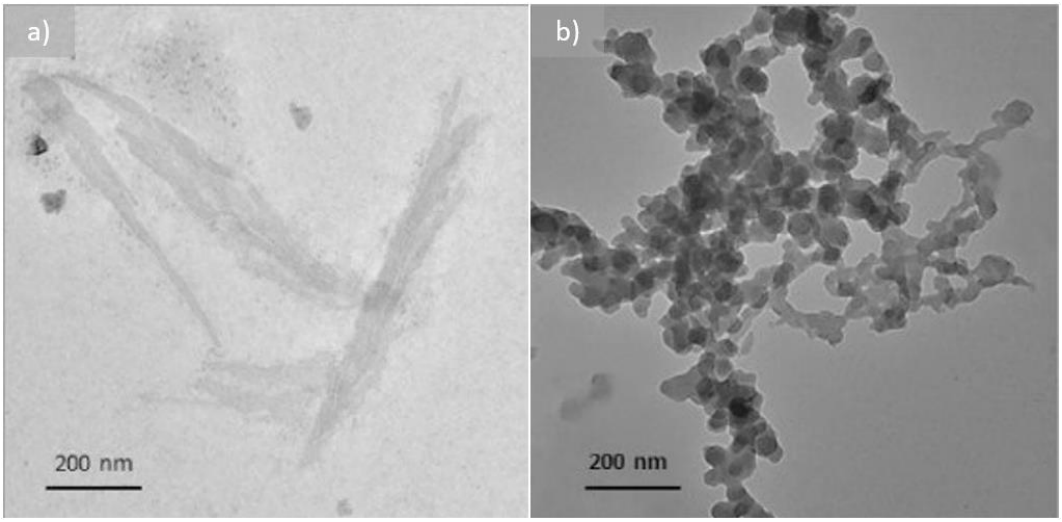

Figure 66: Representative transmission electron micrographs of protein aggregates a) amyloid fibrils and b) amorphous aggregates. Reproduced with permissions from Chandel et al.[199]

Of particular note is the established relationship between the application of heat-treatment and an increased observation of leakiness associated with the outer membrane of Gram-negative bacteria.[204] This is congruent with other reports of sub-lethal heat treatments resulting in outer membrane damage and the subsequent release of lipopolysaccharide (LPS).[205]

An additional contribution to the extracellular milieu of proteins within the culture medium is likely to include the formation of outer membrane vesicles (OMVs).[206-208] OMV formation and secretion is an evolutionarily conserved process, having been observed under various growth conditions, *in vivo* and *in vitro*. While the first instance of this phenomenon was reported for batch cultures of *E. coli*, this process is common to all species of bacteria having been tested so far – both Gram-negative, Gram-positive, pathogenic and non-pathogenic.[207]

OMVs are typically spherical, bilayered and comprised of phospholipids, outer membrane proteins and lipopolysaccharides, ranging from 10 – 300 nm in diameter.[206, 207] OMVs have been found to additionally contain proteins from the periplasm and cell wall, which may become trapped during

their formation and release, although *inner* membrane and cytoplasmic proteins, metabolites, nucleic acids, signalling molecules and other lipids have also been observed within OMVs.[206, 208]

Consequently, is likely that the nature of some of the numerous amorphous aggregates observed in the TEM samples containing *E. coli* are very similar, or in some instances, identical to OMVs.

6.2.2 Uranyl Acetate as a Fixative and Contrast Agent for Biological Specimens using Transmission Electron Microscopy

As biological samples are largely comprised of lighter elements such as carbon, hydrogen, nitrogen, oxygen, sulphur etc., the accelerated electrons within an electron beam do not strongly interact with these atoms, giving poor contrast to samples.[209] To circumvent this issue, sample preparation methods including chemical fixation, dehydration and embedding in resins for ultramicrotome thin-sectioning, or the removal of water from cells by freezing, freeze-substitution, freeze-fracture or vitrification, are often used prior to imaging. This can be used in conjunction with negative staining, whereby heavy metal ions in solution are deposited onto samples to provide significantly increased contrast.[209, 210]

Significant drawbacks with some of the aforementioned sample preparations exist, including; the native state of the sample is generally not maintained and, in some instances, artefacts may be introduced into the sample. For example, mesosomes are convoluted membranous structures found within the cytoplasm of bacterial cells and can be observed through freeze-fracture and thin-section preparations of cells but only when fixed with osmium tetroxide. Mesosomes were later determined to be artefacts caused by fixation with osmium tetroxide.[211]

It is possible to achieve up to 2 nm resolution with air-dried negatively stained biological samples using heavy metal-based stains such as uranyl

acetate (UA). It is the formation of microcrystals of the heavy metal salts upon drying that limits the resolution of this staining/imaging combination.[210, 212] Other negative stains which have been employed successfully for the visualisation and increased contrast of biological specimens include, but are not limited to: osmium tetroxide, other uranyl salts (e.g. formate, sulfate), Na/K- phosphotungstate, Na/methyl-silicotungstate, methylamine tungstate, ammonium molybdate, cadmium thioglycerol and vanadate.[213] Although this may be considered comparatively low resolution compared with techniques such as cryo-imaging (which yields better than 1 nm resolution in some cases), the simplicity and speed of sample preparation makes this a popular preparation technique for bio-TEM.[210] Another often overlooked benefit to the use of some heavy metal stains are their fixative properties, enabling the rapid and simple fixation of biological specimens, structures and intermediates in their near-native states within the order of milliseconds. Negative staining also provides the advantage of enabling aqueous sample preparation.[214] Omission of fixation, dehydration and embedding procedures can be beneficial; it has been shown that these procedures can result in a loss of membrane lipids from cells, particularly during dehydration and fixation processes. Importantly, cells that are fixed with both osmium tetroxide and uranyl acetate, in addition to embedding and dehydration procedures, retain the highest amount of membrane lipids.[215]

Aqueous solutions of uranyl acetate and formate salts have a relatively low pH (~ 4.2 – 4.5) resulting in an electrostatic repulsion between the uranyl ions and bacterial surfaces, so that the ions do not penetrate the surface of the bacteria. This results in clearly contrasted bacterial cells and surface structures.[216]

To provide sufficient contrast to the biological components of the samples intended to be visualized via TEM, UA was used as both a negative stain and fixative. UA was chosen for its fine grain size, and its reported ability to fix protein-level molecular structures within ~ 10 milliseconds.[214] Consequently, additional chemical fixation and dehydration procedures

were able to be omitted to avoid the introduction of artefacts[211] and preserve the near-native state of bacterial membranes and their lipids.[215] It is common to include a washing step after drop-casting the sample onto TEM grids; this helps remove background debris which may be present in the supernatant and prevent the formation of salt crystals as the solvent dries. Within the following experiments, it was of interest to determine if the AuNPs had aggregated in the surrounding medium, on the bacterial cells, or were perhaps loosely associated with the cells. Washing of the drop-cast samples had the potential to remove weakly-associated AuNPs or those that had aggregated in the supernatant as opposed to on/around the bacteria, and was thus omitted to give a more holistic 'picture' of the investigated system.

6.3 Experimental Design and Methods

6.3.1 Chemicals and Materials

Uranyl acetate (UA) was kindly provided by the University of Technology of Sydney for experimental use. A 2% (v/w) solution (100 mL) was prepared by dissolving powdered UA in MQ and subsequently passing the resulting solution through a 0.22 µm filter pre-rinsed with MQ. The solution was stored in a light-proof container. All other chemicals and materials used within the present Chapter are the same as those listed previously. I refer the readers to Sections 3.1 of Chapters 3, 4 and 5 for the complete details. Relevant methodologies to the current Chapter and experiments will be repeated herein for ease of reference.

6.3.2 Preparation of Extra Heat-Killed *E. coli* for Assays and Electron Microscopy

Working solutions of *E. coli* broth were first prepared by incubating a single colony of *E. coli* in sterile LB overnight and adjusting the optical density at 600 nm (OD_{600}) to 0.1 (approximately 5 x 10^7 cells/mL (live *E. coli* working solution)).[74, 182]

For heat-killed *E. coli*, the OD_{600} was first adjusted to 0.1 before the broth was subjected to heating at 75°C, 30 min to significantly reduce the viability (designated as 'heat-killed *E. coli*' working solution).[4]

For extra heat-killed *E. coli*, the OD_{600} was adjusted to 0.1 before the broth was subjected to heating at 75°C for 2 h to further reduce the viability of the bacteria, while remaining below temperatures demonstrated to denature lipopolysaccharides (LPS) and DNA (120°C and 94°C respectively),[4, 217] thus intended to leave the outer membrane and LPS largely intact. This latter preparation was designated as 'extra heat-killed *E. coli*'.

6.3.3 Preparation of Biological and Mixed Samples for Transmission Electron Microscopy

The methods of S.C. Hayden[218] and C. Lin[219] were adapted for use. For TEM grid preparation of bacteria-only samples, bacterial working solutions (see Chapters 4 and 5 for detailed procedures on growth and preparation of live and heat-killed *E. coli* working solutions) were drop cast directly onto holey carbon, formvar-coated copper 200 mesh grids (ProSciTech) in 3 x 2 µL aliquots. Each droplet was allowed to settle on the grid for 20 – 30 sec before being wicked off. Grids were subsequently negatively stained with 2 µL of 2% w/v uranyl acetate (UA) for ~ 20 sec before the excess liquid was wicked off and the grids were left to dry under an upturned Petri-dish to avoid contamination while drying.

For mixed samples, the pre-mixed bacteria and AuNP solutions were drop cast directly onto TEM grids as per the method detailed above. Mixed sample grids were also negatively stained with 2% UA, after drop casting and prior to being imaged. All samples containing biological material were imaged using a JEOL JEM-F200 FE-TEM at 120 kV equipped with a Gatan Rio 1816 camera.

6.4 Results and Discussion

6.4.1 Concentration of Gold Nanoparticles Used in Assays

For details on the calculation of concentration of as-synthesized and washed AuNPs used experimentally, refer to Chapter 4, Section 3.5. For ease of reference, see **Table 6** below.

Table 6: Concentration of As-Synthesized and Washed AuNPs used in assays.

	As-Synthesized AuNPs	**Washed AuNPs**
Conc. (particles/m^3)	4.24 x 10^{17}	2.49 x 10^{17}
Conc. (particles/100 µL)	4.24 x 10^{10}	2.49 x 10^{10}

6.4.2 Transmission Electron Micrographs of Control Samples

Control samples for each type of treatment applied experimentally to the *E. coli* were prepared as detailed in previous Chapters and also in Sections 6.3.2 and 6.3.3 of the current Chapter. A sample of AuNPs stained with uranyl acetate was also prepared and visualized via TEM in order to ensure any artefacts were identified and accounted for.

6.4.2.1 Transmission Electron Micrographs of Gold Nanoparticle Controls

Gold nanoparticles were drop-cast and stained with uranyl acetate (UA) (as per the mixed samples preparation method in Section 6.3.3 of the current Chapter) to examine the effect of UA on the AuNPs. **Figure 67** shows UA stained AuNPs did not exhibit significantly more aggregation when compared to non-stained AuNPs (compare with **Figure 17**). The main observable difference was the increase in visible background of the stained AuNP sample, likely a result of the ample citrate becoming stained.

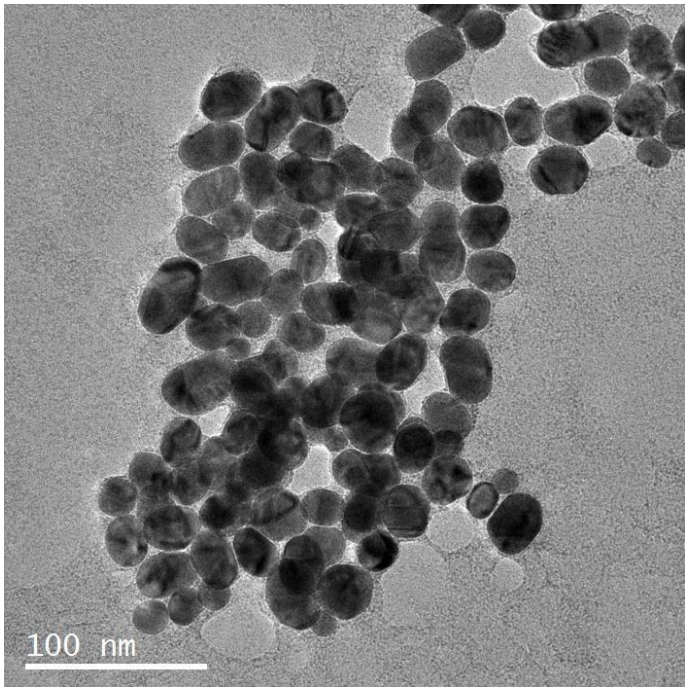

Figure 67: Representative transmission electron micrograph of as-synthesized AuNPs stained with 2% (w/v) UA.

Stained AuNPs exhibited no greater aggregation compared to non-stained AuNPs. Some increase in background is apparent (increase in granularity of the background), likely a result of the abundant citrate becoming stained by the UA.[220] Similar staining effects and contrast of AuNP stabilising moieties have been demonstrated previously, for example, in the works of Yang et al.[221] and Cui et al.[222]

6.4.2.2 Transmission Electron Micrographs of Live *E. coli* Controls

Live *E. coli* controls (not treated with AuNPs) were grown according to the methods outlined in Chapter 4, Section 3.3, and prepared as per Section 6.3.3 of the current Chapter. Briefly, aliquots of live *E. coli* working solution were drop-cast onto TEM grids and stained with 2% (w/v) uranyl acetate to both stain and fix the samples for electron microscopy.

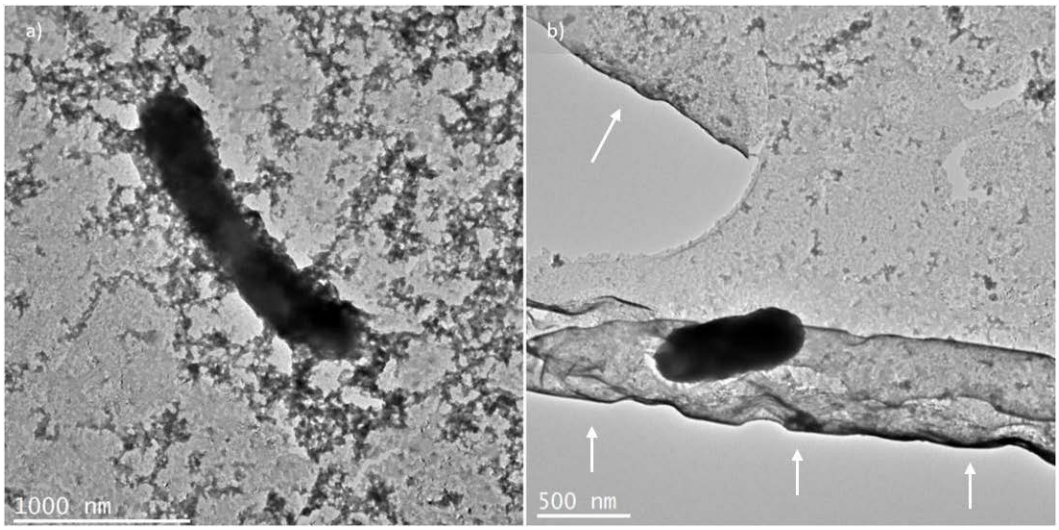

Figure 68: Representative transmission electron micrographs (a) and b)) of live *E. coli* controls stained with UA. White arrows in b) indicate amyloid-like fibril protein aggregates.

In general, the untreated, live *E. coli* exhibited a relatively smooth outer cell envelope and were often seen in the vicinity of protein aggregates (see appendix for additional micrographs). With reference to **Figure 68** a), there was a significant amount of amorphous protein aggregates associated with the cell surface and in its vicinity. In **Figure 68** b) however, the proteinaceous material surrounding the bacterium appears to be mostly comprised of ordered amyloid-like fibril proteinaceous aggregates (indicated by white arrows), with a comparatively low level of amorphous aggregates.

6.4.2.3 Transmission Electron Micrographs of Heat-Killed *E. coli* Controls

Heat-killed *E. coli* controls (not treated with AuNPs) were grown and prepared according to the methods outlined in Sections 6.3.2 and 6.3.3 of the current Chapter. Briefly, aliquots of heat-killed *E. coli* working solution were drop-cast onto TEM grids and fixed/stained with 2% UA.

The following **Figure 69** - **Figure 71**) demonstrate the effect of heat treatment on morphology the *E. coli*. In particular, heat treatment was observed to result in disruption to the cell envelope, and increased aggregation/disorder of the amorphous aggregates within the samples.

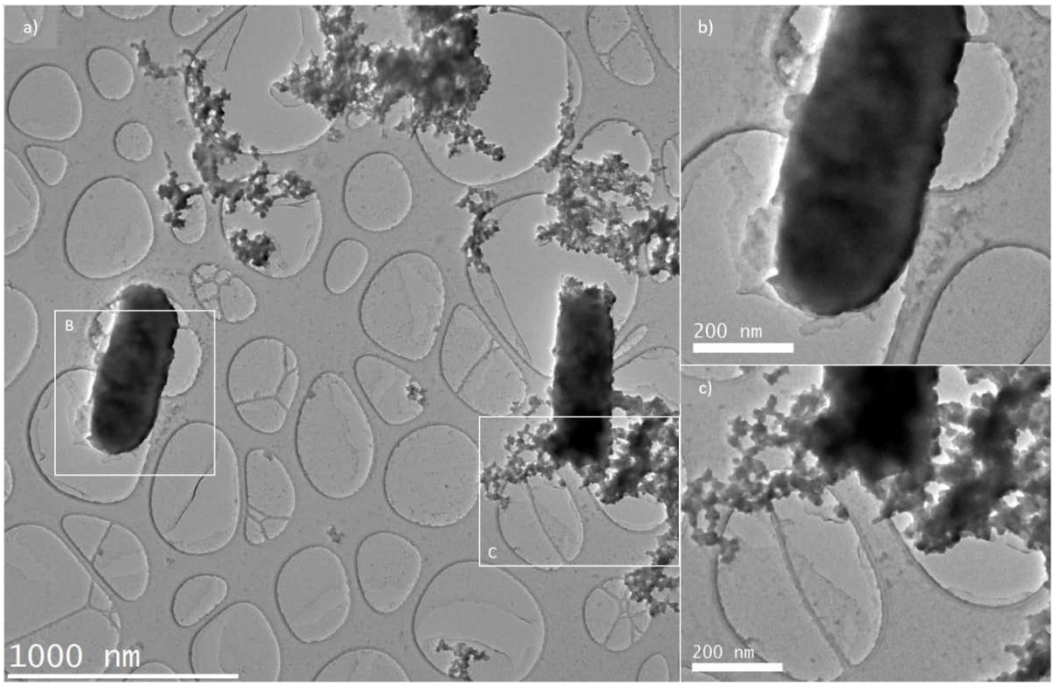

Figure 69: Representative transmission electron micrograph a) of a heat-killed *E. coli* cell stained with UA. Insets b) and c) show magnified regions of the labelled boxes in a).

With reference to **Figure 69** above, the heat treated *E. coli* cells displayed cell envelope disruption, leakage of cellular material and significant aggregation of the amorphous aggregates associated with, and in the

vicinity of the cells. The striations visible on the surface of the left-most cell, (magnified in b)) suggests there are areas of varying electron density. This suggests some level of aggregation within the cytoplasmic contents has occurred.

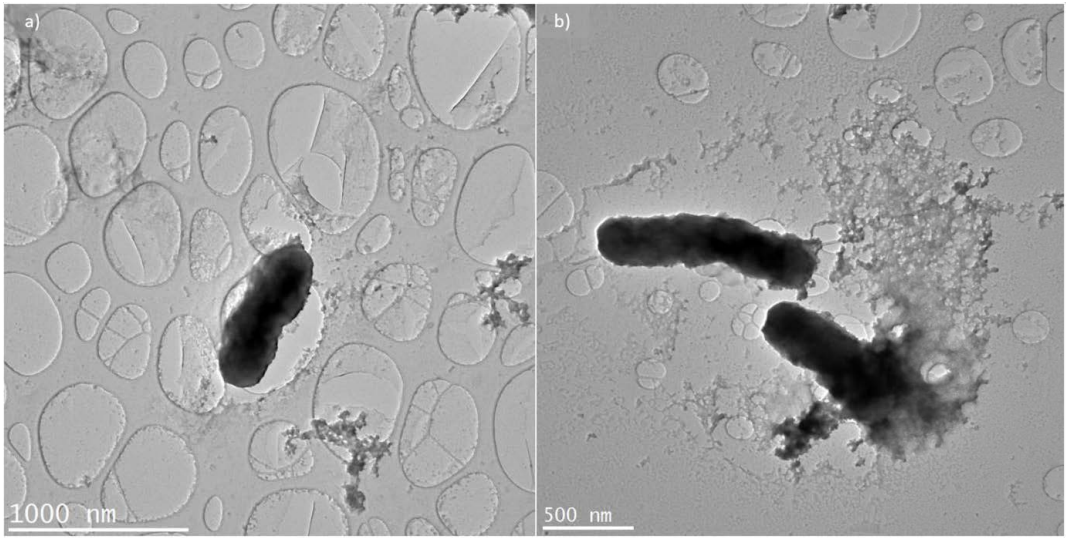

Figure 70: Representative transmission electron micrographs (a) and b)) of heat-killed *E. coli* controls stained with UA.

In general, applying heat treatment to the *E. coli* resulted in damage and disruption to the cellular envelope. In particular, when comparing the heat-killed *E. coli* (**Figure 69** and **Figure 70**) to the live *E. coli* (**Figure 68**), those that were heat treated displayed a more bumpy, pitted and rough looking surface, indicative of disruption and damage to the cell envelope.[223] Additionally, there was an appreciably greater amount of leaked cellular material resulting from the disrupted membranes. This was likely to have originated from the periplasm[204] as there was little cytoplasmic aggregation observed in the heat-treated cells and they remained very electron-dense (i.e. retained a lot of the UA stain), indicating the majority of the cellular contents had remained within the cells.

6.4.2.4 Transmission Electron Micrographs of Extra Heat-Killed *E. coli* Controls

Extra heat-killed *E. coli* controls (not treated with AuNPs) were grown and prepared according to the method outlined in in Sections 6.3.2 and 6.3.3 of the current Chapter. Briefly, aliquots of extra heat-killed *E. coli* working solution were drop-cast onto TEM grids and fixed/stained with 2% UA to simultaneously fix and negatively stain samples for electron microscopy.

Increasing the duration of the heat treatment (i.e. extra heat-killed) applied to the *E. coli* resulted in slight differences to the morphological defects that were similarly observed in the heat-killed *E. coli* (compare **Figure 71** below with heat-killed controls, **Figure 69** and**Figure 70** above). Extra heat-killed *E. coli* cells in general exhibited greater disruption to the cell envelope, and in some instances sections of the cell were no longer present (**Figure 71** b)). Further to this, evidence of cytoplasmic condensation (highlighted by white arrows in **Figure 71** below) and/or loss of inner cellular material was observed, while the leaked contents from the cells had a more granular appearance in the extra heat treated samples.

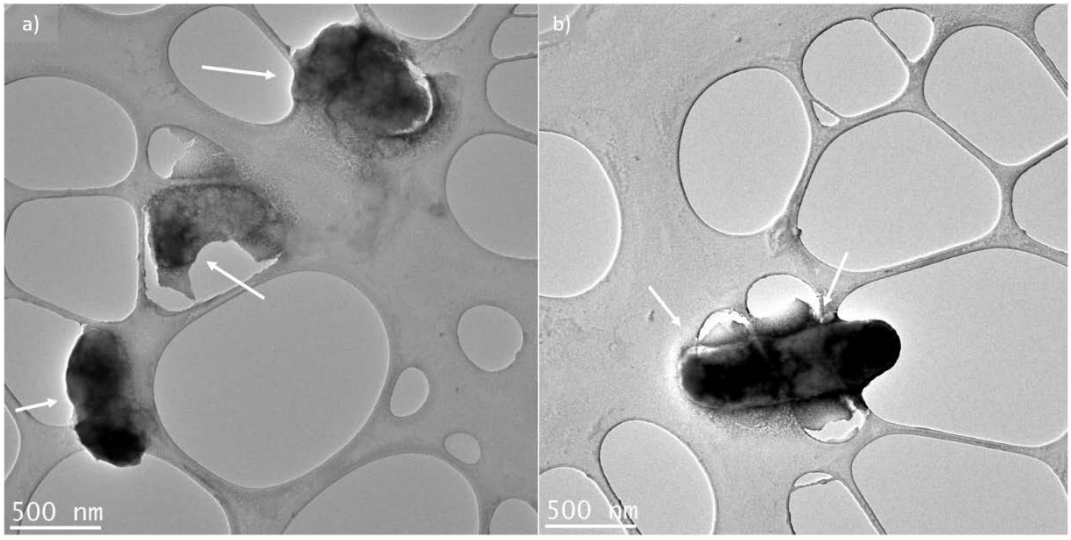

Figure 71: Representative transmission electron micrographs (a) and b)) of extra heat-killed *E. coli* controls stained with UA. White arrows indicate areas of cytoplasmic condensation.

In addition to the further disruption to the cell envelope, extra heat treatment appeared to result in samples with less amorphous aggregates present when visualized via TEM. This may in part be due to the increased length of time at which the cells were exposed to higher temperatures, resulting in the increased orientational disorder of the lipids comprising the cytoplasmic and outer membranes.[224] The more disordered, and thus the larger the proportion of membrane-comprising lipids in the liquid-crystalline phase (compared to gel-phase), the more fluid and leaky the resulting cell.

6.4.3 Transmission Electron Micrographs of Gold Nanoparticles and Live *Escherichia coli*

To visualize the interactions between the live *E. coli* and AuNPs, assays were performed as per the methods outlined previously, with aliquots taken immediately after the addition of AuNPs to the bacterial solutions, and after 2 h of incubation. These aliquots were subsequently prepared for TEM, allowing for a visual representation of the *E. coli*/AuNP interactions, and whether these had an effect on the cell morphologies.

6.4.3.1 Live *E. coli* and As-synthesized Gold Nanoparticles t = 0

Live *E. coli* were assayed with as-synthesized AuNPs, as per the methods previously outlined in Chapter 4 and prepared according to Section 6.3.3 of the current Chapter. Briefly, aliquots of the sample mixtures were taken immediately after addition of AuNPs to the system, and prepared for TEM.

The following figures show that the interaction of the as-synthesized AuNPs with live *E. coli*, even for a very brief amount of time, resulted in an appreciable disruption to the cell envelope with an increased observance of leaked cellular materials when compared to the live *E. coli* controls (compare **Figure 72** below with **Figure 68** for example).

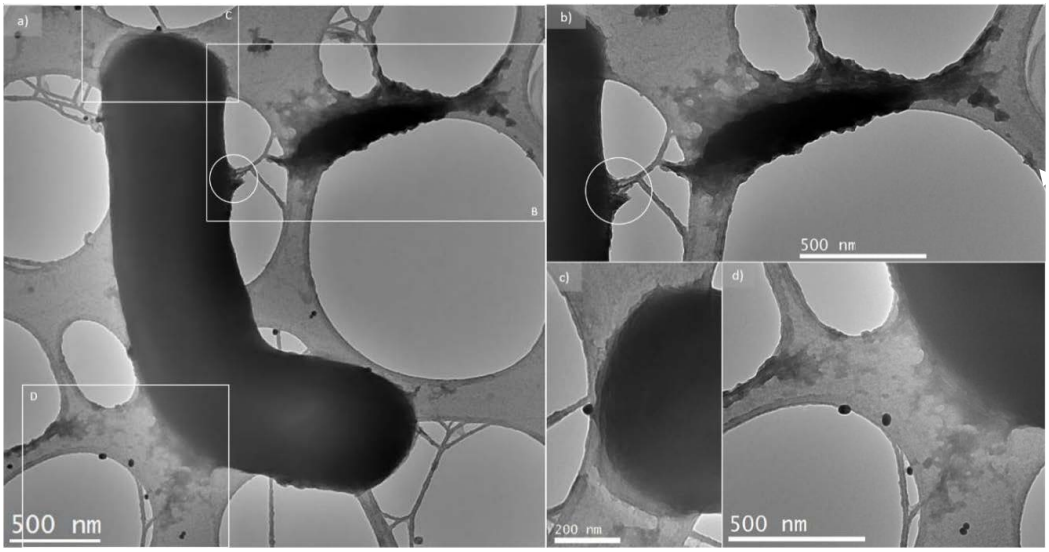

Figure 72: Representative transmission electron micrograph a) of live *E. coli* incubated with as-synthesized AuNPs, aliquoted immediately post-assay and stained UA. Insets b), c) and d) show the magnified regions in a) indicated by labelled boxes.

Although there are areas of the cell surfaces that were observed to have remained smooth and intact (**Figure 72** above), there are notable regions of disruption to the cell envelope, resulting in the leakage of cellular material, as highlighted in the magnified insets b), c) and d). Of particular note, as indicated by the oval in a) and (magnified in c)), there appears to be a rupture in the cell, presumably resulting in additional leakage of cellular and/or cytoplasmic contents, denoted by the white arrow in c). The proximity of the amorphous aggregate to the area that appears ruptured supports the hypothesis that the aggregate is comprised of leaked cellular contents.[218, 223, 225, 226]

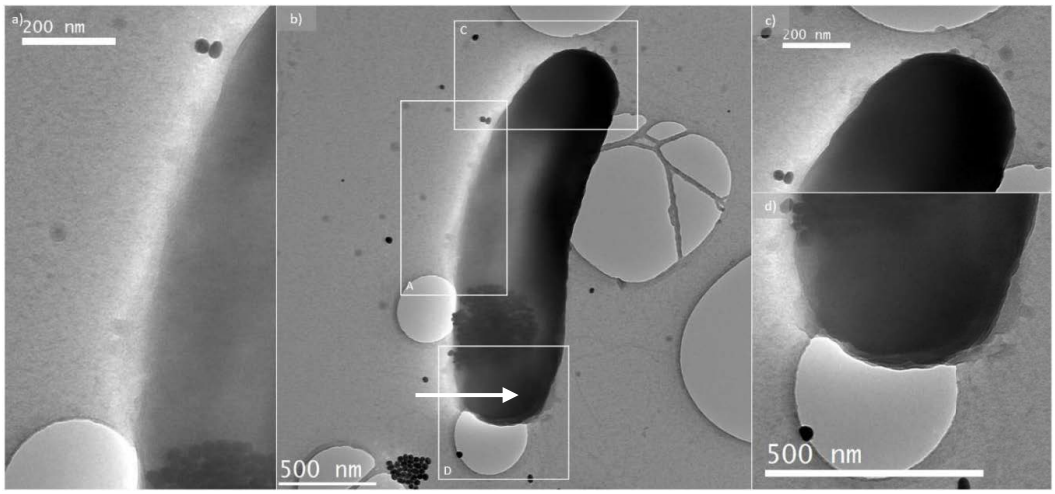

Figure 73: Representative transmission electron micrograph b) of live *E. coli* incubated with as-synthesized AuNPs, aliquoted immediately post-assay and stained UA. Insets a), c) and d) show the magnified regions in b) indicated by labelled boxes.

As was seen in **Figure 72**, the bacterial cell in **Figure 73** above shows evidence of disruption to its cell envelope, resulting in leakage of cellular contents. In this instance however, it is less obvious, with comparatively less material observed leaked from the cell. Two distinct AuNP aggregates were observed in **Figure 73** b) – the aggregate closest to the bottom of the micrograph shows particles that, while aggregated, have not fused. The larger aggregate (denoted by the white arrow) appears to be situated underneath the bacterial cell, and while partially obscured, individual particles can still be observed, indicating at least some of the particles within the aggregate have not fused. The remainder of the AuNPs visible within the micrograph do not seem to be particularly associated with either the surface of the bacterial cell or its leaked contents.

6.4.3.2 Live *E. coli* and As-synthesized Gold Nanoparticles t = 2 h

Live *E. coli* were assayed with as-synthesized AuNPs, as per the methods previously outlined in Chapter 4 and prepared according to Section 6.3.3 of the current Chapter. Briefly, aliquots of the sample mixtures were taken 2 h after addition of AuNPs to the system, and subsequently prepared for TEM.

When compared to the samples taken immediately post-assay, the increased interaction time between the AuNPs and bacteria appeared to result in a greater amount of observable cell leakage (see **Figure 74** and **Figure 75**) as detailed in the following section.

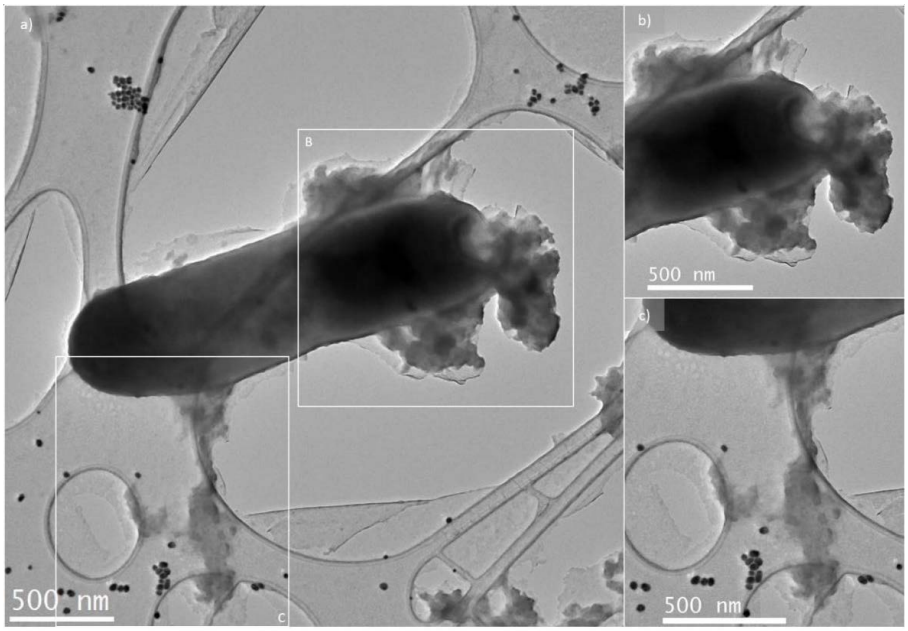

Figure 74: Representative transmission electron micrograph a) of live *E. coli* incubated with as-synthesized AuNPs, aliquoted 2 h post-assay and stained with UA. Insets b) and c) show magnified regions in a) as indicated by the labelled boxes.

Given additional time for the interaction between the as-synthesized AuNPs with the bacteria (compare **Figure 74** to **Figure 72** and**Figure 73**), a greater level of disruption to the cells was observed. Both the number of sites displaying disruption and the relative amounts of leaked cellular contents

were observed to increase between the initial assay and after 2 h of interaction. AuNPs pictured within the above micrograph were comparatively more aggregated, visible in small (but unfused) clusters and in proximity to the cellular excretions.

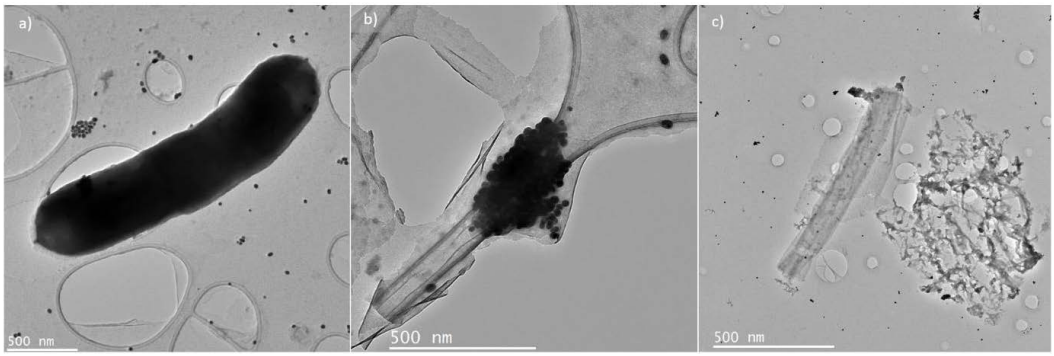

Figure 75: Representative transmission electron micrographs of aliquots taken from a sample of live *E. coli* incubated with as-synthesized AuNPs, 2 h post-assay and stained with UA. a) shows an *E. coli* cell, b) shows a semi-fused cluster of AuNPs aggregated within amyloid-like fibril aggregates and c) shows an amyloid-like fibril (left) and a disordered, amorphous aggregate (right).

In contrast to what was observed in **Figure 74**, the bacterium in **Figure 75** a) appears to have little to no morphological defects. This is of great importance and highlights the incredible variability of *E. coli* cells within cultures with respect to the display and consistency of morphological defects.[227] This, coupled with the inherent variability of the physiological states of *E. coli* cultures grown in LB[74] results in a vastly challenging interpretation.

6.4.3.3 Live *E. coli* and Washed Gold Nanoparticles t = 0

Live *E. coli* were assayed with washed AuNPs, in the same manner as for the as-synthesized AuNPs, in order to discern if the amount of surface-associated citrate produced a visually observable difference in the AuNP-bacteria interactions and/or the resulting morphologies of the bacteria.

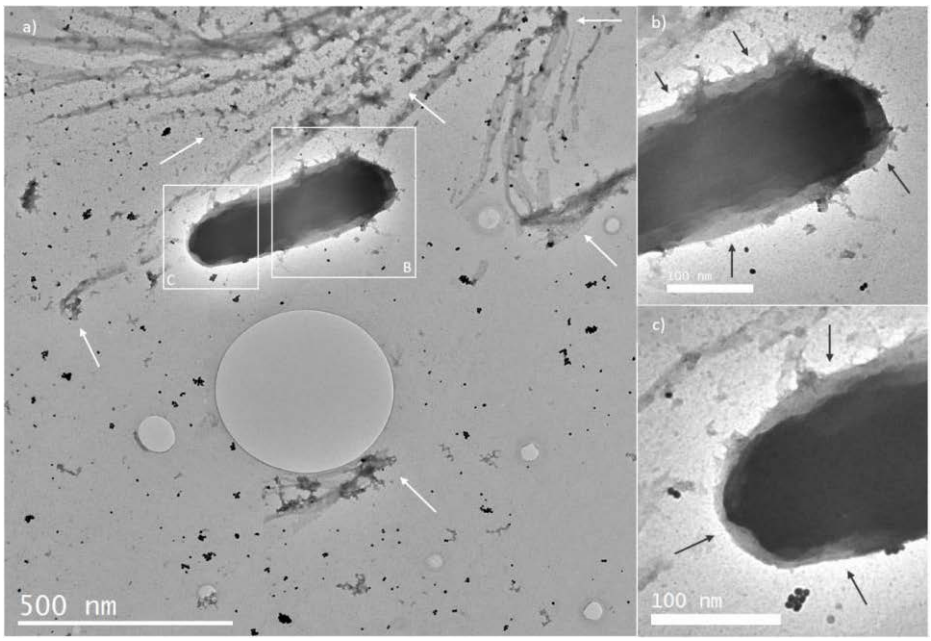

Figure 76: Representative transmission electron micrograph a) of live *E. coli* incubated with washed AuNPs, aliquoted immediately post-assay and stained with UA. Insets b) and c) show magnified regions of a) as indicated by the labelled boxes.

With reference to **Figure 76** above, micrograph a) shows a significant number of amyloid-like fibrils in the upper region of the image, within which many small AuNP aggregates can be observed associated within the proteinaceous matrix. These protein aggregates however, are somewhat more disordered (increased globular appearance and dispersion of the protein sheets) in areas denoted by white arrows, exhibiting morphologies somewhere between a typical amyloid fibril and an amorphous aggregate (refer to **Figure 66**). A comparatively small number of amorphous

aggregates were observed in live *E. coli* samples incubated with washed AuNPs and observed via TEM immediately post-assay.

With reference to the cell's morphology, insets b) and c) of **Figure 76** show magnified regions of a), highlighting the disruption to the cell envelope and what appears to be the inner membrane having shrunk from the cell wall, resulting in a larger than usual periplasmic space[227] (black arrows in b) and c)). Additionally, material can be observed leaking from the cell, likely of periplasmic origin due to the high electron density of the cell, while the enlarged periplasmic space is relatively less electron dense.

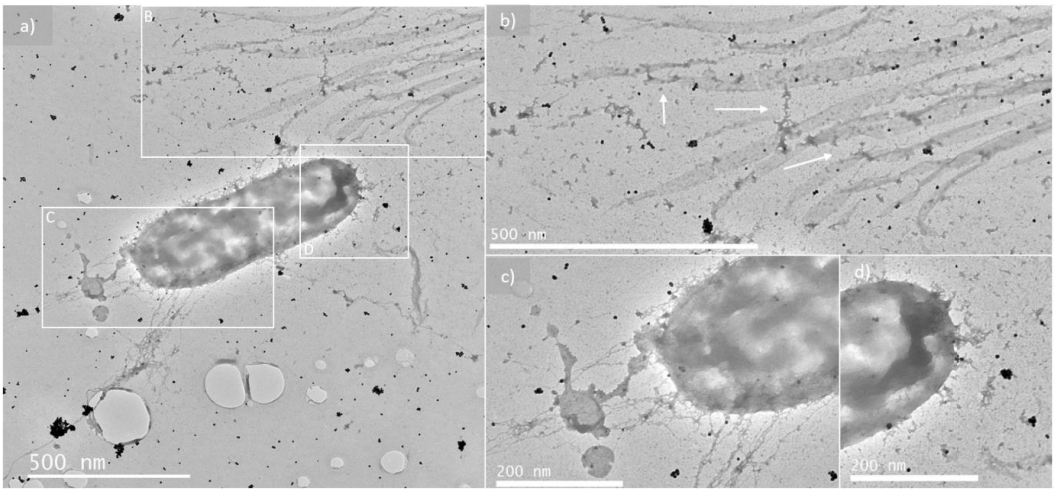

Figure 77: Representative transmission electron micrograph a) of live *E. coli* incubated with washed AuNPs, aliquoted immediately post-assay and stained with UA. Insets b), c) and d) show magnified regions of a) as indicated by the labelled boxes.

Similar to what was observed in **Figure 76**, the micrograph in **Figure 77** shows a number of amyloid-like fibrils. These fibrils were somewhat more ordered than those observed in **Figure 76**, however, their observed morphologies were still somewhat more disordered (white arrows in **Figure 77** inset b) above) than typical conformations (**Figure 66**). Insets c) and d) of **Figure 77** above highlight the morphological defects observed in some of the live *E. coli* incubated with washed AuNPs, even briefly. Namely,

condensation of the cytoplasmic material, as evidenced by the patchy appearance of the cell. These areas of varying electron density, where in some instances AuNPs can be seen *through* the cell, implies that very little cellular material remains within the cell, likely having leaked into the surrounding medium. This is supported by the significant amount of proteinaceous material that can be seen leaking from the cell (highlighted in insets c) and d) of **Figure 77** above).

Common to both **Figure 76** and**Figure 77** were the appearance and association of discreet clusters of AuNP aggregates within the vicinity of the leaked cellular materials, and in particular observed within the amyloid-like fibrils.

6.4.3.4 Live *E. coli* and Washed Gold Nanoparticles t = 2 h

Live *E. coli* were assayed with washed AuNPs, as per the methods previously outlined in Chapter 4 and prepared according to Section 6.3.3 of the current Chapter. Briefly, aliquots of the assays were taken 2 h after addition of AuNPs to the system, drop-cast and wicked off of the TEM grid, before being simultaneously stained and fixed with 2% uranyl acetate.

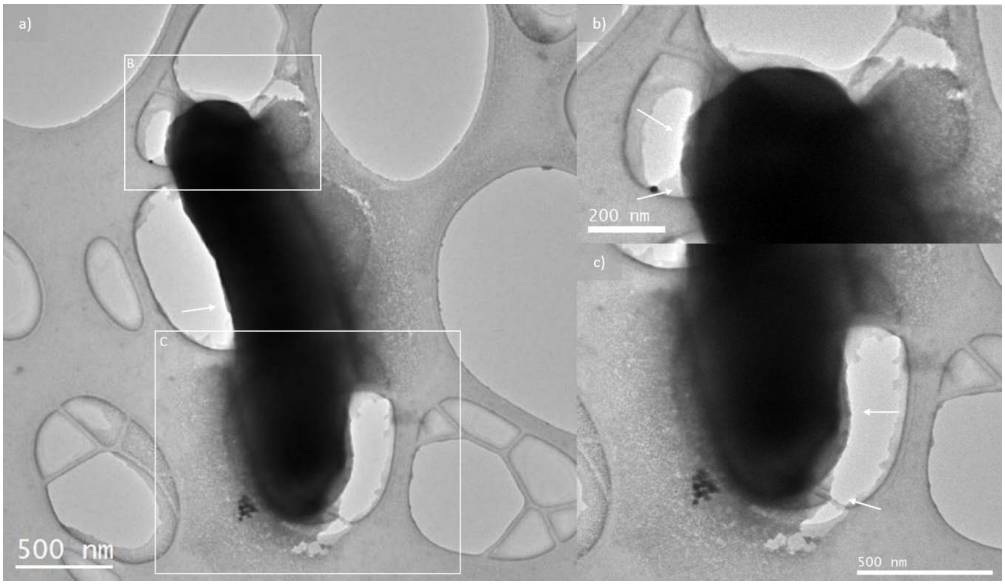

Figure 78: Representative transmission electron micrograph a) of live *E. coli* incubated with washed AuNPs, aliquoted 2 h post-assay and stained with UA. Insets b) and c) show the magnified regions indicated by the labelled white boxes in a). White arrows indicate areas of inner membrane shrinkage.

Figure 78 above shows a representative *E. coli* cell that had been incubated with washed AuNPs for 2 h prior to fixing and visualisation via TEM. The additional interaction time between the bacteria and the washed AuNPs appears to have resulted in disruption to the cell envelope, however the morphological defects observed appear to be more analogous to those seen in the heat-killed and extra heat-killed controls (**Figure 71**). For example, there was a dramatic decrease in the observed proteinaceous material leaked from the cells (**Figure 78**,Figure **79** and Appendix B.2), areas where the cell envelope was disrupted, had a granular appearance. Inner membrane shrinkage from the cell wall was also observed (white arrows in **Figure 78**).

A relatively low number of AuNPs were observed within the live *E. coli* samples that were incubated with washed AuNPs for 2 h, presumably a result of the additional aggregation of the AuNPs within the proteinaceous milieu, likely to the point of flocculation.

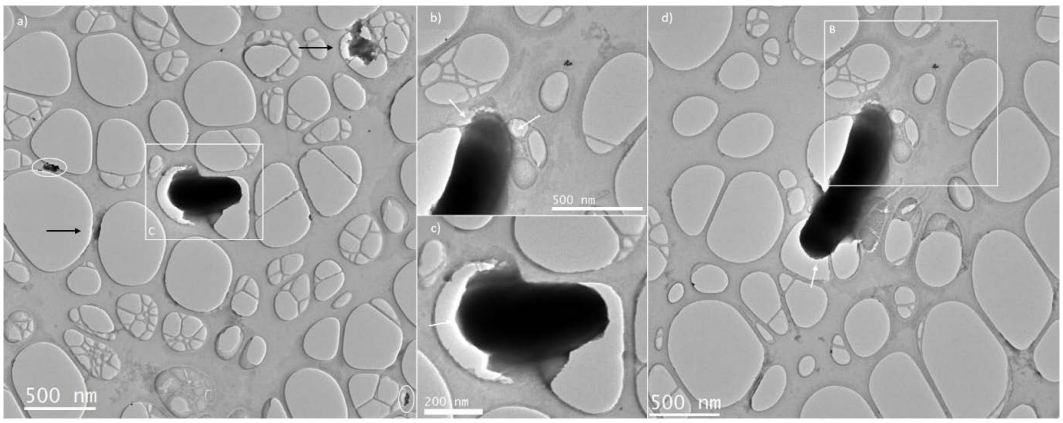

Figure 79: Representative transmission electron micrographs (a) and d)) of live *E. coli* incubated with washed AuNPs, aliquoted 2 h post-assay and

stained with UA. Insets b) and c) show the magnified regions indicated by the labelled white boxes in d) and a) respectively. Black arrows in a) indicate amorphous aggregates, white ovals denote clusters of unfused AuNP aggregates and white arrows indicate areas of inner membrane shrinkage.

Similar to what was observed in **Figure 78**, the cells in the above micrographs (**Figure 79**) had a granular appearance to the contents leaked from the cells, relatively little proteinaceous material observed in the TEM samples (compared to previous sample groups) and very few observable AuNPs (colloidal or aggregated clusters). Additionally, shrinkage of the inner membrane from the cell wall was also observed in the cells in **Figure 79** (white arrows).

6.4.4 Transmission Electron Micrographs of Gold Nanoparticle and Heat-Killed *E. coli* Interactions

The following section presents results from experiments conducted in order to ascertain whether the optically observed differences (previously detailed in Chapters 4 and 5) between the heat-killed and live *E. coli* preparations with AuNPs could be explained when the same samples were visualized. Two key research questions were investigated:

1. Did the morphological defects resulting from heat-treatment result in additional (visible) aggregation and association of the AuNPs with the bacterial cells? and
2. Did the addition of the AuNPs to the heat-killed *E. coli* result in additional, appreciable morphological defects?

6.4.4.1 Heat-killed *E. coli* and As-synthesized Gold Nanoparticles t = 0

Heat-killed *E. coli* were assayed with as-synthesized AuNPs, as per the methods outlined previously (see Chapter 5), and aliquots were taken immediately after the addition of AuNPs to the system. These aliquots were

subsequently prepared for TEM as per Section 6.3.3 of the current Chapter, allowing for a visual assessment of the interactions between the heat-killed bacteria and their interactions with the AuNPs.

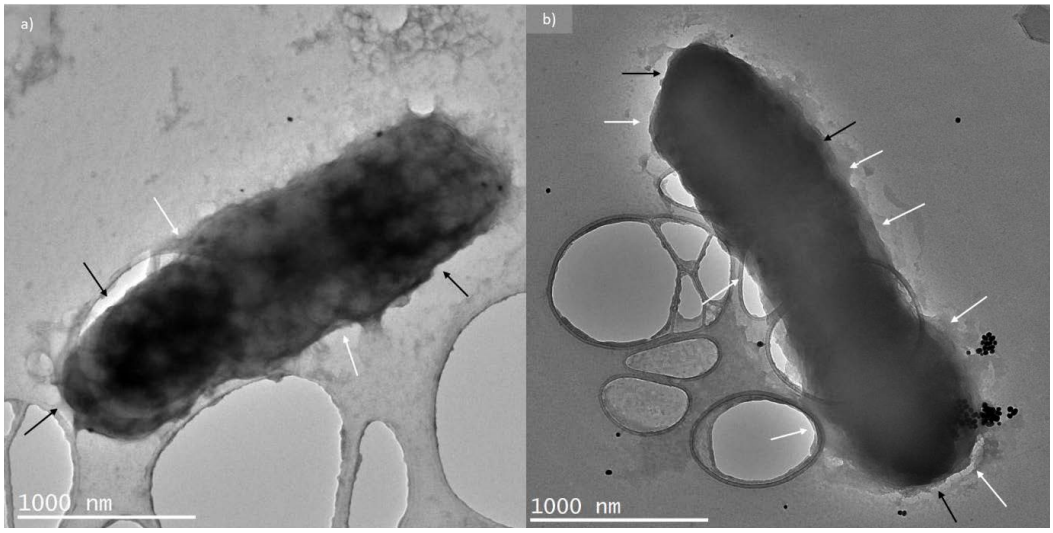

Figure 80: Representative transmission electron micrographs (a) and b)) of heat-killed *E. coli* incubated with as-synthesized AuNPs, aliquoted immediately post-assay and stained with UA. White arrows indicate areas of inner membrane shrinkage and black areas denote cytoplasmic shrinkage.

The morphological defects observed in the cells shown in **Figure 80** above closely resemble those seen in the heat-killed *E. coli* controls (**Figure 69** and**Figure 70**). For example, cytoplasmic condensation (black arrows in **Figure 80**), disruption to the cellular envelope and (an associated) increased leakage of cellular material.

The morphology of the leaked cellular material (**Figure 80**) was less densely aggregated than what was seen in the majority of the heat-killed controls, resembling more closely what was seen in a relatively smaller portion of the leaked cellular material (see **Figure 70** b) for example). Additionally, areas where the inner membrane had shrunk from the cell wall, creating an enlarged periplasmic space were also observed (white arrows in **Figure 80**).

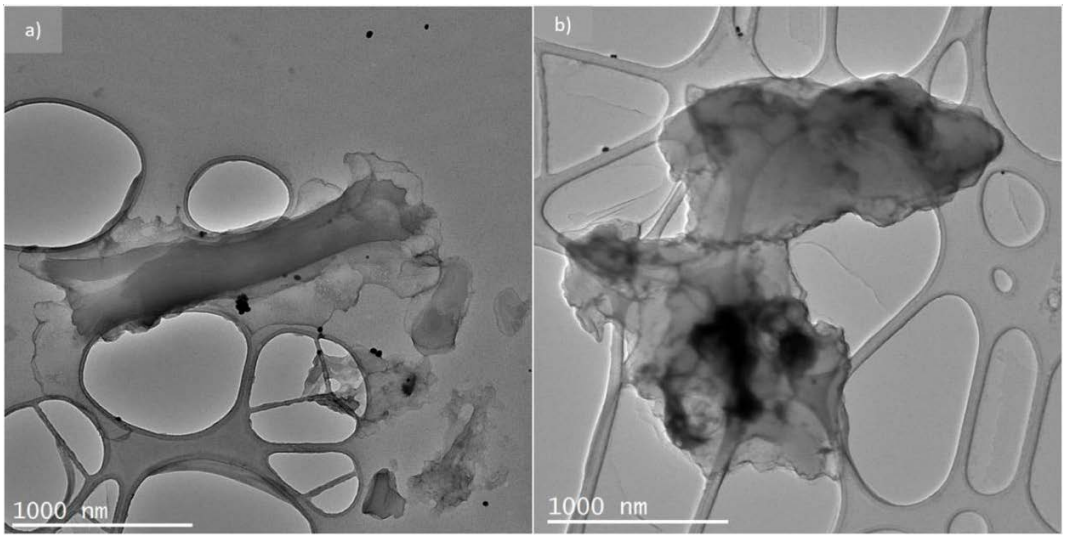

Figure 81: Representative transmission electron micrographs of aliquots taken from a sample of heat-killed *E. coli* incubated with as-synthesized AuNPs, aliquoted immediately post-assay and stained with UA. a) shows an amyloid-like fibril aggregate, and b) a disordered amorphous aggregate.

Present within the heat-killed *E. coli* samples incubated with as-synthesized AuNPs (t = 0) were both amyloid-like fibrils and amorphous aggregates (**Figure 81** a) and b) respectively). A small number of AuNPs were observed aggregating in/around the amyloid-like fibril and associated with proteinaceous milieu surrounding the amorphous aggregate in **Figure 81** a) and b) respectively.

6.4.4.2 Heat-killed *E. coli* and As-synthesized Gold Nanoparticles t = 2 h

Heat-killed *E. coli* were assayed with as-synthesized AuNPs and prepared for TEM, as per the methods previously outlined in Chapter 5 and as per Section 6.3.3 of the current Chapter. Briefly, aliquots of the assays were taken 2 h after addition of AuNPs to the system, drop-cast and wicked off of the TEM grid, before being stained with 2% uranyl acetate.

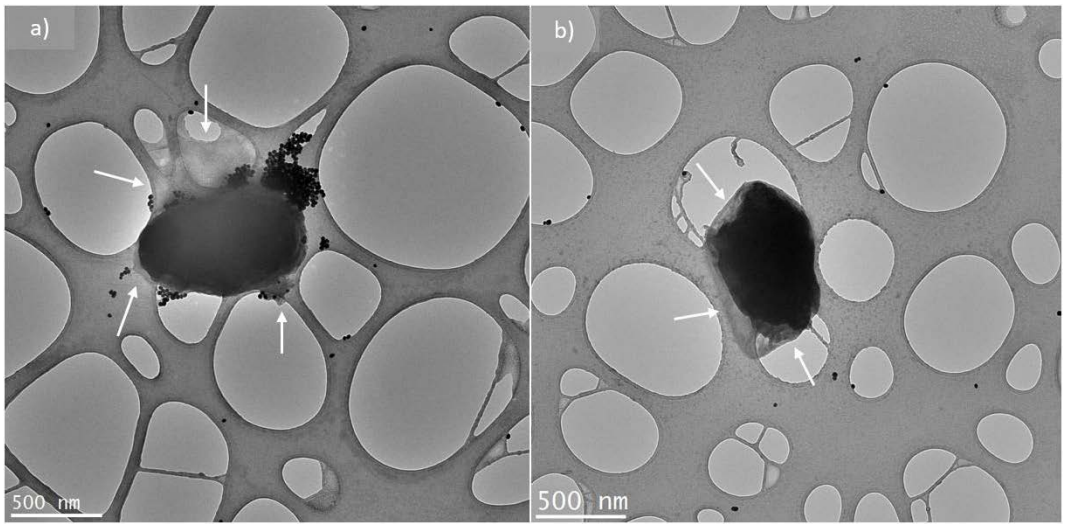

Figure 82: Representative transmission electron micrographs (a) and b)) of heat-killed *E. coli* incubated with as-synthesized AuNPs, aliquoted 2 h post-assay and stained with UA. White arrows denote disruption to the cell envelope and dispersion of cellular material.

As evidenced by the micrographs in **Figure 82** above, the heat-killed *E. coli* that were incubated with as-synthesized AuNPs for 2 h exhibited disruption to the cell envelope, dispersion of the cell wall and outer membrane components (denoted by white arrows). **Figure 82** a) most notably showed an appreciable number of AuNPs associated with and aggregated around the leaky bacterial cell. Considering the associated leakage of cellular material that arises from damage and disruption to the cell envelope, this is likely to account for the adherence of the AuNP clusters to the cell surface. With reference to **Figure 82** b), some inner membrane shrinkage of the bacterial cell is apparent, whereby the (inner) membrane has shrunk from the cell wall, creating an enlarged periplasmic space, similar to what was seen in previous samples.

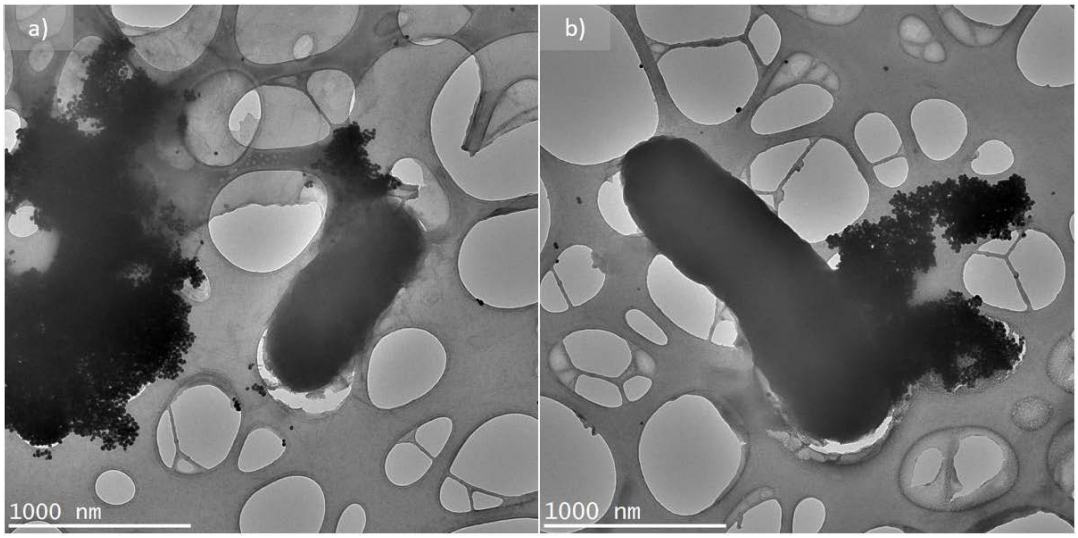

Figure 83: Representative transmission electron micrographs (a) and b)) of heat-killed *E. coli* incubated with as-synthesized AuNPs, aliquoted 2 h post-assay and stained with UA.

Similar to what was observed in **Figure 82**, **Figure 83** shows disrupted bacteria leaking cellular material within which AuNPs can be seen aggregating. **Figure 83** a) demonstrates this most clearly, where significant amounts of proteinaceous material can be visualised, originating from the bacterial cell. The origin of this material as being from the cell is supported by the relatively light electron density of the cell when compared to the cell in **Figure 83** b) which shows a comparatively lower amount of leaked material. Common to both micrographs a) and b) above, are the large clusters of aggregated AuNPs either within the leaked cellular material or associated with the presumably leaky sites of the cell envelope.

6.4.4.3 Heat-killed *E. coli* and Washed Gold Nanoparticles t = 0

Heat-killed *E. coli* were assayed with washed AuNPs, as per the methods outlined previously (see Chapter 5), and prepared for TEM as per the methods outlined in Section 6.3.3 of the current Chapter. Briefly, aliquots of the sample mixtures were taken immediately after addition of washed AuNPs to the system, and prepared for TEM.

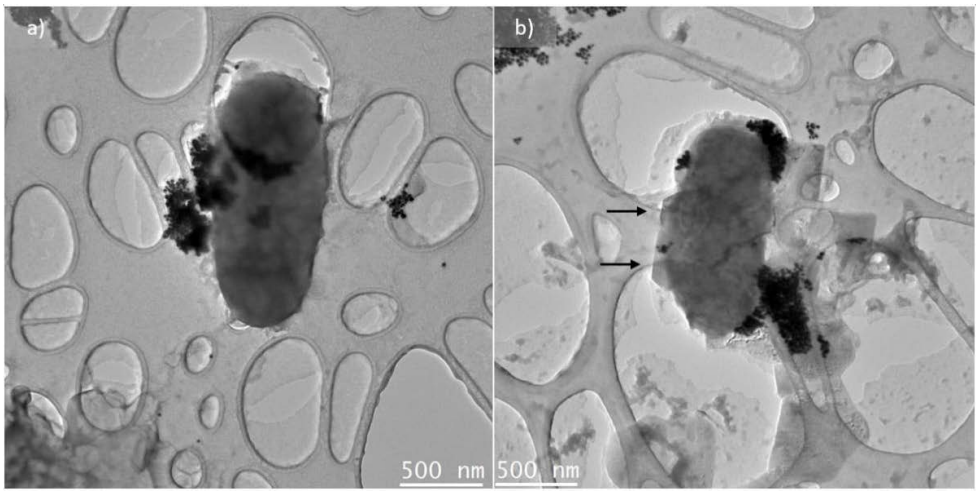

Figure 84: Representative transmission electron micrographs (a) and b)) of heat-killed *E. coli* incubated with washed AuNPs, aliquoted immediately post-assay and stained with UA.

Heat-killed *E. coli* that were incubated with washed AuNPs (**Figure 84** above) appeared relatively less electron-dense than both the live and heat-killed *E. coli* controls (compare with **Figure 68**,**Figure 69** and**Figure 70**), indicating comparatively more cellular material had leaked from the observed cells within this test group. An appreciable amount of cellular material can be observed leaking (and still attached) to the cell in **Figure 84** b), with the damage/disruption to the cellular envelope significant enough to have resulted in a rectangular protrusion of the cell wall (black arrows).

Washed AuNPs can be observed aggregating within the leaked cellular material of the cells, with several large clusters directly associated with the leaky surfaces (**Figure 84** a) and b)). The AuNPs observed in the top-most left corners of **Figure 84** a) and b) appear comparatively less aggregated and fused than those that are directly associated with the cells, presumably due to the relatively lower amounts of associated proteinaceous material.

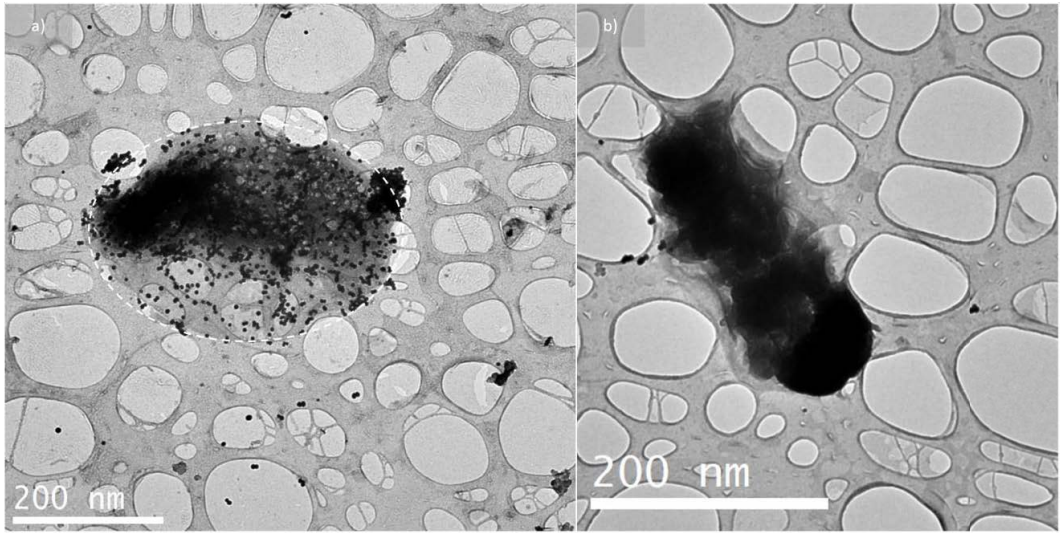

Figure 85: Representative transmission electron micrographs of aliquots taken from a sample of heat-killed *E. coli* incubated with washed AuNPs, aliquoted immediately post-assay and stained with UA. a) shows AuNPs aggregating on a quasi-spherical surface, likely to be an empty cell envelope/dispersed LPS, and b) shows an *E. coli* cell exhibiting significant morphological defects.

Incubating heat-killed *E. coli* with washed AuNPs, even briefly (t = 0) resulted in significant morphological defects such as those seen in **Figure 85** a) and b). For example, the micrograph in a) above shows a cell so disrupted it has resulted in an almost spherical morphology (highlighted by dashed white lines in a)). The bottom-half of the resulting spherical bacterium is essentially devoid of cellular material, noticeable as a result of the slight contrast afforded by the UA in addition to the peppering of washed AuNPs that have aggregated along its surface. In contrast, it appears as if the top-half of the spherical bacterium was likely to be the original cell (prior to disruption and leakage of the envelope), exhibiting areas of relatively concentrated cytoplasmic material (left) and relatively dispersed cellular material (right).

The cell in **Figure 85** b) exhibited comparatively fewer AuNPs associated with the cell and in its vicinity, however the morphology of the bacterium exhibited defects such as cytoplasmic condensation, disruption to the cell

envelope and displayed areas of relatively low electron density, indicating leaked (or displaced – i.e. condensed) cytoplasmic material.

6.4.4.4 Heat-killed *E. coli* and Washed Gold Nanoparticles t = 2 h

Heat-killed *E. coli* were assayed with washed AuNPs, as per methods previously outlined in Chapter 5. Aliquots of the assays were prepared for TEM as per Section 6.3.3 of the current Chapter. Briefly, aliquots of assays were taken 2 h after addition of washed AuNPs to the system, drop-cast and wicked off of the TEM grid, before being stained with 2% (w/v) uranyl acetate.

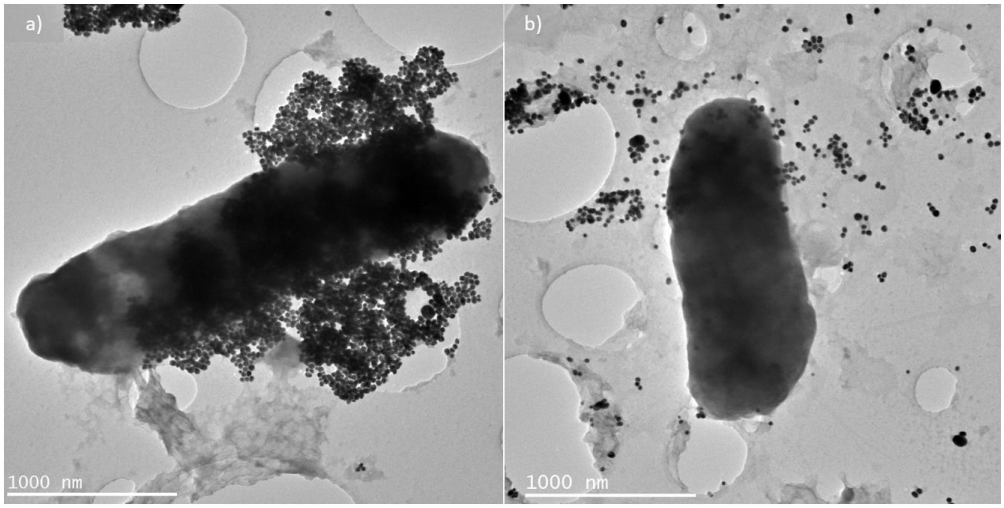

Figure 86: Representative transmission electron micrographs (a) and b)) of heat-killed *E. coli* incubated with washed AuNPs, aliquoted 2 h post-assay and stained with UA.

Increasing the length of time for the interaction between the washed AuNPs and the heat-killed *E. coli* resulted in similar morphological defects to what was observed in the initial assays (t = 0, compare with **Figure 84** andFigure **85**). These include defects such as areas of cytoplasmic condensation and increased leakiness of the cell envelope, resulting in increased association of AuNPs with the cell surfaces. In contrast to the initial assays however, the cells observed after 2 h of incubation (in general, when the majority of

the cell envelope remained in-tact) appeared more electron dense than those observed at t = 0. This is likely to involve the divalent cations Mg^{2+} and Ca^{2+}, both of which are present in LB[76] and play an important role in the protection of *E. coli* from thermal death.[228] For example, it has been demonstrated that Ca^{2+} ions can affect the physico-chemical behaviour of lipids, enhancing the phase transition of both phosphatidylglycerols and LPS, with the potential to induce non-bilayer structures in the total lipids of *E. coli* and thus affecting the overall stability of the bilayers.[228, 229]

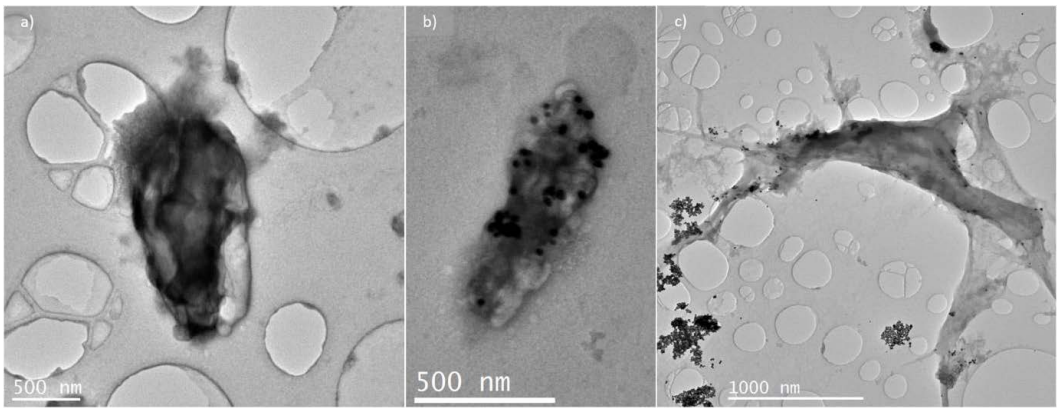

Figure 87: Representative transmission electron micrographs of aliquots taken from a sample of heat-killed *E. coli* incubated with washed AuNPs, aliquoted 2 h post-assay and stained with UA. a) shows a cell with severe morphological defects and cytoplasmic condensation, b) shows a bacterium with the cell envelope severely disrupted and AuNPs associated with its surface, and c) shows an amyloid-like fibril associated with, and in the vicinity of aggregated AuNP clusters.

The micrographs presented in a) through c) of **Figure 87** above highlight the great variability observable within *E. coli* populations, as was seen in previous test groups. For example, the morphological defects visible in the cell pictured in a) include significant levels of cytoplasmic condensation, areas of enlarged periplasmic space, leaked cellular material and a disrupted cell envelope exhibiting multiple bulges. The micrograph in **Figure 87** b) pictures several small clusters of AuNPs aggregated on what could either be an amorphous aggregate or an *E. coli* cell exhibiting defective

morphologies including similar to those seen in a). Finally, micrograph c) highlights the presence of amyloid-like fibril aggregates within the heat-killed *E. coli* assay matrix contributing to the observed level of AuNP aggregation. A number of AuNPs can be seen both caught within and in close proximity to the protein matrix, suggesting an electrostatic-based interaction.

6.4.5 Transmission Electron Micrographs of Gold Nanoparticle and Extra Heat-Killed *E. coli* Interactions

Considering there was an observed difference between the live and heat-killed preparations of *E. coli* and their resultant optical interactions with AuNPs, the previous sections attempted to address if these could be explained by the morphological differences induced by the heat treatment. As the addition of the AuNPs to the *E. coli* was found to result in additional changes to the morphologies of the observed cells and proteinaceous moieties within the samples, an additional test group (extra heat-killed) was used to address the following:

- Did the heat treatment or the presence of the AuNPs result in the observed differences between the control and AuNP test groups?
- If both heat and AuNPs resulted in morphological changes, could one have contributed more significantly?

6.4.5.1 Extra Heat-killed *E. coli* and As-synthesized Gold Nanoparticles t = 0

Extra heat-killed *E. coli* were assayed with as-synthesized AuNPs, as per Section 6.3.3 of the current Chapter. Briefly, extra heat-killed *E. coli* was prepared and aliquots of the assays with as-synthesized AuNPs were taken immediately after post-assay, drop-cast and wicked off of the TEM grid, before being fixed and stained with 2% (w/v) uranyl acetate.

Extra heat-killed *E. coli* assayed with as-synthesized AuNPs in general displayed morphologies consistent with those observed in the heat-killed and extra heat-killed controls (**Figure 69**, **Figure 70** andFigure **71**) and had an appreciable number of aggregated AuNP clusters (generally fused) visible within the micrographs (see the following Section).

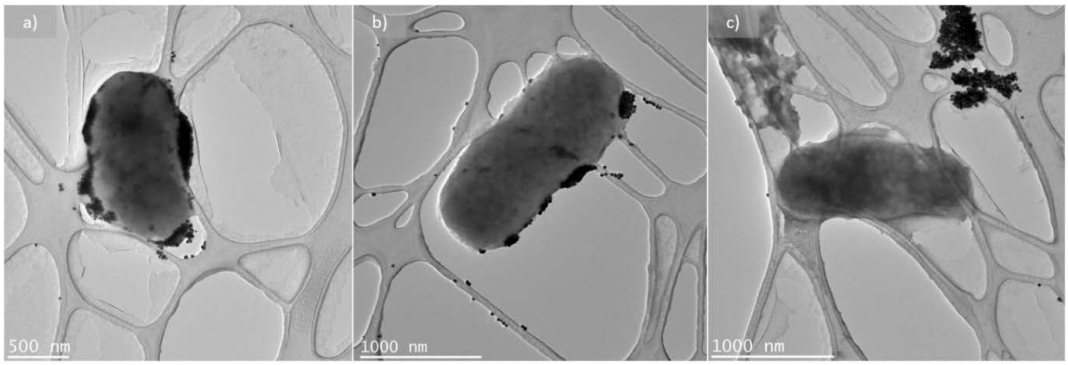

Figure 88: Representative transmission electron micrographs (a) – c)) of extra heat-killed *E. coli* incubated with as-synthesized AuNPs, aliquoted immediately post-assay and stained with UA.

Incubation of the extra heat-killed *E. coli* with as-synthesized AuNPs (**Figure 88** above) resulted in some bacterial cells displaying relatively low electron density, suggesting a loss of cytoplasmic contents. This is consistent with observations in both control samples and previous heat treated samples. Clusters of fused AuNP aggregates can be observed adhering to the (presumably) leaky sites of the cell envelopes in micrographs a) and b) above, while the AuNP cluster in c) is relatively less fused, likely due to being less densely coated in cellular materials. All three cells in **Figure 88** above show evidence of cell envelope disruption, cytoplasmic condensation, and evidence of inner membrane shrinkage.

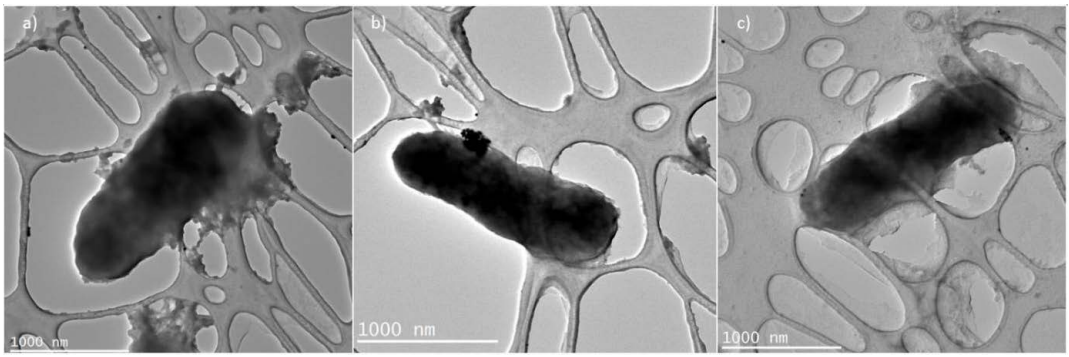

Figure 89: Representative transmission electron micrographs (a) – c)) of extra heat-killed *E. coli* incubated with as-synthesized AuNPs, aliquoted immediately post-assay and stained with UA.

Similar morphological defects to those seen in **Figure 88** can be observed in micrographs a) – c) of **Figure 89**, namely cytoplasmic condensation, areas of variable electron density (indicating a leakage/loss of cytoplasmic material), disruption of the cell envelope (with severity ranging from mild to almost complete loss of integrity) and enlarged periplasmic spaces. Here, comparatively fewer AuNP aggregated were observed to be associated or within the vicinity of these cells.

6.4.5.2 Extra Heat-killed *E. coli* and As-synthesized Gold Nanoparticles t = 2 h

Extra heat-killed *E. coli* were assayed with as-synthesized AuNPs, as per the methods outlined in Section 6.3.3 of the current Chapter. Briefly, aliquots of the assays were taken 2 h post addition of as-synthesized AuNPs to the system, drop-cast and wicked off of the TEM grid, before being simultaneously fixed and stained with 2% uranyl acetate.

An additional 2 h of incubation in the presence of as-synthesized AuNPs appeared to result in more severe morphological defects compared to the initial assay, including deviant cell division,[227] in addition to more significant cytoplasmic condensation, disruption to the cell envelope and/or leakage of cellular material (see the following **Figure 90** andFigure **91**).

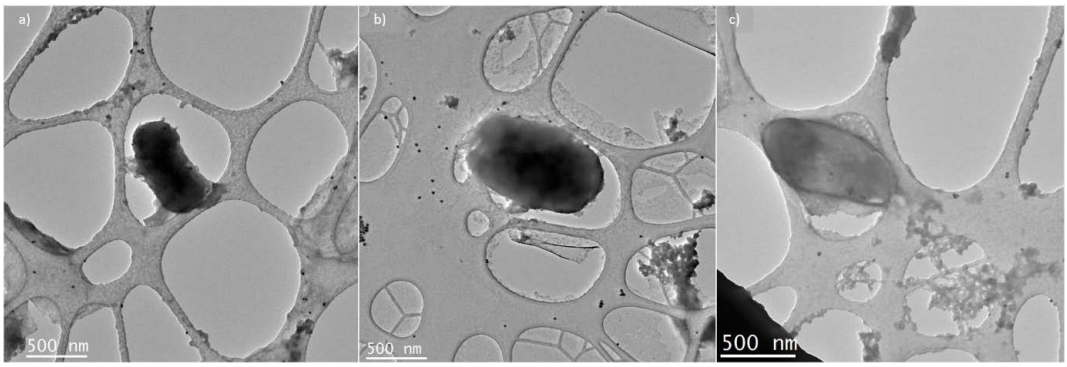

Figure 90: Representative transmission electron micrographs (a) – c)) of extra heat-killed *E. coli* incubated with as-synthesized AuNPs, aliquoted 2 h post-assay and stained with UA.

Additional incubation of the extra heat-killed *E. coli* in the presence of as-synthesized AuNPs appeared to result in more significant morphological defects when compared to the initial assays (**Figure 88** and **Figure 89**). With reference to **Figure 90** above, the cells in a) and b) show evidence of cytoplasmic condensation while remaining relatively electron dense, indicating they have likely retained a fair amount of cellular material, compared to that seen in c) which is almost transparent in some areas and can be seen leaking cellular contents.



Figure 91: Representative transmission electron micrographs (a) – c)) of extra heat-killed *E. coli* incubated with as-synthesized AuNPs, aliquoted 2 h post-assay and stained with UA.

Not often observed in the previous test groups (see Appendix B for other observed instances), is the deleterious 'deviant cell division', seen in micrographs a) and b) of **Figure 91** above. In literature, this phenomenon has been documented in mutant *E. coli* strains lacking both the alarmone ((p)ppGpp) and inorganic polyphosphate (polyP), resulting in cells heterogeneously displaying morphologies including severely mislocalized Z-rings ("deviant cell division"), a high degree of branching and/or large void spaces.[227]

6.4.5.3 Extra Heat-killed *E. coli* and Washed Gold Nanoparticles t = 0

Extra heat-killed *E. coli* were assayed with as-synthesized AuNPs, as per methods outlined in Section 6.3.3 of the current Chapter. Briefly, aliquots of the assays were taken immediately after addition of washed AuNPs to the system, drop-cast and wicked off of the TEM grid, before being stained with 2% (w/v) uranyl acetate.

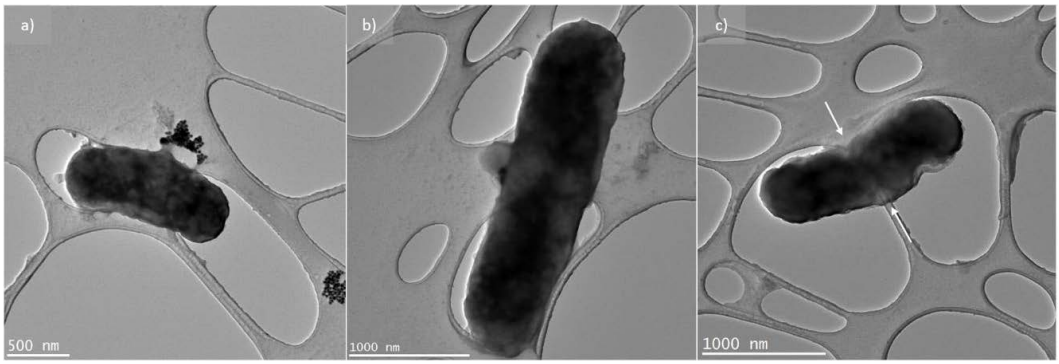

Figure 92: Representative transmission electron micrographs (a) – c)) of extra heat-killed *E. coli* incubated with washed AuNPs, aliquoted immediately post-assay and stained with UA.

The extra heat-killed *E. coli* observed in micrographs a) – c) of **Figure 92** above exhibited cytoplasmic condensation, inner membrane shrinkage and evidence of disrupted cell division in c) (denoted by white arrows). In a), a relatively small cluster of AuNPs can be seen directly associated with leaked contents from the cell.

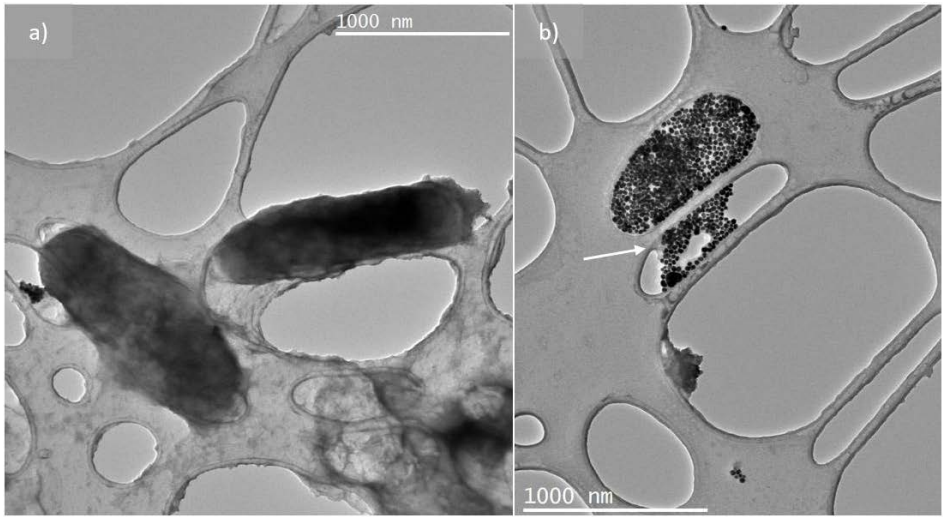

Figure 93: Representative transmission electron micrographs (a) and b)) of a sample of extra heat-killed *E. coli* incubated with washed AuNPs, aliquoted immediately post-assay and stained with UA. b) shows a cluster of quasi-aggregated (unfused) AuNPs surrounded by proteinaceous material (denoted by white arrow in b)).

Figure 93 a) above, showed some cells within the population had more severe morphological defects resulting in the apparent loss of an increased amount of cellular material. Disruption to, and bulging of the cell envelope was notable in several places, in addition to cytoplasmic condensation (areas of high electron density) and areas where relatively little cellular material remained within the cell (areas of low electron density). The micrograph in b) shows a cluster of unfused AuNPs aggregated within leaked proteinaceous material (highlighted by white arrow in b)).

6.4.5.4 Extra Heat-killed *E. coli* and Washed Gold Nanoparticles t = 2 h

Extra heat-killed *E. coli* were assayed with as-synthesized AuNPs, as per the methods outlined in Section 6.3.3 of the current Chapter. In brief, aliquots of the assays were taken 2 h post addition of washed AuNPs to the system, drop-cast and wicked off of the TEM grid, before being fixed and stained with 2% uranyl acetate.

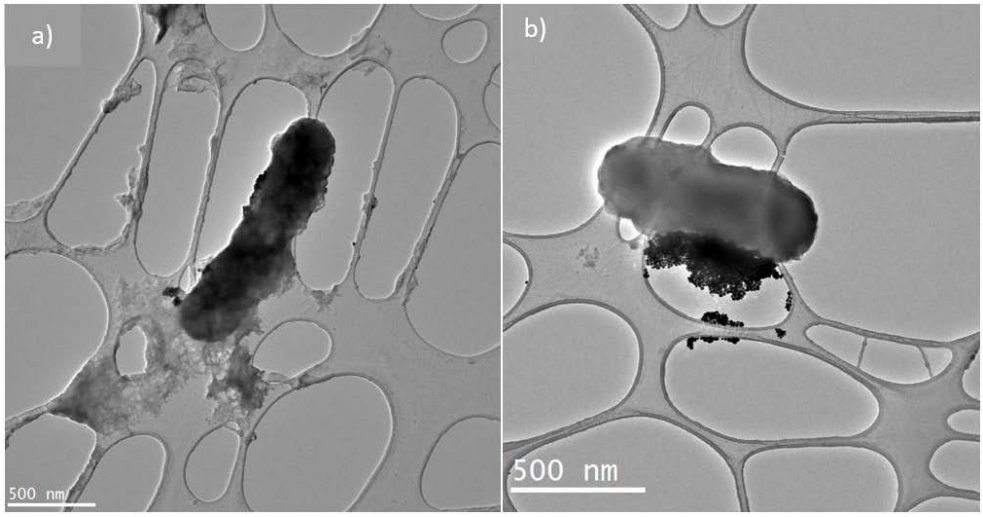

Figure 94: Representative transmission electron micrographs (a) and b)) of extra heat-killed *E. coli* incubated with washed AuNPs, aliquoted 2 h post-assay and stained with UA.

Increasing the incubation time between the extra heat-killed *E. coli* and washed AuNPs appeared to result in an increased incidence of observed AuNP aggregates associated with the disrupted bacterial cells. These aggregates appeared increasingly fused the closer in proximity they were to the cell surfaces. With reference to **Figure 94** above, a similar degree of, and appearance to the morphological defects were observed in the 2 h assay samples when compared to those observed immediately post-assay (**Figure 92** andFigure **93**).

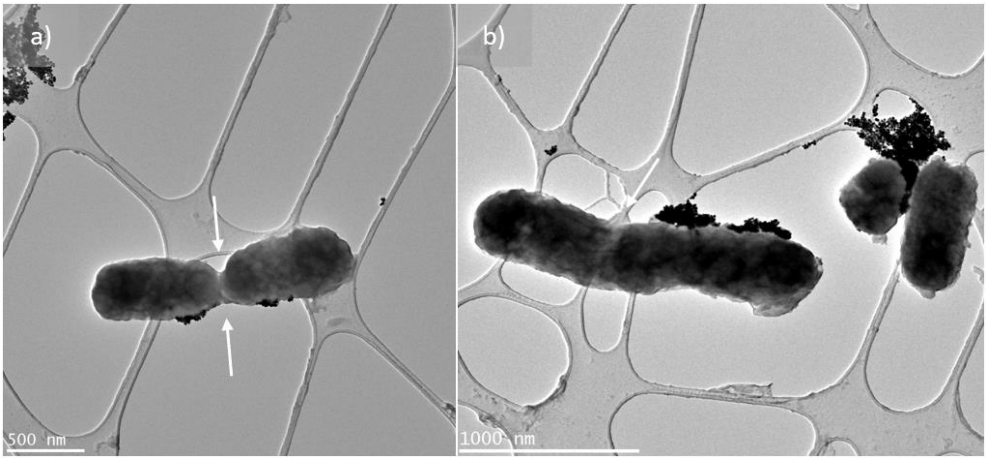

Figure 95: Representative transmission electron micrographs (a) and b)) of extra heat-killed *E. coli* incubated with washed AuNPs, aliquoted 2 h post-assay and stained with UA. White arrows indicate areas of disrupted cell division.

Similar to the deviant cell division observed in the extra heat-killed *E. coli* assays with as-synthesized AuNPs (t = 2 h, **Figure 91**), **Figure 95** a) shows a cell that has failed to undergo complete cell division (denoted by white arrows). While this could be incomplete cell division, it is more likely to be deviant or disrupted cell division due to the stressors applied to the cell culture (extra heat treatment and presence of AuNPs, now established to disrupt and contribute to *further* loss of cell integrity compared to cells only exposed to either stressor singly).

6.5 Summary, Conclusions & Discussion

6.5.1 Summary

Within the present chapter, the interactions between as-synthesized and washed AuNPs with preparations of live, heat-killed and extra heat-killed *E. coli* were investigated through the use of transmission electron microscopy (TEM). This allowed for a visualisation of the systems previously investigated only spectroscopically (i.e. using ultraviolet-visible spectroscopy).

In general, aggregation of the AuNPs were observed in both the supernatant as well as on bacterial cells; increasing the incubation time between the various preparations of bacteria and AuNPs resulted in increased adhesion to the cell surfaces. This AuNP/bacteria interaction appeared to cause additional disruption to the cell envelopes, ultimately leading to leakage of cellular material. Adhesion of the AuNPs to the bacteria appeared to be more frequently associated with areas where the cells showed evidence of damage or disruption. This was supported by the aggregation of both as-synthesized and washed AuNP colloids in and around the proteinaceous moieties present within the samples, supporting their tendency to aggregate in and around these substances. Further to this, an increased degree of aggregation within the AuNPs were observed in samples containing preparations of bacteria that had been subjected to heat treatment (heat-killed and extra heat-killed) prior to assaying. This can be attributed to the heat treatments resulting in an increased concentration of leaked cellular materials from the damaged cells. Concordant with the spectroscopic results presented and discussed in Chapters 4 and 5, the relative amount of surface-associated citrate had an appreciable effect on the morphologies of the *E. coli* cells they were assayed with (i.e. as-synthesized vs washed AuNPs).

6.5.2 Conclusions and Discussion

Proteinaceous moieties were observed in most, if not all bacteria-containing samples observed via TEM. These were most likely comprised of leaked periplasmic contents, disrupted LPS and other lipid-membrane compounds. In the case of severely disrupted cells, the observed moieties may even include cytoplasmic contents, particularly in instances where complete disruption of areas of the cell envelope could be seen. These results are in agreement with the widely reported release of OMVs, a highly-conserved phenomenon amongst pathogenic and non-pathogenic Gram-negative bacteria during *in vivo* and *in vitro* growth.

With reference to the control samples, heat treatment (i.e. heat-killed and extra heat-killed *E. coli* preparations) resulted in morphological defects to the cells, although these defects did not appear to homogeneously apply to the entire population, particularly not to the same degree. This is consistent with the high degree of variability observed within the same populations/cultures of *E. coli* in previous experimental Chapters, as well as observations in literature. In general, however, additional heat treatment was seen to cause further disruption to the cells and more severe morphological defects were observed within this treatment group. For example, the extra heat-killed (compared with heat-killed) *E. coli* cells displayed greater levels of cytoplasmic condensation, increased disruption to the cellular envelope (resulting in complete loss of the cell wall/membrane in some areas), and the leaked cellular material had a comparably increased granular appearance. The increased granularity/decreased (relative) electron density of these materials suggests they are comprised of more dispersed, less aggregated proteins. This is consistent with literature showing that elevated temperatures result in an increased degree of orientational disorder to membrane lipids and are more closely associated with their respective liquid-crystalline phase compared to the gel phase (comparatively more ordered and stable).

Although additional heat treatment (extra heat-killed) appeared to result in more severe morphological defects, the heat-killed *E. coli* still displayed significant defects compared to the live controls. Where the live *E. coli* exhibited relatively smooth, intact cell envelopes, those that were heat-killed showed evidence of disrupted cell envelopes, a higher degree of aggregation associated with their leaked cellular materials and some degree of cytoplasmic condensation.

At this stage, it has been well established that appreciable differences arise from the complex interactions of the various (tested) preparations of *E. coli* with either as-synthesized or washed AuNPs. Within the present Chapter, these interactions were visually examined via TEM, showing that in general, the degree of AuNP association/aggregation for both types of citrate AuNPs

were found to be: heat-killed > extra heat-killed > live *E. coli* preparations, all increasing with increased incubation time.

It was initially postulated that the defects observed within the visualized bacterial cell populations would have resulted predominantly from the heat treatments applied prior to assaying. However, this was later determined to not be the case, as live *E. coli* were observed to display evidence of defects in the presence of either as-synthesized or washed AuNPs. These defects appeared to become more severe in the presence of washed AuNPs (compared to as-synthesized AuNPs), and in general, with an increased incubation time. Thus, it was concluded that the AuNPs caused disruption and damage to the cellular envelopes to the *E. coli* cells. This effect was seen to be exaggerated in the heat treated preparations of *E. coli*. It was also seen that the damage to the bacterial cells as a result of both heat treatment and exposure to AuNPs was greater than that observed by either heat or exposure to AuNPs alone. This was true of both as-synthesized and washed preparations of citrate AuNPs.

Based on the observed tendencies of the AuNPs to aggregate amongst the proteinaceous moieties within the samples, associate more readily with compromised bacterial surfaces, and *in addition* to the increased 'leakiness' of cells assayed with washed AuNPs, it was concluded that electrostatic and/or charge-based interactions predominantly govern the interactions between the bacterial cells and AuNPs. The rationale behind this is as follows; in the case of the washed AuNPs (compared to as-synthesized), the decreased amount of surface-associated citrate resulted in a decreased 'competition' for the surface of the Au, essentially rendering it more active. These washed AuNPs were thus more able to interact with ionisable groups present on the surfaces of the bacterial cells (e.g. carboxyl, amino, sulfhydryl etc.) as well as those present amongst the proteinaceous milieu within the sample matrix. Increased levels of disruption, damage and defects within the heat treated cell populations are likely to be the result of the heat first increasing the fluidity/disruption of the cell envelope, exposing additional surface-active groups usually unable to exert their charge. These

heat-induced conformational changes to lipids, proteins and thus the bacterial membranes likely resulted in the observed increase in surface aggregation of the AuNPs.

Despite the observed morphological defects and damage to the bacteria assayed with AuNPs, examined via TEM in the current Chapter and spectroscopically in Chapters 4 and 5, it was evident that this damage was *not* sufficient to arrest the growth of the bacteria. This finding is important as the *in situ* growth of the *E. coli* in the presence of the AuNPs is a key component of the interaction between the cells and colloid, resulting in the evolution of the optical response and consequently the fundamental output of the proposed sensor.

Chapter 7:

Conditioned Media & Gold Nanoparticle Experiments

7.1 General

This Chapter further explores the processes by which the AuNPs interact with the various preparations of *E. coli* that have been tested. In the preceding Chapters, I examined what occurred in growth media containing either live or heat-killed preparations of *E. coli* to determine whether the time-dependent aggregation of the AuNPs was solely a surface-based interaction with the cells. It was shown that this hypothesis, although often suggested in the literature, was overly simplistic within the tested system. Extensive TEM analysis of the various assays revealed instead that a large proportion of the AuNP aggregation occurred in areas not associated with the bacterial cell surfaces, and were more frequently observed to be aggregated within proteinaceous material within the sample matrices. It also became apparent that the degree of aggregation has a relationship with the concentration of the live bacteria within the assays.

This raised the interesting question of what would occur if the bacterial cells were removed from the sample mixture *after* incubation in the LB growth medium. The key research question to be explored from this being whether the AuNPs are interacting predominantly with solubilized components (such as surface-active metabolites, proteinaceous fragments of cells or leaked cellular contents) in the LB to produce a useable optical signal for detection purposes, as opposed to the whole cells themselves. To this purpose, the various preparations of *E. coli* (live, heat-killed and extra heat-killed) were grown in LB as per the methods detailed in previous Chapters, before being removed from the growth medium. The resulting solutions were designated ‘conditioned media’ and were used in the following section of work.

Should the hypothesis that the AuNPs are predominantly interacting with the surface-active components within conditioned LB be supported, the consequences for the design of a practical sensing system are significant; i.e. it would need to be determined if the additional expense (time, cost, effort) of pre-removal of bacterial cells from the sample matrix is worthwhile.

7.2 Introduction

Within the previous Chapters, it was established that the *in situ* proliferation of the *E. coli* in the presence of the AuNPs is an important component of the sensing mechanism; in the present chapter the experiments conducted using conditioned media seek to determine:

- The contribution of the metabolites and/or leaked cellular materials from the *E. coli* to the aggregation-based sensing
- Whether the method of 'conditioning' affects the sensing ability of the AuNPs - i.e. are the resulting optical signals from the assays between AuNPs and the different conditioned medias significantly different to distinguish between the original bacterial treatments?

As was seen in the previous Chapter, an additional test group was added to more readily identify the effects of the heat treatment that had been applied to produce the heat-killed preparations of *E. coli*. This test group was designated 'extra heat-killed *E. coli*' and was prepared as per the methods detailed in Chapter 6, Section 3.2. In this case, the extra heat-killed *E. coli* solutions were held at elevated temperatures (75°C for 2 h), an additional 1.5 h compared to the heat-killed preparations of *E. coli*. The hypothesis was that the additional heat treatment would cause further disorder of, and disruption to the cellular envelopes of the bacterial cells, resulting in greater levels of leaked cellular materials within the supernatant which may then elicit an enhanced aggregating effect on the AuNPs.

Prior to the presenting the following experimental plan and results, it is worthwhile to briefly review the current understanding of the changes that occur in LB during, and as a consequence of bacterial proliferation. In general, there is no appreciable change in the chloride ion content, while the concentration of carbon-rich sources such as those arising from the tryptone and yeast extract are readily utilised as primary energy sources by the bacteria.[74, 78, 203, 204, 227] As these carbon sources are depleted, there is a corresponding increase in diverse bacterial metabolites. These may include reactive oxygen species (ROS), carboxylic acids,

alcohols, aldehydes, ketones and, importantly (with respect to the pH of the system and stability of AuNPs), ammonium.[230] An accumulation of ammonium ions can cause the pH of the culture medium to rise as high as 9 with deleterious effects to the bacteria.[230-232] This change in pH is also capable of destabilizing and/or causing aggregation of colloidal citrate AuNPs via the protonation/deprotonation of the surface citrate moieties, ultimately disrupting the carboxylate interactions between the surfaces of the citrate and Au, rendering them unable to effectively maintain the interparticle repulsions between the AuNPs necessary for colloidal stability.[233] Simulations have predicted that AuNPs will readily interact with several biologically-relevant amino acids.[73] However, there seems to be no specific assessment in the literature of the effect of bacterial metabolites on AuNP stability or aggregation within a complex system.

7.3 Experimental Design and Methods

The chemicals and materials used herein are identical to those used in previous Chapters. I guide the readers to Sections 3.1 of the preceeding Chapters (3 – 6) for specific details. Experimental methodologies employed within the current Chapter are included herein for ease of reference.

7.3.1 Concentration of Gold Nanoparticles Used in Assays

It is of great importance to note that the AuNPs used experimentally were from the same batches prepared initially, as detailed in Chapter 3, and used experimentally in Chapters 4, 5 and 6. However, three years had lapsed since their original synthesis. Although the UV-visible spectra of the AuNPs showed no appreciable changes over time, some unusual results that will be discussed within the current Chapter led to an interesting finding associated with the age of the utilized citrate AuNPs. As detailed in Chapter 4, Section 3.5, it was assumed all particles were 24 nm in diameter (mean size), the Q_{ext} in water was calculated using the λ_{spr} from control spectral and used in conjunction with the starting concentration of Au (g/L) to calculate the number of particles/m^3. The

concentrations of as-synthesized and washed AuNPs are reported in **Table 7** below for ease of reference.

Table 7: Concentration of As-Synthesized and Washed AuNPs used in assays, reported with respect to concentration of particles/m^3 and particles/100 µL.

	As-Synthesized AuNPs	**Washed AuNPs**
Conc. (particles/m^3)	4.24×10^{17}	2.49×10^{17}
Conc. (particles/100 µL)	4.24×10^{10}	2.49×10^{10}

7.3.2 Gold Nanoparticle Stability in Luria-Bertani Broth

The bacterial culture medium used within the proposed sensor platform is Luria-Bertani broth (see Chapter 4, Section 3.1 for the composition, and Chapter 2, Section 8.1 for the detailed breakdown of the individual components of LB). This was chosen in place of water (or other buffers) to provide a non-selective, nutrient-rich system for potential sub-populations of viable but non-culturable (VBNC) or sub-lethally injured bacteria to recover, *and* to encourage the growth of low numbers of bacteria, thus facilitating the detection of low levels of bacteria.[102, 103] The (relatively) high concentration of chloride ions and other dissolved proteinaceous moieties in this broth can be destabilizing to citrate AuNPs. As the resulting optical spectra of the AuNP and bacterial assays used for sensing are, to a first approximation, the sum of the individual contributions from the AuNPs, the diluent (LB), the bacterial cells, the bacterial metabolites, *and* their dynamic interactions, it was imperative to understand the interaction between LB and AuNPs. This was monitored as the stability of the as-synthesized and washed AuNPs in LB over time.

The stability, or change in stability of AuNPs can be monitored through the LSPR peak position and intensity using UV-vis spectroscopy. When new peaks appear (at a higher wavelength) or if the LSPR peak becomes red-shifted, it can be deduced that a size-increasing event has occurred within the nanoparticle dispersion. Broadening of the LSPR peak indicates a widening size distribution

within the observed NP population, while a decrease in intensity of the LSPR (in the absence of peak shifting) is indicative of removal of the gold from the 'detection zone', likely as a result of aggregation followed by sedimentation and/or coating of the sides of the container.[234]

The initial aggregation of the AuNPs in these experiments is (likely) affected to a large extent by the sodium ion concentration in addition to the milieu of amino acids, amino acid derivatives, vitamins and sugars[74, 76, 77] present within the sample mixture. The additional time-dependent contribution of the metabolites, leaked cellular contents and bacterial cell surfaces will be discussed later on. Since the volume of LB added to each sample well was fixed at 100 μL, this accounts for 1.71×10^{-5} moles of Na^+, given the LB had a concentration of 10 g/L NaCl. Considering the contribution of Na^+ from the as-synthesized AuNPs in other half of the sample mixture (since Na^+ from the tri-sodium citrate used in the AuNP synthesis must be conserved), 100 μL would contain 1.16×10^{-6} moles of Na^+. Since this is $<$ one tenth of the $[Na^+]$ of the LB, the $[Na^+]$ contribution from the as-synthesized AuNPs can be ignored to a first approximation.

7.3.3 Preparation of Extra Heat-Killed *E. coli* for Assays

Working solutions of *E. coli* broth were first prepared by incubating a single colony of *E. coli* in sterile LB overnight and adjusting the optical density at 600 nm (OD_{600}) to 0.1 (approximately 5 x 10^7 cells/mL (live *E. coli* working solution)).[74, 182] For heat-killed *E. coli*, the OD_{600} was first adjusted to 0.1 before the broth was subjected to heating at 75°C, 30 min to significantly reduce the viability (designated as 'heat-killed *E. coli*' working solution).[4] For extra heat-killed *E. coli*, the OD_{600} was adjusted to 0.1 before the broth was subjected to heating at 75°C for 2 h to further reduce the viability of the bacteria, while remaining below temperatures demonstrated to denature lipopolysaccharides (LPS) and DNA (120°C and 94°C respectively), thus intending to leave the outer membrane and LPS largely intact.[4, 217] This latter liquid was designated as 'extra heat-killed *E. coli*'.

7.3.4 Preparation of Conditioned Media

To prepare conditioned media, *E. coli* was first cultured in LB broth at 37°C, 200 rpm overnight, then adjusted to an optical density at 600 nm (OD_{600}) of 0.1. The resulting bacterial solutions were then centrifuged at 5000 x g, 10 min to pellet bacterial cells, and the supernatant was collected for use. Growth medium that had been used to support the growth of bacteria, with the subsequent removal of bacterial cells through means such as centrifugation was designated as "conditioned media"[235, 236] (see **Figure 96** below).

Due to the sensitivity of the citrate AuNPs to changes in their immediate environment, the following experimental design choices should be taken into consideration: In general, when conditioned media is prepared, the whole cells are removed via centrifugation prior to filtration of the resulting supernatant through a steri-filter to ensure the removal of residual cells which may have remained suspended within the solution and/or lighter macromolecules that would not have become pelleted during centrifugation. While it is arguable that the centrifugation conditions applied herein may not have been sufficient to completely remove all cells from the culture medium, use of faster speeds and/or additional centrifuging time can result in mechanical disruption of the cells and consequently an artificially increased concentration of cellular contents within the sample matrix. Additionally, omission of steri-filtration in preparing the conditioned media was deliberately chosen to avoid the capture and removal of proteinaceous macro-molecules within the sample matrices, due to their observed interactions with AuNPs via TEM. This of course, may have resulted in conditioned media with cells remaining therein, capable of resuming (eventual) growth under the tested conditions.

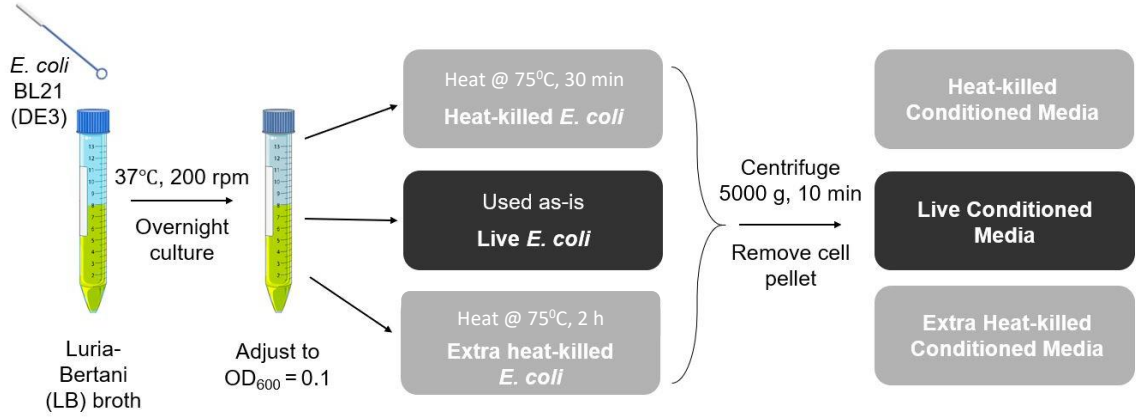

Figure 96: Schematic representation of the preparation of various conditioned media used within the present chapter.

7.3.5 Conditioned Media and Gold Nanoparticle Assays

Assays involving the various preparations of conditioned media and AuNPs were prepared in an identical manner to those detailed in previous Chapters, with the exception of the conditioned media replacing the initial aliquots of the respective *E. coli* working solutions that were subsequently serially diluted. To the prepared serial dilutions of conditioned media, the relevant AuNP colloids were added to perform each assay as detailed.

All UV-visible scans were conducted on three nominally identical wells and the resulting spectra shown are the average of triplicate scans.

7.3.5.1 Live Conditioned Media Assays

Working solutions of *E. coli* were prepared as detailed in Chapter 4, Section 3.3. To prepare live conditioned media, the live *E. coli* working solution (OD_{600} = 0.1) was centrifuged at 5000 x g, 10 min and the bacterial pellet removed, leaving the supernatant – designated as “live conditioned media”. For assays containing AuNPs and conditioned media, the design and setup is identical to that set out in previous chapters, with the exception of live conditioned media replacing the initial aliquot of live *E. coli* working solution that was subsequently serially diluted.

Live conditioned media was prepared according to the schematic in **Figure 96**. In brief, live *E. coli* working solution was cultured according to the methods detailed in Chapter 4, Section 3.3 prior to centrifugation and removal of the supernatant for subsequent use. This supernatant, resulting from the removal of the live *E. coli* cells from the LB was designated as “live conditioned media”.

7.3.5.2 Heat-Killed Conditioned Media Assays

Heat-killed *E. coli* working solutions were prepared as detailed in Chapter 5, Section 3.3. In brief, a live *E. coli* working solution was subjected to heat treatment (75°C, 30 min) to attain heat-killed *E. coli*. The resulting solution was subjected to the preparation scheme shown in **Figure 96** whereby the cells were removed via centrifugation (5000 x g, 10 min). The resulting supernatant was designated “heat-killed conditioned media” and used in subsequent assays as detailed.

7.3.5.3 Extra Heat-Killed Conditioned Media Assays

Extra heat-killed *E. coli* working solutions were prepared as detailed in Chapter 6 Section 3.2. Briefly, a live *E. coli* working solution was subjected to heat treatment (75°C, 2 h) to attain extra heat-killed *E. coli*. The resulting solution was subjected to the preparation scheme shown in **Figure 96** whereby the cells were removed via centrifugation (5000 x g, 10 min). The resulting supernatant was designated “extra heat-killed conditioned media” and used in subsequent assays as detailed.

7.4 Results and Discussion

7.4.1 Experiments to Investigate the Role of Bacterial Metabolites in AuNP Aggregation

To determine the contribution of the metabolism/metabolites of the *E. coli* to the aggregation of the AuNPs within the system, a series of conditioned media solutions were prepared and utilised in assays, as detailed in Section 7.3.4. The

assays utilised live, heat-killed, and extra heat-killed conditioned medias (i.e. the resulting supernatants from the various preparations of *E. coli*) to allow comparison with their bacteria-laden counterparts. In this way, the 10-fold serial dilutions of the conditioned media resulted in the 'equivalent' concentrations of metabolic products as those present in the other assays, with the only difference supposed to be the absence of the bacterial cells. Note that spectra for the undiluted conditioned media are also shown on the figures below as a form of internal 'control' within the assays and are thus labelled 'undiluted conditioned media'.

Conditioned media assays explored the same 'equivalent' concentration range (5 x 10^7 – 5 CFU/mL) as the assays that contained bacterial cells. Importantly, as shown in detail below, the second red-shifted plasmon peak (that indicates aggregation resulting from the increased particle size of AuNP clusters) did not develop in these spectra. This was a surprising result and could be the result of either the absence of the bacterial cells, supporting the hypothesis that they were in fact an essential component within the sample matrix for the aggregation of the AuNPs to occur, *or* as alluded to in Section 7.3.1 of the current Chapter, the explanation could lie in some way with a change in the stability of the colloid over time. Most probably, the true mechanism partly involves both of these things.

In the sections below, I discuss the results first between the as-synthesized AuNPs with various preparations of conditioned media, followed by those with the washed AuNPs.

7.4.1.1 Live Conditioned Media Assays with As-synthesized AuNPs

The following section contains data from the assays of as-synthesized AuNPs with 10-fold serial dilutions of conditioned media from live *E. coli.* The concentrations are reported in 'equivalents' as the bacterial cells were removed prior to serial dilutions being performed as per the same procedures used in previous chapters.

Omitted sequential spectra can be found in Appendix A and have been omitted from this section for ease of reading.

With reference to the following spectra (**Figure 97** -Figure **100**) pertaining to the assays of as-synthesized AuNPs with conditioned media from live *E. coli*, there was no development of the second, red-shifted aggregation LSPR peak, indicative of particle-particle aggregates forming within the colloid. Over time, there was a gradual dampening and very slight broadening of the LSPR peaks, implying a loss of Au from the 'detection zone' and slight increase of particle size distribution within the system, respectively. After ~ 8 h incubation (see Appendix A) there was a total loss of the LSPR for both the highest dilution of conditioned media and the control sample (undiluted conditioned media). Importantly, however, the attenuance of the samples were observed to increase with time, likely resulting from the resumed growth of residual bacterial cells within the conditioned media (after an initial lag).[235, 236] This confirmed that the methods employed herein to prepare the conditioned media was not sufficient to completely remove all viable bacterial cells.

There appears to be two competing occurrences with respect to the resulting spectra from the as-synthesized AuNPs assayed with conditioned media from live *E. coli*; as the concentration of the analyte increased, the LSPR peaks decreased in attenuance. Simultaneously, as residual bacteria resumed growth and proliferated within the sample mixtures over time, the overall attenuance of the samples increased.

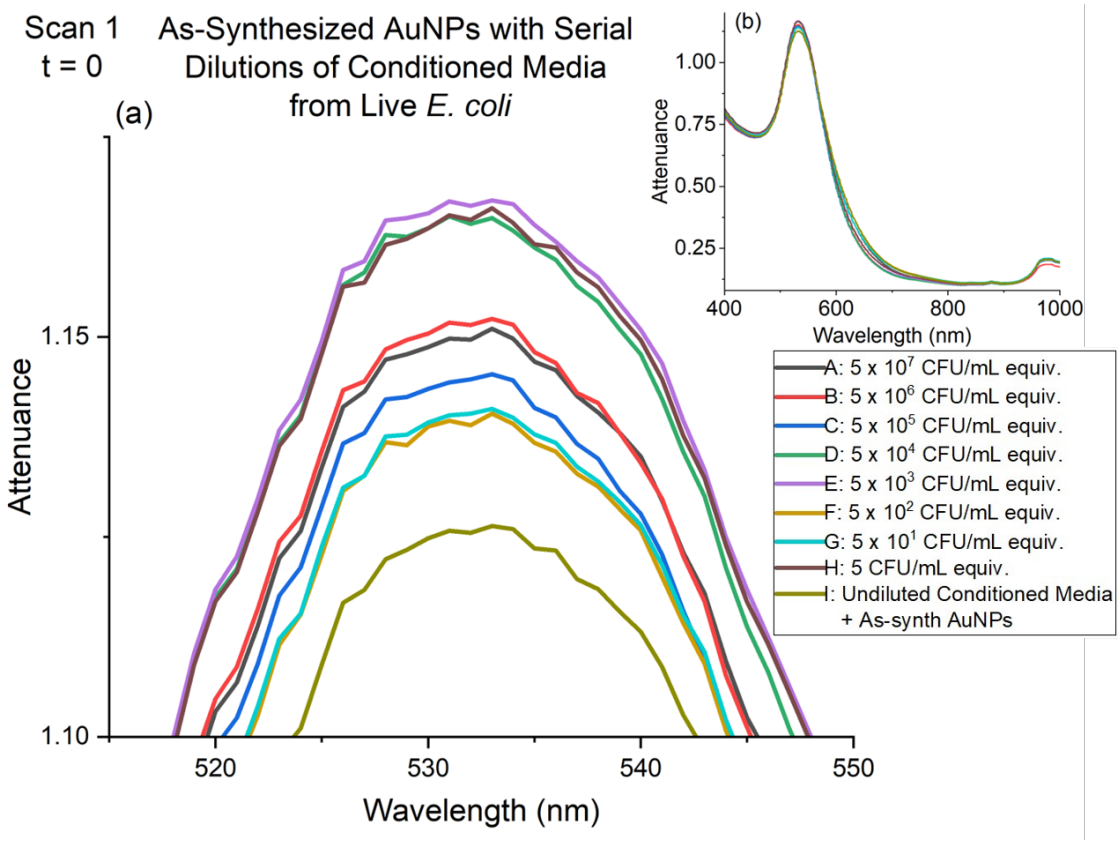

Figure 97: UV-vis spectra of as-synthesized AuNPs with 10-fold serial dilutions of conditioned media from live *E. coli* at ambient temperature, t = 0. a) shows a magnified region of the LSPR peaks and inset b) shows all spectra over the entire range of monitored wavelengths (nm).

Initially there were no appreciable differences between the resulting spectra from the as-synthesized AuNPs assayed with conditioned media from live *E. coli* (**Figure 97**). The absence of the red-shifted LSPR peak indicated no significant aggregation occurred within the system at this time. This suggests either the AuNPs require the presence of the cells to aggregate, additional time is required for the aggregation to occur in the absence of the cells, or there has been some change to the AuNPs over time.

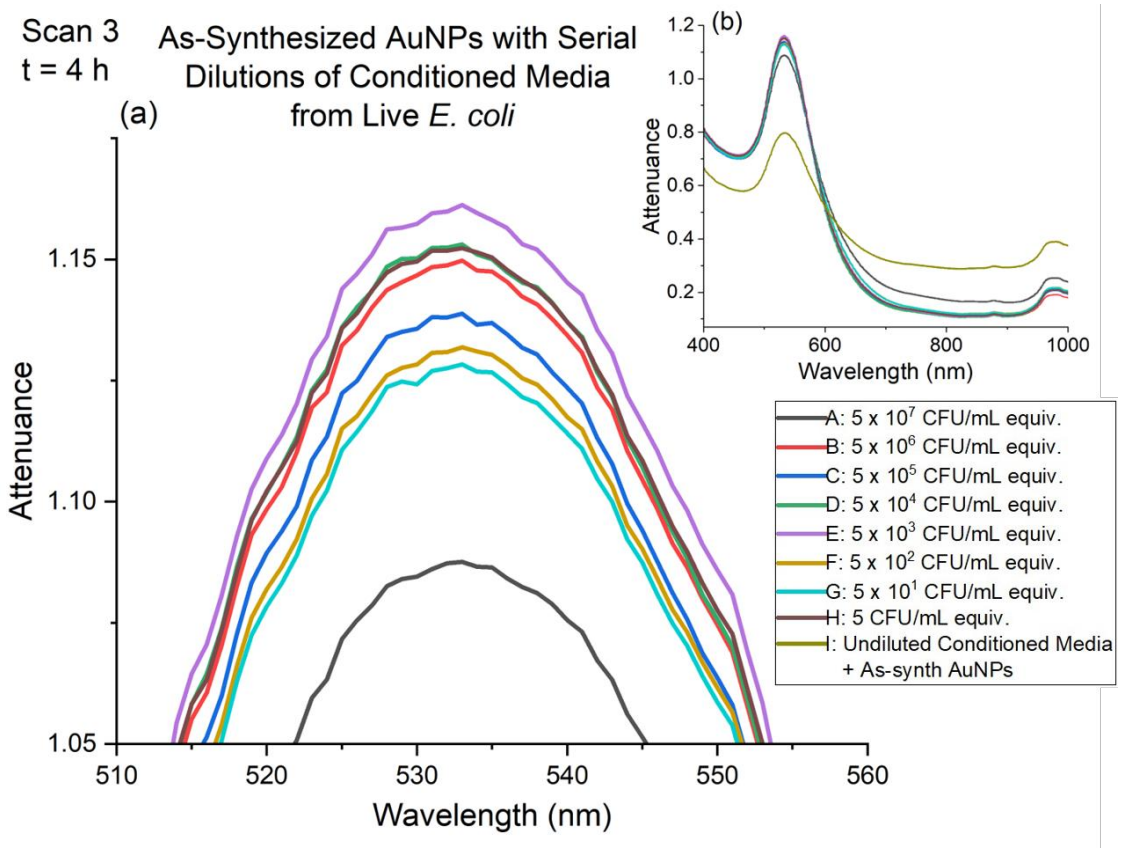

Figure 98: UV-vis spectra of as-synthesized AuNPs with 10-fold serial dilutions of conditioned media from live *E. coli* at ambient temperature, t = 4 h. a) shows a magnified region of the LSPR peaks and inset b) shows all spectra over the entire range of monitored wavelengths (nm).

After 4 h of incubation in the presence of as-synthesized AuNPs (**Figure 98** above), sufficient growth of residual bacterial cells had effected an observable change in attenuance of the most concentrated samples. It had been previously demonstrated in Chapters 4 and 5 that these conditions (incubation at ambient temperature in the presence of as-synthesized AuNPs) were able to support the growth and/or recovery of *E. coli*.

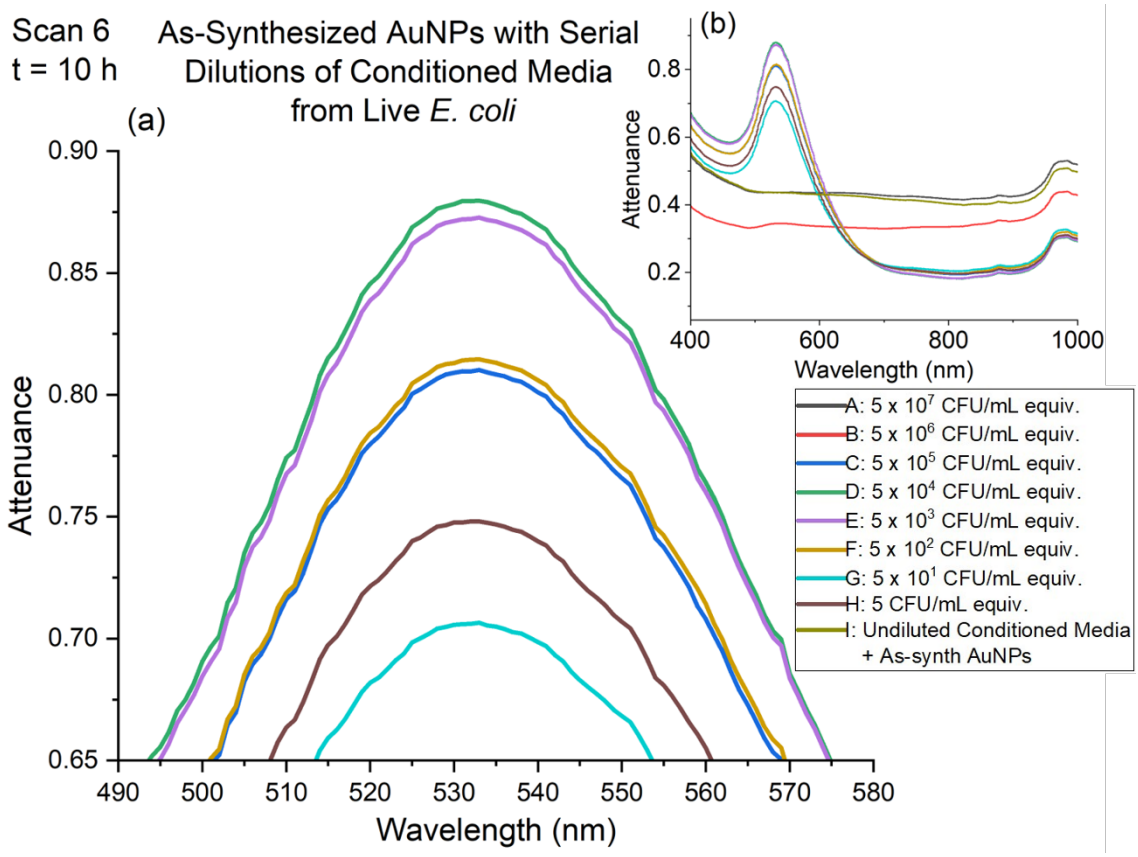

Figure 99: UV-vis spectra of as-synthesized AuNPs with 10-fold serial dilutions of conditioned media from live E. coli at ambient temperature, t = 10 h. a) shows a magnified region of the LSPR peaks and inset b) shows all spectra over the entire range of monitored wavelengths (nm).

With reference to the above **Figure 99**, a complete collapse of the colloid was observed in samples assayed with the highest concentrations of conditioned media: A, B and I (5 x 10^7 – 10^6 CFU/mL and undiluted equivalents, black, red and army green lines respectively). Although the LSPR peaks of these samples were lost (indicating loss of colloidal nature of AuNPs/flocculation), the notable increase in attenuance supports the bacterial growth within these samples. All other (lower) concentrations resulted in slight broadening and dampening of the LSPR peaks, congruent with the gradual aggregation/destabilization of the colloids.

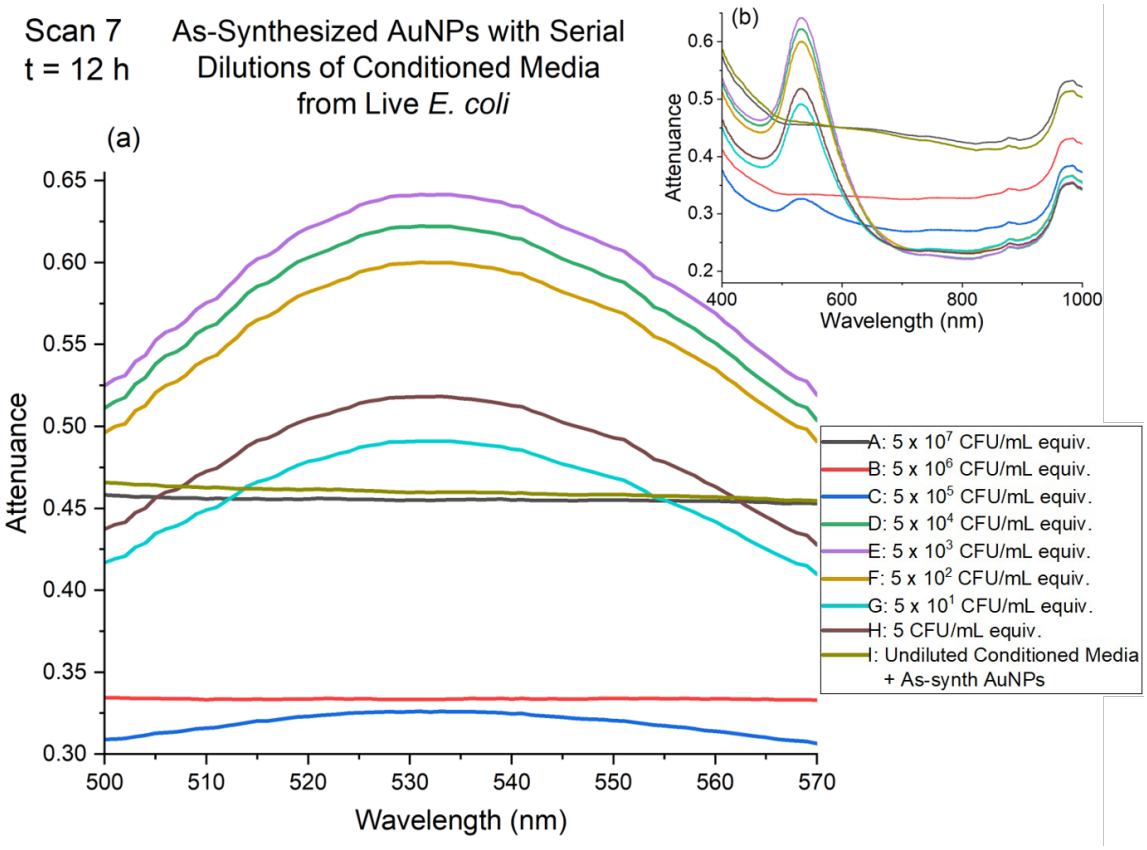

Figure 100: UV-vis spectra of as-synthesized AuNPs with 10-fold serial dilutions of conditioned media from live *E. coli* at ambient temperature, t = 12 h. a) shows a magnified region of the LSPR peaks and inset b) shows all spectra over the entire range of monitored wavelengths (nm).

Comparing **Figure 100** above (12 h incubation), with the spectra from the initial post-assay measurement (**Figure 97**), the spectral changes resulting from the gradual destabilization of the colloid within the conditioned media and as a result of the resumption of growth become magnified. Namely, aggregation (peak broadening and decreased attenuance) was observed in all samples, affecting those that had a higher initial (equivalent) concentration of conditioned media. Sample C (5 x 10^4 CFU/mL equivalent, dark blue line) has very little colloidal gold remaining within the 'detection window', and the colloids assayed with higher equivalent concentrations of conditioned media (already flocculated in **Figure 99**) were observed to further increase in attenuance.

7.4.1.2 Heat-Killed Conditioned Media Assays with As-synthesized AuNPs

The following section contains data from the assays of as-synthesized AuNPs with 10-fold serial dilutions of conditioned media from the preparations of heat-killed *E. coli*. The concentrations are reported in 'equivalents' as the bacterial cells were removed prior to serial dilutions being performed as per the procedures detailed in Section 3.4 of the current Chapter.

Omitted sequential spectra can be found in Appendix A and have been omitted from this section for ease of reading.

Comparing **Figure 97** Figure **100** with the following spectra presented in **Figure 101** -**Figure 103** (as-synthesized AuNPs assayed with conditioned media from heat-killed *E. coli*), the absence of the second, red-shifted aggregation LSPR peak was similarly observed. However, in contrast to **Figure 97** Figure **100**, the conditioned media from heat-killed *E. coli* did not result in complete loss of the LSPR peaks even after 14 h of incubation with colloids, as will be shown below. This suggests that the application of both the heat treatment and removal of cells to prepare the 'conditioned' media was sufficient to retard the growth of any residual bacterial cells enough to prevent the complete flocculation of the colloid within the tested timeframe.

Initially, the colloids assayed with heat-killed conditioned media had a higher attenuance but slightly broader peak width than those assayed with the live conditioned media (**Figure 97** Figure **100**), implying a broader size distribution-type aggregation effect within the heat-killed conditioned media test groups (**Figure 101** -**Figure 103** below) as opposed to a loss of colloidal gold from the detection zone exhibited by the colloids assayed in live conditioned media.

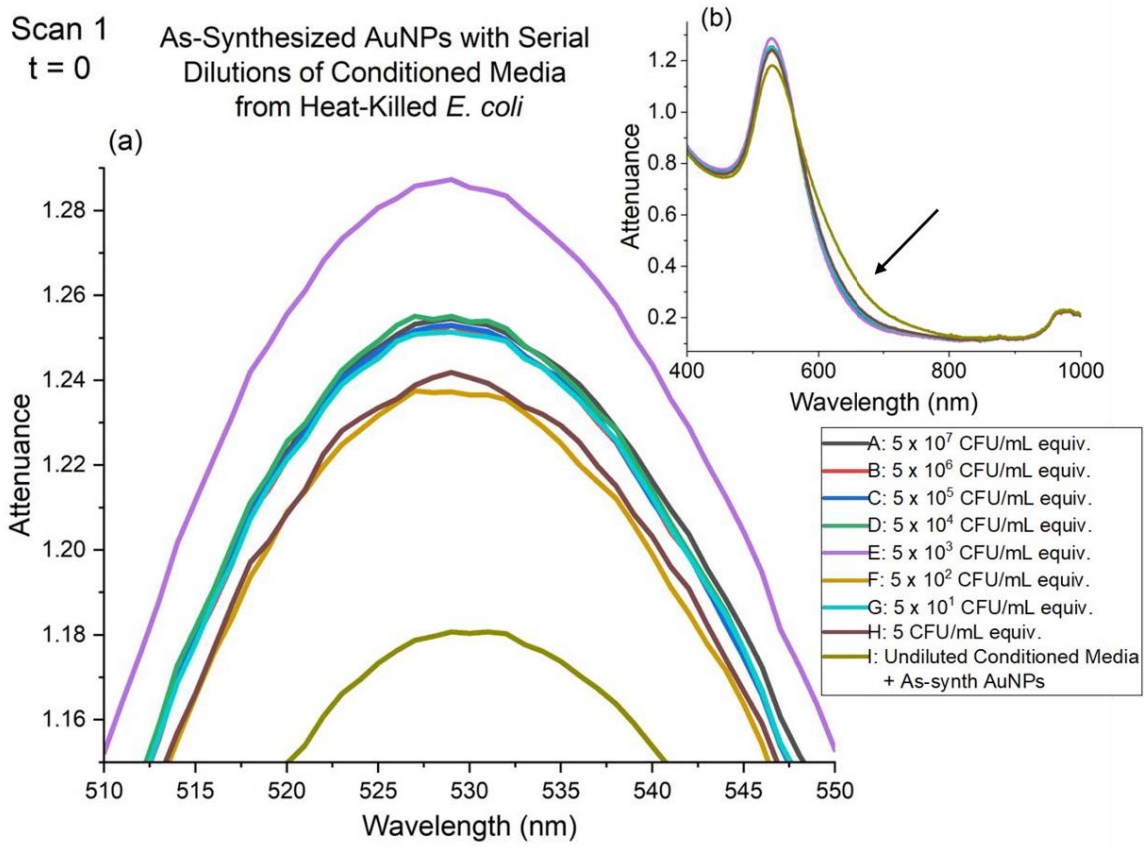

Figure 101: UV-vis spectra of as-synthesized AuNPs with 10-fold serial dilutions of conditioned media from heat-killed *E. coli* at ambient temperature, t = 0. a) shows a magnified region of the LSPR peaks and inset b) shows all spectra over the entire range of monitored wavelengths (nm).

The initial assay between as-synthesized AuNPs and conditioned media from heat-killed *E. coli* (**Figure 101** above) resulted in LSPR peaks of relatively higher attenuance than those arising from the same colloids assayed with conditioned media from live *E. coli* (**Figure 97**). Some slight shouldering is evident in the control sample (I, undiluted heat-killed conditioned media, army green line), as indicated by the arrow in inset b).

This indicates that the heat treatment prior to conditioning resulted in relatively less loss of colloidal gold than the live conditioned media, but caused a comparatively slight increase in size of the particles (peak broadening).

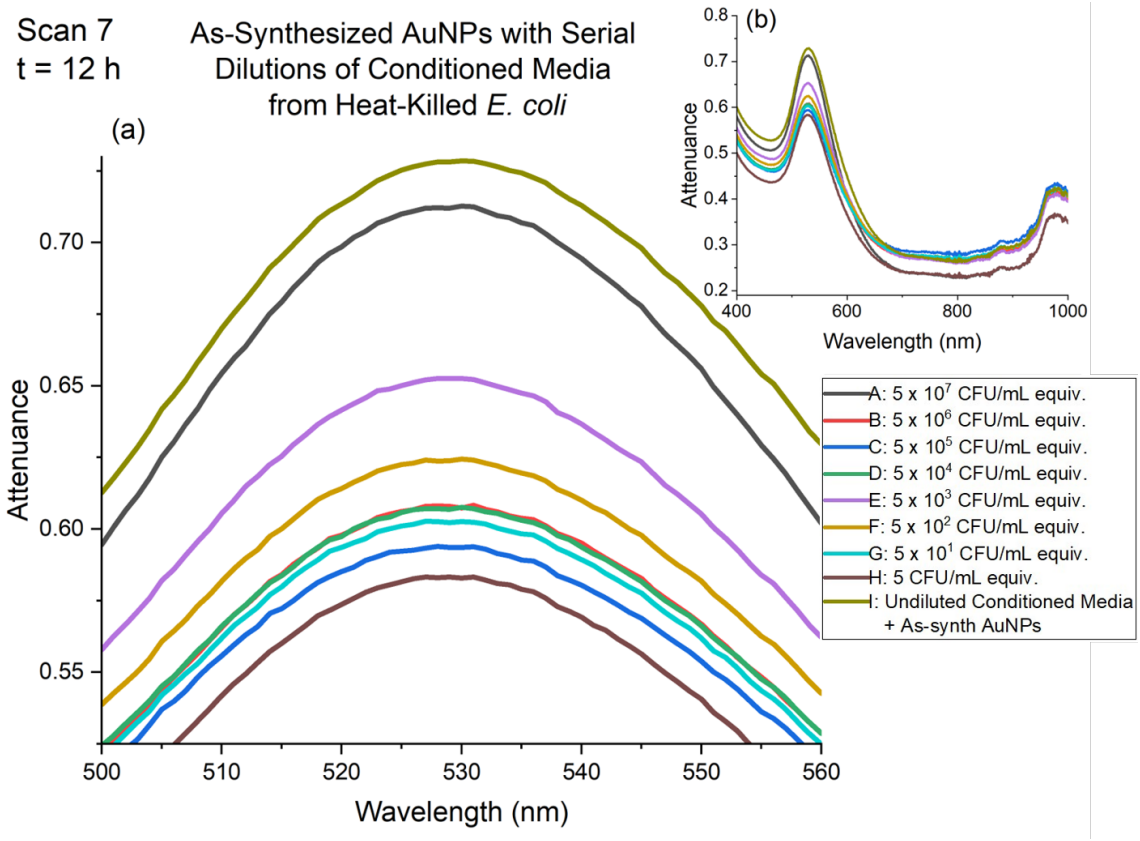

Figure 102: UV-vis spectra of as-synthesized AuNPs with 10-fold serial dilutions of conditioned media from heat-killed *E. coli* at ambient temperature, t = 12 h. a) shows a magnified region of the LSPR peaks and inset b) shows all spectra over the entire range of monitored wavelengths (nm).

After 12 h of incubation in the presence of as-synthesized AuNPs, sufficient growth was evident within the heat-killed conditioned media to produce a notable effect on the attenuance and peak shape of the colloids (**Figure 102**). Compared to the level of aggregation and loss of detectable Au within the sample mixtures seen in the live conditioned media equivalent of this assay (compare the above **Figure 102** with **Figure 100**), comparatively little aggregation/destabilization of the colloid has occurred within the heat-killed conditioned media samples.

Thus, it is likely that a very small number (much lower compared to the live conditioned media) of remaining viable cells, and/or sub-lethally injured cells present within the heat-killed conditioned media were able to resume growth to a noticeable degree by 12 h incubation, in the presence of as-synthesized AuNPs.

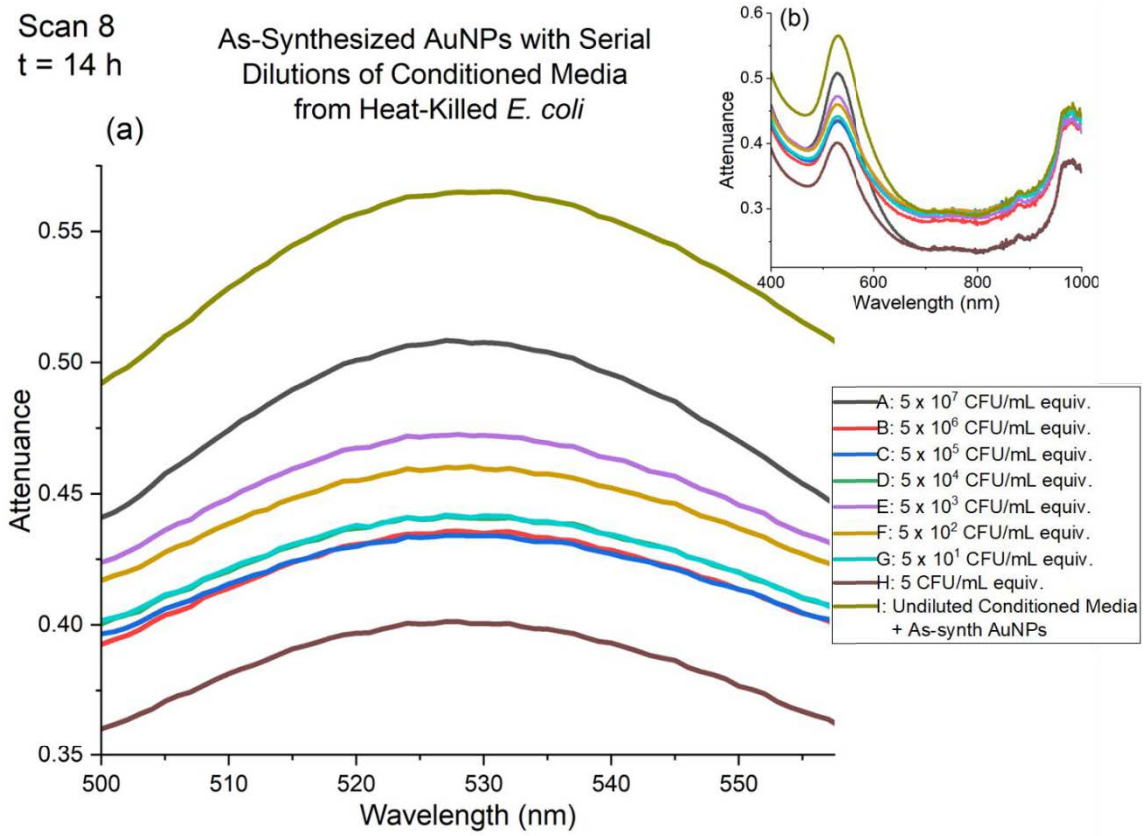

Figure 103: UV-vis spectra of as-synthesized AuNPs with 10-fold serial dilutions of conditioned media from heat-killed *E. coli* at ambient temperature, t = 14 h. a) shows a magnified region of the LSPR peaks and inset b) shows all spectra over the entire range of monitored wavelengths (nm).

An additional 2 h of incubation (total of 14 h) was not sufficient to result in the complete collapse of the as-synthesized AuNPs, at any tested concentrations of the heat-killed conditioned media (**Figure 103**). In contrast, as little as 6 h was sufficient to result in flocculation of as-synthesized AuNPs assayed with highly concentrated samples of live conditioned media (Appendix A).

7.4.1.3 Extra Heat-Killed Conditioned Media Assays with As-synthesized AuNPs

The following section contains data from the assays of as-synthesized AuNPs with 10-fold serial dilutions of conditioned media from extra heat-killed *E. coli*. The concentrations are reported in 'equivalents' as the bacterial cells were removed prior to serial dilutions being performed as per the procedures detailed in Section 3.4 of the current Chapter.

Omitted sequential spectra can be found in Appendix A and have been omitted from this section for ease of reading.

In reference to the following spectra resulting from the assays of as-synthesized AuNPs with conditioned media from extra heat-killed *E. coli* (**Figure 104** -**Figure 107**), and as was seen with the conditioned medias from live and heat-killed preparations of *E. coli*, no red-shifted aggregation peaks were observed to develop. Akin to the results of the 14 h incubation with heat-killed conditioned media (**Figure 103**), the same incubation time with extra heat-killed conditioned media did not result in complete collapse of the as-synthesized colloids, at any tested concentration. Overall, even after 14 h incubation, there is little evidence of bacterial growth which is congruent with both the extended heat treatment and the conditioning of the medium.

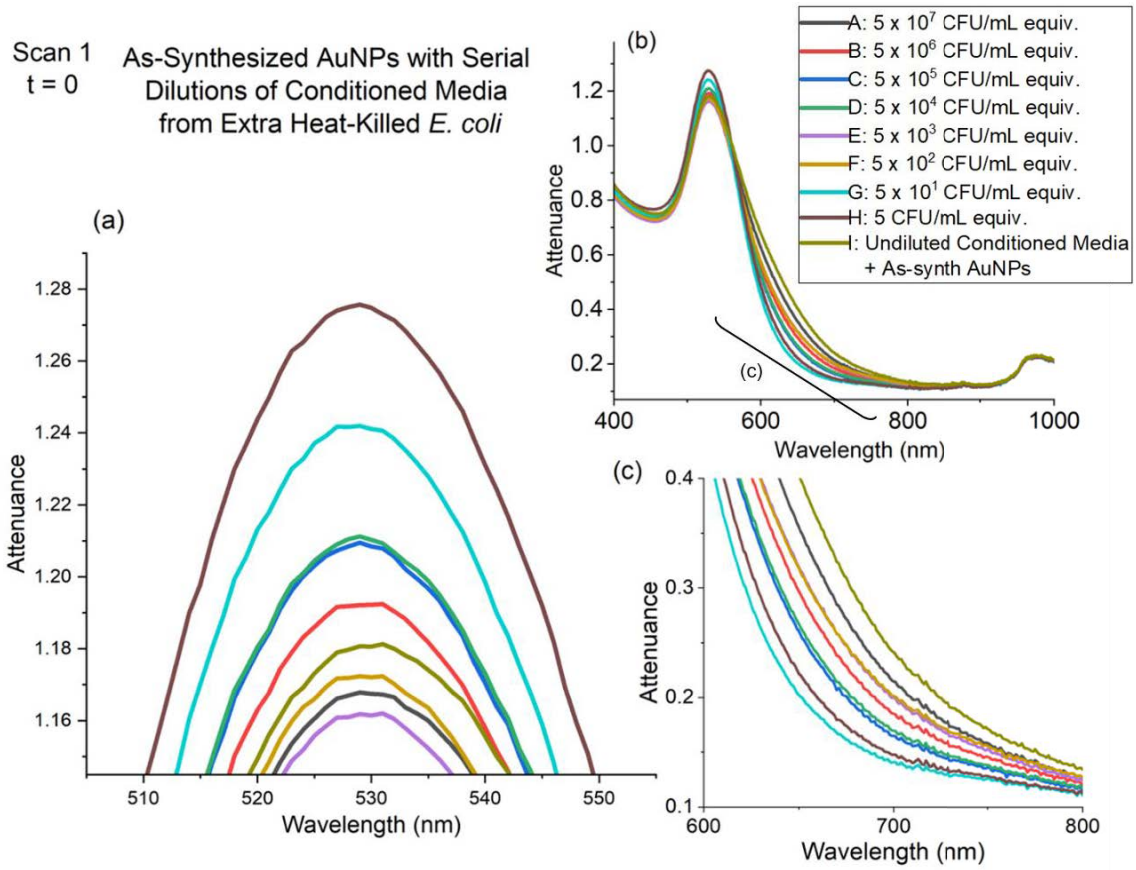

Figure 104: UV-vis spectra of as-synthesized AuNPs with 10-fold serial dilutions of conditioned media from extra heat-killed *E. coli* at ambient temperature, t = 0. a) shows a magnified region of the LSPR peaks, inset b) shows all spectra over the entire range of monitored wavelengths (nm), and inset c) shows the magnified region of interest indicated in b).

Comparing the initial assay between the as-synthesized AuNPs and conditioned media from extra heat-killed *E. coli* (**Figure 104** above) to the initial assays using live and heat-killed conditioned medias (**Figure 97** andFigure **101** respectively), the extra heat-killed conditioned media resulted in a similar range of attenuance (~ 1.16 – 1.28) to that observed in the heat-killed conditioned media initial assay (**Figure 101**). In contrast however, the resulting spectra appeared to be more concentration-dependent in the extra heat-killed conditioned media (**Figure 104** above), with greater separation between the LSPRs of almost all resultant peaks.

Additionally, a slight shouldering or broadening of the peaks (at all tested concentrations) was observed, as shown in the magnified region of inset c)

above. This suggests broadening of the particle size distribution through aggregation. However, the aggregation is not significant enough, or perhaps not forming large AuNP clusters and therefore not appearing as the previously observed red-shifted second LSPR peak.

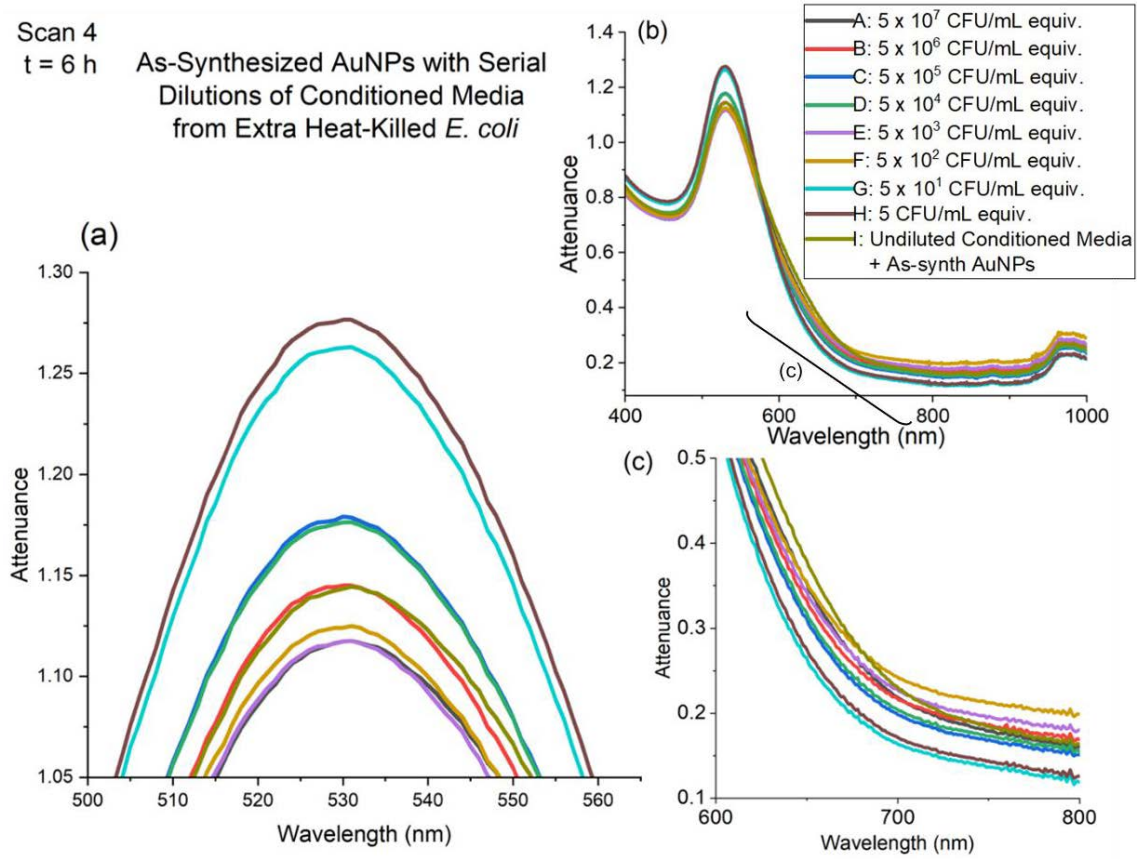

Figure 105: UV-vis spectra of as-synthesized AuNPs with 10-fold serial dilutions of conditioned media from extra heat-killed *E. coli* at ambient temperature, t = 6 h. a) shows a magnified region of the LSPR peaks, inset b) shows all spectra over the entire range of monitored wavelengths (nm), and inset c) shows the magnified region of interest indicated in b).

Overall, after 6 h of incubation, the extra heat-killed conditioned media has resulted in a decrease in attenuance within the majority of the colloidal samples (except the two lowest concentrations tested), **Figure 105**. The same region of interest seen initially (t = 0, **Figure 104**) has become comparatively less broad over time. This, which suggests the larger sized particles/aggregates are no longer present, coupled with the decrease in attenuance of the LSPR peaks

suggests a loss of the total colloidal gold within the 'detection window' of the samples.

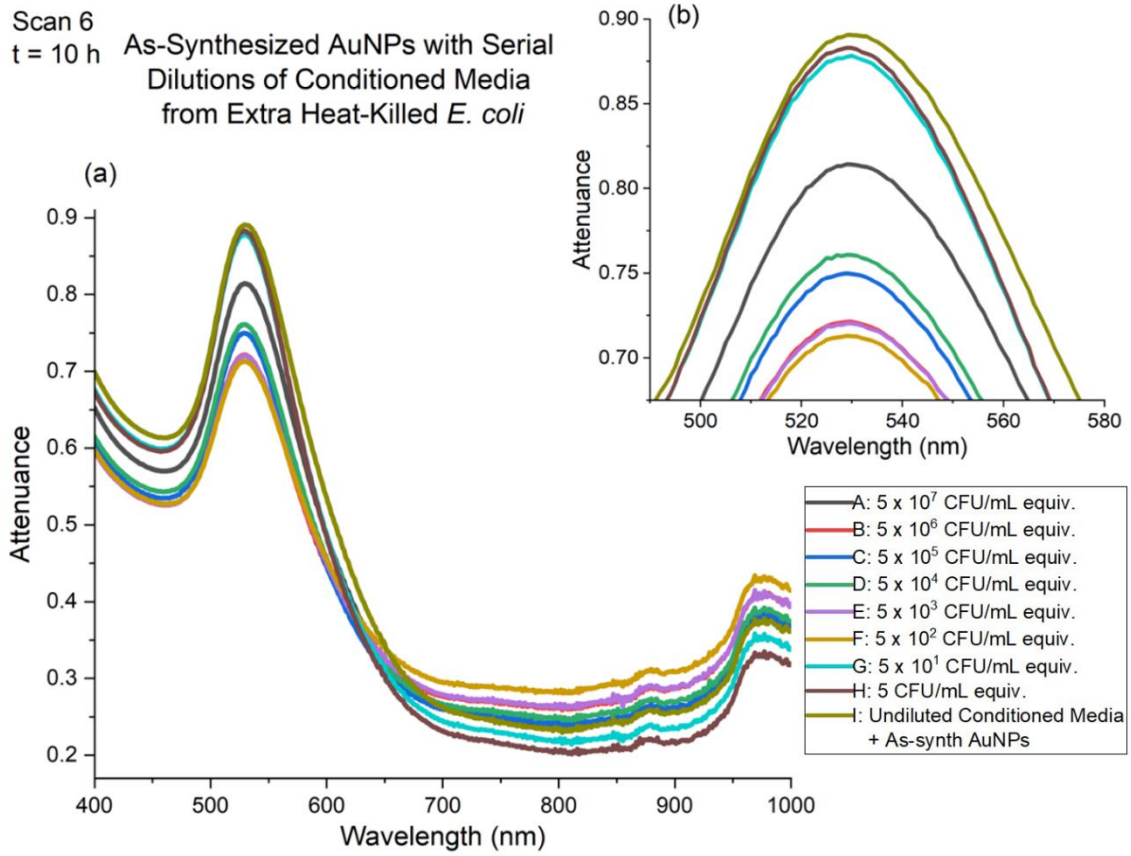

Figure 106: UV-vis spectra of as-synthesized AuNPs with 10-fold serial dilutions of conditioned media from extra heat-killed *E. coli* at ambient temperature, t = 10 h. a) shows all spectra over the entire range of monitored wavelengths (nm), and inset b) shows a magnified region of the LSPR peaks.

An additional 4 h incubation of the as-synthesized AuNPs in extra heat-killed conditioned media (compare **Figure 106** above with **Figure 105**) did not result in appreciably broadened LSPR peaks. However, the attenuance of the LSPR peaks became noticeably lower, suggesting the loss of colloidal gold. The attenuance of the spectra (all tested concentrations) showed an increase in the region between 700 – 1000 nm, although this was not associated with the appearance of an additional LSPR peak and was thus attributed to the eventual resumption of growth of a small population of bacterial cells in the conditioned media.

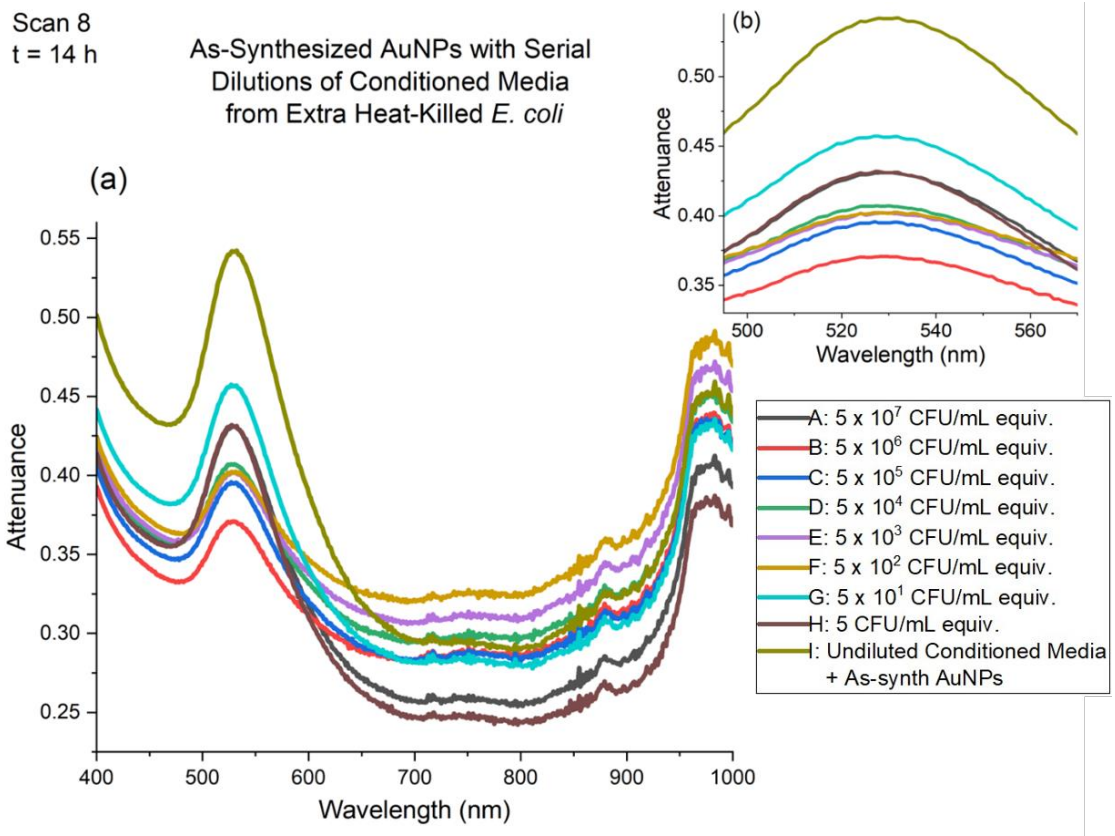

Figure 107: UV-vis spectra of as-synthesized AuNPs with 10-fold serial dilutions of conditioned media from extra heat-killed *E. coli* at ambient temperature, t = 14 h. a) shows all spectra over the entire range of monitored wavelengths (nm), and inset b) shows a magnified region of the LSPR peaks.

Similar to what was observed in **Figure 103**, the extra heat-killed conditioned media did not result in complete collapse/flocculation of the as-synthesized AuNPs at any tested concentration, even after 14 h of incubation (**Figure 107** above). Comparing the above **Figure 107**with **Figure 106**, it appears as though at some point > 10 h of incubation between the extra heat-killed conditioned media and the as-synthesized AuNPs, significant growth of residual, resuscitated and/or recovered cells within the conditioned medium occurred, resulting in a dramatic dampening of the LSPR peaks at all tested *dilutions*. This implies that the addition of fresh LB to the conditioned media was necessary for the eventual repair and/or resumption of growth to a significant degree (compare the relatively high attenuance/undampened LSPR peak of the undiluted conditioned media control to the resulting spectra of all conditioned media dilutions above).

From the changes observed in the spectra of as-synthesized AuNPs with various preparations of conditioned media (live, heat-killed and extra heat-killed), it can be concluded that the as-synthesized AuNPs used experimentally have exhibited different behaviour to what was observed in previous assays (e.g. Chapters 3 – 6), despite coming from the same batch. Upon reflection and careful interpretation of the results as a whole, it can be deduced that these observed differences were not a result of the initial absence of bacterial cells from the samples. This is supported by the absence of the red-shifted plasmon peak from all samples, despite evidence of aggregation of the AuNPs and eventual proliferation of residual bacteria within the samples (**Figure 100** for example).

This change in behaviour, considering the experimental design and conditions remained identical to those employed in previous Chapters, imply that the AuNP colloid has changed over time. Specifically, it appears to have become more resistant to particle-particle aggregation and displayed greater stability in highly complex/high ionic strength solutions. This will be expanded on further in the current chapter.

7.4.1.4 Live Conditioned Media Assays with Washed AuNPs

The following section contains data from the assays of washed AuNPs with 10-fold serial dilutions of conditioned media from live *E. coli*. The concentrations are reported in ‘equivalents’ as the bacterial cells were removed prior to serial dilutions being performed as per the procedures detailed in Section 3.4 of the current Chapter.

Omitted sequential spectra can be found in Appendix A and have been omitted from this section for ease of reading.

With reference to the following spectra (**Figure 108** -Figure **110**) resulting from the assays of washed AuNPs with conditioned media from live *E. coli*, there is a *very slight* suggestion of the beginnings of the formation of the characteristic red-shifted aggregation LSPR peak ~ 750 nm that was notably absent from all conditioned media assays using as-synthesized AuNPs (highlighted in **Figure**

108 by the red arrow). This suggests that the washed AuNPs were still forming (to a much lesser degree than seen in previous Chapters) larger-sized AuNP clusters, indicative of aggregation. This is in agreement with the comparatively reduced colloidal stability of washed AuNPs when compared to the as-synthesized AuNPs.

When washed AuNPs were incubated with conditioned media from live *E. coli* for times > 10 h (Appendix A), a complete collapse of the colloidal LSPR peaks were observed, resulting from the destabilization and eventual flocculation of the colloids. Simultaneously, the attenuance of the samples gradually increased as the residual (viable) bacterial cells in the conditioned media continued.

Additionally, the small peaks ~ 880 nm (indicated by the black arrow in **Figure 108**) in all conditioned media assays utilising washed AuNPs, were present in washed AuNP assays containing bacterial cells. However, the absence of the prominent red-shifted aggregation peak in the conditioned media spectra make these peaks appear more pronounced.

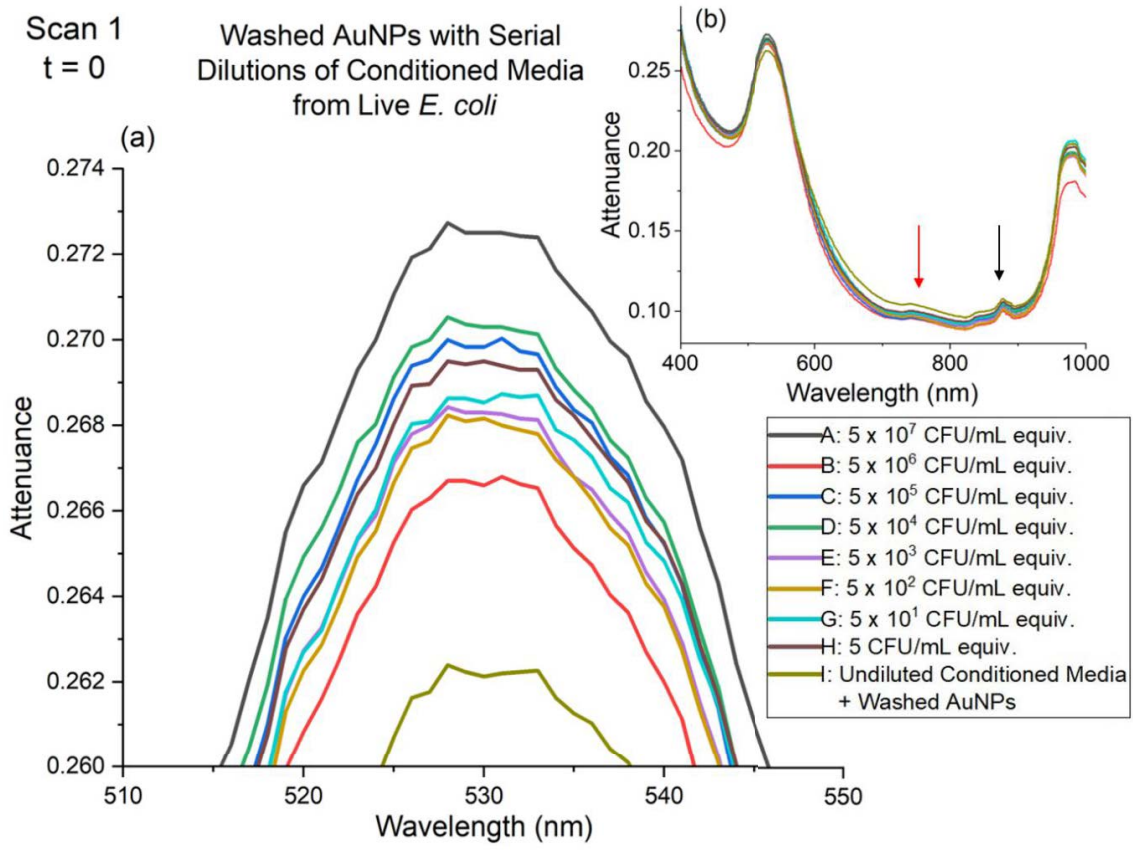

Figure 108: UV-vis spectra of washed AuNPs with 10-fold serial dilutions of conditioned media from live *E. coli* at ambient temperature, t = 0. a) shows a magnified region of the LSPR peaks and inset b) shows all spectra over the entire range of monitored wavelengths (nm).

The initial assay resulting from the incubation of conditioned media from live *E. coli* and washed AuNPs (**Figure 108** above) appears strikingly similar to the equivalent assay performed with as-synthesized AuNPs (**Figure 97**) with respect to the LSPR peaks. The much lower starting attenuance of the washed AuNP assays is partly a result of the reduced concentration of AuNPs within the respective assays.

Of note is the slight 'bump' (indicated by the red arrow above) which appears to be the start of the formation of the absent, red-shifted aggregation peak, suggesting some larger AuNP clusters/aggregates may have formed. It is unclear what is causing the artefact indicated by the black arrow in **Figure 108** b),

however they were also present to a less noticeable degree when the washed AuNPs were comparatively fresher.

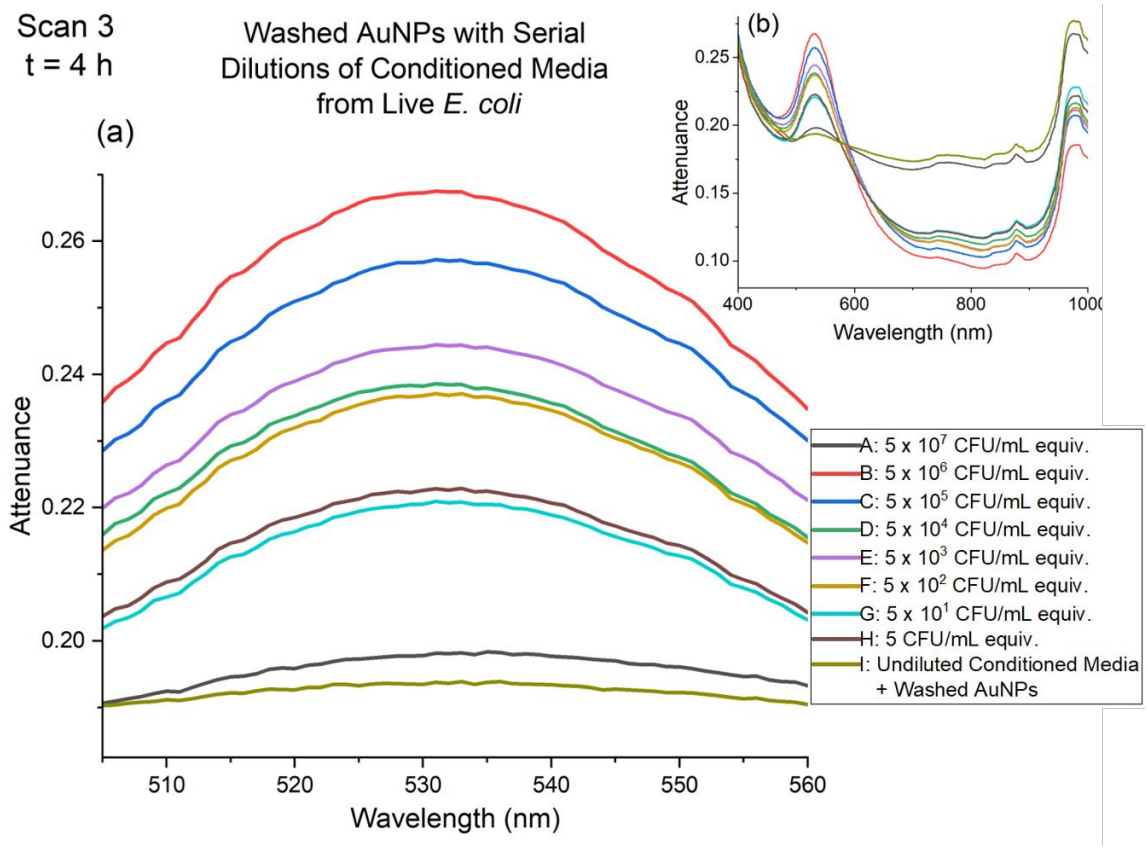

Figure 109: UV-vis spectra of washed AuNPs with 10-fold serial dilutions of conditioned media from live *E. coli* at ambient temperature, t = 4 h. a) shows a magnified region of the LSPR peaks and inset b) shows all spectra over the entire range of monitored wavelengths (nm).

The slight peaks present ~ 750 nm displayed broadening after an additional 4 h incubation in live conditioned media (**Figure 109**) indicating further aggregation and an increasing size dispersity. Aggregation of the more stable, colloidal components of the AuNPs was also evidenced by the peak dampening of the samples. In particular, the two highest concentrations of conditioned media have resulted in a significant reduction of the LSPR peaks. i.e. almost all of the Au has been lost from the 'detection zone'.

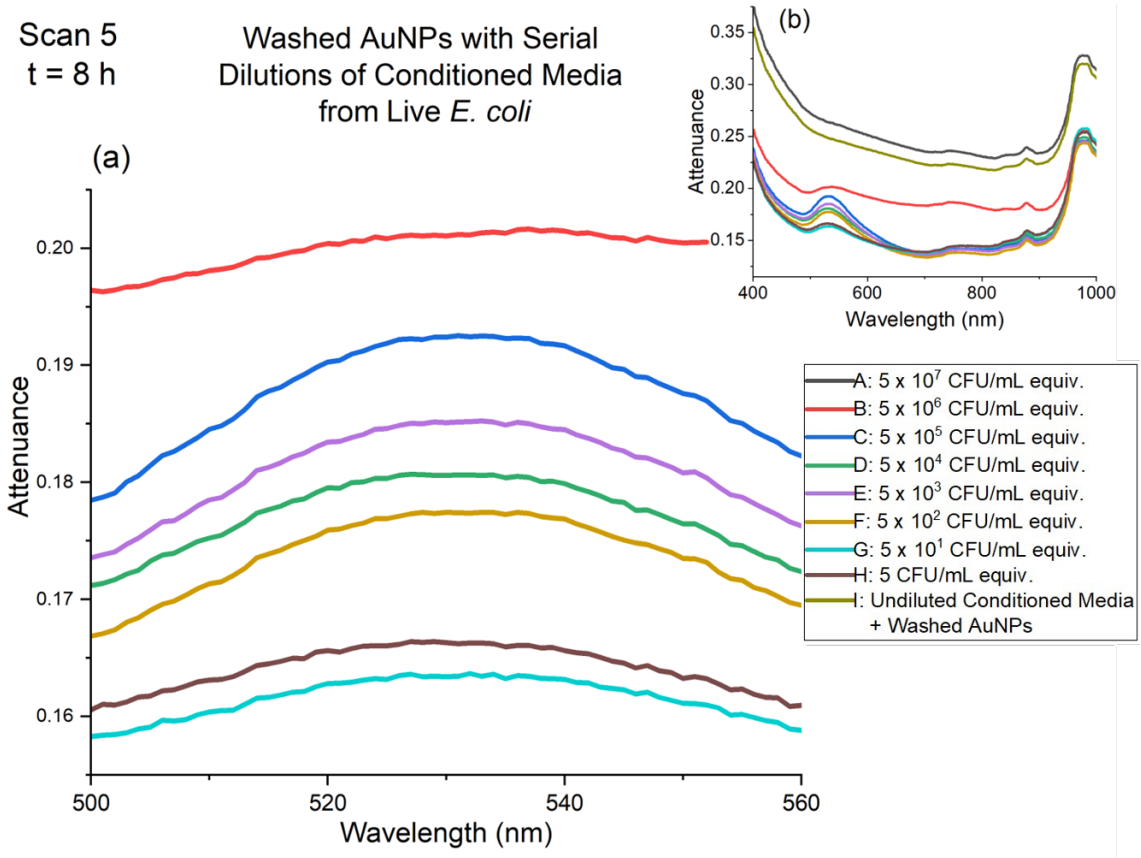

Figure 110: UV-vis spectra of washed AuNPs with 10-fold serial dilutions of conditioned media from live *E. coli* at ambient temperature, t = 8 h. a) shows a magnified region of the LSPR peaks and inset b) shows all spectra over the entire range of monitored wavelengths (nm).

Incubation of washed AuNPs with conditioned media from live *E. coli* for 8 h (**Figure 110**) resulted in the (almost) complete collapse of colloids assayed with concentrations ≥ 5 x 10^6 CFU/mL equivalents. Although sample B (red line) has a very residual LSPR peak, it is almost completely lost to the severe dampening and broadening of the peak resulting from the destabilization of the AuNPs. This, in addition to the marked increased in attenuance for the most concentrated samples tested indicate the significant proliferation of the residual bacteria within the conditioned media and clearly show its concentration-dependent effect on the stability of the washed AuNPs.

Further to this, the (very slight) second aggregation peak was observed to broaden further (from 4 – 8 h incubation), suggesting further

aggregation/increase in large AuNP clusters. Despite this, its relative decreased intensity also suggests these larger particles are likely to have sedimented.

7.4.1.5 Heat-Killed Conditioned Media Assays with Washed AuNPs

The following section contains data from the assays of washed AuNPs with 10-fold serial dilutions of conditioned media from various heat-killed *E. coli*. The concentrations are reported in 'equivalents' as the bacterial cells were removed prior to serial dilutions being performed as per the procedures detailed in Section 3.4 of the current Chapter.

Omitted sequential spectra can be found in Appendix A and have been omitted from this section for ease of reading.

With reference to the following spectra (**Figure 111** -Figure **113**) resulting from the assays of washed AuNPs with conditioned media from heat-killed *E. coli*, a similar red-shifted LSPR peak was observed within the samples ~ 750 nm, albeit very low in relative intensity compared to the initial LSPR peak. This peak was comparable in position and intensity to that observed in the equivalent assays utilizing live conditioned media, **Figure 108** -**Figure 110**.

Comparable trends of LSPR peak dampening were observed for the assays between washed AuNPs and conditioned media from live and heat-killed *E. coli*, with the key differences in the spectra seeming to have risen from the decreased level of resumed bacterial proliferation within the conditioned media. Over time, the heat-killed conditioned media resulted in comparatively lower losses of the total Au from within the detectable range (compare **Figure 113** with **Figure 110** for example). Even after 8 h of incubation with washed AuNPs (**Figure 113**), all tested concentrations of heat-killed conditioned media resulted in spectra with a significantly dampened, but noticeably present LSPR peak.

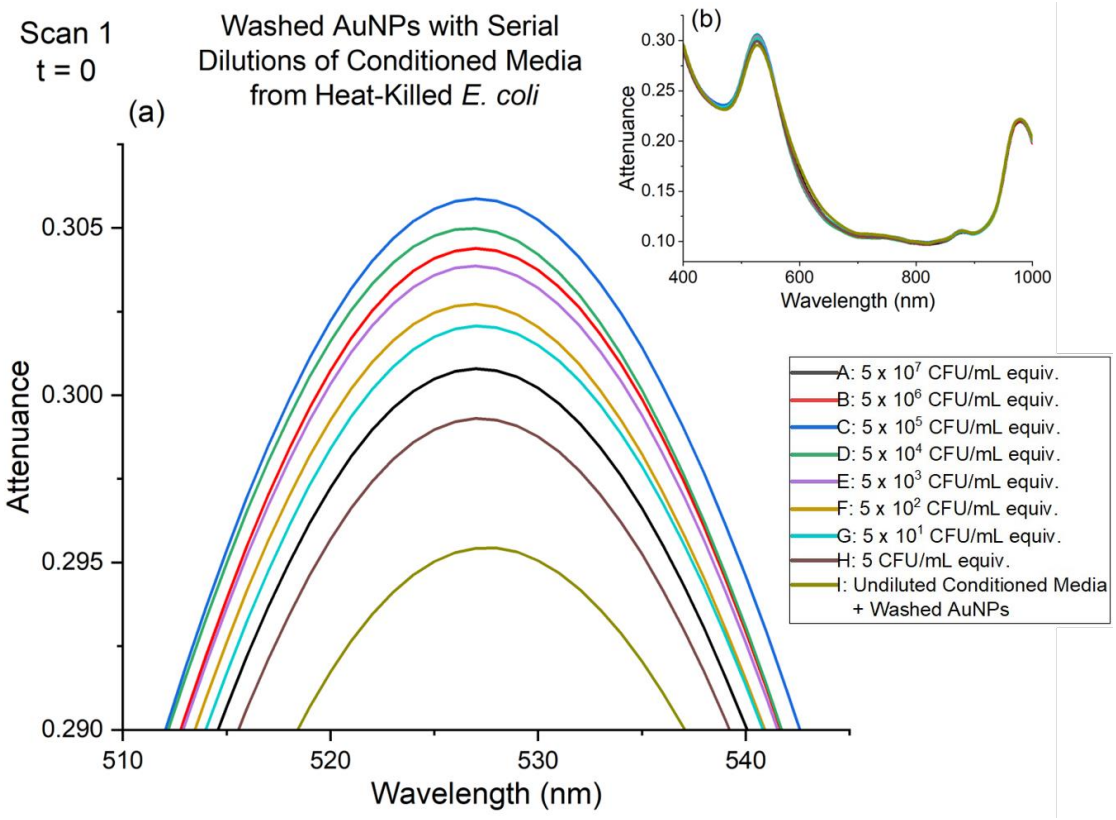

Figure 111: UV-vis spectra of washed AuNPs with 10-fold serial dilutions of conditioned media from heat-killed *E. coli* at ambient temperature, t = 0. a) shows a magnified region of the LSPR peaks and inset b) shows all spectra over the entire range of monitored wavelengths (nm).

Comparison of the initial heat-killed conditioned media/washed AuNP assay (**Figure 111** above) with the live conditioned media equivalent (**Figure 108**), the most notable difference is the relatively higher attenuance of the spectra resulting from the washed AuNPs with the heat-killed conditioned media. This implies the heat-killed conditioned media initially resulted in comparatively less destabilization of the washed colloid. There were no other appreciable differences at this stage.

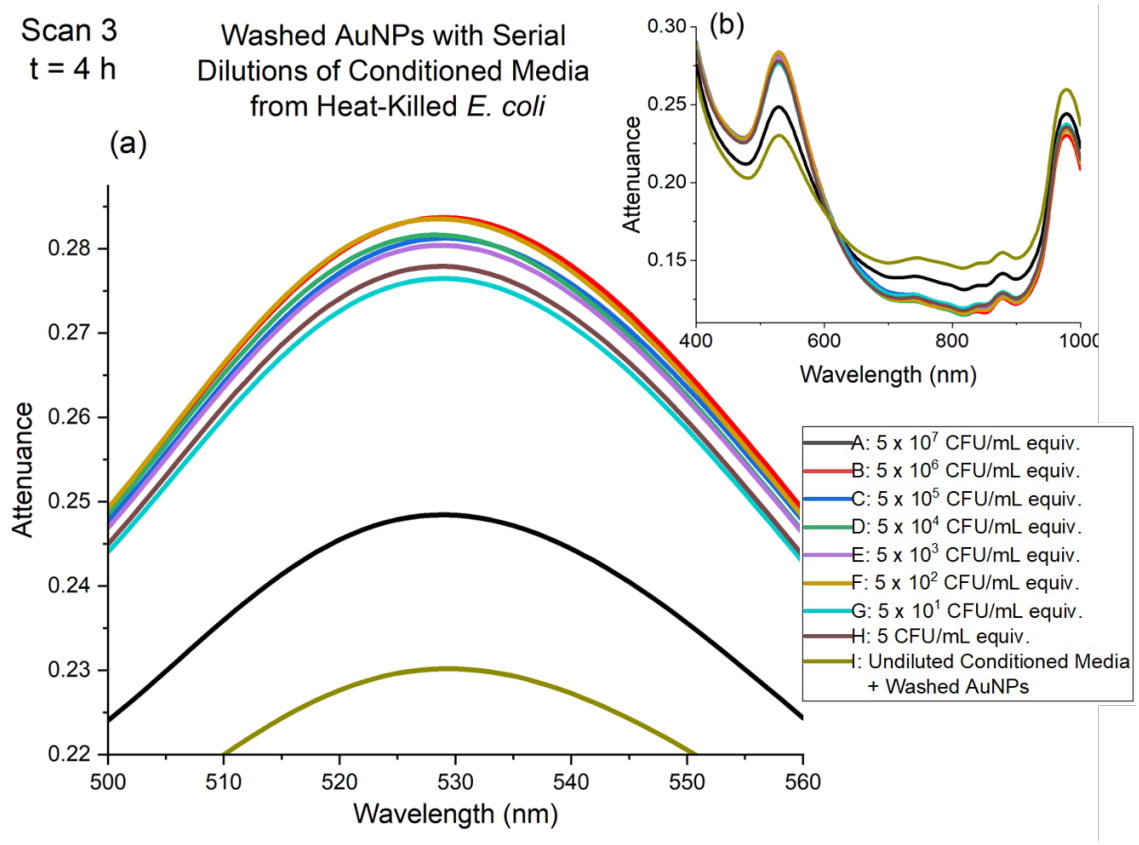

Figure 112: UV-vis spectra of washed AuNPs with 10-fold serial dilutions of conditioned media from heat-killed *E. coli* at ambient temperature, t = 4 h. a) shows a magnified region of the LSPR peaks and inset b) shows all spectra over the entire range of monitored wavelengths (nm).

After 4 h of incubation at ambient temperature in the presence of washed AuNPs, there was sufficient growth, recovery and/or resuscitation of residual cells within the most concentrated samples of heat-killed conditioned media. This was evidenced by the LSPR peak dampening and increase in attenuance in the region > 700 nm.

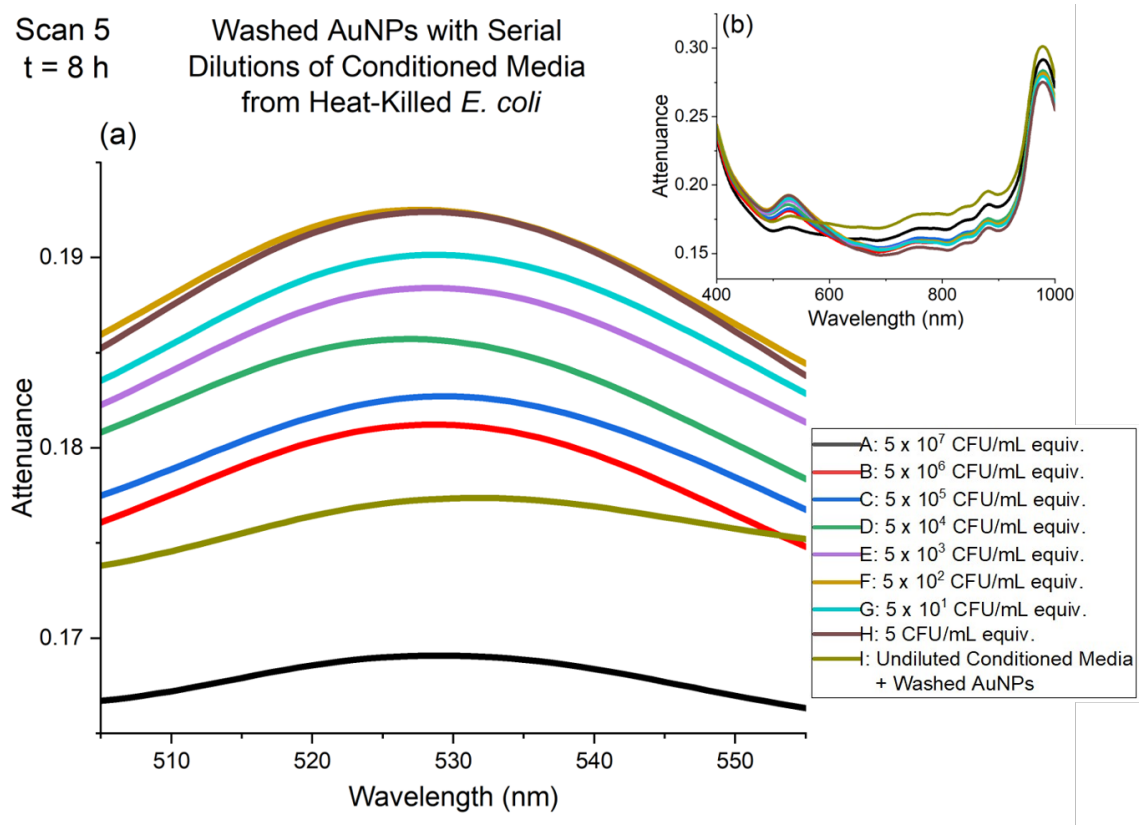

Figure 113: UV-vis spectra of washed AuNPs with 10-fold serial dilutions of conditioned media from heat-killed *E. coli* at ambient temperature, t = 8 h. a) shows a magnified region of the LSPR peaks and inset b) shows all spectra over the entire range of monitored wavelengths (nm).

A further 4 h of incubation (8 h total, **Figure 113** above) resulted in the significant dampening of all resultant LSPR peaks. However, in contrast to the live conditioned media assay equivalent (**Figure 110**), a total loss of the LSPR peaks were not evident here. This suggests the resumption and continued growth of the bacteria within the samples contributes to the destabilization of the washed colloids.

7.4.1.6 Extra Heat-Killed Conditioned Media Assays with Washed AuNPs

The following section contains data from the assays of washed AuNPs with 10-fold serial dilutions of conditioned media from extra heat-killed *E. coli*. The concentrations are reported in 'equivalents' as the bacterial cells were removed prior to serial dilutions being performed as per the procedures detailed in Section 3.4 of the current Chapter.

Omitted sequential spectra can be found in Appendix A and have been omitted from this section for ease of reading.

With reference to the following spectra pertaining to the assays of washed AuNPs with conditioned media from extra heat-killed *E. coli* (**Figure 114** -**Figure 116**), the slight peaks ~ 750 nm that was observed in the previous conditioned media/washed AuNP assays (**Figure 108** -Figure **113**) were again present. The same trend of gradual LSPR peak dampening competing with the slight rise in overall attenuance (most notably at wavelengths > 700 nm) arising from the eventual growth of bacteria within the extra heat-killed conditioned media was similarly observed. There was, of course, appreciably less growth compared to what was produced in the live and heat-killed conditioned media assays, likely a consequence of the additional heat treatment prior to conditioning.

In contrast to the heat-killed conditioned media assays with washed AuNPs, however, the extra heat-killed equivalents (in some instances), resulted in complete flocculation of the washed colloids at high concentrations (compare **Figure 116** with **Figure 113** for example).

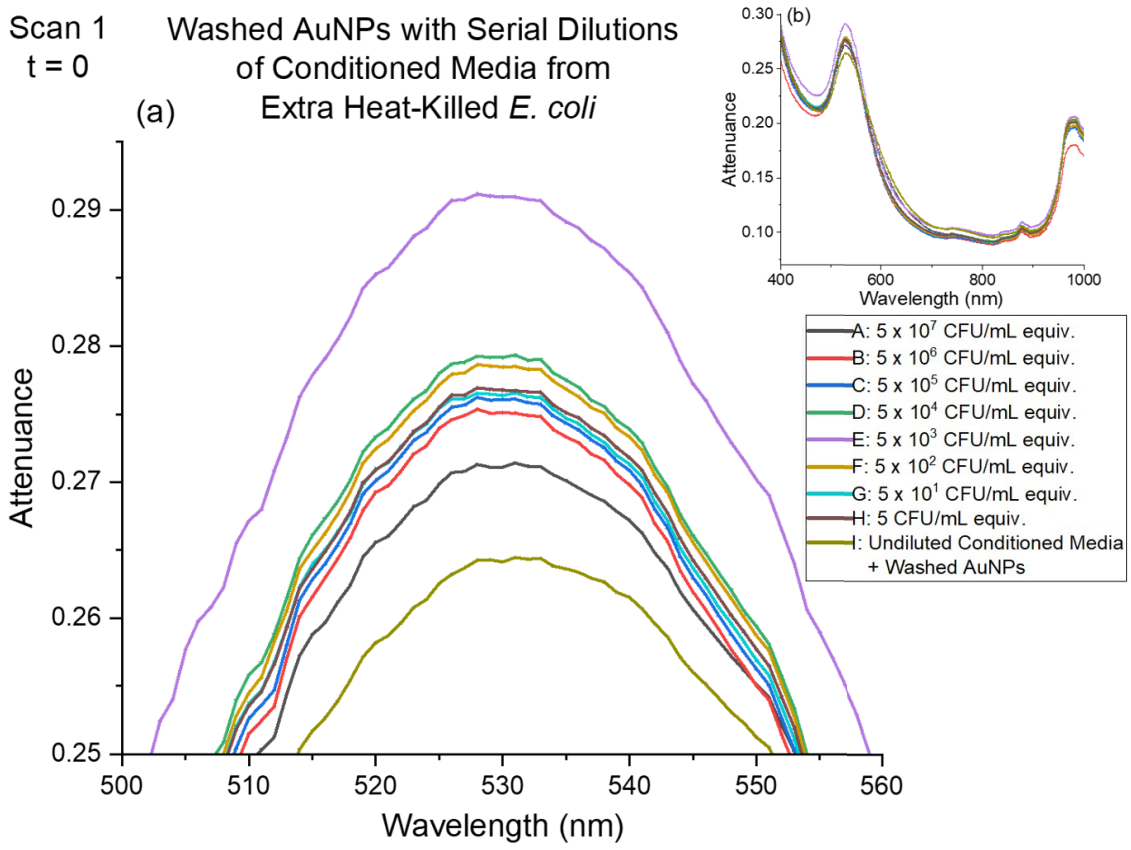

Figure 114: UV-vis spectra of washed AuNPs with 10-fold serial dilutions of conditioned media from extra heat-killed *E. coli* at ambient temperature, t = 0. a) shows a magnified region of the LSPR peaks and inset b) shows all spectra over the entire range of monitored wavelengths (nm).

The resultant spectra from the initial assays between the extra heat-killed conditioned media and washed AuNPs (**Figure 114** above) appeared quite similar to those from the equivalent assay using heat-killed conditioned media (**Figure 111**). The key differences were: the extra heat-killed conditioned media resulted in LSPR peaks of relatively lower attenuance, and the spectra were less tightly clustered, perhaps suggesting greater variability between sample matrices.

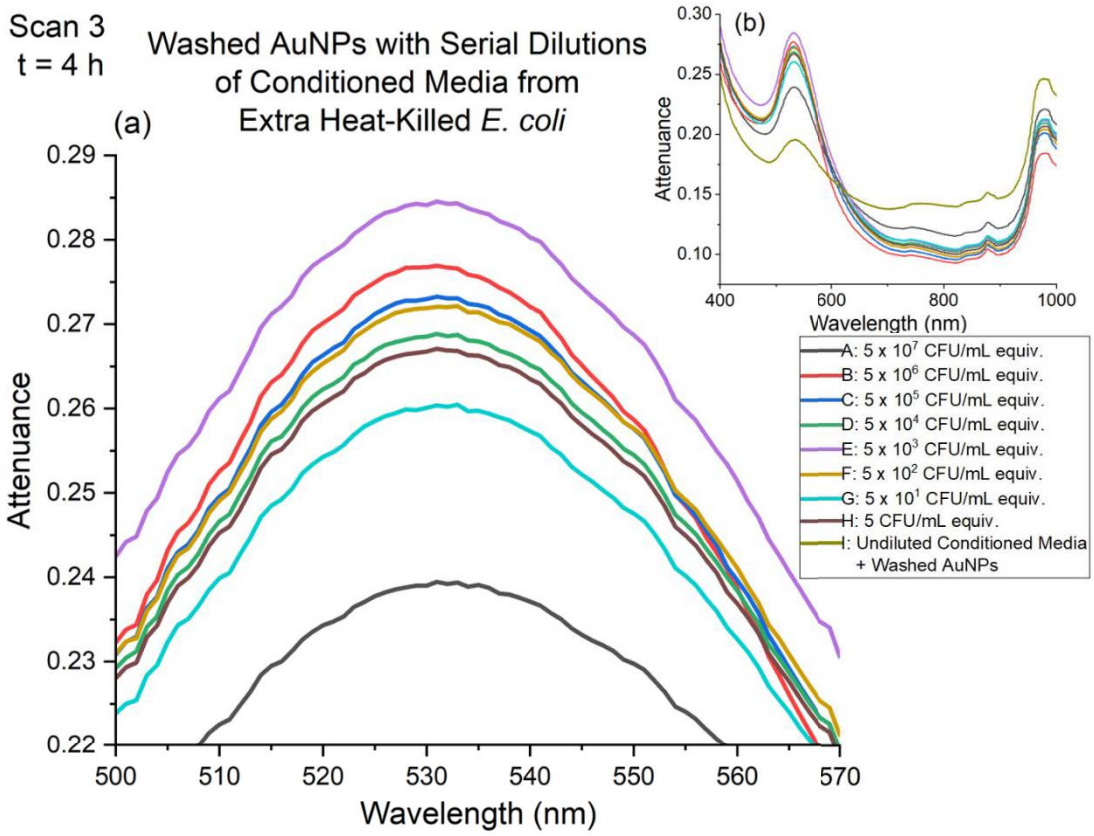

Figure 115: UV-vis spectra of washed AuNPs with 10-fold serial dilutions of conditioned media from extra heat-killed *E. coli* at ambient temperature, t = 4 h. a) shows a magnified region of the LSPR peaks and inset b) shows all spectra over the entire range of monitored wavelengths (nm).

After 4 h of incubation in the presence of washed AuNPs, the resultant effects on the optical spectra appear to have become more concentration-dependent (**Figure 115**). For example, the colloids assayed with higher initial concentrations of the extra heat-killed conditioned media are exhibiting a similar or slightly increased level of LSPR peak dampening compared to the heat-killed conditioned media equivalent (**Figure 112**).

Again, significantly less growth of residual bacteria was apparent within the extra heat-killed conditioned media samples at this time.

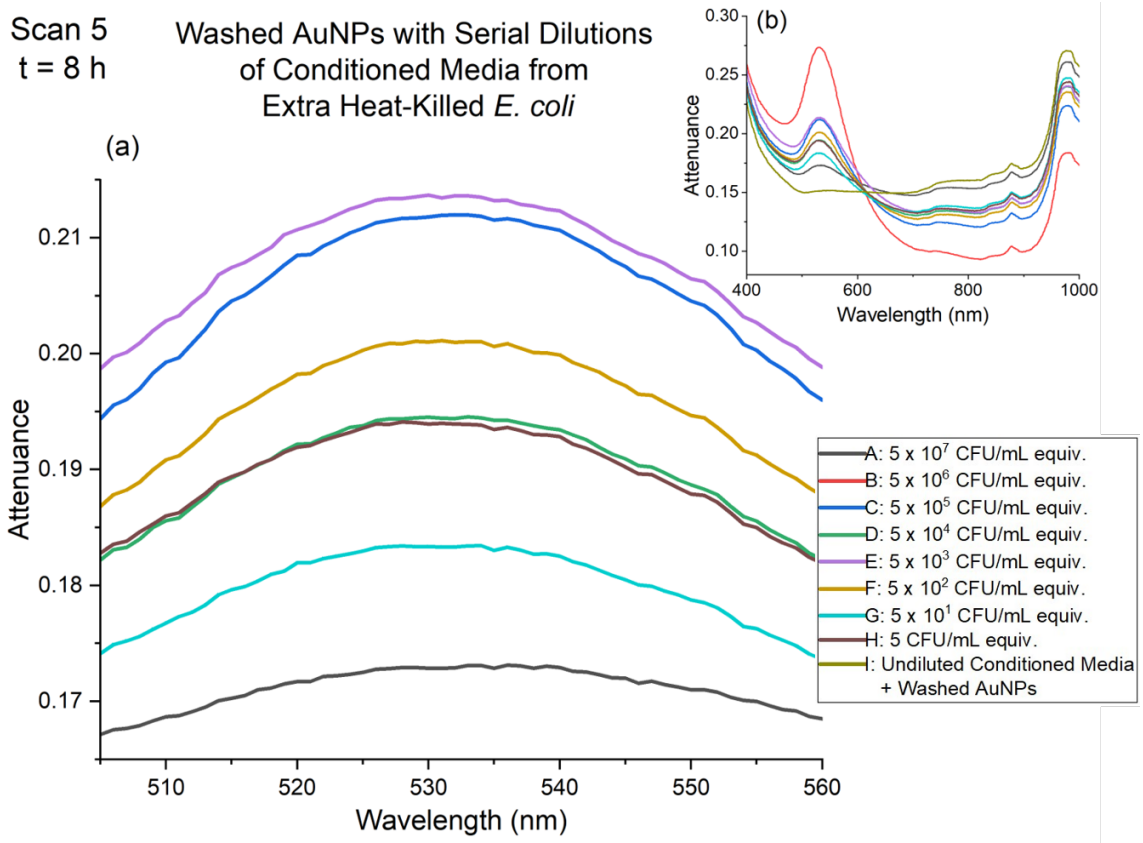

Figure 116: UV-vis spectra of washed AuNPs with 10-fold serial dilutions of conditioned media from extra heat-killed *E. coli* at ambient temperature, t = 8 h. a) shows a magnified region of the LSPR peaks and inset b) shows all spectra over the entire range of monitored wavelengths (nm).

Incubation of extra heat-killed conditioned media in the presence of washed AuNPs for 8 h at ambient temperature produced some interesting and erratic results (**Figure 116**). Initially, it appears as if the attenuance of sample B (red line) has increased dramatically. However, the relative attenuance of all other samples has instead drastically decreased, and the attenuance of B has not changed appreciably since t = 4, **Figure 115**. The most concentrated sample of extra heat-killed conditioned media resulted in flocculation of the colloid. Although this was not yet observed in the heat-killed conditioned media equivalent (**Figure 113**), the equivalent sample was likely on the verge of flocculation, given how slight the residual LSPR peak was observed to be. All other tested concentrations (A, C – H) of extra heat-killed conditioned media displayed relatively less LSPR

peak dampening compared to their heat-killed conditioned media equivalents (compare above **Figure 116**with equivalent concentrations in **Figure 113**).

The notable increase in attenuance for all samples at wavelengths > 700 nm (except B, red line) in the above **Figure 116**indicate the growth of bacteria within the samples. The absence of this increase in B suggests any residual cells present within those specific sample wells were unable to repair, resuscitate and/or resume growth, thus the LSPR peak remained relatively unchanged. This high degree of variability within the bacterial culture had been similarly observed in previous Chapters and has also been documented in literature.[74, 227] It is also worth considering that the additional heat treatment applied to the *E. coli* prior to conditioning the medium is likely to have introduced greater variability into the resulting bacterial culture and thus any residual cells contained within the conditioned media.[227]

From the changes observed in the spectra of washed AuNPs assayed various preparations of conditioned media from *E. coli*, it can be concluded that the washed AuNPs used experimentally are also exhibiting different behaviour to what was observed in previous experiments (see Chapters 3 - 6). Specifically, they did not form the second, red-shifted plasmon peak that was characteristic of aggregation associated with the formation of large AuNP clusters, upon mixing with any preparation of the conditioned medias. These peaks did not form over time, even after the eventual growth of residual bacterial cells within the conditioned media had progressed to a significant degree, resulting in destabilization and gradual flocculation of the colloids. This suggests that the AuNPs themselves had become more stable with age, during storage at ambient conditions. As this increase in stability with time was also observed in the as-synthesized AuNPs, it can be concluded that the cause of this change in AuNP-related stability is unlikely to depend on the relative amount of surface-associated citrate.

7.4.2 Unintuitive Gold Nanoparticle Characteristics in Conditioned Media Assays: The Role of Ageing

The following sections will discuss the significance of the distinct behaviour of the as-synthesized and washed AuNPs observed in the conditioned media assays. These colloids originated from the same batches of AuNPs that were synthesized and characterized in Chapter 3, with the only difference being the age of the colloids. For example, the colloids were relatively "fresh" (i.e. ≤ 1 year since synthesis) for the work in Chapter 3, gradually increasing in age throughout the body of work. The AuNPs had been stored at ambient conditions for ≫ 2 years prior to being used in conditioned media assays.

7.4.2.1 Gold Nanoparticle Stability Increases with Age

The age of AuNPs can play a role in their stability,[52-54] involving processes such as ripening (or coarsening),[55-58] fusion of particles,[53] disruption or degradation of their surface capping moieties,[52, 59] as well as storage conditions (including pH, temperature, additives etc.)[60] contributing to long-term stability, or lack there-of.

In the context of citrate-capped AuNPs, the role of citrate is significant, acting to electrostatically and sterically stabilise the AuNPs via its three carboxylate groups. Citrate has three pK_a values; 3.13, 4.76 and 6.39, corresponding to the central and terminal carboxylates respectively. Therefore, depending on the pH of the colloid, the degree of protonation is affected, ultimately influencing the way in which the citrate moieties are able to coordinate to the Au surfaces. Reflective of the citrate's protonation state, a bidentate mode of coordination is preferred, involving both carboxylate oxygen atoms, as opposed to monodentate binding.[54]

In chloride-rich environments, citrate rearrangement has been observed, shifting from a bidentate to a monodentate coordination. It is speculated that

the presence of chloride ions near the Au surface interferes with the citrate-Au coordination, preventing bidentate coordination and ultimately leading to decreased stability.[54, 61]

7.4.2.2 Ageing of Gold Nanoparticles and its Effect on Sensing

As mentioned in the previous section, the ageing of colloidal AuNPs can affect their stability, involving processes such as Ostwald ripening, gold adatom rearrangement and citrate coordination to the surface of the particles. The AuNPs used over the course of this experimental work were stored at ambient temperature and lighting conditions, and were found to behave differently and have become comparatively more stable over time ($\geq$ 2 years).

This is problematic for the development of unmodified AuNP-based sensors, due to the inability to easily identify or monitor this ageing through standard spectroscopic methods. For example, it is routine to perform UV-vis spectroscopy on AuNPs as part of their characterisation. However, the spectra of fresh and aged AuNPs do not have any distinct differences (see **Figure 117** -Figure **120** for example). Therefore, a more suitable method for assessing the age-related stability of AuNPs is necessary. One such option is to 'challenge' the colloids with a solution of high ionic strength, such as saturated NaCl (or as will be shown in below, LB). Fresh AuNPs produce a characteristic red-shifted LSPR aggregation peak, whereas aged AuNPs do not (under the same experimental conditions).

A study by Grys et al.[54] has reported that aged AuNPs can be refreshed by etching the surfaces to effectively 'refacet' the surfaces of the particles. This can be accomplished by boiling the aged AuNPs in the presence of a strong oxidising agent such as $HAuCl_4$. In contrast, boiling aged AuNPs without an oxidising agent increases the incidence of gold adatoms coordinating to citrate, increasing their stability.[54]

A similar age-related phenomenon was reported by Ding et al.,[161] whereby 13 nm citrate-AuNPs used for label-free DNA sensing were aged for 6 months to assess their relative stability and sensing ability. AuNPs were stored at either room temperature or 4°C, with both conditions resulting in a decrease in colloidal stability, ability to adsorb DNA and therefore decreased sensitivity within the investigated system.[161]

Interestingly, the work by Ding et al. reported a decrease in colloidal stability after 6 months of ageing. This is in disagreement with the results presented within this chapter, as well as those presented by others.[26, 54] Insights provided by the in-depth investigation into the formation and stability of citrate-AuNPs reports that the temperature and duration of the heating used during synthesis of citrate-AuNPs is a crucial factor in the rate of formation, size distribution, and proportion of aggregates with the colloid that contribute to ageing.[26]

By considering the synthetic method employed by Ding et al., it is possible that the relative instability of the colloid arose as a result of the duration and intensity of the heat used in the reduction of $HAuCl_4$. The authors reported refluxing the solution for 20 min, beyond which it was left to cool to room temperature.[161] Although the reduction of Au^{3+} in the presence of sodium citrate is usually conducted in a solution ~ 100°C, it has been demonstrated through dynamic light scattering (DLS) number and volume distributions, that increased heating (i.e. beyond ~ 5 min post formation of the characteristic red colloidal colour) is detrimental to long-term colloidal stability. This was determined to be a result of increased heating durations resulting in an higher probability of AuNPs colliding, forming aggregates and thus contributing to the ageing of the colloid.[26]

In contrast, the AuNPs used herein were synthesized using a lower temperature regime (Chapter 3, Section 3.3) “the solution was held between 90 – 100°C (*without boiling*) for a further 15 min before cooling to ambient temperature.” This is likely to have resulted in comparatively more stable

colloids with fewer aggregates, and could explain the discrepancy in stability of AuNPs over time.

In the context of the proposed sensor, the basis of the optical parameters used rely on the formation of the second (red-shifted) aggregation peak ~ 750 nm that appears as a consequence of adding AuNPs to the bacterial growth medium (**Figure 117** below). This same aggregation was no longer observed (using the same experimental conditions and same batch of AuNPs) after prolonged storage of the AuNPs (**Figure 118**). This same trend was observed for the washed AuNPs (compare **Figure 119** andFigure **120** for example). Therefore, the age of the AuNPs used for the sensor are a limiting factor. It is possible that this may be overcome by refreshing the AuNPs as described above,[54] however this has not yet been confirmed experimentally within the context of the proposed sensing system.

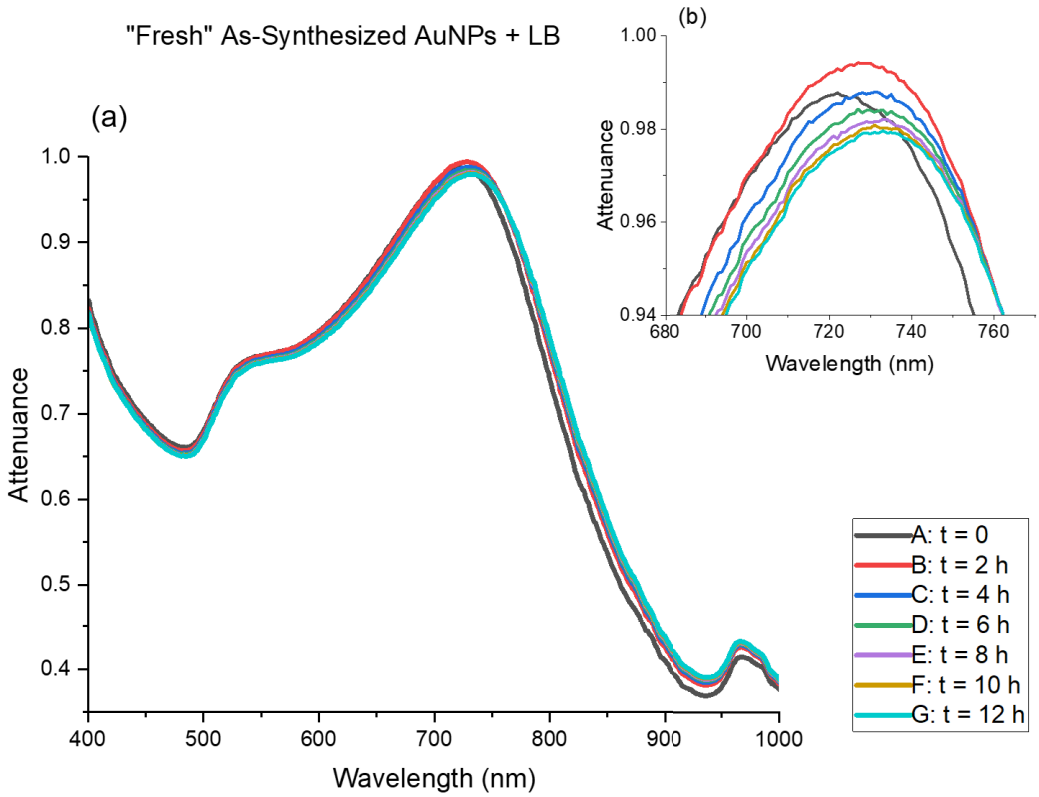

Figure 117: UV-vis spectra of fresh, as-synthesized AuNPs with LB, illustrating the evolution of the spectra over time, measured every 2 h. a)

shows all spectra over the entire range of monitored wavelengths (nm), and inset b) shows a magnified region of the LSPR peaks.

The spectra above indicate the 'freshness' of the AuNPs by their ability to aggregate in a chloride-rich, high ionic-strength environment such as LB. This is evidenced by the appearance of the second, red-shifted aggregation peak that is comparably greater in peak area than the initial LSPR peak. The initial LSPR peak resulting from the colloidal gold has become dampened and shouldered, no longer appearing as a single discreet peak. The relative intensities and proportions of the LSPR peaks suggest that the majority of the fresh as-synthesized AuNPs aggregate into large clusters immediately upon introduction to LB.

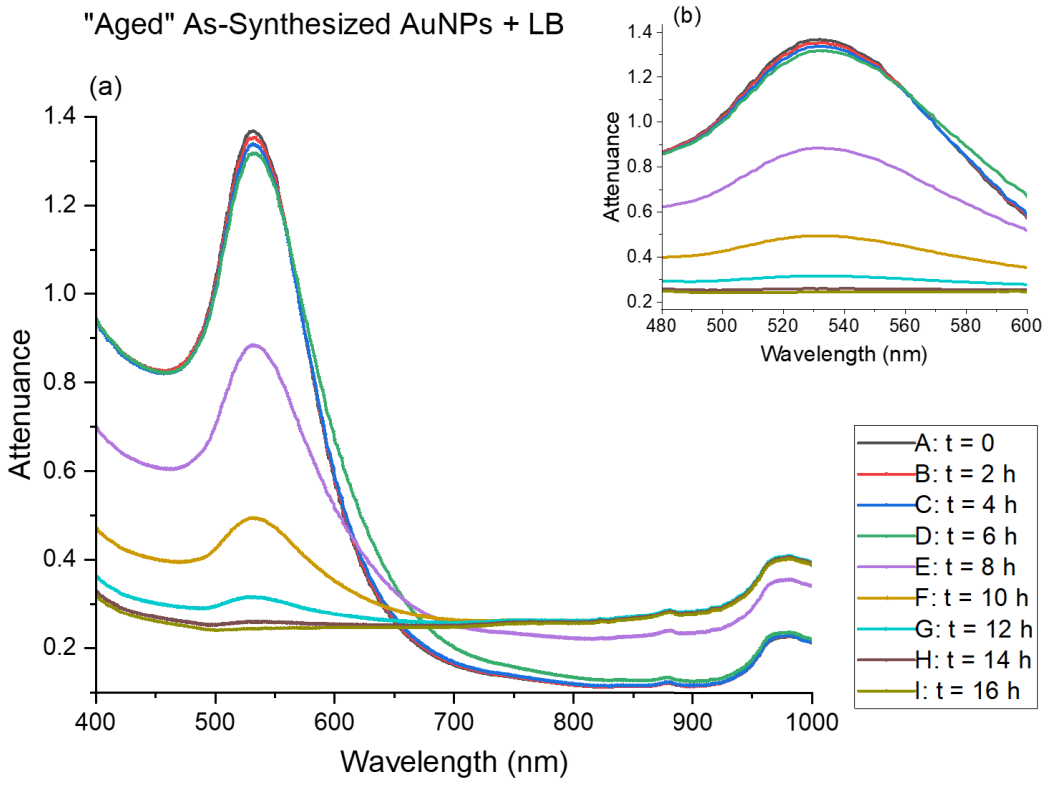

Figure 118: UV-vis spectra of aged, as-synthesized AuNPs with LB, illustrating the evolution of the spectra over time, measured every 2 h. a) shows all spectra over the entire range of monitored wavelengths (nm), and inset b) shows a magnified region of the LSPR peaks.

In contrast to the fresh AuNPs, the aged AuNPs do not exhibit the characteristic red-shifted aggregation peak of the previous set of spectra, obtained from the same batch of AuNPs ≫ 2 years prior (compare **Figure 117** with **Figure 118** above). Although eventual destabilization/aggregation was observed, it did not follow the same mechanism observed with the fresh colloid. Here, instead, > 6 h incubation in LB was necessary to induce a reduction in the optical signal from the colloidal gold (initial LSPR peak), indicating gradual a gradual reduction of the total Au within the detectable range. The absence of the red-shifted second plasmon peak implies that the same, large AuNP clusters that formed in the fresher as-synthesized AuNPs (**Figure 117**) no longer formed in the aged colloid under the same conditions.

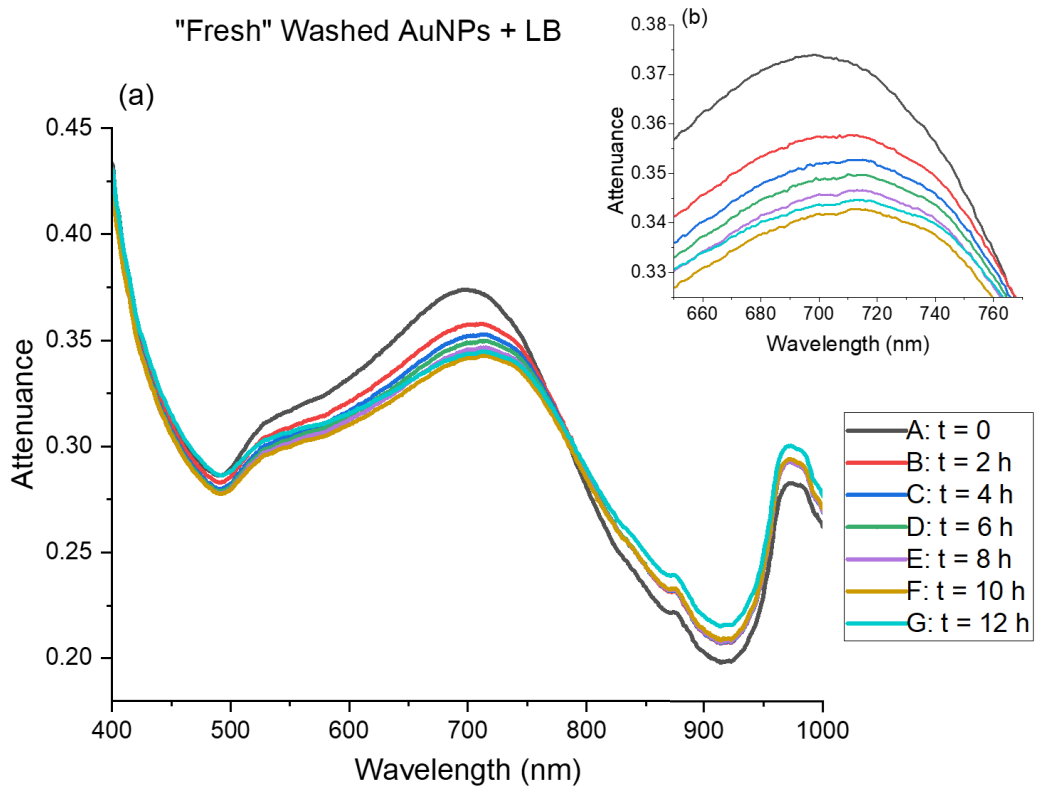

Figure 119: UV-vis spectra of fresh washed AuNPs with LB, illustrating the evolution of the spectra over time, measured every 2 h. a) shows all spectra over the entire range of monitored wavelengths (nm), and inset b) shows a magnified region of the LSPR peaks.

As with the fresh as-synthesized AuNPs seen in **Figure 117**, **Figure 119** above demonstrates that the "fresh" washed AuNPs exhibited the characteristic red-shifted aggregation LSPR peak. Similarly, the relative intensity of this second LSPR peak within the washed AuNP samples in LB indicated a larger proportion of the AuNPs were likely to have aggregated into larger sized clusters, leaving comparatively few in a colloidal or relatively unaggregated state.

The greater difference between the resultant red-shifted LSPR peak can be attributed to the greater sensitivity and reduced colloidal stability of the washed AuNPs when compared to the as-synthesized AuNPs (compare **Figure 119**, inset b) with **Figure 117** inset b)).

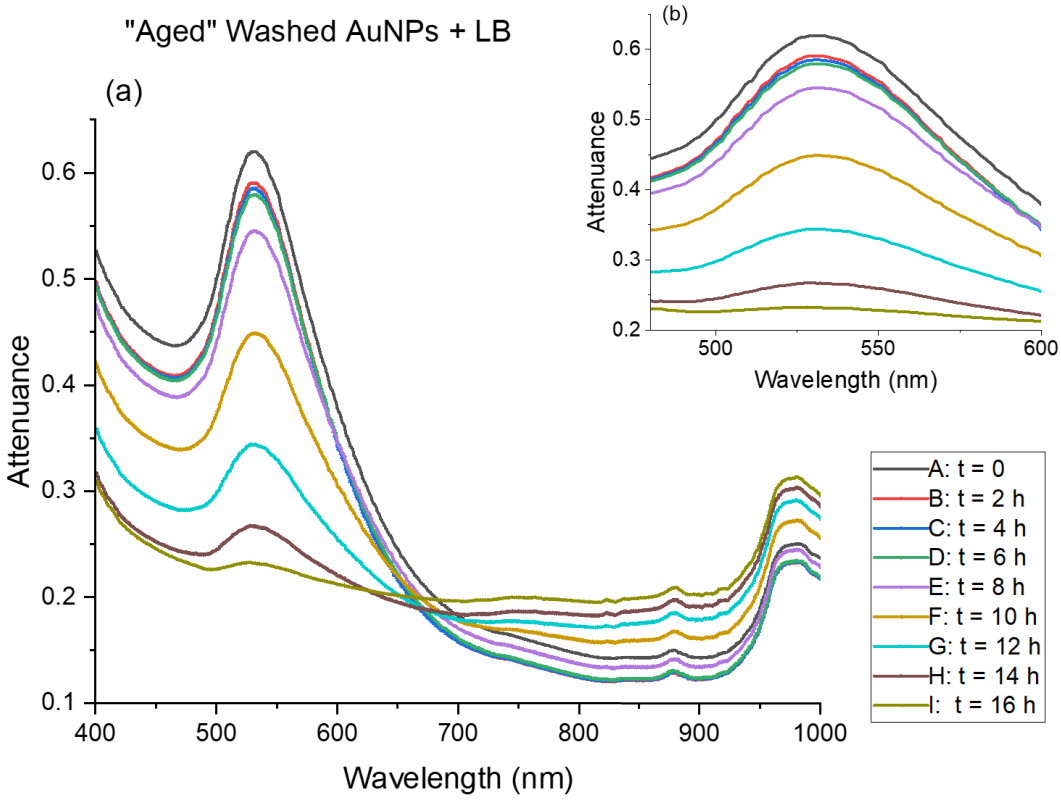

Figure 120: UV-vis spectra of aged washed AuNPs with LB, illustrating the evolution of the spectra over time, measured every 2 h. a) shows all spectra over the entire range of monitored wavelengths (nm), and inset b) shows a magnified region of the LSPR peaks.

The same trend to that observed with the aged as-synthesized AuNPs was seen also in the washed AuNPs that had aged (compare **Figure 118** with **Figure 120** above). These AuNPs similarly lacked the characteristic red-shifted aggregation peak when added with LB, demonstrating the change in behaviour of the washed AuNPs under the same experimental conditions, presumably resulting from their age.

Considering the absence of the characteristic red-shifted, second LSPR peak in both aged colloids (**Figure 118** andFigure **120**), it can be inferred that the increased age-related stability evident in the colloids is not significantly dependent on the amount of surface-associated citrate. However, it does seem to prevent the formation of larger sized AuNP clusters, preferentially resulting in the gradual destabilization of the colloids through sedimentation and/or flocculation.

7.5 Summary, Conclusions and Discussion

Within the present chapter I have investigated the interactions between as-synthesized and washed AuNPs with various preparations of conditioned media from *E. coli* (live, heat-killed and extra heat-killed), to add to the understanding of the contribution of bacterial metabolism and/or metabolites to the proposed sensor. This led to a interesting discovery pertaining to the age-related behaviour of the AuNPs that had been synthesized and characterized as per Chapter 3.

Assays between the various preparations of conditioned media and either as-synthesized or washed AuNPs did not result in the formation of the characteristic, dominant red-shifted LSPR peak ~ 750 nm that was indicative of large AuNP clusters forming and significant aggregation within the colloid. A very slight suggestion of this (mostly absent) peak could be observed in assays between the various conditioned medias and washed AuNPs (**Figure 108** –Figure **116**) but not the as-synthesized AuNPs (**Figure 97** –Figure **107**), suggesting that despite the increased stability of the aged

AuNPs, the relative instability/increased sensitivity afforded by washing remained. This very slight, red-shifted peak (indicated by red arrow in **Figure 108**) could potentially result from a small population of washed AuNPs forming large clusters due to their relatively decreased stability. This hypothesis is supported by the relatively low intensity of this peak, its position (wavelength, nm), and the absence of this same peak in the as-synthesized AuNPs. However, confirmation of this would require further investigation through methods such as comprehensive *in situ* UV-vis spectroscopy in combination with DLS measurements of number, volume and intensity.

With reference to both the as-synthesized and washed AuNPs assayed with all preparations of the conditioned media, it can be said that in general, over time, the initial LSPR peaks associated with the colloidal Au dampened significantly and broadened slightly. This indicates that all preparations of the conditioned media resulted in the gradual destabilization of both as-synthesized and washed colloids, although only very slight size-broadening effects were observed. Herein, it was determined that the relative increased age of the AuNPs had resulted in a marked increase in colloidal stability (given that all other experimental conditions had remained unchanged), thus altering the interactions between the tested particles and the conditioned media.

Aggregation of the aged colloids was still evident and was readily observed by the naked eye (i.e. the characteristic change in colour from red/pink to grey/blue and finally to colourless), indicating the aggregation of the colloids. However, spectroscopically, the mechanism by which the aggregation occurred was noticeably affected by the increased age of the colloids, implying a fundamental change to their colloidal behaviour.

Consequently, the results and conclusions inferred from the assays involving conditioned media are not directly comparable to those resulting from prior experiments containing bacterial cells and “fresh” AuNPs, as was initially intended. Despite this, there were some observable differences

between the optical spectra resulting from assays between the various preparations of conditioned media and both as-synthesized and washed AuNPs. Accordingly, it can be said that the metabolism, metabolites and/or cellular by-products of *E. coli* vary according to their treatment (i.e. live, heat-killed or extra heat-killed) and these contribute to the aggregation and optical properties of citrate AuNPs when combined.

Chapter 8:

Development of a Sensing Platform for *Escherichia coli*

8.1 Introduction

Traditional methods of detection and quantification of bacterial contamination involve methods such as plate counting, polymerase chain reaction (PCR), lateral flow immunochromatography or voltammetry; methods may also be molecular or immunological-based.[237, 238] In general, however, techniques developed for detection of bacteria in health care settings may not be ideal for the food industry (see Gill).[239] The disadvantages of the techniques listed above may include inaccuracies in colony counting, the high cost of materials, the need for specialist equipment and personnel, and the generally more diverse microbiota and complicated matrix interference of food samples.[239, 240] Another potential downfall of standard detection methods is their possible failure to reliably detect injured, sub-lethally injured, or viable but non-culturable (VBNC) cells.[239] These cells may regain their ability to resume growth when supplemented with sufficient nutrients, but may not be detected when cultured on selective media. The detection limits reported in the literature range upwards from about 10 CFU/mL[238] to as high as 10^5 CFU/mL, with traditional bacterial culturing providing a detection limit of the order of 2500 CFU/mL in food samples.[241]

In this chapter, I describe a simple method for the label-free detection of live bacteria, using the optical properties of citrate AuNPs to amplify the optical signal. Whereas most – if not all – previous proposals for nanoparticle-enhanced detection techniques require that the bacteria are first concentrated and/or multiplied following which the Au colloid is added to produce a colorimetric signal, in the present concept the innovative step is that the bacteria are allowed to grow exponentially within a medium that already contains the AuNPs, using typical culture parameters. My hypothesis was that *in situ* proliferation of the *E. coli* in the presence of AuNPs would result in a convenient and sensitive assay. The proposed method simplifies sample preparation and simultaneously allows for the amplification of the signal from low numbers of bacteria. This method also

allows for the simultaneous recovery and detection of sub-lethally injured or VBNC bacteria.[242, 243] In this thesis *E. coli* has been used as model for Gram-negative bacteria in general. The results of the present work will, however, apply to other species of Gram negative bacteria to a large extent due to the highly conserved nature of the processes underlying the sensing mechanism.

The processes occurring between AuNPs and various preparations of *E. coli* are explored with the objective of developing a quantitative platform for the determination of *E. coli*, and, by extension, Gram-negative bacteria in general. Herein, the UV-visible spectra of AuNP/*E. coli* mixtures are analysed in detail and the spectral changes due to aggregating AuNPs identified as a promising parameter for a sensing platform.

Such a sensor utilises the aggregation phenomena described in previous chapters, whereby the colloid aggregates with the surfaces of *E. coli*, in the growth medium, and also as a result of surface-active metabolites or other bacterially-generated proteinaceous materials within the bacterial growth medium itself. A methodology is described herein to fit quantitative models to the various attenuance spectra observed, describing the relationship between the starting concentration of *E. coli* in CFU/mL and the measured optical parameters. It will be shown that it is possible to achieve a limit of detection of 15 CFU/mL for live *E. coli* in LB, at the 95% confidence level, using washed AuNPs in a 6 h assay.

8.2 Experimental Design and Methods

8.2.1 Materials and Methods

Details pertaining to the materials used have been described in detail in previous Chapters. I guide the readers to Sections 3.1 of Chapters 3 – 5 in reference. For brevity, these details will be excluded from the current

Chapter, and only the methods relating to the numerical modelling of the proposed sensor will be detailed herein.

8.2.2 Numerical Methods

Numerical modelling, peak fitting and spectral analysis were performed using a Metropolis Monte Carlo code (PLASMOFIT) that fitted a model to the experimental spectra. The code had been written by a colleague (M.B. Cortie). CURVEEXPERT PROFESSIONAL was used for plotting (www.curveexpert.net).

8.2.3 Optical Parameters

To a first approximation the Beer-Lambert Law is assumed to apply and the UV-vis spectra are therefore the sum of the individual contributions from the AuNP colloid, the LB medium, and the bacteria. To extract and make use of the optical parameters, a model was made whereby the attenuance, A, was constructed from an exponentially decaying background, B_k, two Gaussian plasmon resonance peaks, G_1 and G_2, and a small Gaussian, I_B. The two Gaussians G_1 and G_2 were of variable position, width and amplitude, while I_B was of constant proportions and centered on 463 nm to account for the interband transitions in the Au:

$$A = B_k + G_1 + G_2 + I_B \tag{4}$$

where:

$$B_k = E_{820\,nm} + (E_{400\,nm} - E_{820\,nm}) \cdot e^{-E_d(\lambda - 400)} \tag{5}$$

$E_{400\ nm}$ and $E_{820\ nm}$ are the height of the background at 400 and 820 nm, respectively, and E_d is the decay rate of the exponential background. Using a simple subtraction of the LB background would give an underestimate as the Beer-Lambert Law is not strictly obeyed at higher bacterial concentrations due to increased turbidity. Therefore, to ameliorate this

factor, the background contribution from the LB medium was included within the fitting of the spectra.

The Gaussians are given by:

$$G_n = H_n \cdot e^{-\frac{(eV-P_n)^2}{2W_n^2}} \quad (6)$$

where H_n, P_n, and W_n are the peak height, position, and RMS width of the nth Gaussian, respectively. Note that the values for P_n and W_n are on the electron volt (eV) – not nanometer – scale, as this is more appropriate for electronic resonances.

To produce a fitted model, a Metropolis Monte Carlo code (PLASMOFIT) was used. Within this, there are twelve potentially variable parameters (see **Figure 121** and **Table 8**); these consist of values associated with the exponential background from LB, the interband contribution from Au and two Gaussians.

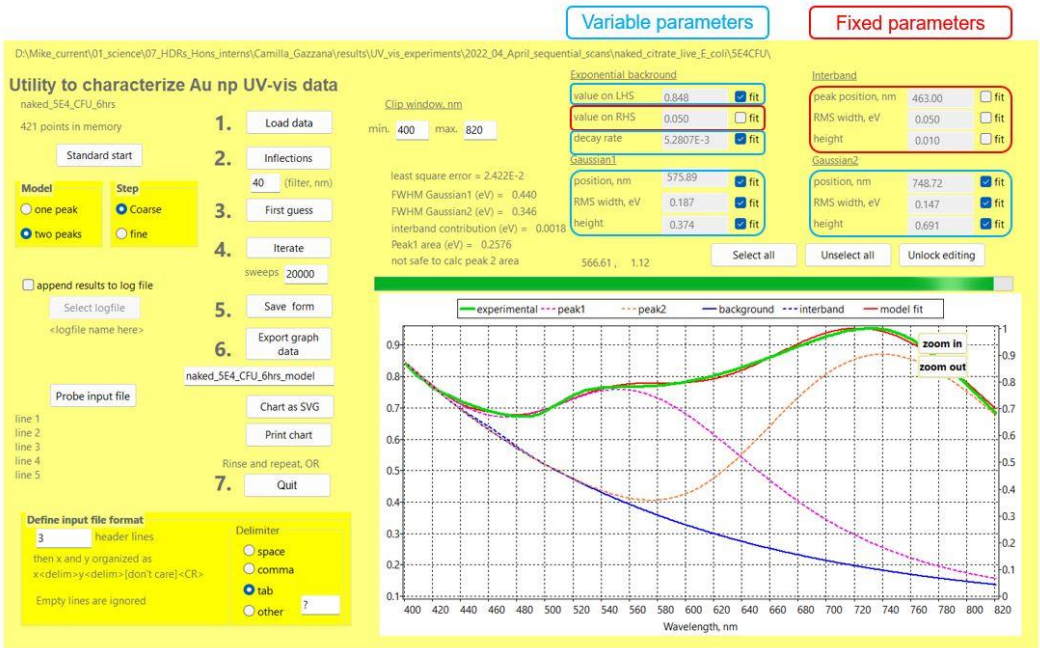

Figure 121: Screen-shot from the program PLASMOFIT, showing how a measured spectrum (green) can be decomposed into an exponentially

decaying background (blue), two LSPR peaks ('peak 1' and 'peak 2') and a small contribution from interband transitions. The model has twelve variable parameters but in practice only eight of them are used, with the other four being held constant at values dependent on the system investigated.

Table 8: Table of optical parameters that contribute to the UV-vis spectra of AuNP and *E. coli* assays, showing their potentially variable parameters. The cells highlighted in green are those that were fixed at a value taken from an average of all scans.

Optical Parameters

Potentially variable parameters	Exponential background	Interband	Gaussian 1	Gaussian 2
	Value on left-hand side	Peak position (nm)	Peak position (nm)	Peak position (nm)
	Value on right-hand side	RMS width (eV)	RMS width (eV)	RMS width (eV)
	Decay rate	Height	Height	Height

It is important to note that a non-linear optimization of this type may produce slightly different results each time it is run. In order to mitigate this, every optimization sequence was started from the same seed values, running off a script with parameters optimized to run in a standard sequence.

Inflection points within the spectra were also calculated using PLASMOFIT, as these have been reported as being useful in the development of bio-sensors, particularly in improving their sensitivity. [244] The first derivative was calculated by linear regression along an overlapping sequence of short linear segments across the data set, and the second derivative was calculated by repeating that process a second time. Non-linear regressions were performed using CURVEEXPERT PROFESSIONAL software.

8.3 Results and Discussion

8.3.1 Regression of Optical Variables

The optical parameters of attenuance at 400 nm, position of the second red-shifted aggregation peak (nm), and the 3rd inflection point (nm) were chosen for regression analysis against the starting bacterial CFU/mL, using the standard input script (i.e. a standard sequence of operations on the data).

The evolution of the optical parameters resulting from the assays of washed AuNPs incubated at ambient temperature with 10-fold serial dilutions of live *E. coli* are illustrated below in **Figure 122** (a – d), representing the system at incubation times of 0, 4, 8 and 12 h.

Over time, the attenuance in each sample increased. This can be attributed to turbidity caused by the proliferation of the *E. coli*. Note that the attenuance of the sterile control sample (LB only) is virtually unchanged in contrast. Plotting the fitted attenuance at 400 nm as a function of time allowed for an estimate of the starting CFU/mL of the sample; the relationship between these two variables, in the instance of the washed AuNPs, was most pronounced $\geq$ 5 h (**Figure 122**). However, the relationship between the positions of the second, red-shifted LSPR peak (nm) and the starting CFU/mL of the sample were found to be a more sensitive metric overall.

As the aggregation within the system increased with time, the second plasmon peak became increasingly red-shifted (**Figure 122**). The sensitivity of this parameter was poor for incubation times < 4 h, was optimal between 6 – 8 h, and declined for times greater than that. The use of the 3rd inflection point has been demonstrated to improve the sensitivity of bio- and chemical sensing between 18 – 55% in a variety of different AuNP shapes and sizes (including spherical AuNPs).[244] However, when the 3rd inflection points were used here as the optical parameter to determine the starting CFU/mL of the bacterial culture, the relationship was found to be less consistent (compare

Table 9 and**Table 10** for example) than the attenuance at 400 nm or the position of the second plasmon peak (**Figure 122**).

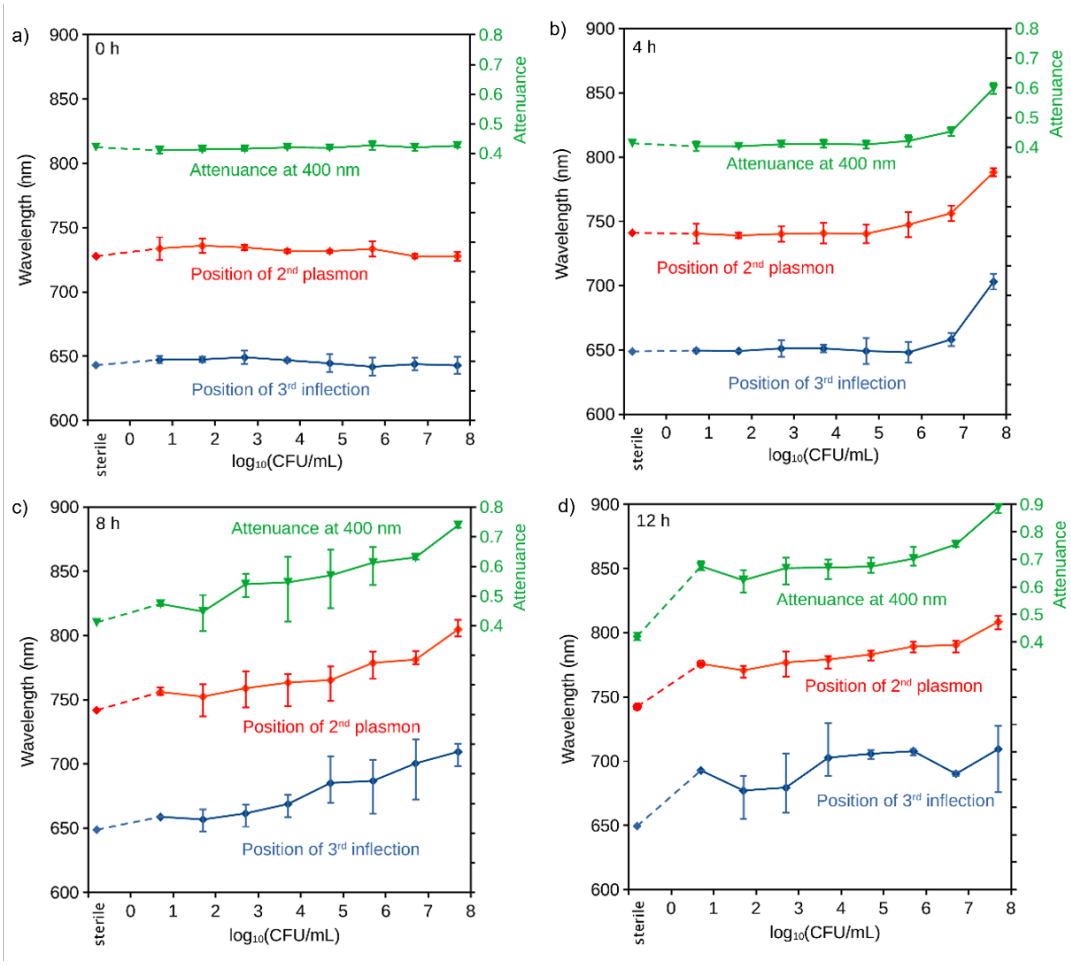

Figure 122: Evolution of the optical parameters of the washed AuNPs incubated at ambient temperature with 10-fold serial dilutions of live *E. coli* at different times. a) 0 h, b) 4 h, c) 8 h and d) 12 h incubation times. The error bars were obtained for each bacterial concentration using the minimum and maximum limits of the triplicate scans.

Table 9: Comparison of r^2 values for as-synthesized AuNPs assayed with live *E. coli* at ambient temperature

Time (h)	Attenuance @400nm	Position 2nd Peak (nm)	3rd Inflection (nm)
0	none	none	none
2	0.829	none	none
4	0.974	0.952	0.964
6	0.923	0.982	0.991
8	0.765	0.920	0.981
10	<0.7	0.887	0.958
12	none	0.818	0.849

Table 10: Comparison of r^2 values for washed AuNPs assayed with live *E. coli* at ambient temperature

Time (h)	Attenuance @400nm	Position 2nd Peak (nm)	3rd Inflection (nm)
0	<0.7	none	none
2	0.951	0.885	0.921
4	0.997	0.985	0.995
6	0.990	0.965	0.880
8	0.945	0.953	0.916
10	0.840	0.870	0.907
12	0.700	<0.7	none

Key:	r^2	>0.98	0.95 – 0.98	0.92 – 0.95

Statistical analysis of other fitted parameters, such as peak width or other points of inflection, did not produce useful correlations. Overall, the washed AuNPs were determined to have a superior sensing capability (in a shorter timeframe) than the as-synthesized AuNPs. Use of the position of the second red-shifted plasmon peak provided the most reliable result. A purely empirical equation, the Gompertz model,

$$y = ae^{(-e^{b-cx})} \tag{7}$$

where x is the position of the second plasmon peak and y the $\log_{10}$ of the starting CFU/mL of the bacterial culture, was found to be the best fit to the data. The resulting empirical models for the 6- and 8- h incubations are shown below in **Figure 123** a) and b) respectively. The 8 h assay using washed AuNPs is capable of detecting levels above approximately 15 CFU/mL in individual assays at the 95% level (outer light pink zone in **Figure 123**). If several measurements are taken and averaged, the limit of detection can be improved to about 2 or 3 CFU/mL (inner pink zone).

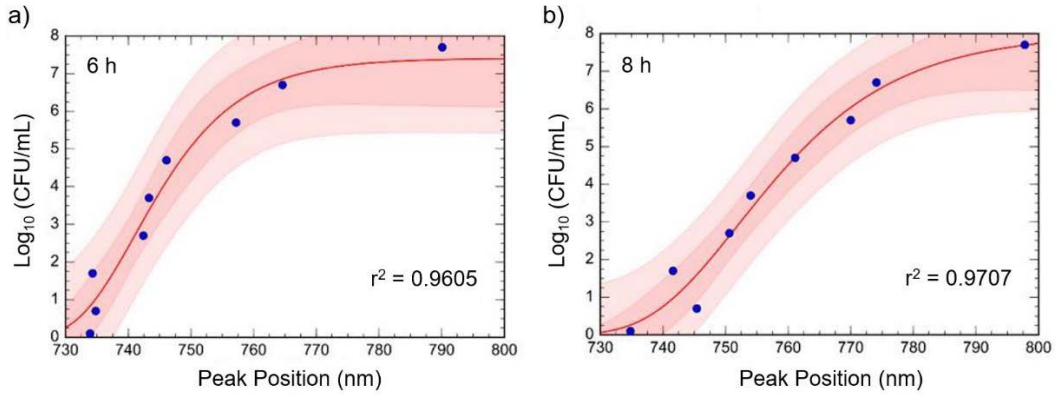

Figure 123: Graphs showing the position of the second plasmon peak (nm) resulting from the incubation of live *E. coli* with washed AuNPs at ambient temperature, allowing the inference of the starting concentration of *E. coli* in CFU/mL. a) after 6 h incubation, and b) after 8 h incubation. Inner pink zones denote the 95% confidence interval for the mean of several measurements. Light pink zones denote the 95% confidence interval for an individual measurement.

8.4 Summary, Conclusions and Discussion

Within the present chapter I have investigated the numerical modelling of various optical parameters that can be used to form the basis for a label-free, AuNP-based optical sensor for the detection of live *E. coli* in a bacterial growth medium. The optical parameters used within the proposed sensor are derived from the UV-vis spectra; that is, the sum of the contributions from the AuNPs, the LB, the *E. coli* and their interactions.

A model was used whereby the attenuance was extracted from a background while simultaneously accounting for the effect of the colloid's two Gaussian plasmon resonance peaks, and a small Gaussian of constant proportions to account for interband transitions in Au. Excellent correlations between the selected optical parameters (attenuance at 400 nm, position of the second plasmon peak (nm), and 3rd inflection point) and the starting concentration of *E. coli* in the sample were found. Consequently, the limit of detection for live *E. coli* in LB was determined to approximately 15 CFU/mL, with a 95% confidence, using washed AuNPs in an 8 h assay at ambient temperature. This could be further enhanced to 2 to 3 CFU/mL by taking the average of several measurements.

The results presented within this chapter suggest that citrate AuNPs present a cost-effective, scalable nanomaterial that could be used as a biological recognition element for the aggregation-based label-free detection of *E. coli*, and, by extension, other Gram-negative bacteria. The exclusion of labels (e.g. antibodies, aptamers, proteins etc.) from the proposed sensor adds to the ease of synthesis, production and design. However, this comes at the (potential) cost of decreased sensitivity and selectivity. It is therefore imperative to perform further testing of the sensor system with different species and strains of bacteria, both Gram-positive and other Gram-negative bacteria to confirm the hypothesis that the mechanism of sensing relies upon a highly conserved process amongst bacteria and should therefore be applicable to other bacterial species.

Key benefits of this type of sensor lie in its simplicity and ease of use; for example, it can readily be used by a layperson, requiring only a relatively inexpensive UV-visible spectrometer and a standard computer to run PLASMOFIT, with the latter providing an intuitive interface to interpret the measured data. Further development could see this process further simplified and/or integration of sample handling with signal processing and display.

Chapter 9:

Conclusions, Discussion & Future Directions

9.1 Conclusions

The primary objective of this thesis was to develop a sensor platform for Gram-negative bacteria through exploitation of the optical properties of unmodified gold nanoparticles (AuNPs). *Escherichia coli* (*E. coli*) was used as a model bacterium considering the plethora of information readily available regarding its characteristics, growth and behaviour under a multitude of different conditions. Further to this, and of great importance, are the highly conserved (among bacteria in general, and Gram-negative bacteria in particular) characteristics that *E. coli* display, truly making it a suitable model micro-organism within this context.

Luria-Bertani (LB) broth was employed as a non-selective growth medium, chosen to facilitate the growth of low levels of bacteria in the presence of the AuNPs. As seen in Chapter 3, a range of different AuNPs were initially synthesized, characterized, and some were further functionalized with moieties such as bovine serum albumin (BSA) or poly(ethylene glycol) (PEG). A portion of the citrate AuNPs were used unmodified ("as-synthesized"), while another portion of these AuNPs were modified to remove the excess surface-associated citrate, becoming "washed" AuNPs. Initial tests between the different types of AuNPs and bacterial preparations revealed that the relatively lower colloidal stability of the citrate AuNPs (compared to the CTAB and functionalized AuNPs), was beneficial with respect to the tested system. This could be attributed to the reduced 'competition' for the active surface area of the AuNPs, resulting in comparatively stronger and increased interactions between citrate AuNPs and *E. coli*. This effect was amplified by washing the citrate AuNPs, thereby further reducing the amount of surface-citrate. In contrast, the BSA- and PEG-functionalized AuNPs were found to be too colloidally stable (even when incubated with bacteria) to produce useful results within the context of the currently investigated aggregation-based sensor. Thus, the citrate AuNPs were pursued further in the design of the sensor with the added benefits of: ease and reproducibility of synthesis, lower cost and longer

shelf-life when compared to both the CTAB AuNPs and further functionalized AuNPs.

With reference to the citrate AuNPs (as-synthesized and washed), their aggregation occurred in a reproducible, time-dependent manner. Assays between various preparations of *E. coli* (live, heat-killed and extra heat-killed) with these same AuNPs showed this relationship to also be concentration-dependent. The resulting UV-vis spectra from these assays yielded useful optical information pertaining to the interactions between the bacteria and the colloids, enabling the extraction of key contributions from the colloids, LB, and the bacteria. It was concluded that use of washed AuNPs was associated with lower limits of detection than the as-synthesized AuNPs. While this has been, for now, attributed to the lower level of surface-citrate and decreased colloidal stability of the washed AuNPs, it would be interesting and potentially very useful to explore this effect further in the future. For example, a series of colloids could be prepared with carefully graduated amounts of surface-associated citrate (post-synthesis so as not to modify the base AuNPs) to determine *if* and where the optimal concentration of surface-associated citrate lies with respect to the interactions of the AuNPs with the bacteria for detection purposes.

An important innovation introduced in this project was the incubation of the bacterial samples in a growth medium that simultaneously contained AuNPs. The synchronicity of the bacteria and AuNPs was expected to amplify the resultant optical signals from their interactions. Extensive analysis of UV-vis spectra in combination with TEM showed that while the AuNPs did induce varying degrees of morphological defects within the bacterial populations observed, these were not deleterious enough to the culture to significantly slow the bacterial growth. *E. coli* that had been heat treated prior to assaying with AuNPs were also able to recover from thermal damage and resume growth, both in LB only and in the presence of AuNPs. Ultimately, it was found that the incubation of the bacteria in the presence of the AuNPs was an essential component to the sensing mechanism,

greatly enhancing the optical signal. It was concluded that an incubation time of the order of 6 – 8 h was optimum for the given system.

A surprising finding was the (unintentional) ageing of the AuNPs for two or three years led to a dramatic increase in colloidal stability, as was shown in Chapter 7. Perusal of the literature suggests that this marked increased in stability was the result of fundamental changes to the surface of the Au, whereby as the colloid ages, there is an increased degree of surface 'roughening' (formation and migration of gold adatoms). These are able to more strongly coordinate with the carboxylate groups of the stabilizing moieties, imparting significantly greater stability to the colloid. Although colloidal stability is often highly desirable, this unfortunately made the colloids significantly less useful for their intended purpose – an aggregation-based sensor. From this, it can be concluded that careful control of not only the imparted properties (design, synthesis etc.), but the *age* of the AuNPs must be taken into consideration. Changes to the AuNPs during storage under various conditions is most definitely an important future direction for further work.

With regard to the mechanism of the sensor (i.e. the interactions between the AuNPs and the bacteria) it was initially hypothesized that aggregation of the colloids would be almost exclusively on the surfaces of the bacteria, resulting in a relatively reliable, concentration-dependent optical signal. However, comprehensive analysis of samples via TEM showed that the AuNP aggregation occurred to a significant degree within the sample matrix, and was often associated with proteinaceous material that was likely to have originated from the cells. This effect became amplified by increased incubation times of the bacteria/AuNP mixtures; the presence of the AuNPs resulted in increased leakiness of the cells. Simultaneously, the AuNPs were found to aggregate in and around these leaked materials and on the bacterial cells (in particular) where they had become leaky. Thus, the growth of the bacteria in the presence of the AuNPs significantly amplified the aggregation-based effect that formed the basis of the proposed sensor.

Finally, it was shown how the optical spectra could be accurately decomposed into its individual components, namely: the growth medium (LB), the bacteria, and the AuNPs. A custom-written program (by my primary supervisor) allowed for the efficient numerical analysis and extraction of quantitative parameters from the spectra. Some of these parameters proved to be good proxies for the starting bacterial concentration (CFU/mL) of the measured samples. There is currently (at the time of thesis submission) a journal paper describing the application of such a system, capable of achieving a detection limit of ~ 15 CFU/mL of *E. coli* at the 95% confidence level using a 9 h incubation at ambient temperature. The current status of the paper is “some revisions requested”.

9.2 Future Directions

In an effort to increase the sensitivity/decrease the required assay time, I believe it to be worthwhile to further test assay conditions at elevated temperatures. Although the experiments at 37°C did not seem to appreciably improve the results within the tested sensor system, the reasons why are still not clear. Understanding the underlying reasons are likely to yield results that would either improve the overall sensitivity of the given system, reduce the time needed to achieve a similar limit of detection, or could be used in further (improved) sensor design.

As mentioned earlier, exploration of the aging of AuNPs is a pertinent topic of further research, having important implications for both commercial production of colloids and researchers alike. As suggested in the literature, it is possible to ‘refresh’ aged AuNPs; consequently, characterization of AuNPs with over time should also include analysis of refreshed AuNPs in an attempt to better understand the chemistry and kinetics behind this ageing.

The proposed sensor platform was tested only with *Escherichia coli* BL21 (DE3) competent cells, chosen as a model Gram-negative bacterium and

as a proof-of-concept. Thus, it is imperative that further testing is completed on additional strains of *E. coli*, particularly those that are clinically relevant. This should then be further expanded to Gram-positive bacteria and/or mixed bacterial samples.

Finally, optimization of the concentration of the colloid should be pursued. It was shown that the concentration of the AuNPs (relative to the analyte/mixture) play a role in their stability and thus sensitivity. Hence, optimizing the concentration of the AuNPs within the system could further improve the sensitivity and is worth exploring further.

References

(1) Bai, Z.; Xu, X.; Wang, C.; Wang, T.; Sun, C.; Liu, S.; Li, D. A comprehensive review of detection methods for Escherichia coli O157: H7. *TrAC Trends in Analytical Chemistry* **2022**, *152*, 116646.

(2) Saxena, T.; Kaushik, P.; Mohan, M. K. Prevalence of E. coli O157: H7 in water sources: an overview on associated diseases, outbreaks and detection methods. *Diagnostic microbiology and infectious disease* **2015**, *82* (3), 249-264.

(3) Amin, N.; Torralba, A. S.; Álvarez-Diduk, R.; Afkhami, A.; Merkoçi, A. Lab in a tube: point-of-care detection of Escherichia coli. *Analytical chemistry* **2020**, *92* (6), 4209-4216.

(4) Lee, J.; Kaletunç, G. Evaluation of the heat inactivation of Escherichia coli and Lactobacillus plantarum by differential scanning calorimetry. *Applied and Environmental Microbiology* **2002**, *68* (11), 5379-5386.

(5) El-Moghazy, A. Y.; Wisuthiphaet, N.; Yang, X.; Sun, G.; Nitin, N. Electrochemical biosensor based on genetically engineered bacteriophage T7 for rapid detection of Escherichia coli on fresh produce. *Food Control* **2022**, *135*, 108811.

(6) Torpdahl, M.; White, E. D.; Schjørring, S.; Søby, M.; Engberg, J.; Engsbro, A. L.; Holt, H. M.; Lemming, L.; Lützen, L.; Olesen, B. Imported spring onions related to the first recorded outbreak of enteroinvasive Escherichia coli in Denmark, November to December 2021. *Eurosurveillance* **2023**, *28* (15), 2200572.

(7) Bojesen, A. M.; Ahmed, U.; Skaarup, H.; Espinosa-Gongora, C. Recurring outbreaks by the same Escherichia coli ST10 clone in a broiler unit during 18 months. *Veterinary Research* **2022**, *53*, 1-7.

(8) Waltenburg, M. A.; Schwensohn, C.; Madad, A.; Seelman, S. L.; Peralta, V.; Koske, S. E.; Boyle, M. M.; Arends, K.; Patel, K.; Mattioli, M. Two multistate outbreaks of a reoccurring Shiga toxin-producing Escherichia coli strain associated with romaine lettuce: USA, 2018–2019. *Epidemiology & Infection* **2022**, *150*, e16.

(9) NHMRC, N. Australian drinking water guidelines paper 6 national water quality management strategy. *National Health and Medical Research Council, National Resource Management Ministerial Council, Commonwealth of Australia, Canberra* **2011**, 5-7.

(10) Hammami, I.; Alabdallah, N. M. Gold nanoparticles: Synthesis properties and applications. *Journal of King Saud University-Science* **2021**, *33* (7), 101560.

(11) Eustis, S.; El-Sayed, M. A. Why gold nanoparticles are more precious than pretty gold: noble metal surface plasmon resonance and its enhancement of the radiative and nonradiative properties of nanocrystals of different shapes. *Chemical society reviews* **2006**, *35* (3), 209-217.

(12) Sardar, R.; Funston, A. M.; Mulvaney, P.; Murray, R. W. Gold nanoparticles: past, present, and future. *Langmuir* **2009**, *25* (24), 13840-13851.

(13) Liu, X.-Y.; Wang, J.-Q.; Ashby Jr, C. R.; Zeng, L.; Fan, Y.-F.; Chen, Z.-S. Gold nanoparticles: Synthesis, physiochemical properties and therapeutic applications in cancer. *Drug discovery today* **2021**, *26* (5), 1284-1292.

(14) Nejati, K.; Dadashpour, M.; Gharibi, T.; Mellatyar, H.; Akbarzadeh, A. Biomedical applications of functionalized gold nanoparticles: a review. *Journal of Cluster Science* **2021**, 1-16.

(15) Daniel, M.-C.; Astruc, D. Gold nanoparticles: assembly, supramolecular chemistry, quantum-size-related properties, and applications toward biology, catalysis, and nanotechnology. *Chemical reviews* **2004**, *104* (1), 293-346.

(16) Dykman, L. A.; Khlebtsov, N. G. Uptake of engineered gold nanoparticles into mammalian cells. *Chemical reviews* **2014**, *114* (2), 1258-1288.

(17) Wang, W.; Wang, J.; Ding, Y. Gold nanoparticle-conjugated nanomedicine: design, construction, and structure–efficacy relationship studies. *Journal of Materials Chemistry B* **2020**, *8* (22), 4813-4830.

(18) Amendola, V.; Pilot, R.; Frasconi, M.; Maragò, O. M.; Iatì, M. A. Surface plasmon resonance in gold nanoparticles: a review. *Journal of Physics: Condensed Matter* **2017**, *29* (20), 203002.

(19) Schröfel, A.; Kratošová, G. Biosynthesis of metallic nanoparticles and their applications. *Intracellular Delivery* **2011**, 373-409.

(20) Turkevich, J.; Stevenson, P. C.; Hillier, J. A study of the nucleation and growth processes in the synthesis of colloidal gold. *Discussions of the Faraday Society* **1951**, *11*, 55-75.

(21) Shah, M.; Badwaik, V.; Kherde, Y.; Waghwani, H. K.; Modi, T.; Aguilar, Z. P.; Rodgers, H.; Hamilton, W.; Marutharaj, T.; Webb, C. Gold nanoparticles: various methods of synthesis and antibacterial applications. *Frontiers in Bioscience-Landmark* **2014**, *19* (8), 1320-1344.

(22) Santhosh, P. B.; Genova, J.; Chamati, H. Green Synthesis of Gold Nanoparticles: An Eco-Friendly Approach. *Chemistry* **2022**, *4* (2), 345-369.

(23) Chowdhury, N. K.; Choudhury, R.; Gogoi, B.; Chang, C.-M.; Pandey, R. P. Microbial synthesis of gold nanoparticles and their application. *Curr. Drug Targets* **2022**, *23*.

(24) Sylvestre, J.-P.; Kabashin, A. V.; Sacher, E.; Meunier, M.; Luong, J. H. Stabilization and size control of gold nanoparticles during laser ablation in aqueous cyclodextrins. *Journal of the American Chemical Society* **2004**, *126* (23), 7176-7177.

(25) Polte, J. r.; Ahner, T. T.; Delissen, F.; Sokolov, S.; Emmerling, F.; Thünemann, A. F.; Kraehnert, R. Mechanism of gold nanoparticle formation in the classical citrate synthesis method derived from coupled in situ XANES and SAXS evaluation. *Journal of the American Chemical Society* **2010**, *132* (4), 1296-1301.

(26) Vityuk, N.; Eremenko, A.; Rusinchuk, N.; Lozovski, V.; Lokshyn, M.; Lysenko, V.; Mukha, I. P. FORMATION AND STABILITY OF GOLD NANOPARTICLES IN COLLOIDS PREPARED BY CITRATE METHOD. *Chemistry, Physics & Technology of Surface/Khimiya, Fizyka ta Tekhnologiya Poverhni* **2023**, *14* (3).

(27) Yahaya, M. L.; Zakaria, N. D.; Noordin, R.; Razak, K. A. Synthesis of large and stable colloidal gold nanoparticles (AuNPs) by seeding-growth method. *Materials Today: Proceedings* **2022**.

(28) Ali, S.; Chen, X.; Shi, W.; Huang, G.; Yuan, L.-m.; Meng, L.; Chen, S.; Zhonghao, X.; Chen, X. Recent advances in silver and gold nanoparticles-based colorimetric sensors for heavy metal ions detection: a review. *Critical Reviews in Analytical Chemistry* **2021**, 1-33.

(29) Zuber, A.; Purdey, M.; Schartner, E.; Forbes, C.; Van der Hoek, B.; Giles, D.; Abell, A.; Monro, T.; Ebendorff-Heidepriem, H. Detection of gold nanoparticles with different sizes using absorption and fluorescence based method. *Sensors and Actuators B: Chemical* **2016**, *227*, 117-127.

(30) Jeon, H. B.; Tsalu, P. V.; Ha, J. W. Shape effect on the refractive index sensitivity at localized surface plasmon resonance inflection points of single gold nanocubes with vertices. *Scientific reports* **2019**, *9* (1), 1-8.

(31) Kołątaj, K.; Krajczewski, J.; Kudelski, A. Plasmonic nanoparticles for environmental analysis. *Environmental Chemistry Letters* **2020**, *18* (3), 529-542.

(32) Arruebo, M.; Valladares, M.; González-Fernández, Á. Antibody-conjugated nanoparticles for biomedical applications. *Journal of Nanomaterials* **2009**, *2009*, 37.

(33) Hermanson, G. T. *Bioconjugate Techniques*; Elsevier Science, 2013.

(34) Kumar, S.; Aaron, J.; Sokolov, K. Directional conjugation of antibodies to nanoparticles for synthesis of multiplexed optical contrast agents with both delivery and targeting moieties. *Nature protocols* **2008**, *3* (2), 314.

(35) Huang, W.-C.; Tsai, P.-J.; Chen, Y.-C. Functional gold nanoparticles as photothermal agents for selective-killing of pathogenic bacteria. **2007**.

(36) Mout, R.; Moyano, D. F.; Rana, S.; Rotello, V. M. Surface functionalization of nanoparticles for nanomedicine. *Chemical Society Reviews* **2012**, *41* (7), 2539-2544.

(37) Jazayeri, M. H.; Amani, H.; Pourfatollah, A. A.; Pazoki-Toroudi, H.; Sedighimoghaddam, B. Various methods of gold nanoparticles (GNPs) conjugation to antibodies. *Sensing and bio-sensing research* **2016**, *9*, 17-22.

(38) Barreto, A.; Luis, L. G.; Girão, A. V.; Trindade, T.; Soares, A. M.; Oliveira, M. Behavior of colloidal gold nanoparticles in different ionic strength media. *Journal of Nanoparticle Research* **2015**, *17* (12), 493.

(39) Bolaños, K.; Kogan, M. J.; Araya, E. Capping gold nanoparticles with albumin to improve their biomedical properties. *International journal of nanomedicine* **2019**, *14*, 6387.

(40) Oliveira, J.; Keijok, W.; Prado, A.; Guimarães, M. Tracking the effect of binder length on colloidal stability and bioconjugation of gold nanoparticles. *Applied Nanoscience* **2018**, *8* (7), 1781-1790.

(41) International, A. *Standard Terminology Relating to Nanotechnology*; West Conshohocken, PA, 2020.

(42) Lee, J. W.; Choi, S.-R.; Heo, J. H. Simultaneous stabilization and functionalization of gold nanoparticles via biomolecule conjugation: Progress and perspectives. *ACS Applied Materials & Interfaces* **2021**, *13* (36), 42311-42328.

(43) Fleischer, C. C.; Payne, C. K. Nanoparticle–cell interactions: molecular structure of the protein corona and cellular outcomes. *Accounts of chemical research* **2014**, *47* (8), 2651-2659.

(44) Chenthamara, D.; Subramaniam, S.; Ramakrishnan, S. G.; Krishnaswamy, S.; Essa, M. M.; Lin, F.-H.; Qoronfleh, M. W. Therapeutic efficacy of nanoparticles and routes of administration. *Biomaterials research* **2019**, *23* (1), 1-29.

(45) Kim, Y.-J.; Kim, H.-S.; Chon, J.-W.; Kim, D.-H.; Hyeon, J.-Y.; Seo, K.-H. New colorimetric aptasensor for rapid on-site detection of Campylobacter jejuni and Campylobacter coli in chicken carcass samples. *Analytica chimica acta* **2018**, *1029*, 78-85.

(46) Li, F.; Li, F.; Yang, G.; Aguilar, Z. P.; Lai, W.; Xu, H. Asymmetric polymerase chain assay combined with propidium monoazide treatment and unmodified gold nanoparticles for colorimetric detection of viable emetic Bacillus cereus in milk. *Sensors and Actuators B: Chemical* **2018**, *255*, 1455-1461.

(47) Ma, X.; Song, L.; Zhou, N.; Xia, Y.; Wang, Z. A novel aptasensor for the colorimetric detection of S. typhimurium based on gold nanoparticles. *International journal of food microbiology* **2017**, *245*, 1-5.

(48) Niu, S.; Lv, Z.; Liu, J.; Bai, W.; Yang, S.; Chen, A. Colorimetric aptasensor using unmodified gold nanoparticles for homogeneous multiplex detection. *PLoS One* **2014**, *9* (10), e109263.

(49) Verma, M. S.; Chen, P. Z.; Jones, L.; Gu, F. X. Controlling “chemical nose” biosensor characteristics by modulating gold nanoparticle shape and concentration. *Sensing and bio-sensing research* **2015**, *5*, 13-18.

(50) Du, J.; Singh, H.; Dong, W.-j.; Bai, Y.-h.; Yi, T.-H. Colorimetric detection of Listeria monocytogenes using one-pot biosynthesized flower-shaped gold nanoparticles. *Sensors and Actuators B: Chemical* **2018**, *265*, 285-292.

(51) Bui, M.-P. N.; Ahmed, S.; Abbas, A. Single-digit pathogen and attomolar detection with the naked eye using liposome-amplified plasmonic immunoassay. *Nano letters* **2015**, *15* (9), 6239-6246.

(52) Lupusoru, R. V.; Simion, L.; Sandu, I.; Pricop, D. A.; Chiriac, A.; Poroch, V. Aging study of gold nanoparticles functionalized with chitosan in aqueous solutions. *Rev. Chim* **2017**, *68*, 2385-2388.

(53) Gubicza, J.; Labar, J. L.; Quynh, L. M.; Nam, N. H.; Luong, N. H. Evolution of size and shape of gold nanoparticles during long-time aging. *Materials Chemistry and Physics* **2013**, *138* (2-3), 449-453.

(54) Grys, D.-B.; de Nijs, B.; Salmon, A. R.; Huang, J.; Wang, W.; Chen, W.-H.; Scherman, O. A.; Baumberg, J. J. Citrate coordination and bridging of gold nanoparticles: The role of gold adatoms in AuNP aging. *ACS nano* **2020**, *14* (7), 8689-8696.

(55) Pattadar, D. K.; Zamborini, F. P. Effect of size, coverage, and dispersity on the potential-controlled Ostwald ripening of metal nanoparticles. *Langmuir* **2019**, *35* (50), 16416-16426.

(56) Gentry, S. T.; Kendra, S. F.; Bezpalko, M. W. Ostwald ripening in metallic nanoparticles: stochastic kinetics. *The Journal of Physical Chemistry C* **2011**, *115* (26), 12736-12741.

(57) Wang, F.; Richards, V. N.; Shields, S. P.; Buhro, W. E. Kinetics and mechanisms of aggregative nanocrystal growth. *Chemistry of Materials* **2014**, *26* (1), 5-21.

(58) Madras, G.; McCoy, B. J. Ostwald ripening with size-dependent rates: Similarity and power-law solutions. *The Journal of Chemical Physics* **2002**, *117* (17), 8042-8049.

(59) Caporali, S.; Muniz-Miranda, F.; Pedone, A.; Muniz-Miranda, M. SERS, XPS and DFT study of xanthine adsorbed on citrate-stabilized gold nanoparticles. *Sensors* **2019**, *19* (12), 2700.

(60) Burtt, C. M.; Senanayake, G. Effect of reductants and stabilizers on ageing of gold nanoparticles at pH 2–12 and application of nano-gold to study non-cyanide leaching in sodium hypochlorite/chloride solutions using UV–Visible spectroscopy. *Hydrometallurgy* **2016**, *164*, 166-176.

(61) Park, J.-W.; Shumaker-Parry, J. S. Structural study of citrate layers on gold nanoparticles: role of intermolecular interactions in stabilizing nanoparticles. *Journal of the American Chemical Society* **2014**, *136* (5), 1907-1921.

(62) Javadi-Zarnaghi, F.; Hosseini, F.; Mohammadrezaei, D. Distinct pH-dependent Aggregation of Citrate-Capped Colloidal Gold in Presence of Citrate Competitors. *Pertanika Journal of Science & Technology* **2018**, *26* (3).

(63) Li, X.; Robinson, S. M.; Gupta, A.; Saha, K.; Jiang, Z.; Moyano, D. F.; Sahar, A.; Riley, M. A.; Rotello, V. M. Functional gold nanoparticles as potent antimicrobial agents against multi-drug-resistant bacteria. *ACS nano* **2014**, *8* (10), 10682-10686.

(64) Lima, E.; Guerra, R.; Lara, V.; Guzmán, A. Gold nanoparticles as efficient antimicrobial agents for Escherichia coli and Salmonella typhi. *Chemistry Central Journal* **2013**, *7* (1), 11.

(65) Pal, S.; Tak, Y. K.; Song, J. M. Does the antibacterial activity of silver nanoparticles depend on the shape of the nanoparticle? A study of the gram-negative bacterium Escherichia coli. *Applied and environmental microbiology* **2007**, *73* (6), 1712-1720.

(66) Zhou, Y.; Kong, Y.; Kundu, S.; Cirillo, J. D.; Liang, H. Antibacterial activities of gold and silver nanoparticles against Escherichia coli and bacillus Calmette-Guérin. *Journal of nanobiotechnology* **2012**, *10* (1), 19.

(67) Luna-Guevara, J. J.; Arenas-Hernandez, M. M.; Martínez de la Peña, C.; Silva, J. L.; Luna-Guevara, M. L. The role of pathogenic E. coli in fresh vegetables: Behavior, contamination factors, and preventive measures. *International journal of microbiology* **2019**, *2019*.

(68) Glass, K. L., Emily; Kirk, Martyn; Bourke, Siobhan; McLure, Angus; Cribb, Danielle. *The annual cost of foodborne illness in Australia*; Australian National University, https://www.foodstandards.gov.au/; https://openresearch-repository.anu.edu.au/, 2022.

(69) Parija, S. C. *Textbook of Microbiology & Immunology-E-book*; Elsevier Health Sciences, 2014.

(70) Silhavy, T. J.; Kahne, D.; Walker, S. The bacterial cell envelope. *Cold Spring Harbor perspectives in biology* **2010**, *2* (5), a000414.

(71) Erridge, C.; Bennett-Guerrero, E.; Poxton, I. R. Structure and function of lipopolysaccharides. *Microbes and infection* **2002**, *4* (8), 837-851.

(72) Sherbet, G.; Lakshmi, M. Characterisation of Escherichia coli cell surface by isoelectric equilibrium analysis. *Biochimica Et Biophysica Acta (BBA)-Biomembranes* **1973**, *298* (1), 50-58.

(73) Ramezani, F.; Amanlou, M.; Rafii-Tabar, H. Comparison of amino acids interaction with gold nanoparticle. *Amino Acids* **2014**, *46* (4), 911-920.

(74) Sezonov, G.; Joseleau-Petit, D.; d'Ari, R. Escherichia coli physiology in Luria-Bertani broth. *Journal of bacteriology* **2007**, *189* (23), 8746-8749.

(75) Baev, M. V.; Baev, D.; Radek, A. J.; Campbell, J. W. Growth of Escherichia coli MG1655 on LB medium: monitoring utilization of sugars, alcohols, and organic acids with transcriptional microarrays. *Applied microbiology and biotechnology* **2006**, *71*, 310-316.

(76) Hanko, V. P.; Rohrer, J. S. Determination of amino acids in cell culture and fermentation broth media using anion-exchange chromatography with integrated pulsed amperometric detection. *Analytical biochemistry* **2004**, *324* (1), 29-38.

(77) Tao, Z.; Yuan, H.; Liu, M.; Liu, Q.; Zhang, S.; Liu, H.; Jiang, Y.; Huang, D.; Wang, T. Yeast extract: characteristics, production, applications and future perspectives. *Journal of microbiology and biotechnology* **2023**, *33* (2), 151.

(78) Pletnev, P.; Osterman, I.; Sergiev, P.; Bogdanov, A.; Dontsova, O. Survival guide: Escherichia coli in the stationary phase. *Acta Naturae (англоязычная версия)* **2015**, *7* (4 (27)), 22-33.

(79) Maier, R. M.; Pepper, I. L. Bacterial growth. In *Environmental microbiology*, Elsevier, 2015; pp 37-56.

(80) Fishov, I.; Zaritsky, A.; Grover, N. On microbial states of growth. *Molecular microbiology* **1995**, *15* (5), 789-794.

(81) Vulić, M.; Kolter, R. Evolutionary cheating in Escherichia coli stationary phase cultures. *Genetics* **2001**, *158* (2), 519-526.

(82) Kram, K. E.; Henderson, A. L.; Finkel, S. E. Escherichia coli has a unique transcriptional program in long-term stationary phase allowing identification of genes important for survival. *Msystems* **2020**, *5* (4), e00364-00320.

(83) Ratib, N. R.; Seidl, F.; Ehrenreich, I. M.; Finkel, S. E. Evolution in long-term stationary-phase batch culture: emergence of divergent Escherichia coli lineages over 1,200 days. *MBio* **2021**, *12* (1), 10.1128/mbio. 03337-03320.

(84) Saha, K.; Kim, S. T.; Yan, B.; Miranda, O. R.; Alfonso, F. S.; Shlosman, D.; Rotello, V. M. Surface functionality of nanoparticles determines cellular uptake mechanisms in mammalian cells. *Small* **2013**, *9* (2), 300-305.

(85) Chithrani, B. D.; Ghazani, A. A.; Chan, W. C. Determining the size and shape dependence of gold nanoparticle uptake into mammalian cells. *Nano letters* **2006**, *6* (4), 662-668.

(86) Grogan, D. W. Physiology of prokaryotic cells. In *Cell Physiology Source Book*, Elsevier, 2001; pp 1063-1075.

(87) Zhao, Y.; Tian, Y.; Cui, Y.; Liu, W.; Ma, W.; Jiang, X. Small molecule-capped gold nanoparticles as potent antibacterial agents that target gram-negative bacteria. *Journal of the American Chemical Society* **2010**, *132* (35), 12349-12356.

(88) Zhang, Y.; Shareena Dasari, T. P.; Deng, H.; Yu, H. Antimicrobial activity of gold nanoparticles and ionic gold. *Journal of Environmental Science and Health, Part C* **2015**, *33* (3), 286-327.

(89) Gaspar, R. Pushed off target with proteins. *Nature Nanotechnology* **2013**, *8* (2), 79-80.

(90) Jin, D.; Liu, M.; Zhang, Y.; Yu, W.; Yu, J.; Luo, Y.; Cheng, J.; Liu, Y. Active regulation of protein coronas for enhancing the in vivo biodistribution and metabolism of nanoparticles. *Inorganic Chemistry Frontiers* **2024**, *11* (17), 5741-5752.

(91) Mahmoudi, M.; Lynch, I.; Ejtehadi, M. R.; Monopoli, M. P.; Bombelli, F. B.; Laurent, S. Protein− nanoparticle interactions: opportunities and challenges. *Chemical reviews* **2011**, *111* (9), 5610-5637.

(92) Nandakumar, A.; Wei, W.; Siddiqui, G.; Tang, H.; Li, Y.; Kakinen, A.; Wan, X.; Koppel, K.; Lin, S.; Davis, T. P. Dynamic protein corona of gold nanoparticles with an evolving morphology. *ACS applied materials & interfaces* **2021**, *13* (48), 58238-58251.

(93) Salvati, A.; Pitek, A. S.; Monopoli, M. P.; Prapainop, K.; Bombelli, F. B.; Hristov, D. R.; Kelly, P. M.; Åberg, C.; Mahon, E.; Dawson, K. A. Transferrin-functionalized

nanoparticles lose their targeting capabilities when a biomolecule corona adsorbs on the surface. *Nature nanotechnology* **2013**, *8* (2), 137-143.

(94) Shah, J.; Singh, S. Nanoparticle–protein corona complex: composition, kinetics, physico–chemical characterization, and impact on biomedical applications. **2019**.

(95) Sun, Z.; Zheng, W.; Zhu, G.; Lian, J.; Wang, J.; Hui, P.; He, S.; Chen, W.; Jiang, X. Albumin broadens the antibacterial capabilities of nonantibiotic small molecule-capped gold nanoparticles. *ACS applied materials & interfaces* **2019**, *11* (49), 45381-45389.

(96) Tao, X.; Chang, X.; Wan, X.; Guo, Y.; Zhang, Y.; Liao, Z.; Song, Y.; Song, E. Impact of protein corona on noncovalent molecule–gold nanoparticle-based sensing. *Analytical Chemistry* **2020**, *92* (22), 14990-14998.

(97) Yang, J.; Wang, B.; You, Y.; Chang, W.-J.; Tang, K.; Wang, Y.-C.; Zhang, W.; Ding, F.; Gunasekaran, S. Probing the modulated formation of gold nanoparticles–beta-lactoglobulin corona complexes and their applications. *Nanoscale* **2017**, *9* (45), 17758-17769.

(98) Ferone, M.; Gowen, A.; Fanning, S.; Scannell, A. G. Microbial detection and identification methods: Bench top assays to omics approaches. *Comprehensive Reviews in Food Science and Food Safety* **2020**, *19* (6), 3106-3129.

(99) Nnachi, R. C.; Sui, N.; Ke, B.; Luo, Z.; Bhalla, N.; He, D.; Yang, Z. Biosensors for rapid detection of bacterial pathogens in water, food and environment. *Environment international* **2022**, *166*, 107357.

(100) Foddai, A. C.; Grant, I. R. Methods for detection of viable foodborne pathogens: Current state-of-art and future prospects. *Applied Microbiology and Biotechnology* **2020**, *104*, 4281-4288.

(101) Shen, Y.; Zhang, Y.; Gao, Z. F.; Ye, Y.; Wu, Q.; Chen, H.-Y.; Xu, J.-J. Recent advances in nanotechnology for simultaneous detection of multiple pathogenic bacteria. *Nano Today* **2021**, *38*, 101121.

(102) Pazos-Rojas, L. A.; Cuellar-Sánchez, A.; Romero-Cerón, A. L.; Rivera-Urbalejo, A.; Van Dillewijn, P.; Luna-Vital, D. A.; Muñoz-Rojas, J.; Morales-García, Y. E.; Bustillos-Cristales, M. d. R. The Viable but Non-Culturable (VBNC) State, a Poorly Explored Aspect of Beneficial Bacteria. *Microorganisms* **2023**, *12* (1), 39.

(103) Chen, S.; Li, X.; Wang, Y.; Zeng, J.; Ye, C.; Li, X.; Guo, L.; Zhang, S.; Yu, X. Induction of Escherichia coli into a VBNC state through chlorination/chloramination and differences in characteristics of the bacterium between states. *Water research* **2018**, *142*, 279-288.

(104) Al-Hindi, R. R.; Teklemariam, A. D.; Alharbi, M. G.; Alotibi, I.; Azhari, S. A.; Qadri, I.; Alamri, T.; Harakeh, S.; Applegate, B. M.; Bhunia, A. K. Bacteriophage-based biosensors: A platform for detection of foodborne bacterial pathogens from food and environment. *Biosensors* **2022**, *12* (10), 905.

(105) Garg, N.; Ahmad, F. J.; Kar, S. Recent advances in loop-mediated isothermal amplification (LAMP) for rapid and efficient detection of pathogens. *Current Research in Microbial Sciences* **2022**, *3*, 100120.

(106) Tiburzi, O.; Papadakis, S.; Gerasopoulos, K.; Astatke, M. NASBA Coupled to Paper Microfluidics for RNA Detection. In *RNA Amplification and Analysis: Methods and Protocols*, Springer, 2024; pp 51-64.

(107) Liu, L.; Ma, W.; Wang, X.; Li, S. Recent progress of surface-enhanced Raman spectroscopy for bacteria detection. *Biosensors* **2023**, *13* (3), 350.

(108) Wen, P.; Yang, F.; Zhao, H.; Xu, Y.; Li, S.; Chen, L. Novel Digital SERS-Microfluidic Chip for Rapid and Accurate Quantification of Microorganisms. *Analytical Chemistry* **2024**, *96* (4), 1454-1461.

(109) Parvathy, N. A.; Sruthi, R.; Darshana, A. NEXT GENERATION SEQUENCING TECHNOLOGIES IN PLANT GENETICS. *GENETICS AND PLANT BREEDING* **2024**, 378.

(110) Bharadwaj, S.; Dwivedi, V. D.; Kirtipal, N. Application of whole genome sequencing (WGS) approach against identification of foodborne bacteria. *Microbial Genomics in Sustainable Agroecosystems: Volume 1* **2019**, 131-148.

(111) Parkhe, V. S.; Tiwari, A. P. Gold nanoparticles-based biosensors: pioneering solutions for bacterial and viral pathogen detection—a comprehensive review. *World Journal of Microbiology and Biotechnology* **2024**, *40* (9), 269.

(112) Mao, K.; Min, X.; Zhang, H.; Zhang, K.; Cao, H.; Guo, Y.; Yang, Z. Paper-based microfluidics for rapid diagnostics and drug delivery. *Journal of Controlled Release* **2020**, *322*, 187-199.

(113) Castillo-Henríquez, L.; Brenes-Acuña, M.; Castro-Rojas, A.; Cordero-Salmerón, R.; Lopretti-Correa, M.; Vega-Baudrit, J. R. Biosensors for the detection of bacterial and viral clinical pathogens. *Sensors* **2020**, *20* (23), 6926.

(114) Lakshmipriya, T.; Gopinath, S. C. An introduction to biosensors and biomolecules. In *Nanobiosensors for biomolecular targeting*, Elsevier, 2019; pp 1-21.

(115) Metkar, S. K.; Girigoswami, K. Diagnostic biosensors in medicine–a review. *Biocatalysis and agricultural biotechnology* **2019**, *17*, 271-283.

(116) Pourakbari, R.; Shadjou, N.; Yousefi, H.; Isildak, I.; Yousefi, M.; Rashidi, M.-R.; Khalilzadeh, B. Recent progress in nanomaterial-based electrochemical biosensors for pathogenic bacteria. *Microchimica Acta* **2019**, *186*, 1-13.

(117) Yadav, N.; Chhillar, A. K.; Rana, J. S. Detection of pathogenic bacteria with special emphasis to biosensors integrated with AuNPs. *Sensors International* **2020**, *1*, 100028.

(118) Bhalla, N. Biosensors for drug discovery applications. University of Bath, 2015.

(119) Malhotra, B. D.; Ali, M. A. Nanomaterials in biosensors: Fundamentals and applications. *Nanomaterials for biosensors* **2018**, 1.

(120) Hegde, M.; Pai, P.; Shetty, M. G.; Babitha, K. S. Gold nanoparticle based biosensors for rapid pathogen detection: A review. *Environmental Nanotechnology, Monitoring & Management* **2022**, *18*, 100756.

(121) Yazdi, M. K.; Zarrintaj, P.; Bagheri, B.; Kim, Y. C.; Ganjali, M. R.; Saeb, M. R. Nanotechnology-based biosensors in drug delivery. In *Nanoengineered biomaterials for advanced drug delivery*, Elsevier, 2020; pp 767-779.

(122) Naresh, V.; Lee, N. A review on biosensors and recent development of nanostructured materials-enabled biosensors. *Sensors* **2021**, *21* (4), 1109.

(123) Chaubey, A.; Malhotra, B. Mediated biosensors. *Biosensors and bioelectronics* **2002**, *17* (6-7), 441-456.

(124) Chen, C.; Wang, J. Optical biosensors: An exhaustive and comprehensive review. *Analyst* **2020**, *145* (5), 1605-1628.

(125) Si, P.; Razmi, N.; Nur, O.; Solanki, S.; Pandey, C. M.; Gupta, R. K.; Malhotra, B. D.; Willander, M.; de la Zerda, A. Gold nanomaterials for optical biosensing and bioimaging. *Nanoscale Advances* **2021**, *3* (10), 2679-2698.

(126) Chen, Y.-T.; Lee, Y.-C.; Lai, Y.-H.; Lim, J.-C.; Huang, N.-T.; Lin, C.-T.; Huang, J.-J. Review of integrated optical biosensors for point-of-care applications. *Biosensors* **2020**, *10* (12), 209.

(127) Zhao, X.; Bhat, A.; O'Connor, C.; Curtin, J.; Singh, B.; Tian, F. Review of detection limits for various techniques for bacterial detection in food samples. *Nanomaterials* **2024**, *14* (10), 855.

(128) Gill, A. The importance of bacterial culture to food microbiology in the age of genomics. *Frontiers in microbiology* **2017**, *8*, 777.

(129) Sachdeva, P.; Nath, G.; Jain, U. Phage based biosensors: Enhancing early detection of emerging pathogens in diagnostics. *Talanta Open* **2024**, *10*, 100345.

(130) Chauhan, A.; Goyal, P.; Varma, A.; Jindal, T. Microbiological evaluation of drinking water sold by roadside vendors of Delhi, India. *Applied Water Science* **2017**, *7*, 1635-1644.

(131) Kim, S. O.; Kim, S. S. Bacterial pathogen detection by conventional culture-based and recent alternative (polymerase chain reaction, isothermal amplification, enzyme linked immunosorbent assay, bacteriophage amplification, and gold nanoparticle aggregation) methods in food samples: A review. *Journal of Food Safety* **2021**, *41* (1), e12870.

(132) Wang, Z.; Cai, R.; Gao, Z.; Yuan, Y.; Yue, T. Immunomagnetic separation: An effective pretreatment technology for isolation and enrichment in food microorganisms detection. *Comprehensive Reviews in Food Science and Food Safety* **2020**, *19* (6), 3802-3824.

(133) Khalid, S. A.; Hashem, H. M. Recent Trends in Bacterial Sensors. In *Handbook of Nanosensors: Materials and Technological Applications*, Springer, 2024; pp 1045-1076.

(134) Farooq, U.; Ullah, M. W.; Yang, Q.; Wang, S. Applications of phage-based biosensors in the diagnosis of infectious diseases, food safety, and environmental monitoring. In *Biosensors for Environmental Monitoring*, IntechOpen, 2019.

(135) Martelet, A.; L'Hostis, G.; Nevers, M.-C.; Volland, H.; Junot, C.; Becher, F. o.; Muller, B. H. Phage amplification and immunomagnetic separation combined with

targeted mass spectrometry for sensitive detection of viable bacteria in complex food matrices. *Analytical chemistry* **2015**, *87* (11), 5553-5560.

(136) Craw, P.; Balachandran, W. Isothermal nucleic acid amplification technologies for point-of-care diagnostics: a critical review. *Lab on a Chip* **2012**, *12* (14), 2469-2486.

(137) Das, D.; Lin, C.-W.; Chuang, H.-S. LAMP-based point-of-care biosensors for rapid pathogen detection. *Biosensors* **2022**, *12* (12), 1068.

(138) Rodriguez, L.; Zhang, Z.; Wang, D. Recent advances of Raman spectroscopy for the analysis of bacteria. *Analytical Science Advances* **2023**, *4* (3-4), 81-95.

(139) Yin, M.; Li, J.; Huang, L.; Li, Y.; Yuan, M.; Luo, Y.; Armato, U.; Zhang, L.; Wei, Y.; Li, Y. Identification of microbes in wounds using near-infrared spectroscopy. *Burns* **2022**, *48* (4), 791-798.

(140) Kozyreva, V. K.; Truong, C.-L.; Greninger, A. L.; Crandall, J.; Mukhopadhyay, R.; Chaturvedi, V. Validation and implementation of clinical laboratory improvements act-compliant whole-genome sequencing in the public health microbiology laboratory. *Journal of clinical microbiology* **2017**, *55* (8), 2502-2520.

(141) Deshmukh, R. A.; Joshi, K.; Bhand, S.; Roy, U. Recent developments in detection and enumeration of waterborne bacteria: a retrospective minireview. *MicrobiologyOpen* **2016**, *5* (6), 901-922.

(142) Bonyadi, F.; Kavruk, M.; Ucak, S.; Cetin, B.; Bayramoglu, G.; Dursun, A. D.; Arica, Y.; Ozalp, V. C. Real-time biosensing bacteria and virus with quartz crystal microbalance: Recent advances, opportunities, and challenges. *Critical reviews in analytical chemistry* **2024**, *54* (8), 2888-2899.

(143) Mayaka, R. K.; Alocilja, E. C. Genomic nano-biosensor for rapid detection of the carbapenem-resistant gene bla NDM-1 in carbapenemase-producing bacteria. *Nanoscale Advances* **2025**.

(144) Landa, G.; Miranda-Calderon, L. G.; Sebastian, V.; Irusta, S.; Mendoza, G.; Arruebo, M. Selective point-of-care detection of pathogenic bacteria using sialic acid functionalized gold nanoparticles. *Talanta* **2021**, *234*, 122644.

(145) Han, D.; Li, X.; Bian, X.; Wang, J.; Kong, L.; Ding, S.; Yan, Y. Localized surface plasmon-enhanced electrochemiluminescence biosensor for rapid, label-free, and single-

step detection of broad-spectrum bacteria using urchin-like Au and Ag nanoparticles. *Sensors and Actuators B: Chemical* **2022**, *355*, 131120.

(146) Luo, J.; Liu, X.; Tian, Q.; Yue, W.; Zeng, J.; Chen, G.; Cai, X. Disposable bioluminescence-based biosensor for detection of bacterial count in food. *Analytical biochemistry* **2009**, *394* (1), 1-6.

(147) Yaghubi, F.; Zeinoddini, M.; Saeedinia, A. R.; Azizi, A.; Samimi Nemati, A. Design of localized surface plasmon resonance (LSPR) biosensor for immunodiagnostic of E. coli O157: H7 using gold nanoparticles conjugated to the chicken antibody. *Plasmonics* **2020**, *15* (5), 1481-1487.

(148) Maldonado, J.; Estévez, M.-C.; Fernández-Gavela, A.; González-López, J. J.; González-Guerrero, A. B.; Lechuga, L. M. Label-free detection of nosocomial bacteria using a nanophotonic interferometric biosensor. *Analyst* **2020**, *145* (2), 497-506.

(149) Banada, P. P.; Huff, K.; Bae, E.; Rajwa, B.; Aroonnual, A.; Bayraktar, B.; Adil, A.; Robinson, J. P.; Hirleman, E. D.; Bhunia, A. K. Label-free detection of multiple bacterial pathogens using light-scattering sensor. *Biosensors and Bioelectronics* **2009**, *24* (6), 1685-1692.

(150) Tetyana, P.; Shumbula, P. M.; Njengele-Tetyana, Z. Biosensors: design, development and applications. In *Nanopores*, IntechOpen, 2021.

(151) Klos-Witkowska, A.; Martsenyuk, V. Stability in biosensors derived from domain map analysis of bibliometric data. *Acta Biochimica Polonica* **2024**, *71*, 12196.

(152) Gibson, T. D. Biosensors: The stabilité problem. *Analusis* **1999**, *27* (7), 630-638.

(153) Morales, M. A.; Halpern, J. M. Guide to selecting a biorecognition element for biosensors. *Bioconjugate chemistry* **2018**, *29* (10), 3231-3239.

(154) McNaught, A. D.; Wilkinson, A. *Compendium of chemical terminology*; Blackwell Science Oxford, 1997.

(155) Scientific, C. *Gold (III) Chloride Trihydrate AR (tetrachloroauric (III) acid, trihydrate) (ACS)*. ChemSupply Australia, 2025. (accessed 2025 23.09.2025).

(156) Alkilany, A. M.; Abulateefeh, S. R.; Murphy, C. J. Facile Functionalization of Gold Nanoparticles with PLGA Polymer Brushes and Efficient Encapsulation into PLGA

Nanoparticles: Toward Spatially Precise Bioimaging of Polymeric Nanoparticles. *Particle & Particle Systems Characterization* **2018**, 1800414.

(157) Dong, J.; Carpinone, P. L.; Pyrgiotakis, G.; Demokritou, P.; Moudgil, B. M. Synthesis of precision gold nanoparticles using Turkevich method. *KONA Powder and Particle Journal* **2020**, *37*, 224-232.

(158) Gharatape, A.; Davaran, S.; Salehi, R.; Hamishehkar, H. J. R. A. Engineered gold nanoparticles for photothermal cancer therapy and bacteria killing. **2016**, *6* (112), 111482-111516.

(159) Herizchi, R.; Abbasi, E.; Milani, M.; Akbarzadeh, A. Current methods for synthesis of gold nanoparticles. *Artificial cells, nanomedicine, and biotechnology* **2016**, *44* (2), 596-602.

(160) Shah, M.; Badwaik, V.; Kherde, Y.; Waghwani, H.; Modi, T.; Aguilar, Z.; Rodgers, H.; Hamilton, W.; Marutharaj, T.; Webb, C. Gold nanoparticles: various methods of synthesis and antibacterial applications. *Frontiers in bioscience (Landmark edition)* **2014**, *19*, 1320.

(161) Ding, Y.; Huang, P.-J. J.; Zandieh, M.; Wang, J.; Liu, J. Gold nanoparticles synthesized using various reducing agents and the effect of aging for DNA sensing. *Langmuir* **2022**, *39* (1), 256-264.

(162) BenchChem. *Chloroauric acid hydrate*. Bench Chemicals, 2025. https://www.benchchem.com/product/b6360573 (accessed 2025 02/06/2025).

(163) 王永旗, 王., 吕明, 王铮, 萧瑞雪. Preparation method of chloroauric acid. China 2016.

(164) King, S.; Massicot, J.; McDonagh, A. A straightforward route to tetrachloroauric acid from gold metal and molecular chlorine for nanoparticle synthesis. *Metals* **2015**, *5* (3), 1454-1461.

(165) Brewer, S. H.; Glomm, W. R.; Johnson, M. C.; Knag, M. K.; Franzen, S. Probing BSA binding to citrate-coated gold nanoparticles and surfaces. *Langmuir* **2005**, *21* (20), 9303-9307.

(166) Matei, I.; Buta, C. M.; Turcu, I. M.; Culita, D.; Munteanu, C.; Ionita, G. Formation and stabilization of gold nanoparticles in bovine serum albumin solution. *Molecules* **2019**, *24* (18), 3395.

(167) La Spina, R.; Spampinato, V.; Gilliland, D.; Ojea-Jimenez, I.; Ceccone, G. Influence of different cleaning processes on the surface chemistry of gold nanoparticles. *Biointerphases* **2017**, *12* (3), 031003.

(168) Sánchez-Iglesias, A.; Winckelmans, N.; Altantzis, T.; Bals, S.; Grzelczak, M.; Liz-Marzán, L. M. High-yield seeded growth of monodisperse pentatwinned gold nanoparticles through thermally induced seed twinning. *Journal of the American Chemical Society* **2016**, *139* (1), 107-110.

(169) Sau, T. K.; Murphy, C. J. Seeded high yield synthesis of short Au nanorods in aqueous solution. *Langmuir* **2004**, *20* (15), 6414-6420.

(170) Pissuwan, D. Selective targeting and thermal destruction of live cells using antibody functionalised gold nanoparticles. 2008.

(171) Hinterwirth, H.; Stübiger, G.; Lindner, W.; Lämmerhofer, M. Gold nanoparticle-conjugated anti-oxidized low-density lipoprotein antibodies for targeted lipidomics of oxidative stress biomarkers. *Analytical chemistry* **2013**, *85* (17), 8376-8384.

(172) Haller, E.; Lindner, W.; Lämmerhofer, M. Gold nanoparticle–antibody conjugates for specific extraction and subsequent analysis by liquid chromatography–tandem mass spectrometry of malondialdehyde-modified low density lipoprotein as biomarker for cardiovascular risk. *Analytica chimica acta* **2015**, *857*, 53-63.

(173) Ltd., A. *Zeta Potential – What is it and how can it be characterised?* https://analytik.co.uk/zeta-potential-what-is-it-and-how-can-it-be-characterised/ (accessed 2025.

(174) Nobbmann, U. *What is the zeta deviation?* Malvern Panalytical Ltd, 2017. (accessed 2025.

(175) Tong, W.; Walsh, M. J.; Mulvaney, P.; Etheridge, J.; Funston, A. M. Control of symmetry breaking size and aspect ratio in gold nanorods: underlying role of silver nitrate. *The Journal of Physical Chemistry C* **2017**, *121* (6), 3549-3559.

(176) Razali, N. L.; Shah, N. Z. A. n. M.; Morsin, M.; Noh, F. H. M.; Salleh, M. M. Seed-mediated synthesis of gold nanorods with variation of silver nitrate (AgNO3)

concentration. *Journal of Telecommunication, Electronic and Computer Engineering (JTEC)* **2017**, *9* (3-8), 123-127.

(177) Scarabelli, L.; Sánchez-Iglesias, A.; Pérez-Juste, J.; Liz-Marzán, L. M. A "tips and tricks" practical guide to the synthesis of gold nanorods. ACS Publications: 2015; Vol. 6, pp 4270-4279.

(178) Cui, M.; Liu, R.; Deng, Z.; Ge, G.; Liu, Y.; Xie, L. Quantitative study of protein coronas on gold nanoparticles with different surface modifications. *Nano Research* **2014**, *7*, 345-352.

(179) De Carlo, S.; Harris, J. R. Negative staining and cryo-negative staining of macromolecules and viruses for TEM. *Micron* **2011**, *42* (2), 117-131.

(180) Rodríguez-Fernández, J.; Pérez-Juste, J.; Mulvaney, P.; Liz-Marzán, L. M. Spatially-directed oxidation of gold nanoparticles by Au (III)− CTAB complexes. *The Journal of Physical Chemistry B* **2005**, *109* (30), 14257-14261.

(181) Willey, T. M.; Vance, A. L.; Bostedt, C.; van Buuren, T.; Meulenberg, R. W.; Terminello, L. J.; Fadley, C. S. Surface structure and chemical switching of thioctic acid adsorbed on Au (111) as observed using near-edge X-ray absorption fine structure. *Langmuir* **2004**, *20* (12), 4939-4944.

(182) Agilent. *E. coli Cell Culture Calculator*. Agilent, https://www.agilent.com/store/biocalculators/calcODBacterial.jsp?_requestid=3508959 (accessed.

(183) Haiss, W.; Thanh, N. T.; Aveyard, J.; Fernig, D. G. Determination of size and concentration of gold nanoparticles from UV− Vis spectra. *Analytical chemistry* **2007**, *79* (11), 4215-4221.

(184) Vilela, D.; González, M. C.; Escarpa, A. Sensing colorimetric approaches based on gold and silver nanoparticles aggregation: chemical creativity behind the assay. A review. *Analytica chimica acta* **2012**, *751*, 24-43.

(185) Yang, S.; Piao, Y.; Li, X.; Mu, D.; Ji, S.; Wu, R.; Wu, J. A new decontamination method for Bacillus subtilisin pasteurized milk: Thermosonication treatment. *Food Research International* **2023**, *163*, 112291.

(186) Phebus, R. K.; Nutsch, A. L.; Schafer, D. E.; Wilson, R. C.; Riemann, M. J.; Leising, J. D.; Kastner, C. L.; Wolf, J. R.; Prasai, R. K. Comparison of steam

pasteurization and other methods for reduction of pathogens on surfaces of freshly slaughtered beef. *Journal of Food Protection* **1997**, *60* (5), 476-484.

(187) Spinks, A. T.; Dunstan, R.; Harrison, T.; Coombes, P.; Kuczera, G. Thermal inactivation of water-borne pathogenic and indicator bacteria at sub-boiling temperatures. *Water research* **2006**, *40* (6), 1326-1332.

(188) Biswas, S.; Nazmi, A.; Pitesky, M.; Gallardo, R.; Pandey, P. Thermal inactivation of Escherichia coli and Salmonella Typhimurium in poultry carcass and litter at thermophilic temperatures. *Journal of Applied Poultry Research* **2019**, *28* (2), 307-317.

(189) Pebdeni, A. B.; Roshani, A.; Mirsadoughi, E.; Behzadifar, S.; Hosseini, M. Recent advances in optical biosensors for specific detection of E. coli bacteria in food and water. *Food Control* **2022**, 108822.

(190) Singha, S.; Thomas, R.; Viswakarma, J. N.; Gupta, V. K. Foodborne illnesses of Escherichia coli O157origin and its control measures. *Journal of Food Science and Technology* **2022**, 1-10.

(191) Puligundla, P.; Lim, S. Biocontrol approaches against Escherichia coli O157: H7 in foods. *Foods* **2022**, *11* (5), 756.

(192) D'aoust, J.-Y.; Park, C.; Szabo, R.; Todd, E.; Emmons, D.; McKellar, R. Thermal inactivation of Campylobacter species, Yersinia enterocolitica, and hemorrhagic Escherichia coli 0157: H7 in fluid milk. *Journal of Dairy Science* **1988**, *71* (12), 3230-3236.

(193) Mukherjee, A.; Yoon, Y.; Belk, K. E.; Scanga, J. A.; Smith, G. C.; Sofos, J. N. Thermal inactivation of Escherichia coli O157: H7 in beef treated with marination and tenderization ingredients. *Journal of food protection* **2008**, *71* (7), 1349-1356.

(194) Feng, G.; Churey, J. J.; Worobo, R. W. Thermal inactivation of Salmonella and Escherichia coli O157: H7 on alfalfa seeds. *Journal of food protection* **2007**, *70* (7), 1698-1703.

(195) Kou, X.; Li, R.; Zhang, L.; Ramaswamy, H.; Wang, S. Effect of heating rates on thermal destruction kinetics of Escherichia coli ATCC25922 in mashed potato and the associated changes in product color. *Food Control* **2019**, *97*, 39-49.

(196) Liu, Y.; Kumblathan, T.; Uppal, G. K.; Zhou, A.; Moe, B.; Hrudey, S. E.; Li, X.-F. A hidden risk: Survival and resuscitation of Escherichia coli O157: H7 in the viable but nonculturable state after boiling or microwaving. *Water Research* **2020**, *183*, 116102.

(197) Marcén, M.; Cebrián, G.; Ruiz-Artiga, V.; Condón, S.; Mañas, P. Protective effect of glutathione on Escherichia coli cells upon lethal heat stress. *Food research international* **2019**, *121*, 806-811.

(198) Han, A.; Paek, J.; Lee, S.-Y. Thermal resistance of Escherichia coli O157: H7 in laboratory media, milk, and beef extracts during non-isothermal processing at various heating rates. *Food Microbiology* **2023**, *110*, 104187.

(199) Chandel, T. I.; Zaman, M.; Khan, M. V.; Ali, M.; Rabbani, G.; Ishtikhar, M.; Khan, R. H. A mechanistic insight into protein-ligand interaction, folding, misfolding, aggregation and inhibition of protein aggregates: An overview. *International journal of biological macromolecules* **2018**, *106*, 1115-1129.

(200) Lin, Z.; Zhou, B.; Wu, W.; Xing, L.; Zhao, Q. Self-assembling amphipathic alpha-helical peptides induce the formation of active protein aggregates in vivo. *Faraday discussions* **2013**, *166*, 243-256.

(201) Anderson, J. J.; Wilson, J. M.; Oxender, D. L. Defective transport and other phenotypes of a periplasmic" leaky" mutant of Escherichia coli K-12. *Journal of bacteriology* **1979**, *140* (2), 351-358.

(202) Chen, Z. Y.; Cao, J.; Xie, L.; Li, X. F.; Yu, Z. H.; Tong, W. Y. Construction of leaky strains and extracellular production of exogenous proteins in recombinant E scherichia coli. *Microbial Biotechnology* **2014**, *7* (4), 360-370.

(203) Wu, X.; Ren, J.; Liu, Z.; Su, Z.; Ren, J.; Zha, J. Controllable autolytic leaky E. coli platform for the recovery of intracellular proteins. *Journal of Agricultural and Food Chemistry* **2024**, *72* (44), 24632-24642.

(204) Wurm, D.; Slouka, C.; Bosilj, T.; Herwig, C.; Spadiut, O. Comparative analysis of how to trigger periplasmic release in recombinant E. coli cultivations. *Eng. Life Sci* **2017**, *17*, 215-222.

(205) Hitchener, B. J.; Egan, A. F. Outer-membrane damage in sublethally heated Escherichia coli K-12. *Canadian Journal of Microbiology* **1977**, *23* (3), 311-318.

(206) Avila-Calderón, E. D.; Ruiz-Palma, M. d. S.; Aguilera-Arreola, M. G.; Velázquez-Guadarrama, N.; Ruiz, E. A.; Gomez-Lunar, Z.; Witonsky, S.; Contreras-Rodríguez, A. Outer membrane vesicles of gram-negative bacteria: an outlook on biogenesis. *Frontiers in microbiology* **2021**, *12*, 557902.

(207) Roier, S.; Zingl, F. G.; Cakar, F.; Durakovic, S.; Kohl, P.; Eichmann, T. O.; Klug, L.; Gadermaier, B.; Weinzerl, K.; Prassl, R. A novel mechanism for the biogenesis of outer membrane vesicles in Gram-negative bacteria. *Nature communications* **2016**, *7* (1), 10515.

(208) Xuan, S.; Xuan, G. Bacterial membrane vesicles: formation, functions, and roles in bacterial-phage interactions. *World Journal of Microbiology and Biotechnology* **2024**, *40* (10), 329.

(209) Maaz, K. *The transmission electron microscope: theory and applications*; BoD–Books on Demand, 2015.

(210) Harris, J. R.; De Carlo, S. Negative staining and cryo-negative staining: applications in biology and medicine. *Electron Microscopy: Methods and Protocols* **2014**, 215-258.

(211) Muller-Reichert, T. *Electron microscopy of model systems*; Academic Press, 2010.

(212) Ohi, M.; Li, Y.; Cheng, Y.; Walz, T. Negative staining and image classification—powerful tools in modern electron microscopy. *Biological procedures online* **2004**, *6*, 23-34.

(213) Bremer, A.; Henn, C.; Engel, A.; Baumeister, W.; Aebi, U. Has negative staining still a place in biomacromolecular electron microscopy? *Ultramicroscopy* **1992**, *46* (1-4), 85-111.

(214) Zhao, F.-Q.; Craig, R. Capturing time-resolved changes in molecular structure by negative staining. *Journal of structural biology* **2003**, *141* (1), 43-52.

(215) Weibull, C.; Christiansson, A.; Carlemalm, E. Extraction of membrane lipids during fixation, dehydration and embedding of Acholeplasma laidlawii-cells for electron microscopy. *Journal of Microscopy* **1983**, *129* (2), 201-207.

(216) Mörgelin, M. Negative Staining and transmission electron microscopy of bacterial surface structures. *Bacterial Pathogenesis: Methods and Protocols* **2017**, 211-217.

(217) Rodriguez-Torres, A.; Ramos-Sanchez, M.; Orduna-Domingo, A.; Martin-Gil, F.; Martin-Gil, J. Differential scanning calorimetry investigations on LPS and free lipids A of the bacterial cell wall. *Research in microbiology* **1993**, *144* (9), 729-740.

(218) Hayden, S. C.; Zhao, G.; Saha, K.; Phillips, R. L.; Li, X.; Miranda, O. R.; Rotello, V. M.; El-Sayed, M. A.; Schmidt-Krey, I.; Bunz, U. H. Aggregation and interaction of cationic nanoparticles on bacterial surfaces. *Journal of the American Chemical Society* **2012**, *134* (16), 6920-6923.

(219) Lin, C.-C.; Yeh, Y.-C.; Yang, C.-Y.; Chen, C.-L.; Chen, G.-F.; Chen, C.-C.; Wu, Y.-C. Selective binding of mannose-encapsulated gold nanoparticles to type 1 pili in Escherichia coli. *Journal of the American Chemical Society* **2002**, *124* (14), 3508-3509.

(220) Wurm, D. J.; Slouka, C.; Bosilj, T.; Herwig, C.; Spadiut, O. How to trigger periplasmic release in recombinant Escherichia coli: A comparative analysis. *Engineering in life sciences* **2017**, *17* (2), 215-222.

(221) Yang, H.; Chen, Z.; Zhang, L.; Yung, W. Y.; Leung, K. C. F.; Chan, H. Y. E.; Choi, C. H. J. Mechanism for the cellular uptake of targeted gold nanorods of defined aspect ratios. *Small* **2016**, *12* (37), 5178-5189.

(222) Cui, M.; Liu, R.; Deng, Z.; Ge, G.; Liu, Y.; Xie, L. Quantitative study of protein coronas on gold nanoparticles with different surface modifications. *Nano Research* **2014**, *7* (3), 345-352.

(223) Chandran, K.; Song, S.; Yun, S.-I. Effect of size and shape controlled biogenic synthesis of gold nanoparticles and their mode of interactions against food borne bacterial pathogens. *Arabian Journal of Chemistry* **2019**, *12* (8), 1994-2006.

(224) Nichol, C. P.; Davis, J. H.; Weeks, G.; Bloom, M. Quantitative study of the fluidity of Escherichia coli membranes using deuterium magnetic resonance. *Biochemistry* **1980**, *19* (3), 451-457.

(225) Feng, Z. V.; Gunsolus, I. L.; Qiu, T. A.; Hurley, K. R.; Nyberg, L. H.; Frew, H.; Johnson, K. P.; Vartanian, A. M.; Jacob, L. M.; Lohse, S. E. Impacts of gold nanoparticle charge and ligand type on surface binding and toxicity to Gram-negative and Gram-positive bacteria. *Chemical science* **2015**, *6* (9), 5186-5196.

(226) Sawosz, E.; Chwalibog, A.; Szeliga, J.; Sawosz, F.; Grodzik, M.; Rupiewicz, M.; Niemiec, T.; Kacprzyk, K. Visualization of gold and platinum nanoparticles interacting with Salmonella enteritidis and Listeria monocytogenes. *International journal of nanomedicine* **2010**, 631-637.

(227) Hamm, C. W.; Gray, M. J. Inorganic polyphosphate and the stringent response coordinately control cell division and cell morphology in Escherichia coli. *Mbio* **2025**, *16* (2), e03511-03524.

(228) Van Die, I. M.; Bergmans, H. E.; Hoekstra, W. P. Transformation in Escherichia coli: studies on the role of the heat shock in induction of competence. *Microbiology* **1983**, *129* (3), 663-670.

(229) Findlay, E. J.; Barton, P. G. Phase behavior of synthetic phosphatidylglycerols and binary mixtures with phosphatidylcholines in the presence and absence of calcium ions. *Biochemistry* **1978**, *17* (12), 2400-2405.

(230) Osborne, M. G.; Geiger, C. J.; Corzett, C. H.; Kram, K. E.; Finkel, S. E. Removal of toxic volatile compounds in batch culture prolongs stationary phase and delays death of *Escherichia coli*. *Appl. Environ. Microbiol.* **2021**, *87*, 01860-01821.

(231) Sezonov, G.; Joseleau-Petit, D. I.; D'Ari, R. *Escherichia coli* physiology in Luria-Bertani broth. *J. Bacteriol.* **2007**, *189* (23), 8746–8749. DOI: 10.1128/JB.01368-07.

(232) Sánchez-Clemente, R.; Igeño, M. I.; Población, A. G.; Guijo, M. I.; Merchán, F.; Blasco, R. Study of pH changes in media during bacterial growth of several environmental strains. *Proceedings* **2018**, *2*, 1297. DOI: 10.3390/proceedings2201297.

(233) Wagers, K.; Chui, T.; Adem, S. Effect of pH on the stability of gold nanoparticles and their application for melamine detection in infant formula. *IOSR J. Appl. Chem* **2014**, *7* (8), 15-20.

(234) Cho, T. J.; Hackley, V. A. Assessing the chemical and colloidal stability of functionalized gold nanoparticles. *NIST Special Publication* **2018**, *1200*, 26.

(235) Dantur, K. I.; Pizarro, R. A. Effect of growth phase on the Escherichia coli response to ultraviolet-A radiation: influence of conditioned media, hydrogen peroxide and acetate. *Journal of Photochemistry and Photobiology B: Biology* **2004**, *75* (1-2), 33-39.

(236) Jandu, N.; Ceponis, P. J.; Kato, S.; Riff, J. D.; McKay, D. M.; Sherman, P. M. Conditioned medium from enterohemorrhagic Escherichia coli-infected T84 cells inhibits signal transducer and activator of transcription 1 activation by gamma interferon. *Infection and immunity* **2006**, *74* (3), 1809-1818.

(237) Maphalla, L. Functionalisation of green synthesised gold nanoparticles (AuNPs) with biotinylated polyclonal specific an-tibodies and its application in an immunoassay for the detection of waterborne *Escherichia coli*. Masters thesis, University of Johannesburg, 2021.

(238) Zhao, X.; Bhat, A.; O'Connor, C.; Curtin, J.; Singh, B.; Tian, F. Review of Detection Limits for Various Techniques for Bacterial Detection in Food Samples. *Nanomater.* **2024**, *14*, 855. DOI: https://doi.org/10.3390/nano14100855.

(239) Gill, A. The Importance of Bacterial Culture to Food Microbiology in the Age of Genomics. *Front. Microbiol.* **2017**, *8*, 777. DOI: doi: 10.3389/fmicb.2017.00777.

(240) Wen, J.; Zhu, Y.; Liu, J.; He, D. Smartphone-based surface plasmon resonance sensing platform for rapid detection of bacteria. *RSC Adv.* **2022**, *12*, 13045-13051.

(241) Nnachi, R. C.; Sui, N.; Ke, B.; Luo, Z.; Bhalla, N.; He, D.; Yang, Z. Biosensors for rapid detection of bacterial pathogens in water, food and environment. *Environ. Int.* **2022**, *166*, 107357.

(242) Zhang, R.; Lan, L.; Shi, H. Sublethal injury and recovery of *Escherichia coli* O157: H7 after freezing and thawing. *Food Control* **2021**, *120*, 107488.

(243) Chen, S.; Li, X.; Wang, Y.; Zeng, J.; Ye, C. L. X.; Guo, L.; Zhang, S.; Yu, X., I. Induction of *Escherichia Coli* into a VBNC State through Chlorination/Chloramination and Differences in Characteristics of the Bacterium between States. *Water Res.* **2018**, *142*, 279-288.

(244) Chen, P.; Tran, N. T.; Wen, X.; Xiong, Q.; Liedberg, B. Inflection point of the localized surface plasmon resonance peak: a general method to improve the sensitivity. *ACS sensors* **2017**, *2* (2), 235-242.

Appendix A

Appendix A contains ultraviolet-visible (UV-vis) spectra that were excluded from the main thesis for brevity and/or ease of reading. Where necessary, they were referred to in the main bodies of text.

A.1 Controls and Background Spectra

The following section contains spectra pertaining to controls and UV-vis spectra used for background analysis/correction for spectral analysis.

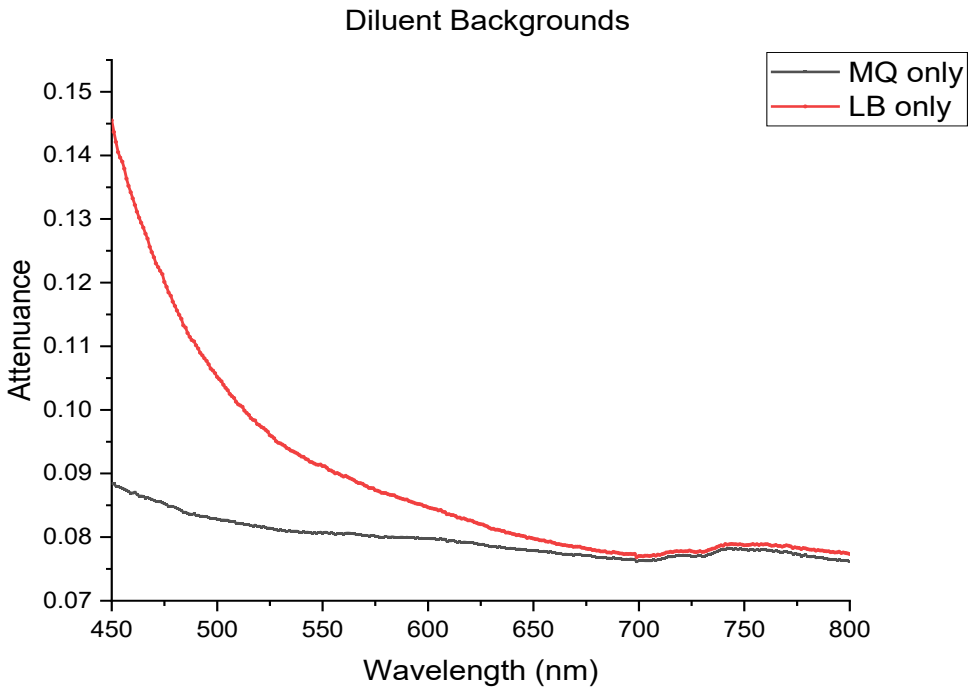

Figure 1: UV-vis spectra of the diluents (MQ and LB) used to in experimental assays. Spectrum of MQ in black and LB broth shown in red.

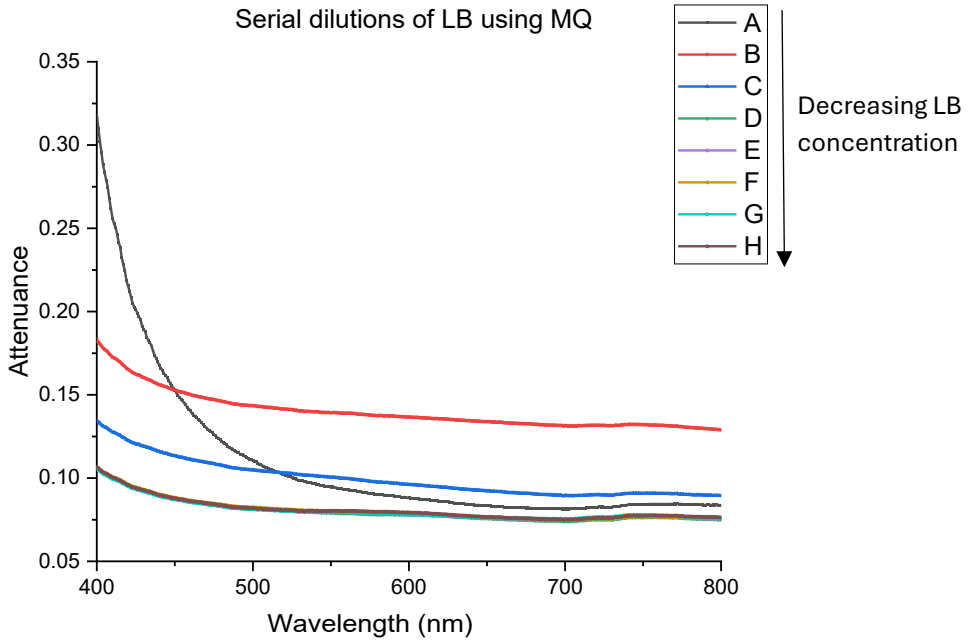

Figure 2: UV-vis spectra of LB, serially diluted with MQ. A contains LB only, whilst B – H are 10-fold serial dilutions of the LB, performed in the same manner as all other assay serial dilutions were performed to mimic the ratio of LB:MQ.

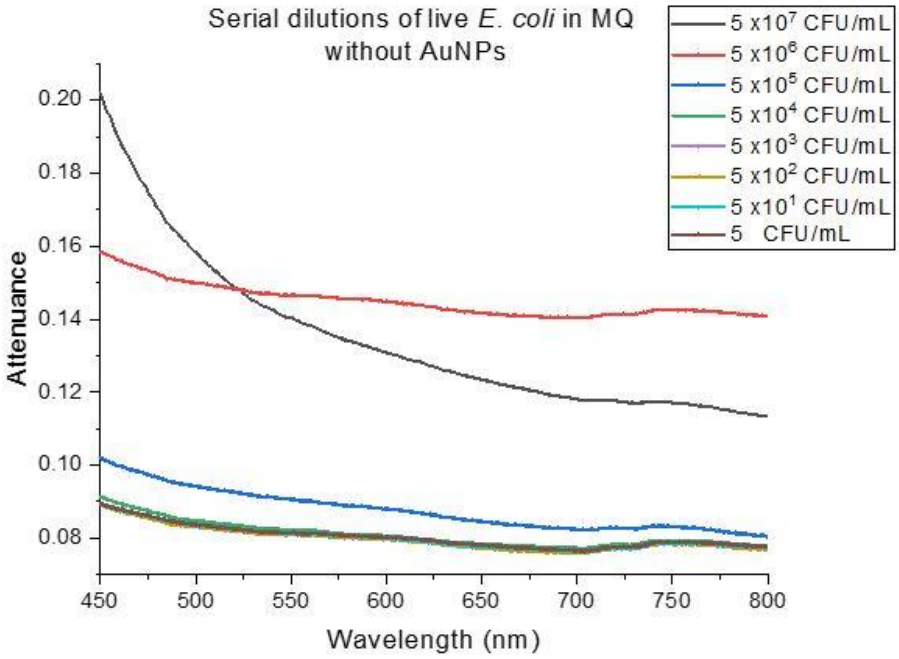

Figure 3: UV-vis spectra of live *E. coli* serially diluted with MQ, without the addition of AuNPs. The 10-fold serial dilutions and preparation were identical to all AuNP and bacterial assays.

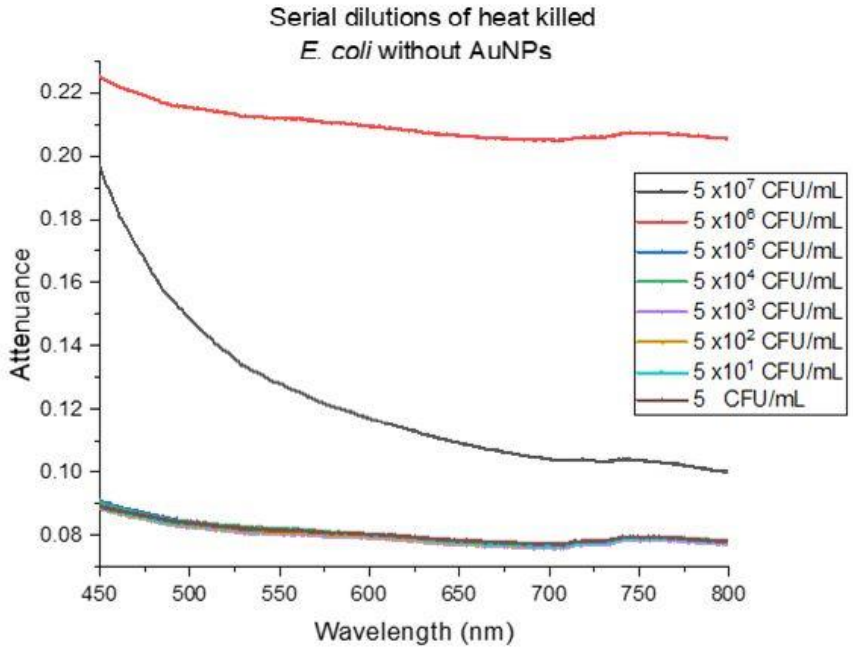

Figure 4: UV-vis spectra of 10-fold serial dilutions of heat-killed *E. coli* in MQ, without the addition of AuNPs, and measured immediately post assay.

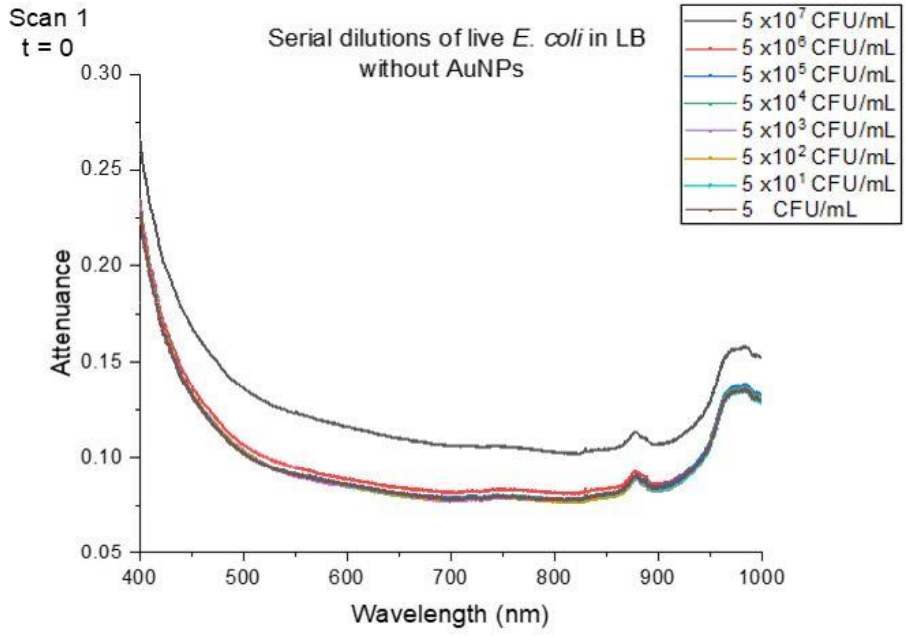

Figure 5: UV-vis spectra of 10-fold serial dilutions of live *E. coli* in LB, without the addition of AuNPs, and measured immediately post assay.

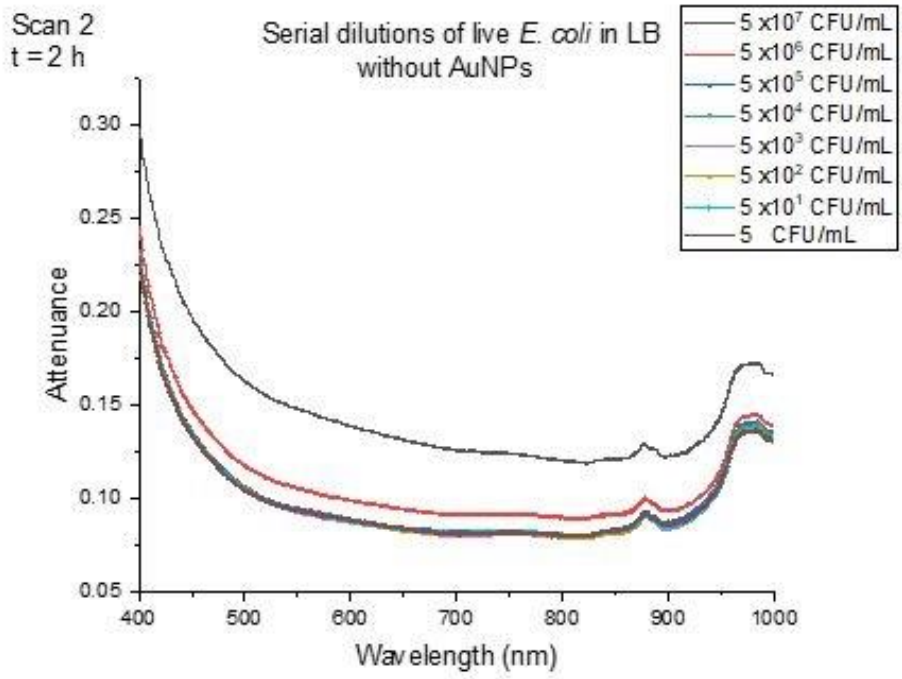

Figure 6: UV-vis spectra of 10-fold serial dilutions of live *E. coli,* diluted in LB, without the addition of AuNPs, and measured after 2 h of incubation at ambient temperature.

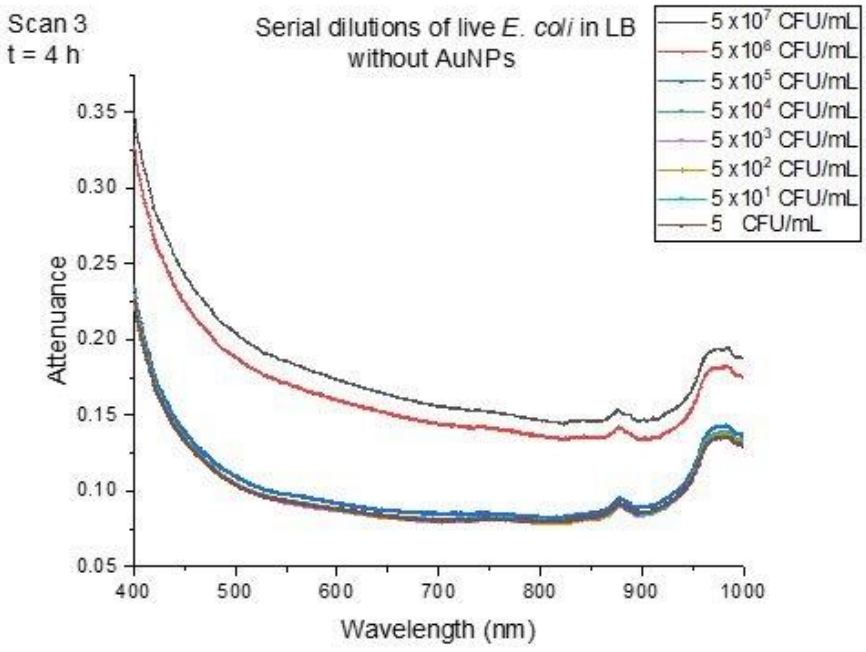

Figure 7: UV-vis spectra of 10-fold serial dilutions of live *E. coli,* diluted in LB, without the addition of AuNPs, and measured after 4 h of incubation at ambient temperature.

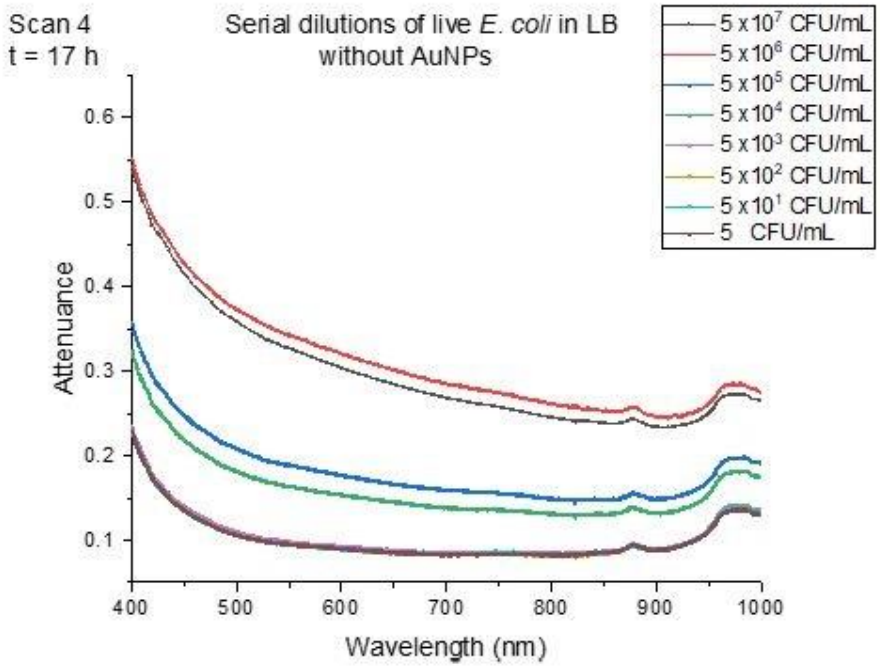

Figure 8: UV-vis spectra of 10-fold serial dilutions of live *E. coli,* diluted in LB, without the addition of AuNPs, and measured after 17 h of incubation at ambient temperature (overnight incubation).

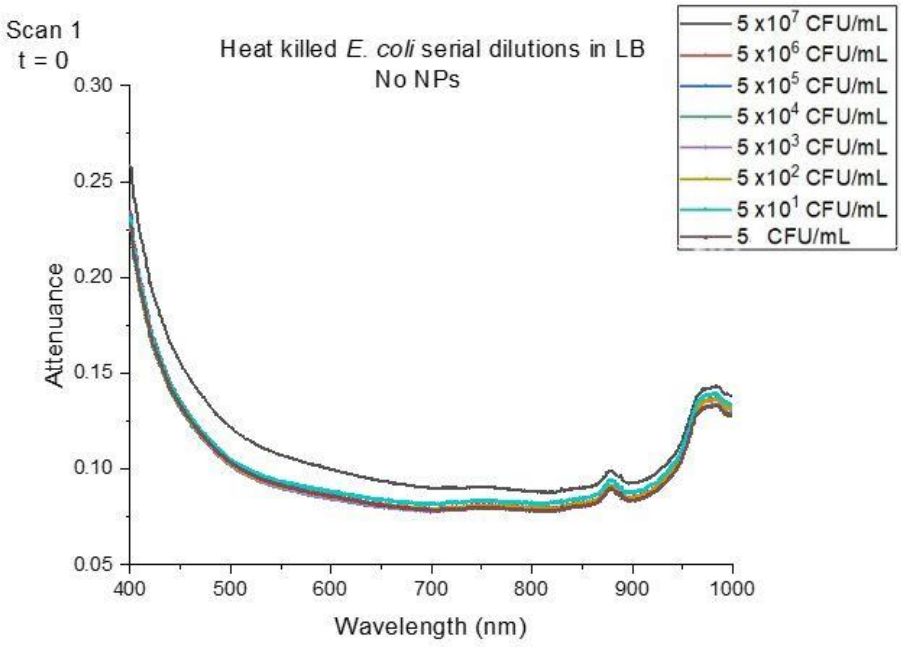

Figure 9: UV-vis spectra of 10-fold serial dilutions of heat-killed *E. coli* in LB, without the addition of AuNPs, and measured immediately post assay.

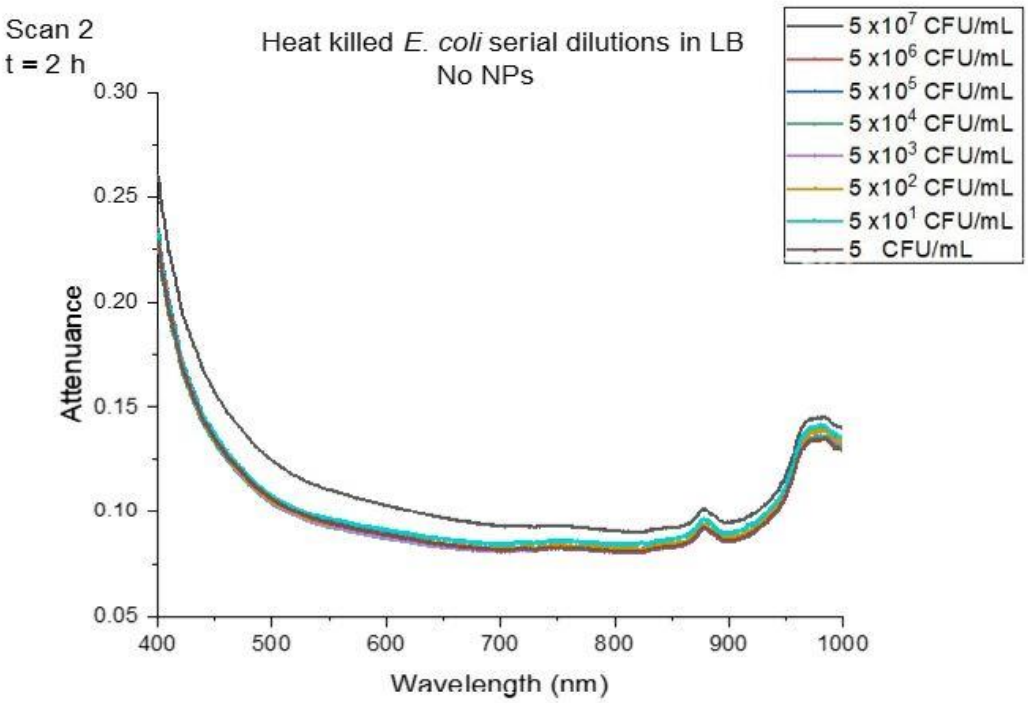

Figure 10: UV-vis spectra of 10-fold serial dilutions of heat-killed *E. coli* in LB, without the addition of AuNPs, and measured after 2 h of incubation at ambient temperature.

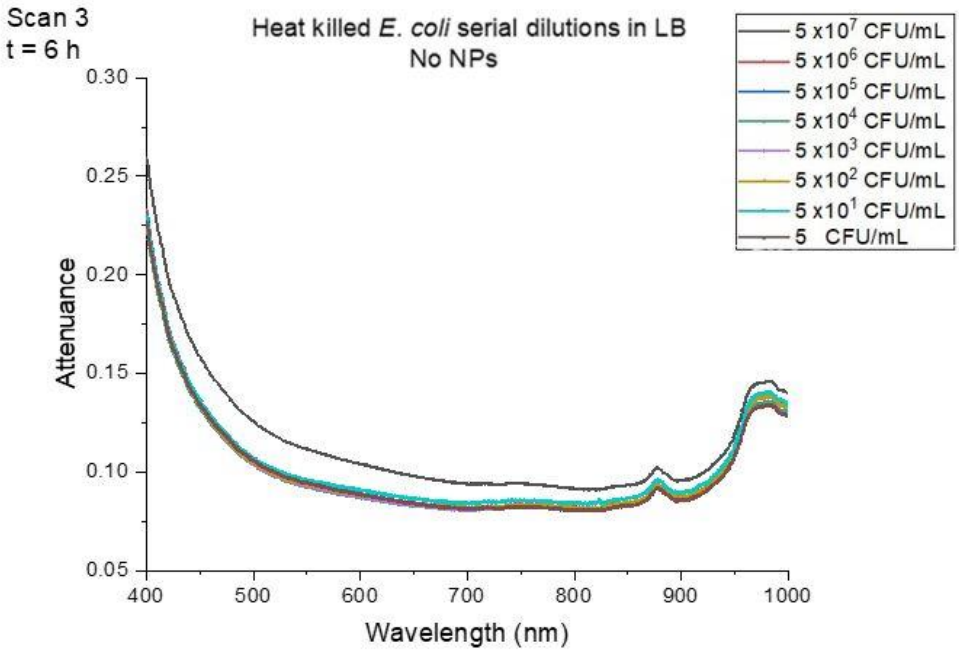

Figure 11: UV-vis spectra of 10-fold serial dilutions of heat-killed *E. coli* in LB, without the addition of AuNPs, and measured after 6 h of incubation at ambient temperature.

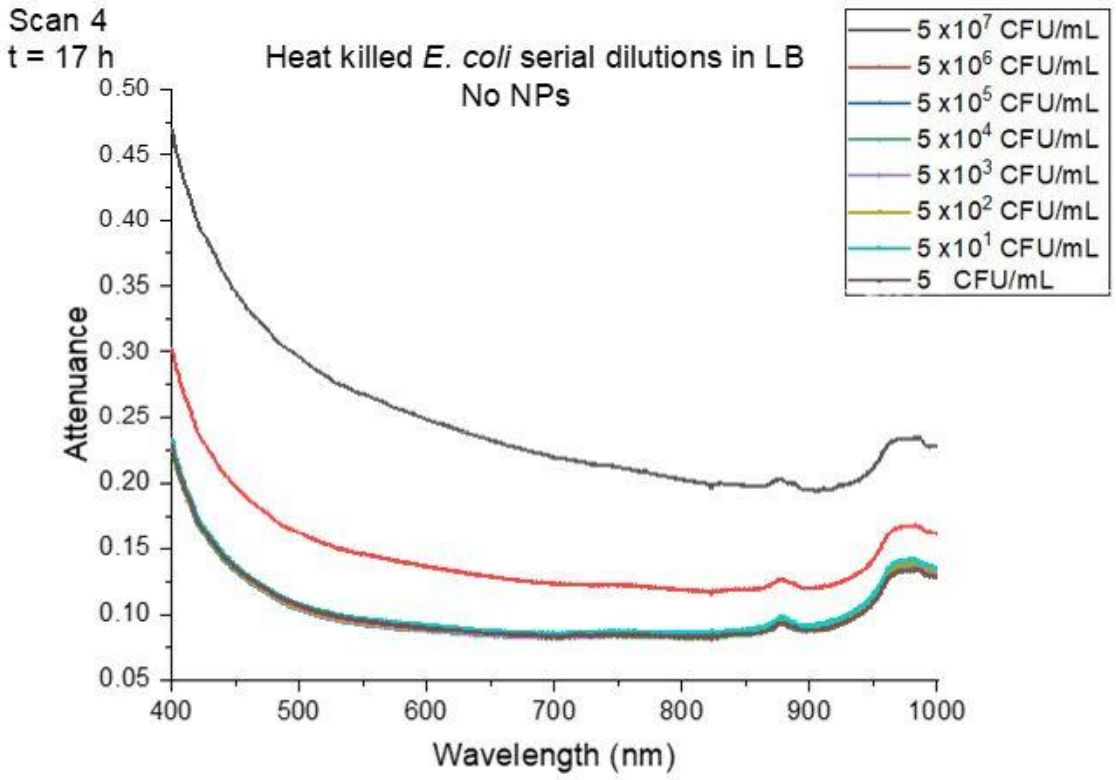

Figure 12: UV-vis spectra of 10-fold serial dilutions of heat-killed *E. coli* in LB, without the addition of AuNPs, and measured after 17 h of incubation at ambient temperature (overnight incubation).

A.2 Spectra from Live *E. coli* and As-synthesized Citrate AuNP Assays

The following section contains UV-vis spectra pertaining to the assays from live *E. coli* and as-synthesized AuNPs, taken sequentially over time, that were excluded from the main thesis for brevity and/or ease of reading. Where necessary, they were referred to in the main bodies of text.

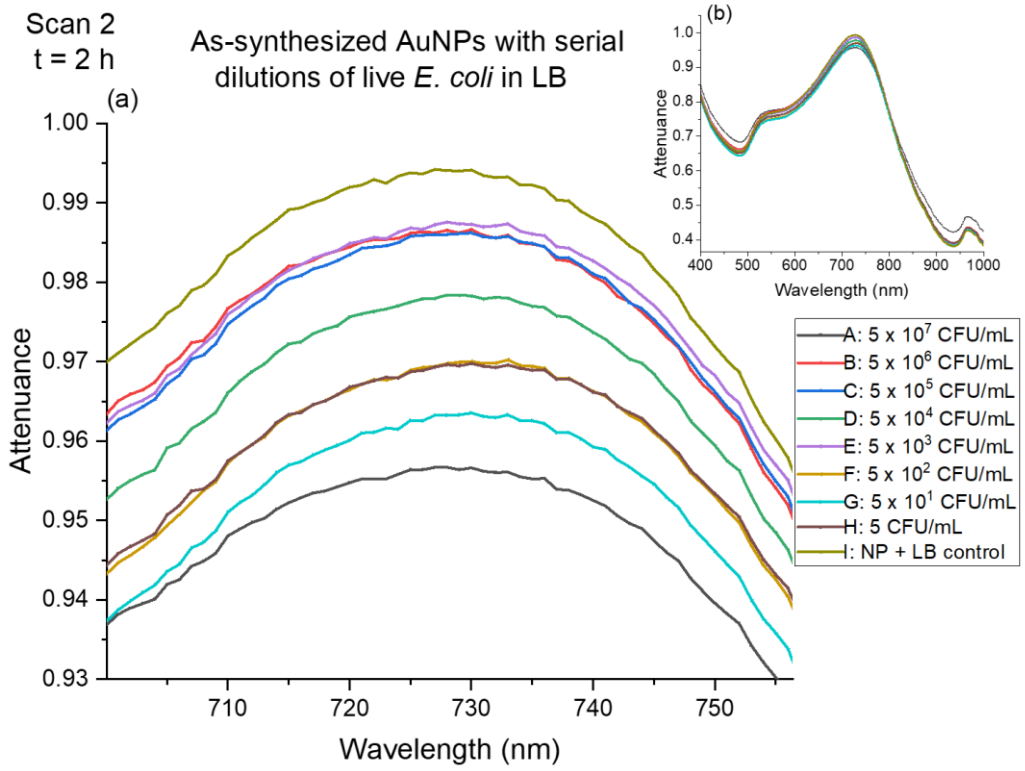

Figure 13: UV-vis spectra of as-synthesized citrate AuNPs assayed with 10-fold serial dilutions of live *E. coli* in LB. Concentrations of *E. coli* range from 5 x 10^7 – 5 cells/mL, t = 2 h. (a) shows a close-up region of the relative positions of the red-shifted plasmon peaks, and inset (b) shows the spectra over the entire range of monitored wavelengths (nm).

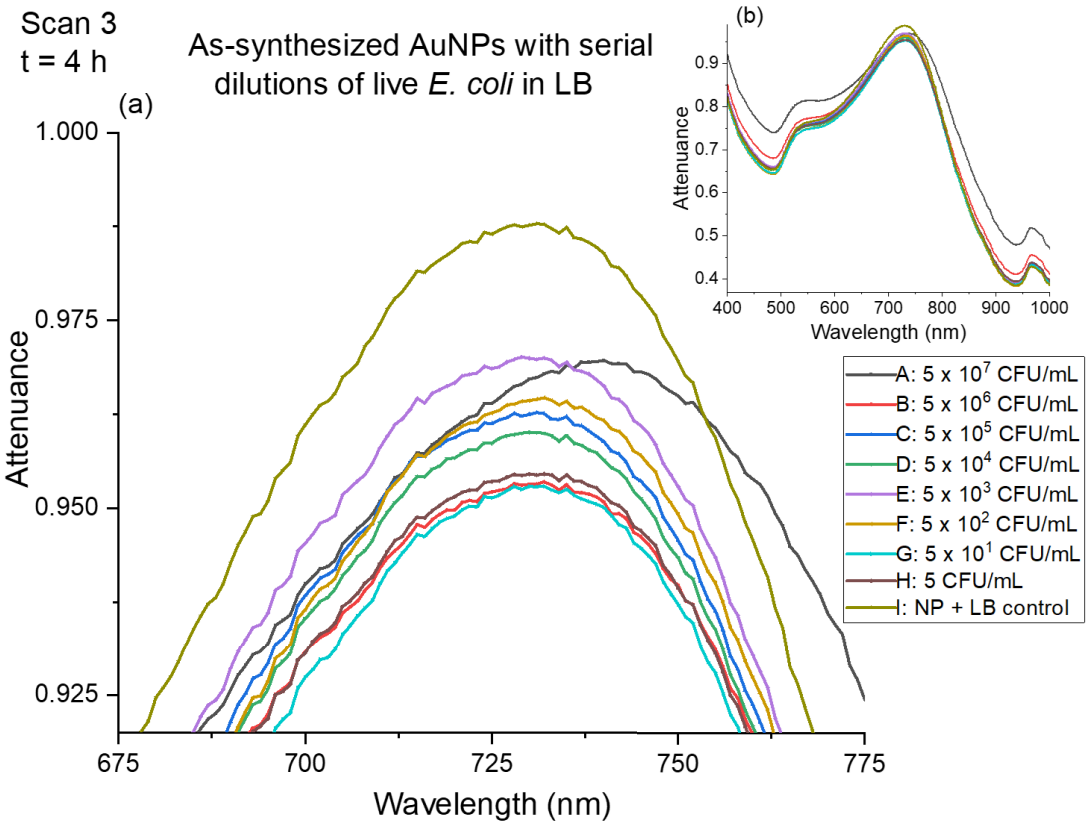

Figure 14: UV-vis spectra of as-synthesized citrate AuNPs assayed with 10-fold serial dilutions of live *E. coli* in LB. Concentrations of *E. coli* range from 5 x 10^7 – 5 cells/mL, t = 4 h. (a) shows a close-up region of the relative positions of the red-shifted plasmon peaks, and inset (b) shows the spectra over the entire range of monitored wavelengths (nm).

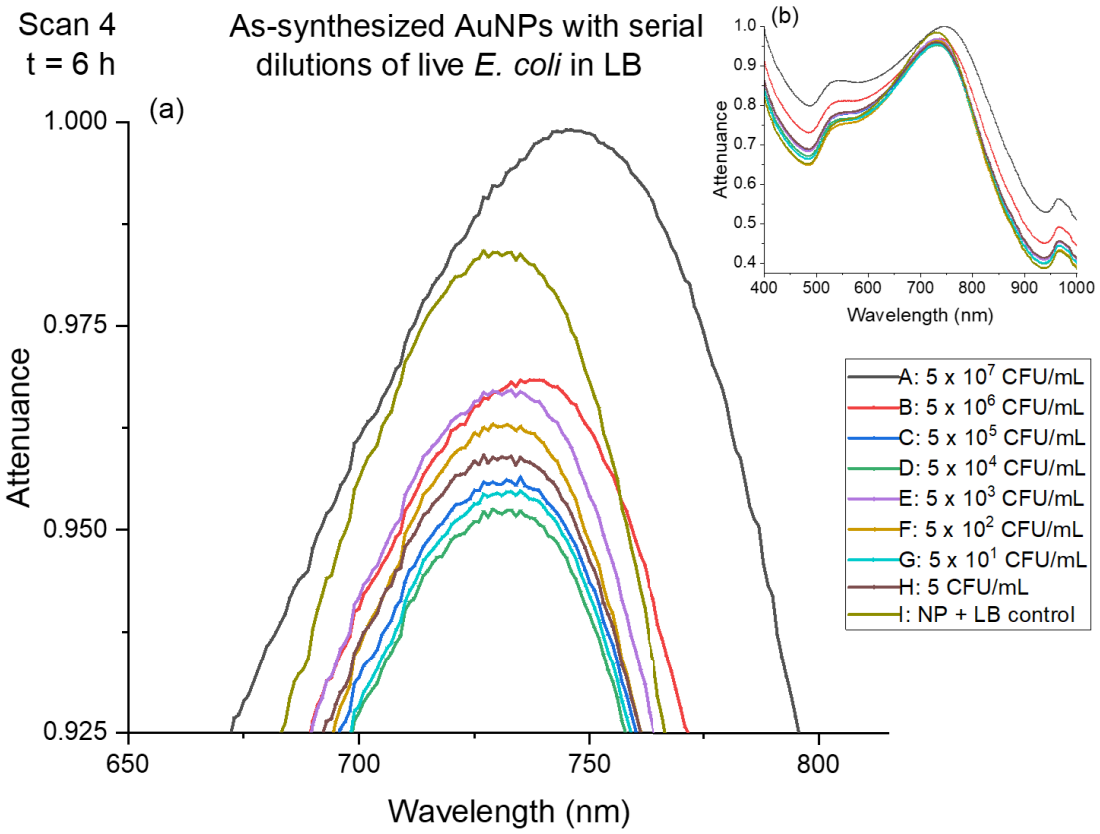

Figure 15: UV-vis spectra of as-synthesized citrate AuNPs assayed with 10-fold serial dilutions of live *E. coli* in LB. Concentrations of *E. coli* range from 5 x 10^7 – 5 cells/mL, t = 6 h. (a) shows a close-up region of the relative positions of the red-shifted plasmon peaks, and inset (b) shows the spectra over the entire range of monitored wavelengths (nm).

A.3 Spectra from Live *E. coli* and Washed Citrate AuNPs Time Point Assays

The following section contains UV-vis spectra pertaining to the assays from live *E. coli* and as-synthesized AuNPs, taken sequentially over time, that were excluded from the main thesis for brevity and/or ease of reading. Where necessary, they were referred to in the main bodies of text.

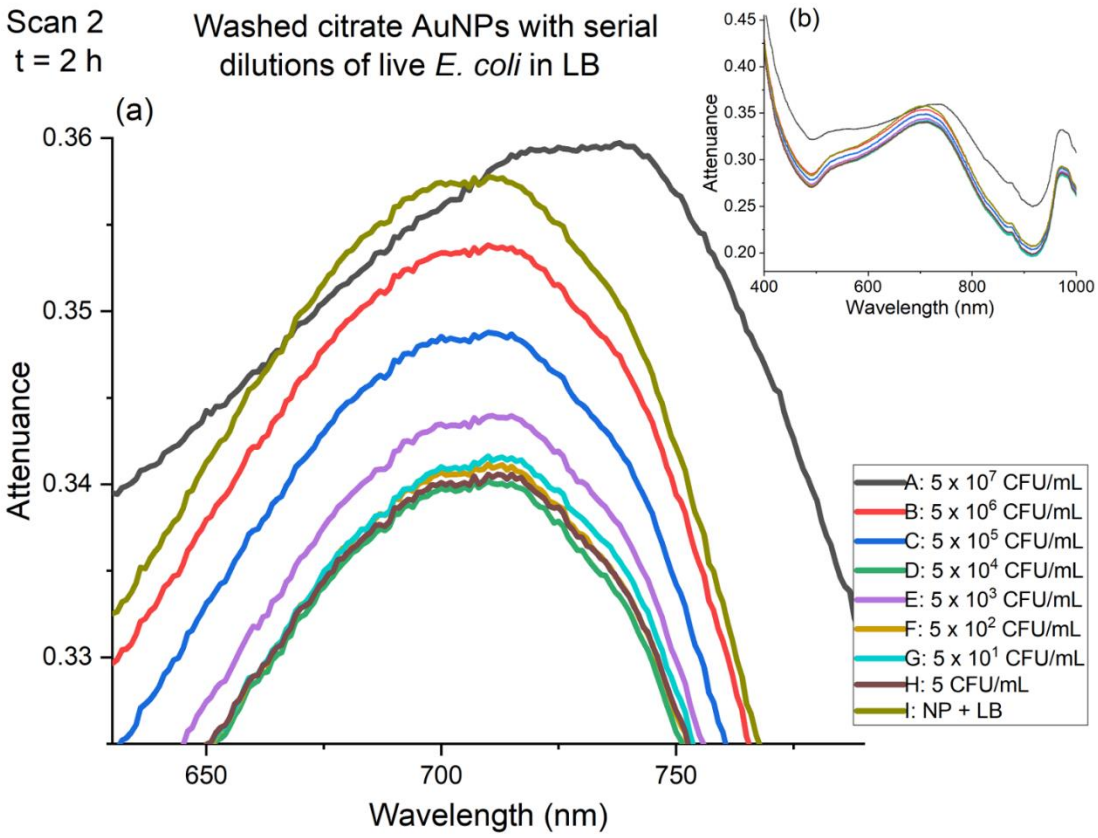

Figure 16: UV-vis spectra of washed citrate AuNPs assayed with 10-fold serial dilutions of live *E. coli* in LB. Concentrations of *E. coli* range from 5 x 10^7 – 5 cells/mL, t = 2 h. (a) shows a close-up region of the relative positions of the red-shifted plasmon peaks, and inset (b) shows the spectra over the entire range of monitored wavelengths (nm).

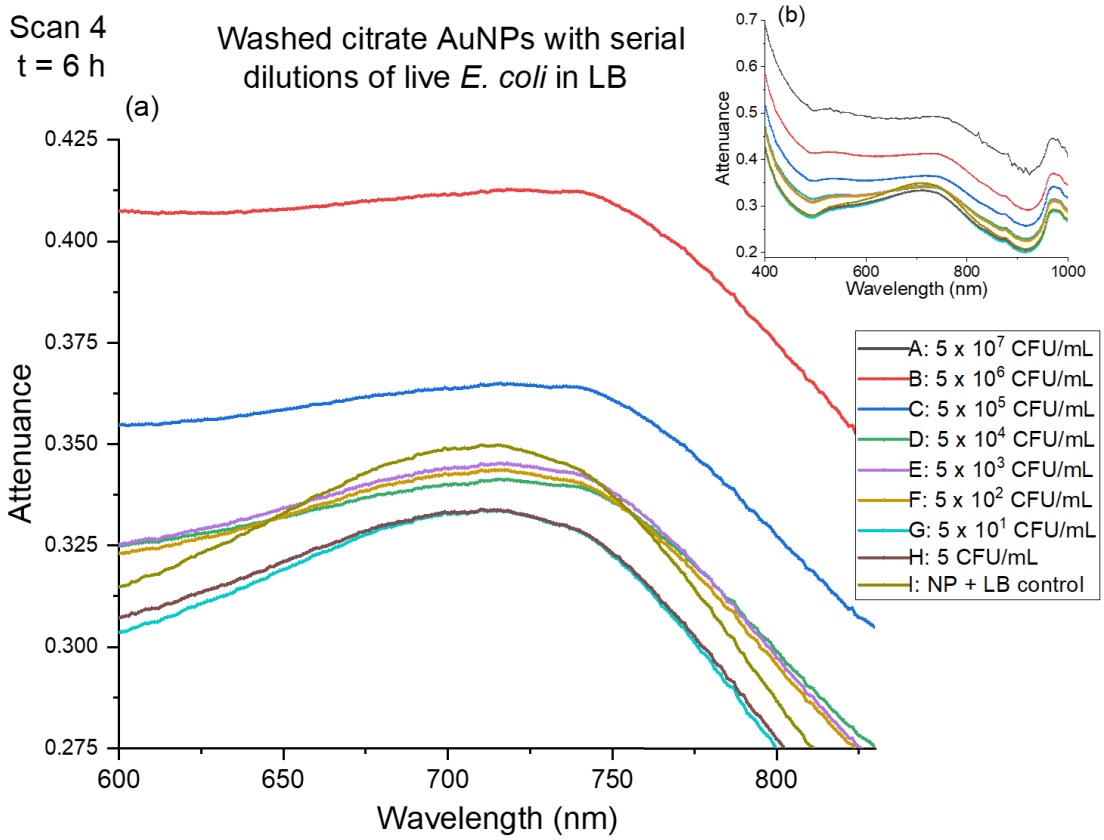

Figure 17: UV-vis spectra of washed citrate AuNPs assayed with 10-fold serial dilutions of live *E. coli* in LB. Concentrations of *E. coli* range from 5 x 10^7 – 5 cells/mL, t = 6 h. (a) shows a close-up region of the relative positions of the red-shifted plasmon peaks, and inset (b) shows the spectra over the entire range of monitored wavelengths (nm).

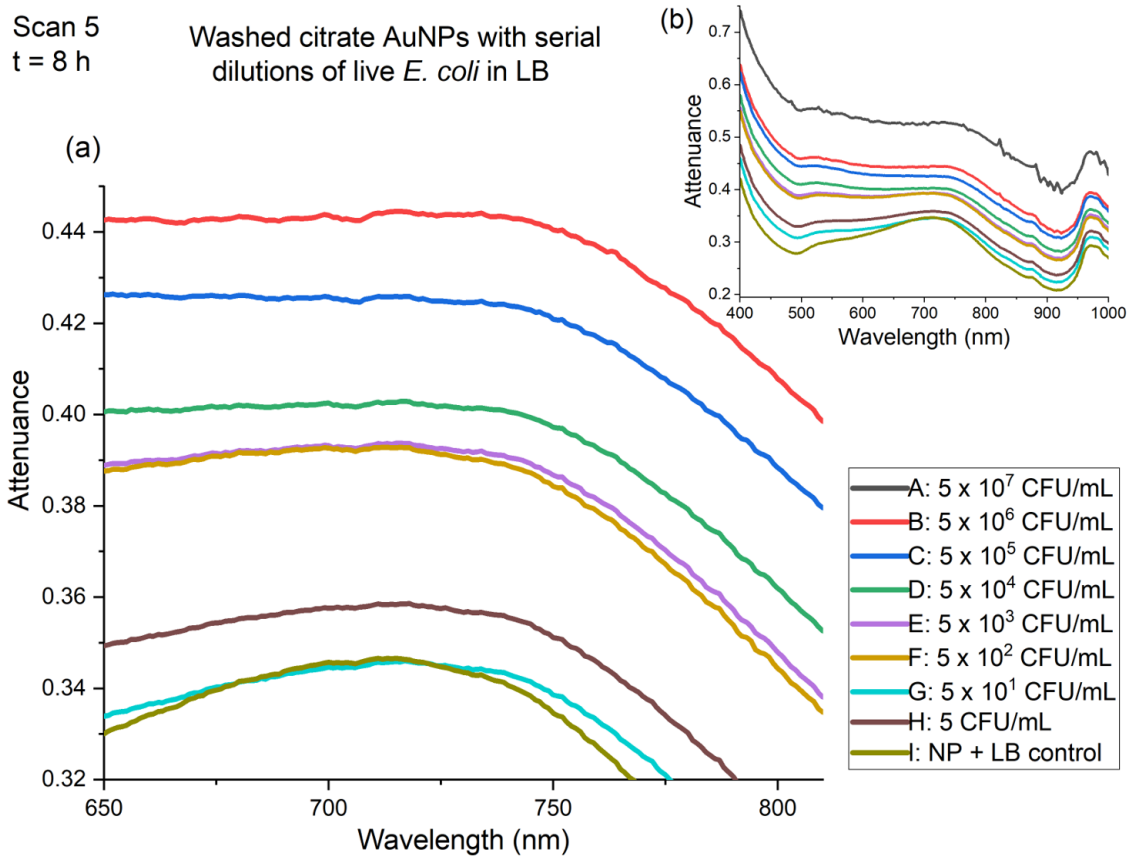

Figure 18: UV-vis spectra of washed citrate AuNPs assayed with 10-fold serial dilutions of live *E. coli* in LB. Concentrations of *E. coli* range from 5 x 10^7 – 5 cells/mL, t = 8 h. (a) shows a close-up region of the relative positions of the red-shifted plasmon peaks, and inset (b) shows the spectra over the entire range of monitored wavelengths (nm).

A.4 Spectra of Live *E. coli* and As-synthesized Citrate AuNP Assays at Elevated Temperature (37°C)

The following section contains UV-vis spectra pertaining to the assays from live *E. coli* and as-synthesized AuNPs, taken sequentially over time at 37°C, that were excluded from the main thesis for brevity and/or ease of reading. Where necessary, they were referred to in the main bodies of text.

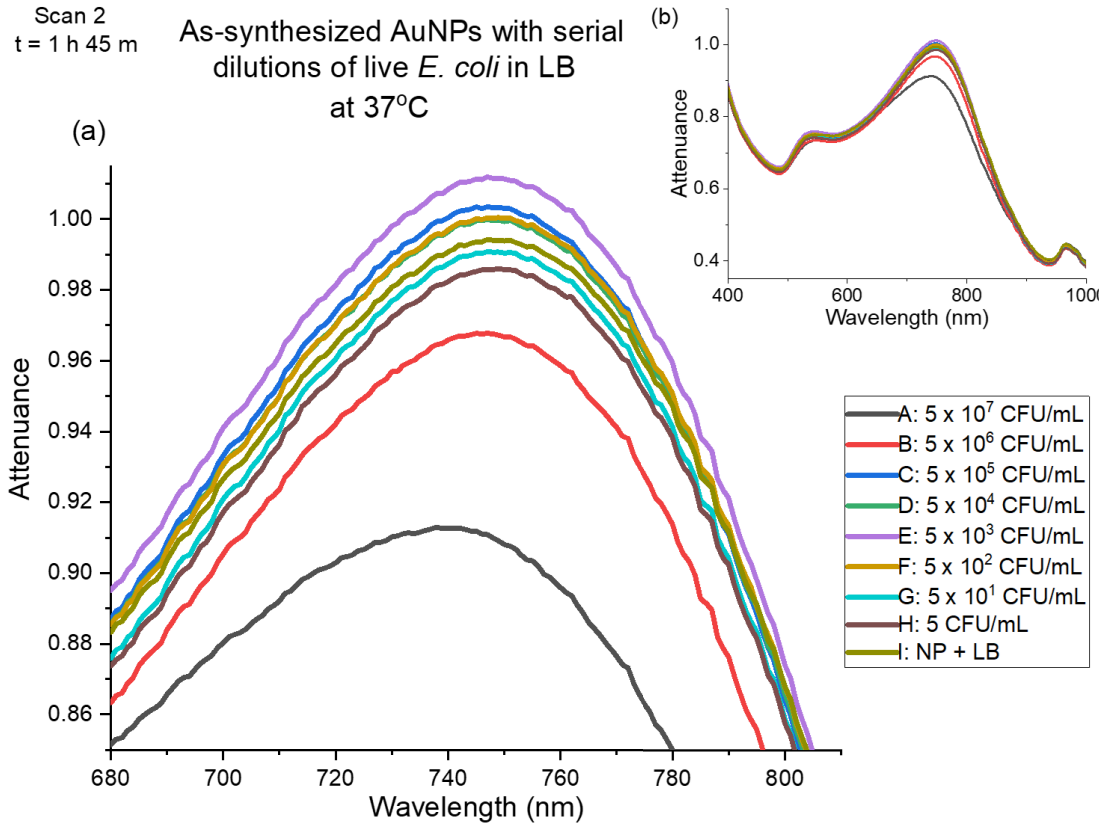

Figure 19: UV-vis spectra of as-synthesized AuNPs assayed with 10-fold serial dilutions of live *E. coli* in LB at 37°C, t = 1 h, 45 min. (a) shows a close-up region of the relative positions of the red-shifted plasmon peaks, and inset (b) shows the spectra over the entire range of monitored wavelengths (nm).

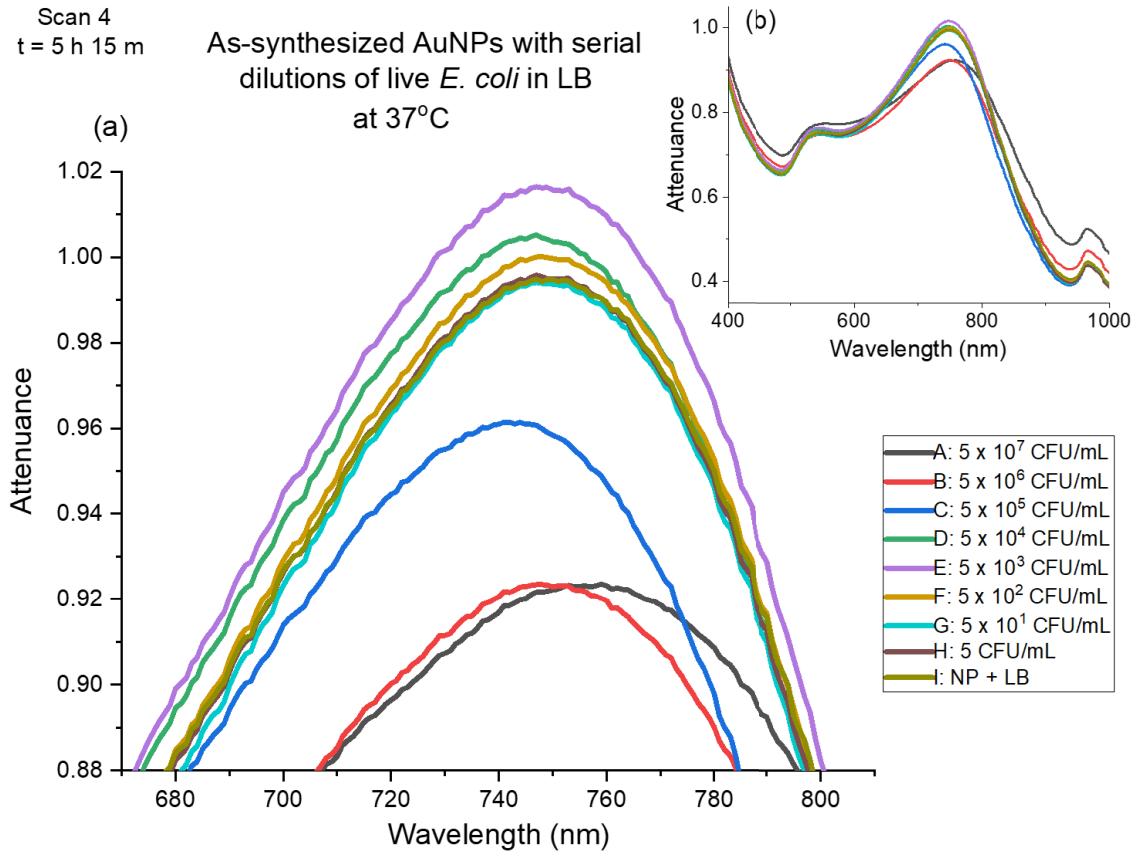

Figure 20: UV-vis spectra of as-synthesized AuNPs assayed with 10-fold serial dilutions of live *E. coli* in LB at 37°C, t = 5 h, 15 min. (a) shows a close-up region of the relative positions of the red-shifted plasmon peaks, and inset (b) shows the spectra over the entire range of monitored wavelengths (nm).

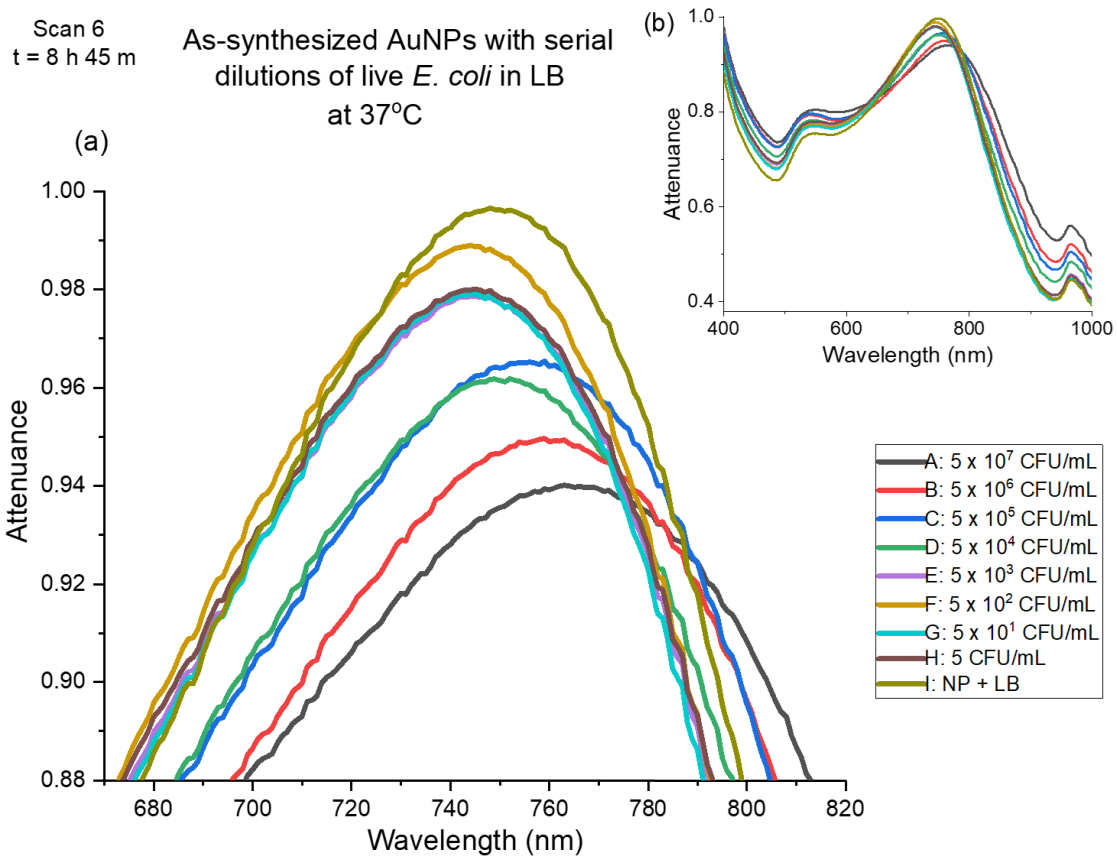

Figure 21: UV-vis spectra of as-synthesized AuNPs assayed with 10-fold serial dilutions of live *E. coli* in LB at 37°C, t = 8 h, 45 min. (a) shows a close-up region of the relative positions of the red-shifted plasmon peaks, and inset (b) shows the spectra over the entire range of monitored wavelengths (nm).

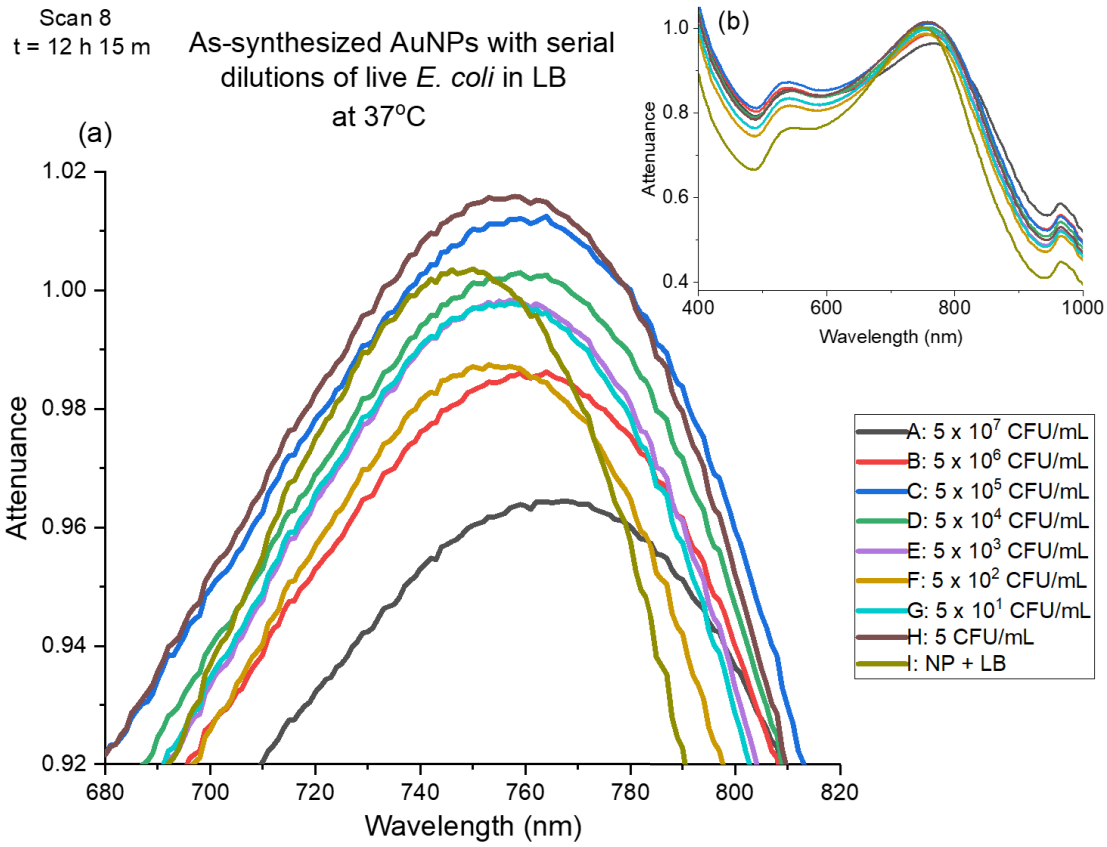

Figure 22: UV-vis spectra of as-synthesized AuNPs assayed with 10-fold serial dilutions of live *E. coli* in LB at 37°C, t = 12 h, 15 min. (a) shows a close-up region of the relative positions of the red-shifted plasmon peaks, and inset (b) shows the spectra over the entire range of monitored wavelengths (nm).

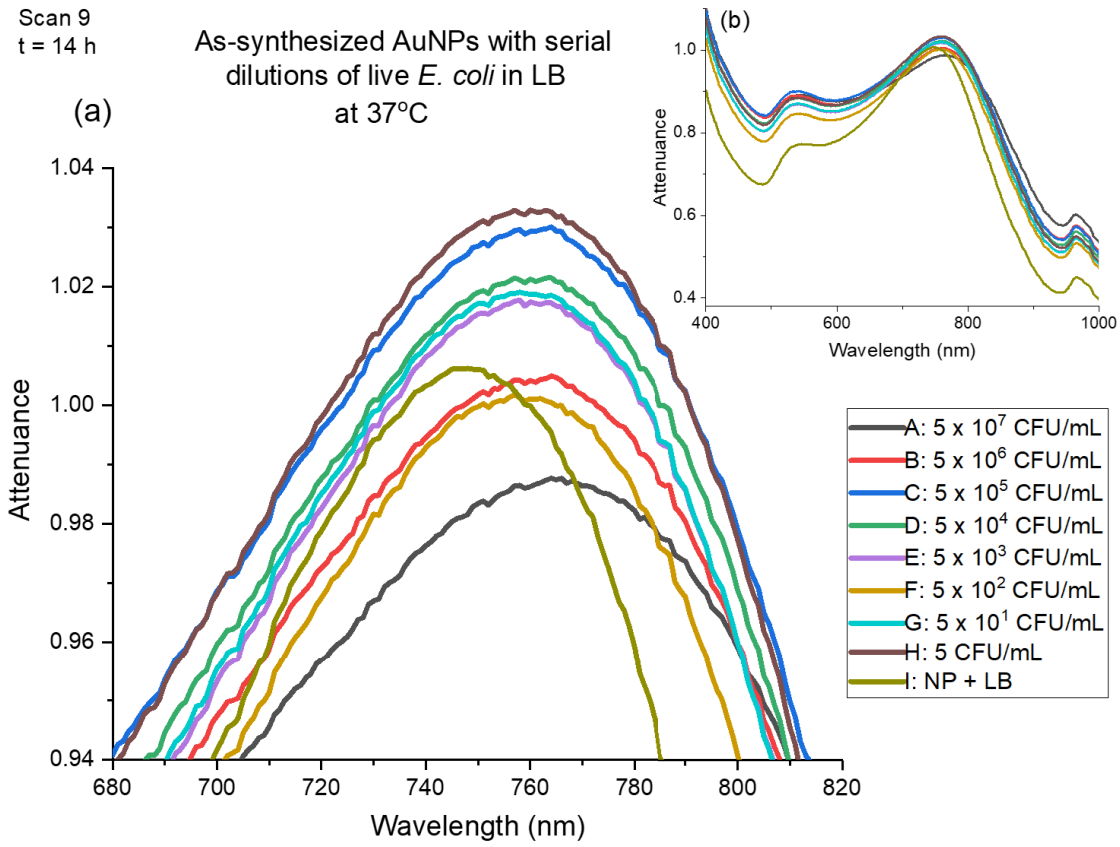

Figure 23: UV-vis spectra of as-synthesized AuNPs assayed with 10-fold serial dilutions of live *E. coli* in LB at 37°C, t = 14 h. (a) shows a close-up region of the relative positions of the red-shifted plasmon peaks, and inset (b) shows the spectra over the entire range of monitored wavelengths (nm).

A.5 Spectra of Live *E. coli* and Washed Citrate AuNPs at Elevated Temperatures (37**°C**)

The following section contains UV-vis spectra pertaining to the assays from live *E. coli* and washed AuNPs, taken sequentially over time at 37°C, that were excluded from the main thesis for brevity and/or ease of reading. Where necessary, they were referred to in the main bodies of text.

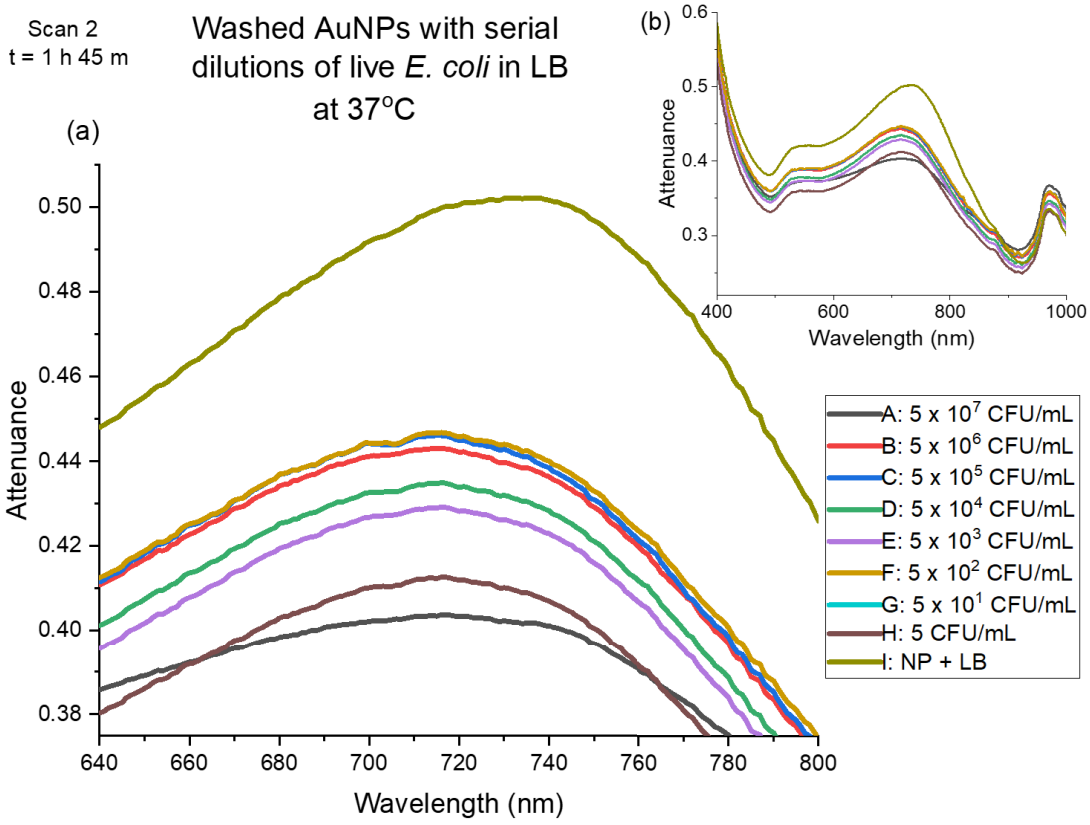

Figure 24: UV-vis spectra of washed AuNPs assayed with 10-fold serial dilutions of live *E. coli* in LB at 37°C, t = 1 h, 45 min. (a) shows a close-up region of the relative positions of the red-shifted plasmon peaks, and inset (b) shows the spectra over the entire range of monitored wavelengths (nm).

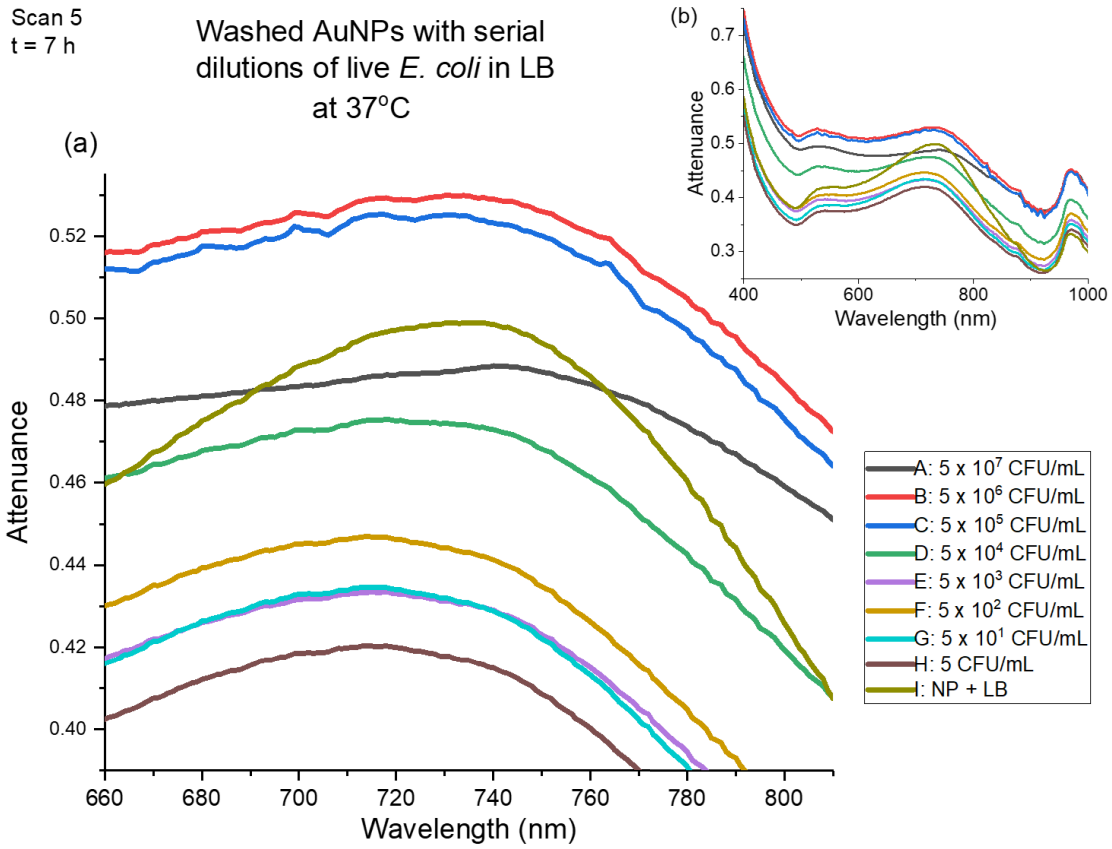

Figure 25: UV-vis spectra of washed AuNPs assayed with 10-fold serial dilutions of live *E. coli* in LB at 37°C, t = 7 h. (a) shows a close-up region of the relative positions of the red-shifted plasmon peaks, and inset (b) shows the spectra over the entire range of monitored wavelengths (nm).

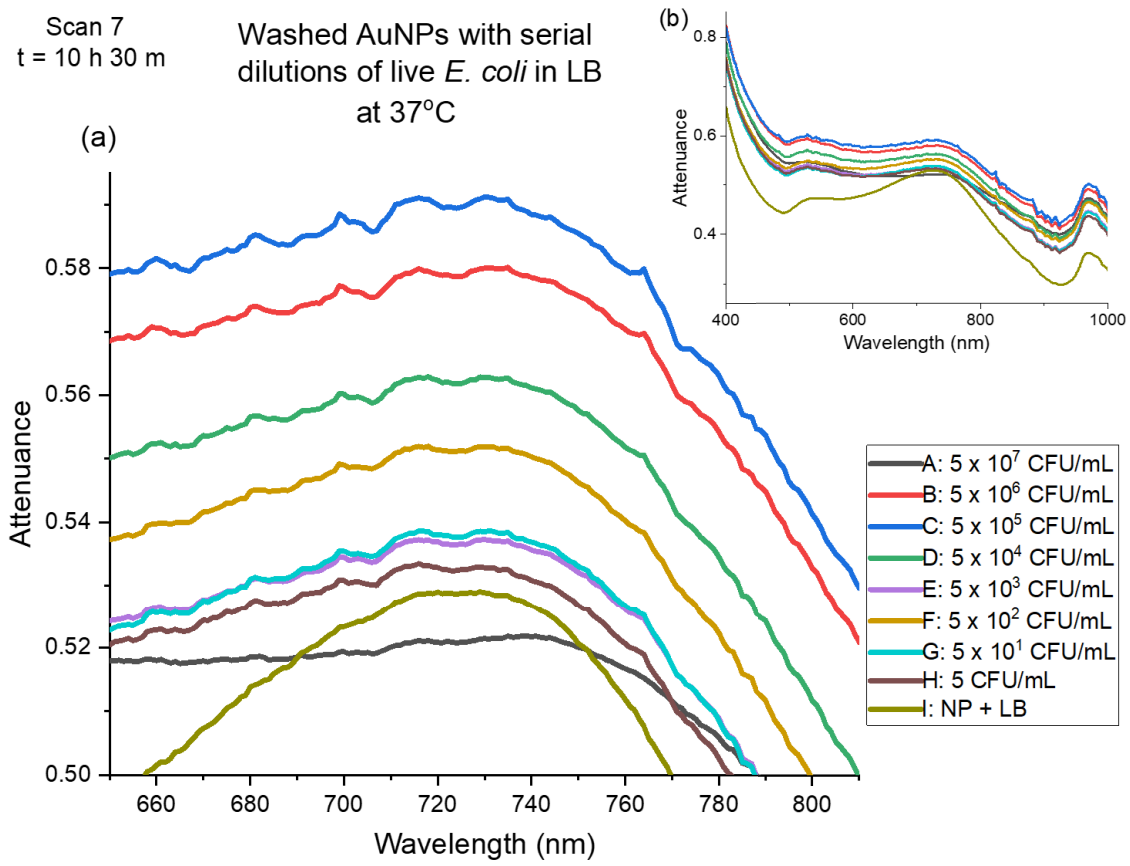

Figure 26: UV-vis spectra of washed AuNPs assayed with 10-fold serial dilutions of live *E. coli* in LB at 37°C, t = 10 h, 30 min. (a) shows a close-up region of the relative positions of the red-shifted plasmon peaks, and inset (b) shows the spectra over the entire range of monitored wavelengths (nm).

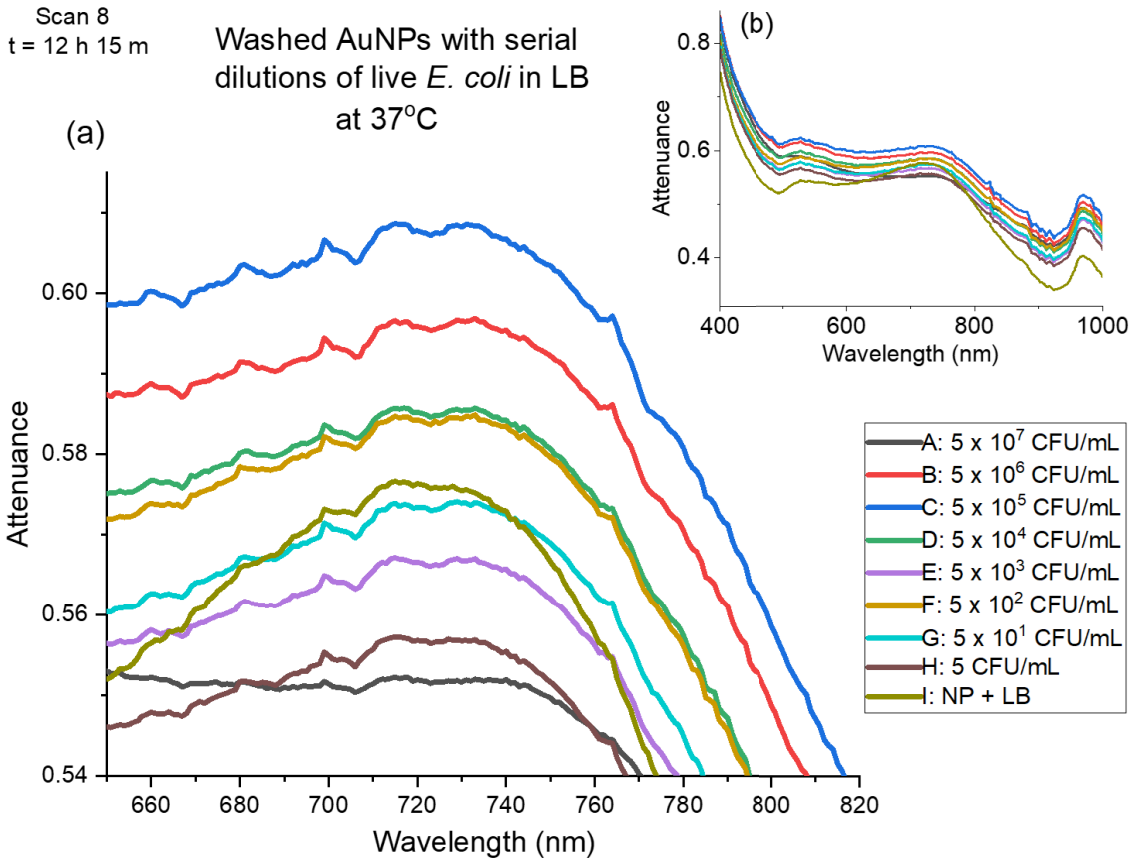

Figure 27: UV-vis spectra of washed AuNPs assayed with 10-fold serial dilutions of live *E. coli* in LB at 37**°C**, t = 12 h, 15 min. (a) shows a close-up region of the relative positions of the red-shifted plasmon peaks, and inset (b) shows the spectra over the entire range of monitored wavelengths (nm).

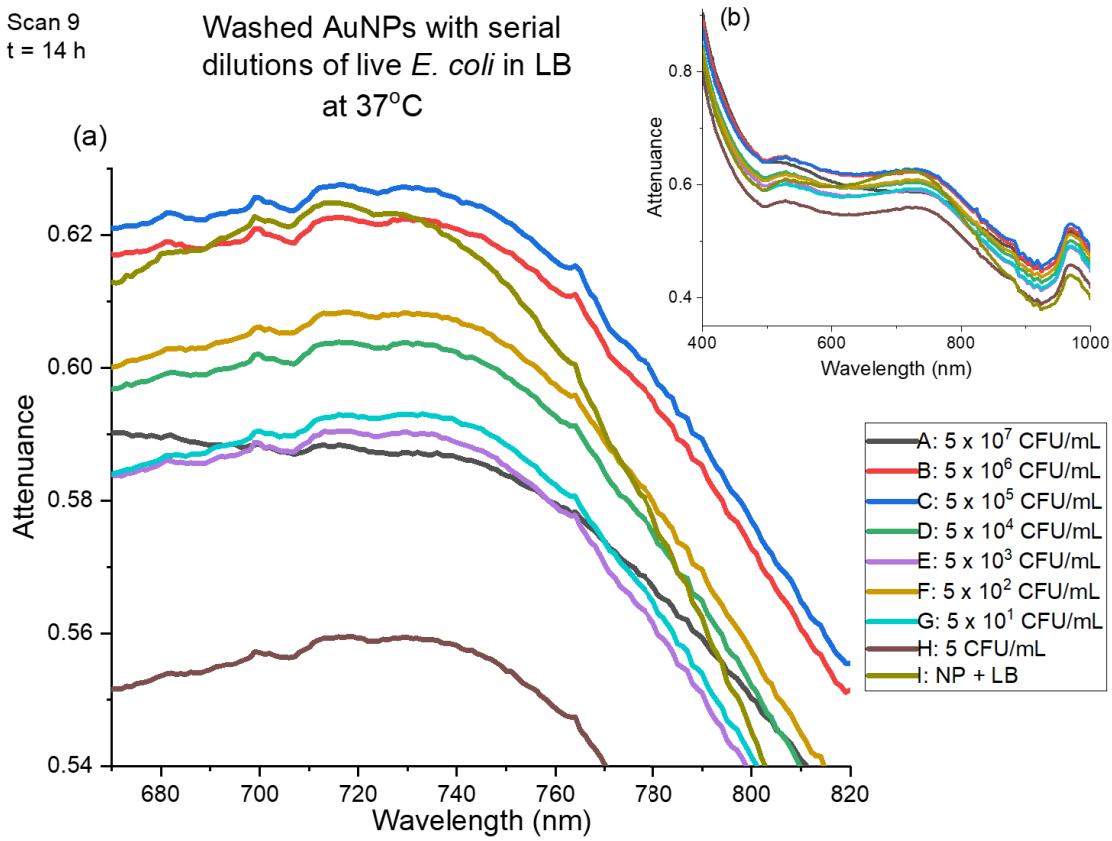

Figure 28: UV-vis spectra of washed AuNPs assayed with 10-fold serial dilutions of live *E. coli* in LB at 37**°C**, t = 14 h. (a) shows a close-up region of the relative positions of the red-shifted plasmon peaks, and inset (b) shows the spectra over the entire range of monitored wavelengths (nm).

A.6 Spectra of Washed Citrate AuNPs and Heat Killed *E. coli* Assays at Elevated Temperatures (37°C)

The following section contains UV-vis spectra pertaining to the assays from heat-killed preparations of *E. coli* and washed AuNPs, taken sequentially over time at 37°C, that were excluded from the main thesis for brevity and/or ease of reading. Where necessary, they were referred to in the main bodies of text.

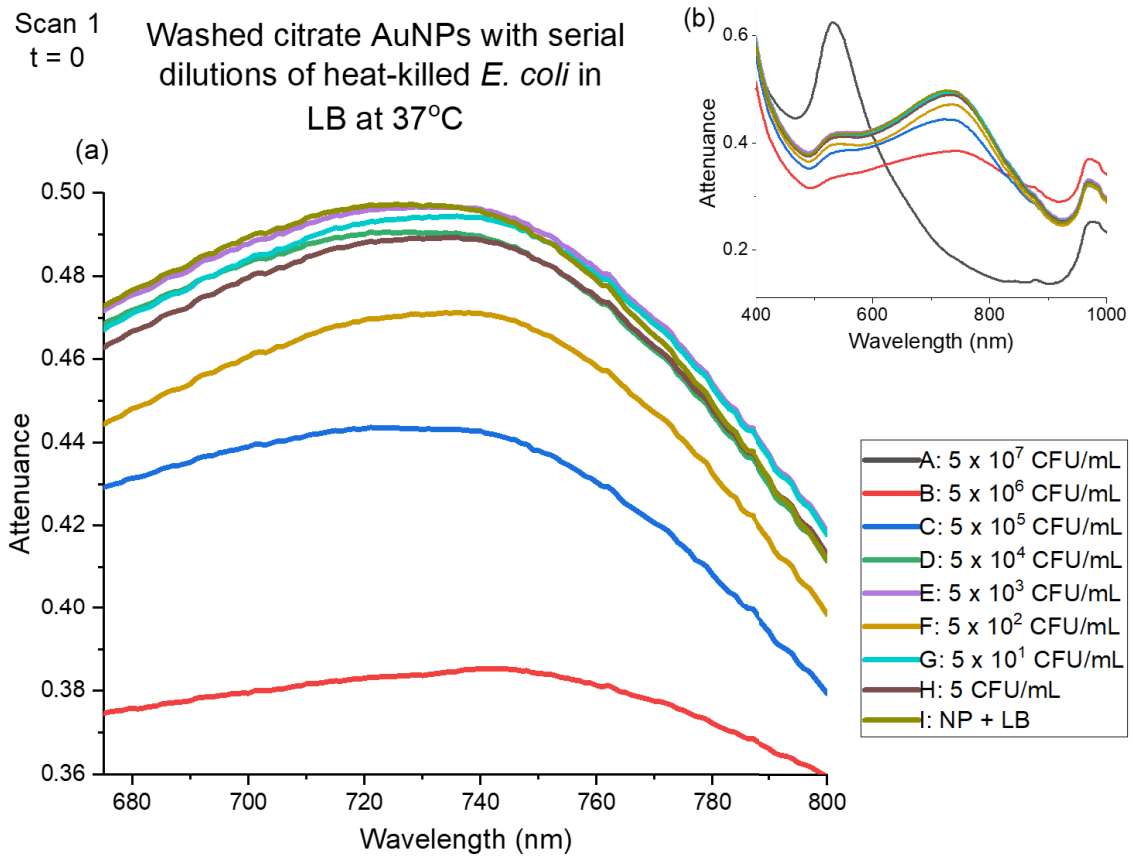

Figure 29: UV-vis spectra of washed AuNPs assayed with 10-fold serial dilutions of heat-killed *E. coli* in LB at 37°C, t = 0. (a) shows a close-up region of the relative positions of the red-shifted plasmon peaks, and inset (b) shows the spectra over the entire range of monitored wavelengths (nm).

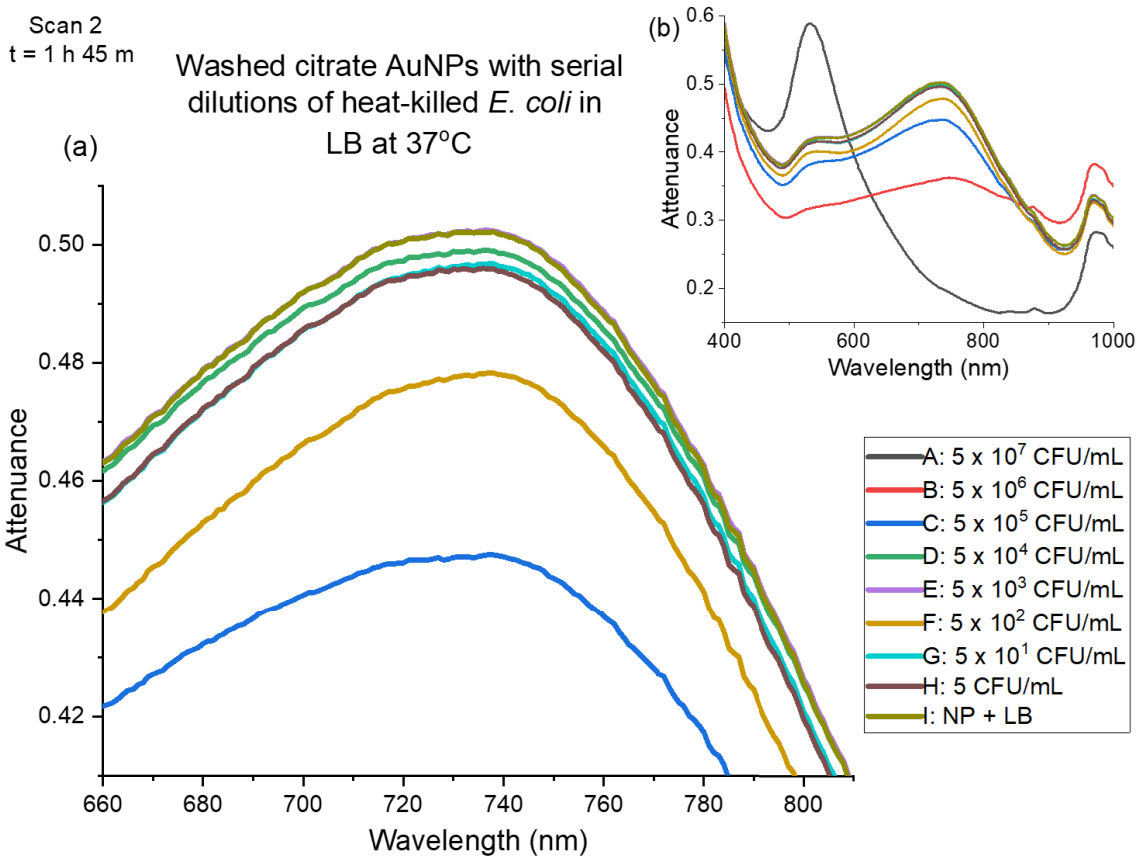

Figure 30: UV-vis spectra of washed AuNPs assayed with 10-fold serial dilutions of heat-killed *E. coli* in LB at 37°C, t = 1 h, 45 min. (a) shows a close-up region of the relative positions of the red-shifted plasmon peaks, and inset (b) shows the spectra over the entire range of monitored wavelengths (nm).

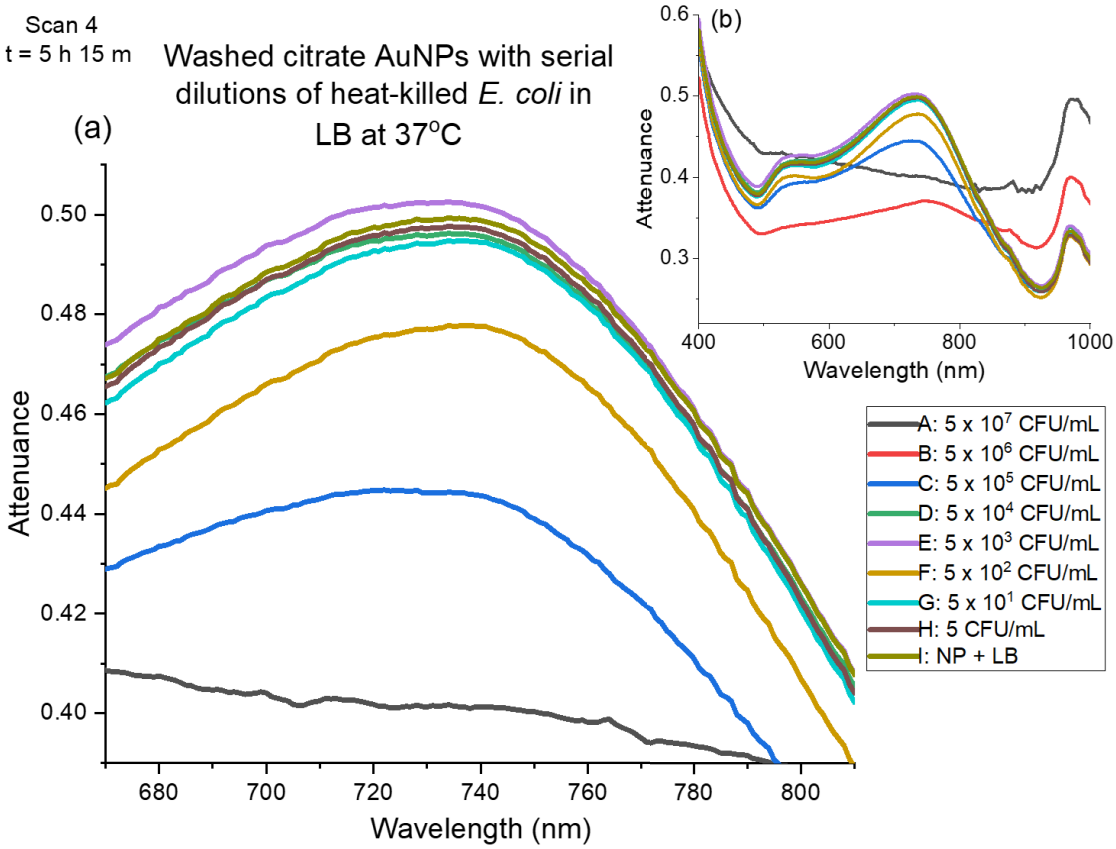

Figure 31: UV-vis spectra of washed AuNPs assayed with 10-fold serial dilutions of heat-killed *E. coli* in LB at 37°C, t = 5 h, 15 min. (a) shows a close-up region of the relative positions of the red-shifted plasmon peaks, and inset (b) shows the spectra over the entire range of monitored wavelengths (nm).

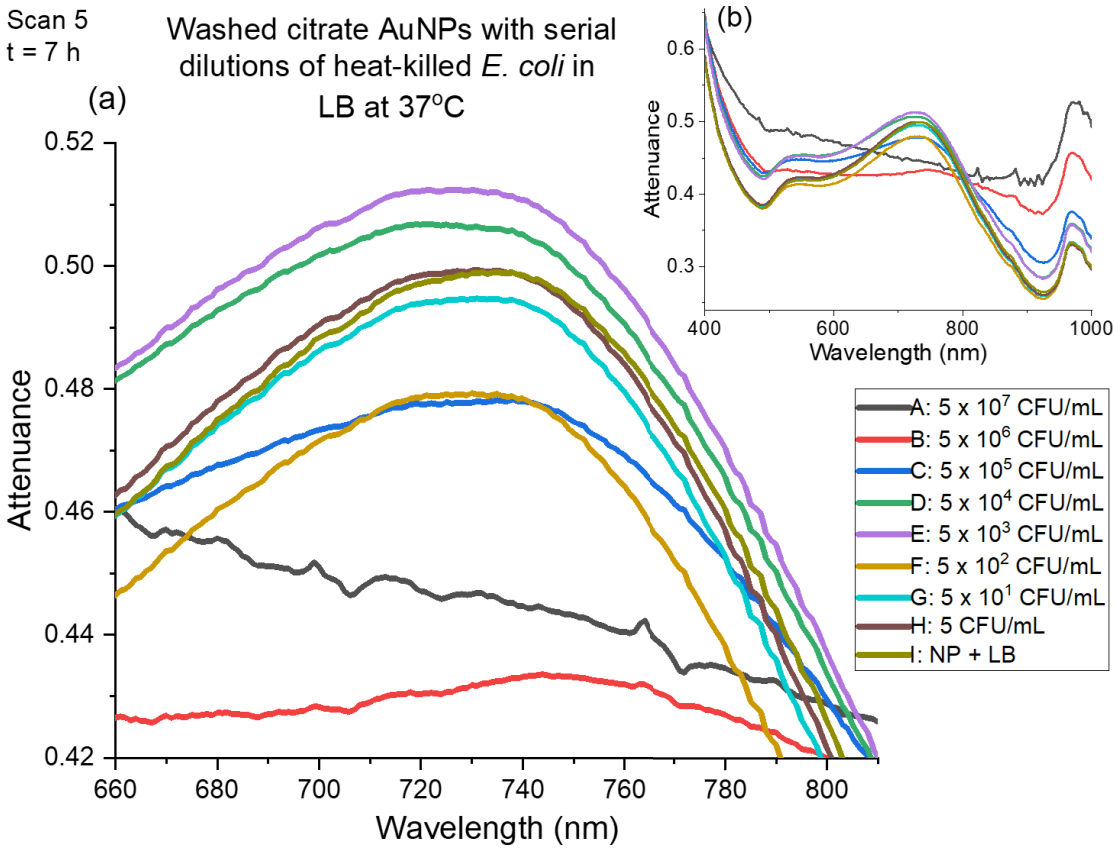

Figure 32: UV-vis spectra of washed AuNPs assayed with 10-fold serial dilutions of heat-killed *E. coli* in LB at 37°C, t = 7 h. (a) shows a close-up region of the relative positions of the red-shifted plasmon peaks, and inset (b) shows the spectra over the entire range of monitored wavelengths (nm).

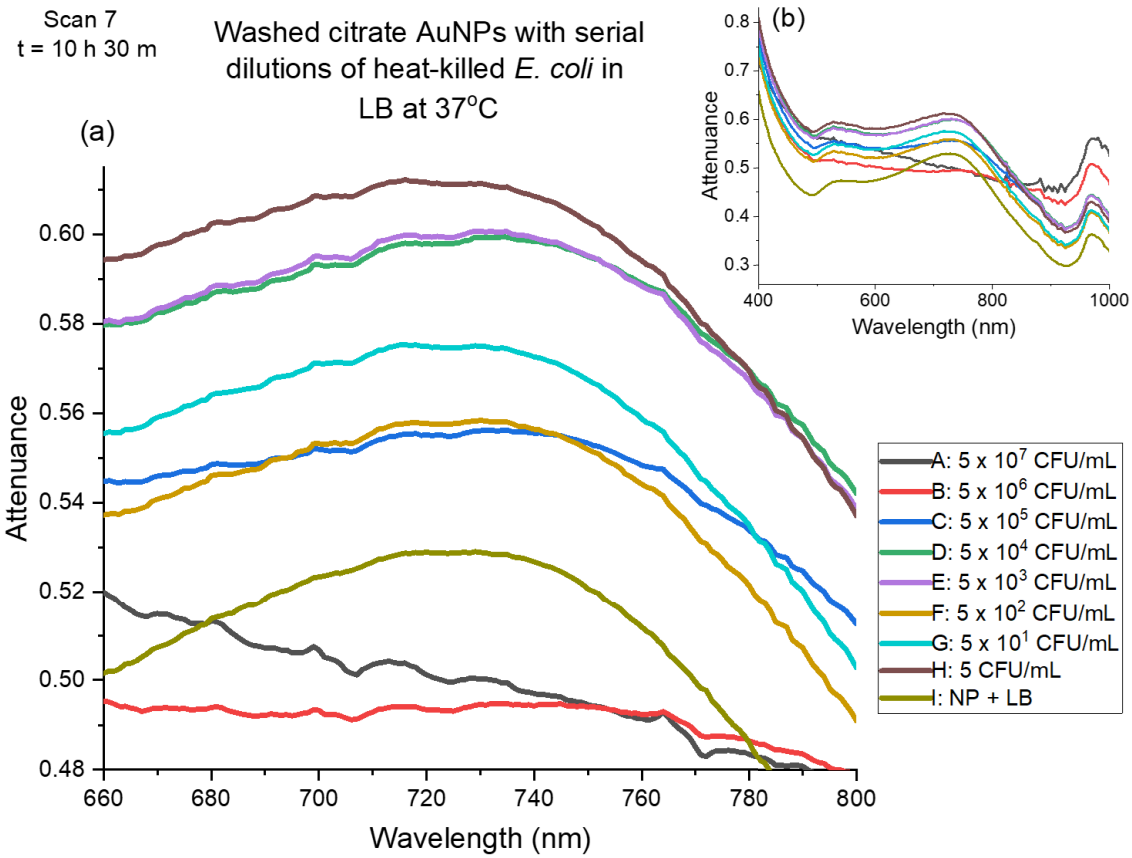

Figure 33: UV-vis spectra of washed AuNPs assayed with 10-fold serial dilutions of heat-killed *E. coli* in LB at 37°C, t = 10 h, 30 min. (a) shows a close-up region of the relative positions of the red-shifted plasmon peaks, and inset (b) shows the spectra over the entire range of monitored wavelengths (nm).

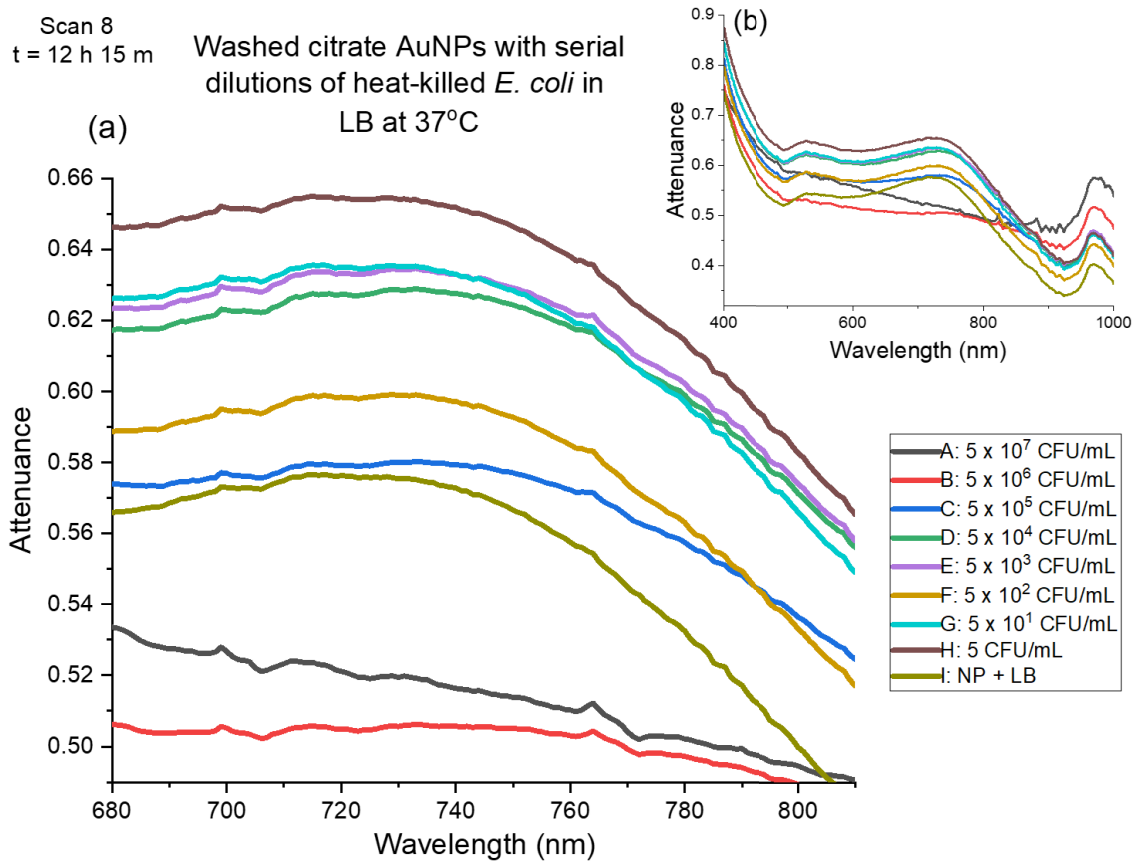

Figure 34: UV-vis spectra of washed AuNPs assayed with 10-fold serial dilutions of heat-killed *E. coli* in LB at 37°C, t = 12 h, 15 min. (a) shows a close-up region of the relative positions of the red-shifted plasmon peaks, and inset (b) shows the spectra over the entire range of monitored wavelengths (nm).

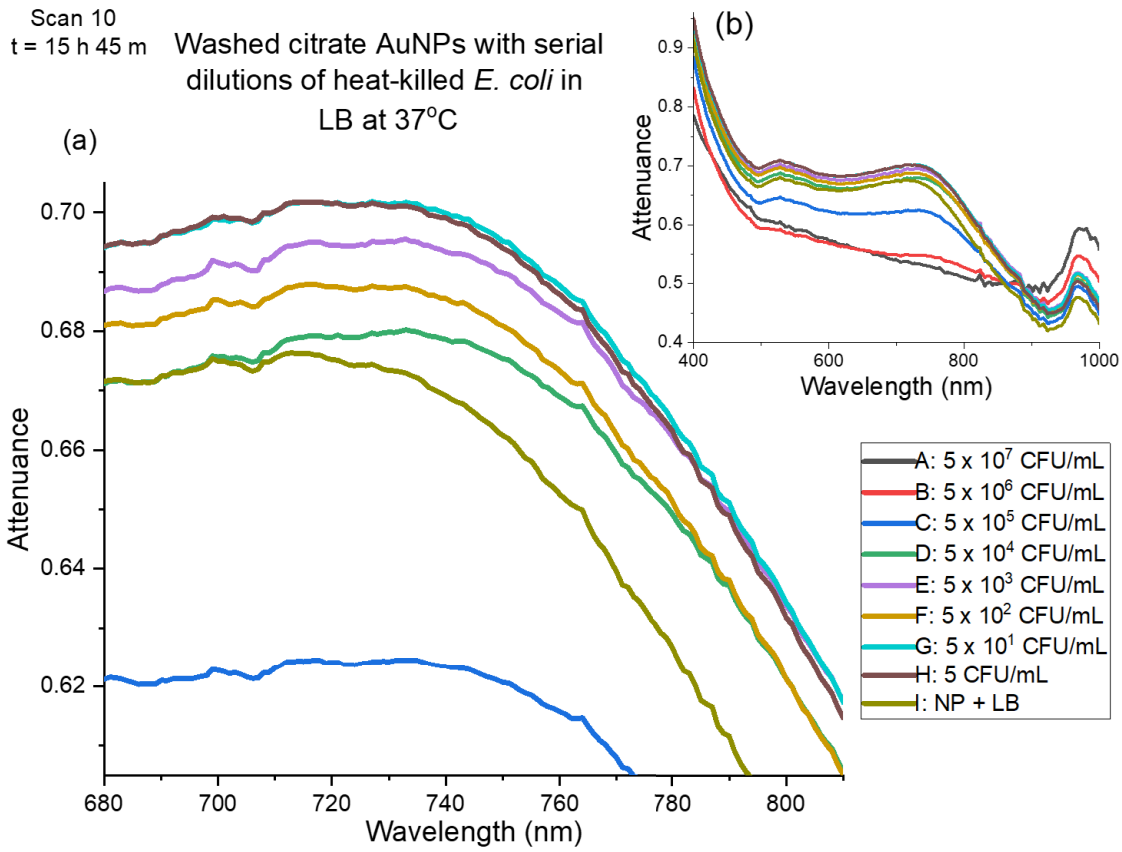

Figure 35: UV-vis spectra of washed AuNPs assayed with 10-fold serial dilutions of heat-killed *E. coli* in LB at 37°C, t = 15 h, 45 min. (a) shows a close-up region of the relative positions of the red-shifted plasmon peaks, and inset (b) shows the spectra over the entire range of monitored wavelengths (nm).

A.7 Live Conditioned Media Assays with As-Synthesized AuNPs

The following section contains UV-vis spectra pertaining to the assays between as-synthesized AuNPs and the conditioned media from live *E. coli* that were excluded from the main thesis for brevity and/or ease of reading. Where necessary, they were referred to in the main bodies of text.

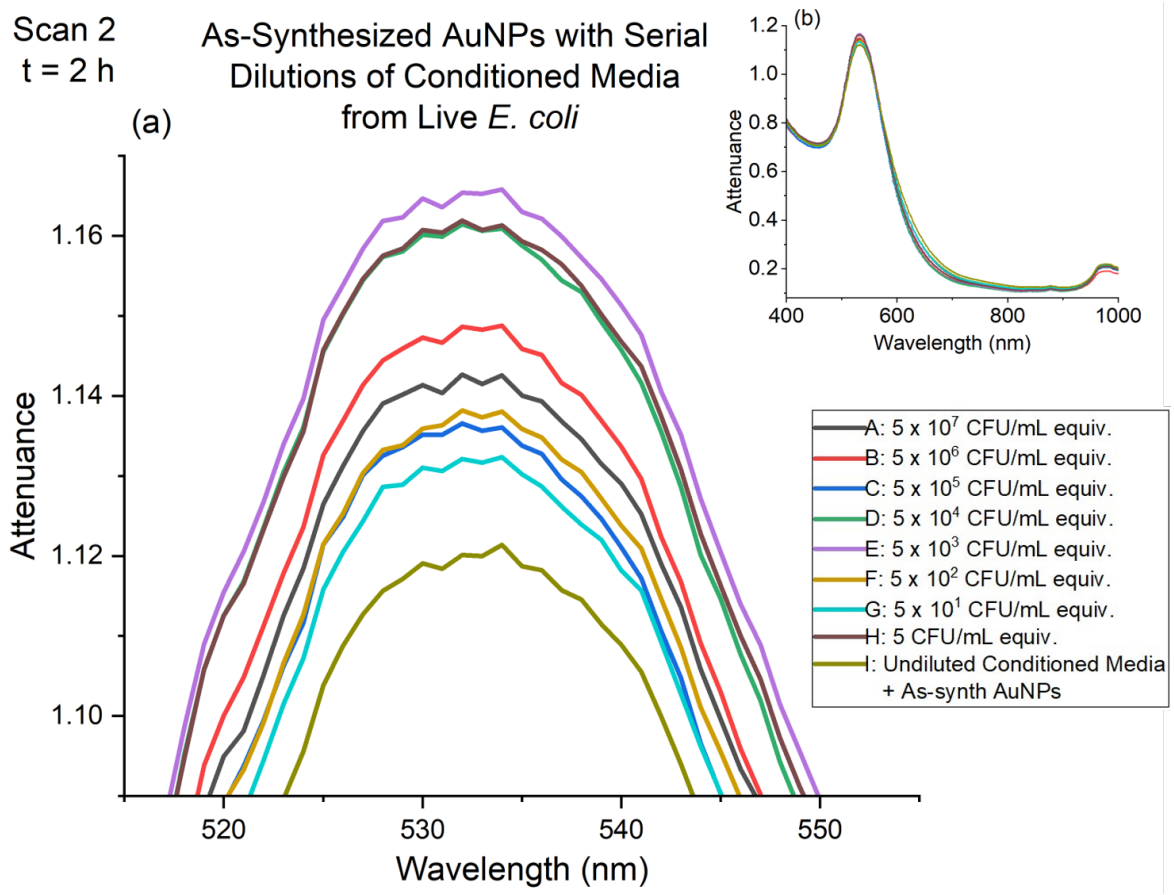

Figure 36: UV-vis spectra of as-synthesized AuNPs with 10-fold serial dilutions of conditioned media from live *E. coli* at ambient temperature, t = 2 h. (a) shows a close-up region of the relative positions of the red-shifted plasmon peaks, and inset (b) shows the spectra over the entire range of monitored wavelengths (nm).

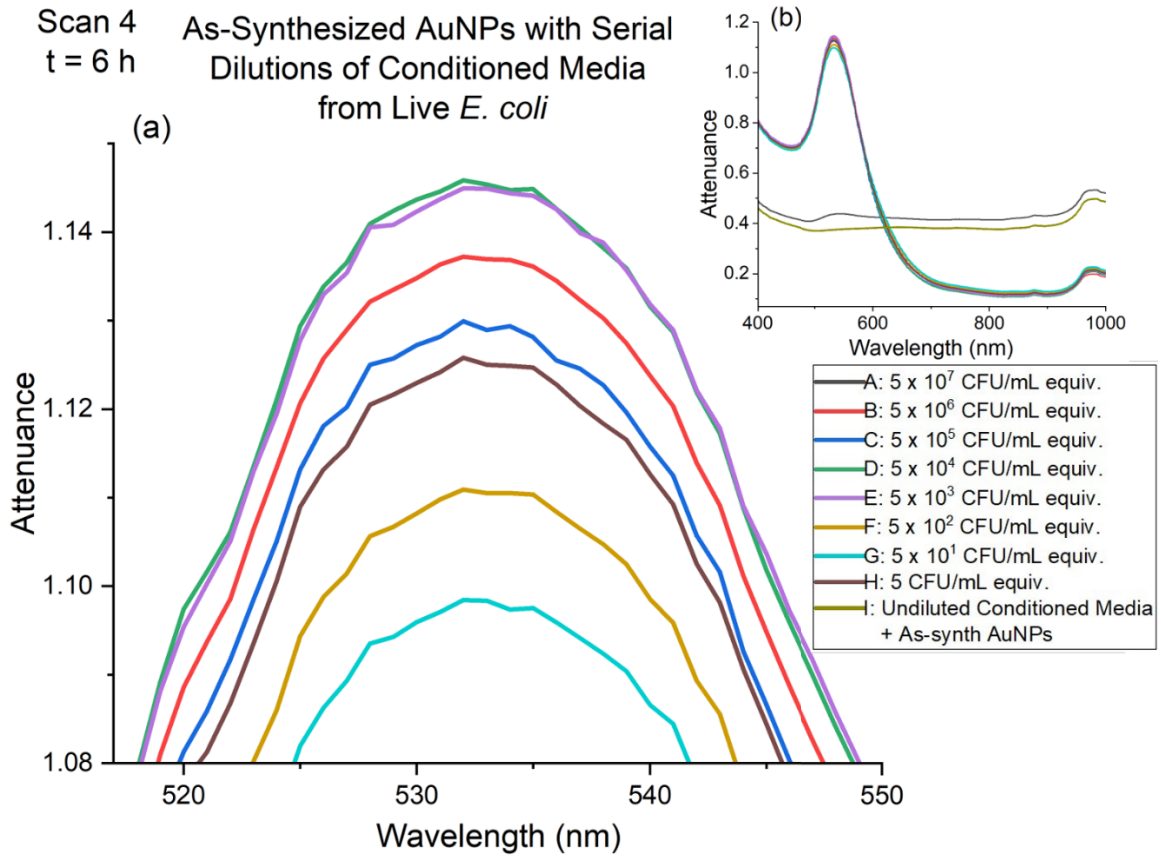

Figure 37: UV-vis spectra of as-synthesized AuNPs with 10-fold serial dilutions of conditioned media from live *E. coli* at ambient temperature, t = 6 h. (a) shows a close-up region of the relative positions of the red-shifted plasmon peaks, and inset (b) shows the spectra over the entire range of monitored wavelengths (nm).

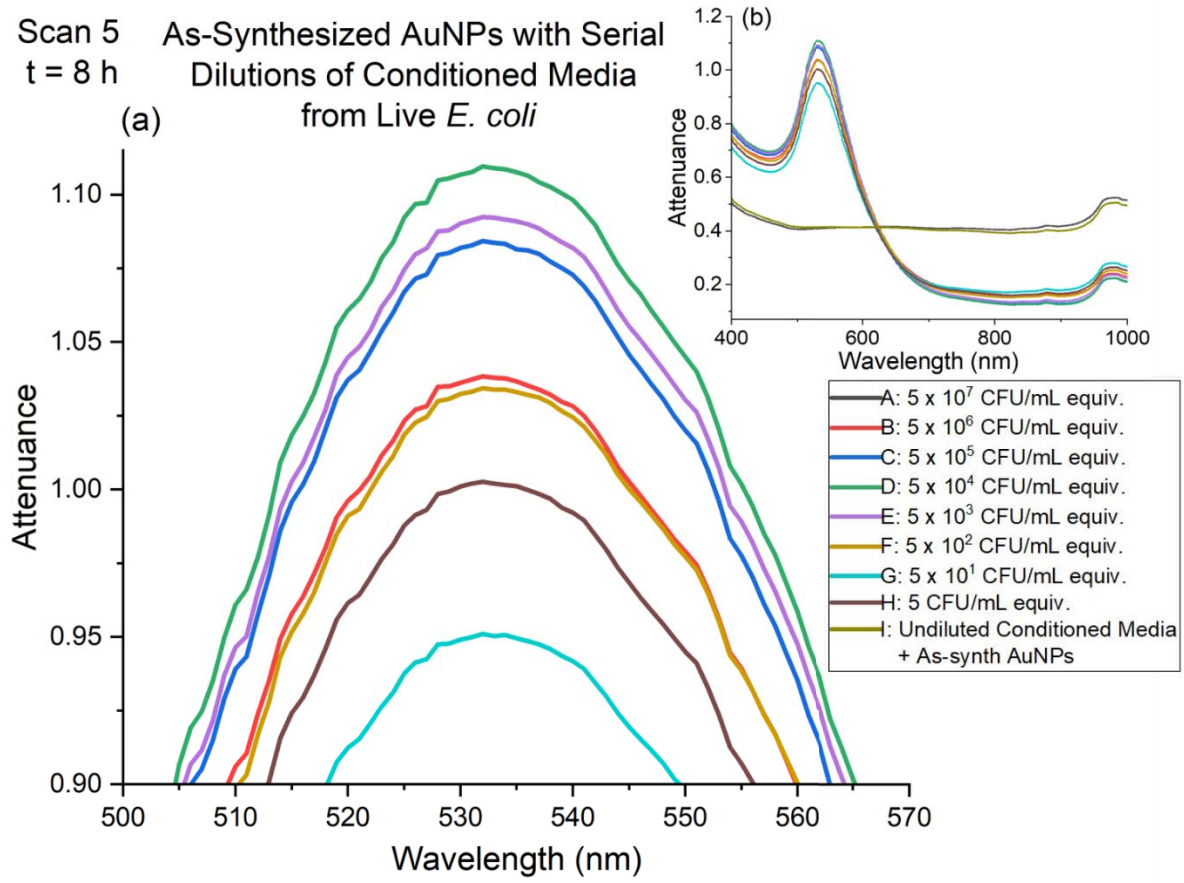

Figure 38: UV-vis spectra of as-synthesized AuNPs with 10-fold serial dilutions of conditioned media from live *E. coli* at ambient temperature, t = 8 h. (a) shows a close-up region of the relative positions of the red-shifted plasmon peaks, and inset (b) shows the spectra over the entire range of monitored wavelengths (nm).

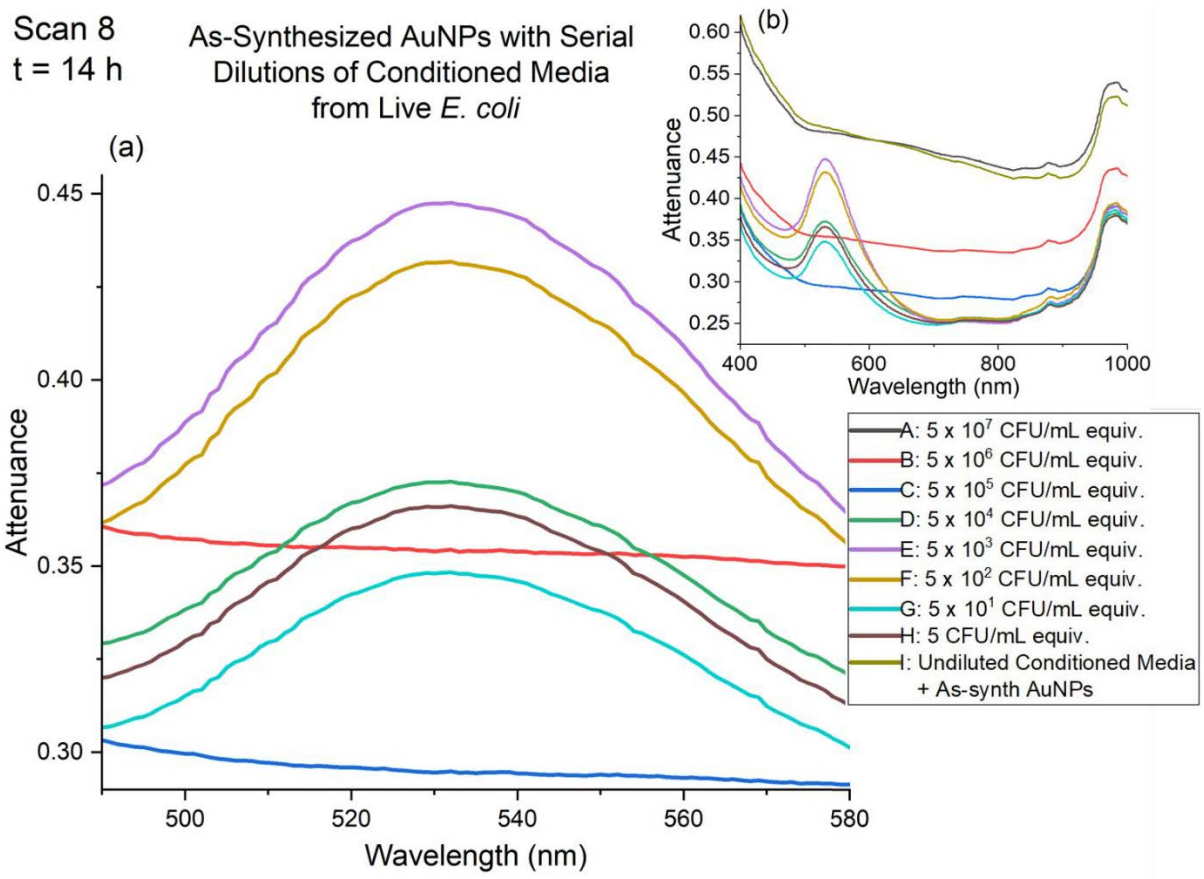

Figure 39: UV-vis spectra of as-synthesized AuNPs with 10-fold serial dilutions of conditioned media from live *E. coli* at ambient temperature, t = 14 h. (a) shows a close-up region of the relative positions of the red-shifted plasmon peaks, and inset (b) shows the spectra over the entire range of monitored wavelengths (nm).

A.8 Heat-killed Conditioned Media Assays with As-Synthesized AuNPs

The following section contains UV-vis spectra pertaining to the assays between as-synthesized AuNPs and the conditioned media from heat-killed preparations of *E. coli* that were excluded from the main thesis for brevity and/or ease of reading. Where necessary, they were referred to in the main bodies of text.

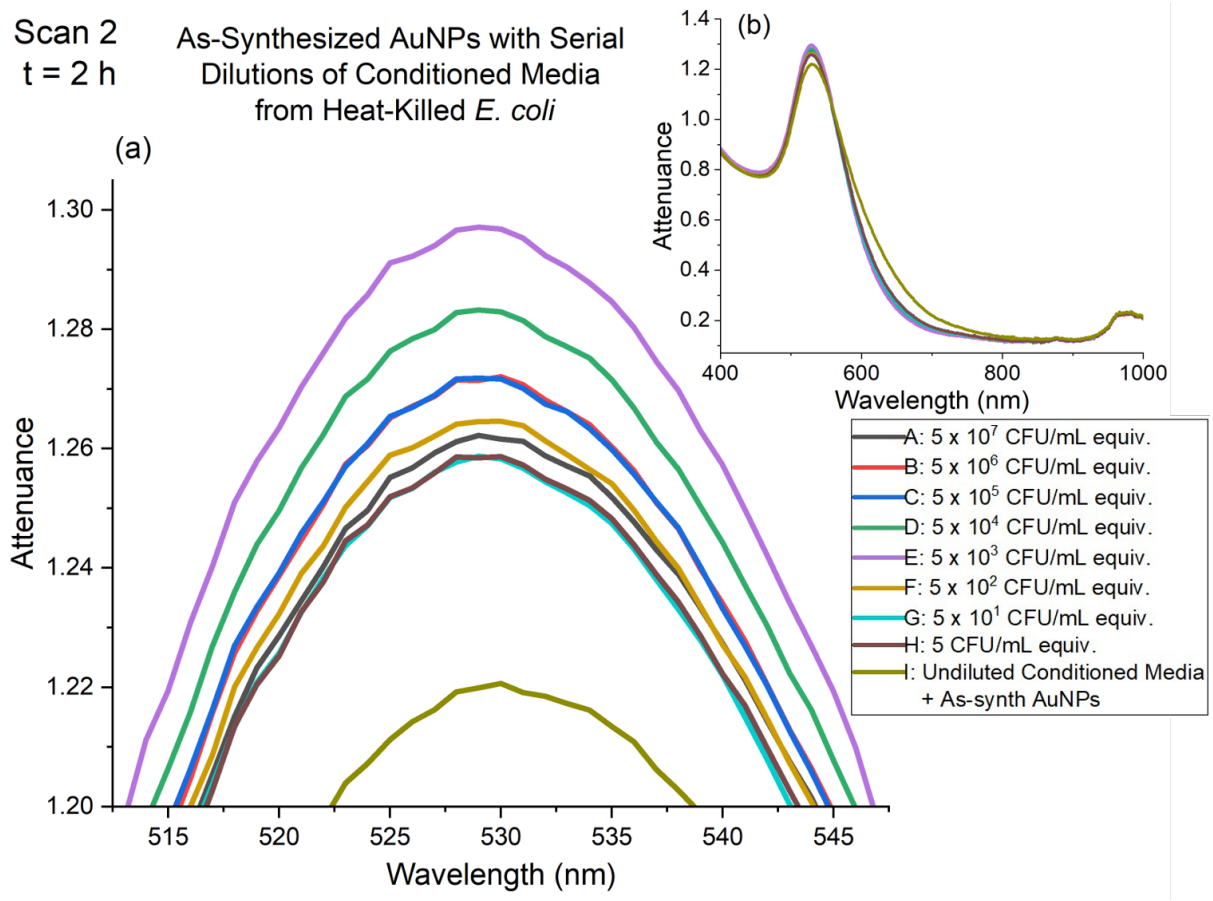

Figure 40: UV-vis spectra of as-synthesized AuNPs with 10-fold serial dilutions of conditioned media from heat-killed *E. coli* at ambient temperature, t = 2 h. (a) shows a close-up region of the relative positions of the red-shifted plasmon peaks, and inset (b) shows the spectra over the entire range of monitored wavelengths (nm).

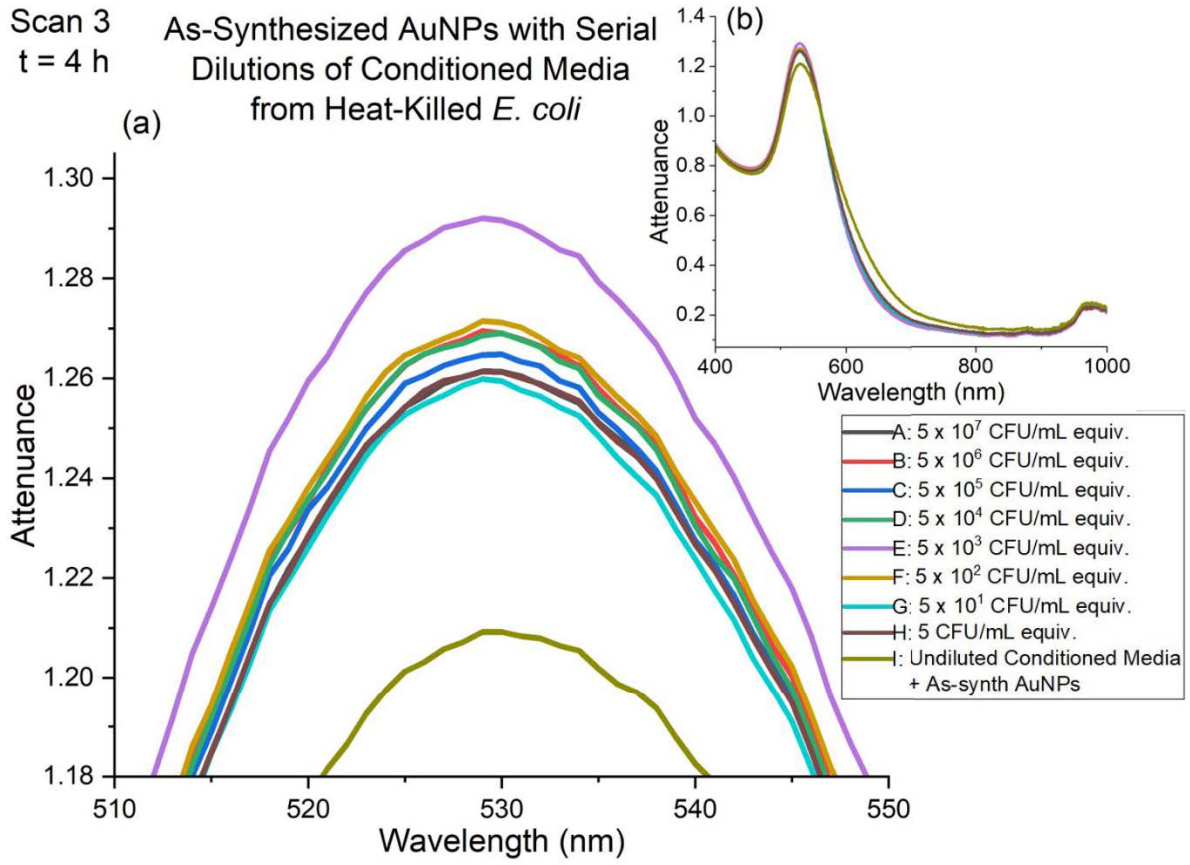

Figure 41: UV-vis spectra of as-synthesized AuNPs with 10-fold serial dilutions of conditioned media from heat-killed *E. coli* at ambient temperature, t = 4 h. (a) shows a close-up region of the relative positions of the red-shifted plasmon peaks, and inset (b) shows the spectra over the entire range of monitored wavelengths (nm).

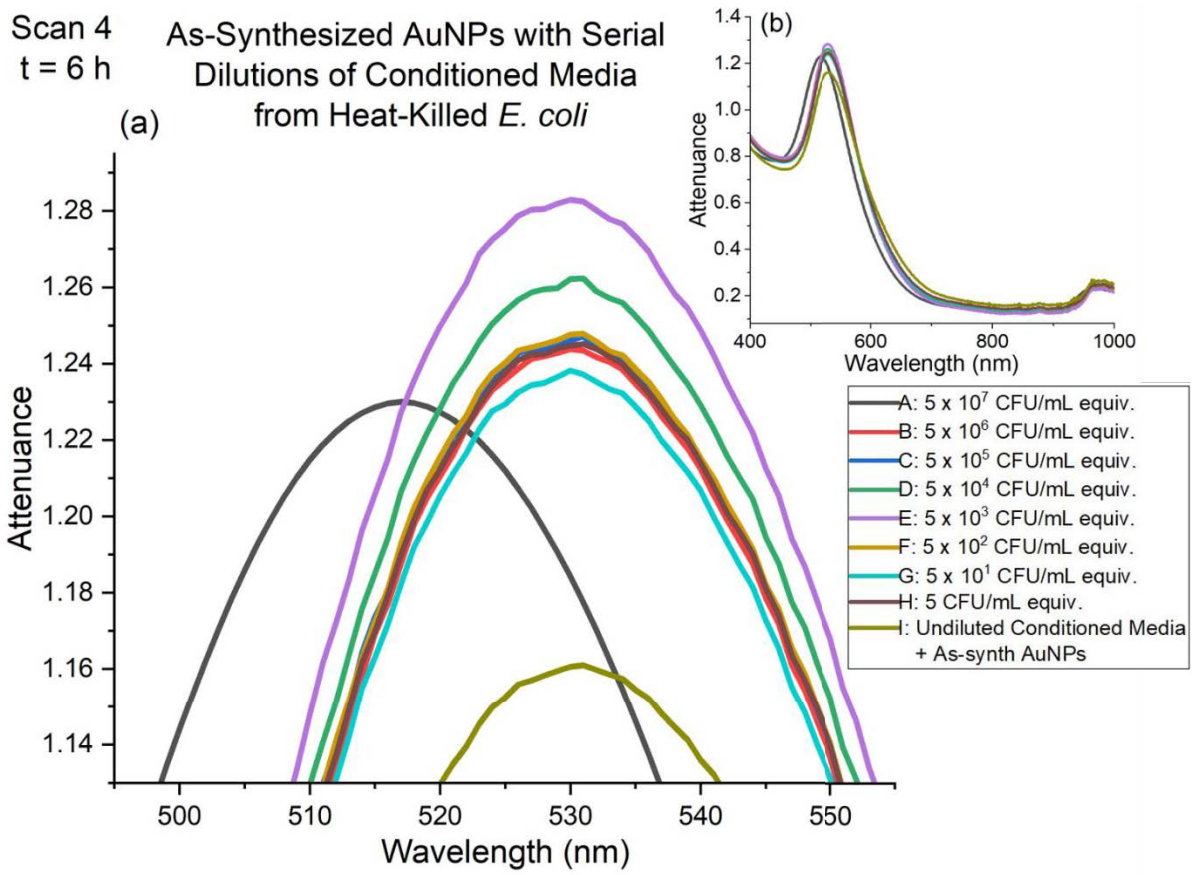

Figure 42: UV-vis spectra of as-synthesized AuNPs with 10-fold serial dilutions of conditioned media from heat-killed *E. coli* at ambient temperature, t = 6 h. (a) shows a close-up region of the relative positions of the red-shifted plasmon peaks, and inset (b) shows the spectra over the entire range of monitored wavelengths (nm).

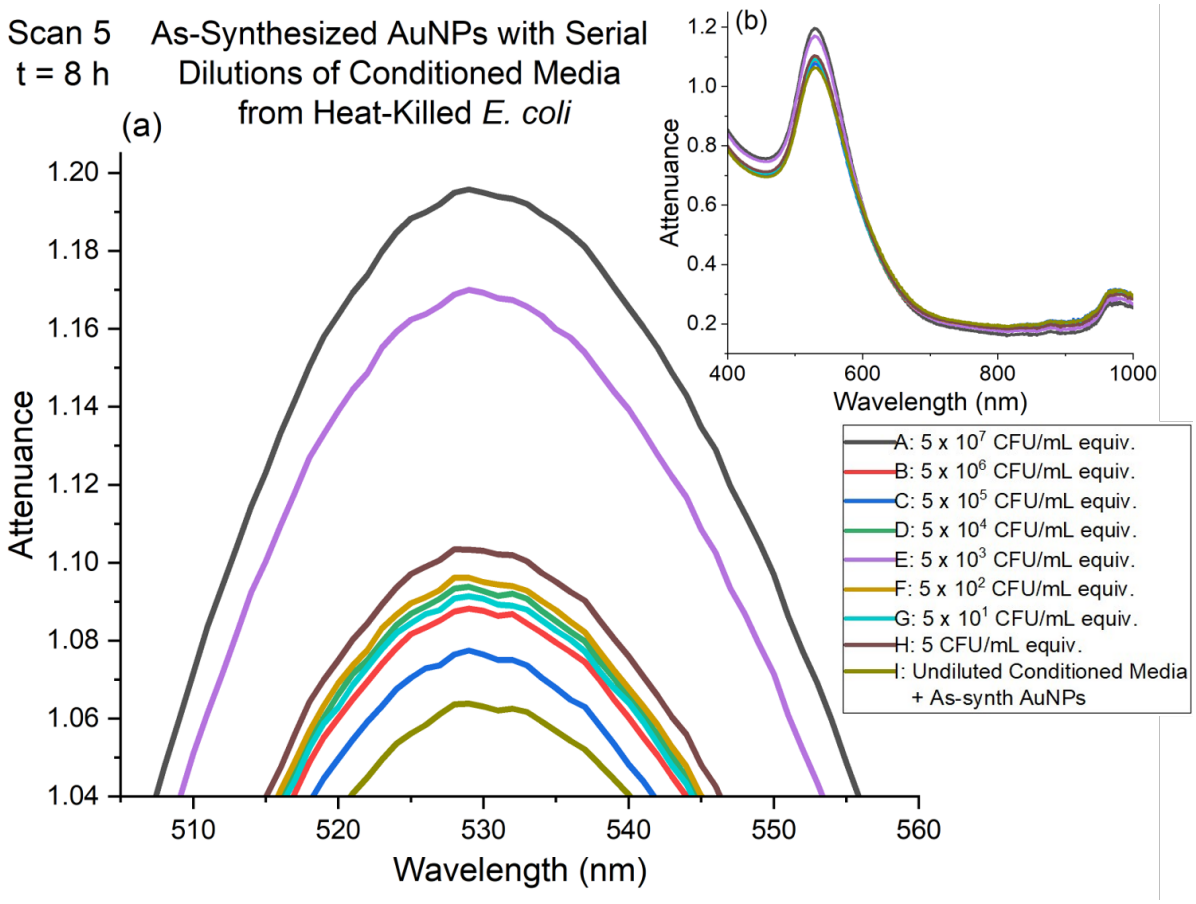

Figure 43: UV-vis spectra of as-synthesized AuNPs with 10-fold serial dilutions of conditioned media from heat-killed *E. coli* at ambient temperature, t = 8 h. (a) shows a close-up region of the relative positions of the red-shifted plasmon peaks, and inset (b) shows the spectra over the entire range of monitored wavelengths (nm).

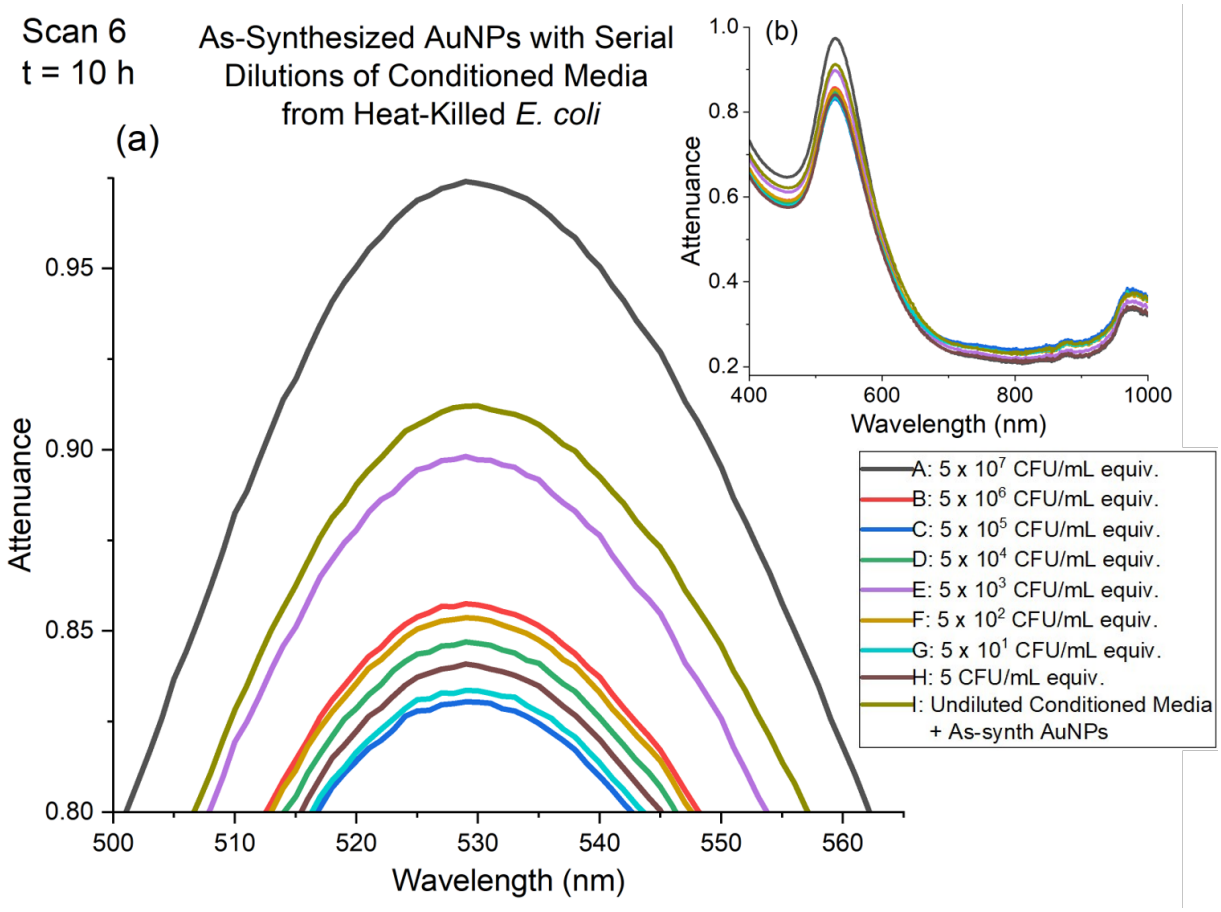

Figure 44: UV-vis spectra of as-synthesized AuNPs with 10-fold serial dilutions of conditioned media from heat-killed *E. coli* at ambient temperature, t = 10 h. (a) shows a close-up region of the relative positions of the red-shifted plasmon peaks, and inset (b) shows the spectra over the entire range of monitored wavelengths (nm).

A.9 Extra Heat-killed Conditioned Media Assays with As-synthesized AuNPs

The following section contains UV-vis spectra pertaining to the assays between as-synthesized AuNPs and the conditioned media from extra heat-killed preparations of *E. coli* that were excluded from the main thesis for brevity and/or ease of reading. Where necessary, they were referred to in the main bodies of text.

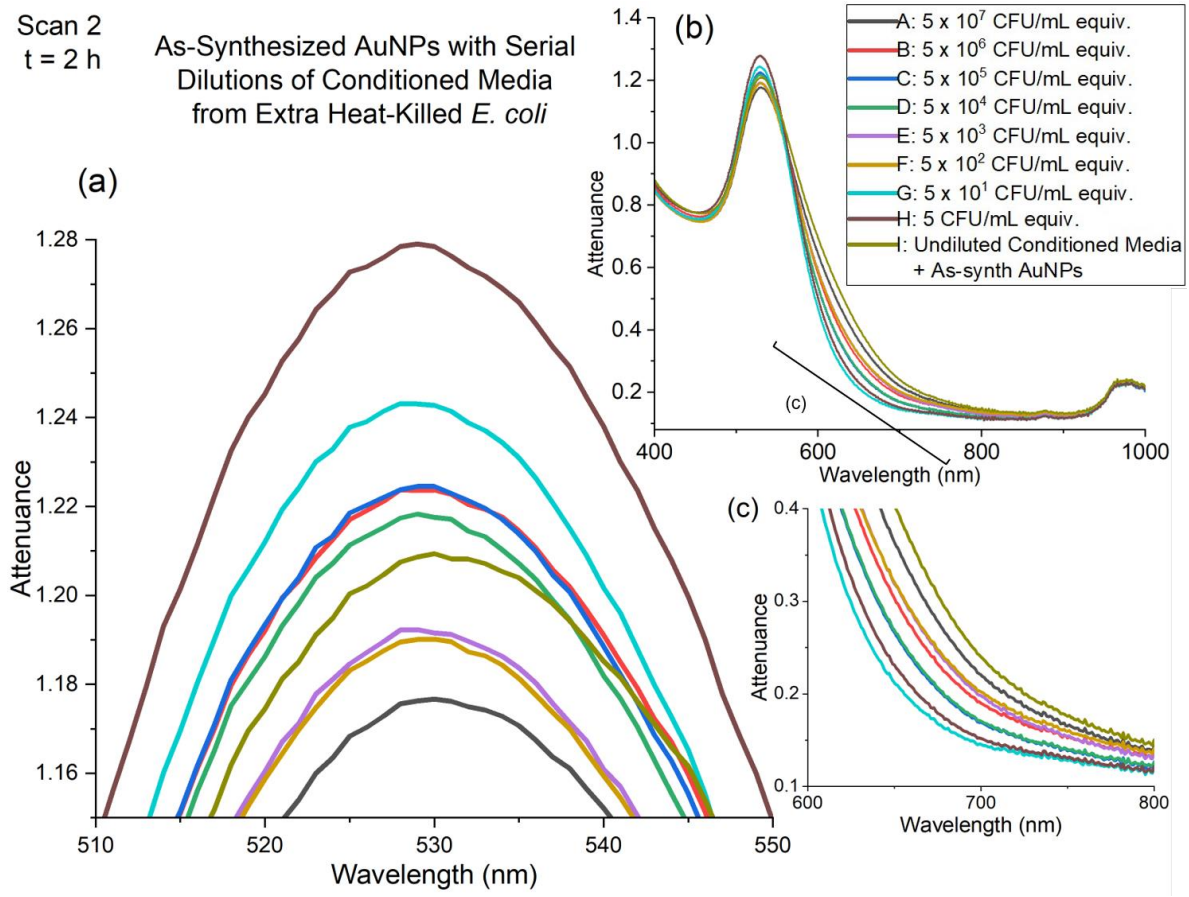

Figure 45: UV-vis spectra of as-synthesized AuNPs with 10-fold serial dilutions of conditioned media from extra heat-killed *E. coli* at ambient temperature, t = 2 h. (a) shows a close-up region of the relative positions of the red-shifted plasmon peaks, and inset (b) shows the spectra over the entire range of monitored wavelengths (nm). Inset (c) shows a magnified view of the region of interest labelled in (b).

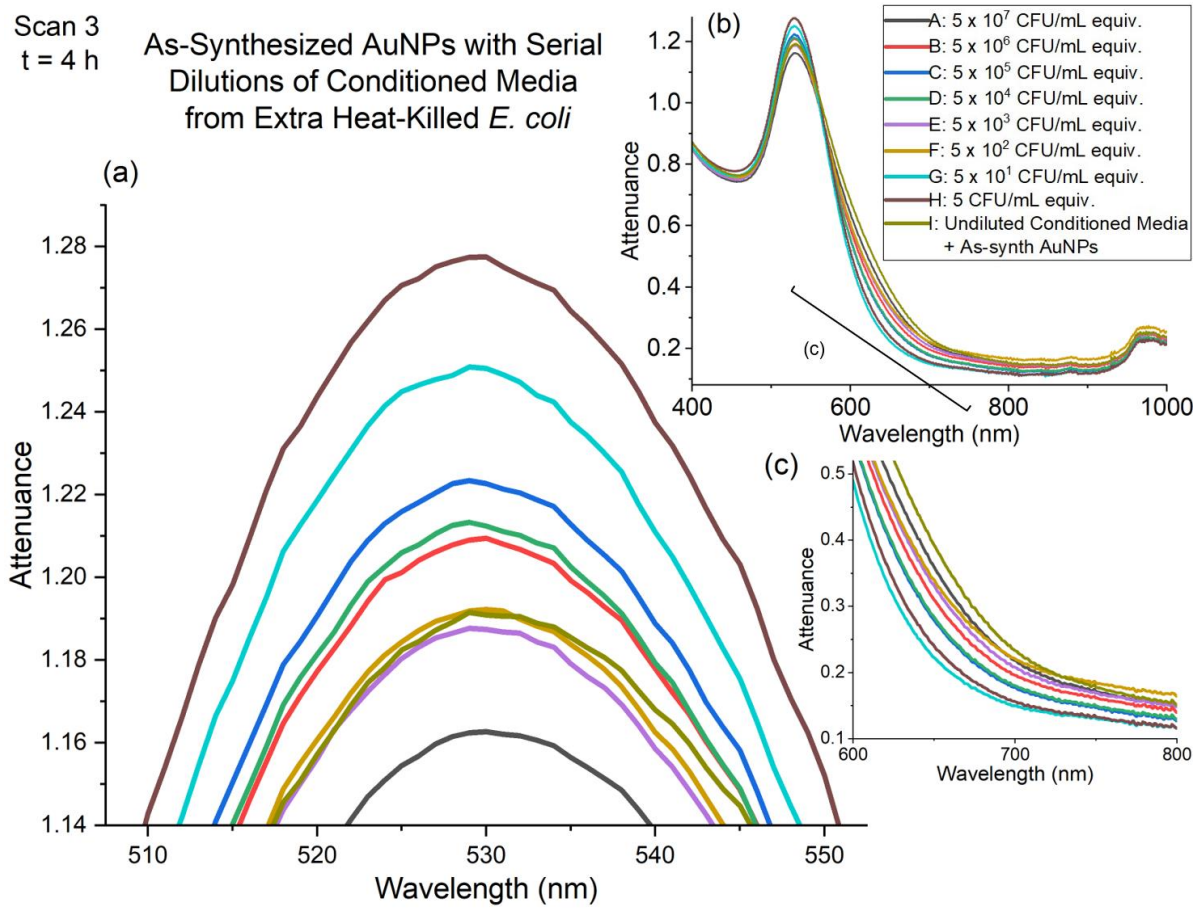

Figure 46: UV-vis spectra of as-synthesized AuNPs with 10-fold serial dilutions of conditioned media from extra heat-killed *E. coli* at ambient temperature, t = 4 h. (a) shows a close-up region of the relative positions of the red-shifted plasmon peaks, and inset (b) shows the spectra over the entire range of monitored wavelengths (nm). Inset (c) shows a magnified view of the region of interest labelled in (b).

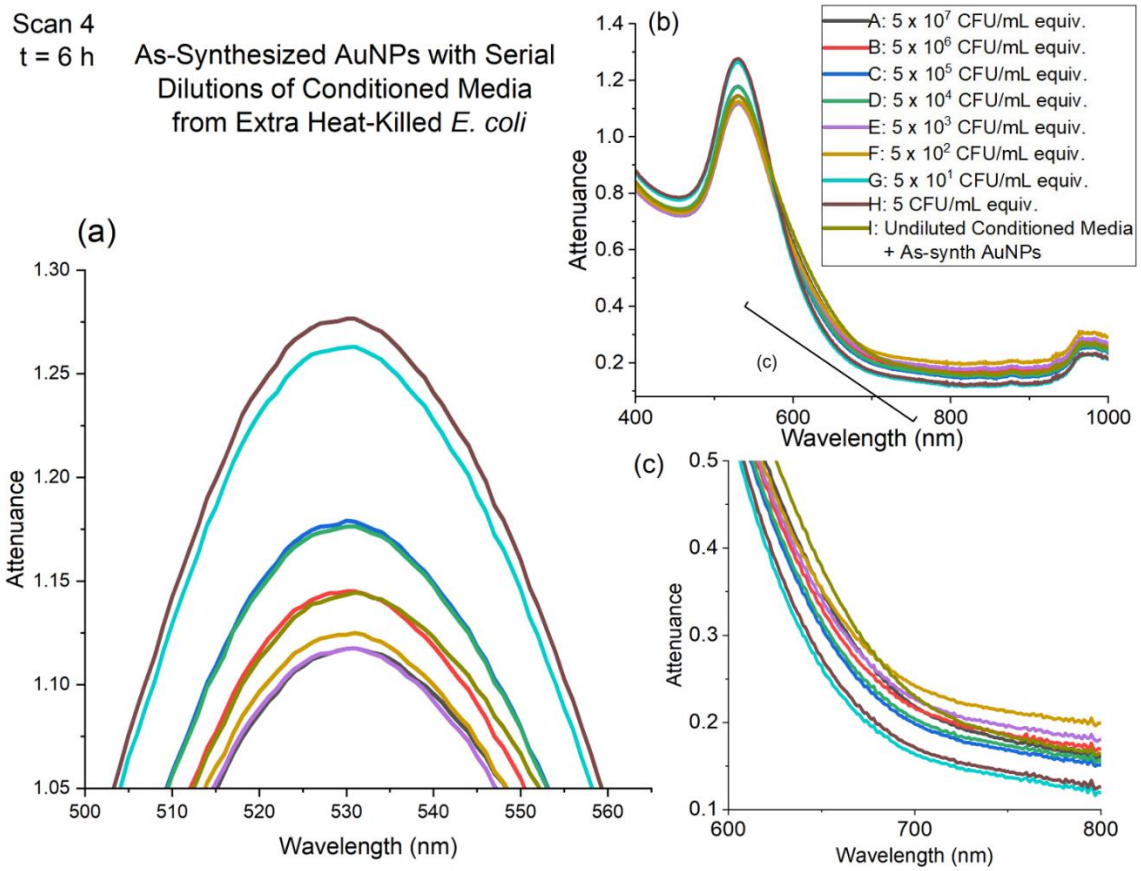

Figure 47: UV-vis spectra of as-synthesized AuNPs with 10-fold serial dilutions of conditioned media from extra heat-killed *E. coli* at ambient temperature, t = 6 h. (a) shows a close-up region of the relative positions of the red-shifted plasmon peaks, and inset (b) shows the spectra over the entire range of monitored wavelengths (nm). Inset (c) shows a magnified view of the region of interest labelled in (b).

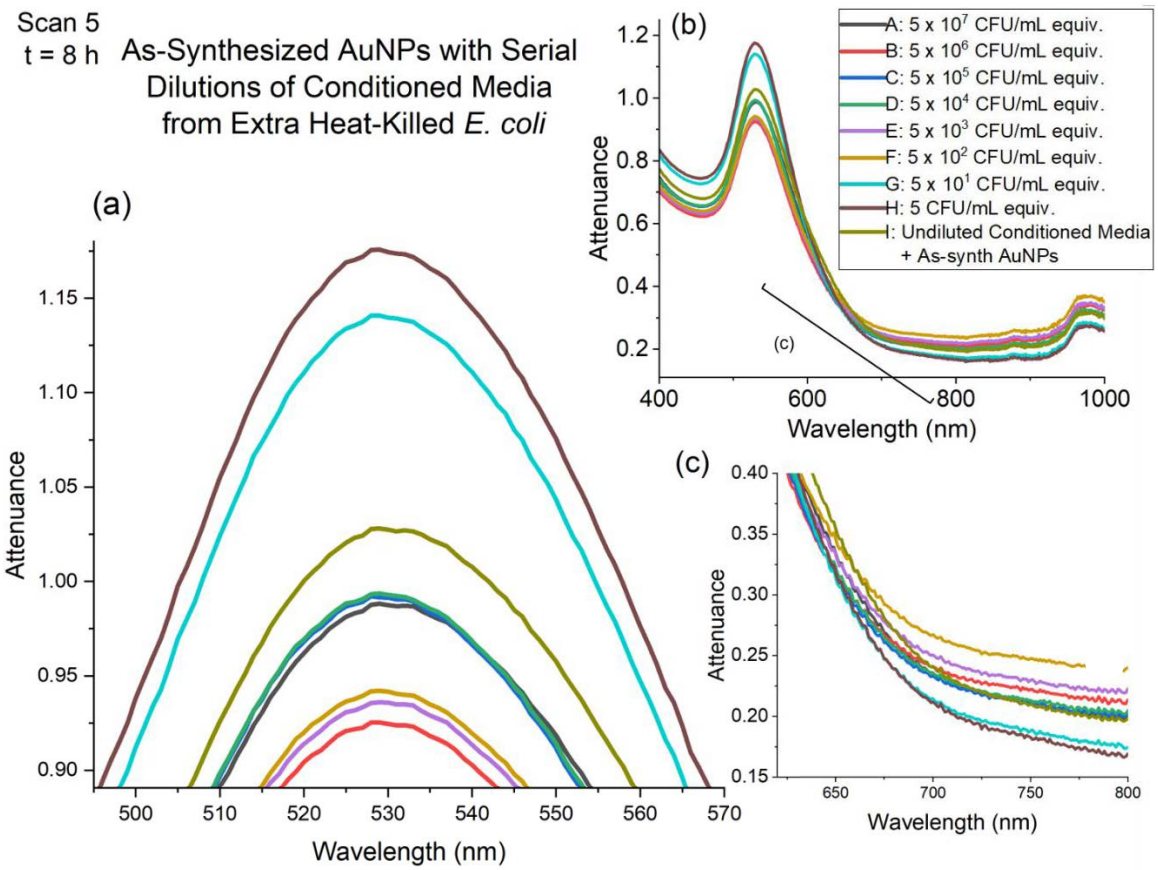

Figure 48: UV-vis spectra of as-synthesized AuNPs with 10-fold serial dilutions of conditioned media from extra heat-killed *E. coli* at ambient temperature, t = 8 h. (a) shows a close-up region of the relative positions of the red-shifted plasmon peaks, and inset (b) shows the spectra over the entire range of monitored wavelengths (nm). Inset (c) shows a magnified view of the region of interest labelled in (b).

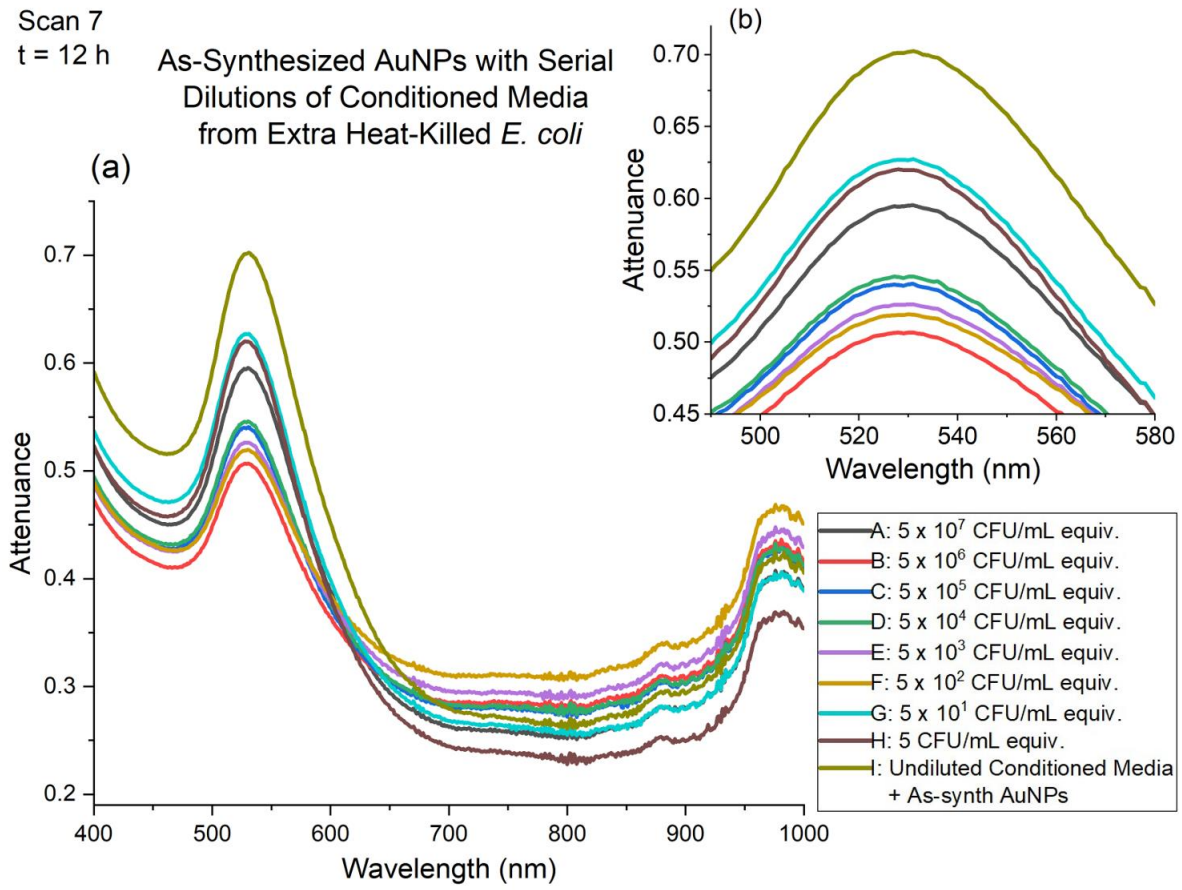

Figure 49: UV-vis spectra of as-synthesized AuNPs with 10-fold serial dilutions of conditioned media from extra heat-killed *E. coli* at ambient temperature, t = 12 h. (a) shows the spectra over the entire range of monitored wavelengths (nm) and inset (b) shows a close-up region of the relative positions of the red-shifted plasmon peaks.

A.10 Live Conditioned Media Assays with Washed AuNPs

The following section contains UV-vis spectra pertaining to the assays between washed AuNPs and the conditioned media from live *E. coli* that were excluded from the main thesis for brevity and/or ease of reading. Where necessary, they were referred to in the main bodies of text.

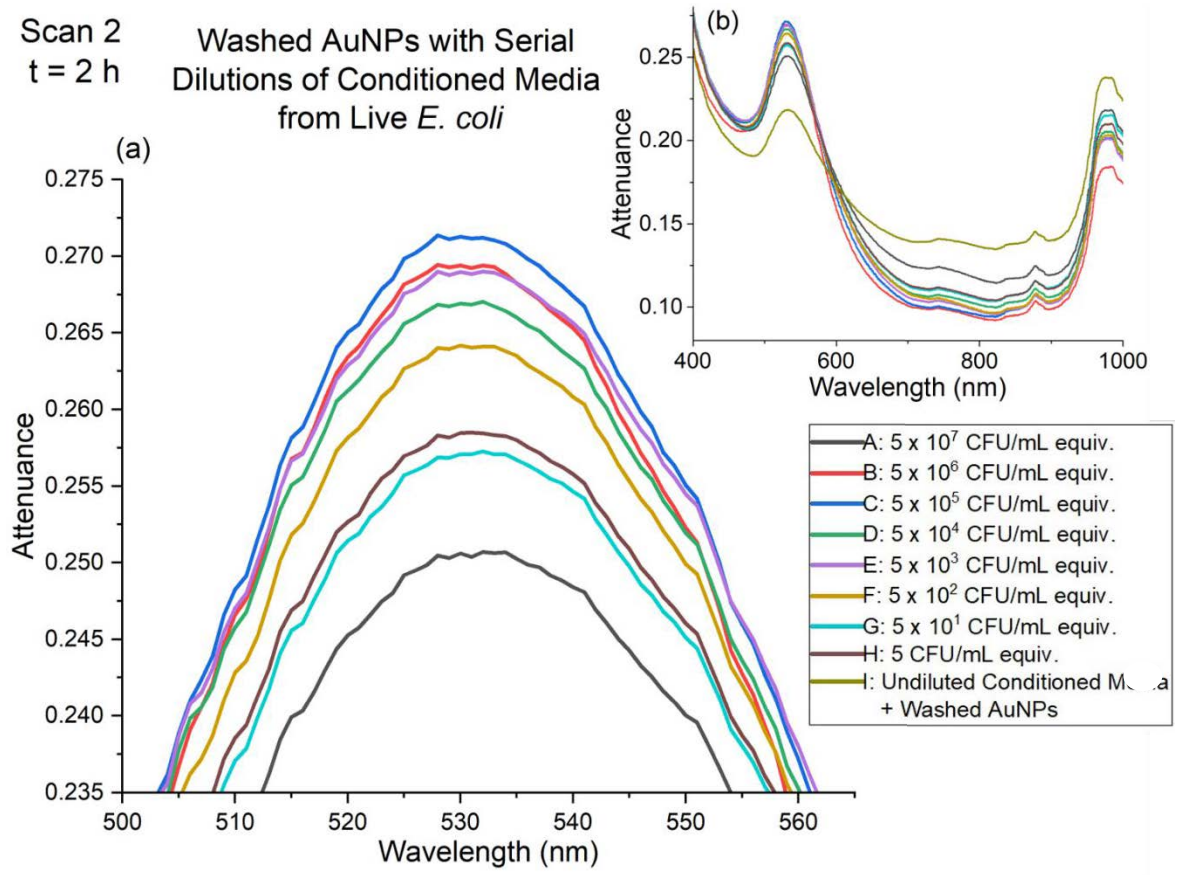

Figure 50: UV-vis spectra of washed AuNPs with 10-fold serial dilutions of conditioned media from live *E. coli* at ambient temperature, t = 2 h. (a) shows a close-up region of the relative positions of the dampened plasmon peaks, and inset (b) shows the spectra over the entire range of monitored wavelengths (nm).

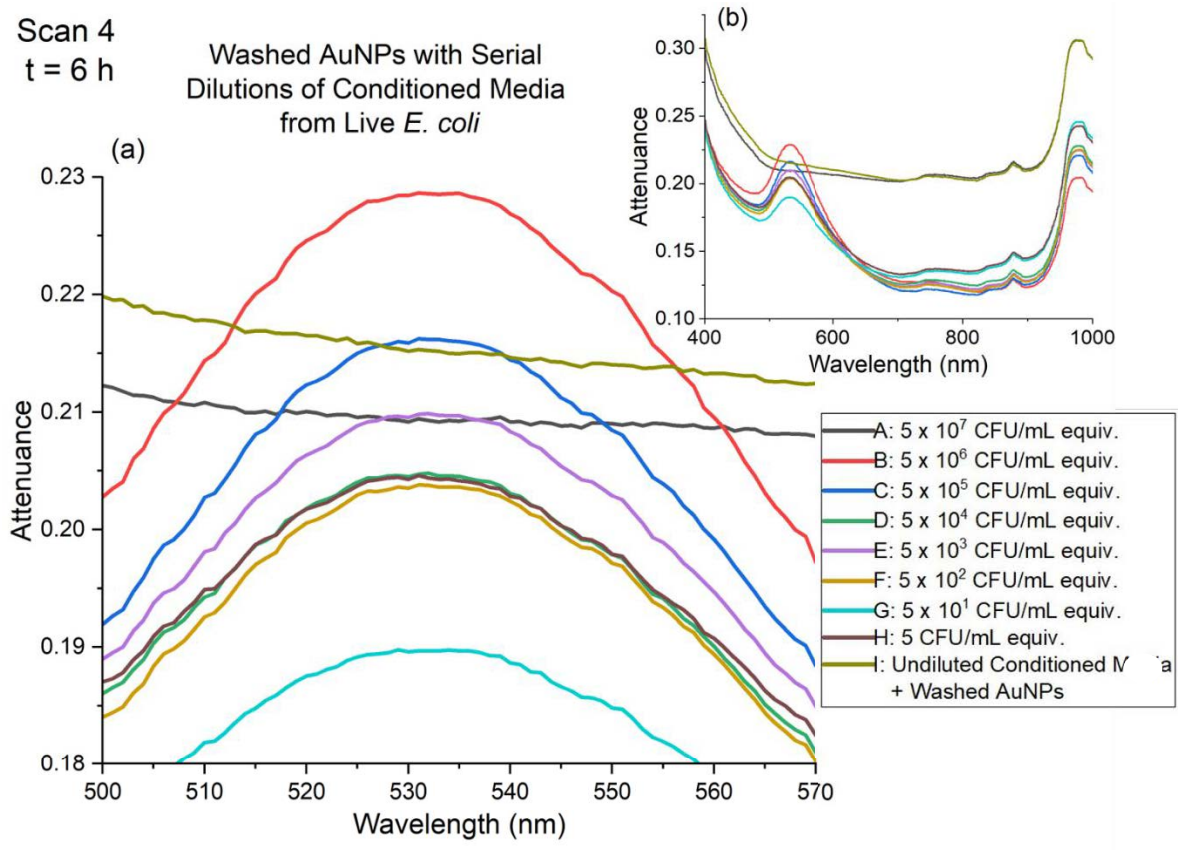

Figure 51: UV-vis spectra of washed AuNPs with 10-fold serial dilutions of conditioned media from live *E. coli* at ambient temperature, t = 6 h. (a) shows a close-up region of the relative positions of the dampened plasmon peaks, and inset (b) shows the spectra over the entire range of monitored wavelengths (nm).

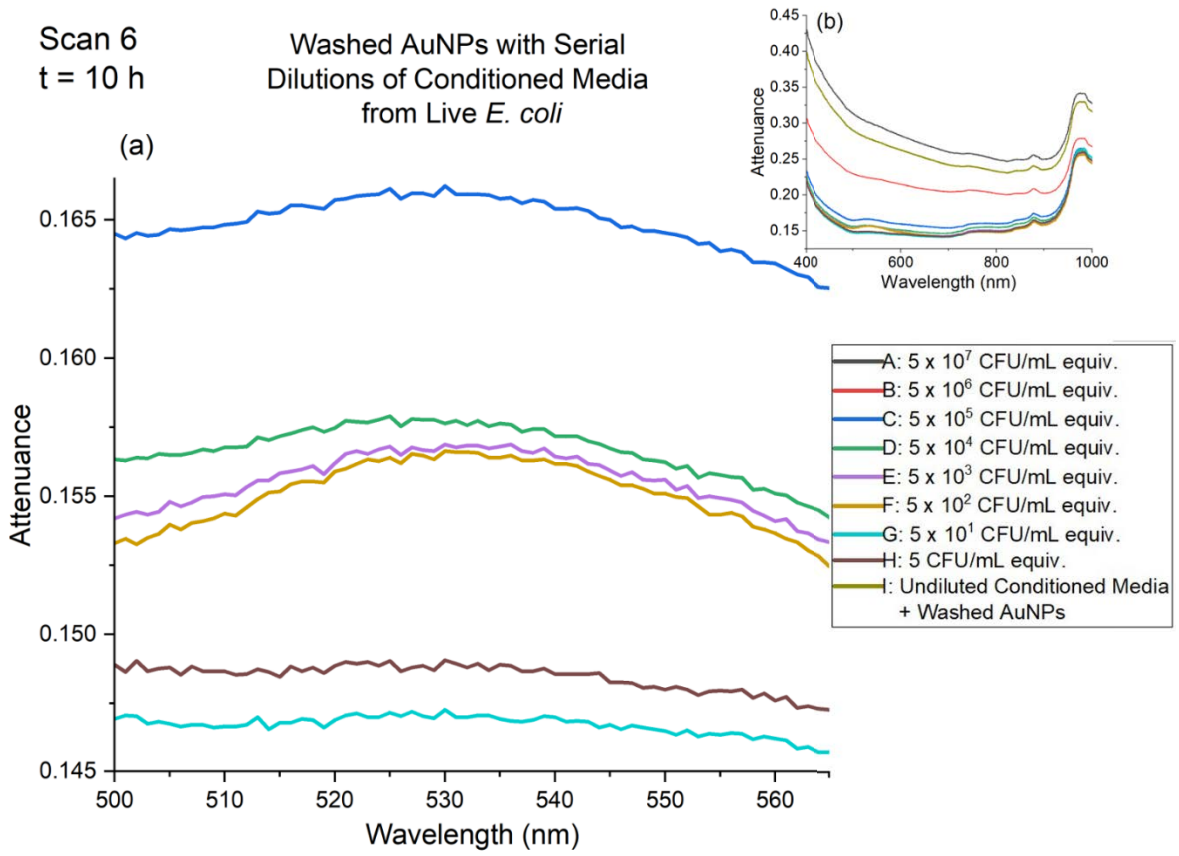

Figure 52: UV-vis spectra of washed AuNPs with 10-fold serial dilutions of conditioned media from live *E. coli* at ambient temperature, t = 10 h. (a) shows a close-up region of the relative positions of the dampened plasmon peaks, and inset (b) shows the spectra over the entire range of monitored wavelengths (nm).

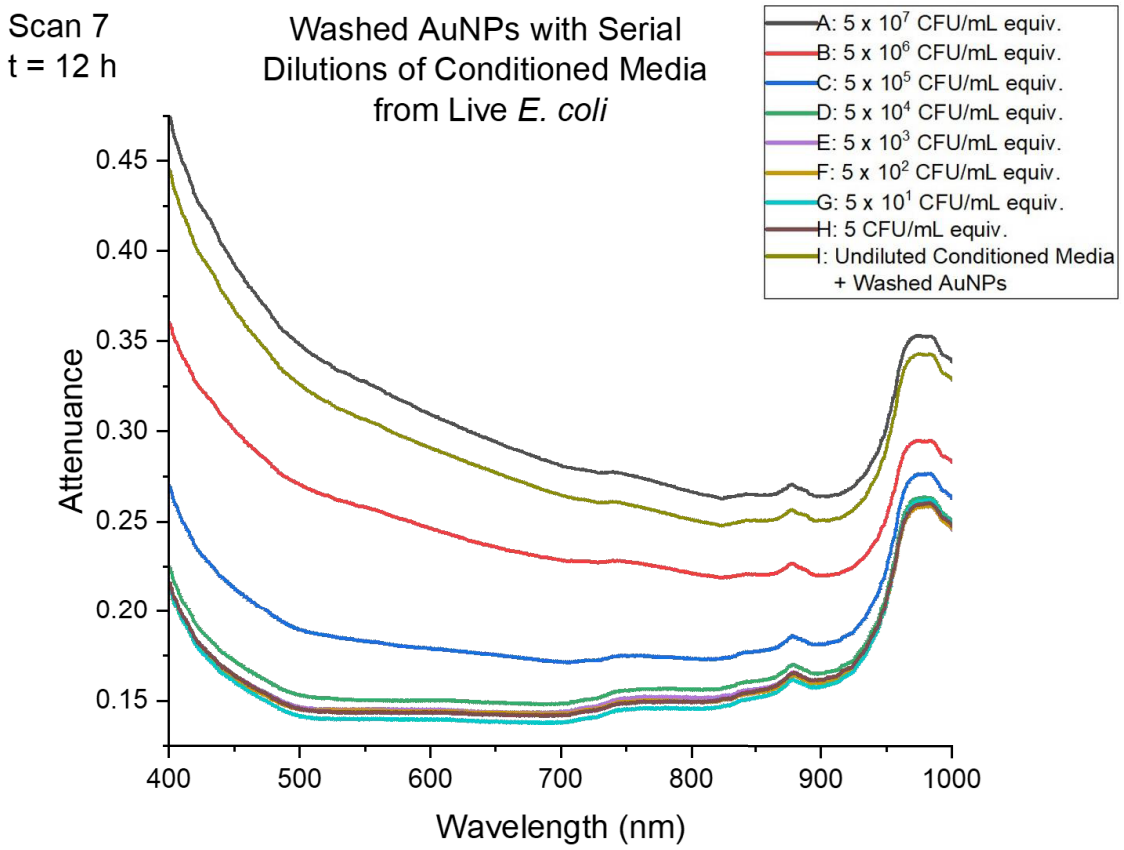

Figure 53: UV-vis spectra of washed AuNPs with 10-fold serial dilutions of conditioned media from live *E. coli* at ambient temperature, t = 12 h.

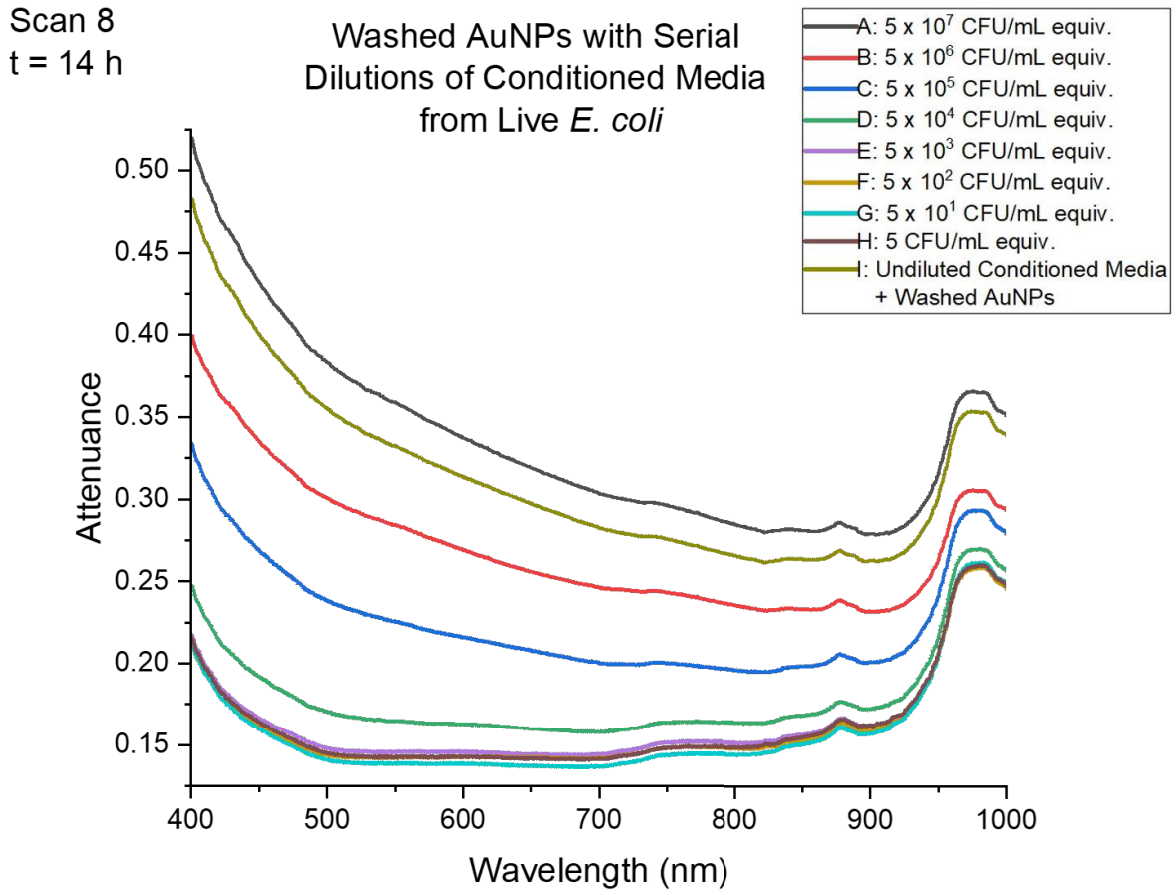

Figure 54: UV-vis spectra of washed AuNPs with 10-fold serial dilutions of conditioned media from live *E. coli* at ambient temperature, t = 14 h.

A.11 Heat-killed Conditioned Media Assays with Washed AuNPs

The following section contains UV-vis spectra pertaining to the assays between washed AuNPs and the conditioned media from heat-killed preparations of *E. coli* that were excluded from the main thesis for brevity and/or ease of reading. Where necessary, they were referred to in the main bodies of text.

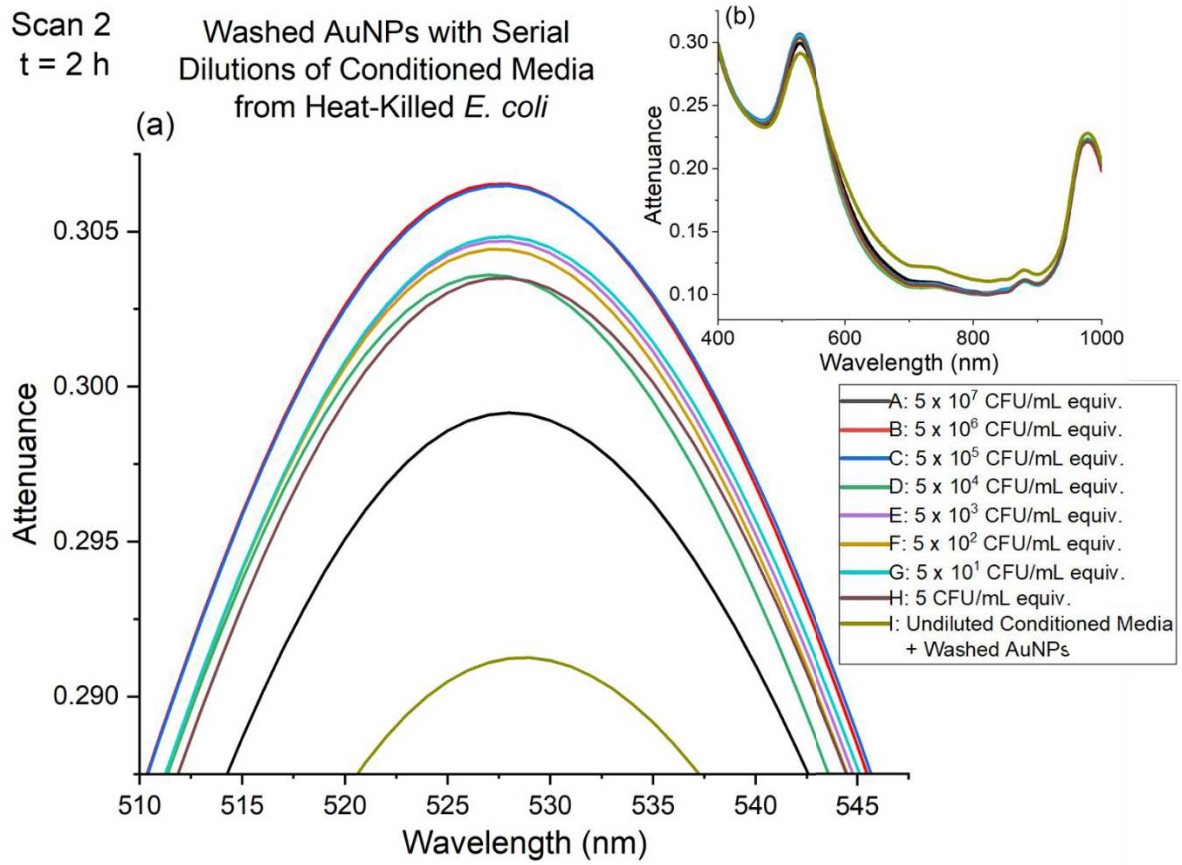

Figure 55: UV-vis spectra of washed AuNPs with 10-fold serial dilutions of conditioned media from heat-killed *E. coli* at ambient temperature, t = 2 h. (a) shows a close-up region of the relative positions of the dampened plasmon peaks, and inset (b) shows the spectra over the entire range of monitored wavelengths (nm).

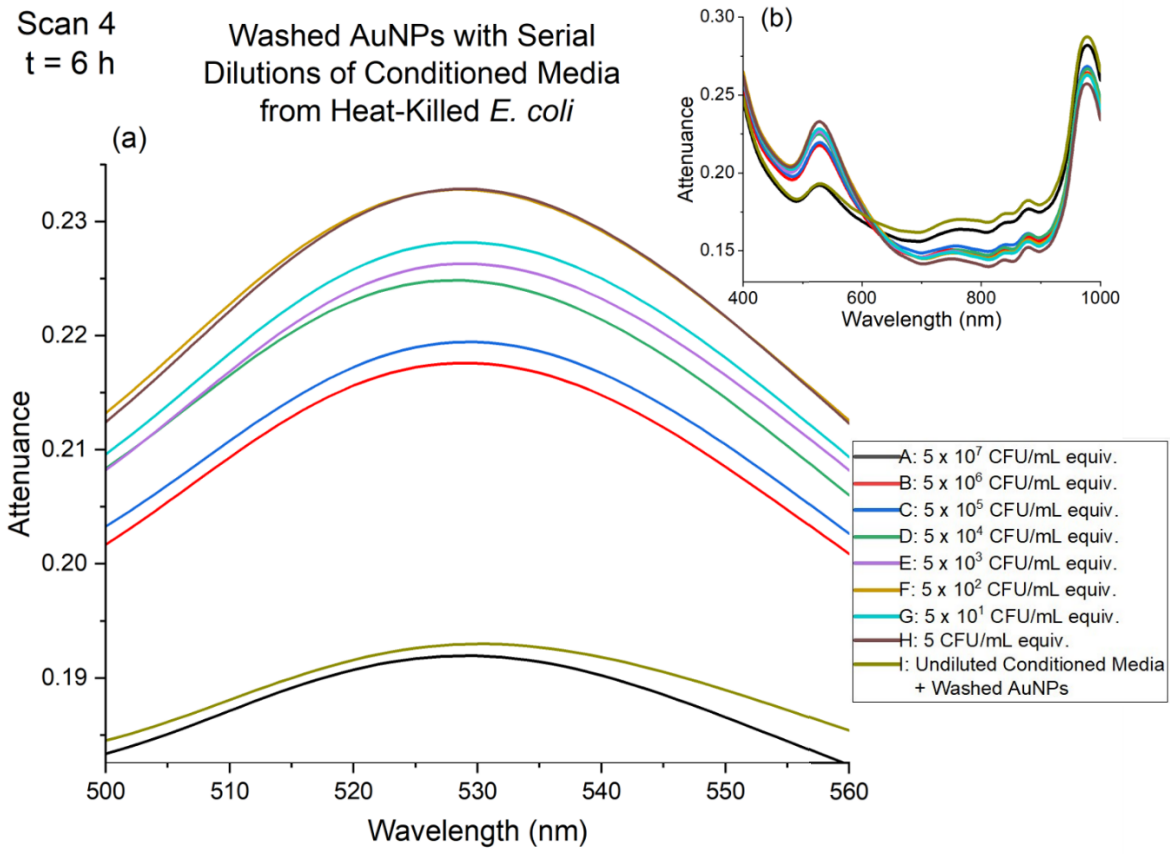

Figure 56: UV-vis spectra of washed AuNPs with 10-fold serial dilutions of conditioned media from heat-killed *E. coli* at ambient temperature, t = 6 h. (a) shows a close-up region of the relative positions of the dampened plasmon peaks, and inset (b) shows the spectra over the entire range of monitored wavelengths (nm).

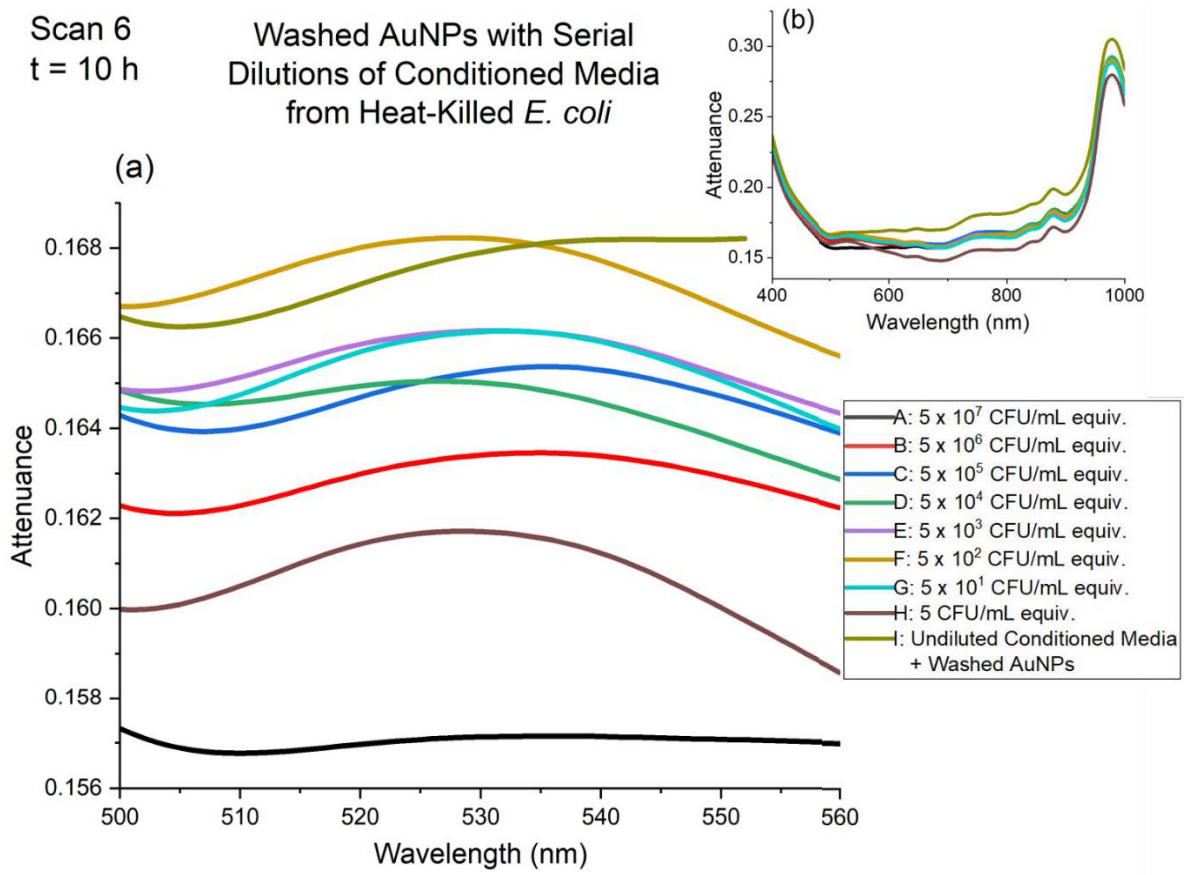

Figure 57: UV-vis spectra of washed AuNPs with 10-fold serial dilutions of conditioned media from heat-killed *E. coli* at ambient temperature, t = 10 h. (a) shows a close-up region of the relative positions of the dampened plasmon peaks, and inset (b) shows the spectra over the entire range of monitored wavelengths (nm).

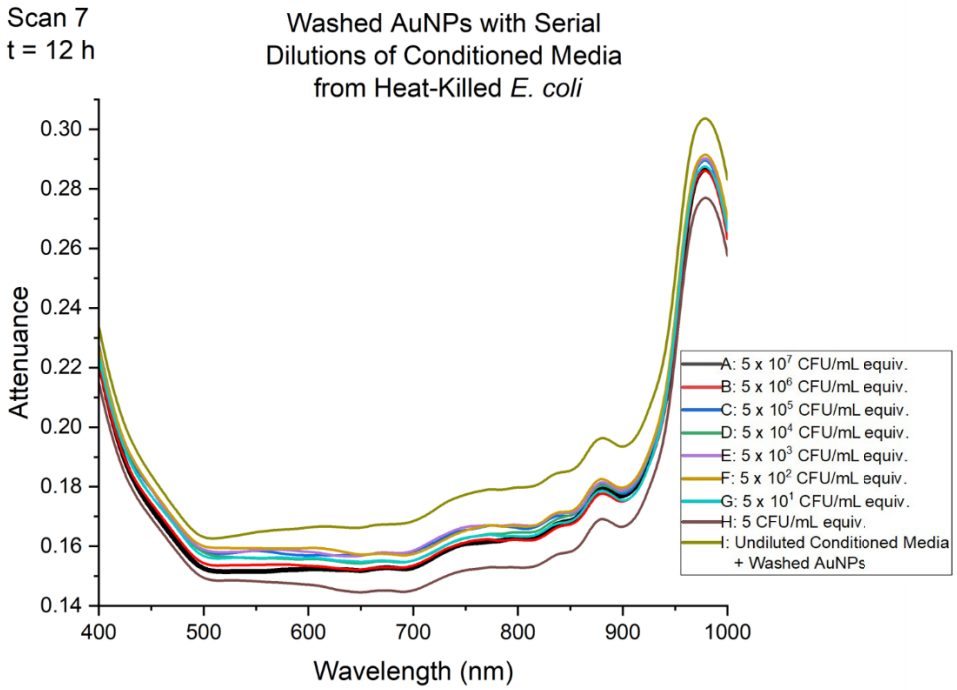

Figure 58: UV-vis spectra of washed AuNPs with 10-fold serial dilutions of conditioned media from heat-killed *E. coli* at ambient temperature, t = 12 h.

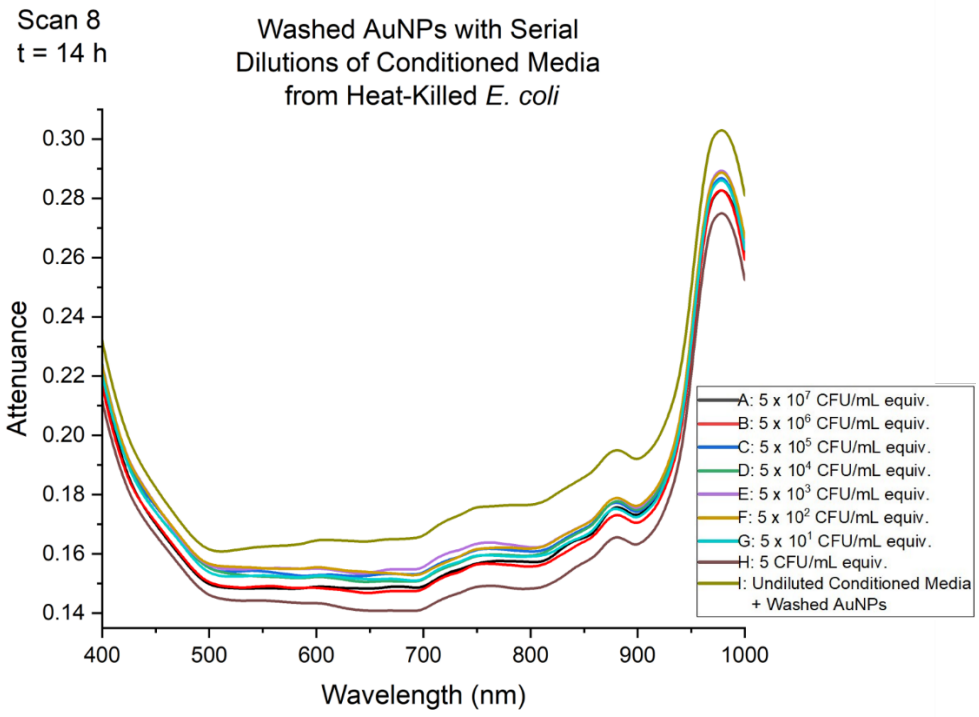

Figure 59: UV-vis spectra of washed AuNPs with 10-fold serial dilutions of conditioned media from heat-killed *E. coli* at ambient temperature, t = 14 h.

A.12 Extra Heat-killed Conditioned Media Assays with Washed AuNPs

The following section contains UV-vis spectra pertaining to the assays between washed AuNPs and the conditioned media from extra heat-killed preparations of *E. coli* that were excluded from the main thesis for brevity and/or ease of reading. Where necessary, they were referred to in the main bodies of text.

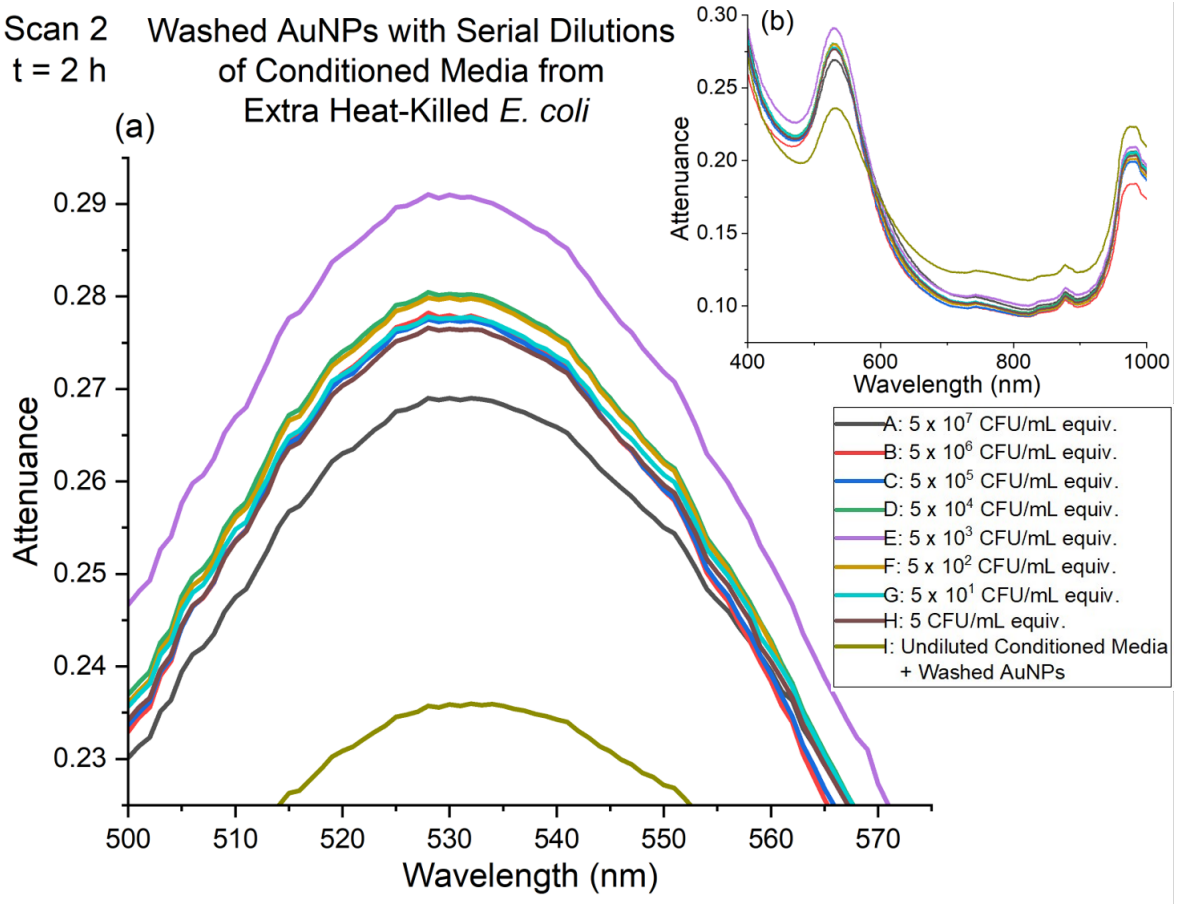

Figure 60: UV-vis spectra of washed AuNPs with 10-fold serial dilutions of conditioned media from extra heat-killed *E. coli* at ambient temperature, t = 2 h. (a) shows a close-up region of the relative positions of the dampened plasmon peaks, and inset (b) shows the spectra over the entire range of monitored wavelengths (nm).

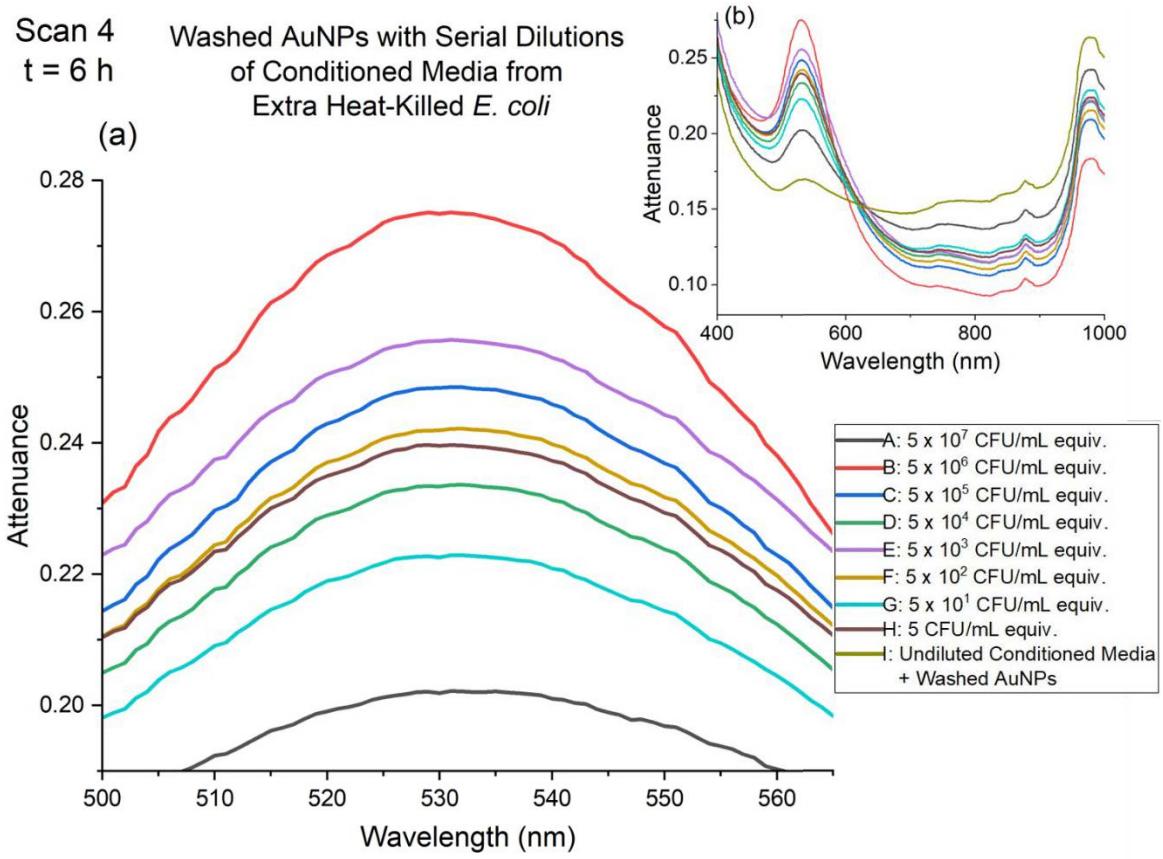

Figure 61: UV-vis spectra of washed AuNPs with 10-fold serial dilutions of conditioned media from extra heat-killed *E. coli* at ambient temperature, t = 6 h. (a) shows a close-up region of the relative positions of the dampened plasmon peaks, and inset (b) shows the spectra over the entire range of monitored wavelengths (nm).

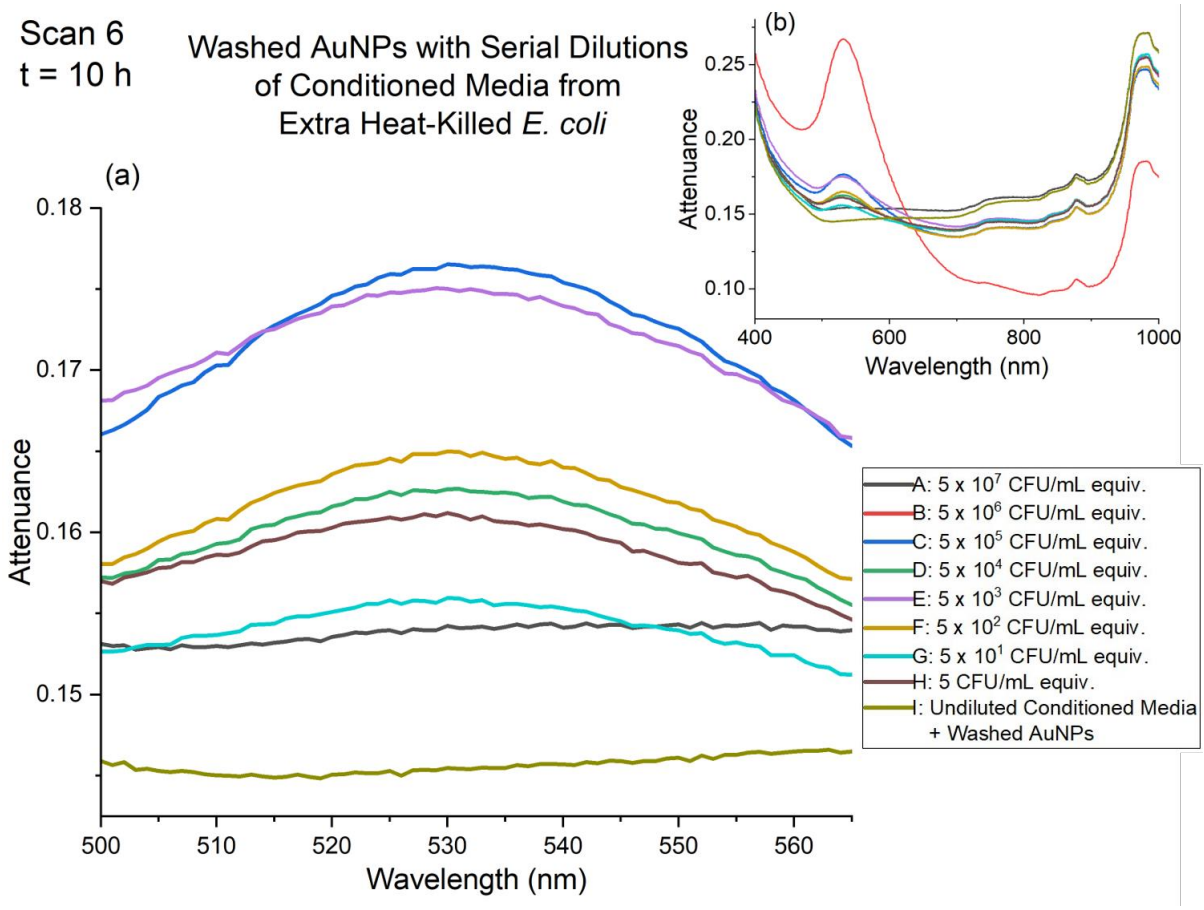

Figure 62: UV-vis spectra of washed AuNPs with 10-fold serial dilutions of conditioned media from extra heat-killed *E. coli* at ambient temperature, t = 10 h. (a) shows a close-up region of the relative positions of the dampened plasmon peaks, and inset (b) shows the spectra over the entire range of monitored wavelengths (nm).

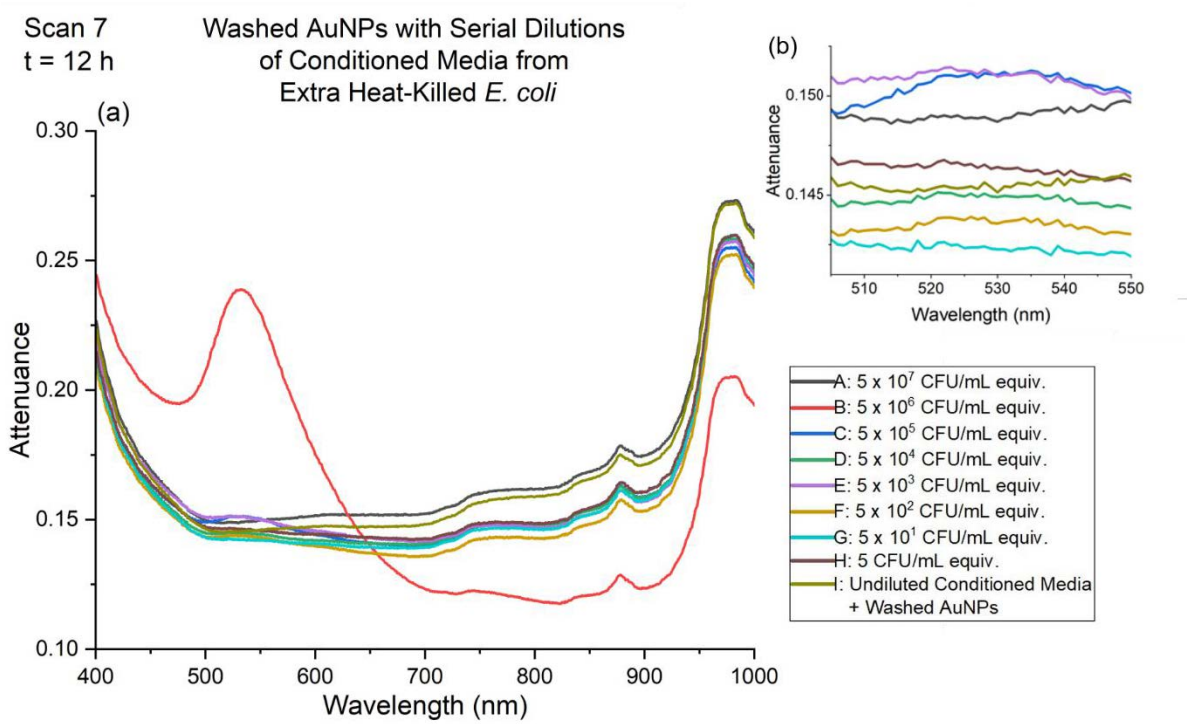

Figure 63: UV-vis spectra of washed AuNPs with 10-fold serial dilutions of conditioned media from extra heat-killed *E. coli* at ambient temperature, t = 12 h. (a) shows the spectra over the entire range of monitored wavelengths (nm) and inset (b) shows a close-up region of the relative positions of the dampened plasmon peaks.

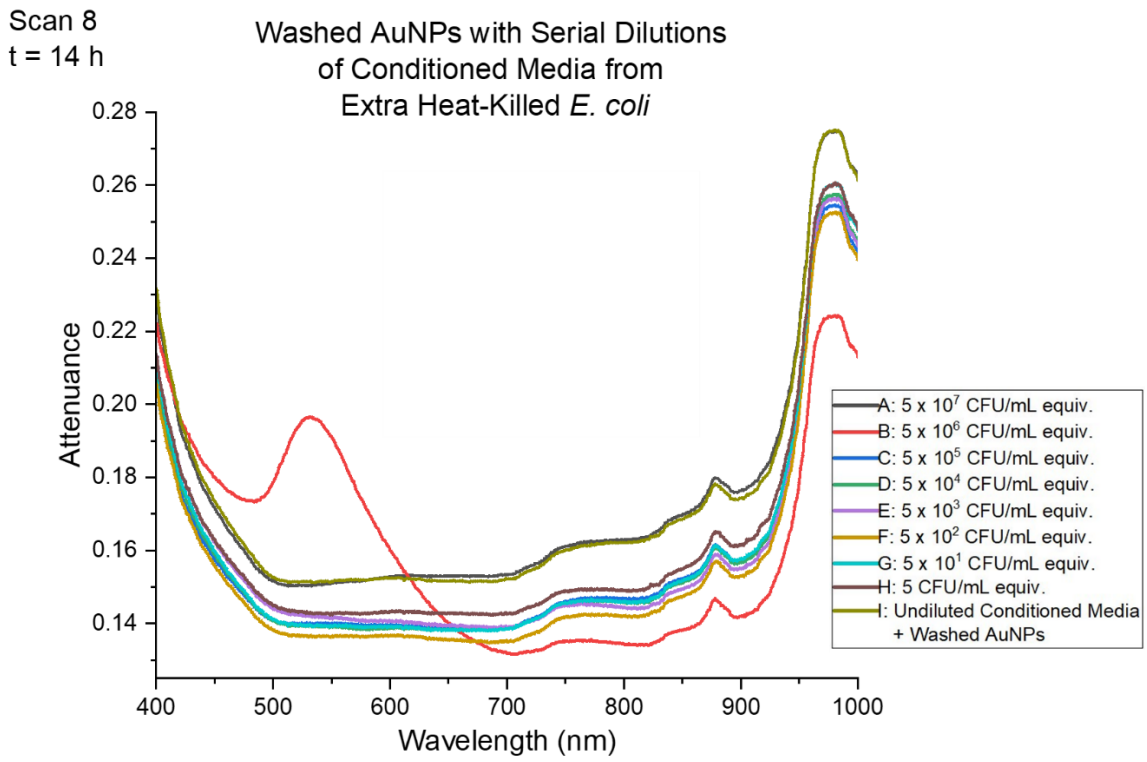

Figure 64: UV-vis spectra of washed AuNPs with 10-fold serial dilutions of conditioned media from extra heat-killed *E. coli* at ambient temperature, t = 14 h.

Appendix B

Appendix B contains transmission electron microscopy (TEM) micrographs that were excluded from the main thesis for brevity and/or ease of reading. Where necessary, they were referred to in the main bodies of text.

B.1 Transmission Electron Micrographs of Controls

The following section contains representative transmission electron micrographs of control samples, as per the figure captions.

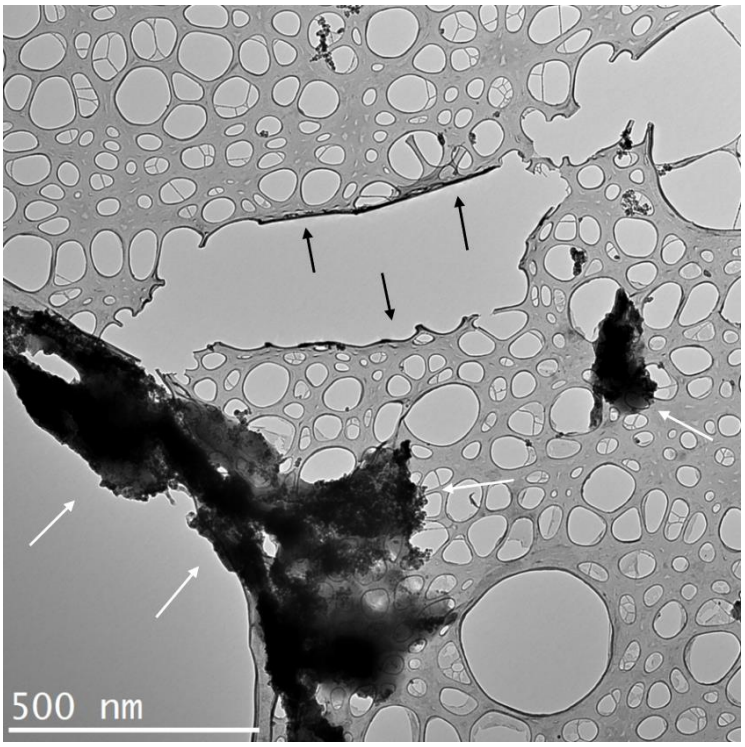

Figure 65: Representative transmission electron micrograph highlighting the difference between the appearance of amorphous proteinaceous aggregates (indicated by white arrows) and the appearance of a torn TEM grid (black arrows).

In instances where proteinaceous aggregates were not so densely aggregated/electron dense, they at times could appear strikingly similar to a torn grid. Particularly one additionally damaged by the electron beam, whereby it was possible to observe the fragile grid curling beneath the focussed beam.

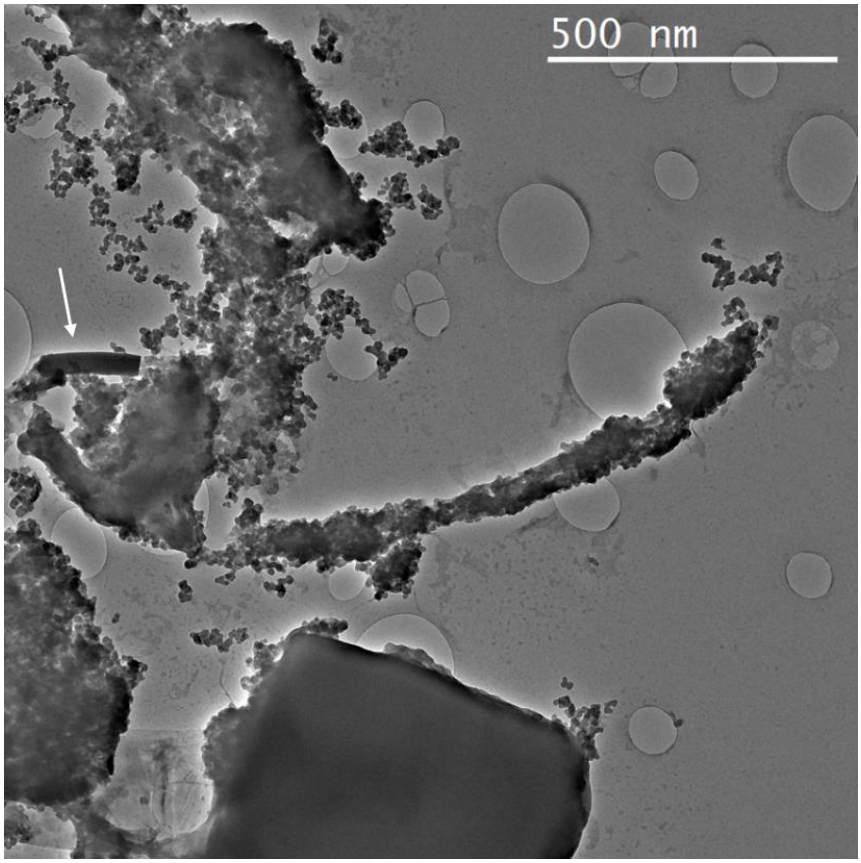

Figure 66: Representative transmission electron micrograph of an aliquot taken from a live *E. coli* control sample.

The micrograph above emphasizes the presence of relatively large protein aggregates within populations of untreated *E. coli*. It is currently unclear what has resulted in the angular, electron-dense entity towards the bottom of the micrograph. The similarity in its appearance to the smaller, more ordered aggregate (similarly electron-dense, indicated by the white arrow) suggests it may be an abnormally large amyloid-like fibril.

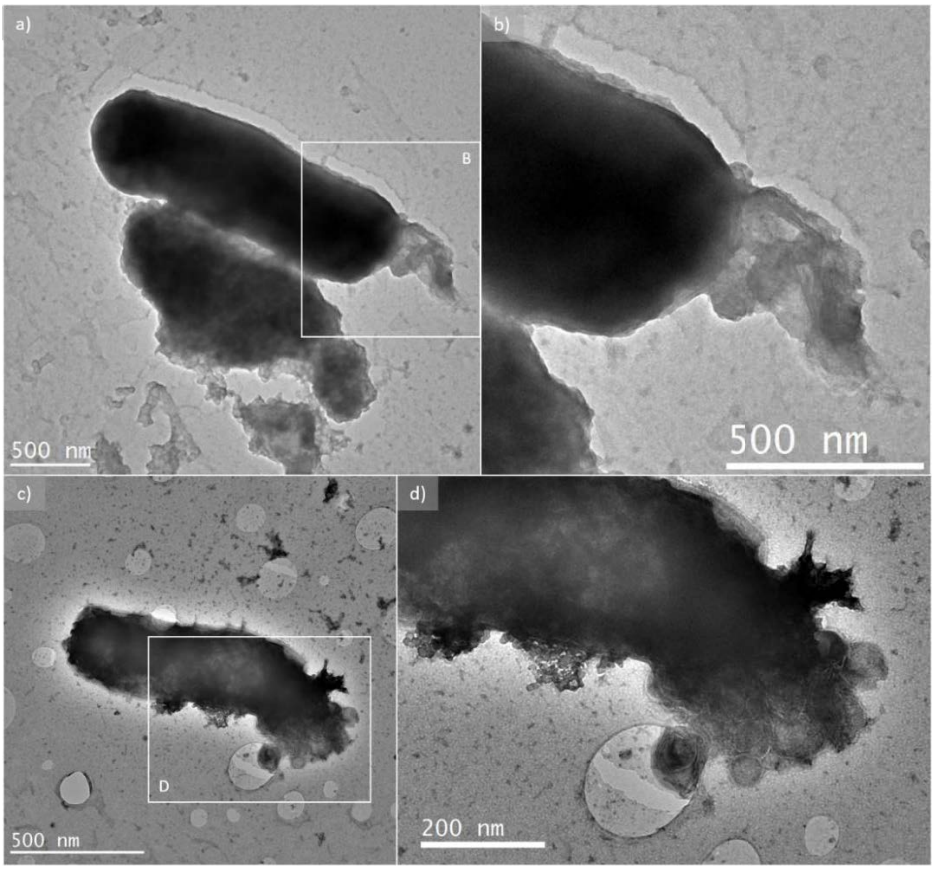

Figure 67: Representative transmission electron micrographs (a) and c)) of live *E. coli* (not incubated with AuNPs). Insets b) and d) show magnified regions of a) and c) respectively, as indicated by the labelled white boxes.

The above micrograph highlights the variability in morphologies across a single population of *E. coli*.

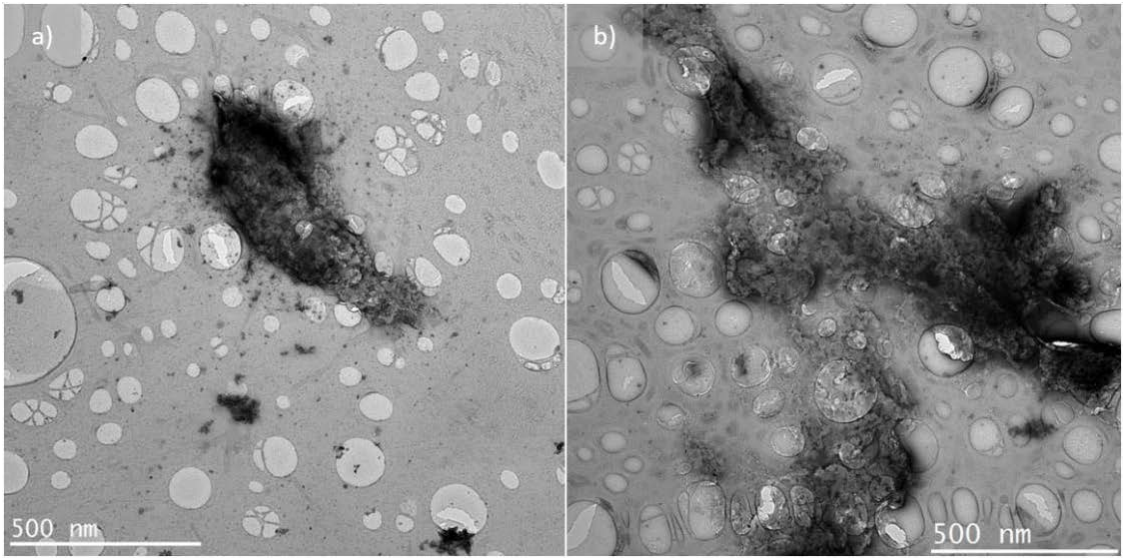

Figure 68: Representative transmission electron micrographs (a) and b)) of an aliquot taken from a heat-killed *E. coli* control sample.

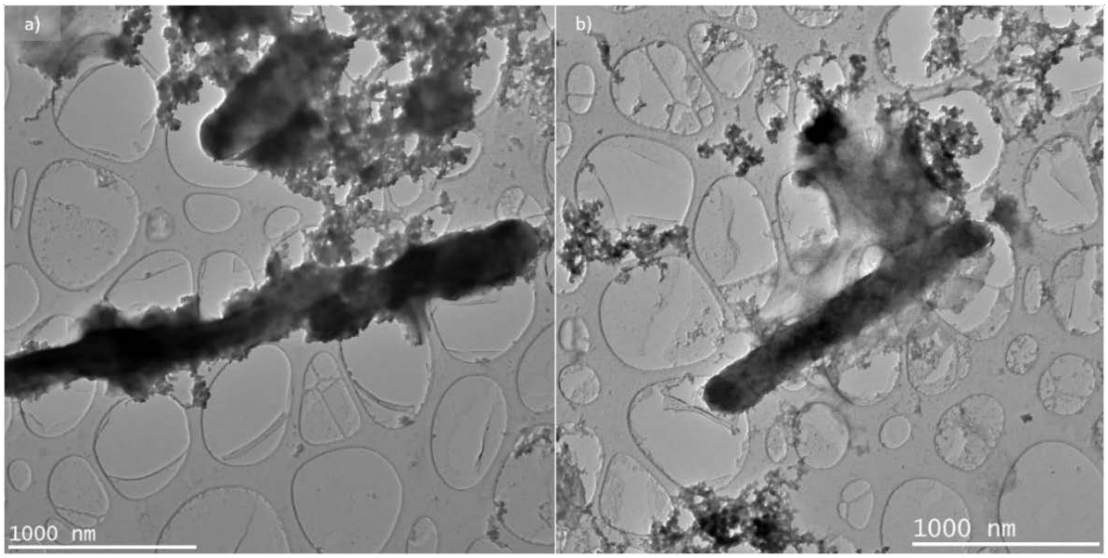

Figure 69: Representative transmission electron micrographs (a) and b)) of a heat-killed *E. coli* control sample.

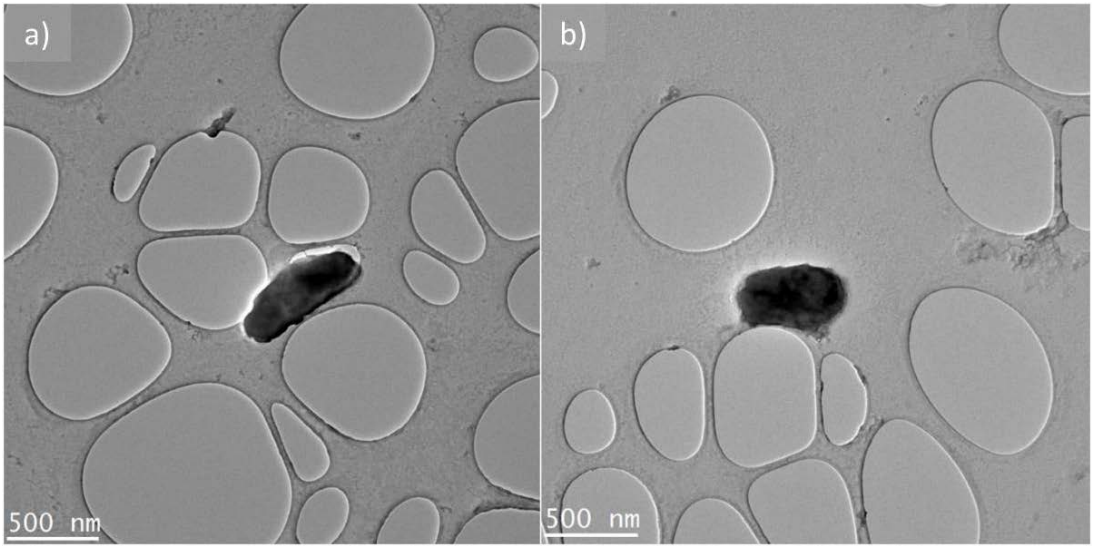

Figure 70: Representative transmission electron micrographs (a) and b)) of an extra heat-killed *E. coli* control sample.

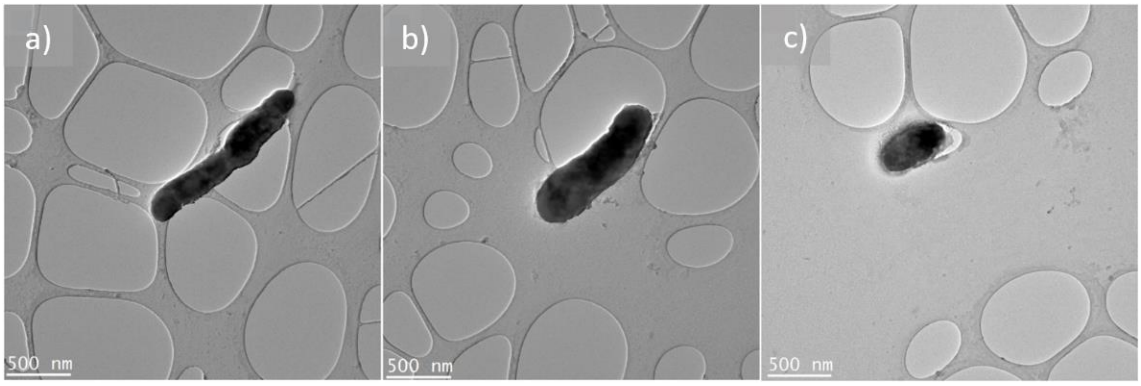

Figure 71: Representative transmission electron micrographs (a), b) and c)) of extra heat-killed *E. coli* cells.

B.2 Transmission Electron Micrographs of Gold Nanoparticle and *E. coli* Samples

The following section contains representative transmission electron micrographs of various preparations of *E. coli*, assayed with AuNPs, as per the figure captions.

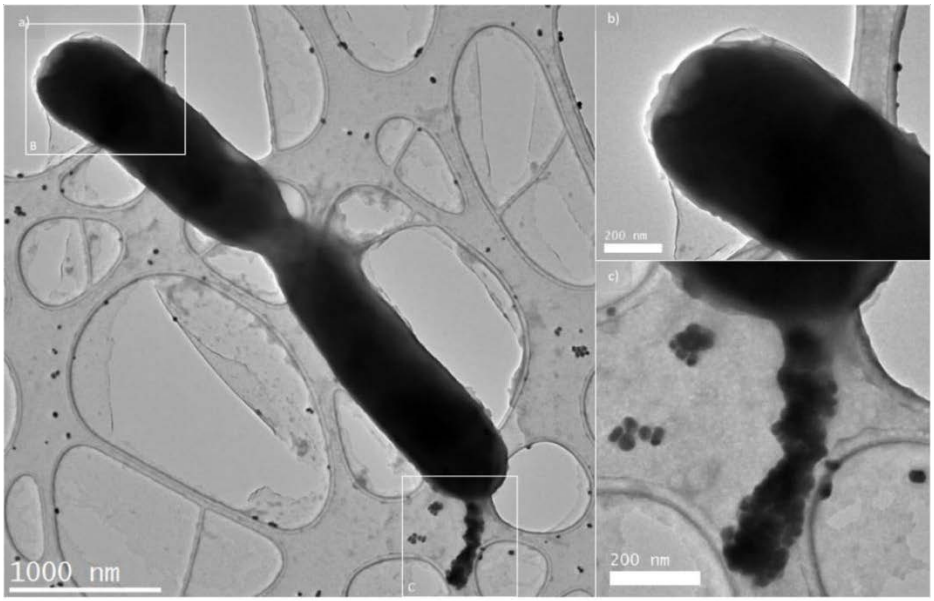

Figure 72: Representative transmission electron micrograph (a)) of live *E. coli* incubated with as-synthesized AuNPs for 2 h. Insets b) and c) show magnified regions of a), as indicated by the labelled white boxes.

Inset b) of the above **Figure** 72highlights the morphological defects shown by the live *E. coli* when incubated with as-synthesized AuNPs for 2 h, while inset b) shows evidence of AuNPs aggregating within cellular materials leaking (and still attached) to the cell.

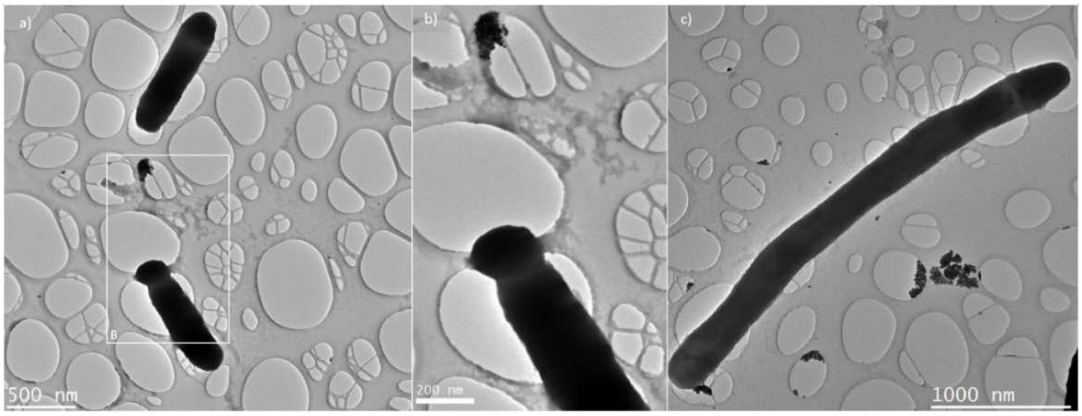

Figure 73: Representative transmission electron micrographs (a) and c)) of live *E. coli* incubated with washed AuNPs for 2 h. Inset b) shows a magnified region of the area indicated by the labelled box in a), highlighting a cluster of aggregated AuNPs associated with a relatively electron-light, amorphous protein aggregates towards the top of the micrograph.

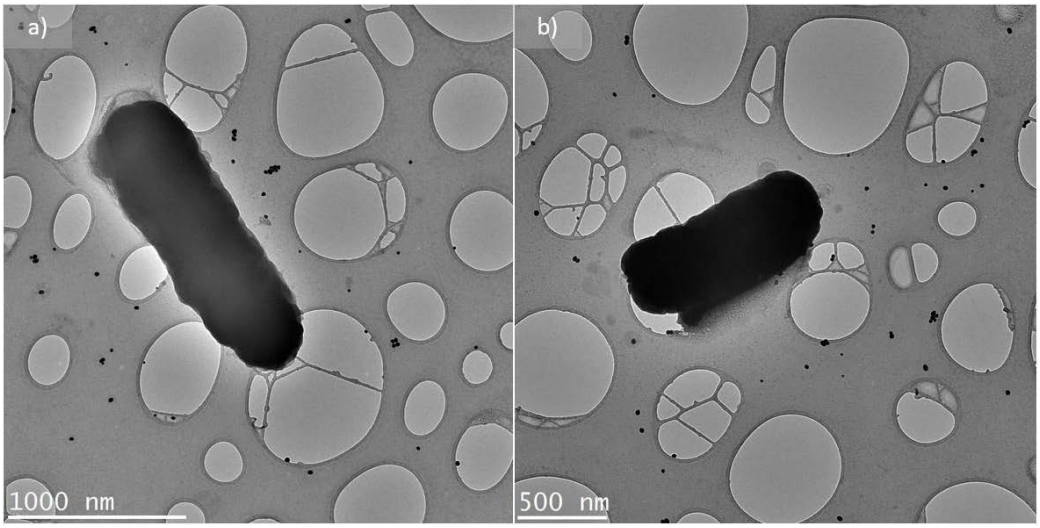

Figure 74: Representative transmission electron micrographs (a) and b)) of heat-killed *E. coli* incubated with as-synthesized AuNPs for 2 h.

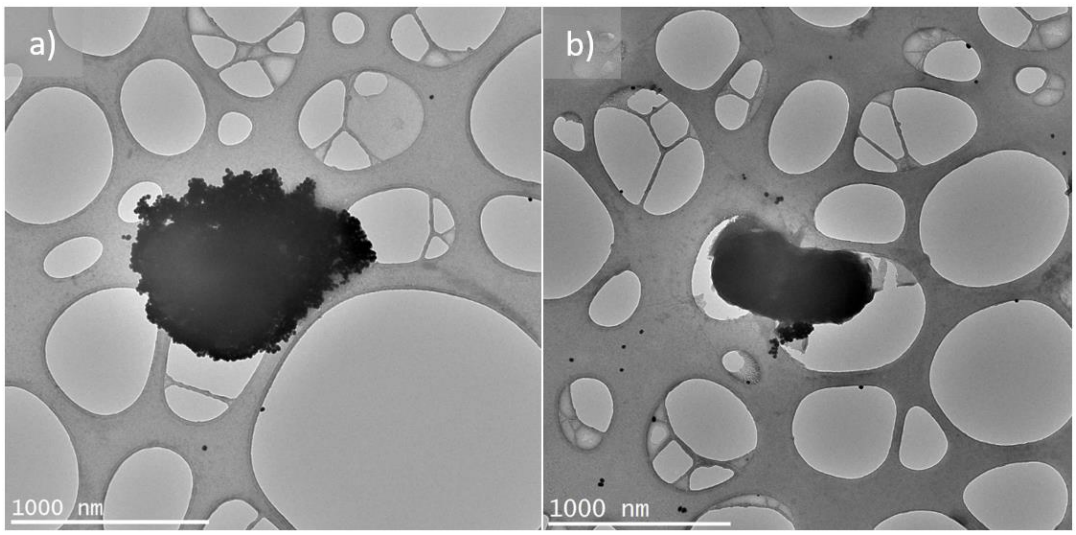

Figure 75: Representative transmission electron micrographs (a) and b)) of heat-killed *E. coli* incubated with as-synthesized AuNPs for 2 h.

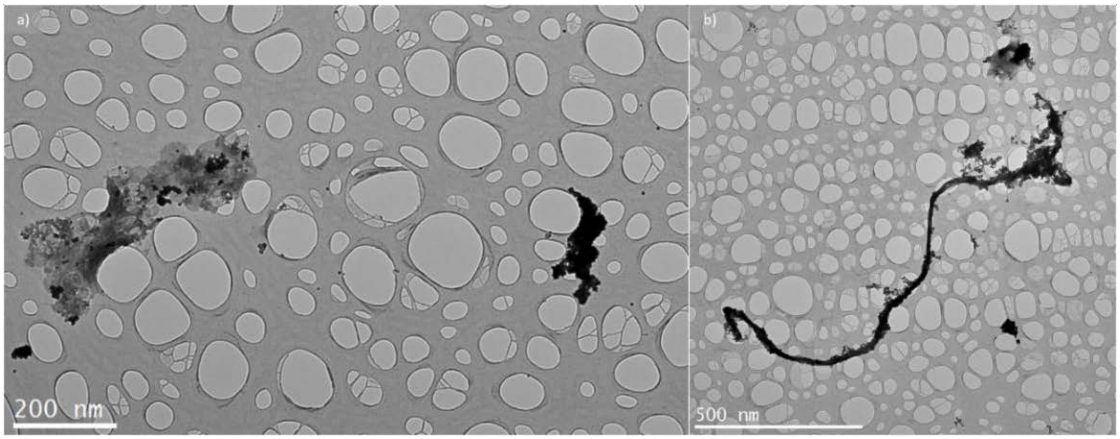

Figure 76: Representative transmission electron micrographs (a) and b)) of an aliquot taken from a heat-killed *E. coli* sample incubated with washed AuNPs. The aliquot was taken immediately post-assay (t = 0). a) shows an amorphous aggregate (left) with AuNPs aggregated within it, and a cluster of aggregated AuNPs (right). b) shows a ~ 1.5 µm protein aggregate.

The aggregate in **Figure 76** b) above exhibits morphologies predominantly consistent with amyloid-like fibrils (long, chain-like), with areas that are comparatively more

disordered and globular, more closely resembling the morphologies of amorphous aggregates.

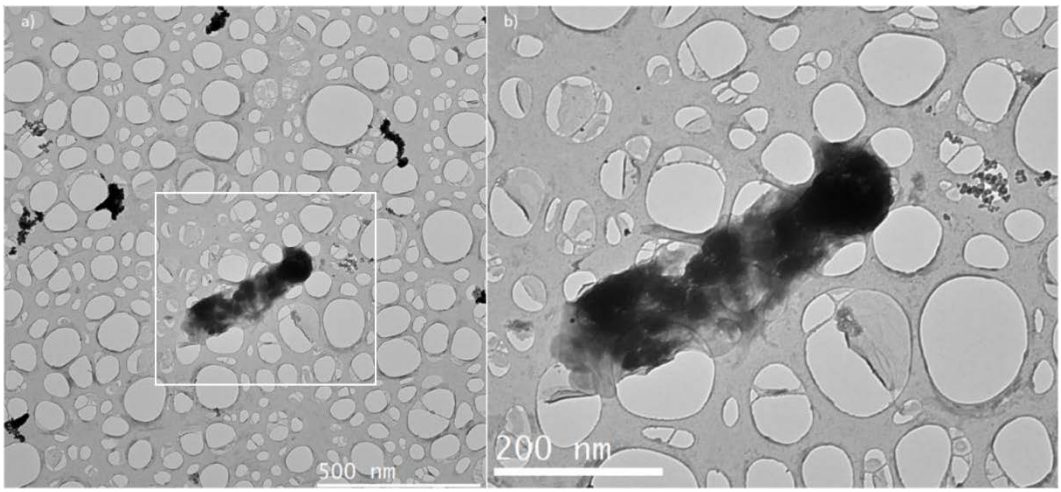

Figure 77: Representative transmission electron micrograph (a)) of heat-killed *E. coli* incubated with washed AuNPs and aliquoted immediately post-assay (t = 0). Inset b) shows a magnified view of the defective/damaged cell, as indicated by the white box in a).

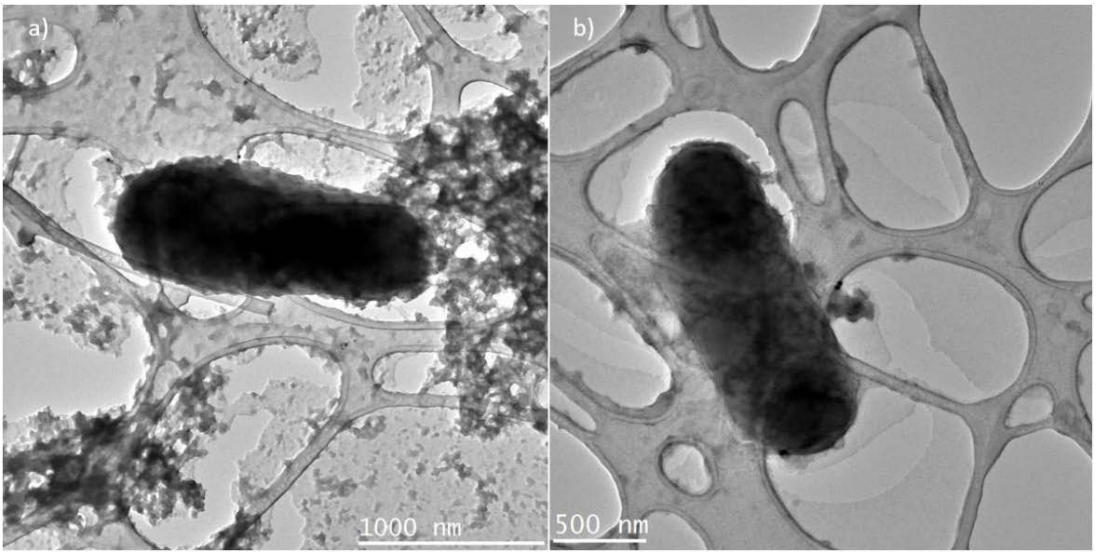

Figure 78: Representative transmission electron micrographs (a) and b)) of heat-killed *E. coli* incubated with washed AuNPs for 2 h.

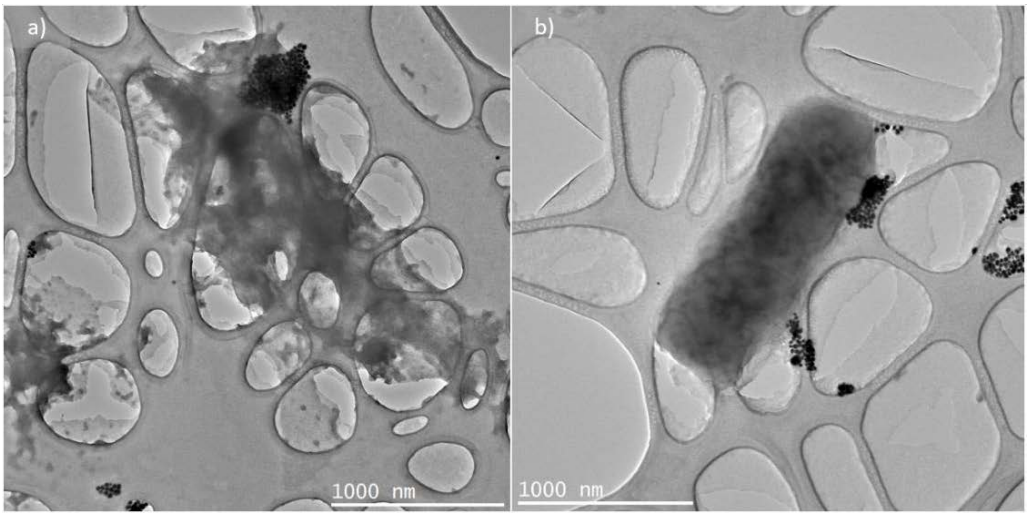

Figure 79: Representative transmission electron micrographs (a) and b)) of aliquots from a sample of heat-killed *E. coli* incubated with washed AuNPs for 2 h. a) shows an amorphous aggregate with clusters of AuNPs aggregated within and around it. b) shows an *E. coli* cell displaying defective morphologies resulting from both the heat treatment and AuNPs, resulting in adhesion of AuNP aggregated to leaky areas of the cell surface.

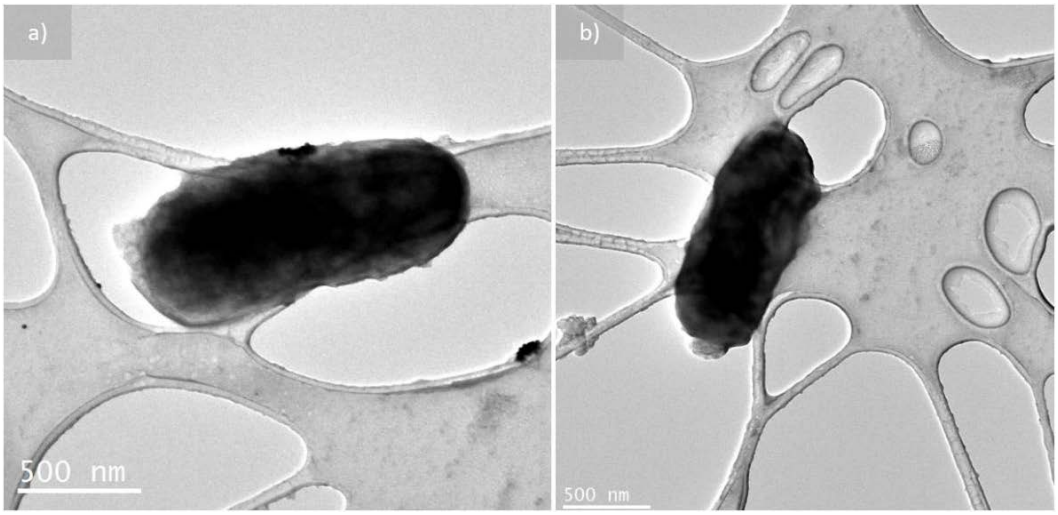

Figure 80: Representative transmission electron micrographs (a) and b)) of extra heat-killed *E. coli* incubated with as-synthesized AuNPs (t = 0). Both cells show

evidence of defective morphologies with the cell in a) showing a cluster of aggregated AuNPs associated with the surface of the bacteria.

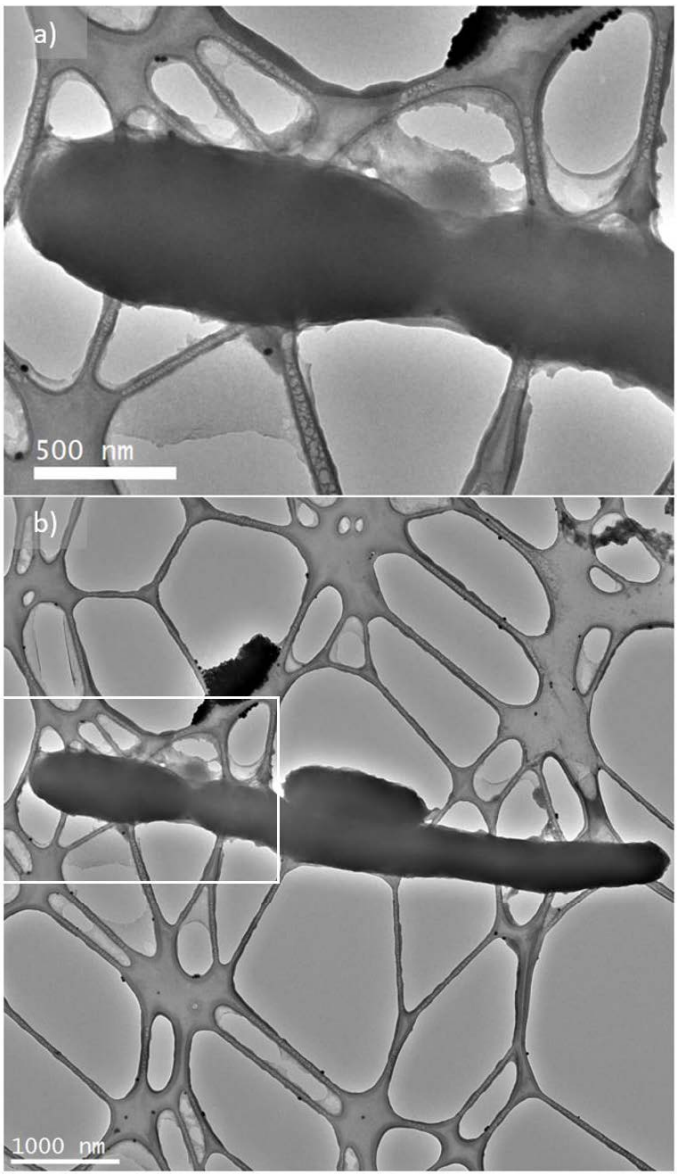

Figure 81: Representative transmission electron micrograph (b)) of extra heat-killed *E. coli* incubated with washed AuNPs (t = 0). a) shows the magnified region indicated in b) by the white box, highlighting the deviant cell-division (failure to correctly/appropriately complete cell division) observed within a number of the samples.

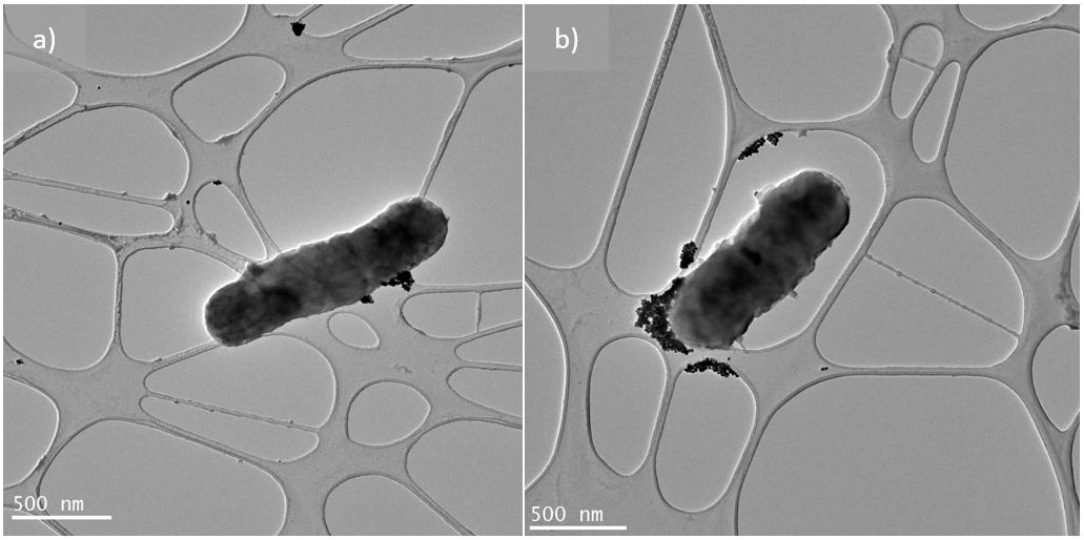

Figure 82: Representative transmission electron micrographs (a) and b)) of extra heat-killed *E. coli*, incubated with washed AuNPs for 2 h. AuNPs can be observed aggregating on and around the cells in both micrographs

Appendix C

Appendix C contains information pertaining to my research outputs and publications to date, resulting from my doctoral studies. These were mentioned in the introductory Chapter and are restated here for completeness.

1. D. Pissuwan, C. Gazzana, S. Mongkolsuk, and M.B. Cortie, Single and multiple detections of foodborne pathogens by gold nanoparticle assays, *Wiley Interdisciplinary Reviews: Nanomedicine and Nanobiotechnology*, vol.12(1), 2020, article e1584. https://doi.org/10.1002/wnan.1584

2. C. Gazzana, S. Valenzuela, A. McDonagh, M. Cortie, Exploiting the interaction between live Escherichia coli and citrate Au nanoparticles to form a label-free diagnostic test for bacterial contamination, *Gold 2022*, Quebec City July 2022, and

3. C. Gazzana, S. Valenzuela, A. McDonagh, M. Cortie, Exploiting the interaction between live *E. coli* and citrate Au nanoparticles to form a label-free diagnostic test for bacterial contamination, *13th International Nanomedicine Conference*, 19-21 June 2023, Sydney, Australia.

4. C.R. Gazzana, M.J. A. Phillips, S.M. Valenzuela, A.M. McDonagh and M.B. Cortie, Label-free detection of live bacteria using growth medium enhanced with Au nanoparticles, under review, *Biochemical and Biophysical Research Communications*